

---

# Development of New Atomic Force Microscopy Methods to Investigate Interfaces of Semiconductor Materials

---

## Dissertation

zur Erlangung des Grades

**„Doktor der Naturwissenschaft“**

DOCTOR RERUM NATURALIUM (DR. RER. NAT.)

im Promotionsfach Chemie

vorgelegt am Fachbereich Chemie, Pharmazie, Geographie und  
Geowissenschaften der Johannes Gutenberg-Universität in Mainz

am 14. Mai 2025

von

**PASCAL NIKO ROHRBECK**

geboren am 10.10.1995 in Wiesbaden-Dotzheim

---

Dekanin: Univ.-Prof. Dr. Eva Rentschler

1. Berichterstatter: [REDACTED]

2. Berichterstatter: [REDACTED]

Tag der mündlichen Prüfung: 17. Juli 2025





---

# Eigenständigkeitserklärung zur Doktorarbeit

Die vorliegende Arbeit wurde in der Zeit vom 01. Juni 2021 bis zum 14. Mai 2025 am Max-Planck-Institut für Polymerforschung in Zusammenarbeit mit dem Department Chemie der Johannes Gutenberg-Universität Mainz unter Betreuung von Prof. Dr. Stefan Weber und Univ.-Prof. Dr. Sebastian Seiffert angefertigt.

Hiermit erkläre ich, Pascal Rohrbeck, Matrikelnummer 2714712, dass ich die vorliegende Arbeit mit dem Titel "Development of New Atomic Force Microscopy Methods to Investigate Interfaces of Semiconductor Materials" selbstständig verfasst und keine anderen als die angegebenen Quellen und Hilfsmittel (dazu zählen auch KI-basierte Anwendungen oder Werkzeuge) benutzt habe. Sämtliche wörtlichen oder sinngemäßen Übernahmen und Zitate sind kenntlich gemacht und nachgewiesen (dies gilt auch für Texte, die durch generative KI, wie ChatGPT erzeugt wurden). Ich versichere, dass ich keine Hilfsmittel verwendet habe, deren Nutzung die Prüferin oder der Prüfer explizit ausgeschlossen hat. Im Anhang in „Chapter 9“ („Nutzung KI-Tools“) habe ich die verwendeten KI-Tools in „Table 9.1“ dokumentiert. Mit Abgabe der vorliegenden Leistung übernehme ich die Verantwortung für das eingereichte Gesamtprodukt. Ich verantworte damit auch jegliche KI-generierten Inhalte, die ich in meine Arbeit übernommen habe. Die Richtigkeit übernommener (KI-generierter) Aussagen und Inhalte habe ich nach bestem Wissen und Gewissen geprüft. Mir ist bekannt, dass ein Verstoß gegen die genannten Punkte prüfungsrechtliche Konsequenzen hat und insbesondere dazu führen kann, dass die Promotionsleistung als mit „nicht bestanden“ bewertet wird. Die Einschreibung kann für bis zu zwei Jahre widerrufen werden, wenn Studierende zweimal oder häufiger bei Prüfungsleistungen täuschen (§ 69 Abs. 4 und 5 HochSchG)

Mainz, 14.05.25

Ort, Datum

P. Rohrbeck

Unterschrift



---

# Zitat

*”Der praktische Wert [der Entdeckung] wird ebenso offensichtlich sein, wenn man bedenkt, dass die Versorgung mit Sonnenenergie sowohl unbegrenzt als auch ohne Kosten ist und dass sie noch unzählige Jahrhunderte lang auf uns herabstrahlen wird, nachdem alle Kohlevorkommen der Erde erschöpft sind.”*

- Werner von Siemens, 1885, *Erfinder und Unternehmer*

*”[the discovery’s] practical value will be no less obvious when we reflect that the supply of solar energy is both without limit and without cost, and that it will continue to pour down upon us for countless ages after all the coal deposits of the earth have been exhausted and forgotten.”*

- Werner von Siemens, 1885, *Inventor and entrepreneur*

*”Ich habe gelernt, dass man nie zu klein dafür ist, einen Unterschied zu machen”*

- Greta Thunberg, *Klimakonferenz Kattowitz 2018*



---

# Acknowledgements - Danksagung

Zu aller erst möchte ich mich bei allen bedanken, die mich in all den Jahren des Studiums und der Doktorarbeit unterstützt haben und Teil dieser Reise waren. Besonders sind dabei die [REDACTED] [REDACTED] [REDACTED] zu nennen. Mit euch hat das anstrengende Studium viel mehr Spaß gemacht und ich habe durch euch sehr gute Freund:innen gefunden.

Zudem das Team am MPIP rund um [REDACTED], das mich so herzlich aufgenommen, ausgebildet und bis heute geprägt hat. Besonderer Dank möchte ich dabei an [REDACTED] [REDACTED] [REDACTED] aussprechen. Es war eine großartige Zeit am MPIP und ich werde mich mit Freude an gemeinsame Konferenzen, die Weihnachtsfeiern, Ausflüge, Wanderungen, Spieleabende, Filmabende, Pub Quizze oder tiefgründige Gespräche erinnern. Ihr seid mir alle sehr ans Herz gewachsen.

Ein sehr großes Dankeschön geht an [REDACTED] für die hervorragende, tolle und kompetente Betreuung in all den Jahren. Ich habe mich in seiner Gruppe immer sehr wohl gefühlt, obwohl ich von der „ebschen“ Seite kam und genoss das gute Arbeitsklima sowie die vielen hilfreichen Gespräche und Anregungen sehr. [REDACTED] hat immer ein offenes Ohr und ist in der Zeit meiner Master- und Doktorarbeit ein guter Freund geworden. Ich werde die gemeinsamen Abende in Regensburg und Boston immer in guter Erinnerung behalten. Danke für all die Möglichkeiten während meiner Ausbildung und vor allem für die Möglichkeit zweieinhalb Monate in die USA zu reisen.

Zudem bedanke ich mich bei [REDACTED] für die Aufnahme in seinen Arbeitskreis, die Bereitstellung des Forschungsthemas und der Forschungseinrichtung sowie

---

für die ausgezeichneten Arbeitsbedingungen. Danke auch für die Unterstützung und das Vertrauen in all diesen Jahren. Darüber hinaus danke ich den Gruppenleitern [REDACTED] [REDACTED] und den Menschen in der Personalabteilung wie [REDACTED] für die Unterstützung. Danke auch allen ehemaligen und derzeitigen Mitarbeiter:innen im Arbeitskreis Butt, insbesondere [REDACTED] [REDACTED] für die herzliche Aufnahme und die gute Arbeitsatmosphäre während der letzten 4 Jahre.

Zuletzt möchte ich mich bei meiner kleinen Familie und meinen Freunden, meiner Freund:in und allen, die ich vergessen haben sollte bedanken.

Ein ganz liebevolles Danke geht an meine [REDACTED].





---

# Scope, aim, and outline of this Study

This PhD Thesis focuses on the development of new Atomic Force Microscopy (AFM) methods to study semiconductor materials on the nanoscale. I focused in particular perovskite solar cells (PSCs) with the aim of unveiling the effects and dynamics of changes at the interface.

Chapter 1 provides a broad introduction to the field of study, while Chapter 2 gives a more theoretical background about the basic knowledge and a conceptual overview of the experimental methods. In the following Chapters 3 to 5 the scientific results of the studies are given in detail. In Chapter 6 a brief summary as well as an outlook will be given.

The objective of the study in Chapter 3 is to demonstrate the significance of defect management in both grain boundaries (GBs) and the surface of PSCs. The field of PSCs has seen rapid advancements, particularly in the inverted p-i-n architecture, which holds promise for flexible and tandem photovoltaic applications.<sup>1,2</sup> However, these devices face significant challenges due to non-radiative recombination losses at GBs and the perovskite/electron-transporting layer (ETL) interface, which limit their open circuit voltage ( $V_{OC}$ ) and fill factor (FF).<sup>3-9</sup> Addressing these issues is vital for achieving higher power conversion efficiencies (PCE) of p-i-n PSCs given their low-temperature processability ( $<100\text{ }^{\circ}\text{C}$ ), and their promising operational stability along with negligible hysteresis.<sup>3</sup> Despite the implementation of diverse passivation strategies, targeting either the GB or interfaces,<sup>10-15</sup> comprehensive approaches targeting both remain limited in scope.

The present study introduces a novel approach to the field: the utilization of phenethylammonium chloride ( $\text{Ph}-\text{C}_2\text{H}_4-\text{NH}_3^+ + \text{Cl}^-$ ) (PEACl) as a dual-passivation strategy agent, operating as both an additive and a surface treatment. This multifaceted method aims to address the limitations associated with defect mitigation at the GB and the perovskite/ $\text{C}_{60}$  interface. The dual passivation approach leverages PEACl in two roles: as an additive combined with  $\text{PbCl}_2$  to passivate GBs during film formation and as a post-deposition surface treatment to address defects at the perovskite/ $\text{C}_{60}$  interface. This method promotes a combination of surface and grain passivation that leads to the formation of a heterogeneous 2D RUDDLESDEN-POPPER phase  $(\text{PEA})_2(\text{Cs}_{1-x}\text{FA}_x)_{n-1}\text{Pb}_n(\text{I}_{1-y}\text{Cl}_y)_{3n+1}$ , which passivate defects and improves charge carrier dynamics. The strategy was validated through various characterization techniques, including

---

time-resolved photoluminescence (tr-PL), Kelvin Probe Force Microscopy (KPFM), and X-ray photoelectron spectroscopy (XPS).

This research achieved one of the highest reported efficiencies for inverted p-i-n PSCs, with a stabilized PCE of 22.3%, alongside significant improvements in  $V_{OC}$  (up to 1.162 V) and FF (up to 88.2%). Furthermore, KPFM imaging revealed that dual passivation effectively reduced heterogeneity in work function across the film surface, particularly at GBs, where the passivation molecules systematically accumulate. The passivation process has been shown to enhance charge extraction efficiency and to demonstrate reduced non-radiative recombination as well as improved electronic properties across the films. These results underscore the importance of simultaneous grain boundary and surface passivation in advancing high-efficiency and stable PSCs.

The study in Chapter 4 further investigates the properties of interfaces and in particular the dynamics during and after operation. Due to interface optimization, the PCE has increased in the last decade. Besides the bulk photovoltaic (PV) properties, the interface properties determine to a large extent the performance of a hybrid PSC device.<sup>16–19</sup> Slow dynamic effects such as hysteresis in  $J - V$  curves are associated with ionic motion effects.<sup>20</sup> However, a deterministic relationship between the ionic displacement and the observed kinetic variations of the external electronic current has not yet been established.<sup>21</sup> The work provided insight into the defects within the active perovskite layers as well as the dynamics at the hole-transporting layer (HTL)/perovskite interface.

Understanding the intricate dynamics of electron and ion behavior in halide perovskites is critical for advancing their application in optoelectronic devices such as solar cells. Despite their high defect tolerance,<sup>22</sup> defects in perovskite films, particularly at GBs or interfaces, lead to increased non-radiative recombination losses,<sup>23</sup> limiting device efficiency. Current macroscopic techniques fail to resolve nanoscale variations in charge carrier dynamics and defect distributions,<sup>24,25</sup> which are vital for optimizing these materials. This study addresses this gap by employing time-resolved Kelvin Probe Force Microscopy (tr-KPFM) to introduce nanoscale surface photovoltage spectroscopy (nano-SPV) and nanoscale ideality factor mapping (nano-IFM), enabling high-resolution mapping of charge carrier recombination, ion migration, and defect distributions in perovskite films.

We adopt a novel approach using nano-SPV and nano-IFM to investigate the local charge carrier dynamics in triple-cation perovskite films with varying morphologies, including small grains, large grains, and passivated surfaces following the work showed in Chapter 3. Nano-SPV tracks surface photovoltage dynamics during and after light pulses to assess charge extraction

---

and recombination times, while nano-IFM evaluates the local ideality factor to identify recombination mechanisms. These methods provide insights into how processing techniques such as solvent annealing and methylamine treatment influence the defect density and ion migration within perovskite films.

We were able to show why significant improvements in perovskite film quality correlates with larger grains and passivation. Passivation with phenylethylammonium iodide ( $\text{Ph}-\text{C}_2\text{H}_4-\text{NH}_3^+ + \text{I}^-$ ) (PEAI) reduces defect density at GBs, leading to more uniform SPV distributions and suppressed ion migration. Methylamine-treated films exhibit enhanced crystallinity and fewer GBs, resulting in longer SPV decay times and reduced recombination losses. The tr-KPFM imaging highlights that optimized films still exhibit localized variations in defect density, emphasizing the need for further targeted optimizations. Overall, this study demonstrates the potential of nano-SPV and nano-IFM for guiding the development of high-efficiency perovskite solar cells by providing a deeper understanding of nanoscale structure-function relationships.

Chapter 5 introduce a new technique to obtain dielectric information about samples with a multi-frequency Electrostatic Force Microscopy (EFM) approach. Besides the direct observation of the change in the CPD (e.g. SPV), shown in Chapter 4, the investigation of the capacitance at the nanoscale is also important for the charge mobilities at interfaces and therefore the efficiency of the solar cell itself.<sup>26-28</sup> Furthermore, the analysis of dopant profiles in semiconductors is of particular importance, especially with regard to the performance of the devices. Conventionally, Scanning Capacitance Microscopy (SCM) and spreading resistance profiling (SRP) are utilized to assess dopant profiles, though they are limited in terms of spatial resolution. Capacitance-voltage ( $C - V$ ) spectroscopy can also be used for failure analysis for semiconductors. In addition, device performance and reliability of solar cells are affected by dielectric film quality.<sup>28,29</sup> However, as devices continue to miniaturize, the conventional  $C - V$  measurements based on a probe are inadequate for the characterization of nano-scale devices.<sup>28,29</sup> Additionally, the change in the dielectric constant of the crystal ( $\epsilon_r$ ) affects the strength of the exciton binding energy, thereby influencing the extraction of charge carriers. This aspect necessitates further study to facilitate a comprehensive understanding of the influences on the charge extraction.<sup>27</sup> Furthermore, in doped semiconductors, the attractive potential energy between an impurity and an electron is reduced by the relative dielectric constant  $\epsilon_r$  of the host atoms in the crystal lattice.<sup>26</sup>

My investigation, presented in Chapter 5, addresses the critical need for advanced nanoscale characterization techniques to study dielectric properties, which are fundamental to understand material behavior in microelectronics, energy storage, nanomedicine, and photonics.<sup>30</sup> For in-

---

stance, the optical properties of a solid are related to the complex refractive index as a function of photon energy. In a non-magnetic solid, the reflective index is the square-root of the relative dielectric constant  $\varepsilon_r$ , which is dependent on the photon energy. This is known as the dielectric function. The optical dielectric constant, denoted by  $\varepsilon_{\text{opt}}$ , manifest at lower frequencies compared to the electronic absorption and are determined solely by the electronic polarizability of the solid. At even lower frequencies, the static dielectric constant  $\varepsilon_s$  provides information about ionic motion as a whole, and this value is typically larger than  $\varepsilon_{\text{opt}}$ .<sup>26</sup>

Traditional methods, such as single-frequency EFM<sup>31-51</sup> and SCM,<sup>52-77</sup> are limited by non-local stray capacitances<sup>63</sup> and resolution constraints,<sup>31,39</sup> particularly at high frequencies.<sup>44,78-80</sup> These limitations hinder the accurate correlation of dielectric properties with nanoscale structural heterogeneity, which is essential for optimizing material performance in applications like high- $\kappa$  dielectrics,<sup>81-83</sup> polymer-ceramic composites,<sup>84</sup> and perovskite solar cells.<sup>85</sup> To overcome these challenges, I introduce multi-frequency heterodyne Electrostatic Force Microscopy (MFH-EFM), a novel multi-frequency EFM approach that enhances spatial resolution and minimizes background signal interference.

The approach employed in this study utilizes multi-frequency excitation to measure the second capacitance gradient ( $C''$ ), which significantly reduces long-range contributions from the tip cone and cantilever. Multi-frequency AFM involves the excitation and/or detection of the deflection at two or more frequencies. This method has the potential to overcome limitations in the spatial resolution and acquisition times of conventional force microscopes.<sup>30</sup> Since the conception of multi-frequency AFM, pioneered by RODRÍGUEZ AND GARCÍA,<sup>86</sup> this method has empowered the probing of material properties at greater distances, thereby enhancing sensitivity. Secondly, material contrast can be obtained for exclusively conservative interactions. This leads to the suppression or minimization of surface damage.<sup>87</sup> Consequently, the acquisition of images in a single scan is possible with enhanced sensitivity and increased information content compared to the standard tapping mode AFM.<sup>88</sup> Multi-frequency AFM represents a promising new field in the realm of force microscopy. However, it should be noted that multi-frequency AFM methods are more demanding than conventional AFM methods.<sup>30</sup> This is due to the non-linear response caused by motion of the lever at higher harmonics, which distorts the frequency response characteristics of the system by interacting with the tip and surface<sup>89,90</sup> Additionally, the amount of data collected during operation requires the use of automated data methods.<sup>91</sup> In general, it is challenging to integrate the sophisticated force sensitivity of force spectroscopy with molecular-resolution imaging. Consequently, obtaining simultaneous high spatial resolution and material properties mapping is difficult.<sup>30</sup> In previous studies, viruses,<sup>92</sup> cells,<sup>93,94</sup> CPD, current distributions,<sup>95</sup> as well as the CPD and the  $\partial^2 C / \partial z^2$  signals simultaneously<sup>96</sup> have been

---

obtained so far with multi-frequency AFM. This novel heterodyne technique enables operation at arbitrary frequencies, allowing for high-frequency dielectric spectroscopy without the need for specialized equipment beyond a lock-in amplifier (LIA). The validity of the method was demonstrated through experiments on microfabricated SiO<sub>2</sub> microcapacitors and self-assembled molecular structures, thereby demonstrating its ability to provide highly localized capacitance measurements. Analytical simulations confirmed that  $C''$ -based detection offers superior lateral resolution compared to first-order gradients ( $C'$ ), albeit at the cost of reduced signal-to-noise ratio.

The findings highlight the effectiveness of MFH-EFM in characterizing nanoscale dielectric properties with unprecedented precision. Experimental results from force-distance spectroscopy and frequency sweeps on SiO<sub>2</sub> microcapacitors revealed that  $C''$ -sensitive detection suppresses stray contributions, achieving highly localized measurements even at MHz frequencies. Imaging experiments on perfluoroalkyl-alkane aggregates further demonstrated sharp contrast between nanostructures and substrates, underscoring the potential of MFH-EFM for high-resolution imaging. These advances pave the way for quantitative studies of dielectric effects in materials science, biology, and nanotechnology and will enlighten properties especially at the interface between the active and the transport layers within solar cells.<sup>1</sup>

The Chapters 3 to 5 of this PhD Thesis present collaborative research projects. In these studies, my contributions includes contributing AFM experiments to research, in which Chapter 5 included developing an entirely new technique. Moreover, I designed the concept of a research project, execute all the experiments followed by analyzing and interpretation of taken measurement data (Chapter 5) and leading or co-leading the manuscript writing process (Chapters 4 and 5). For the study in Chapter 3 I was one of the co-authors of the manuscript writing process of the paper, while in Chapter 4 I was co-leading the project including writing, and in Chapter 5 I was single first author of this project. A summary of the specific individual contributions can be found on page XX.

---

<sup>1</sup>This chapter has been initially prepared with the help of artificial intelligence (AI) chatbot Perplexity AI, which provided a first version of the scope, aim and outline chapter. The text created by an AI algorithm has been further edited by the human author.



---

# Publications and contributions covered in this PhD thesis

## Chapter 3:

Gharibzadeh, S.; Fassel, P.; Hossain, I. M.; **Rohrbeck, P.**; Frericks, M.; Schmidt, M.; Duong, T.; Khan, M. R.; Abzieher, T.; Nejand, B. A.; Schackmar, F.; Almora, O.; Feeney, T.; Singh, R.; Fuchs, D.; Lemmer, U.; Hofmann, J. P.; Weber, S. A. L.; Paetzold, U. W. Two Birds with One Stone: Dual Grain-Boundary and Interface Passivation Enables >22 % Efficient Inverted Methylammonium-Free Perovskite Solar Cells. *Energy Environ. Sci.* **2021**, 14 (11), 5875–5893. DOI: 10.1039/D1EE01508G.<sup>97</sup>

## Chapter 4:

Yalçınkaya, Y.; **Rohrbeck, P. N.**; Schütz, E. R.; Fakharuddin, A.; Schmidt-Mende, L.; Weber, S. A. L. Nanoscale Surface Photovoltage Spectroscopy. *Adv. Opt. Mater.* **2024**, 12 (8), 1–12. DOI: 10.1002/adom.202301318.<sup>98</sup>

## Chapter 5:

**Rohrbeck, P. N.**; Cavar, L. D.; Weber, F.; Reichel, P. G.; Niebling, M.; Weber, S. A. L. Nanoscale capacitance spectroscopy based on multi-frequency electrostatic force microscopy. *Beilstein J. Nanotechnol.* **2025**, 16, 637–651. DOI: 10.3762/bjnano.16.49.<sup>99</sup>

---

The author contributions are as follows:

### Chapter 3:

S. G. conceived the initial idea for this study and developed it further with support of P. F., I. M. H. and U. W. P. Furthermore, S. G. designed the experiments, fabricated the perovskite films and performed the J–V, EQE and long-term stability measurements. P. F. performed the absolute and intensity-dependent PLQY measurements and data analysis. I. M. H. performed the transient photoluminescence measurements and data analysis. S. G. performed the XRD measurements. M. F. performed the XPS/UPS measurements and data analysis and P. F. and J. P. H. supported in data interpretation. M. S. helped for device fabrication. **P. R. performed the KPFM measurements, supervised by S. A. L. W., and the data was analysed by P.R.,S.G.,P.F.and S.A.L.W.** The CL measurements were performed by T. D. The TAS measurements were performed by S.G.and M. R. K.,and O. A. and M.R.K. analysed the data. T. A. and B. A. N. performed the SEM measurements. F. S. performed the contact angle measurement. T. F. applied and optimized the antireflection coating. R. S. helped for long-term stability measurement. B. A. N. helped with designing the schematics. D. F. performed additional high-resolution XRD measurements. U. L. and U. W. P. supervised the whole project. S. G., P. F. and U. W. P. drafted the manuscript. **All authors reviewed and commented on the paper.**

### Chapter 4:

**Y.Y. and P.N.R. contributed equally to this work including measurements, analyzing, and drafting the manuscript.** S.A.L.W. supervised the whole project.

### Chapter 5:

**Pascal N. Rohrbeck: conceptualization; data curation; formal analysis; investigation; methodology; project administration; resources; software; validation; visualization; writing – original draft; writing – review & editing.** Lukas D. Cavar: resources; software; writing – review & editing. Franjo Weber: software. Peter G. Reichel: investigation. Mara Niebling: resources; software. Stefan A. L. Weber: conceptualization; funding acquisition; resources; supervision; validation; writing – original draft; writing – review & editing.

---

## Other Publications:

Liang, J.; Ender, C. P.; **Rohrbeck, P.**; Graf, R.; Lieberwirth, I.; Räder, H.-J.; Wagner, M.; Weber, S. A. L.; Müllen, K.; Weil, T. High Pressure Induced Formation of Carbon Nanorods from Tetracosane. *Diam. Relat. Mater.* **2024**, 143, 110913. DOI: 10.1016/j.diamond.2024.110913.<sup>100</sup>

Pious, J. K.; **Rohrbeck, P. N.**; Widmer, R.; Oechsle, A. H.; Shivarudraiah, S. B.; Kothandaraman, R. K.; Siegrist, S.; Shih, C.; Jung, T. A.; Weber, S. A. L.; Tiwari, A. N. ; Fu, F. Efficient Blade-Coated Wide-Bandgap Perovskite Solar Cells via Interface Engineering. *ACS Appl. Mater. Interfaces* **2025**, 17 (16), 24040–24047. DOI: 10.1021/acsami.5c03709.



---

# Abbreviations

<b>AC</b>	alternating current
<b>AFM</b>	Atomic Force Microscopy
<b>AI</b>	artificial intelligence
<b>AM</b>	amplitude modulation
<b>AM-AFM</b>	amplitude modulation Atomic Force Microscopy
<b>AM-KPFM</b>	amplitude modulation Kelvin Probe Force Microscopy
<b>AO</b>	atomic orbital
<b>BCP</b>	bathocuproine (2,9-Dimethyl-4,7-diphenyl-1,10-phenanthroline)
<b>c-AFM</b>	conductive Atomic Force Microscopy
<b>CB</b>	conduction band
<b>CPD</b>	contact potential difference
<b>CTL</b>	charge transport layer
<b>DC</b>	direct current
<b>DOS</b>	density of states
<b>EFM</b>	Electrostatic Force Microscopy
<b>ETL</b>	electron-transporting layer
<b>FA</b>	formamidinium
<b>FAI</b>	formamidinium iodide
<b>FAPbI<sub>3</sub></b>	formamidinium lead iodide (FAPbI <sub>3</sub> )
<b>FF</b>	fill factor
<b>FFM</b>	fast force mapping
<b>FM</b>	frequency modulation

---

<b>FM-AFM</b>	frequency modulation Atomic Force Microscopy
<b>FM-KPFM</b>	frequency modulation Kelvin Probe Force Microscopy
<b>FTO</b>	fluorine doped tin(IV) oxide; (F@SnO <sub>2</sub> )
<b>GB</b>	grain boundary
<b>G-mode KPFM</b>	general acquisition mode Kelvin Probe Force Microscopy
<b>H-KPFM</b>	heterodyne Kelvin Probe Force Microscopy
<b>HOMO</b>	highest occupied molecular orbital
<b>HOPG</b>	highly oriented pyrolytic graphite
<b>HTL</b>	hole-transporting layer
<b>InvOLS</b>	inverse optical lever sensitivity
<b>IR</b>	infrared
<b>ITO</b>	indium tin oxide (In <sub>2</sub> O <sub>3</sub> ·(SnO <sub>2</sub> ) <sub>x</sub> )
<b>KPFM</b>	Kelvin Probe Force Microscopy
<b>LCAO</b>	linear combination of atomic orbital
<b>LIA</b>	lock-in amplifier
<b>LED</b>	light-emitting diode
<b>LUMO</b>	lowest unoccupied molecular orbital
<b>MA</b>	methylammonium
<b>MAI</b>	methylammoniumiodide
<b>MAPI</b>	methyl ammonium lead iodide (MAPbI <sub>3</sub> )
<b>MFH-EFM</b>	multi-frequency heterodyne Electrostatic Force Microscopy
<b>MO</b>	molecular orbital
<b>nano-IFM</b>	nanoscale ideality factor mapping
<b>nano-SPV</b>	nanoscale surface photovoltage spectroscopy
<b>PCBM</b>	[6,6]-phenyl-C <sub>61</sub> -butyric acid methyl ester
<b>PEA<sup>+</sup></b>	Phenylethylammonium (Ph-C <sub>2</sub> H <sub>4</sub> -NH <sub>3</sub> <sup>+</sup> )
<b>PCE</b>	power conversion efficiency
<b>PEACl</b>	phenethylammonium chloride (Ph-C <sub>2</sub> H <sub>4</sub> -NH <sub>3</sub> <sup>+</sup> + Cl <sup>-</sup> )

---

<b>PF</b>	Peak Force
<b>PL</b>	photoluminescence
<b>PLL</b>	phase-locked loop
<b>PLQY</b>	photoluminescence quantum yield
<b>PM</b>	phase modulation
<b>pp-KPFM</b>	pump-probe Kelvin Probe Force Microscopy pp-KPFM
<b>PSC</b>	perovskite solar cell
<b>PTAA</b>	poly[bis(4-phenyl)(2,4,6-trimethylphenyl)amine]
<b>PV</b>	photovoltaic
<b>QFLS</b>	quasi-FERMI level splitting
<b>qi</b>	quantitative imaging
<b>SCM</b>	Scanning Capacitance Microscopy
<b>SEM</b>	Scanning Electron Microscopy
<b>SFM</b>	Scanning Force Microscopy
<b>SNR</b>	signal-to-noise ratio
<b>SPV</b>	surface photovoltage
<b>SRH</b>	Shockley-Read-Hall
<b>STM</b>	Scanning Tunneling Microscopy
<b>RE</b>	radiative efficiency
<b>TAS</b>	thermal admittance spectroscopy
<b>ToF-SIMS</b>	Time-of-Flight Secondary Ion Mass Spectrometry
<b>tr</b>	time-resolved
<b>tr-KPFM</b>	time-resolved Kelvin Probe Force Microscopy
<b>tr-PL</b>	time-resolved photoluminescence
<b>UHV</b>	ultra-high vacuum
<b>UV</b>	ultraviolet
<b>VB</b>	valence band
<b><math>V_{oc}</math></b>	open circuit voltage



---

# Abstract

This PhD Thesis investigates nanoscale structures in semiconductor devices and their structure-property relationships, with a particular focus on perovskite solar cells (PSCs). Over the past two decades, PSCs have attracted significant attention due to their high power conversion efficiency (PCE) and low production costs, positioning them as promising alternatives to traditional silicon solar cells.<sup>101</sup> However, to fully exploit their potential for commercial applications, a fundamental understanding of their nanoscale physical properties is essential.<sup>102–105</sup> Features such as grain boundaries (GBs) and crystal lattice and interfacial defects has been observed to function as recombination centers for charge carriers. This property is critical to the functionality of the device. However, direct visualization at this scale has remained challenging.

The aim of this PhD Thesis is to develop tools and methods that enable a deeper understanding through visualization of promising semiconductor materials and their buried interfaces at the nanoscale. This knowledge will facilitate targeted engineering of surfaces and defects to optimize device performance without compromising efficiency.

To probe electronic properties at the nanoscale, I employed conventional Kelvin Probe Force Microscopy (KPFM) alongside two newly developed Atomic Force Microscopy (AFM) techniques based on Electrostatic Force Microscopy (EFM) principles. The first method, nanoscale surface photovoltage spectroscopy (nano-SPV), enables the study of charging and discharging processes in PSCs. The second method, multi-frequency heterodyne Electrostatic Force Microscopy (MFH-EFM), enhances the spatial resolution of the second capacitance derivative signal, allowing for more detailed investigation of interfaces in semiconductor devices.

As demonstrated by KPFM measurements, passivation molecules have been found to preferentially accumulate at grain boundaries, where dangling bonds are present. Utilizing tr-KPFM and the newly developed nano-SPV method has revealed that surface passivation not only leads to more homogeneous extraction and recombination of charge carriers but also increases recombination times, indicating fewer defects that hinder carrier extraction.

The novel MFH-EFM method enabled superior localization of dielectric properties compared to standard approaches and the possibility to do dielectric spectroscopy.

This PhD thesis presents new functional methods with improved resolution for the AFM and further improves the versatility of the EFMs for nanocharacterization of new energy materials.

---

# Kurzfassung

Diese Dissertation untersucht nanoskalige Strukturen in Halbleiterbauelementen und deren Struktur-Eigenschafts-Beziehungen, mit dem Hauptfokus auf Perowskit-Solarzellen (PSCs). PSCs haben sich in den letzten Jahren durch hohe Energieumwandlungseffizienz (PCE) und niedrige Produktionskosten als vielversprechende Alternative zu Siliziumsolarzellen etabliert.<sup>101</sup> Für ihr volles Potenzial ist ein grundlegendes Verständnis ihrer nanoskaligen Eigenschaften entscheidend.<sup>102–105</sup> Merkmale wie Korngrenzen (GBs) und Kristallgitterdefekte fungieren als Rekombinationszentren für Ladungsträger, aber eine direkte Visualisierung auf dieser Skala ist bisher nicht möglich.

Ziel dieser Arbeit ist die Entwicklung von Werkzeugen, die ein tieferes Verständnis vielversprechender Halbleitermaterialien auf der Nanoskala ermöglichen und so ein gezieltes Design von Oberflächen und Defekten zur Optimierung der Leistungsfähigkeit ohne großen Effizienzverlust zu optimieren. Um die elektronischen Eigenschaften auf der Nanoskala zu untersuchen, wurden neben konventioneller KELVIN-Sonden-Kraftmikroskopie (KPFM) zwei neuartige Rasterkraftmikroskopie-Techniken (AFM) eingesetzt, die auf elektrostatischer Kraftmikroskopie (EFM) basieren: Die nanoskalige Oberflächen-Photospannungs-Spektroskopie (nano-SPV) ermöglicht die Analyse von Lade- und Entladevorgängen in PSCs, während die multifrequente heterodyne EFM (MFH-EFM)-Methode die räumliche Auflösung Grenzflächenuntersuchung verbessert, indem es das zweite Kapazitätsableitungssignal nutzt.

Wie durch KPFM-Messungen nachgewiesen wurde, sammeln sich Passivierungsmoleküle bevorzugt an Korngrenzen an, wo ungesättigte Bindungen vorhanden sind. Durch den Einsatz von tr-KPFM und der neu entwickelten nano-SPV-Methode wurde ferner festgestellt, dass die Oberflächenpassivierung nicht nur zu einer homogeneren Extraktion und Rekombination von Ladungsträgern führt, sondern auch die Rekombinationszeiten verlängert, was auf weniger Defekte hinweist, die die Ladungsträgerextraktion behindern. Die neuartige MFH-EFM-Methode ermöglichte eine im Vergleich zu Standardverfahren überlegene Lokalisierung dielektrischer Eigenschaften und die Durchführung dielektrischer Spektroskopie.

Diese Dissertation stellt neue funktionelle Methoden mit verbesserter Auflösung für das AFM vor und verbessert die Vielseitigkeit von EFMs für die Nanokarakterisierung neuer Energiematerialien.





# Contents

<b>Eigenständigkeitserklärung zur Doktorarbeit</b>	<b>V</b>
<b>Acknowledgements - Danksagung</b>	<b>IX</b>
<b>Scope, aim, and outline of this Study</b>	<b>XIII</b>
<b>Publications and contributions covered in this PhD thesis</b>	<b>XIX</b>
<b>Abbreviations</b>	<b>XXIII</b>
<b>Abstract</b>	<b>XXVII</b>
<b>Kurzfassung</b>	<b>XXVIII</b>
<b>1 Introduction</b>	<b>1</b>
<b>2 Fundamentals</b>	<b>5</b>
2.1 Chemical classification of solids . . . . .	5
2.1.1 Electrons in solids - Orbitals, molecular orbitals and band structures . . . . .	6
2.1.2 Metallic and non-metallic solids - Difference between a metal, a semiconductor and an insulator . . . . .	8
2.2 Semiconductor Materials . . . . .	10
2.2.1 Excited states and extraction of charge carriers . . . . .	10
2.2.2 Types of crystal defects . . . . .	12
2.2.3 Consequences of defects, impurities and doping in semiconductors . . . . .	14
2.2.4 p-n junctions . . . . .	16
2.2.5 Recombination Mechanisms . . . . .	16
2.2.6 Oxide semiconductors . . . . .	19
2.2.7 Amorphous semiconductors . . . . .	19
2.3 Surface . . . . .	20
2.3.1 The work function . . . . .	20

---

2.3.2	Surface electronic states . . . . .	20
2.3.3	Band bending at semiconductor surfaces . . . . .	21
2.4	Working principles and fundamentals of photovoltaics and solar cells . . . . .	23
2.4.1	Light absorption . . . . .	23
2.4.2	Quasi-FERMI level splitting (QFLS) after light absorption . . . . .	23
2.4.3	Separation via p-n- or heterojunction . . . . .	25
2.4.4	Semiconductor materials used in solar cells . . . . .	25
2.5	Halide perovskites and perovskite solar cells . . . . .	26
2.5.1	Crystal structure of halide perovskites . . . . .	26
2.5.2	Electronic Structure of halide perovskites . . . . .	28
2.5.3	Architecture of perovskite solar cells . . . . .	30
2.5.4	Defects in perovskite solar cells . . . . .	31
2.5.5	Performance, stability, and passivation of perovskite solar cells . . . . .	32
2.5.6	Illumination of perovskite solar cells . . . . .	33
2.6	Characterization Methods . . . . .	33
2.6.1	Atomic Force Microscopy . . . . .	34
2.6.2	Basic modes in conventional Atomic Force Microscopy (AFM) . . . . .	35
2.6.3	Conductive Atomic Force Microscopy (c-AFM) . . . . .	36
2.6.4	Electrostatic Force Microscopy (EFM) . . . . .	38
2.6.5	Kelvin Probe Force Microscopy (KPFM) . . . . .	40
2.6.6	Amplitude modulation Kelvin Probe Force Microscopy (AM-KPFM) . . . . .	41
2.6.7	Frequency modulation Kelvin Probe Force Microscopy (FM-KPFM) . . . . .	42
2.6.8	Sideband FM-KPFM . . . . .	43
2.6.9	Heterodyne Kelvin Probe Force Microscopy (H-KPFM) . . . . .	44
2.6.10	Influences on the local contact potential difference . . . . .	45
2.6.11	Time-resolved Kelvin Probe Force Microscopy (tr-KPFM) . . . . .	47
2.6.12	Scanning Capacitance Microscopy (SCM) . . . . .	50
2.6.13	Multi-frequency Electrostatic Force Microscopy . . . . .	52
2.6.14	Multi-frequency heterodyne Electrostatic Force Microscopy (MFH-EFM) . . . . .	53
<b>3</b>	<b>Two birds with one stone: dual grain-boundary and interface passivation enables &gt;22 % efficient inverted methylammonium-free perovskite solar cells</b>	<b>59</b>
<b>4</b>	<b>Nanoscale Surface Photovoltage Spectroscopy</b>	<b>135</b>

5	Nanoscale capacitance spectroscopy based on multi-frequency electrostatic force microscopy	175
6	Summary and Outlook	213
7	Bibliography	217
8	List of Figures	253
9	Nutzung KI-Tools	257
10	Curriculum Vitae	259



---

# 1 Introduction

Global electricity production has grown and will continue to grow in the coming decades.<sup>106–108</sup> In Figure 1.1 the increase of the worldwide electricity production from 1985 until 2023 is visible. For a sustainable and healthy society, a secure, environmentally friendly, and efficient energy

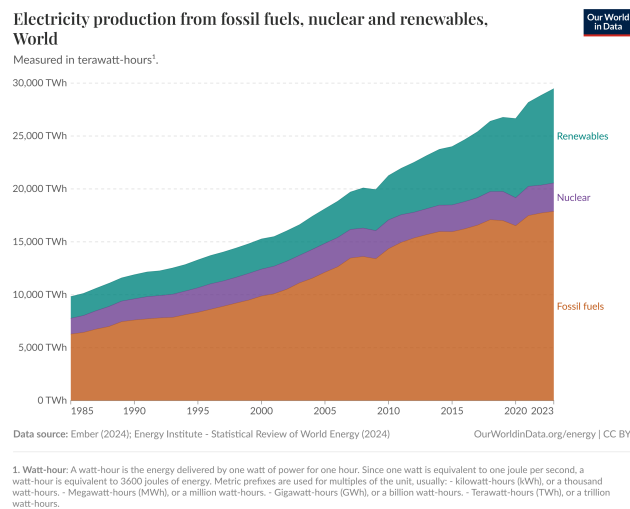


**Figure 1.1:** Electricity production from fossil fuels, nuclear and renewables on the entire world measured in TWh from 1985 to 2023.<sup>109</sup>

source is needed.<sup>108,110–114</sup> Interestingly, the percentage of renewable electricity production has been increased to 30 % of the global production which sums up to almost 8914 TWh in 2023 while the percentage of electricity production by fossil fuels is decreasing slowly (see Figure 1.1). 1630 TWh of the renewable fraction are produced by solar power.<sup>109</sup> That is 18 % of all renewable energy sources in 2023 and growing.<sup>109</sup> In 2023, approximately 61 % of the global production (17 879 TWh) was fossil fueled-based electricity production.<sup>109</sup>

The electricity production process that utilizes fossil fuels, particularly coal, oil, and gas (see Figure 1.2(a)), has resulted in substantial atmospheric carbon dioxide (CO<sub>2</sub>) emissions, contributing to an increase in the average global CO<sub>2</sub> concentration (see Figure 1.2(b)). As a result, the annual global land-sea temperature has also increased since the Industrial Revolution. In

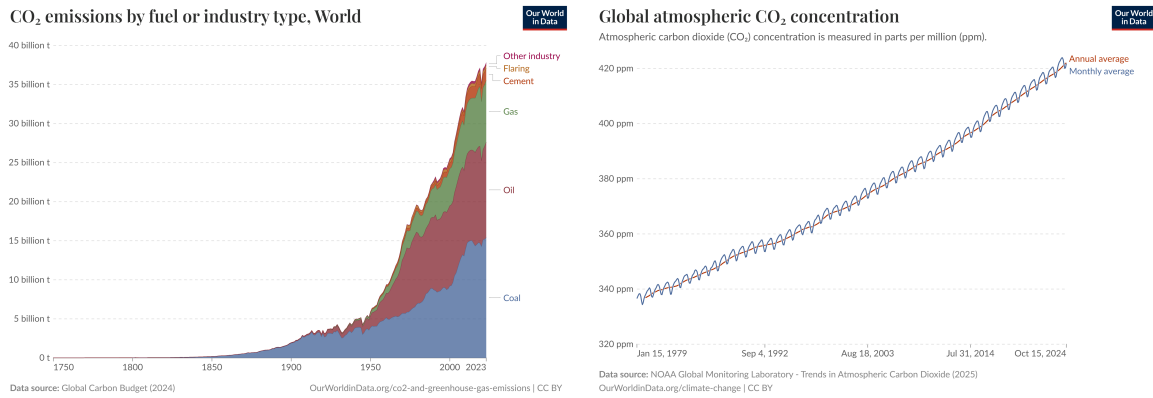


**Figure 1.2:** (a) CO<sub>2</sub> emissions by fuel or industry type on the entire world measured in billion t from 1750 to 2023<sup>115</sup> and (b) the global atmospheric CO<sub>2</sub> concentration from January 15, 1979 to October 15, 2024 measured in parts per million (ppm).<sup>116</sup>

2024 the earth has increased the average temperature up by 1.18 °C.<sup>117</sup> This has led to a number of dangerous environmental problems, such as land drought,<sup>108,118,119</sup> heat waves, forest fires, sea level rise, floods, and other extreme weather events around the globe.<sup>108,120–122</sup> The observed increase in global surface temperatures is a phenomenon that has been anticipated since the late 1970s, as evidenced by the findings of a study conducted by ExxonMobil. This study made a precise prediction of the actual increase in the average global land-sea temperature.<sup>123</sup> This is shown in Figure 1.3.

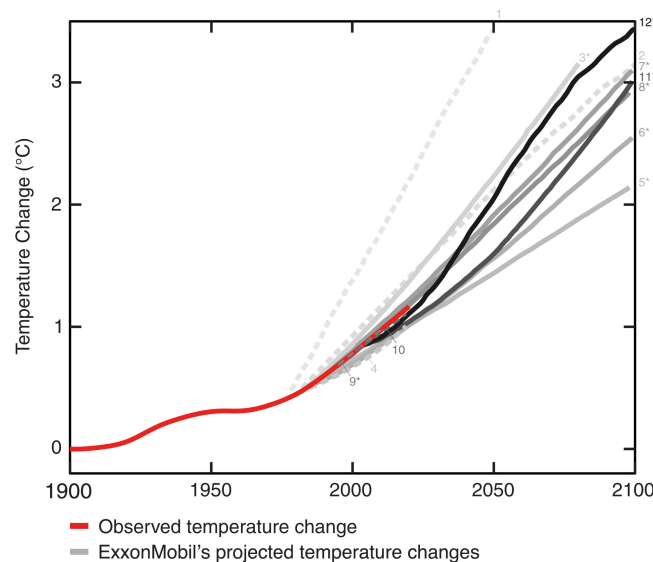


**Figure 1.3:** Summary of all global warming projections (nominal scenarios) reported by ExxonMobil scientists in internal documents and peer-reviewed publications (gray lines), superimposed on historically observed temperature change (red).<sup>123</sup>

---

Consequently, it is imperative to expedite the implementation of renewable energy sources at the earliest opportunity.<sup>124</sup> Studies have been conducted to find several environmentally friendly and efficient alternatives for the conventional energy market, taking into account their limited sources and environmental impacts.<sup>108,125–127</sup> From the recent growth statistics on renewable technologies, it can be seen that many countries in the world are highly interested in solar-powered systems, with a global photovoltaic capacity installation of 456 GW in 2024.<sup>128</sup> This interest in solar cell technology is driven by the many benefits of solar energy, including its availability, low cost, and environmental friendliness.<sup>108</sup> The earth's surface receives a direct solar radiation of  $1366 \frac{\text{W}}{\text{m}^2}$ , which decreases to a maximum normal surface radiation intensity of approximately  $1000 \frac{\text{W}}{\text{m}^2}$  at sea level on a clear day due to the atmosphere.<sup>108,129</sup> Solar radiation is particularly high in the vicinity of the equator. Assuming a radiation intensity of approximately  $1000 \frac{\text{W}}{\text{m}^2}$  over the entirety of a year, it can be estimated that in 2023, an area no larger than the island of Mallorca in Spain would be sufficient to generate the world's annual electricity output, if we assume 24 h sunshine, 365 d in a year, and a power conversion efficiency (PCE) of 100 %. In general, photovoltaic (PV) systems are known for their production of energy with no CO<sub>2</sub> emission during operation but in the making of the solar cells, they cause a certain amount of CO<sub>2</sub> and other greenhouse gas emissions. They are therefore characterized by a relatively short payback period compared to other conventional and renewable energy sources. After the manufacturing phase and completed installation, PV systems do not produce any environmental burden. They do not generate noise or emit toxic or greenhouse gases. In order to stop the climate crisis and make energy generation CO<sub>2</sub>-neutral, solar cells are a key technology that needs to be studied more closely for efficient design. However, like any industrial product, the production of solar cells and modules has health and environmental impacts such as the use of toxic chemicals during preparation or the use of a lot of energy for the production of defect-free silicon single crystals.<sup>108</sup>

For example, in 2023, 739 kWh electricity was produced per capita from solar cells in Germany alone<sup>130</sup> and therefore the emission decreased to 381 gCO<sub>2</sub>/kWh.<sup>109</sup> As more solar cells increase their efficiency, the amount of electricity produced will grow exponentially, while the amount of CO<sub>2</sub> emitted per kWh will decrease. To improve solar cells, the absorber materials needs to be examined in particular. Making thin films from solution, especially for the perovskite materials, will result in a heterogeneous formation of crystals and nanostructures. These nanostructures such as grain boundaries (GBs) as well as interfaces limit the performance of solar cells due to non-radiative recombinations taking place at these defects/interfaces. Investigation of these

nanostructures requires nano resolution devices such as Atomic Force Microscopy (AFM) to conduct surface investigations. Surface science was revolutionized in 1982 by the invention of the Scanning Tunneling Microscopy (STM) by BINNIG and ROHRER.<sup>131,132</sup> In 1986, the invention of the AFM expanded the sample range from conductive to non-conductive.<sup>132,133</sup> By combining the AFM with other measurement methods, a wide range of applications has been opened up, allowing additional sample properties to be obtained on a lateral scale in the nanometer range.<sup>132</sup> To learn more about electronic properties of nanostructures the electrostatic interaction between the tip and the sample is in focus of research. Electrostatic Force Microscopy (EFM) detects the electrostatic interaction and with that it is possible to map the local surface potential with a method called Kelvin Probe Force Microscopy (KPFM),<sup>41,132,134,135</sup> or dielectric properties with methods called Scanning Capacitance Microscopy (SCM). KPFM has significantly contributed to the understanding of the electronic properties and structure-property relationships on the nanoscale.

In many applications, knowledge of the dynamics of electronic processes is of great importance in understanding existing limitations and improving the performance of solar cells.<sup>132</sup> However, only a few studies have used the time-resolution method to study dynamic effects, as the time resolution is getting better through various methods.<sup>132</sup>

Research in perovskite solar cells (PSCs) has started with methyl ammonium lead iodide (MAPbI<sub>3</sub>) (MAPI) introduced by KOJIMA ET AL.<sup>136</sup> making it an interesting light-absorbing material for almost two decades to study.<sup>20</sup> The current record efficiency of metal halide perovskites is 27.0%.<sup>137</sup> As progress in perovskite research continues, the understanding of fundamental properties in the length range of morphology, that is, at the scale of grain boundaries or grains, must also be clarified.<sup>103</sup> With new AFM methods we will get a better understanding of the basic physics of PSCs and other semiconductor materials. Local differences especially in the perovskite/electron-transporting layer (ETL) interface need to be studied to improve energy production and storage in order to pave the way towards more efficient cells to fight the climate crisis. The following questions will be addressed in this thesis: First, how the dual passivation strategy influences defects at GBs in PSCs, and which methods are useful to analyze these defects. Second, to what extent can methods like nanoscale surface photovoltage spectroscopy (nano-SPV) and nanoscale ideality factor mapping (nano-IFM) resolve charge carrier dynamics in perovskite films, including the role of GBs and crystallographic facets. Third, how multi-frequency heterodyne Electrostatic Force Microscopy (MFH-EFM) could transform the characterization of nanoscale dielectric properties, and what technical advances are needed to broaden its applicability.

---

## 2 Fundamentals

In this chapter I will introduce the fundamentals necessary for the research addressed in this PhD Thesis. This includes solid state chemistry, semiconductors, role of defects and the surface as well as photovoltaics and the basics of Atomic Force Microscopy (AFM) and the electric modes as characterization method.

Sections 2.1 to 2.3 are based on the book "The Electronic Structure and Chemistry of Solids" by COX<sup>26</sup> if not cited otherwise.

### 2.1 Chemical classification of solids

The first section discusses what characterizes a crystalline solid and how electrons can be described at single atoms, molecules and ultimately in solids. This leads to the band theory and the differences between a metal, a semiconductor, and an insulator.

In Chemistry, there are different solids based on the type of the force which hold the atoms together. All of them have the characteristics of being solid under standard conditions and of having completely or partially crystalline structures. The four most important classes are molecular, ionic, covalent and metallic solids. While molecular solids held together by weak and short range VAN DER WAALS forces, ionic solids are bonding via electrostatic forces between ions. The energy of the interaction of two individual neighbors is given by the COULOMB law in general and by the BORN-LANDÉ equation as an extension for ionic crystals (Equation (2.1))

$$E_{\text{BORN-LANDÉ}} = \frac{N_{\text{A}} \cdot z^{+} \cdot z^{-} \cdot A \cdot e^2}{4 \pi \cdot \varepsilon_0 \cdot r_0} \cdot \left(1 - \frac{1}{n}\right) \quad (2.1)$$

with the AVOGADRO constant  $N_{\text{A}}$ ,  $z^{+}$  and  $z^{-}$  the numerical charge of the cation and anion, the MADELUNG constant  $A$ , the elementary charge  $e$ , the vacuum permittivity  $\varepsilon_0$ , and the distance between the nearest cation and anion  $r_0$ .  $n$  is the BORN exponent, typically a number between 5 and 12, determined experimentally by measuring the compressibility of the solid, or derived theoretically. Covalent solids are characterized by covalent bonds while metallic solids are characterized to have delocalized sharing of electrons throughout the solid. These

individual solid types represent only extreme ideal cases. Solids such as in energy devices have a more complex and combination of the different type of bondings. In this particular context, the concept of bonding in solids is built upon the fundamental principles of orbitals, which are derived from the solution of the SCHRÖDINGER equation for the hydrogen molecule (Equation (2.2) without  $U(r)$ ).

### 2.1.1 Electrons in solids - Orbitals, molecular orbitals and band structures

The SCHRÖDINGER equation for a single electron in a periodic potential, e.g., in a crystalline solid, is shown in Equation (2.2).

$$\hat{H} \psi = \left( \frac{-\hbar^2}{2m} \nabla^2 + U(r) \right) \psi = E \psi \quad (2.2)$$

$\hat{H}$  is the HAMILTONIAN operator,  $\psi$  is the wave function,  $\hbar$  the reduced PLANCK constant,  $m$  the mass of the particle, and  $E$  the energy. The term  $U(r)$  is given for the periodic potential coming from the periodic lattice of the crystal which satisfies  $U(r + a) = U(r)$ . The so-called free electron model try to get the wave function for electrons moving freely through the solid, which means the potential is zero ( $U(r) = 0$ ). Because of its simplicity, this free electron model is used widely to treat the electronic properties especially of pre-transition metals and some semiconductors, where the interaction of the atoms are strong and therefore the atoms lose their individual identities. However, this model breaks down for compounds of transition metals and lanthanides. The quasi-free electron model can be used instead.

The quasi-free electron model is using a small but nearly constant potential  $U(r)$ , which cause band gaps to appear in the electron structure. The band gaps come from the interaction of the quasi-free electrons with the periodic potential in a lattice. These electrons are referred as "BLOCH electrons", which obey the SCHRÖDINGER equation shown in Equation (2.2).

Covalent and even ionic solids, can be treated from a free electron starting point, although with a much stronger periodic potential. From a chemical point of view, though, it is much easier to think of these solids in terms of overlapping atomic orbitals (AOs). And chemical bondings are described better by overlapping BLOCH functions. In the orbital model, the electron repulsion is treated in an approximated way, and it is assumed that the electrons are quasi-free.

For molecules, the same ideas are used in the molecular orbital (MO) theory. Here, the AOs are combined with the method of the so called linear combination of atomic orbitals

(LCAOs). The schematic illustration of orbital energies of single AOs, to MOs, and ultimately crystal orbitals is shown in Figure 2.1. By combination of different AOs of single atoms (see

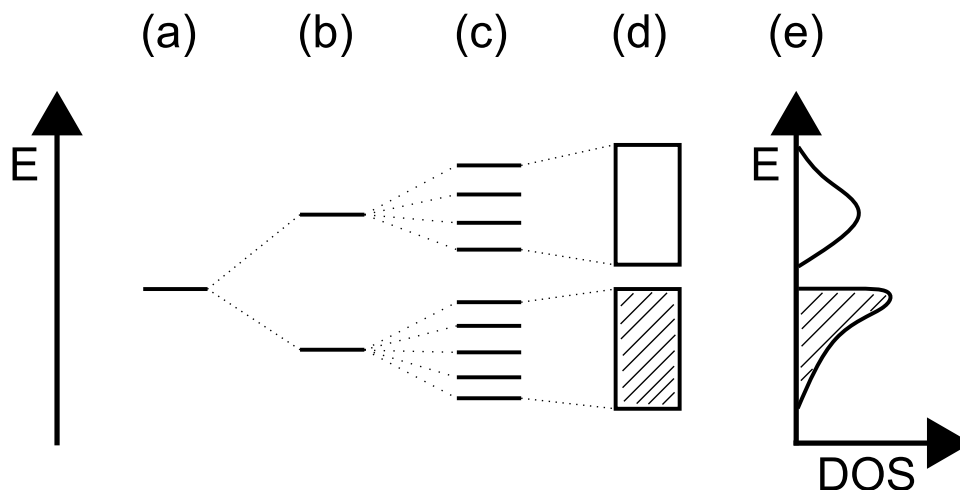


**Figure 2.1:** Orbital Energies of (a) an atom, (b) a small molecule, (c) a large molecule, (d) a solid, and (e) the density of states corresponding to (d).

Figure 2.1(a)), bonding and anti-bonding MOs will form (see Figure 2.1(b)). Therefore, in most cases, covalent bonding can be described as a charge build-up due to overlap of AOs in the internuclear region of mostly valence AOs. And the strength is based on the degree of overlap. As the number of AOs is getting larger the resulting MO is becoming larger (see Figure 2.1(c)). We can think of a solid as a very large molecule. For a finite solid, there is a finite number of valence AOs, however because of the large number of orbitals we can neglect the energy spacing between them and we can estimate a formation of a continuous band shown in Figure 2.1(d). These new orbitals can be called crystal orbitals. The energy levels at which electrons can occupy are now called energy bands.<sup>138</sup>

The MOs of the imaginary large molecule will not distribute equally over all energies. If there are no orbitals this is called a gap between the bands of the solid. But even within the bands some orbitals are more concentrated together at some energies compared to others, which is why the concept of density of states (DOS) was introduced. The DOS is the number of allowed energy levels per unit volume of the solid, in the energy range  $E$  to  $E + dE$ .  $DOS = 0$  stands for the band gap of a solid, where no energy level is located. The electronic properties of a solid depend on the energies of the bands, their widths, and the gaps between them. As a rule of thumb, if the band width is wider, the interaction with neighbouring atoms is stronger and vice versa. It's therefore the band structure with the electrons which decides if it is a metal or an insulator. But what differentiates a metal from an insulator?

### 2.1.2 Metallic and non-metallic solids - Difference between a metal, a semiconductor and an insulator

The difference between a metal and an insulator is based on their different electric conductivity. While metals are electrical conductive down to the lowest attainable temperatures, non-metallic crystalline solids up to a certain band gap have some conductivity at high temperatures, but it declines as the temperature is lowered.<sup>139</sup>

In order to understand this, we need to understand filling of bands, the meaning of the FERMI level, and what electric conductivity means and what it influences.

Bands can either be empty, partly filled or completely filled (see Figure 2.2). In a filled

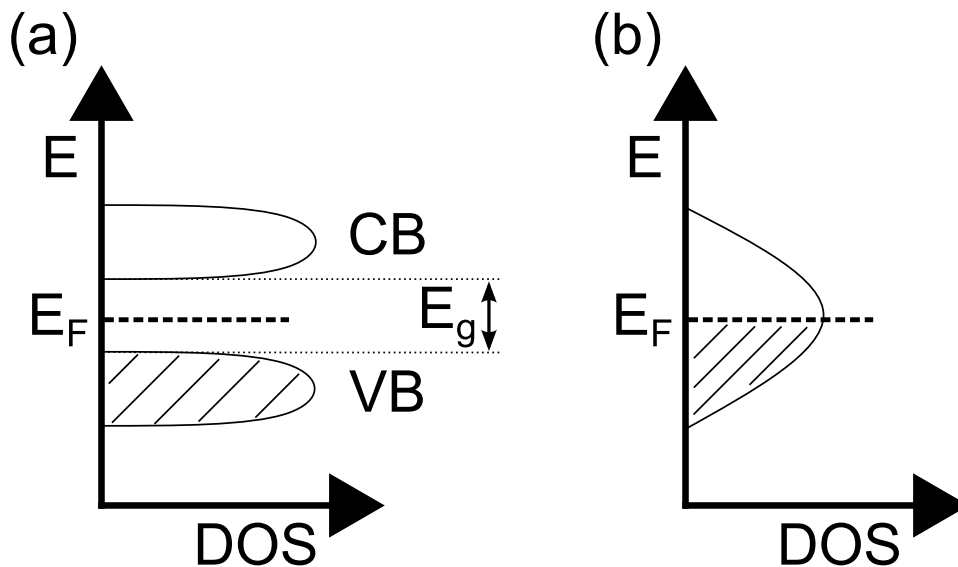


**Figure 2.2:** Density of states (DOS) in (a) non-metallic solid with the band gap  $E_g$ , and (b) metal. The respective FERMI level is marked with  $E_F$ . Shading represents occupied levels.

band (lower band in Figure 2.2(a)), the net motion of the electrons, due to the temperature  $T > 0\text{K}$ , cancels, and there is no electric conductivity. Therefore, a filled valence band (VB) with a band gap to the next empty conduction band (CB) (upper band in Figure 2.2(a)) is an insulator in the ground state. The energy gap in between the highest level of the VB, also called highest occupied molecular orbital (HOMO), and the lowest level in the CB, also called lowest unoccupied molecular orbital (LUMO), is called the band gap  $E_g$ . The FERMI level  $E_F$  is located in the middle of this band gap and has a fundamental importance as the thermodynamic chemical potential for electrons in the solid. This will be discussed in the Section 2.6.5 to measure the contact potential difference (CPD) via the Kelvin Probe Force

Microscopy (KPFM) method. A metal, however, has a partially filled band with no energy gap above the uppermost level (HOMO) (see Figure 2.2(b)). This top-filled energy level represents the FERMI level  $E_F$  in the metal.

These descriptions are only true for the extreme ideal case of 0 K. The FERMI-DIRAC distribution (Equation (2.3)) describes the probability for an allowed energy level with energy  $E$  to be occupied by an electron at a certain temperature  $T$ .

$$f(E) = \frac{1}{1 + \exp\left(\frac{E - E_F}{k_B T}\right)} \quad (2.3)$$

At 0 K the FERMI-DIRAC distribution corresponds to a sharp cut-off between completely filled levels below the energy  $E_F$  and completely empty levels above it. At higher temperatures, the distribution is smeared out, showing that some electrons are excited thermally to higher energies. Nevertheless, the FERMI level stays in the middle of the band gap ( $E_F = 0.5 \cdot E_g$ ).

A crystalline solid is electronic conductive when a net motion of electrons within the band is possible. In a metal, electrons from the formal VB can easily be excited by thermal excitation to the energy levels above the FERMI level, and the electron in the formal CB as well as the resulting hole in the lower energy band can move freely throughout the crystal. In case of the insulator or semiconductor, electronic conductivity requires the excitation of some electrons from the VB into the CB. If the band gap is small, however, electrons also can get thermally excited into the CB, which is called thermal conductivity. Another method by which to achieve electrical conduction in nonmetallic crystalline solids is by photoconductivity, in which an electron absorbs energy from a photon greater than the band gap. The distinction between insulators and semiconductors is predicated on the ability to undergo photoconductivity, which is determined by the variation in their band gap. The visible spectrum of the sun extends from photon energies of 1.5 eV to 3 eV, thereby defining a semiconductor as an insulator with a band gap smaller than 3 eV.

Optical properties of a metal are different due to the missing band gap at the FERMI energy (Figure 2.2(b)), which means there is a range of electronic excitation energies available.<sup>139</sup> Apart from infrared (IR) absorption, due to vibrations of the atoms, a non-metallic crystalline solid generally does not absorb radiation below a certain threshold energy. That is why, by simple absorption spectroscopy, it is possible to measure the band gap of a crystalline insulators and semiconductors.

## 2.2 Semiconductor Materials

In this section, I give an overview of semiconductor physics to lay the groundwork for understanding the photovoltaic effect and photovoltaics in general. This includes discussions on the electronic consequences of defects and impurities in energy bands, electron-hole excitation and recombination as well as discussions on some oxide semiconductors.

Semiconductors are non-metallic crystalline solids that conduct electricity only through thermal or photonic excitation across an energy gap. However, this fundamental principle can be hindered by defects, leading to a disruption in the regular periodicity of the crystal lattice. These defects interact with charge carriers, resulting in a perturbation in the electronic structure. It is noteworthy that all crystalline solids, even those of the highest degree of perfection, such as single crystals, are subject to the presence of defects and impurities, and are characterized by the existence of surfaces. In many cases, these defects and impurities significantly influence the electronic and optical properties of the material. A notable example is that of solid-state devices composed of semiconductors, which are contingent upon the electronic levels of deliberately introduced impurities, known as "doping". The subsequent sections will go into more detail about the intricate nature of defect types and their electronic consequences, but first I want to discuss the different types of excitons and the charge extraction.

### 2.2.1 Excited states and extraction of charge carriers

Excited electronic states are produced in crystalline solids by absorption of photons of sufficient energy, or by bombardment with charged particles like electrons. The resulting free electrons in the CB and free holes in the VB of a semiconductor are held together by electrostatic COULOMB attraction, similar to that between an electron and a positively charged defect. Furthermore, their relative motion is quantized, provided that this interaction is stronger than the random thermal fluctuation. These excited states are referred to as non-equilibrium defects, and they can also interact with other defects. The stable quasi-particle state associated with this electron-hole interaction is known as an exciton.

In a first approximation, the exciton can be treated as a hydrogenic atom of reduced mass  $m_{e,h}^*$  in a medium of dielectric constant  $\epsilon_r$ . Utilizing the BOHR model, the binding energy of the  $n_l$  level relative to the ionization limit can be calculated as

$$E_B(n_l) = -\frac{m_{e,h}^* R_H}{m_0 \epsilon_r n_l^2} \quad (2.4)$$

Here,  $m_0$  denotes the mass of a free, noninteracting electron, and  $R_H = h \cdot c \cdot R_\infty = \frac{m_e e^4}{8 \epsilon_0 h^2} = 13.6 \text{ eV}$  is the RYDBERG constant of the hydrogen atom with the electron mass  $m_e$ , the elementary charge  $e$ , and the PLANCK constant  $h$ .<sup>27</sup> ( $n_l = 1$ ) stands for an electron in the lowest energy level of hydrogen. An electron in the lowest energy level of hydrogen ( $n_l = 1$ ) therefore has about 13.6 eV less energy than a motionless electron infinitely far from the nucleus. For larger values of  $n$ , these are also the binding energies of a highly excited atom with one electron in a large circular orbit around the rest of the atom. The average distance between an electron and a hole at the level  $n_l = 1$ , also called the effective BOHR radius, is henceforth defined as

$$a_X = \frac{m_{e,h}^*}{m_0 \epsilon_r} a_B \quad (2.5)$$

where  $a_B = 0.053 \text{ nm}$  is the BOHR radius of the hydrogen atom.<sup>27</sup>

The photon energy necessary to form an electron-hole pair is determined by the band gap  $E_g$  minus the binding energy due to the COULOMB interaction (see Equation (2.6)).

$$E_n = E_g - \frac{m_{e,h}^* e^4}{32 \pi^2 \epsilon_0^2 \epsilon_r^2 \hbar^2 n^2} \quad (2.6)$$

The symbol  $\hbar$  is used to represent the reduced PLANCK constant. Due to the finite difference in Equation (2.6), a significant optical absorption is anticipated below the band edge energy. This results in an optical gap that is lower than the transport gap.<sup>27</sup>

In general, for semiconductors with a wide band and a small band gap, the dielectric constant is large and the effective masses  $m_{e,h}^*$ , as well as the binding energy, are small. Consequently, the binding energy tends to increase, and the radius decreases as the band gap of the semiconductor increases.<sup>27</sup> Excitons with small binding energy, where an electron and a hole "orbit" around each other with a large radius, are referred to as the WANNIER-MOTT excitons. These delocalized states can move freely through the crystal (represented by the exciton center of mass).<sup>27</sup>

In organic materials, the dielectric constant is typically lower compared to inorganic semiconductors, and the exciton-binding energy is higher.<sup>27</sup> This tends to make excitons more stable in organic materials.<sup>27</sup> In insulators and certain organic crystals, the tightly bound electron-hole pair wave function is confined to one crystal unit, the same atom, or one molecule.<sup>27</sup> These excitons are known as FRENKEL excitons. Impurities within the crystal structure are capable of trapping these excitons, thereby impeding their movement through the crystal lattice.

Generally, free carriers, which are present in heavily doped samples, typically act to shield the COULOMB interaction. This, in turn, reduces the binding forces by screening, impeding the formation of excitons.<sup>27,140</sup> The DEBYE-HÜCKEL theory posits that the exciton-binding energy exhibits a pronounced decrease for concentrations exceeding approximately  $n \approx 1 \cdot 10^{17} \frac{1}{\text{cm}^3}$ .<sup>27,141</sup>

Another noteworthy phenomenon is the thermal dissociation of excitons. According to classical statistics, thermal effects appear to be an unlikely cause of excitons dissociating, as the thermal energy at room temperature ( $k_B T \approx 0.026 \text{ eV}$ ) is considerably less than the exciton binding energy.<sup>142</sup> However, systematic studies have shown that the diffusion coefficient of excitons and length monotonically decrease with cooling at the high-temperature region, while it remains nearly constant at lower temperatures<sup>142-144</sup> It was observed further, that the dissociation of a charge-transfer state is a temperature-dependent process, where the exciton dissociation probability increases with temperature<sup>145</sup> and even that thermal energy is sufficient to separate most of the thermalized charge transfer states into free charges.<sup>142,146,147</sup> These studies underscore the vital role of temperature in exciton migration and dissociation. While the significance of thermal fields in this process is evident, further investigation is necessary to ascertain their precise function.<sup>142</sup>

In certain instances, electrons and holes may become trapped at defect sites that are distant from one another. The probability of recombination, whether radiative or non-radiative, is found to be exceptionally low in such circumstances. In the event that the trapped energy is sufficiently large, the lifetime of such an "excited state" can be very long indeed. The recombination process is governed by specific recombination mechanisms. They will be discussed in Section 2.2.5. The following section will go into detail about defects, because they can influence the behavior of the excitons.

## 2.2.2 Types of crystal defects

A defect is a interruption in the lattice periodicity. There are several types of defects in crystals.

First, there is the possibility for single point defects (see Figure 2.3), which are perturbations of the crystal that involve a single lattice site, or at most a group of two defect sites combined. As a simple example there is lattice vacancies (Figure 2.3(a)) and interstitial atoms (Figure 2.3(b)). In ionic solids, the defects are often charged, so a significant number of charged defects can only exist if the electrical charge is compensated by that of other defects. The simplest combination is also shown in Figure 2.3(c) and (d). The SCHOTTKY defect (see Figure 2.3(c)) consists of an anion and a cation vacancy while the FRENKEL defect combines a vacancy of one type with an interstitial of the same type. Another possible point defect in terms of the electric structure is

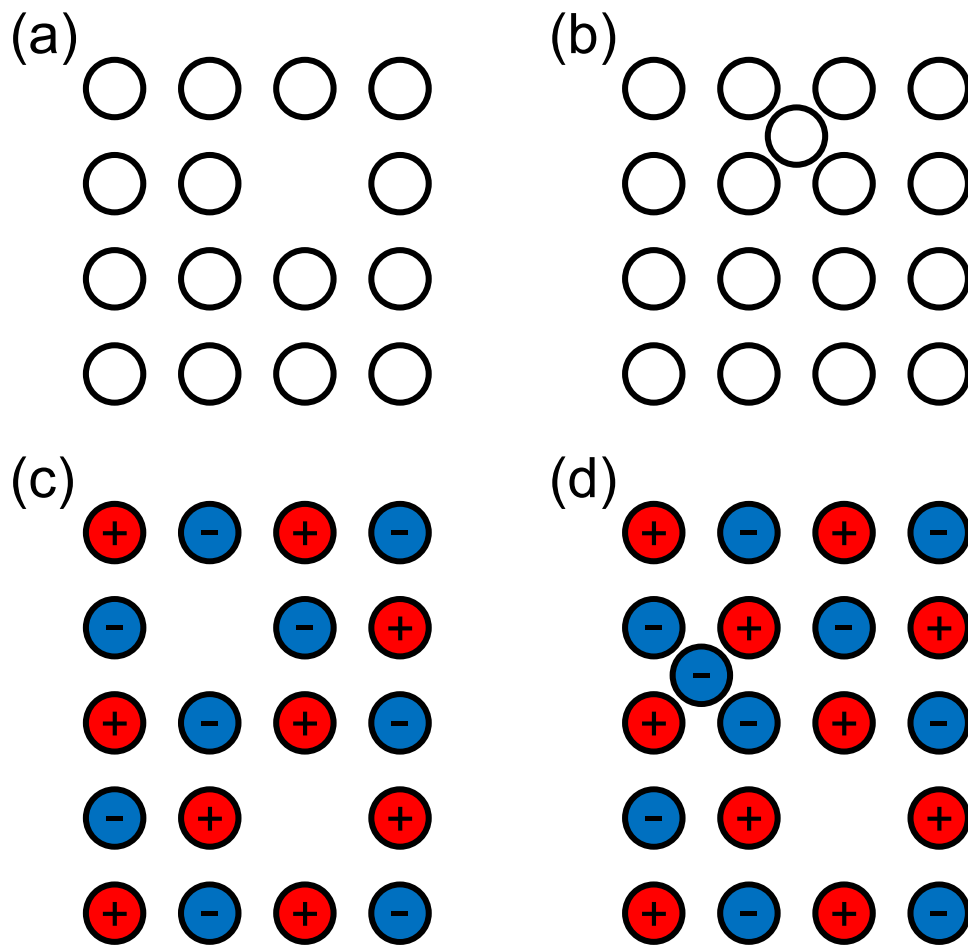


**Figure 2.3:** Simple point defects. (a) Lattice vacancy. (b) Interstitial atom. (c) SCHOTTKY defect, consisting of cation and anion vacancy. (d) FRENKEL defect, with vacancy balanced by interstitial.

doping, in which an atom is replaced by another atom, resulting in either a one-electron excess or deficit compared to the previous atom. For instance, the Silicon (Si) atom can be exchanged for either a Boron (B) or a Nitrogen (N) atom, thereby inducing a hole or an extra electron in the crystal, respectively.

Conversely, solids are also characterized by extended defects, such as linear or planar interruptions of the crystal periodicity. When a fault in the arrangement of atoms in the crystal lattice is associated with a dislocation, it serves as an example of a linear defect. An example of a planar defect is a shear plane or a grain boundary (GB) between two crystallites in a polycrystalline solid. The most prevalent type of planar defect, however, is the crystal surface, where dangling bonds, which are unsatisfied valence bonds on immobilized atoms, are predominantly located.<sup>148</sup>

### 2.2.3 Consequences of defects, impurities and doping in semiconductors

As all the defects described in Section 2.2.2 break the regular periodicity of the ideal crystal lattice, electrons traveling through the crystal are scattered into other orbitals. Consequently, defects and impurities arising from vacancies or interstitials in metals tend to reduce the electrical conductivity. This holds true for a semiconductor with a small band gap, where electrons can be thermally excited into the CB. However, in semiconductors with a band gap in the region available for solar radiation, defects and impurities can have significantly more substantial effects. This is due to the fact that they can introduce additional electronic levels into the energy gap. Two factors must be considered in order to determine the electrostatic consequences of defects. First, the energies of the extra levels introduced by the defects, separating them into shallow or deep defect states, and second, the number of electrons occupying them. As illustrated in Figure 2.4, there are several possible outcomes.

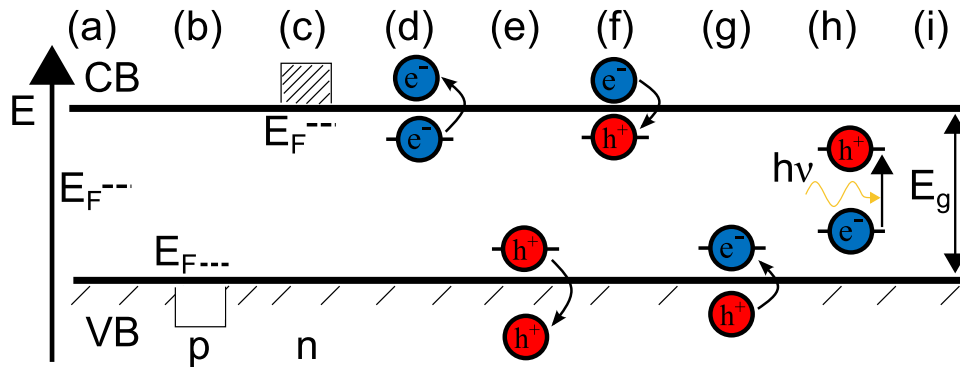


**Figure 2.4:** Electronic consequences of defects in semiconductors are illustrated with the respected valence band (VB) and the conduction band (CB). FERMI-DIRAC distribution in a (a) pure crystalline solid; (b) p-type; and (c) n-type semiconductor with extra holes or electrons in valence or conduction band. (d) and (e): Defect levels providing free electrons or holes by thermal excitation. (f) and (g): Defect levels acting as traps for electrons or holes. (h): Levels giving optical absorption at energies below the band gap. (i) the corresponding band gap  $E_g$  of the semiconductor. Shading represents occupied levels.

In a perfectly stoichiometric crystalline semiconductor (see Figure 2.4(a)), the FERMI level  $E_F$  is precisely at the half of the band gap  $E_g$  (illustrated in Figure 2.4(i)), because at any temperature the number of electrons in the CB is exactly the same as the number of holes in the VB.

The introduction of a small concentrations of defects will result in trapped electrons or holes in energy levels close to the band edges (see Figure 2.4(d) and (e)). The donor or acceptor states

caused by the presence of defects are typically referred to as defect states or trap-states. In the context of defect states in proximity to band edges, these states are designated as "shallow trap states" due to the minimal energy required for the ionization of the trapped electron (Figure 2.4(d)) or hole (Figure 2.4(e)). These states function primarily as dopants of charge carriers, contributing to the overall electrical properties of the material. Figure 2.4(f) shows a defect level just below the edge of the CB, where there is no electron in the ground state. This means it does not add extra electrons or change the FERMI level in the ground state. However, these defect levels can act as trap states for optical excited electrons. A similar defect level is shown in Figure 2.4(g) shows a similar defect level, where an occupied level just above the VB edge is forming a trap for holes in the VB. In rare instances, the defect levels are found to be significantly distant from the boundaries of the band edges, as illustrated in Figure 2.4(h). Consequently, the generation of free carriers by thermal excitation becomes unfeasible at ambient temperatures. Such defect states are designated as deep trap states. In the case of shallow traps, their impact on the performance of the semiconductor is typically negligible. In contrast, the phenomenon of deep traps has been demonstrated to be responsible for non-radiative recombination.<sup>149–151</sup>

In addition to point defects, extended defects have been shown to have significant electronic consequences. For semiconductors, dislocations increase the electrical resistivity and can act as centers for recombination of electrons and holes. This phenomenon is attributed to the elimination of the charge carriers. A more thorough explanation of recombination mechanisms can be found in Section 2.2.5. The electronic properties of surfaces have been the focus of extensive research in recent years. The surfaces of semiconductors, particularly in conjunction with defects or adsorbed species, manifest a comprehensive array of electronic phenomena, as depicted in Figure 2.4. An in-depth discussion of surfaces can be found in Section 2.3.

Doping, in contrast to defects, is defined as the intentional introduction of impurity atoms into a pure semiconductor. This process involves the addition of atoms with different valences to a semiconductor crystal, thereby altering its electrical, optical, and physical properties. In doped semiconductors, a particular type of carrier becomes predominant. For instance, one of the tetrahedrally bonded silicon atoms can be substituted by a Group V or Group III element as a substitute defect. Figure 2.4(b) and (c) illustrate the band structure of a p-type and a n-type semiconductor, respectively. In a n-type semiconductor, negative electrons are the predominant current carriers because the number of electrons in the CB exceeds the number of holes in the VB. The filled VB of silicon doped with an Group V atom, such as phosphorus, introduce an additional electron from each Group V atom. However, it also possesses a greater nuclear charge.

Therefore, the additional electron will "orbit" around the Group V atom in the ground state. This configuration is referred to as a donor state, in which an electron is trapped at an energy level just below the CB. This is illustrated in Figure 2.4(d). Conversely, a p-type semiconductor exhibits an excess of positive holes in the VB relative to the number of electrons in the CB. In this particular instance, silicon may be substituted by an Group III atom, such as aluminum. In this situation there is one less valence electron, and the result is an unfilled level, or hole, in the VB. This hole subsequently forms a bound state of similar nature, designated as an acceptor level, which is situated just above the VB. This is illustrated in Figure 2.4(e). This causes a shift of the FERMI level towards the VB in an p-type semiconductor (see Figure 2.4(b)) and towards the CB in case of a n-type semiconductor (see Figure 2.4(c)).<sup>148,152</sup> In semiconductors that are doped with small concentrations of defects, where the electrons or holes are trapped in levels near or close the band edges (see Figure 2.4(d) and (e)), carriers are likely to be released, increasing the conductivity and also changing the FERMI level in the semiconductor. The properties of doped semiconductors are a consequence of both the dopant effect and the trap states present within the material. The fundamental difference between beneficial doping (p- and n-type) and detrimental defects lies in the inherent nature of defects, which are virtually inevitable in any crystalline solid. Conversely, doping constitutes a deliberate process aimed at modifying the optical and physical properties.

## 2.2.4 p-n junctions

A fundamental component of a solid-state device based on doped semiconductors is the p-n junction. When you bring a p-type semiconductor and an n-type semiconductor together, the energy of the bands will initially be equal. However, if the energy of the bands is the same, the junction cannot be in equilibrium because the FERMI levels on both sides are not the same. Electrons will pass from the n- to the p-type material, forming a space charge region where there are no carriers. The unbalanced charge of the ionized impurities causes the bands to bend, until a point is reached where the FERMI levels are equal. This phenomenon, known as rectification, leads to the preferential flow of current in one direction, a property that is advantageous in the context of solar cells.

## 2.2.5 Recombination Mechanisms

As we learned, the photovoltaic (PV) effect, which is used in solar cells, will generate excited electron-hole pairs by absorbing photons with an energy greater than the band gap of a semiconductor. Typically, the resulting electrons in the CB and holes in the VB undergo

rapid recombination by either collide into each other or by transferring their energy.<sup>151</sup> This process of elimination of charge carriers, which occurs in semiconductors, is referred to as the recombination process. There are three types of recombination that occur in a semiconductor solid depending on the energy emission illustrated in Figure 2.5.<sup>151</sup> (I) Radiative recombination where a photon is emitted, with an energy corresponding to the band gap of the semiconductor (see Figure 2.5(a)), (II) non-radiative recombination where the energy of recombination passes into lattice vibrations, and so appears as heat (see Figure 2.5(b)), and (III) AUGER recombination where the energy of another free charge carrier increases (see Figure 2.5(c)).<sup>151</sup> Alternatively, they may move in opposite directions. In this case, they can be collected by metal electrodes and utilized to perform work within an electric circuit.<sup>151</sup> Although, I will be

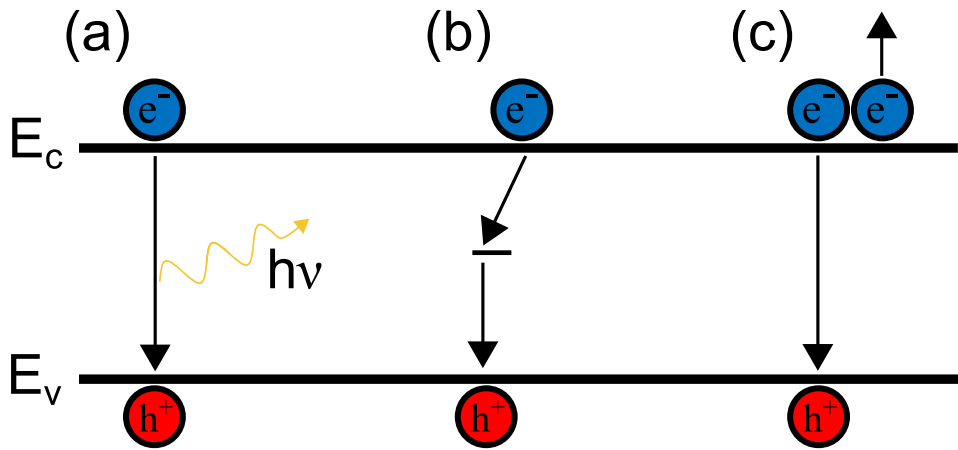


**Figure 2.5:** Illustration of recombination mechanisms in semiconductors. (a) Radiative, (b) non-radiative, and (c) AUGER.<sup>151</sup>

describing radiative and non-radiative recombinations since they are the most common ones in solar cells.<sup>27</sup>

In the context of radiative or band-to-band recombination processes (see Figure 2.5(a)), the electron undergoes a direct transition from the CB to the VB, thereby engaging in an interaction with a free hole.<sup>151</sup> This process is referred to as recombination due to the fact that the electron-hole interaction, as a result of the band-to-band transition, results in a photon emission that has the same energy as the band gap.<sup>151</sup> The density dependence of the radiative recombination is given by  $U_{np} = B_{np}$ , where  $n$  is the number of free electrons,  $p$  is the number of free holes, and  $B$  is a recombination coefficient which depends amongst other conditions on temperature.<sup>27,151</sup> The radiative recombination for Si and GaAs at 300 K are  $B \approx 1 \cdot 10^{-14} \frac{\text{cm}^3}{\text{s}}$  and  $B \approx 7.2 \cdot 10^{-10} \frac{\text{cm}^3}{\text{s}}$ , respectively.<sup>151,153-156</sup> The radiative recombination process can be

expressed in a more comprehensible form by expressing the dependence of the recombination rate on the voltage applied to the solid as follows in Equation (2.7):<sup>27,151</sup>

$$U_{np} = B n_i^2 \exp\left(\frac{q \cdot V}{k_B T}\right) \quad (2.7)$$

The recombination rate  $k_{rec}$  is generally linked to the free electron lifetime  $\tau$ .<sup>151</sup> An enhanced recombination rate is associated with a reduced electron lifetime.<sup>151</sup> For a linear recombination rate, this relationship is expressed by Equation (2.8):<sup>27,151</sup>

$$\tau = \frac{1}{k_{rec}} \quad (2.8)$$

Accordingly, the recombination rate can be estimated quantitatively by measuring the free electron lifetime.<sup>151</sup> For instance, time-resolved photoluminescence (tr-PL) measurements monitor the photoluminescence (PL) from a sampled material over time, thereby determining the point at which the PL diminishes, which in turn provides the free electron lifetime.<sup>151</sup>

The recombination process is inextricably linked to the emission of energy, which is a direct consequence of the fundamental principle of energy conservation.<sup>151</sup> In the case of non-radiative recombination, the energy is primarily absorbed by either electrons or holes, as in the AUGER recombination process, or by phonons in defect-related recombination processes.<sup>151</sup> In normal semiconductor devices the recombination is mostly non-radiative. Recombination also occurs through trap levels within the band gap (see Figure 2.5(b)).<sup>151</sup> Therefore, when an electron descends from the CB to the midgap state, it emits a photon that is redshifted relative to the band gap photons.<sup>151</sup> When recombination occurs via a midgap state, it more frequently involves a multiphonon process.<sup>151</sup> In this process, the energy of the band gap is transferred to a multitude of phonons.<sup>151</sup> This is unlike the emission of photons.<sup>151</sup> This type of recombination is referred to as non-radiative recombination.<sup>151</sup> Non-radiative recombination is often associated with defects in the bulk or on the surface of the semiconductor,<sup>151</sup> but this type of recombination can also occur at impurity sites. The semiconductor's surface, particularly in proximity to contact points, often harbors defects and recombination sites.<sup>151</sup> These sites are termed surface recombination sites.<sup>151</sup> The Shockley-Read-Hall (SRH) recombination model is a typical model for recombination.<sup>151</sup> It occurs within the band gap, taking both electrons and holes from the conduction and valence band.<sup>151</sup> The recombination rate of excess charge carries is given by Equation (2.9):<sup>27</sup>

$$U_{SRH} = \frac{np - n_i^2}{\tau_p(n + n_1) + \tau_n(p + p_1)} \quad (2.9)$$

where  $\tau_n$  is the electron lifetime for a large density of holes,  $\tau_p$  is the hole lifetime for a large density of electrons, and  $n_1, p_1 = n_i^2/n_1$  are the electron and hole densities when the FERMI level overlaps with the trap state energy that is the recombination center:<sup>27,151</sup>

$$\begin{aligned} n_1 &= N_c \exp\left(\frac{E_t - E_c}{k_B T}\right) \\ p_1 &= N_v \exp\left(\frac{E_v - E_t}{k_B T}\right) \end{aligned} \quad (2.10)$$

These recombination mechanisms take usually place at defects, which can appear also intrinsically from the material itself.

### 2.2.6 Oxide semiconductors

Simple oxides like MgO have rather low concentration of defects under equilibrium conditions within the lattice structure. On the other hand, many oxides of transition elements can have quite high concentrations of defects under equilibrium conditions. The defects are often associated with derivation from perfect stoichiometry, and are formed because of the relative ease of reduction oxidation of the metal ion. Due to the higher dielectric constants the electrons and holes are not so firmly bound to the defects. Thus, carriers can be thermally excited into the conduction or VBs, giving semiconductor properties. TiO<sub>2</sub> for example has oxygen vacancies or interstitial titanium and therefore has a n-type behaviour due to slight reduction of the titanium. This can be found within compounds such as TiO<sub>2</sub>, ZnO, and SnO<sub>2</sub>, which are materials used in perovskite solar cells (PSCs) as electron-transporting layer (ETL). At higher temperatures, the electrons will be mobile in the CB, but in the ground state they are normally trapped by the lattice defect. An interstitial cation in the lattice will give a positive potential that can trap an electron in a bound orbital just below the CB edge, similar to the impurity levels introduced earlier.

### 2.2.7 Amorphous semiconductors

In the solids considered so far, the disorder is associated with defects that are relatively well isolated from one another. In a solid with high degree of disorder this picture is not longer valid. The most important difference is that the local coordination is different to the structure in the whole solid, in other words, how the local coordinations are bound to each other. Therefore, there is the possibility for dangling bonds within the crystal, which is also known at crystal surfaces and at lattice vacancies. These can either be stabilized by disproportionation  $A \cdot + A \cdot \longrightarrow A^+ + A^-$ , where the electron transfer therefore needs to be stabilized by a relaxation in

the positions of surrounding atoms. The disordered structure leads to lower electron mobilities but is superior in where a large area is needed but single crystal cannot be made, or would be prohibitively expensive. The alternative to an amorphous solid is a polycrystalline film, with many GBs between the crystallites. Such GBs can have a very deleterious effect on the electrical behaviour of a semiconductor, since they form traps for electrons and holes, and centers where they can recombine.

GBs are also present at interfaces, especially, when looking at a surface of a polycrystalline material. I will highlight the characteristics of surfaces in the next section.

## 2.3 Surface

The ideal surface is defined as the planar termination of the bulk crystal. However, in practice, surfaces may exhibit significant roughness, which is known to possess their own point defects and impurities. Exceptional smooth surfaces are represented by materials such as highly oriented pyrolytic graphite (HOPG) and monocrystalline silicon. The electronic structure of a surface is important because it may control the way in which molecules adsorb and react. For these reasons surfaces have been the subject of intensive research in recent years and specially for microscope users. In this section, the focus will be on surface-related semiconductor physics, a critical component of the understanding of the research topics of this PhD Thesis.

### 2.3.1 The work function

A reference point for energies within a solid is the FERMI level  $E_F$ . Outside the solid, however, the natural zero of energy is the vacuum level  $E_{vac}$ . This is the energy of an electron at rest and infinitely far away from the surface and any electrical charge. The relation between the two energies is given by the work function  $\Phi$  shown in Equation (2.11)

$$\Phi = E_{vac} - E_F \quad (2.11)$$

Besides the energy of electrons in the bulk of the solid, also various surface effects have influence to the local work function  $\Phi$ , so that different crystal faces of the same solid may have different work functions.

### 2.3.2 Surface electronic states

Because the atoms on the surface are in a different environment from those of the bulk solid, there are a distinct electronic levels associated with a surface, similar to those produced by

defects. In the case of covalent solids, the reduction in coordination is anticipated to result in the formation of dangling bonds. The atoms may undergo a relaxation from their ideal bulk position, thereby stabilizing the filled levels. For surfaces that are clean and flat, there is less change in the electronic structure compared to the more significant changes that occur when the surface is rough or has defects present on it. For example, in the structure of strontium titanate ( $\text{SrTiO}_3$ ), oxygen vacancies can be introduced by Ar etching, which removes oxygen more easily than it does with the heavier elements, resulting in a reduction of some surface titanium from  $\text{Ti}^{4+}$  to  $\text{Ti}^{3+}$ . In the case of a study by KLASSEN ET AL. of a  $\text{TiO}_2$  interface, Ar-etching removes oxygen-atoms and can be repaired by ultraviolet (UV)/Ozone ( $\text{O}_3$ ) treatment.<sup>157</sup> Surface defects such as these are quite important, since they may often be the sites at which catalytic reactions take place, or these defects are recombination centers.

### 2.3.3 Band bending at semiconductor surfaces

In the bulk of a semiconductor, the position of the FERMI level is controlled by the energy levels introduced by doping. At the surface, the energies of the surface states and adsorbates, as well as the energy of the FERMI level relative to the band edges, play a significant role because they can differ from the bulk. However, in equilibrium, the FERMI level needs to be the same throughout the solid. Therefore, the band energies at the surface must be different. This is called band bending and describes a semiconductor with surface states in the band gap. An overview of the effect in the band alignment is shown in Figure 2.6.

Electrons and holes are moving towards the depletion and/or accumulation layer and forming an unbalanced electric field that shifts the band energies.

The degree of band bending depends on the amount of charge transferred to the surface and is therefore a result of charge accumulation.<sup>151</sup> The variation of the electrostatic potential  $V$  is given in terms of the charge density  $\rho$  and the relative dielectric constant  $\varepsilon_r$  of the medium by POISSON'S equation:

$$\frac{d^2V}{dx^2} = \frac{\rho}{\varepsilon_0 \varepsilon_r} \quad (2.12)$$

The two boundary conditions for Equation (2.12) are that the potential is zero in the bulk and assuming there is no electric field away from the depletion layer. We end up with a total band bending  $V_0$  at the surface of

$$V_0 = \frac{\rho}{2 \varepsilon_0 \varepsilon_r w^2} \quad (2.13)$$

with  $w$  the width of the layer. When the band bending in the junction corresponds to the normal equilibrium value there is no potential, since the effective energy of electrons and holes reaching each electrode is the same. In order to do electric work, the photocell must generate

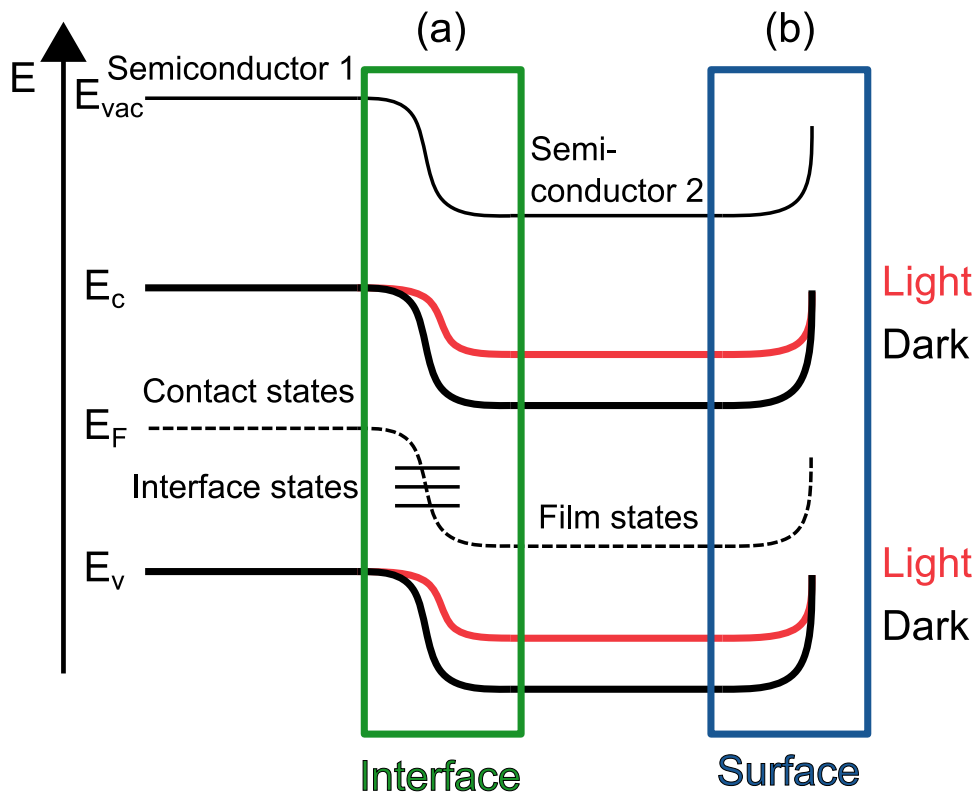


**Figure 2.6:** Energy band alignment illustration for two semiconductor heterojunction. (a) Band bending shown at the interface between two semiconductors and (b) the band bending at the surface of a n-type semiconductor.<sup>98</sup>

a potential. This will reduce the band bending in the junction. Some current will flow so long as the potential developed by the cell does not completely eliminate the bending necessary to separate the carriers. Since the equilibrium band bending is determined by the difference of FERMI levels in the n- and p-type materials, it is the difference that controls the maximum voltage obtainable from a single junction. The band gap of the semiconductor must obviously be low enough for a reasonable proportion of photons to be absorbed. Normally, solids with a band gap less than 3 eV can be used, due to the radiation spectrum of the sun. The occupancy of the surface states can be altered by the adsorption of molecules from the gas phase. But in most of the applications, it is the interface between the semiconductor and some other medium that is important.<sup>158</sup>

In the next section I want to go into detail how photovoltaics work and which semiconductor materials are used for them.

## 2.4 Working principles and fundamentals of photovoltaics and solar cells

The internal photoelectric effect is a fundamental process that enables the conversion of solar radiation into electricity by solar cells and modules.<sup>27</sup> Consequently, each solar cell must contain a photovoltaic active absorption material that can efficiently absorb the incoming light and generate mobile charge carriers, such as electrons and holes, which can be transported at the cell's terminals with minimal energy dissipation.<sup>159</sup> The extraction of these electron-hole pairs and the subsequent circulation through an external load result in a net delivery of electric power, with no other change in the device.<sup>27,160</sup> This is generally accomplished by utilizing semiconductor materials, as previously outlined in Section 2.2.

### 2.4.1 Light absorption

The band gap of the semiconductor is the most significant factor in determining the efficiency of a solar cell material. Sunlight is absorbed only when the energy is sufficiently significant to cause an electron transition from the VB to the CB. Given the fixed spectrum of solar radiation, the band gap of the semiconductor plays a key role in determining the maximum achievable efficiency of a single junction solar cell. A reduced band gap in a semiconductor results in an increased number of free charge carriers. However, this also leads to a decreased electrochemical potential difference.<sup>151</sup> Conversely, an augmented band gap results in a reduced number of free charge carriers, along with an increased electrochemical potential difference.<sup>151</sup> Therefore, the existence of an optimal band gap is a crucial property that governs the efficiency of the system. The limit is denoted as radiative efficiency<sup>1</sup> limit.<sup>162,163</sup> This maximum possible efficiency is reached when there is no non-radiative recombination and all of the generated carriers are either gathered as current or recombined and emit one photon per electron-hole pair.<sup>105,163,164</sup> The maximum radiative efficiency limit lays at 33.2% with a band gap of 1.34 eV.<sup>165</sup>

### 2.4.2 Quasi-Fermi level splitting (QFLS) after light absorption

As demonstrated in Section 2.2.1, the successful absorption of a photon and the subsequent formation of an electron-hole pair result in the modification of the Fermi level. This modification can be utilized for powering external systems or can be lost through recombination processes, as outlined in Section 2.2.5.<sup>27</sup> At ambient temperature, the solar cell is in a thermal equilibrium,

---

<sup>1</sup>The radiative efficiency limit was formally known as the SHOCKLEY–QUEISSER limit, but because SHOCKLEY had an advance racist ideology,<sup>161</sup> I will use the term radiative efficiency limit.<sup>162</sup>

due to the FERMI-DIRAC distribution (see Equation (2.3) in Section 2.1.2). In equilibrium, the FERMI level  $E_F$  of a semiconductor is unique, indicating that the electrochemical potentials of electrons and holes ( $\mu_{e,h}$ ) are equal. However, upon illumination or applied voltage, an excess population of photogenerated carriers—electrons and holes—is generated within the semiconductor. This deviation from the equilibrium FERMI-DIRAC distribution results in the emergence of two independent quasi-FERMI levels. The electron quasi-FERMI level ( $E_{F_e}$ ) and the hole quasi-FERMI level ( $E_{F_h}$ ), respectively.<sup>27</sup> The phenomenon is referred to as quasi-FERMI level splitting (QFLS) and is described by Equation (2.14).<sup>27,151</sup>

$$\mu_{e,h} = \mu_e + \mu_h = E_{F_e} - E_{F_h} \quad (2.14)$$

The quasi-FERMI level splitting is shown in Figure 2.7 and gives an illustration of a diode with contact layers with different work functions. After all materials have been brought into contact,

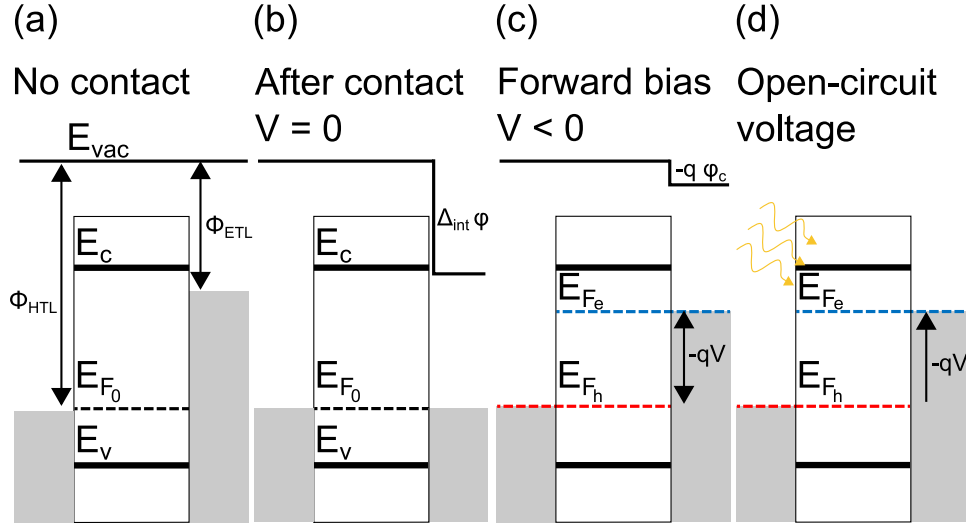


**Figure 2.7:** Schematic illustration of energy diagram of a semiconductor layer with CB for electrons  $E_C$  and VB for holes  $E_V$  and two contacts: an electron selective contact (ETL) with work function  $\Phi_{ETL}$  and hole selective contact (HTL) with work function  $\Phi_{HTL}$ . The contacts are considered as metals in which the carrier energy level is at the respective FERMI level. Contacting, forward bias voltage or light illumination modifies the FERMI level of the ETL with respect to  $E_C$ , while holes remain at equilibrium at the left contact (HTL). (a) Energies of the separate materials. (b,c) Different situations of bias voltage  $V$  indicating the FERMI levels of electrons ( $E_{F_e}$ ) and holes ( $E_{F_h}$ ). In (d), the semiconductor is illuminated and minority carrier generation raises the FERMI level of electrons consequently producing a photovoltage (SPV).<sup>27</sup>

we see an equalization of the materials on an identical FERMI level (see Figure 2.7(b)).<sup>151</sup> This equalization process can occur by band bending in the absorber layer or by changing the vacuum level,  $E_{vac}$ . Any potential drop (change in vacuum level) associated with an applied voltage will

occur exactly at this interface, as shown for the forward bias in Figure 2.7(c).<sup>151</sup> The internal chemical potential  $\mu_{e,h}$  is extracted and a voltage  $V$  generates which has the relation given in Equation (2.15) assuming low device thickness, high mobilities, no losses at interfaces, and neglecting surface recombination.<sup>27,151</sup>

$$q \cdot V = E_{F_e} - E_{F_h} \quad (2.15)$$

### 2.4.3 Separation via p-n- or heterojunction

A secondary significant factor for an efficient solar cell material is the fitting band energies of the contact layers. The discrepancy in the electrochemical potential shown in Section 2.4.2 necessitates a conversion into a voltage through the diode configuration of the solar cell.<sup>27</sup> This diode structure provides directionality for the carrier flow with respect to the external contacts.<sup>27</sup> Electrons exhibit this directionality either via a p-n junction (see Section 2.2.4) or with selective contacts (called heterojunctions), which require a correct band alignment.<sup>27,166</sup>

It is imperative to note that electron-hole recombinations (covered in Section 2.2.5), known as loss mechanisms, are unfavorable processes. The impact of defects, which result in the elimination of carriers, is a key factor in the reduction of efficiency. This necessitates the utilization of a defect-free semiconductor to ensure an effective conversion process in solar cells.<sup>151</sup> Therefore, the control of defects, non-radiative recombination, and interfacial losses is a crucial aspect for the functionality of solar cell materials.<sup>151</sup>

### 2.4.4 Semiconductor materials used in solar cells

Currently, the photovoltaic market is primarily controlled by crystalline silicon solar cells, which have reached power conversion efficiencies (PCE) of around 22.6%. For a silicon heterojunction solar cell the PCE is at 27.6% due to six decades of research.<sup>137,167,168</sup> However, the potential of these cells is restricted by the indirect band gap of silicon and there has been limited progress in improving their efficiencies over the last five years. Presently, the highest performing single-junction solar cells are those that contain GaAs. The efficiency of these devices has been demonstrated to be close to the radiative efficiency limit of 33%, with a measured efficiency of  $\approx 30\%$ .<sup>162,163,165,168</sup> Due to seven times higher costs of raw materials for GaAs solar cells,<sup>168,169</sup> their feasibility is limited for example to extraterrestrial applications where efficiency is more important than cost.<sup>168,170</sup>

In the past decade, hybrid halide perovskite solar cells (PSCs) have become a viable alternative to traditional silicon-based solar cells.<sup>168</sup> Research interest in this field has led to a high

efficiency of 27.0 %<sup>137</sup> for single junction PSCs<sup>168</sup> and 34.6 % for perovskite/silicium hybrid tandem cells.<sup>137</sup> Metal halide perovskites possess exceptional properties for optoelectronic devices, including photovoltaic solar cells and light-emitting diodes (LEDs).<sup>103,105</sup> This is attributed to the simplicity of their fabrication process, which can also be easily modified to adjust electrical and optical properties.<sup>103,105</sup>

In the next section I want to go into detail into the PSCs, due to their relevance to this PhD Thesis.

## 2.5 Halide perovskites and perovskite solar cells

Perovskite solar cells (PSCs) is a type of photovoltaic cell that utilizes the halide perovskite material as the photoabsorbing material. This semiconductor material has many of the ideal characteristics for a solar absorber, such as a direct band gap in between 1.45 eV for formamidinium lead iodide (FAPbI<sub>3</sub>) (FAPbI<sub>3</sub>) and 1.55 eV for methyl ammonium lead iodide (MAPbI<sub>3</sub>) (MAPI), close to the optimum in the radiative efficiency limit.<sup>162,163</sup> Also, PSCs have small exciton binding energies, high levels of defect self-regulation, exceptional charge carrier diffusion lengths, and outstanding charge carrier mobilities.<sup>168,171–178</sup> That are some of the reasons it was studied intensively in the last two decades.

### 2.5.1 Crystal structure of halide perovskites

The first halide perovskite material to be used in solar cells was MAPI and introduced by KOJIMA ET AL.<sup>136</sup> The perovskite structure derives its nomenclature from the mineral calcium titanate (CaTiO<sub>3</sub>), which was first discovered by GUSTAV ROSE in the Ural Mountains and subsequently named after LEV PEROVSKI.<sup>151,179</sup> The general crystal structure of halide perovskite materials is based on the molecular formula ABX<sub>3</sub> and shown in Figure 2.8. Thereby the A-cation mostly represents the MA-cation (CH<sub>3</sub>NH<sub>3</sub><sup>+</sup>), but also the formamidinium (FA)-cation (CH(NH<sub>2</sub>)<sub>2</sub><sup>+</sup>). The B-cation represents lead ions (Pb<sup>2+</sup>) and in a few cases tin ions (Sn<sup>2+</sup>), manganese (Mn<sup>2+</sup>), or germanium ions (Ge<sup>2+</sup>).<sup>103,183</sup> In accordance to its name, the X in the molecular formula stands for halides such as iodine (I<sup>-</sup>), bromine (Br<sup>-</sup>) or chlorine (Cl<sup>-</sup>).<sup>103,105</sup> In detail it consists of [BX]<sup>2-</sup> octahedras surrounded by A<sup>2+</sup> cations. In case of MAPbI<sub>3</sub>, it consists of [PbI<sub>6</sub>]<sup>-</sup> octahedras surrounded by MA<sup>+</sup> cations (see Figure 2.8).<sup>184</sup>

The term "perovskite" is now applied to any crystalline solid that exhibits a similar crystal structure. This encompasses oxide perovskites, such as BaTiO<sub>3</sub> or PbTiO<sub>3</sub>, among others.<sup>151,185</sup> In a manner akin to oxide perovskites, alternative perovskite configurations may be established, exhibiting varied oxidation states, a phenomenon exhibited by halide perovskites.<sup>151</sup>

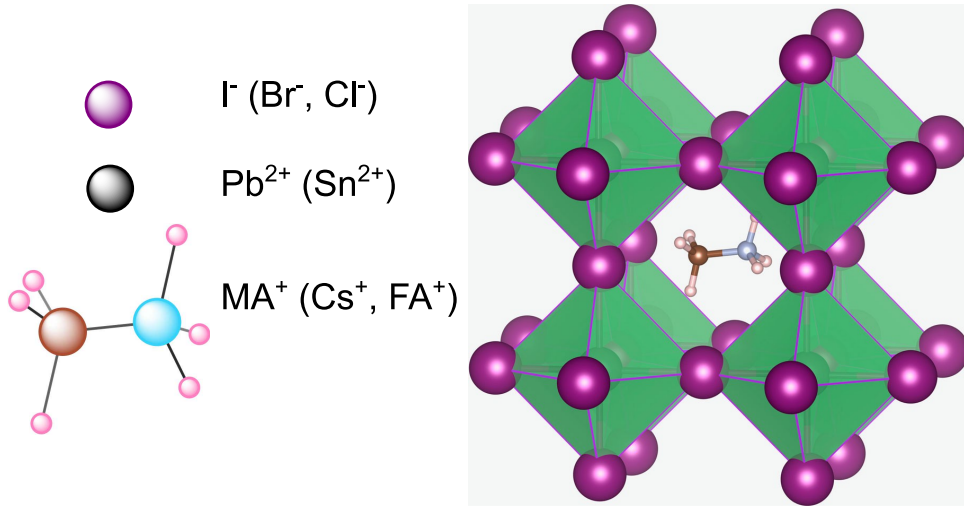


**Figure 2.8:** Crystal structure of metal halide perovskites of the molecular formula  $ABX_3$  in the cubic phase ( $T > 330$  K). A methylammonium (MA) molecule occupies the A site in the crystal surrounded by 12 direct iodine neighbor atoms and corner-linked octahedra. The octahedra are built up by the iodine atoms (purple) sitting on the A-position. The lead atoms (black) form the centers of the octahedra on the B-position.<sup>105,180–182</sup>

Substitutions of the organic cations with caesium ( $\text{Cs}^+$ ) or rubidium ( $\text{Rb}^+$ ) cations lead to improved stabilities of the resulting solar cells.<sup>103,105</sup> By varying the halide composition, the optical band gap can be changed from 1.6 eV to 2.3 eV,<sup>103</sup> and thus the maximum possible efficiency of the absorption material can also be changed via the above mentioned radiative efficiency limit.<sup>162,163</sup> An illustration of the crystal structure can be seen in Figure 2.8.<sup>105</sup> The advantages of the halide perovskite material are the high absorption coefficient,<sup>186</sup> low electron-hole binding energies,<sup>187</sup> long charge carrier diffusion lengths,<sup>188</sup> direct and tunable band gaps,<sup>189</sup> and indifferent electronic properties in presence of bulk defects, namely defect tolerance.<sup>151,190</sup> Furthermore, the ease with which these thin films can be produced from solution renders this group of materials well suited for low-cost and large-scale manufacturing and they have been proven to perform well with a variety of hole and electron contact materials, making them suitable for a wide range of applications.<sup>151,168,191–193</sup>

However, the inherent long-term stability under ambient conditions of the MAPI structure and halide perovskites in general is poor<sup>168,194–196</sup> and, despite ongoing efforts, remains a significant challenge for the hybrid perovskite community.<sup>168,197–199</sup> Additionally, the presence of a high defect density at layer interfaces,<sup>200</sup> grain boundaries,<sup>201</sup> and ion migration<sup>202</sup> during device operations has been observed to hinder their performance in practical applications.<sup>151</sup> The composition of MAPI has undergone significant changes since it was first proposed as a

solar cell material. Currently, triple cation and mixed anion materials are commonly used in solar cells. Perovskite materials with triple cations [(MA/FA/Cs)Pb(I/Br)<sub>3</sub>], and those with quadrupole cations [(MA/FA/Cs/Rb)Pb(I/Br)<sub>3</sub>] in which Rb serves as an additional cation, have gained significant attention due to their stability over time and high cell efficiency.<sup>101</sup>

The GOLDSCHMIDT tolerance factor is a quantitative indicator of the stability and distortion of the perovskite structure. It is measured by the parameters of the ions involved.<sup>151</sup> This estimation is based on the ionic radii of the components.<sup>151</sup> Equation (2.16) gives the GOLDSCHMIDT tolerance factor.<sup>203</sup>

$$\tau = \frac{r_A + r_X}{\sqrt{2}(r_B + r_X)} \quad (2.16)$$

where  $\tau$  is the tolerance factor and  $r_A$ ,  $r_B$ , and  $r_X$  stand for the ionic radii of A, B, and X ions, respectively.<sup>151</sup> The value of the parameter  $\tau$  is a factor in determining the feasibility of the perovskite structure formation.<sup>151</sup> It has been observed that if the parameter  $\tau$  ranges between 0.8 and 1, the formation of the perovskite structure is favored.<sup>203</sup> Furthermore, it has been demonstrated that values of  $\tau$  between 0.9 and 1 result in the formation of a cubic perovskite structure, while values between 0.8 and 0.9 yield distorted perovskite crystals.<sup>151,204</sup> According to the  $\tau$  values, the ions in a perovskite structure can be substituted with ions mentioned above. By exchanging the  $A^+$  with larger inorganic or organic cationsthis may lead to unstable or metastable perovskite phases due to the  $\tau$  value.<sup>151,183</sup>

## 2.5.2 Electronic Structure of halide perovskites

It is important to note that, e.g., in organic absorption materials, the majority of light absorption processes result in the formation of excitons and a preliminary step of charge separation is necessary to dissociate these excitons into free carriers as well as a direct band gap, to allow the direct excitation with light. Therefore, the band alignment is very important to ensure the extraction of charge carriers. The band alignment of a typical PSC is demonstrated in Figure 2.9. Halide perovskites are direct band gap semiconductors that demonstrate strong absorption in the visible or near-infrared portion of the electromagnetic spectrum.<sup>151,206,207</sup> Their high optical absorption coefficients allow for efficient light absorption even in thin active layers, consequently making them excellent candidates for use as an active layer in solar cells or photodetectors.<sup>151</sup>

Charge-selective contacts can affect the photogenerated electron-hole population through electron and hole extraction, non-radiative recombination due to interfacial defects, and charge accumulation in the contacting semiconductor. The band alignment (see Figure 2.9) allows electrons to relax to the CB of the ETL instead of the VB of perovskite, which enhances

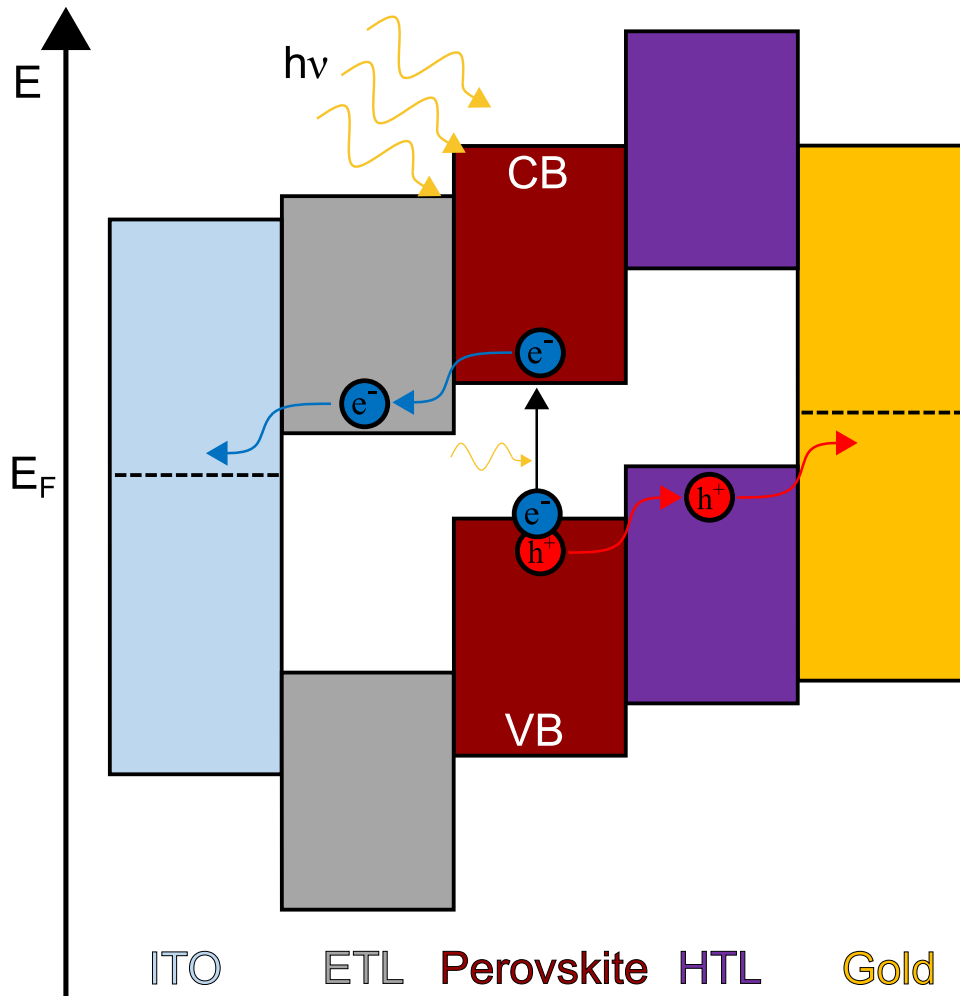


**Figure 2.9:** Band diagram of a typical perovskite solar cell. Light passes through the indium tin oxide ( $\text{In}_2\text{O}_3 \cdot (\text{SnO}_2)_x$ ) (ITO) layer and the ETL and is absorbed by the perovskite layer (red), where an electron is promoted from the VB into the CB as indicated by the arrow in between the valence and CB. Excited electrons can migrate into the CB of the electron transport layer. Since the hole transport layer has no corresponding energy level, that layer act as an electron blocking layer. The photon-generated electrons migrate from the ETL into the bottom electrode, the ITO. The remaining hole in the VB of the perovskite layer is filled with electrons from the VB of the hole transport layer. This process corresponds to migration of holes from the perovskite layer into the hole transport layer (violet). Since the ETL has no corresponding energy level, that layer acts as a hole blocking layer. The holes migrate from the hole-transporting layer (HTL) into the gold electrode.<sup>205</sup>

electron extraction and charge carrier lifetime. Similarly, the bands of HTL stand at a higher energy level compared to the that of perovskite layer. Therefore, the photo-generated holes move towards the HTL.

The VB of halide perovskites formed by anti-bonding of s-orbital from  $B^{2+}$  cation and p-orbital from  $X^{-}$  halide. The CB consists of anti-bonding p-orbitals from  $B^{2+}$  cation and  $X^{-}$  halide.<sup>151,208,209</sup> Ion substitution in halide perovskites modify their band structure. Substitutions of the  $B^{2+}$  cation or  $X^{-}$  anion directly impact this structure. As the halide undergoes a replacement from  $Cl^{-}$  to  $Br^{-}$  and consequently to  $I^{-}$ , the energy of the p-orbital increases.<sup>151,210</sup> This increase in energy leads to an enhancement in the VB maximum, which is also referred to as the band gap reduction.<sup>151,210</sup> A comparable phenomenon occurs when  $Pb^{2+}$  is substituted with  $Sn^{2+}$ .<sup>151,211</sup> This results in an increase of the s-orbital, leading to a decrease in the band gap.<sup>151,211</sup> The ability to manipulate the composition of metal halide perovskites allows for precise control over their band gap, which can be adjusted to encompass a wide spectral range.<sup>151</sup> For example, the wide band gap of  $MAPbCl_3$  (3.11 eV) can be decreased to 2.35 eV for  $MAPbBr_3$ , and further to 1.55 eV for  $MAPbI_3$ . By means of partial substitution, the band gap of the material can be tuned between these values, thereby enabling coverage of nearly the entire visible spectrum.<sup>151,212–214</sup>

### 2.5.3 Architecture of perovskite solar cells

PSCs are typically based on three device architecture type. These are p-i-n, n-i-p mesoporous, and n-i-p planar solar cells. The n, i, and p represent the n-type, intrinsic, and p-type semiconductor material, respectively. A typical n-i-p PSC illustration is given in Figure 2.10. Here,

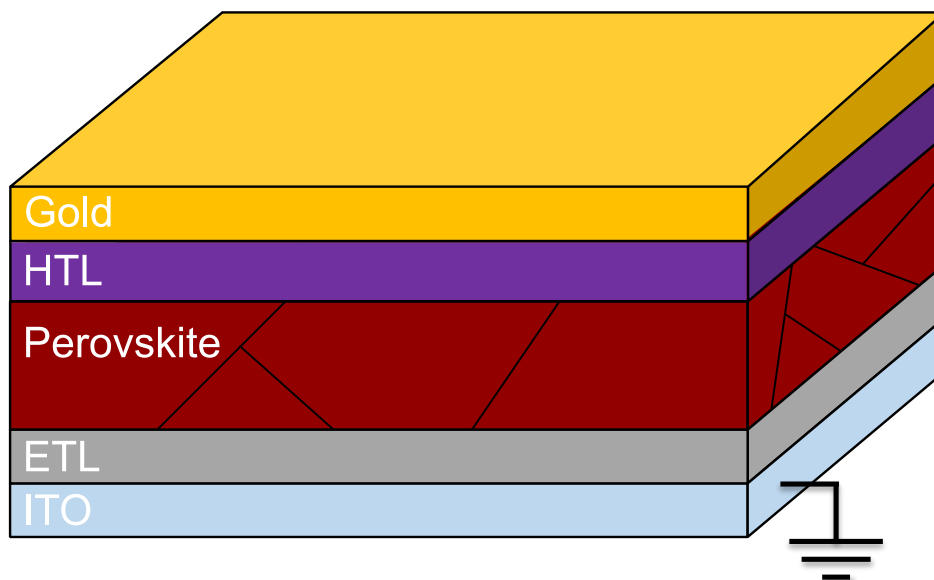


**Figure 2.10:** Typical architecture for a PSC.

ETL is coated on top of indium tin oxide ( $In_2O_3 \cdot (SnO_2)_x$ ) (ITO) or fluorine doped tin(IV) oxide;

(F@SnO<sub>2</sub>) (FTO). The most common ETL materials for n-i-p PSCs are TiO<sub>2</sub> and SnO<sub>2</sub>.<sup>215</sup> The perovskite absorber layer is coated on an ETL and then a HTL is coated on top of perovskite. The typical HTL materials for n-i-p PSCs are Spiro-OMeTAD and poly[bis(4-phenyl)(2,4,6-trimethylphenyl)amine (PTAA)].<sup>216</sup> Lastly, a metal layer (gold, silver, aluminium, copper etc.) is evaporated on top of the PSC as an electrode.<sup>217</sup> When the ETL in a n-i-p PSC includes a mesoporous component to improve the contact and charge extraction from the perovskite layer, the device architecture is named mesoporous n-i-p PSC. Usually TiO<sub>2</sub> based PSCs are built as mesoporous n-i-p PSCs which consists of a compact TiO<sub>2</sub> and on top a mesoporous TiO<sub>2</sub> layer.<sup>218</sup> On the other hand, SnO<sub>2</sub> based PSCs are usually built as planar n-i-p PSCs.<sup>219</sup> If a HTL is coated on top of ITO or FTO to be further coated by the perovskite layer, then the device is called a p-i-n PSC. The common HTLs for p-i-n PSCs are NiO<sub>x</sub><sup>220</sup> or PTAA<sup>221</sup> whereas common ETLs for p-i-n PSCs are C<sub>60</sub>/bathocuproine (2,9-Dimethyl-4,7-diphenyl-1,10-phenanthroline) (BCP) or [6,6]-phenyl-C<sub>61</sub>-butyric acid methyl ester (PCBM).<sup>151,222</sup>

The band alignment (see Figure 2.9 in Section 2.5.2) is responsible for the desirable charge extraction from the absorption material. Therefore, the ETL/perovskite and perovskite/HTL interfaces are extremely important regarding the efficiency of a PSC. The defects at the devices interfaces can act as non-radiative recombination sites and decrease the efficiency of the device. To counter this issue, the contact layers can be improved<sup>223</sup> or thin interlayers between perovskite and the contact layers can be formed.<sup>224</sup>

PSCs are used in this thesis as a photoactive model system in order to investigate new AFM methods and have insights into a photoactive material on the nanoscale.

## 2.5.4 Defects in perovskite solar cells

The presence of defect states in a semiconductor material, mentioned in Section 2.2.2, particularly in halide perovskites, can impede the functionality of certain applications due to the trapping of excited charge carriers, as discussed in Section 2.2.3. As we saw in Section 2.2.3, the trapping behavior and its consequences in the band structures of VBs and CBs are determined by the changes in the FERMI level due to the trapped charges or empty defect levels. In halide perovskites, deep traps can occur due to interstitials. However, the most common defect type is the point defect, which leads to the formation of shallow trap states because they have a low formation energy.<sup>151,225</sup> These defects typically do not compromise the performance of perovskite-based devices. While the bulk of halide perovskites exhibit defect tolerance, their surfaces are more susceptible to deep traps due to surface defects.<sup>151,226</sup> Consequently, high defect areas, such as GBs, have been identified as contributing to trap-assisted recombination<sup>227,228</sup> and ion migration.<sup>151,229–231</sup>

### 2.5.5 Performance, stability, and passivation of perovskite solar cells

One of the major challenges facing the commercialization of PSCs is the instability of the material.<sup>105,232</sup> Unlike calcium titanate ( $\text{CaTiO}_3$ ) or barium titanate ( $\text{BaTiO}_3$ ), hybrid organic-inorganic perovskites experience instability on a wide range of time scales, from nanoseconds to days. This instability is caused by various environmental factors, including oxygen,<sup>105,232</sup> water or moisture,<sup>105,232</sup> applied voltage, temperature or thermal stress,<sup>105,232</sup> and/or light.<sup>103,105</sup> During this process, the material reacts with the water to form  $\text{PbI}_2$  and methylammonium iodide (MAI) or formamidinium iodide (FAI). Iodides of the MA and FA cations may also evaporate out of the perovskite layer.<sup>105,233</sup> Moisture can also penetrate through the surface of the film, migrate along the GBs, and ultimately degrade the entire film.<sup>105,233</sup>

Furthermore, the movement of ions within the perovskite crystal lattice, known as ion migration, has also been demonstrated to affect the performance, efficiency, and stability of PSCs by influencing the charge carrier recombination dynamics and the transport properties of the perovskite material.<sup>151,234</sup> It is therefore essential to develop effective strategies for the control of ion migration to enhance the performance and stability of PSCs.<sup>151</sup> The mechanisms of ion migration in PSCs are influenced by both intrinsic and extrinsic factors.<sup>151</sup> Intrinsic factors include the presence of defects in the perovskite crystal lattice, such as vacancies or interstitials, which can create a gradient of ion concentration and lead to ion migration.<sup>151,225</sup> Extrinsic factors, such as the presence of external electric fields, thermal gradients, or light irradiation, can also induce ion migration in PSCs.<sup>151,235</sup> There are several ways to prevent this degradation. One approach is to chemically encapsulate or confine the PSCs by using hydrophobic materials on the surface of the perovskites, which prevents the penetration of molecules such as water, oxygen, or iodide ions.<sup>105,232</sup> This is called surface passivation. Additionally, the introduction of diverse cations, the incorporation of supplementary materials into the perovskite structure, the utilization of interface layers, and the refinement of device fabrication conditions have been demonstrated to diminish ion migration, thereby enhancing device performance and stability.<sup>151</sup> The post-treatment of perovskite films is a well-established strategy for suppressing interfacial recombination and optimizing the performance of PSCs.<sup>97,236–243</sup>

There are several prominent examples of tailored passivation schemes, including the use of (alkyl)ammonium salts,<sup>10–13,244–270</sup> other organic compounds,<sup>271–281</sup> and fluoride-containing materials.<sup>1,5,8,97,270,280,282,283</sup> In the case of  $\text{CsPbI}_3$ , an attempt was made to cover the  $\alpha$  phase of the surface with a protective capsulation by using Phenylethylammonium ( $\text{Ph}-\text{C}_2\text{H}_4-\text{NH}_3^+$ ) ( $\text{PEA}^+$ ) cations. This resulted in cells being stable for several months.<sup>105,232</sup>

In conjunction with established chemical passivation techniques, which have been demonstrated to reduce the density of surface/interface defects,<sup>97,263,277,279,284</sup> this strategy also en-

hances performance through the formation of 2D/3D heterostructures.<sup>13,246,247,251,255,257–259,263,266</sup> These heterojunctions can be caused by varying the cation composition at the surface or by building 2D / 3D stacking structures to change the dimensionality of the perovskites<sup>105,232</sup> or combinations of two-dimensional and 3D structures.<sup>105,233</sup> 2D perovskites of MAPI with PEA cations as spacers of the form  $(\text{PEA})_2(\text{MA})_2\text{PbI}_{10}$  exhibited superior moisture stability, too.<sup>105,232</sup> Furthermore, the performance can be enhanced by wide-band gap interface layers.<sup>97,250,253,285,286</sup> The latter enhancements can be the result of improved energy level alignment that promotes selectivity and carrier transport across perovskite/charge transport layer (CTL) interfaces and/or a reduced probability for interfacial recombination due to charge blocking.<sup>5,13,97,248,272,284,287,288</sup>

### 2.5.6 Illumination of perovskite solar cells

When a PSC is illuminated, an additional offset potential from the quasi-FERMI level splitting increases the CPD.<sup>103</sup> This additional potential is called surface photovoltage (SPV). This is illustrated in Figure 2.7(d) by the value  $-q \cdot V$  for the FERMI level separation which is described by  $\Delta\mu$ .<sup>289</sup>

A detailed discussion about SPV is after explaining what CPD is and how to measure it in Section 2.6.10.

## 2.6 Characterization Methods

As demonstrated above, modern energy devices, such as batteries and solar cells like PSCs, often consist of a combination of organic, hybrid organic or monomolecular films. Here interfaces and surfaces between the different materials play an important role, as they can be the source of efficiency losses through charge carrier recombination, series resistance or chemical reactions and degradation. In this section, I will focus on Atomic Force Microscopy (AFM), which is a powerful tool to investigate structural and electronic properties at interfaces.<sup>98,105,157,205,290</sup> In particular, the electrical modes, such as conductive Atomic Force Microscopy (c-AFM), Electrostatic Force Microscopy (EFM), Kelvin Probe Force Microscopy (KPFM), and Scanning Capacitance Microscopy (SCM) combine the lateral resolution with electrical information of the material. Here, I will introduce the AFM itself, the working mechanism behind electrical AFM modes and discuss the limitations in terms of resolution and imaging artifacts. In addition, I will discuss the capabilities of static and dynamic measurements by discussing examples from the field of PSCs and silicon based devices such as capacitors.

### 2.6.1 Atomic Force Microscopy

Atomic Force Microscopy (AFM) is a type of scanning probe microscopy that visualizes and measures surface features on the nanoscale.<sup>105,291</sup> The invention of the Scanning Tunneling Microscopy (STM)<sup>131</sup> and the following invention of the AFM (also named Scanning Force Microscopy (SFM)) by BINNIG ET AL.<sup>133</sup> was the starting point for modern surface science.<sup>132</sup> It works by using a probe, typically made of a sharp tip attached to a flexible cantilever, to scan the surface of a sample.<sup>105,291</sup> The setup is shown in Figure 2.11. The AFM measures the

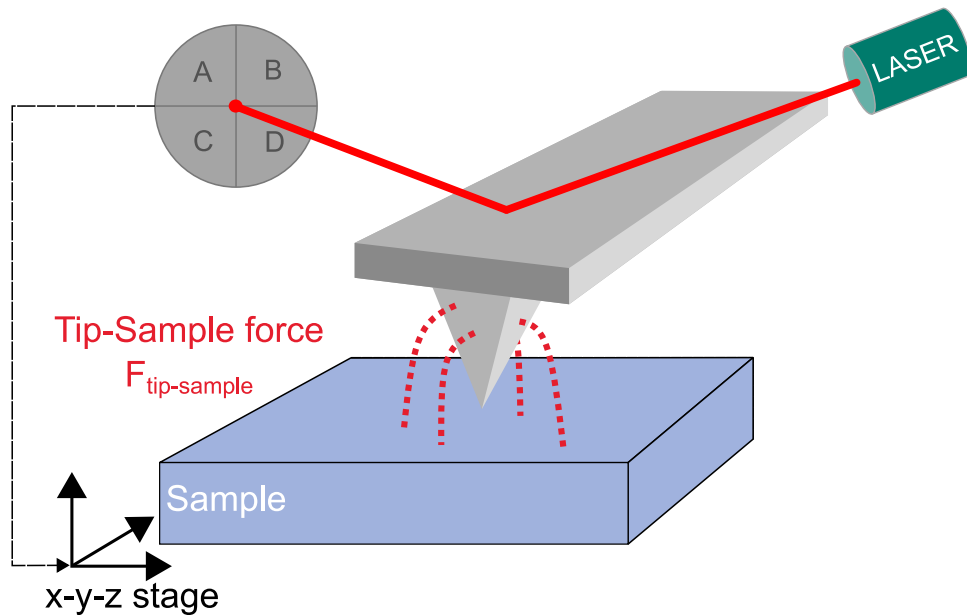


**Figure 2.11:** Fundamental setup of a contact mode AFM during operation.<sup>132,292–295</sup>

tip-sample interaction, e.g., via an optical beam deflection system (shown in Figure 2.11).<sup>296</sup> This optical lever system reflects a laser beam on the backside of the cantilever, effectively magnifying the small cantilever deviations with the four phase photo diode caused by the interactions between the tip and the sample (see Figure 2.11).<sup>291</sup> While the probe is moving over the surface of the sample in a raster pattern by the nano-positioning system, the force between the tip and the sample gets measured via this optical lever system.<sup>105,294</sup> With the help of the HOOK's law the tip-sample force  $F_{\text{tip-sample}}$  between the tip and the sample surface can be calculated with the knowledge of the spring constant  $k$  and the bending distance in  $z$  via  $F_{\text{tip-sample}} = -k \cdot z$ .<sup>294</sup> The interaction between the tip and the sample is compensated by a feedback circuit that utilizes a piezoelectric element to displace the sample or tip in the  $z$ -direction. With the help of a force feedback loop, which maintain a specific force setpoint constant, the resulting topography corresponds to a contour at constant tip-sample force.<sup>294</sup>

Through that the AFM can therefore be utilized to generate a high-resolution map of the surface features of the specimen, including surface roughness, topography, and mechanical properties such as elasticity, HAMAHER constant, and adhesion.<sup>297</sup>

Most groups use AFM to characterize surface topography by keeping the tip-sample force constant with a feedback loop, due to an accuracy of typically less than one nanometer laterally and less than 1 nm vertically. However, AFM also enables to measure additional tip-sample interactions, which are related to the sample's functionality. AFM has a number of advantages over other microscopy techniques, including its ability to operate in a wide range of environments (including air, liquids, and vacuum), its high spatial resolution, and its ability to measure a variety of physical properties of samples.<sup>291</sup> It is widely used in a variety of fields, including materials science,<sup>97</sup> and biology<sup>298</sup> to study the structure and properties of materials on the nanoscale.

## 2.6.2 Basic modes in conventional Atomic Force Microscopy (AFM)

Here, I want to introduce the basic modes of every AFM.

Contact mode AFM is a method of measuring small bending of a scanning cantilever from its initial position. This is achieved by utilizing the aforementioned force-feedback circuit. The topography of the given sample is obtained by measuring the static deflection of the bending cantilever with a reflecting laser positioned at the tip of the cantilever. This deflection is then detected with a photodiode and the  $z$ -correction (height) of the scanned surface is plotted pixel by pixel. This is illustrated in Figure 2.11

Dynamical AFM employs oscillating cantilevers. There, the tip-sample interaction can be measured via the dynamic deflection via amplitude (amplitude modulation (AM)) or phase (phase modulation (PM)) changes of the cantilever oscillating at its resonance frequency.<sup>294</sup> Different AM modes, such as "intermittent contact", "tapping", or "oscillating" mode, use feedback controls to oscillate the cantilever at its resonant frequency and constant lock-in amplitude by detecting the change in the mechanical amplitude  $\Delta A_m$ .<sup>291,299</sup>

Other oscillating modes use feedback control through frequency (frequency modulation (FM)) or phase modulation (PM). The principle of frequency modulation detection is that any force gradient in the tip sample interaction will lead to a shift  $\Delta\omega$  of the cantilever's resonance frequency  $\omega_{\text{res}}$ .<sup>132</sup>

$$\frac{\Delta\omega}{\omega_{\text{res}}} = \frac{1}{2k} \frac{\partial F}{\partial z} \quad (2.17)$$

During the cantilever oscillation, a so-called phase-locked loop (PLL) tracks  $\Delta\omega$ . These dynamic modes allow for a gentler tip-sample interaction due to the shorter time of direct interaction

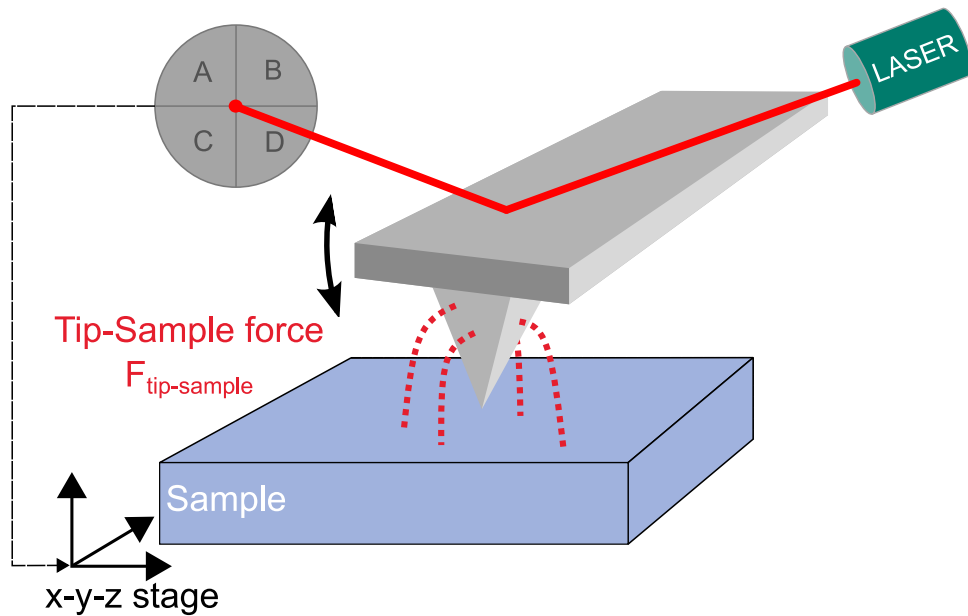


**Figure 2.12:** Fundamental setup of an dynamic / AC mode AFM during operation.<sup>132,292–295</sup>

and typically less force is needed to get into a stable contact, reducing in general the forces involved and the possibility for tip wear. Imaging modes relying on AM operation like amplitude modulation Atomic Force Microscopy (AM-AFM) are sensitive to tip sample forces, whereas FM modes like frequency modulation Atomic Force Microscopy (FM-AFM) are sensitive to force gradients, which usually leads to better spatial resolution.<sup>134,300–305</sup> FM-AFM is commonly used in ultra-high vacuum (UHV) and low-temperature physics,<sup>291,306</sup> as well as in biological applications.<sup>291,307</sup> However, in air and liquid, where the  $Q$ -factor is higher, force detection through AM-AFM is simpler and faster, and the amplitude changes with the tip-sample distance in a nearly monotonic manner.

An operation mode in between static and dynamic mode is the jumping mode (commercially called as PeakForce™ mode (PF mode), quantitative imaging (qi), or fast force mapping (FFM), ...),<sup>308</sup> where the tip performs a succession of force-distance curves at repetition rates of 100 Hz up to a couple of kHz. In torsional resonance mode, the tip vibrates laterally with respect to the surface, making this operation mode sensitive to lateral friction between tip and surface.<sup>294,309–311</sup>

### 2.6.3 Conductive Atomic Force Microscopy (c-AFM)

With conductive Atomic Force Microscopy (c-AFM), it is possible to probe the local electronic or ionic conductivity or capacitive currents<sup>312,313</sup> of the sample, although capacitive currents

only have minor influences on the steady-state photovoltaic operation.<sup>313</sup> In c-AFM, a voltage is applied between the sample and a conductive probe. A sensitive current amplifier, which is usually integrated into the cantilever holder, detects the tip-sample current and acts therefore as an "ampere meter" for collecting the current-voltage (I-V) response.<sup>28,314</sup> Depending on the conductivity and the probe bias, currents are on the order of fA up to  $\mu\text{A}$ . The most common

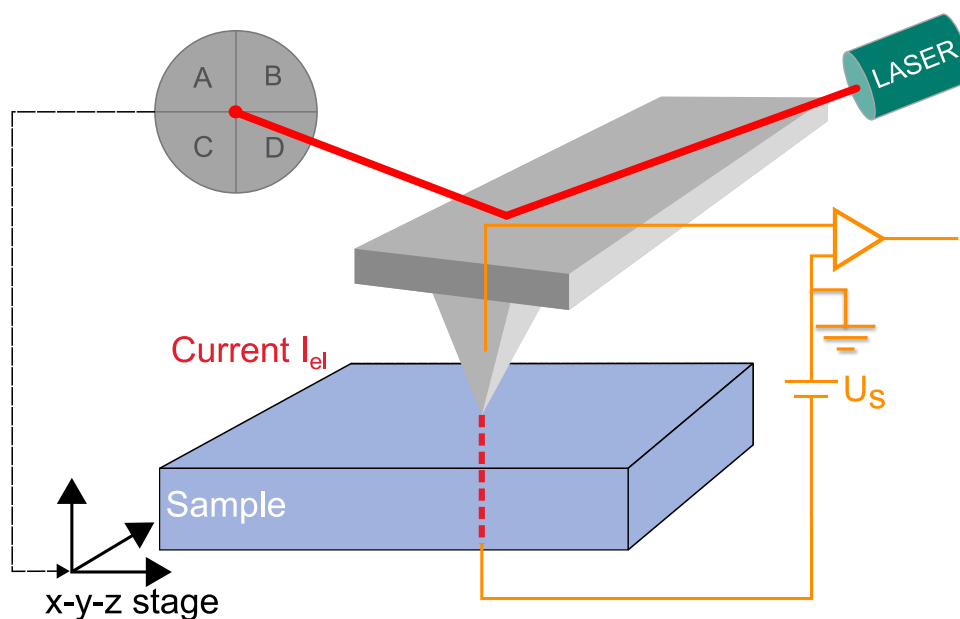


**Figure 2.13:** Fundamental setup of an c-AFM during operation.<sup>132,292-295</sup>

operation mode of c-AFM is contact mode, where the probe tip and the sample are in constant mechanical contact. However, high shear forces during the scanning motion of the tip make this method unsuitable for soft materials such as organic materials or nanorods. In the PF- or FFM-mode, the tip only touches the surface for a short time, reducing lateral forces that would damage delicate samples. Nevertheless, the contact time is long enough to measure a tip sample current.<sup>157,314-316</sup> Moreover, c-AFM can be used to measure photoconductivity of photo-active materials by measuring the current under light illumination.<sup>317,318</sup> A dynamic mode that still allows for a continuous electrical contact between tip and sample is the conductive time-resolved (tr) mode.<sup>309,310</sup> For energy research, c-AFM has become a powerful tool in investigating the underlying interplay between the topography and its electrical performance of organic solar cell materials, devices, and nanostructures.<sup>28,314</sup>

### 2.6.4 Electrostatic Force Microscopy (EFM)

When two semiconductors (in the form of tip and sample) with different work functions  $\Phi_{\text{tip}}$  and  $\Phi_{\text{sample}}$  (see Figure 2.14(a)) are electrically connected, their FERMI levels will align because electrons will move from the higher to the lower FERMI level (see Figure 2.14(b)), resulting in an electric field  $E$  between them. As long as the contact potential difference (CPD) is not

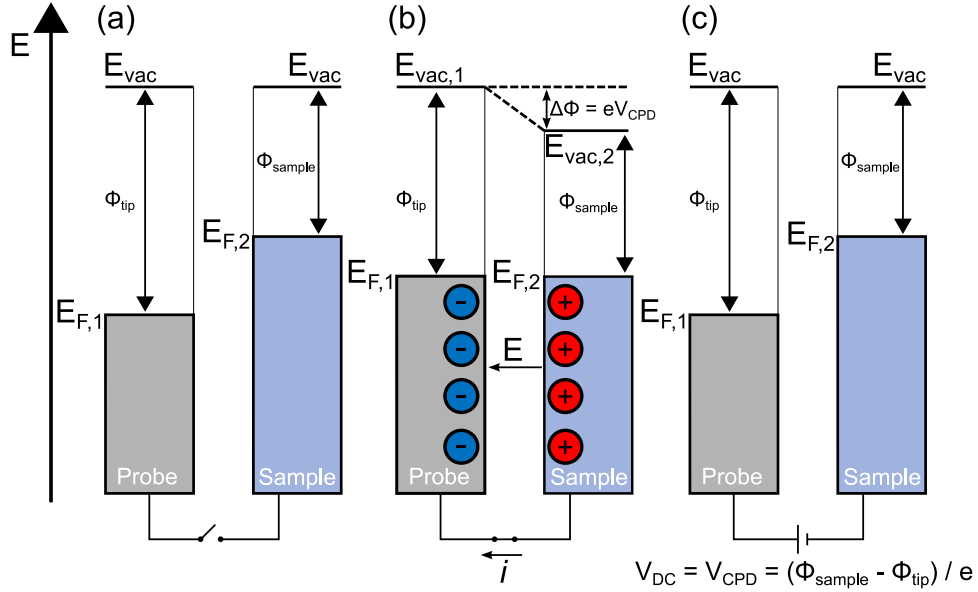


**Figure 2.14:** The following illustration provides a visual representation of the band gap diagrams, illustrating the principle behind the KELVIN method, which is utilized in KPFM. The potential energy diagram for the probe and the sample, with work functions  $\Phi_{\text{tip}}$  and  $\Phi_{\text{sample}}$ , initially not connected and thus sharing a common vacuum level  $E_{\text{vac}}$ , is depicted in (a). (b) If the two materials are connected by a conducting wire, the FERMI levels  $E_{\text{F},1}$  and  $E_{\text{F},2}$  of the two materials align. A buildup of surface charge leads to a macroscopic potential gradient, which compensates the difference between the work functions ( $\Delta\Phi$ ) of the two materials. (c) The surface charges and the corresponding electric field  $E$  vanish if a voltage  $V_{\text{DC}} = V_{\text{CPD}} = (\Phi_{\text{sample}} - \Phi_{\text{tip}})/e = \Delta\Phi/e$  is applied between the materials.<sup>27,28,151,294,319</sup>

compensated, this electric field will lead to an attractive force between tip and sample in the AFM. The CPD corresponds to:<sup>132</sup>

$$V_{\text{CPD}} = \frac{\Phi_{\text{sample}} - \Phi_{\text{tip}}}{e} \quad (2.18)$$

with  $\Phi_{\text{sample}}$  and  $\Phi_{\text{tip}}$  as the work function of the sample and tip, respectively. And  $e$  the elementary charge of an electron. On insulating surfaces, such as polymers and ceramics, electrostatic fields can arise from uncompensated static charges close to the surface. These charges will generate image charges in a metallic tip, leading to an attractive force. Here, we

will focus on the case of metallic and semiconducting surfaces, as they are more relevant to energy materials.

To detect the local variations in the electric field close to the surface, Electrostatic Force Microscopy (EFM) is used by observing the deflection and/or oscillation of the tip in contact or tapping mode using an AFM (see Figure 2.15).<sup>33</sup> In the most common implementation, EFM

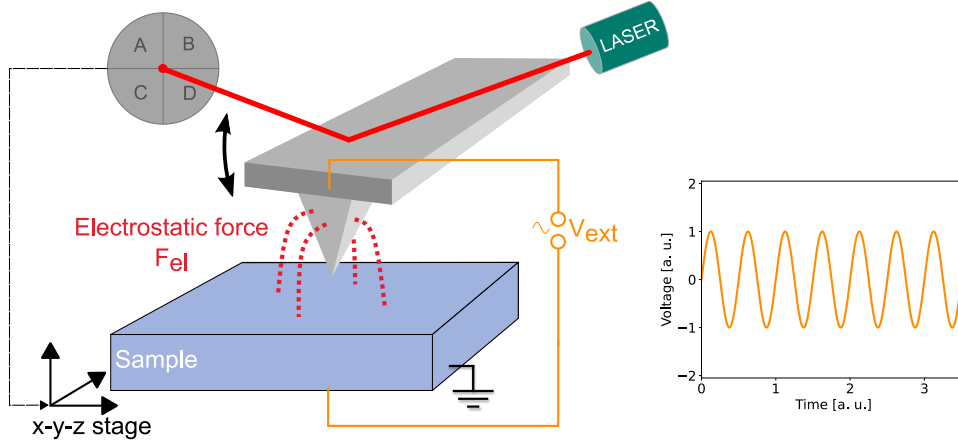


**Figure 2.15:** Fundamental setup of an EFM during operation.<sup>132,292–295</sup>

operates in a two-pass or lift mode. During the first pass, the topography is measured. During the second pass, the cantilever follows the measured topography several nanometers over the surface and the electrostatic force is measured by monitoring the response to an alternating current (AC) voltage applied to the tip at the frequency  $\omega_{AC}$ .<sup>132</sup> This is achievable because a variation in the tip-sample interaction is indicated by the alteration in the electrostatic force (Equation (2.19)) in relation to the grounded sample. This electrostatic force  $F_{el}$ , based on electrostatic interactions of two charges (compare Equation (2.1)), is given by

$$F_{el} = \frac{\partial W_C}{\partial z} = \frac{1}{2} \cdot \frac{\partial C}{\partial z} \cdot V_{\text{tip-sample}}^2, \quad (2.19)$$

with  $W_C$  as the capacitive energy,  $C$  as the capacitance,  $z$  the distance between tip and sample in the axis normal to the sample surface and  $V_{\text{tip-sample}}$  the bias voltage between the tip and sample. This voltage is the difference between all external voltages  $V_{\text{ext}}$  and the CPD given in Equation (2.20). This tip-sample voltages gets applied to the tip, while the sample stays grounded.

$$V_{\text{tip-sample}} = V_{\text{ext}} - V_{\text{CPD}} = V_{\text{DC}} - V_{\text{CPD}} + V_{\text{AC}} \cdot \sin(\omega_{\text{AC}} t). \quad (2.20)$$

with  $V_{\text{DC}}$  the DC-voltage offset,  $V_{\text{AC}}$  the AC bias voltage amplitude with the frequency  $\omega_{\text{AC}}$  at a certain time  $t$  and  $V_{\text{CPD}}$  the CPD. This electrostatic force in Equation (2.19) can be used to

map the surface for electrical properties, such as surface potential (CPD),<sup>41,97</sup> SPV,<sup>98,105,320</sup> or capacitance and dielectric properties.<sup>32,37,39,57,99</sup> When combining Equations (2.19) and (2.20), the electrostatic force is divided into a static (see Equation (2.21)) and two dynamic contributions (see Equations (2.22) and (2.23)):<sup>135</sup>

$$F_{\text{stat}} = \frac{1}{2} \frac{\partial C}{\partial z} \left( (V_{\text{CPD}})^2 + \frac{V_{\text{AC}}^2}{2} \right) \quad (2.21)$$

$$F_{\omega} = \frac{\partial C}{\partial z} \cdot V_{\text{CPD}} \cdot V_{\text{AC}} \cdot \sin(\omega_{\text{AC}} t) \quad (2.22)$$

$$F_{2\omega} = -\frac{1}{4} \frac{\partial C}{\partial z} \cdot V_{\text{AC}}^2 \cdot \cos(2\omega_{\text{AC}} t) \quad (2.23)$$

In case of not applying a direct current (DC)-offset ( $V_{\text{DC}} = \text{const.}$ ), the first harmonic response at the first eigenmode of the cantilever ( $A(\omega_{\text{AC}}) = \frac{Q \cdot F(\omega_{\text{AC}})}{k}$ ) with the spring constant  $k$  and the  $Q$ -factor is commonly used in EFM (Equation (2.22)). The amplitude is sensitive to the damping factor  $Q$  because at the resonance frequency this amplitude  $A(\omega_{\text{AC}})$  is  $Q$  times higher than the excitation amplitude  $A(\omega_{\text{drive}})$  ( $A(\omega_0) = Q \cdot A(\omega_{\text{drive}})$ ).<sup>294</sup> Besides that the amplitude varies with the CPD and the tip-sample capacitance. The latter varies further with the local dielectric properties. Please note that the amplitude and therefore the dielectric properties also varies owing to geometric variations between tip and sample caused by surface topography and the shape of the cantilever.<sup>99</sup> The influences of the shape and excitation frequency on the measurements of the dielectric properties will be discussed later in Sections 2.6.13 and 2.6.14. Thus, EFM is prone to topographical cross talk. Furthermore, uncompensated electric fields between the tip and sample surface can affect the topography measurement. Therefore, although EFM is relatively easy to implement, it only provides qualitative information about local electric fields. For quantification of the electric properties KPFM is necessary.<sup>132</sup>

### 2.6.5 Kelvin Probe Force Microscopy (KPFM)

Kelvin Probe Force Microscopy (KPFM) is the standard technique of choice to map the local surface potential.<sup>41,135,321</sup>

KPFM is a microscopic version of measuring CPD that follows the fundamental principle of the KELVIN probe.<sup>322</sup> KELVIN discovered that the total charge  $Q$  over each object's surface depends on the capacitance  $C$  between the two objects, by the relation  $Q = C \cdot \Delta\Phi$ .<sup>323</sup> By varying  $C$  by a known value, e.g., by changing the distance between them a current flows between the two connected materials.<sup>323</sup> This current can be compensated with a DC voltage, which equals the CPD.<sup>323</sup> Unlike traditional measurements, KPFM uses the electrostatic force between the tip and the sample as the controlling parameter, rather than the current.<sup>105,132,294</sup>

The setup for KPFM experiments (see Figure 2.16) are similar to the EFM setup shown in Figure 2.15. AFM is a highly sensitive tool for measuring forces, which makes it an ideal

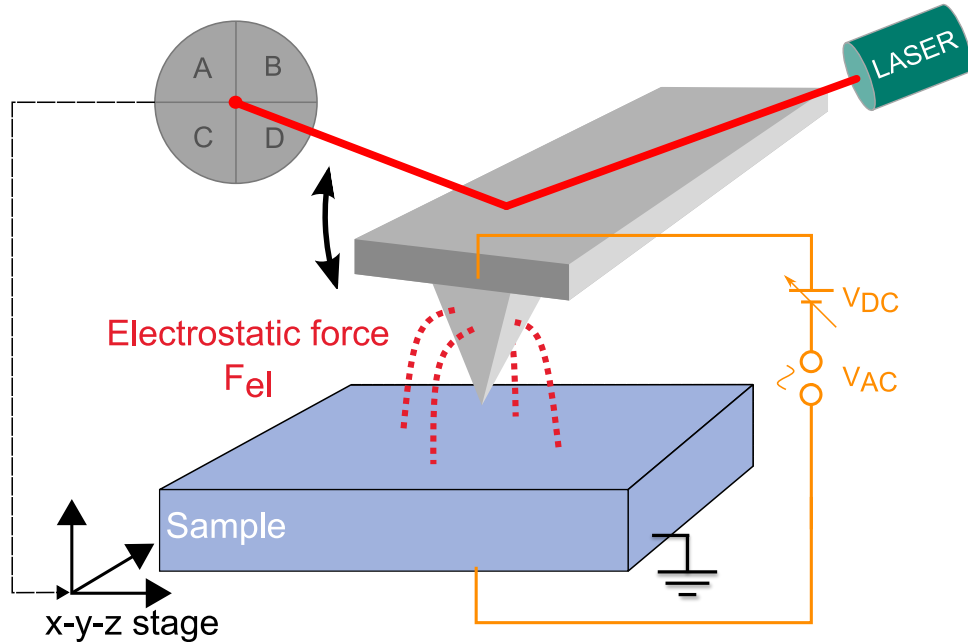


**Figure 2.16:** Fundamental setup of an KPFM during operation.<sup>105,132,294</sup>

method, e.g., for measuring CPD.<sup>105,132</sup> KPFM is an extension of EFM where a additional control loop (feedback loop) compensates the electrostatic force via an additional external DC voltage (closed-loop) (see Figure 2.16).<sup>105,132</sup> Alternatively, both the first ( $A(\omega_{AC})$ ) and the second harmonic response ( $A(2\omega_{AC})$ ) to the electrostatic excitation is measured (open loop operation).<sup>324</sup> Here, I will focus on closed-loop KPFM modes.

If the work function of the tip  $\Phi_{tip}$  is known, the work function of the sample can be quantitatively calculated at each location (see Equation (2.18)).<sup>105,132</sup> Similar to dynamic AFM, CPD can be measured by KPFM mainly in two modes: amplitude modulation Kelvin Probe Force Microscopy (AM-KPFM)- and frequency modulation Kelvin Probe Force Microscopy (FM-KPFM)-based modes.<sup>105,132</sup> In either mode, KPFM enables the precise recording of potential differences and distributions at the nanometer level.<sup>135</sup>

## 2.6.6 Amplitude modulation Kelvin Probe Force Microscopy (AM-KPFM)

As outlined in Section 2.6.2, the AM method assesses the changes in the amplitude of the cantilever at the resonance frequency, while the FM method evaluates the changes in the resonance

frequency itself.<sup>105,135</sup>

If the sample is grounded at all times and an external voltage with both a DC and an AC voltage of the form shown in Equation (2.20) is applied to the cantilever, the electrostatic force at the first harmonic from Equation (2.22) becomes Equation (2.24).<sup>135</sup>

$$F_\omega = \frac{\partial C}{\partial z} \cdot (V_{\text{DC}} - V_{\text{CPD}}) \cdot V_{\text{AC}} \cdot \sin(\omega_{\text{AC}} t) \quad (2.24)$$

Equation (2.24) is the fundamental equation for the AM-KPFM mode. If the contact potential difference (CPD) is compensated by the DC-voltage ( $V_{\text{DC}} = V_{\text{CPD}}$ ), the electric oscillation  $A(\omega_{\text{AC}})$  will vanish. Thus, we can determine the local CPD by using a feedback that regulates  $V_{\text{DC}}$  to minimize the oscillation amplitude. This method is called AM-KPFM.<sup>132,135</sup> AM-KPFM can be operated both in lift mode and simultaneously with topography mapping by using different cantilever resonance frequencies for topography and CPD detection.

AXT ET AL. reported that choosing two different frequencies for the detection of the two different signals for AM-KPFM is more reliable than the lift-mode AM-KPFM method, yielding a more quantitative CPD value.<sup>135</sup> Amongst other reasons, this is because the frequency of the electronic excitation in case of the lift-mode AM-KPFM is the same as the frequency of the mechanical oscillation of the cantilever.<sup>105,135</sup> Although the compensation approach should reduce the influence of the tip-sample capacitance, AM-KPFM is prone to imaging artefacts such as cross-coupling with the mechanical drive signal, for example, the excitation piezo<sup>135</sup> or cross talk and reduced lateral resolution from long-ranged electrostatic interactions with the tip cone and the cantilever, limiting the lateral resolution.<sup>135,300,305,325,326</sup> To reach the highest resolution and quantitative results, FM methods are usually preferable.

### 2.6.7 Frequency modulation Kelvin Probe Force Microscopy (FM-KPFM)

In frequency modulation Kelvin Probe Force Microscopy (FM-KPFM) we apply a low frequency (typically  $\omega_{\text{AC}} \approx 0.1 - 5$  kHz) AC voltage to the tip. The resulting periodic fluctuations in the frequency of the electric oscillation  $\Delta\omega(t)$  (see Equation (2.17)) are then detected by a PLL processed by a lock-in amplifier (LIA) and minimized via a feedback loop similar to FM-AFM.<sup>105,294</sup> Due to the FM detection, this operation mode is directly proportional to the electrostatic force gradient, and therefore also to the second derivative of the capacitance  $\frac{\partial^2 C}{\partial z^2} = C''$  (Equations (2.17) and (2.24)).<sup>135</sup> This makes FM detection more sensitive to the electrostatic interaction between the tip and the sample surface<sup>135</sup> and leads to a superior lateral resolution by the cost of a poorer signal-to-noise ratio.<sup>99</sup> Nevertheless, the implementation and

stable operation of FM-KPFM with a PLL and additional LIA and feedback loop is complicated. That is the reason why there are alternatives to detect the FM-KPFM signal. Namely, sideband-FM-KPFM and heterodyne Kelvin Probe Force Microscopy (H-KPFM)

### 2.6.8 Sideband FM-KPFM

For applications in air, alternative force gradient sensitive KPFM modes are available that rely on the detection of sidebands caused by frequency mixing between the mechanical and the electrical excitation. A full derivation can be found in the work of AXT ET AL.,<sup>135</sup> here I show a simplified calculation to illustrate the appearance of sidebands. The electrostatic force (Equation (2.19)) contains the capacity gradient. If the tip oscillates at a frequency  $\omega_m$  and amplitude  $A_m$  around a certain distance  $z_0$  but close to the surface, the tip-sample capacitance and therefore the capacity gradient will be oscillating monotonically with  $\omega_m$ , as well. This is because the capacitance is dependent on the tip-sample distance of the tip and the sample surface. To a first approximation, we can linearize the capacity gradient over the oscillation range  $\Delta z$  by a TAYLOR series (see Equation (2.25)).<sup>134,135</sup>

$$\frac{\partial C}{\partial z}(z_0 + \Delta z) \approx \left. \frac{\partial C}{\partial z} \right|_{z_0} + \left. \frac{\partial^2 C}{\partial z^2} \right|_{z_0} \cdot \Delta z + \dots \quad (2.25)$$

Using this equation, we can approximate this fluctuation with a periodic function with the mechanical frequency  $\omega_m$ :

$$F_\omega = \left[ \left. \frac{\partial C}{\partial z} \right|_{z_0} + \left. \frac{\partial^2 C}{\partial z^2} \right|_{z_0} \cdot A_m \cdot \sin(\omega_m t) \right] \cdot ((V_{DC} - V_{CPD}) \cdot V_{AC} \cdot \sin(\omega_{AC} t)) \quad (2.26)$$

The first term in the square bracket yields an expression identical to Equation (2.22) of AM-KPFM. The second term contains a product of the mechanical and the electrical oscillation. Rearranging yields

$$F_{\omega_m \pm \omega_{AC}} = \frac{1}{2} A_m \left. \frac{\partial^2 C}{\partial z^2} \right|_{z_0} \cdot (V_{DC} - V_{CPD}) \cdot V_{AC} \cdot \sin((\omega_m \pm \omega_{AC})t)^{135} \quad (2.27)$$

Equation (2.27) represents the fundamental equation for the force gradient-based methods. So, the modulation of the capacity gradient by the mechanical cantilever oscillation generates sidebands at frequencies  $\omega_m \pm \omega_{AC}$ . The force component in Equation (2.27) has the same CPD dependence on the DC-offset ( $V_{DC} - V_{CPD}$ ) as Equation (2.24) for AM-KPFM. The main difference is the second capacity gradient that puts a stronger emphasis of the resulting signal

on the tip apex compared to tip cone and cantilever, providing a spatial resolution superior to AM-KPFM modes.<sup>99,134,301–305</sup> Strictly speaking, this so-called sideband KPFM is not a FM mode. Nevertheless, both methods are force-gradient-sensitive, so we will use the term FM-KPFM for modes using the sideband detection, as well. In the early implementations of sideband FM-KPFM, a low frequency AC voltage was applied. This way, the sidebands are still within the resonance band of the cantilever, limiting the detection bandwidth and thereby the detection speed. Therefore, a further improvement lead to a new method called heterodyne Kelvin Probe Force Microscopy (H-KPFM).

### 2.6.9 Heterodyne Kelvin Probe Force Microscopy (H-KPFM)

SUGAWARA ET AL.<sup>327</sup> introduced the heterodyne Kelvin Probe Force Microscopy (H-KPFM) method, which is a refined method for detecting electrostatic force gradients by frequency mixing. In contrast to sideband FM-KPFM, H-KPFM is much faster due to the wider bandwidth possible during operation. This method, similar to sideband FM-KPFM, uses the nonlinear mixing of a mechanical cantilever vibration with an angular frequency  $\omega_m$  and an electrical frequency  $\omega_{AC}$ . But in case of H-KPFM, these frequencies are separated by hundreds of kHz.<sup>134</sup> A subsequent study from GARRETT AND MUNDAY<sup>134</sup> modified the H-KPFM method further.<sup>134</sup> This means for Equation (2.27) if  $\omega_{m,1} + \omega_{AC} = \omega_{m,2}$  the signal falls on the second mechanical resonance  $\omega_{m,2}$  of the cantilever, where the detection is enhanced due to the higher signal-to-noise ratio on the resonance peaks.

The H-KPFM method, as it is with the sideband FM-KPFM, simplifies the measurement process by eliminating the need for direct acquisition of the periodic oscillations  $\Delta\omega$  using a PLL in the non-contact mode of the AFM under UHV conditions.<sup>134,135</sup> Furthermore, H-KPFM allows for a detection of the sideband signal with high bandwidth, providing a superior time resolution compared to a low-frequency AC excitation.<sup>134</sup> This leads to an increased speed (single pass mode) and a higher signal-to-noise ratio compared to lift mode AM-KPFM.<sup>134,135</sup> Additionally, the electrical excitation is shifted in frequency from the electrical detection, which eliminates any interference or coupling.<sup>135</sup> The electric oscillation amplitude ( $A(\omega_{m,2})$ ) is compensated with the use of a LIA by applying a DC-bias, similar to the AM-KPFM method. And similar to the AM-KPFM method, this DC-bias is equivalent to the CPD.

The force signal in the AM-KPFM method is often stronger than the force gradient signal in the H-KPFM method. As a result, higher electrical drive amplitudes ( $A(\omega_{AC})$ ) are typically needed for the H-KPFM method, which can cause other problems, such as electronic band bending.<sup>135,328</sup> In a comparative study AXT ET AL. reported that FM-KPFM and in particular H-KPFM is more reliable than the lift-mode AM-KPFM method, yielding the most quantitative

CPD value.<sup>135</sup> Therefore, I used H-KPFM in my studies, when mentioned KPFM or CPD measurements. For studying dynamics, I used H-KPFM to study the time-trace of the KPFM signal which is called time-resolved Kelvin Probe Force Microscopy (tr-KPFM). But before that in the next section, I want to focus on the Influences on the local CPD value.

### 2.6.10 Influences on the local contact potential difference

The CPD maps of a sample can be obtained after a KPFM measurement and can be used to characterize the electronic properties of the sample on the nanoscale.<sup>151</sup> However, great care must be taken when interpreting CPD maps.<sup>151</sup> Thus, possible contributions to CPD during KPFM measurement should be discussed.<sup>151</sup>

#### Crosstalk / Tip artifacts

The first possible contribution to the CPD image is crosstalk between the topography image and the CPD image.<sup>151</sup> Even if the FM- or heterodyne mode is used during the KPFM measurement, this effect cannot be completely eliminated.<sup>151</sup> This phenomenon is especially significant in contexts marked by pronounced topographical features, such as sharp edges or deep trenches. The impact of tip geometry on the CPD map is attributable to the non-uniformity of the cantilever cone, which can present as a triangular-shaped cone. The variation in cone geometry gives rise to distinct electrostatic interactions, thereby influencing the orientation-dependent behavior observed between the tip and the surface.<sup>151</sup> Furthermore, phase jumps in the oscillation of the cantilever will be reflected in the CPD images. This is due to the dependency of Equation (2.27) on the mechanical amplitude,  $A_m$ , and the amplitude is subject to variation if the interaction undergoes a shift, consequently modifying the phase.<sup>151,329</sup>

#### Crystallinity

The CPD values can also change due to chemical features at the surface the sample.<sup>151</sup> In the context of crystalline materials, it has been demonstrated that the presence of two distinct crystal phases within a single sample, each exhibiting different work functions, results in the variation of CPD values when mapped.<sup>330</sup> Furthermore, the different facets of a particular phase can also manifest distinct CPD signals, as evidenced by research conducted by ABDELLATIF ET AL.<sup>151,331</sup> Consequently, the use of KPFM allows for the detection of segregated phases and the orientation of grains within films.<sup>151</sup>

### Band bending

The CPD of the sample will also be affected by the local changes within the band structure such as band bending.<sup>151,332,333</sup> As we learned in Section 2.3.3 band bending is caused by the charge accumulation caused by defect states within the material (e.g., internal interfaces between layers) or at the surface, e.g., at its GBs.<sup>151</sup> The band bending can occur at defect positions in two ways as upward band bending and downward band bending (see Figure 2.17).<sup>151</sup> The

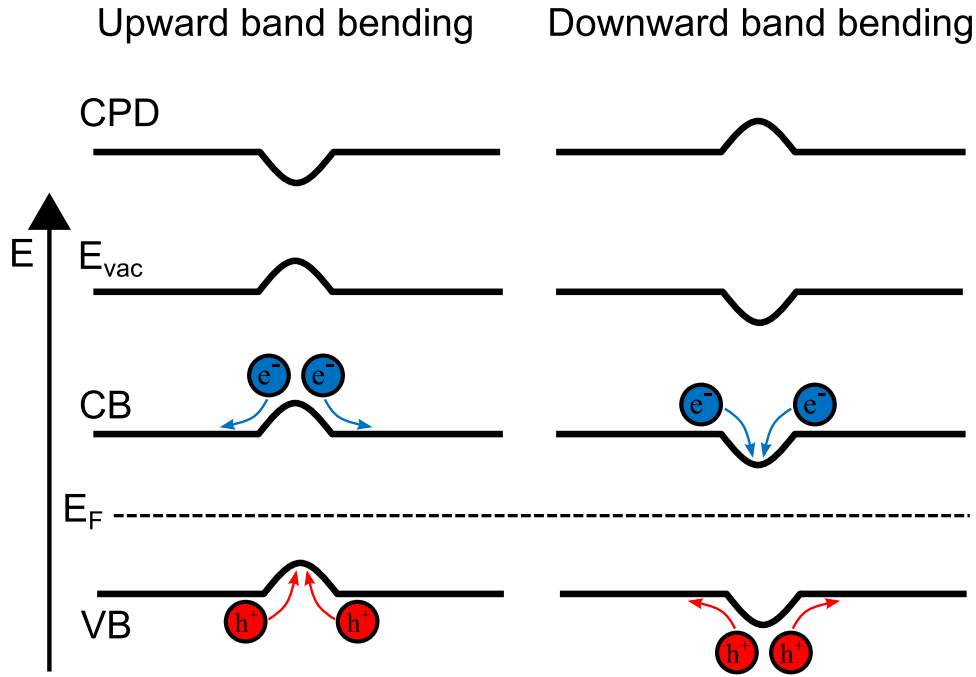


**Figure 2.17:** The upward and downward band bending effecting the VB, the CB, the vacuum level  $E_{vac}$ , and the CPD signal at a defect position like a GB.<sup>98,151</sup>

type of band bending depends on the type of defect present in the structure which affect the type of charge that accumulates.<sup>151</sup> Downward band bending occurs due to donor type defect states which results in electron accumulation and increase in CPD.<sup>151</sup> On the contrary, upward band bending occurs due to acceptor type defect states which leads to hole accumulation and it decreases CPD.<sup>151</sup> Since the CPD changes can be tracked via CPD maps, KPFM stands as a useful tool to localize defects in the halide perovskite films.<sup>151</sup>

### Surface photovoltage (SPV)

The surface photovoltage (SPV) is defined as the difference between the surface potential (CPD) of a sample in the dark and under illumination.<sup>320</sup> The SPV is defined in Equation (2.28).<sup>98</sup>

$$V_{SPV} = V_{CPD, \text{illum.}} - V_{CPD, \text{dark}}. \quad (2.28)$$

By illuminating the photoactive material, as we learned in Section 2.4.2 a splitting of the FERMI level takes place which is equal to a voltage shown in Equation (2.15). SPV is an observed phenomenon in semiconductor physics and photovoltaic devices, providing valuable insight into carrier behavior and material properties. A non-zero SPV indicates a redistribution of photogenerated free charges.<sup>320,334</sup>

In crystalline inorganic semiconductors with domains larger than a few nanometers, SPV typically results from a decrease in the built-in electrical potential gradient and band flattening in a space-charge region, either near the surface or around a buried interface.<sup>320,335,336</sup> In photovoltaic device stacks, the buried interfaces can be in between the absorber and a charge-selective contact.<sup>98</sup> Since the SPV signal depends on the FERMI level and the FERMI level change in the sample under illumination (see Section 2.5.6), it is influenced by band bending, doping,<sup>337</sup> and stoichiometry in the sample.<sup>338</sup> During illumination, the increased carrier concentration screens the trapped surface charges, resulting in band flattening.<sup>98,339</sup> This change in the band bending and therefore the surface potential is observed as the SPV signal.

The behavior of the SPV is influenced by the distribution of charge carriers resulting from n-type or p-type doping, which affects the initial band bending of the semiconductor.<sup>98</sup> N-type semiconductors typically produce positive SPV values, while p-type semiconductors yield negative SPV values.<sup>98</sup> Consequently, the doping status of a sample can be determined by the sign of its SPV value.<sup>98,340</sup>

Moreover, The redistribution of photogenerated carriers across the heterojunction depends on the characteristics of the charge-selective layer. An ETL results in a positive SPV due to an imbalance of free charges in the film volume, while a HTL results in a negative SPV due to an excess of electrons. The SPV can be measured using KELVIN probe experiments at both the macro- and nanoscale (see the tr-KPFM method in Section 2.6.11), providing insight into the underlying processes within solar cells. It can provide information about material properties, carrier behavior,<sup>341,342</sup> and open circuit voltage ( $V_{OC}$ ) loss processes.<sup>320</sup> This knowledge can be applied to optimize solar cell performance and improve efficiency.<sup>320</sup> In addition, SPV can be used to study charge recombination at the interface of the perovskite layer,<sup>98,105,342</sup> which is crucial for the performance of PSCs. One possibility to map the SPV in the domain of time is given by a method called time-resolved Kelvin Probe Force Microscopy (tr-KPFM) shown in Figure 2.18.<sup>98</sup>

### 2.6.11 Time-resolved Kelvin Probe Force Microscopy (tr-KPFM)

The time-resolved Kelvin Probe Force Microscopy (tr-KPFM) method gives the possibility to measure the surface photovoltage (SPV) on the nanoscale.<sup>98</sup> This method was investigated

during this PhD Thesis and published by YALÇINKAYA/ROHRBECK ET AL. with me as second first author.<sup>98</sup> The schematic setup of the tr-KPFM experiments investigating characteristic voltage decays following an illumination pulse with a laser positioned underneath the sample is shown in Figure 2.18.<sup>98</sup> As mentioned in Section 2.6.10 this is possible by tracking the change

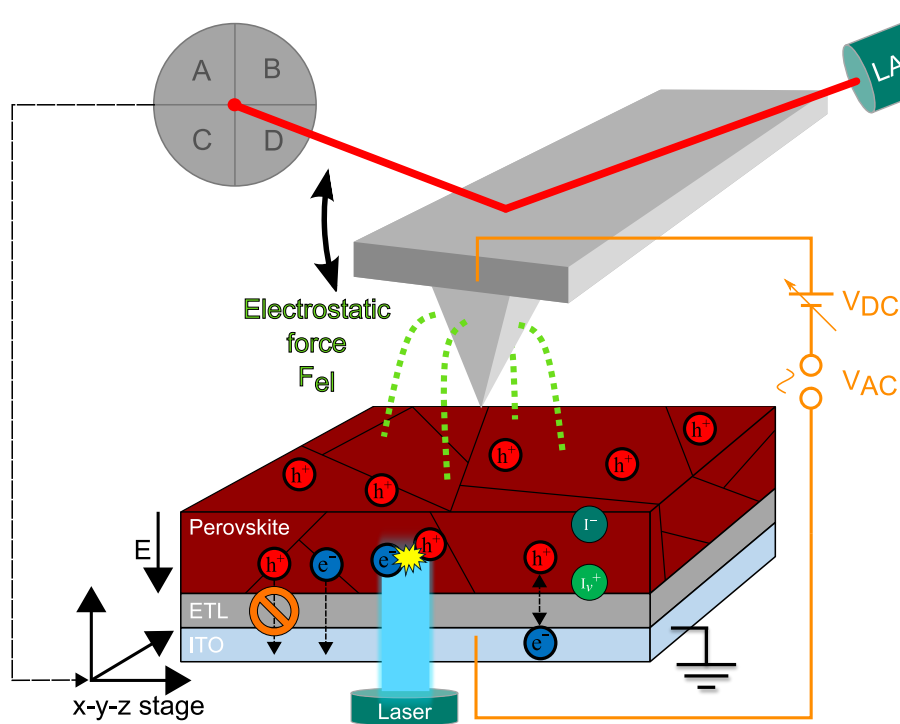


**Figure 2.18:** Fundamental setup of an tr-KPFM during operation.<sup>98</sup>

of the CPD ( $\Delta CPD = SPV$ ) of the photosensitive semiconductor like PSCs with respect to the time and illumination intensity of the PSC.

As the study of YALÇINKAYA/ROHRBECK ET AL., covered in detail in Chapter 4, showed the SPV transients contain information about recombination rates,<sup>343</sup> trap density,<sup>334</sup> and ion migration<sup>344</sup> effects.<sup>98</sup> The distinguishing factor between these contributions lies in their respective dynamics. Therefore, in order to separate the different components, the use of tr-KPFM is necessary to differentiate the dynamics across their respective time domains. Our study utilizes a CPD trajectory acquired via a tr-KPFM configuration, offering insights into the nature of contributing charge carriers. This analysis is accomplished by the observation of the decay of the SPV following the application of a light pulse, a process referred to as SPV spectroscopy.<sup>98</sup> While the fast decaying components typically representing electronic contributions and slow decaying components usually indicating ionic contributions.<sup>98,344</sup> The decay of SPV after light illumination was fitted in respect to time with an double-exponential fit of the form shown in

Equation (2.29) to separate and extract the fast electronic and slow ionic decay effects within the measured data:<sup>98</sup>

$$\text{CPD}(t) = \text{CPD}_\infty + A_{\text{ion}} \cdot \exp\left(\frac{x_0 - x}{\tau_{\text{ion}}}\right) + A_{\text{elec}} \cdot \exp\left(\frac{x_0 - x}{\tau_{\text{elec}}}\right) \quad (2.29)$$

with  $\text{CPD}_\infty$  the equilibrium CPD state,  $A_{\text{ion}}$  the amplitude of the ionic exponential decay or rise with the time  $\tau_{\text{ion}}$  at the laser impulse point  $x_0$ .  $A_{\text{elec}}$  and  $\tau_{\text{elec}}$  represent the amplitude and time constant of the electronic exponential decay or rise.<sup>98</sup> The electronic decay is correlated with the electron-hole recombination mechanisms occurring at the perovskite bulk or at the interface between perovskite and the ETL.<sup>98,105</sup> The rate of SPV decay is proportional to the extent of trap-assisted recombination.<sup>98</sup> Accordingly, it can be employed to investigate the localization of the passivation.<sup>105</sup> This information can be used to optimize passivation strategies, thereby enhancing the performance of solar cells through the further improvement of their efficiency. The ionic decay is linked to the redistribution of ions from the surface, which can occur through migration from the crystal lattice<sup>345</sup> or adsorption from the environment.<sup>98</sup> Additionally, the electric field generated by electron movement and hole accumulation at the surface exerts a force on the ions within the film, influencing their movement.<sup>98</sup>

An analysis of the dynamics of SPV formation at the onset of a light pulse reveals that this phenomenon can be further interpreted as interfacial extraction of charge carriers,<sup>98</sup> in addition to the internal  $RC$ -time of the solar cell. This interpretation is supported by other experimental studies using photoluminescence (PL)<sup>346</sup> or photoconductivity measurements.<sup>98,347</sup> The research suggests that only the ETL or HTL interface is a charge transport limiting factor in the device and not the perovskite itself.<sup>98,347,348</sup> This implies that the interfacial properties of the device can be observed by tracking changes in the SPV.<sup>98,348</sup>

The tr-KPFM is conducted by setting up a H-KPFM measurement and place the cantilever in the middle of the laser spot shown schematically in Figure 2.18.

Due to the AM detection scheme on the second eigenmode the method has an intrinsic time resolution limit. This time resolution limit of tr-KPFM is proportional to  $\frac{Q}{f_0 \cdot \pi}$ .<sup>294</sup> It includes  $Q$ , also known as the quality factor ( $Q$ -factor), and is defined near the resonance frequency ( $\omega \approx \omega_m$ ) as  $Q \approx \frac{\omega_0}{\gamma}$ , where  $\gamma$  is the damping factor of the cantilever oscillation.<sup>294</sup>  $f_0$  is the mechanical resonance frequency at which the cantilever oscillates. Similar time resolution can be achieved by using spiral-mode data acquisition.<sup>349,350</sup> Faster time resolution is only possible by using methods like pump-probe Kelvin Probe Force Microscopy (pp-KPFM)<sup>351-353</sup> or general acquisition mode Kelvin Probe Force Microscopy (G-mode KPFM)<sup>354</sup> using open loop KPFM.<sup>324</sup>

In addition to the application of the KPFM methods, another approach to gaining insights into the electrical properties of a given sample is through an analysis of its dielectric properties. One possibility to get dielectric properties via the capacity gradients  $C'$  or  $C''$  by detecting the force component independent of the CPD shown in Equation (2.23). This widely used method is called Scanning Capacitance Microscopy (SCM).

### 2.6.12 Scanning Capacitance Microscopy (SCM)

Scanning Capacitance Microscopy (SCM) is a widely used technique for capacitance measurements, e.g., on the nanoscale.<sup>99</sup> It can directly provide local information about 2D carrier distributions or profiles,<sup>39,52,54,64,67</sup> image surface dielectric properties and permittivity values,<sup>32,34–38,57–59,355</sup> measure the thickness of bio-membranes,<sup>58,62,63,66</sup> investigate memory devices,<sup>40,55</sup> and identify particles or nanostructures.<sup>36</sup> Moreover, SCM detects capacitance with superior spatial resolution compared to conventional methods like ellipsometry or reflectance spectroscopy.<sup>58,99</sup> In energy materials like PSCs, SCM allows the localization of defects by understanding the capacitance signal on the nanoscale with an AFM. By analyzing the capacitive responses, it is possible to address not only the nature of the charge distribution in the device, but also the kinetics of the charging processes and how they change the solar cell current.<sup>312</sup>

Equation (2.23) is the fundamental equation used for SCM.<sup>99</sup> For semiconductors such as perovskites,  $\frac{\partial C}{\partial z}$  is not constant with respect to the applied bias voltage<sup>31</sup> and is also strongly dependent on the dopant concentration.<sup>31,39,64,99</sup> The capacitance of a material depends, among other things, on the dielectric constant  $\epsilon_r$  of the material. Conversely, this means that the capacitance gradient  $C'$  also depends on the dielectric constant. Furthermore, is only constant at a certain frequency ( $\epsilon_r(f)$ ), because the dielectric function is a function of the applied frequency  $f$ . With the information from the capacitance gradient and the exact model of complicated the tip-sample capacitance illustrated in Figure 2.19, it is possible to extract local dielectric information at certain frequencies from a SCM experiment. Historically, the capacitance was measured with an electrode placed over a flat surface and electrically connected with an capacitance sensor.<sup>55,356,357</sup> This sensor is a ultra-high frequency coaxial resonator. In a widely used system, a specific sensor is employed to detect changes in capacitance by measuring the fluctuations in its electric amplitude at a fixed frequency of approximately 915 MHz across the cantilever that is in contact with the sample.<sup>52,55,57,358</sup> The feedback of the sensor get tracked via a LIA.<sup>56</sup> The disadvantages are possible cross-talk from the capacitance signal and the topography<sup>55</sup> and these kind of measurements are only possible for materials with a voltage-dependent capacitance such as semiconductors due to the need of a changing contact capacitance upon electric excitation.<sup>57</sup>

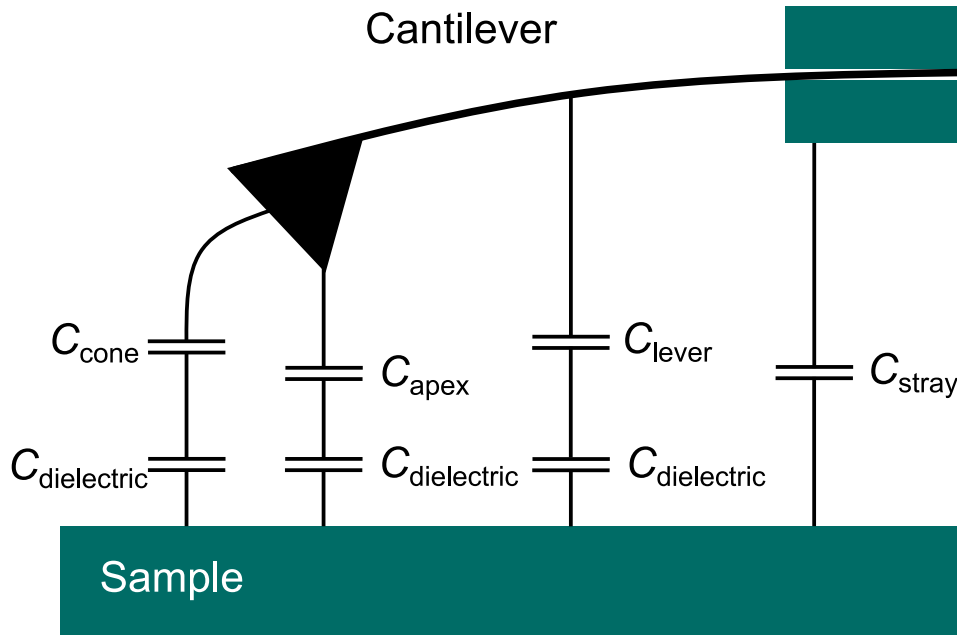


**Figure 2.19:** Schematic illustration of tip apex, tip cone, lever, and stray capacitances. The contribution of the tip apex contains the most localized part of the overall capacitance signal. The mesoscopic tip cone and the macroscopic cantilever, in contrast, contribute to the long-range stray capacitance, effectively delocalizing the signal.<sup>99</sup>

A fundamental problem is set by the small tip-sample contact area, which is approximately  $\sim 100$  nm,<sup>56</sup> thereby limiting the lateral resolution. Another limiting factor is the sensitivity of the sensor used.<sup>31,39</sup> Moreover, the cone and lever of the cantilever is significantly contributing to the absolute capacitance signal (see Figure 2.19).<sup>63</sup> That is the reason why it is hard to measure the absolute contact capacitance of the dielectric material  $C_{\text{dielectric}}$  in presence of the stray capacitance ( $C_{\text{stray}}$ ),<sup>53,54,63,75,358</sup> also because the stray capacitance is much larger than the contact capacitance.<sup>53</sup>

So far, it was shown by FUMAGALLI ET AL.<sup>57</sup> and GRAMSE ET AL.<sup>37</sup> that capacitance imaging with a resolution of aF is possible by detecting the capacitive current with a current-to-voltage amplifier<sup>57</sup> or modulate the force signal with a AC excitation frequency to the cantilever to detect the force itself.<sup>31,37</sup>

As we know by applying a single frequency excitation without a DC component (see Equation (2.20)) an electrostatic force signal is created at the second harmonic of the excitation frequency ( $2\omega_{\text{AC}}$ ) seen in Equation (2.23). This allows in principle to detect the force created by changes in the first capacitive gradient ( $C'$ ) between tip and sample by observing the deflection and/or oscillation of the tip in contact or tapping mode with an AFM.<sup>33</sup> A single frequency approach using Equation (2.20) as electric excitation has the disadvantage of limited excitation

and/or detection frequencies. Only an enhanced signal-to-noise ratio at the harmonics of the cantilever can provide sufficient signals. However, it is also possible to extract electric properties by applying at least two various frequencies to the cantilever. This approach is called multi-frequency EFM.

### 2.6.13 Multi-frequency Electrostatic Force Microscopy

Multi-frequency Electrostatic Force Microscopy (MF-EFM) uses excitation and/or detection of the deflection at two or more frequencies.<sup>30</sup> Detecting or applying at different frequencies would normally require dual or multiple pass methods to scan similarly to lift mode AM-KPFM. Multiple scans over the same area are time-consuming. However, a multi-frequency approach with the detection similar to H-KPFM on the second eigenmode has the potential to overcome limitations in the spatial resolution and acquisition time limitations of conventional force microscopes.<sup>30</sup> This combination takes advantage of the superior resolution of H-KPFM detection scheme in comparison to the crosstalk-prone AM-KPFM method and time consuming sideband/FM-KPFM method.

In dynamic modes of AFM, the motion of the cantilever is highly nonlinear, and information about the sample that is encoded in the deflection at frequencies other than the excitation frequency is typically lost.<sup>30</sup> When using a single excitation frequency (see Figure 2.15), specific force components are generated as described in Equations (2.21) to (2.23). In multi-frequency EFM (see Figure 2.20), this changes. Mixing the electrostatic force and the TAYLOR expansion at  $z_0$  (see Section 2.6.8) leads to sidebands at frequencies  $\omega_{SB,1} = (\omega_m \pm \omega_{AC})$  and  $\omega_{SB,2} = (\omega_m \pm 2\omega_{AC})$  next to the the mechanical oscillation at  $\omega_m$ .<sup>99,135</sup> Both of these methods are applied in the aforementioned techniques, namely FM-KPFM, H-KPFM, and SCM.<sup>99</sup> In order to guarantee an adequate signal-to-noise ratio, it is essential that the resulting frequencies align with one of the cantilever's resonance frequencies.<sup>99</sup> This restriction in single-excitation frequency selection, shown schematically in Figure 2.15, can be circumvented by implementing a multi-frequency excitation approach (see Figure 2.20).<sup>99</sup> With a double-frequency excitation, we can write the tip-sample voltage as:<sup>99</sup>

$$V_{\text{tip-sample}} = V_{AC,1} \cdot \sin(\omega_{e,1} t) + V_{AC,2} \cdot \sin(\omega_{e,2} t) \quad (2.30)$$

with  $V_{AC,1}$  and  $V_{AC,2}$  as the amplitude voltages and  $\omega_{e,1}$  and  $\omega_{e,2}$  the AC excitation frequencies. In the case of two drives with identical amplitude  $V_{AC,1} = V_{AC,2} = \frac{V_{AC}}{2}$ , Equation (2.30) can be

rearranged as shown in Equation (2.31).

$$V_{\text{tip-sample}} = V_{\text{AC}} \cdot \sin\left(\frac{\omega_{e,1} - \omega_{e,2}}{2} t\right) \cdot \sin\left(\frac{\omega_{e,1} + \omega_{e,2}}{2} t\right) \quad (2.31)$$

Thus, the waveform can be viewed as a high-frequency oscillation at  $(\omega_{e,1} + \omega_{e,2})/2$  with a low-frequency amplitude modulation at frequency  $(\omega_{e,1} - \omega_{e,2})/2 = \Delta\omega_e/2$ . This effect is also known as "beating" (shown schematically in Figure 2.20) and is utilized in the AFM context for example in intermodulation AFM.<sup>88,95,359,360</sup> This principle of the multi-frequency EFM is used in the new multi-frequency heterodyne Electrostatic Force Microscopy (MFH-EFM) method, which was developed by me during this PhD.

### 2.6.14 Multi-frequency heterodyne Electrostatic Force Microscopy (MFH-EFM)

I recently introduced a new version of SCM in which I use a multi-frequency EFM approach called multi-frequency heterodyne Electrostatic Force Microscopy (MFH-EFM) to detect signals dependent on the second capacitance gradient signal.<sup>99</sup>

MFH-EFM provides the capability to assess dielectric properties with high lateral resolution. This method involves the use of an EFM and the application of two sinusoidal signals to the cantilever, resulting in the generation of an intermodulation signal in conjunction with a LIA for detection.<sup>99</sup> The setup, based on multi-frequency EFM, is shown in Figure 2.20. GIL ET

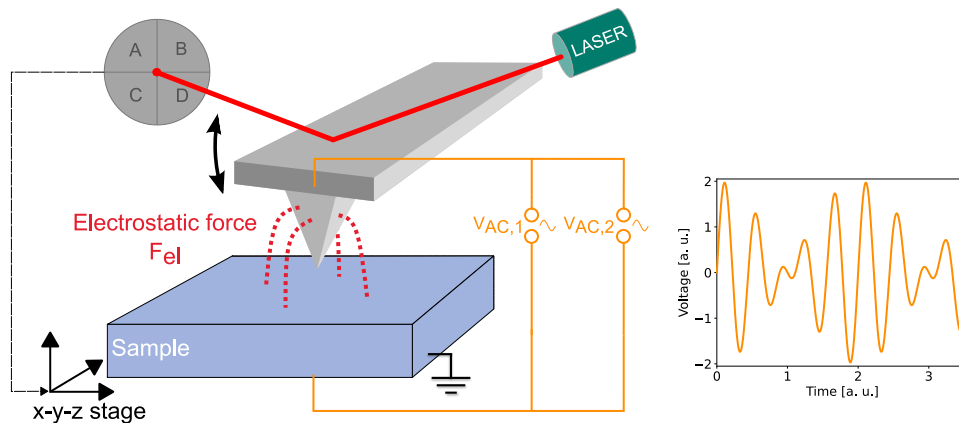


**Figure 2.20:** The fundamental setup of a MFH-EFM during operation is demonstrated in the presence of a schematic intermodulation signal consisting of two sinusoidal frequencies, specifically 2 Hz and 2.5 Hz.<sup>99</sup>

AL. suggested to use the force gradient, which is dependent on the second capacitance gradient

$\left(\frac{\partial^2 C}{\partial z^2}\right) = C''$ .<sup>43</sup> The force contribution of the cone and the lever will be "derived away".<sup>43</sup> Consequently, the force signal will be localized on the tip apex.<sup>99</sup>

In Chapter 5 the complete work is provided, but here I would like to frame the theory in the context of the previous sections on multi-frequency EFM and provide a complete picture.

If we ignore higher orders of the TAYLOR expansion for now, the combination of Equation (2.19), Equation (2.25) up to the first order, and using the double excitation approach from Equation (2.31) and separating by spectral components yields among others the following Equation (2.32). The full expression for the electrostatic force can be found in the work of ROHRBECK ET AL.<sup>99</sup> Here, I will focus on the DC force component and set  $V_{\text{DC}} - V_{\text{CPD}} = \Delta$ :

$$F_{\text{DC}} = \frac{1}{2}(C' + C'' A_m \sin(\omega_m t) + \dots) \cdot \left[ \Delta^2 + \frac{V_{\text{AC}}^2}{2} \sin^2\left(\frac{\Delta\omega_e}{2} t\right) \right]$$

$$= \frac{1}{2}C' \left[ \Delta^2 + \frac{V_{\text{AC}}^2}{4} \right] + \frac{1}{8}C'V_{\text{AC}}^2 \cos(\Delta\omega_e t) \quad (2.32a)$$

$$+ \frac{1}{2}C'' A_m \left[ \Delta^2 + \frac{V_{\text{AC}}^2}{4} \right] \sin(\omega_m t) + \frac{1}{16}C'' A_m V_{\text{AC}}^2 \sin((\omega_m \pm \Delta\omega_e) t) \quad (2.32b)$$

In addition to a static force term identical to Equation (2.21), Equation (2.32a) contains a term proportional to  $C'$  at frequency  $2\omega_{\text{mod}} = \Delta\omega$ .<sup>99</sup> This force has been used for AM-based dielectric spectroscopy.<sup>41,47,79,99,355,361-364</sup> The second term Equation (2.32b) contains a force component at the mechanical drive frequency  $\omega_m$  and at a sideband frequency  $\omega_m \pm 2\omega_{\text{mod}}$ .<sup>99</sup> This last term is independent of the local CPD, making it interesting for dielectric measurements.<sup>99</sup> The forces in Equation (2.32b) are only dependent on the frequency difference,  $\Delta\omega_e$ , of the electrical drive frequencies.<sup>99</sup> Thus, the experiments can be performed at almost arbitrarily high AC frequencies.<sup>99</sup> The lower limit for the frequency range is given by the second resonance of the cantilever.<sup>99</sup> Towards higher frequencies, the impedance of the electrical connection will introduce a damping of the excitation signal that has to be considered.<sup>99</sup> By using appropriate means of coupling the electrical excitation into the tip-sample gap, experiments at microwave or even at optical frequencies are possible.<sup>99</sup> In the setup shown in the publication, the two excitation frequencies can be varied in frequency from  $\approx 600$  kHz up to at least 50 MHz, limited by the bandwidth of the lock-in amplifier.<sup>99</sup>

To reach a nanoscale sensitive measurement of the dielectric constant in media besides air, a detection at higher excitation frequencies in the MHz regime is strictly necessary.<sup>37,99</sup> The main difference between Equation (2.32) and Equation (2.19) is the proportionality to the second derivative of the capacitance  $\frac{\partial^2 C}{\partial z^2} = C''$  rather than to the first derivative  $\frac{\partial C}{\partial z} = C'$ . This improves sensitivity because the electrostatic force acting at the tip apex still dominates at longer distances, where stray capacitance normally takes over, compared to  $C'$  signals at

the cost of lower signal-to-noise ratio (see Figure 2.21).<sup>99,365</sup> Since the magnitude of this force

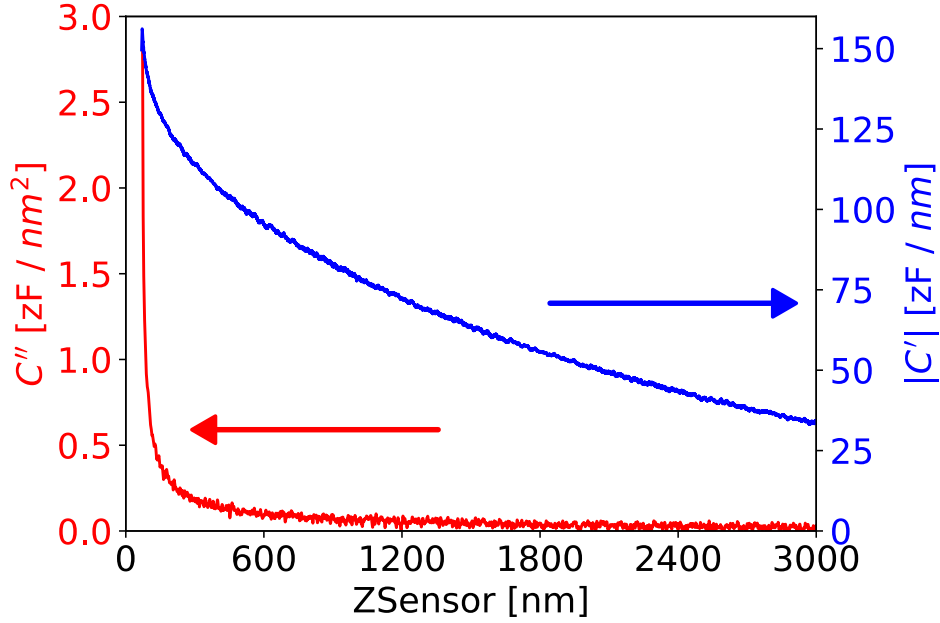


**Figure 2.21:** Comparison of the  $C''$  and the  $C'$  single force curves of a microcapacitor while doing MFH-EFM (see Equations (2.32b) and (2.33)) and compared with the detection of  $2\omega$  (see Equation (2.23)).<sup>99</sup>

component depends on  $C''$ , superior lateral resolution is expected by reducing the long-range force contributions from the tip cone and cantilever.<sup>99</sup> This improved lateral resolution was demonstrated by comparing the  $C'$  and the  $C''$  signal (see Figure 2.21).<sup>99</sup> By fitting the second capacitance gradient signal  $C''$  with respect to the tip-surface distance  $z$  to an appropriate capacitance model of a cantilever over a surface, e.g., from COLCHERO ET AL., HUDLET ET AL.,<sup>300,366</sup> it will be possible to extract the local capacitance and the dielectric properties of the measured sample.

In case of PSCs this is a central element to understand the physical processes in the perovskite photovoltaic devices<sup>367,368</sup> As in the case of conventional EFM, signal-to-noise is greatly improved by choosing  $\Delta\omega_e$  such that one of the induced sidebands falls on one of the cantilever's mechanical resonances.<sup>99</sup>

In addition to the standard setup for an EFM experiment, MFH-EFM is performed by applying two high-frequency electrical excitations of equal magnitude ( $V_{AC,1} = V_{AC,2}$ ) at the frequencies  $\omega_{e,1}$  and  $\omega_{e,2}$  (see Equation (2.30)). A schematic of the excitation frequencies is shown in Figure 2.22. The electrical detection frequency (300 - 420 kHz) is several hundred kilohertz away from the frequency of mechanical oscillation (65 - 80 kHz), effectively reducing crosstalk between the topographical and capacitive images.<sup>99</sup> It is important to note that the

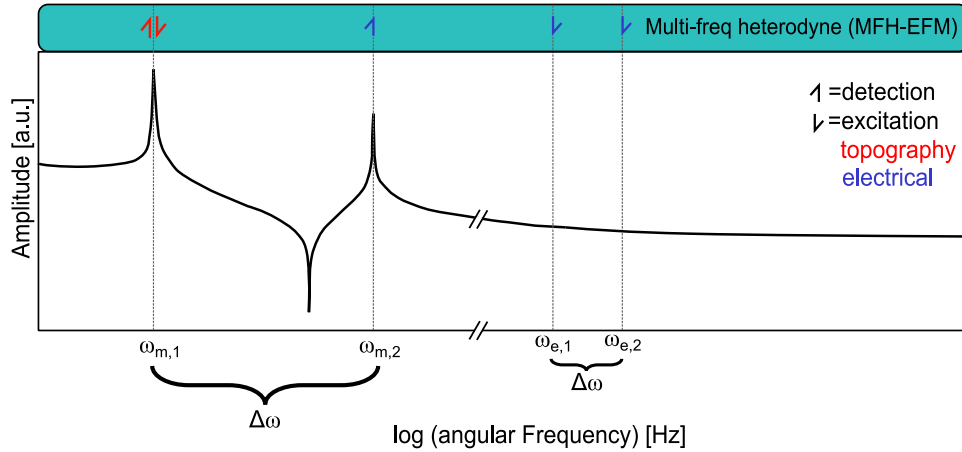


**Figure 2.22:** Schematic illustration of the excitation and detection frequencies in MFH-EFM. The lower part shows the transfer function of the cantilever, where the amplitude is plotted vs the logarithmic angular frequency. The upper part shows the excitation frequencies (↓) and the detection frequencies (↑) of the applied frequencies. The red arrow corresponds to topography- and the blue arrow to the electrical signal.<sup>99,134,135,369</sup> A comparison of H-KPFM and MFH-EFM can be found in the work of ROHRBECK ET AL.<sup>99</sup>

excitation frequencies are to be situated at the  $n$ th and the  $(n + 1)$ th multiple of the frequency gap  $\Delta\omega = (\omega_{m,2} - \omega_{m,1})$  (see Figure 2.22), respectively. The indirect detection of local capacity variations by means of an electrostatic force at the second harmonic of the cantilever ( $\omega_{m,2}$ ) has the advantage that it does not require additional devices for the measurement except for the LIA similar to the work of GRAMSE ET AL.<sup>34,99</sup> Nevertheless, to quantify the total tip-sample capacitance will require varying the distance, e.g., by force-distance spectroscopy.<sup>99</sup>

The second capacitance gradient itself can be calculated from the electrostatic force by the detected amplitude signal from the LIA,  $A_{\text{det}}$ .<sup>99</sup> This is shown in detail in Equation (2.33)<sup>99</sup>

$$\frac{\partial^2 C}{\partial z^2}(\omega) = C''(\omega) = \frac{16 \cdot V_{\text{MFH-EFM}}(\omega) \cdot \text{InvOLS}_2(\omega) \cdot k_2(\omega)}{A_m \cdot V_{\text{AC}}^2 \cdot \Xi_{\text{amp,d2C}} \cdot Q} \quad (2.33)$$

This amplitude contains in detail the voltage from the LIA output ( $V_{\text{MFH-EFM}}$ ) and the amplification factor  $\Xi_{\text{amp,d2C}}$  of this voltage from the LIA in MFH-EFM mode.<sup>99</sup> Additionally, we need to take the cantilever's frequency-dependent spring constant or transfer function ( $k(\omega)$ ) as well as the  $Q$ -factor discussed in Section 2.6.4 ( $A(\omega_{m,2}) = \frac{Q \cdot F(\omega_{m,2})}{k}$ ) into account.<sup>99</sup> The cantilever's transfer function  $k(\omega)$  corresponds to the inverse optical lever sensitivity (InvOLS) of the second harmonic ( $\text{InvOLS}_2$ ) and the spring constant of the second resonance ( $k_2$ ).<sup>99</sup>

It is important to note that the InvOLS and the spring constant on the second resonance is not the same as measured on the first resonance by the method of SADER ET AL.<sup>370</sup> It is

rather necessary to calculate the properties of the cantilever for the respective eigenmodes.<sup>371</sup> The InvOLS of the second harmonic (*InvOLS*<sub>2</sub>) is determined through the measurement of the cantilever's oscillation at its second mechanical resonance ( $\omega_{m,2}$ ), while conducting force-distance curves and quantifying the reciprocal slope of the mechanical voltage of the detector ( $V_m$ ) against the tip-sample distance ( $z$ ). The spring constant of the second resonance ( $k_2$ ) can be estimated through the method of SADER, while at the second resonance. Alternatively,  $k_2$  can be calculated with the formula by LABUDA ET AL.:<sup>371</sup>

$$k_n = k_1 \left( \frac{f_n}{f_1} \right)^\zeta \quad (2.34)$$

The power-law exponent  $\zeta$  can be determined empirically; it has been shown to be approximately 1.72 for a rectangular cantilever with a resonance frequency of  $f_1 = 70$  kHz and a spring constant of  $k_1 = 2 \frac{\text{N}}{\text{m}}$ .<sup>371</sup>

The newly developed MFH-EFM method is an advantageous addition to the toolkit of the AFM, given its facile capacity to be integrated into existing EFM setups.

In the following chapters, I will present the three research projects that were concluded during my doctoral studies. The present study in Chapter 3 will initiate with a thorough examination of the passivation strategies employed to the PSCs, utilizing KPFM.



---

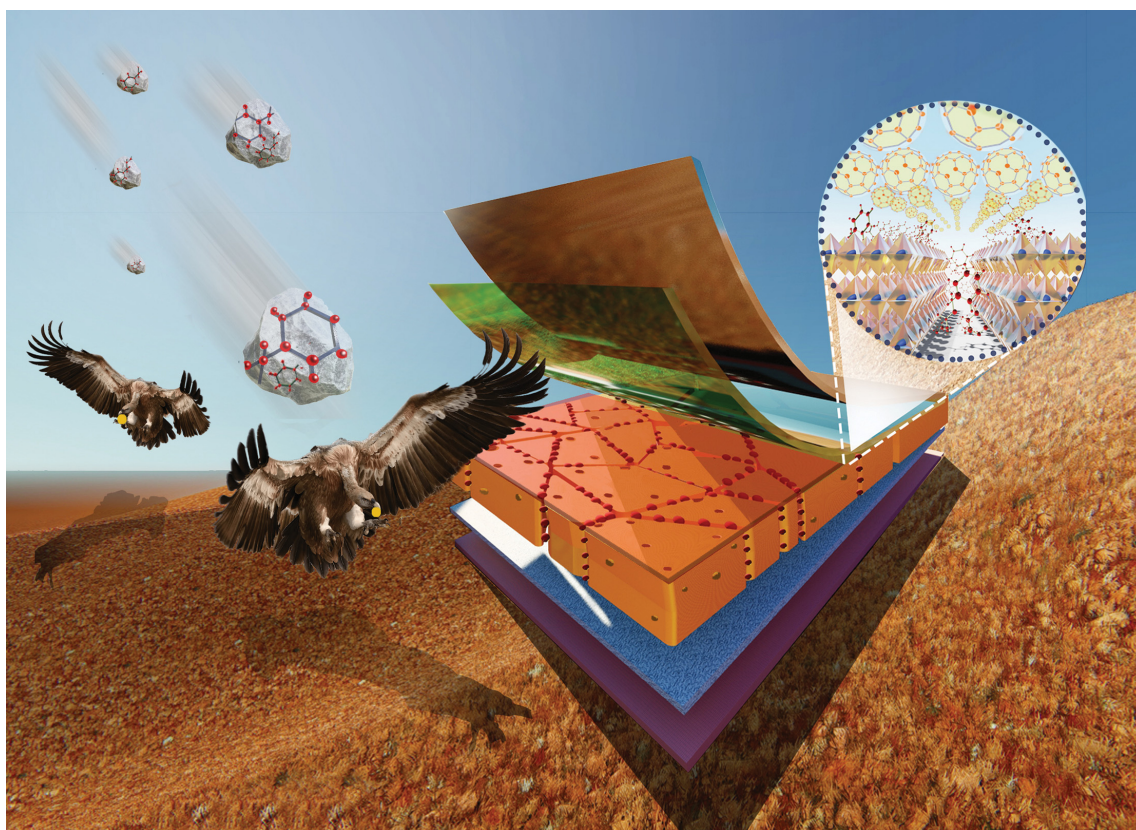
### 3 Two birds with one stone: dual grain-boundary and interface passivation enables >22 % efficient inverted methylammonium-free perovskite solar cells

Reproduced from Ref. 'Gharibzadeh, S.; Fassel, P.; Hossain, I. M.; Rohrbeck, P.; Frericks, M.; Schmidt, M.; Duong, T.; Khan, M. R.; Abzieher, T.; Nejand, B. A.; Schackmar, F.; Almora, O.; Feeney, T.; Singh, R.; Fuchs, D.; Lemmer, U.; Hofmann, J. P.; Weber, S. A. L.; Paetzold, U. W. Two Birds with One Stone: Dual Grain-Boundary and Interface Passivation Enables >22 % Efficient Inverted Methylammonium-Free Perovskite Solar Cells. *Energy Environ. Sci.* **2021**, 14 (11), 5875–5893. DOI: 10.1039/D1EE01508G.<sup>97</sup> with permission from the Royal Society of Chemistry.

In this paper, we used the KPFM method to investigate defect passivation strategies within halide perovskites materials.

Pascal Niko Rohrbeck is one of the co-authors of this paper. Pascal Niko Rohrbeck measured KPFM on the different samples (Figure 6) and analysed among Saba Gharibzadeh, Paul Fassel, and Stefan A. L. Weber the data. Also, Pascal Niko Rohrbeck reviewed and commented on the paper among all the other authors.

## CHAPTER 3. TWO BIRDS WITH ONE STONE: DUAL GRAIN-BOUNDARY AND INTERFACE PASSIVATION ENABLES >22 % EFFICIENT INVERTED METHYLAMMONIUM-FREE PEROVSKITE SOLAR CELLS



Showcasing research of Ulrich Paetzold's laboratory, Institute of Microstructure Technology & Light Technology Institute, Karlsruhe Institute of Technology, Germany.

Two birds with one stone: dual grain-boundary and interface passivation enables >22% efficient inverted methylammonium-free perovskite solar cells

Perovskite solar cells in p-i-n architecture have demonstrated great potential for flexible and perovskite-based tandem photovoltaics. This study introduces a dual passivation strategy using the long chain alkylammonium salt phenethylammonium chloride both as an additive and for surface treatment to simultaneously passivate the grain boundaries and the interface. We achieve one of the highest efficiencies for p-i-n perovskite solar cells by advancing simultaneously the open-circuit voltage and the fill factor. The presented dual passivation strategy highlights the importance of advanced defect management of the perovskite absorber layer to achieve highest performance.

As featured in:



See Ulrich W. Paetzold *et al.*, *Energy Environ. Sci.*, 2021, **14**, 5875.



Cite this: *Energy Environ. Sci.*,  
2021, 14, 5875

## Two birds with one stone: dual grain-boundary and interface passivation enables >22% efficient inverted methylammonium-free perovskite solar cells†

Saba Gharibzadeh,<sup>†‡</sup> Paul Fassel,<sup>†‡</sup> Inteaz M. Hossain,<sup>ab</sup> Pascal Rohrbeck,<sup>†c</sup> Markus Frericks,<sup>†de</sup> Moritz Schmidt,<sup>†de</sup> The Duong,<sup>†g</sup> Motiur Rahman Khan,<sup>†a</sup> Tobias Abzieher,<sup>a</sup> Bahram Abdollahi Nejad,<sup>†ab</sup> Fabian Schackmar,<sup>ab</sup> Osbel Almora,<sup>†h</sup> Thomas Feeney,<sup>a</sup> Roja Singh,<sup>†ab</sup> Dirk Fuchs,<sup>†</sup> Uli Lemmer,<sup>a</sup> Jan P. Hofmann,<sup>†de</sup> Stefan A. L. Weber<sup>c</sup> and Ulrich W. Paetzold<sup>†\*ab</sup>

Advancing inverted (p–i–n) perovskite solar cells (PSCs) is key to further enhance the power conversion efficiency (PCE) and stability of flexible and perovskite-based tandem photovoltaics. Yet, the presence of defects at grain boundaries and in particular interfacial recombination at the perovskite/electron transporting layer interface induce severe non-radiative recombination losses, limiting the open-circuit voltage ( $V_{OC}$ ) and fill factor (FF) of PSCs in this architecture. In this work, we introduce a dual passivation strategy using the long chain alkylammonium salt phenethylammonium chloride (PEACl) both as an additive and for surface treatment to simultaneously passivate the grain boundaries and the perovskite/ $C_{60}$  interface. Using [2-(9H-carbazol-9-yl)ethyl]phosphonic acid (2PACz) as a hole transporting layer and a methylammonium (MA)-free  $Cs_{0.18}FA_{0.82}PbI_3$  perovskite absorber with a bandgap of  $\sim 1.57$  eV, prolonged charge carrier lifetime and an on average 63 meV enhanced internal quasi-Fermi level splitting are achieved upon dual passivation compared to reference p–i–n PSCs. Thereby, we achieve one of the highest PCEs for p–i–n PSCs of 22.7% (stabilized at 22.3%) by advancing simultaneously the  $V_{OC}$  and FF up to 1.162 V and 83.2%, respectively. Using a variety of experimental techniques, we attribute the positive effects to the formation of a heterogeneous 2D Ruddlesden–Popper (PEA)<sub>2</sub>(Cs<sub>1–x</sub>FA)<sub>n–1</sub>Pb<sub>n</sub>(I<sub>1–y</sub>Cl)<sub>3n+1</sub> phase at the grain boundaries and surface of the perovskite films. At the same time, the activation energy for ion migration is significantly increased, resulting in enhanced stability of the PSCs under light, humidity, and thermal stress. The presented dual passivation strategy highlights the importance of defect management both in the grain boundaries and the surface of the perovskite absorber layer using a proper passivation material to achieve both highly efficient and stable inverted p–i–n PSCs.

Received 18th May 2021,  
Accepted 3rd August 2021

DOI: 10.1039/d1ee01508g

rsc.li/ees

This article is licensed under a Creative Commons Attribution 3.0 Unported Licence.



<sup>a</sup> Light Technology Institute, Karlsruhe Institute of Technology, Engesserstrasse 13, 76131 Karlsruhe, Germany. E-mail: ulrich.paetzold@kit.edu

<sup>b</sup> Institute of Microstructure Technology, Karlsruhe Institute of Technology, Hermann-von-Helmholtz-Platz 1, 76344 Eggenstein-Leopoldshafen, Germany

<sup>c</sup> Max Planck Institute for polymer research, department physics at interfaces, Ackermannweg 10, 55128 Mainz, Germany

<sup>d</sup> Technical University of Darmstadt, Department of Materials and Earth Sciences, Surface Science Laboratory, Otto-Berndt-Strasse 3, 64287 Darmstadt, Germany

<sup>e</sup> InnovationLab GmbH, Speyerer Strasse 4, 69115 Heidelberg, Germany

<sup>f</sup> Center for Nanophotonics, AMOLF, 1098 XG Amsterdam, The Netherlands

<sup>g</sup> School of Engineering, The Australian National University, Canberra, 2601, Australia

<sup>h</sup> Institute of Advanced Materials, Universitat Jaume I, 12006 Castelló, Spain

<sup>i</sup> Institute for Quantum Materials and Technologies, Karlsruhe Institute of Technology, Hermann-von-Helmholtz-Platz 1, 76344 Eggenstein-Leopoldshafen, Germany

† Electronic supplementary information (ESI) available. See DOI: 10.1039/d1ee01508g

‡ These authors contributed equally to this work.

# CHAPTER 3. TWO BIRDS WITH ONE STONE: DUAL GRAIN-BOUNDARY AND INTERFACE PASSIVATION ENABLES >22 % EFFICIENT INVERTED METHYLAMMONIUM-FREE PEROVSKITE SOLAR CELLS

View Article Online

Paper

Energy & Environmental Science

## Broader context

Due to the rapid increase in power conversion efficiency of perovskite solar cells (PSCs), they are considered an emerging area of research in photovoltaic technologies. While inverted p-i-n PSCs have demonstrated great potential for flexible and perovskite-based tandem photovoltaics, key challenges still need to be addressed as compared to their n-i-p counterparts. In particular, severe non-radiative recombination losses induced by the presence of defects at grain boundaries (GBs) and interfacial recombination at the perovskite/electron transporting layer interface limit the open-circuit voltage ( $V_{OC}$ ) and fill factor (FF) of PSCs in this architecture. To address this issue, we demonstrate that utilizing a dual passivation strategy using phenethylammonium chloride both as an additive and for surface treatment simultaneously passivates defects at the GBs and the perovskite/ $C_{60}$  interface. We show that this is due to the formation of a heterogeneous 2D Ruddlesden-Popper phase, leading to a significant improvement in both the  $V_{OC}$  and FF. In view of the urge to advance p-i-n PSCs for flexible and perovskite-based tandem photovoltaics, our findings stress the importance of defect management both at the GBs and the surface of the perovskite absorber layer in order to achieve both highly efficient and stable inverted p-i-n PSCs.

## Introduction

Single-junction organic-inorganic metal halide perovskite solar cells (PSCs) have demonstrated outstanding performance in laboratory-scale devices, closing the gap to the highest reported power conversion efficiencies (PCEs) of the market-dominating Si solar cells.<sup>1,2</sup> While PCEs above 23% have been demonstrated using the mesoporous<sup>3-12</sup> and planar<sup>13-22</sup> n-i-p architecture (up to 25.5% certified<sup>23</sup>), inverted planar p-i-n PSCs still lag behind despite several recent studies reporting PCEs above 22% (up to 22.75% certified<sup>24</sup>) (see Fig. S1, ESI†).<sup>20,24-30</sup> Further increasing the PCE of p-i-n PSCs is crucial given (1) their compatibility with p-type Si bottom solar cells for monolithic perovskite/Si tandem photovoltaics (PV),<sup>31,32</sup> (2) their low-temperature processability ( $\leq 100$  °C), and (3) their promising operational stability along with negligible hysteresis.<sup>33</sup>

The most relevant bottleneck limiting the PCE of p-i-n PSCs is the apparent non-radiative recombination losses at the interface between the perovskite and the charge transport layers (CTLs).<sup>33-39</sup> As a result, the open-circuit voltage ( $V_{OC}$ ) of p-i-n PSCs relative to the Shockley-Queisser (S-Q) limit for a given bandgap has long been significantly lower as compared to their n-i-p counterparts (Fig. S2a, ESI†), while recently specifically the  $V_{OC} \times$  fill factor (FF) product is lagging behind (Fig. S2b, ESI†).<sup>31,33,34</sup> Considering that the novel self-assembled monolayer (SAM) hole transport layers (HTLs) 2PACz ([2-(9H-carbazol-9-yl)ethyl]phosphonic acid) and Me-4PACz ([2-(3,6-dimethoxy-9H-carbazol-9-yl)ethyl]phosphonic acid) developed by Albrecht and coworkers form a practically lossless interface,<sup>31,32</sup> the remaining challenge is interfacial recombination at the electron transport layer (ETL), which is commonly the fullerene  $C_{60}$  or phenyl- $C_{61}$ -butyric acid methyl ester (PCBM). The second most relevant bottleneck is bulk defects in conjunction with the abundance of grain boundaries in perovskite films. Although the electronic properties of grain boundaries are still debated,<sup>40-42</sup> they are commonly associated with an increased defect density, facilitated ion migration and an accelerated degradation under light and thermal stress.<sup>43-47</sup> The latter aspect is particularly important considering that stability is one of the main concerns for the future commercialization of perovskite PVs.<sup>48-51</sup> For these reasons, effective strategies to reduce both, (1) interfacial recombination at surface/interface defects and (2) bulk recombination at bulk or grain boundary

defects are pivotal to maximize both the  $V_{OC}$  and FF as well as the stability of planar p-i-n PSCs.

Post-treatment of perovskite films is a widely established strategy to suppress interfacial recombination and optimize the performance of PSCs.<sup>49,52-58</sup> Prominent examples for tailored passivation schemes are the use of (alkyl)ammonium salts,<sup>3,4,6,10,11,13,14,20,22,59-80</sup> other organic compounds<sup>16,19,24,45,81-87</sup> and fluoride-containing materials.<sup>31,35,38,74,86,88,89</sup> Alongside established chemical passivation that reduces the density of surface/interface defects,<sup>53,63,83,85</sup> this strategy also encompasses performance enhancements by the formation of 2D/3D heterostructures<sup>10,59-61,63,64,70,76-78</sup> and/or wide-bandgap interface layers.<sup>6,66,90,91</sup> The latter enhancements can be the result of improved energy level alignment that promotes selectivity and carrier transport across perovskite/CTL interfaces and/or a reduced probability for interfacial recombination due to charge blocking.<sup>19,25,35,53,67,77,92</sup> Recently, lithium fluoride (LiF) has been identified as an interlayer at the perovskite/ETL interface that significantly enhances the performance of p-i-n PSCs.<sup>31,35,38,88,89,93</sup> However, PSCs with LiF undergo severe long-term degradation which limits the applicability of this approach.<sup>31,93</sup>

In order to reduce non-radiative recombination in the bulk and grain boundaries, the use of non-stoichiometric precursors<sup>94-96</sup> or incorporation of different additives into the perovskite precursor solution or antisolvent such as metal cations,<sup>97</sup> anions,<sup>98</sup> chloride (Cl) or thiocyanate (SCN),<sup>4-6,10,14,15,17,19,88</sup> (alkyl)ammonium salts,<sup>3,25,26,64,98-105</sup> other organic compounds,<sup>74,84,106</sup> and fluoride-containing materials<sup>74,107</sup> have been proposed. Given that these additives directly assist in perovskite film formation, changes in crystallization dynamics as well as a reduced defect density are commonly observed.<sup>55,108,109</sup> For instance, Xu *et al.* demonstrated that by alloying MAPbCl<sub>3</sub> into the perovskite film, the  $V_{OC}$  of the wide-bandgap p-i-n PSCs significantly improved due to a reduced bulk defect density.<sup>88</sup> In other works, the addition of various long chain alkylammonium cations was shown to self-assemble into a wide-bandgap 2D perovskite phase passivating the surface and/or grain boundaries of the 3D perovskite film.<sup>25,58,64,99-105</sup> However, due to the insulating nature of such 2D phases, adding too large amounts typically results in an overall lower PCE compared to control devices.<sup>25,64,99,101,103,104,107</sup>

Despite the apparent wide range of strategies suggested to reduce non-radiative recombination losses in PSCs,<sup>49,54,57,110,111</sup>

This article is licensed under a Creative Commons Attribution 3.0 Unported Licence.



to our knowledge there is only one recent report that used the same passivation material both as an additive and for surface treatment to improve the performance of p-i-n PSCs.<sup>84</sup> In this work, we report on an effective dual passivation approach using the long chain alkylammonium salt phenethylammonium chloride (PEACl) to simultaneously passivate the grain boundaries and the perovskite/C<sub>60</sub> interface by using PEACl:PbCl<sub>2</sub> as the additive and PEACl for surface treatment, respectively. Employing time-resolved photoluminescence (TRPL) and photoluminescence quantum yield (PLQY) measurements, dual passivation is proven to be most effective in reducing non-radiative recombination compared to either of the individual passivation strategies. By analyzing cathodoluminescence (CL), scanning electron microscopy (SEM), X-ray/ultraviolet photoelectron spectroscopy (XPS/UPS), X-ray diffraction (XRD) and Kelvin probe force microscopy (KPFM) measurements, we attribute the positive effects to the formation of a heterogeneous 2D Ruddlesden–Popper (RP) (PEA)<sub>2</sub>(Cs<sub>1-x</sub>FA<sub>x</sub>)<sub>n-1</sub>Pb<sub>n</sub>(I<sub>1-y</sub>Cl<sub>y</sub>)<sub>3n+1</sub> perovskite phase with  $n \sim 1-2$  at the surface and grain boundaries of the film that exhibits a lower work function (WF) and hole blocking properties. Finally, thermal admittance spectroscopy (TAS) reveals that the activation energy for ion migration is strongly increased upon dual passivation, which is reflected in an enhanced device stability under maximum power point (MPP) tracking and heat treatment for 1000 h. In summary, by using PEACl both as the additive and for surface treatment, we could not only effectively reduce interfacial recombination at the perovskite/C<sub>60</sub> interface, but simultaneously passivate the grain boundary defects. Employing dual passivation for

methylammonium (MA)-free p-i-n PSCs with a bandgap of  $\sim 1.57$  eV leads to a very high PCE of 22.7% (stabilized at 22.3%) with a remarkable  $V_{OC}$  and FF of up to 1.162 V and 83.2%, respectively. In view of the urge to advance the p-i-n structure for flexible and perovskite-based tandem photovoltaics, this development is pivotal.

## Results and discussion

The dual passivation strategy developed in this work is based on combining the incorporation of PEACl:PbCl<sub>2</sub> into the perovskite precursor solution and PEACl surface treatment (Fig. 1). Since using long chain alkylammonium salts as additive mainly passivates the grain boundaries, as will be shown later and has been proposed in previous works,<sup>26,98,101-103</sup> it is for simplicity referred to as grain boundary passivation (GBP) in the following, while surface treatment is referred to as surface passivation (SP). For the reference perovskite films (referred to as Ref), we adapt an established fabrication route,<sup>112</sup> yielding high-quality MA-free films with a composition of Cs<sub>0.18</sub>FA<sub>0.82</sub>PbI<sub>3</sub> (10% excess PbI<sub>2</sub>) and a bandgap of  $\sim 1.57$  eV. In case of GBP, PEACl:PbCl<sub>2</sub> (1 : 1 molar ratio) dissolved in dimethyl sulfoxide (DMSO) is added into the Ref precursor solution (optimized at a concentration of 2 mol%; see Fig. S3, ESI†). The Ref and GBP precursor solutions are spin-coated on top of ITO/2PACz and annealed at 150 °C for 30 min (Fig. 1a). In case of SP, PEACl dissolved in isopropanol (optimized at a concentration of 1.5 mg ml<sup>-1</sup>; see Fig. S4, ESI†), is dynamically spin-coated on the surface of Cs<sub>0.18</sub>FA<sub>0.82</sub>PbI<sub>3</sub>

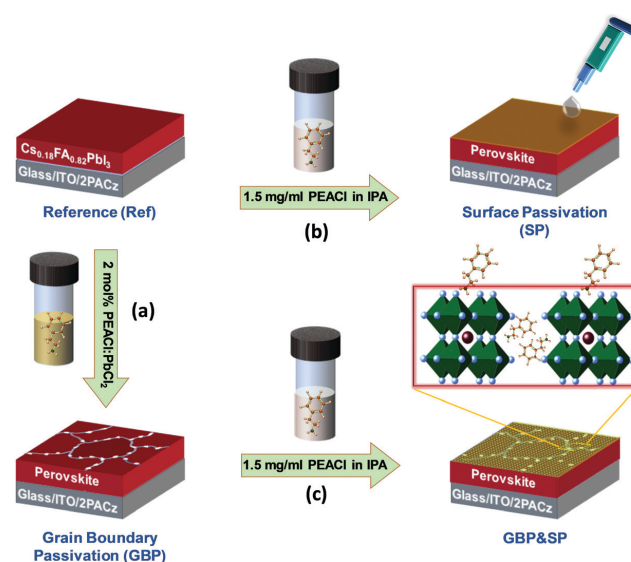


Fig. 1 Schematic of the perovskite absorber deposition process employing the dual passivation strategy developed in this work: (a) grain boundary passivation (GBP) by incorporation of PEACl:PbCl<sub>2</sub> into the perovskite precursor solution, (b) surface passivation (SP) by treatment of PEACl in IPA on top of the perovskite absorber layer and (c) combination of grain boundary and surface passivation (GBP&SP).

# CHAPTER 3. TWO BIRDS WITH ONE STONE: DUAL GRAIN-BOUNDARY AND INTERFACE PASSIVATION ENABLES >22 % EFFICIENT INVERTED METHYLAMMONIUM-FREE PEROVSKITE SOLAR CELLS

View Article Online

Paper

Energy & Environmental Science

films and subsequently annealed at 100 °C for 10 min (Fig. 1b). Finally, both individual passivation strategies are exploited together, referred to as GBP&SP (Fig. 1c). Further details are provided in the Experimental Section (ESI†).

## Photovoltaic performance

In order to demonstrate the trend in performance of planar p-i-n PSCs upon employing either individual passivation (GBP or SP) as well as dual passivation (GBP&SP) compared to Ref PSCs, devices in the layer stack ITO/2PACz/perovskite/C<sub>60</sub>/BCP/Ag with an active area of 12.3 mm<sup>2</sup> were prepared (Fig. 2a). Fig. 2b and Table S1 (ESI†) summarize the current density–voltage (*J*-*V*) characteristics and PV parameters of the best-performing p-i-n PSCs. The corresponding statistics (in total 147 devices) that emphasize the very high yield and good reproducibility of the key trends are shown in Fig. 2c. The best Ref PSC exhibits a PCE of 20.4% with a short-circuit current density (*J*<sub>SC</sub>) of 23.9 mA cm<sup>-2</sup>, a *V*<sub>OC</sub> of 1.086 V, and a FF of 78.6%. This denotes a very respectable starting point in performance for p-i-n PSCs compared to literature (see Fig. S1, ESI†). The PCE of the best GBP PSC is slightly improved to 20.7%, which is mainly associated with a 26 mV enhancement in *V*<sub>OC</sub> as well as a slightly improved FF. The small decrease in *J*<sub>SC</sub> to 23.6 mA cm<sup>-2</sup> is attributed to the formation of a 2D RP perovskite (see discussion in the following) and, thus, a slight decrease in 3D perovskite absorber volume (see ultraviolet-visible (UV-vis) measurements in Fig. S5, ESI†).<sup>64,99</sup> The best SP PSC already exhibits a very high PCE of 22.1% with a

significant improvement in both the *V*<sub>OC</sub> (1.131 V) and FF (82.3%) as compared to the Ref PSC.

Strikingly, upon dual passivation, the *V*<sub>OC</sub> and FF are further enhanced to 1.162 V and 83.2% respectively, which leads to a remarkable PCE of 22.7% for the best GBP&SP PSC (see Fig. 2d). This corresponds to a *V*<sub>OC</sub> × FF product of 0.891 with respect to the S-Q limit, the highest reported for p-i-n PSCs with a PCE above 21% (compare Fig. S1 and S2b, ESI†). Furthermore, the GBP&SP PSC also exhibits a remarkable stabilized PCE (under MPP tracking), *V*<sub>OC</sub> and *J*<sub>SC</sub> of 22.3%, 1.161 V and 23.4 mA cm<sup>-2</sup> under continuous AM1.5G illumination for 5 min, respectively (Fig. 2e). It should be noted that the *V*<sub>OC</sub> enhancements are not governed by an increase in the bandgap, as shown by analysis *via* the Tauc plot method and the inflection point of the EQE spectra (Fig. S6a and b, ESI†),<sup>113</sup> but relate to reduced non-radiative recombination, as we will later elaborate on in detail. We note that when increasing the concentration of PEACl to 3 mg ml<sup>-1</sup> (beyond the optimum concentration), the *V*<sub>OC</sub> of GBP&SP PSCs increases further up to 1.184 V (see Fig. S4, ESI†), which represents a voltage deficit of only 393 mV and 104 mV with respect to the bandgap and radiative limit respectively (90.9% of the S-Q limit),<sup>113</sup> that are among the lowest reported for p-i-n PSCs (Fig. S2a, ESI†). However, since the *J*<sub>SC</sub> and FF decline at the same time, possibly due to the insulating nature of a thicker 2D RP passivation layer at the surface,<sup>63,64,81,82,99</sup> the PCE of the best GBP&SP PSC drops to 21.8%. It should be noted that the reported *J*<sub>SC</sub> for all PSCs is corrected using the ratio of *J*<sub>SC</sub> derived from the external quantum efficiency (EQE) and *J*-*V* measurements of the best PSCs (Fig. 2b and Fig. S7, ESI†).

This article is licensed under a Creative Commons Attribution 3.0 Unported Licence.

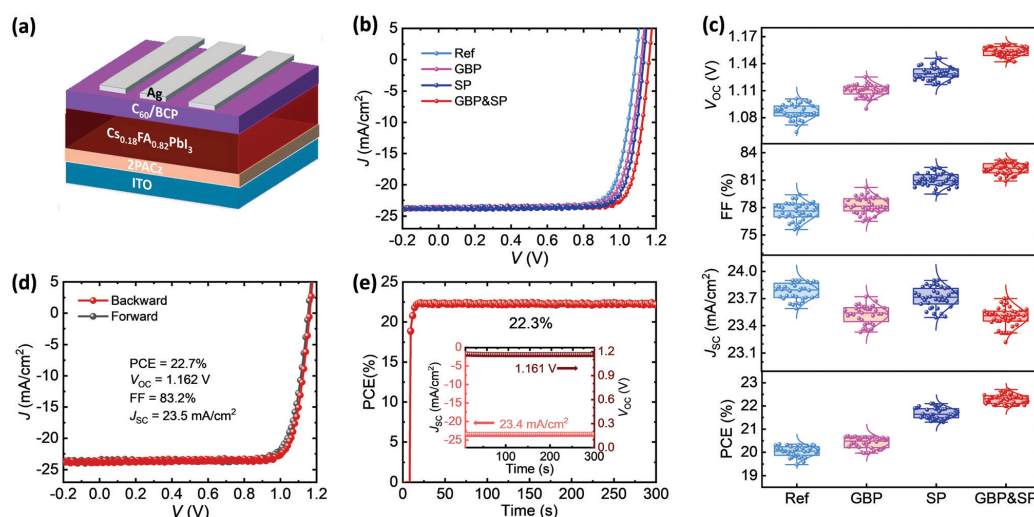


Fig. 2 (a) Schematic of the employed perovskite solar cell configuration with a layer stack sequence of ITO/2PACz/perovskite/C<sub>60</sub>/BCP/Ag. (b) Current density versus voltage (*J*-*V*) characteristics and (c) statistical distribution of the open-circuit voltage (*V*<sub>OC</sub>), fill factor (FF), short-circuit current density (*J*<sub>SC</sub>), and power conversion efficiency (PCE) of perovskite solar cells without any modification (Ref), with surface passivation (SP), grain boundary passivation (GBP) and combined grain boundary and surface passivation (GBP&SP). (d) *J*-*V* characteristics and (e) maximum power point (MPP) tracking of the best-performing GBP&SP perovskite solar cell, demonstrating a stabilized PCE of 22.3%. The inset shows the stabilized *J*<sub>SC</sub> and *V*<sub>OC</sub>.

This results in a rather conservative determination of PCE in this work. To summarize, the combined enhancements in  $V_{OC}$  and FF are highest for GBP&SP PSCs, which highlights the necessity of the simultaneous passivation of the perovskite/ $C_{60}$  interface, and – as we will show later – the grain boundaries of the perovskite thin film.

Next to dual passivation by PEACl, we first evaluated the effect on the  $V_{OC}$  upon employing PEAI and PEABr, since they have been used in numerous previous reports for passivation of perovskite films.<sup>62,65,69,77,99,103</sup> As shown in Fig. S8 (ESI<sup>†</sup>), PEACl-based GBP&SP PSCs show a much higher average of  $V_{OC}$  of  $\sim 1.15$  V as compared to  $\sim 1.12$  V in case of PEAI and PEABr. Therefore, we focussed in more detail on alternative chloride-based long chain alkylammonium salts namely *n*-butylammonium chloride (BACl) and *n*-octylammonium chloride (OACl), since BAI,<sup>63,64,71,72,76,102</sup> BABr,<sup>10,59,60,64</sup> OAI,<sup>4,72,75,76,101</sup> and OABr<sup>10,71</sup> have previously been reported to serve as efficient passivation molecules as additive as well as for surface treatment.

While SP PSCs all exhibit an enhanced  $V_{OC}$  and FF as compared to Ref PSCs, the enhancements are most pronounced in case of PEACl (Fig. S9, ESI<sup>†</sup>). Employing the dual passivation strategy leads to a  $\sim 30$  mV  $V_{OC}$  enhancement in case of OACl and BACl, which is much lower compared to  $\sim 70$  mV for PEACl-based GBP&SP PSCs (see Fig. S10, ESI<sup>†</sup>). Furthermore,

while for BACl-based GBP&SP PSCs the FF remains similar and only a slight drop in  $J_{SC}$  is observed compared to Ref PSCs, these parameters are even reduced in case of OACl, as expected based on previous reports employing too large amounts of alkylammonium salts as additive.<sup>25,64,99,102</sup> Therefore, an overall lower average PCE of only 18.6% is obtained for OACl-based GBP&SP PSCs compared to 20.1% for Ref PSCs, while the average PCE is slightly higher at 20.9% in case of BACl. These results highlight that our dual GBP&SP passivation strategy in principle is compatible with other Cl-based long chain alkylammonium salts, but reduced charge carrier transport (*i.e.*, lower  $J_{SC}$  and/or FF) can easily impede any positive effects from reduced interfacial recombination (*i.e.*, higher  $V_{OC}$ ). Hence, careful optimization of the fabrication parameters is required. Targeting high efficiency and reproducibility, we identified PEACl as the superior choice for the dual passivation strategy of p–i–n PSCs studied in this work.

### Photophysical properties

To discriminate the effect of GBP, SP and GBP&SP on non-radiative recombination of the PSCs, we first show representative TRPL transients measured for ITO/2PACz/perovskite/ $C_{60}$  layer stacks in Fig. 3a. While the detailed interpretation of such transients can be challenging,<sup>114</sup> a longer monomolecular

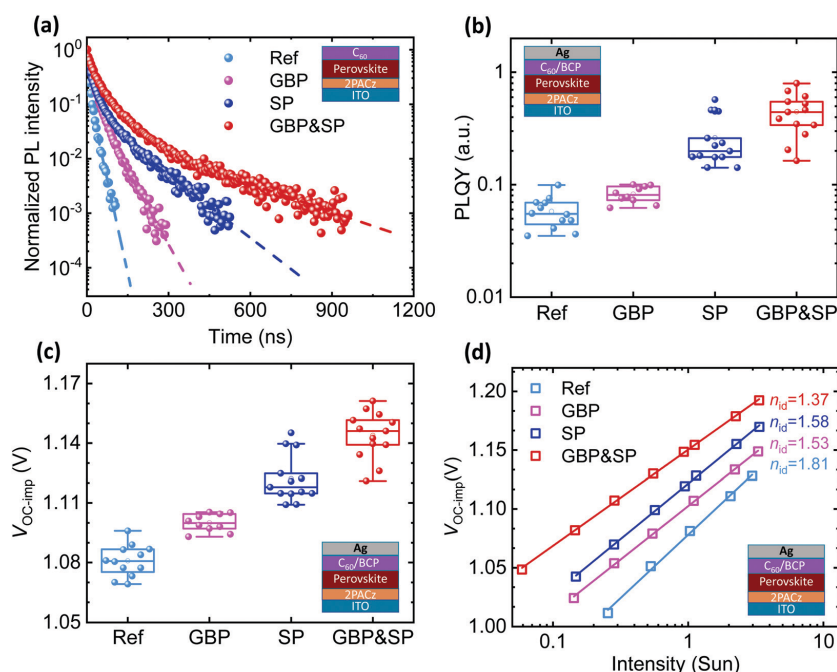


Fig. 3 (a) Time-resolved photoluminescence (TRPL), (b) photoluminescence quantum yield (PLQY), (c) the obtained implied  $V_{OC}$  ( $V_{OC-imp}$ ), and (d) ideality factor ( $n_{id}$ ) extracted from a fit to the intensity-dependent  $V_{OC-imp}$  of the perovskite films prepared on ITO/2PACz substrates for the reference (Ref), surface passivation (SP), grain boundary passivation (GBP) and grain boundary & surface passivation (GBP&SP) films. TRPL in (a) is measured with a  $C_{60}$  layer on top, while (b–d) are measured for a full device stack.

# CHAPTER 3. TWO BIRDS WITH ONE STONE: DUAL GRAIN-BOUNDARY AND INTERFACE PASSIVATION ENABLES >22 % EFFICIENT INVERTED METHYLAMMONIUM-FREE PEROVSKITE SOLAR CELLS

View Article Online

Paper

Energy & Environmental Science

lifetime at low-level injection can be attributed to reduced non-radiative recombination either within the bulk (including the grain boundaries) or the perovskite/CTL interfaces.<sup>114–117</sup> The lifetime increases considerably by more than one order of magnitude in the order ref (19 ns) → GBP (48 ns) → SP (113 ns) → GBP&SP (256 ns) (dashed lines Fig. 3a). This indicates that non-radiative recombination is effectively suppressed in the same order as the observed  $V_{OC}$  enhancement of the PSCs.<sup>114–117</sup>

To quantify the reduction of non-radiative recombination, PLQY measurements along with the internal quasi-Fermi level splitting ( $E_F$ ), that are attributed to the 'implied  $V_{OC}$ ' via  $V_{OC\_imp} = \Delta E_F/q = V_{OC\_rad} + k_B T/q \ln(\text{PLQY})$ , are discussed next.<sup>34,118</sup> Analysing PLQY and  $V_{OC\_imp}$  for the stack ITO/2PACz/perovskite without  $C_{60}$  allows identification of whether non-radiative recombination at the HTL/perovskite limits the  $V_{OC}$  of our PSCs.<sup>34,35,39</sup> For the Ref films, we find an already very high average PLQY ( $V_{OC\_imp}$ ) of 7.2% (1.206 V) which only slightly increases to 7.9% (1.218 V), 9.8% (1.218 V) and 9.7% (1.225 V) for GBP, SP and GBP&SP films, respectively (Fig. S11, ESI<sup>†</sup>), with  $V_{OC\_imp}$  being well above the obtained  $V_{OC}$  of all PSCs presented in Fig. 2c. This shows that our perovskite films are of very high quality and that the nearly lossless 2PACz/perovskite interface does not limit the  $V_{OC}$ , in line with previous reports.<sup>31,32,35</sup> Upon addition of  $C_{60}$ /BCP/Ag, the PLQY for Ref films severely drops to a low average value of 0.058% correlating to  $V_{OC\_imp}$  of 1.081 V, clearly showing that the perovskite/ $C_{60}$  interface limits the  $V_{OC}$  (Fig. 2b and c). Impressively, the average PLQY increases by roughly one order of magnitude to 0.083%, 0.26% and 0.45% for GBP, SP, and GBP&SP films respectively (Fig. 3b), correlating to an enhanced  $V_{OC\_imp}$  of 1.100 V, 1.122 V and 1.144 V, respectively (Fig. 3c). Notably, the values of  $V_{OC\_imp}$  closely match with the average  $V_{OC}$  of the respective PSCs (compare Fig. 2c), implying that all PSCs have a proper energetic alignment that does not result in an offset between  $V_{OC\_imp}$  and  $V_{OC}$ .<sup>34,35,92,118,119</sup> We note that increasing the PEACL concentration to 3 mg ml<sup>-1</sup> for GBP&SP films further increases the PLQY and  $V_{OC\_imp}$  to remarkable values of up to 2.21% and 1.190 V, respectively, which is in line with the results discussed above for the respective PSCs (see Fig. S12, ESI<sup>†</sup>).

At first sight, the role of the PEACL:PbCl<sub>2</sub> additive for the improved device performance remains unclear, since  $V_{OC\_imp}$  for the half layer stack without  $C_{60}$  only slightly increases for all passivation strategies as compared to Ref films. To shed more light on this aspect, we show representative TRPL transients for the stack ITO/2PACz/perovskite in Fig. S13 (ESI<sup>†</sup>). Here, we find a clear trend with the monomolecular lifetime for GBP films (~1624 ns) and GBP&SP films (~1497 ns) being considerably longer as compared to Ref films (~335 ns). Interestingly, for perovskite films with surface passivation only, the lifetime is solely slightly increased to ~464 ns. At this point, we hypothesize that the enhanced lifetimes in case of GBP relate to the passivation of shallow grain boundary traps *via* the self-assembly of PEA<sup>+</sup> molecules and/or the formation of a PEACL-based 2D RP phase.<sup>25,26,36,41,46,102,104–106,120,121</sup> We note that shallow traps are typically filled at high illumination intensities

around 1 Sun, possibly explaining why the values of PLQY and  $V_{OC\_imp}$  for stacks without  $C_{60}$  are only slightly enhanced by all three passivation strategies. This explanation is in line with the common implication that grain boundaries are not necessarily detrimental to device performance at solar illumination intensities.<sup>40,41,120</sup> To shed more light on this, we evaluate the trap-state density ( $n_t$ ) and charge carrier mobility ( $\mu$ ) of electrons and holes for the different passivation strategies *via* space charge limited current (SCLC) measurements. We fabricated both electron- and hole-only devices with the configuration of ITO/SnO<sub>2</sub>/perovskite/ $C_{60}$ /BCP/Ag and ITO/2PACz/perovskite/Spiro-MeOTAD/Ag, respectively. The dark  $J$ - $V$  characteristics of the devices are plotted in Fig. S14 and S15 (ESI<sup>†</sup>) and are analyzed according to the SCLC method (see further details in the ESI<sup>†</sup>). The electron mobility of the Ref device is  $4.9 \times 10^{-3} \text{ cm}^2 \text{ V}^{-1} \text{ s}^{-1}$ , while both SP and GBP devices demonstrate a comparable increase in mobility to  $6.3 \times 10^{-3}$  and  $7.2 \times 10^{-3} \text{ cm}^2 \text{ V}^{-1} \text{ s}^{-1}$  (see Table S2, ESI<sup>†</sup>), respectively. Applying our dual passivation strategy, the electron mobility further increases to  $10.0 \times 10^{-3} \text{ cm}^2 \text{ V}^{-1} \text{ s}^{-1}$ . Furthermore, the trap-filled limit voltage ( $V_{TFL}$ ), which is linearly proportional to the trap-state density, demonstrates a substantial decrease in the order Ref → GBP → SP → GBP&SP, correlating to a reduction in electron trap density from  $9.2 \times 10^{15} \text{ cm}^{-3}$  to  $6.5 \times 10^{15}$ ,  $5.4 \times 10^{15}$  and  $3.7 \times 10^{15} \text{ cm}^{-3}$ , respectively (see Fig. S14 and Table S2, ESI<sup>†</sup>). A very similar trend is also observed for the calculated hole mobilities, while the reduction in the hole trap density is apparently slightly less pronounced (see Fig. S15 and Table S3, ESI<sup>†</sup>). Therefore, the TRPL and SCLC results indicate that both GBP and SP independently contribute to enhancing both the electron- and hole mobilities by roughly a factor of 2, while at the same time specifically reducing the electron trap density at the grain boundaries and surface of the perovskite film.

To assess the impact of the reduced trap-state density on device performance, we perform intensity-dependent PLQY measurements to obtain the internal ideality factor ( $n_{id}$ ) from a fit to the calculated  $V_{OC\_imp}$ .<sup>34</sup> The ideality factor has been proven to be governed by bulk as well as interfacial recombination properties.<sup>34,122,123</sup> For high-performing PSCs that are not limited by failures at either of the perovskite/CTL interfaces, a reduction of  $n_{id}$  towards a value of 1 is typically associated with a predominant bimolecular radiative and reduced trap-assisted Shockley-Read Hall recombination and there is a direct correlation between  $n_{id}$  and FF.<sup>31,34,122,124</sup> Again, we first analyse half-layer stacks without  $C_{60}$  and find a considerable reduction of  $n_{id}$  from 1.71 for Ref films to 1.48 and 1.60 for GBP and SP films, respectively, while GBP&SP films show by far the lowest  $n_{id}$  of 1.30 (Fig. S16, ESI<sup>†</sup>). The observation that  $n_{id}$  in case of GBP is slightly lower as compared to SP is in line with the enhanced monomolecular lifetime for GBP films without a  $C_{60}$  layer. Yet, despite the apparently improved bulk recombination properties, GBP PSCs remain severely limited by interfacial recombination at the perovskite/ $C_{60}$  interface, as exemplified by the lower device  $V_{OC}$  and FF. Interestingly,  $n_{id}$  of complete PSC layer stacks shows a very similar trend, with Ref PSCs exhibiting  $n_{id}$  of 1.81, which considerably reduces to 1.53 and 1.58 for GBP and SP PSCs,

This article is licensed under a Creative Commons Attribution 3.0 Unported Licence.



respectively (Fig. 3d). Critically, GBP&SP PSCs again show by far the lowest  $n_{\text{id}}$  of 1.37, only slightly higher as for the half-layer stack without  $C_{60}$ . This is among the lowest  $n_{\text{id}}$  values reported in the literature for p-i-n PSCs with a PCE > 20% and slightly below the value reported by Al Ashouri *et al.* for 2PACz-based wide-bandgap PSCs.<sup>26,31,34,38</sup> We note that when increasing the PEACl concentration to 3 mg ml<sup>-1</sup>,  $n_{\text{id}}$  of SP and GBP&SP PSCs increases again to 1.49 and 1.42 (Fig. S17, ESI<sup>†</sup>), respectively, showing that while the  $V_{\text{OC}}$  of the respective PSCs further increases (Fig. S4, ESI<sup>†</sup>), the recombination behaviour does not further benefit from too thick passivation layers, to some extent contributing to the reduced FF.

Finally, using the ideality factor and PLQY values we can determine the implied PCE and FF without and with  $C_{60}$  and compare it with an ideal device (*i.e.*,  $n_{\text{id}} = 1$ ) that has the same bandgap and  $J_{\text{SC}}$ .<sup>34</sup> This allows us to estimate the remaining losses in our devices, *i.e.* the FF losses due to series/shunt resistance, non-ideal  $n_{\text{id}}$  and non-radiative recombination.<sup>34,125</sup> As shown in Fig. S18 (ESI<sup>†</sup>), the ideal device exhibits a PCE of 27.8% with a FF of 90.3% for both Ref and GBP&SP. Without and with  $C_{60}$ , Ref (GBP&SP) exhibits an implied FF of 84.8% (87.7%) and 82.8% (86.6%), respectively, while the respective best PSCs show a FF of 78.6 (83.2%). This relates to a FF loss due to series/shunt resistance of roughly 4.2% (3.4%), while non-ideal  $n_{\text{id}}$  and non-radiative recombination account for another 2% (1.1%) from  $C_{60}$  and 5.5% (2.6%) from the bulk. This analysis reveals that, in addition to strongly enhancing the  $V_{\text{OC}}$ , our dual passivation approach (GBP&SP) reduces the FF losses by 4.6% absolute as compared to Ref PSCs due to a reduced series/shunt resistance (0.8%) as well as simultaneous passivation of the perovskite/ $C_{60}$  interface (0.9%) and grain boundaries (2.9%).

In summary, the TRPL and PLQY results show that (i) the perovskite/ $C_{60}$  interface limits the  $V_{\text{OC}}$  of our PSCs and (ii) that grain boundary passivation becomes specifically crucial in the case where the perovskite/CTL interfaces are already well passivated. Therefore, in line with the device data presented, we find that dual passivation is required to reach both the lowest non-radiative recombination losses and the lowest  $n_{\text{id}}$  that only together result in the highest  $V_{\text{OC}}$  and FF.

### Material characterization

Having demonstrated that the superior performance of our dual passivation strategy stems from reduced non-radiative recombination at the grain boundaries as well as at the perovskite/ $C_{60}$  interface, the question arises: How do SP and GBP modify the perovskite film morphology, structure or composition? To start with, we examine the films by SEM and identify a similar surface morphology and grain size distribution for the Ref and SP perovskite films (see Fig. S19a and b, ESI<sup>†</sup>). This observation is in line with the literature as surface treatment with low concentration long chain alkylammonium salts commonly does not alter the perovskite film morphology; more distinct changes to the morphology are only observed for higher concentrations (see Fig. S20, ESI<sup>†</sup>).<sup>59,60,62,64,65,90</sup> Further analysis of atomic force microscopy (AFM) images reveals a slight reduction in the root-mean-square surface roughness,

which we attribute to the fact that PEACl preferentially fills regions close to the grain boundaries (Fig. S21, ESI<sup>†</sup>).<sup>10,14</sup> For all perovskite films, the grains that appear brighter in SEM are attributed to  $\text{PbI}_2$ -rich crystallites as will be discussed later in more detail.<sup>17,95</sup>

By incorporating PEACl: $\text{PbCl}_2$  in the film for GBP films, the size of the perovskite grains remains largely unchanged, however, the number and size of the  $\text{PbI}_2$ -rich grains slightly increase (Fig. S19c, ESI<sup>†</sup>). Interestingly, notable small bright crystallites appear on the surface of the perovskite film which are specifically embedded close to the grain boundaries. This indicates that PEACl: $\text{PbCl}_2$  leads to passivation mainly near the grain boundaries. Upon additional surface treatment with PEACl for GBP&SP films, the size of these small bright crystallites is reduced and they appear more dispersed all over the surface, growing with a plate-like appearance perpendicular to the perovskite grains (Fig. S19d, ESI<sup>†</sup>). This implies that some reaction with these crystallites occurs when PEACl is deposited on top of GBP films.

To gain a better understanding about the phase or composition of the small and large bright grains observed in SEM at the surface of the perovskite films as well as their potential relevance in the context of this work, we carry out CL measurement.<sup>126</sup> For the Ref film, the grains which appear darker in SEM (highlighted by a green circle in Fig. 4) exhibit higher CL intensities (Fig. 4b) with the emission peak located at  $\sim 774$  nm (Fig. S22, ESI<sup>†</sup>) that correlates with the 3D perovskite phase with a bandgap of  $\sim 1.57$  eV (note that the CL setup is not spectrally calibrated). The grains which appear brighter and exhibit a different texture in the SEM images (highlighted by a yellow circle in Fig. 4; see further top-view SEM images in Fig. S23, ESI<sup>†</sup>) demonstrate lower CL intensities (dark spots in Fig. 4b) with a CL emission peak around 500 nm (Fig. S22, ESI<sup>†</sup>). By applying a 500 nm  $\pm$  40 nm bandpass filter to record the CL image, these grains can be clearly distinguished from the 3D perovskite grains (Fig. 4c). These regions are therefore attributed to  $\text{PbI}_2$ -rich crystallites, in line with previous reports,<sup>17,64</sup> and as seen from cross-sectional SEM images, they appear to be located on top of 3D perovskite grains (Fig. S24, ESI<sup>†</sup>). Looking specifically at the CL signal from individual large  $\text{PbI}_2$ -rich grains, there is indeed still a signal from the (underlying) 3D perovskite phase (Fig. S22, ESI<sup>†</sup>). For the SP film, we observe a slight charging of the SEM images (Fig. 4d), which we attribute to the insulating nature of a 2D RP phase forming at the surface. No noticeable change in the CL images of the SP film without and with 500 nm  $\pm$  40 nm bandpass filter is observed compared to the Ref film (Fig. 4e and f). This indicates that the large  $\text{PbI}_2$ -rich grains are not completely chemically reacting upon PEACl surface treatment, which is in contrast to previous observations that bright  $\text{PbI}_2$  related grains vanish upon treatment with various organic halides.<sup>11,20,66,77,78,84</sup> Nevertheless, due to the passivation effect, the CL signal of the 3D perovskite phase exhibits a much higher intensity compared to the Ref film (Fig. S25, ESI<sup>†</sup>), in line with the PLQY results. For the GBP film, the grains which appear as small bright grains close to the grain boundaries in SEM (highlighted by a red circle in Fig. 4g) are detected as dark small spots around the perovskite grains in the CL image (Fig. 4h). This stresses that these small grains exhibit lower CL intensities similar to the large  $\text{PbI}_2$ -rich grains. Interestingly,



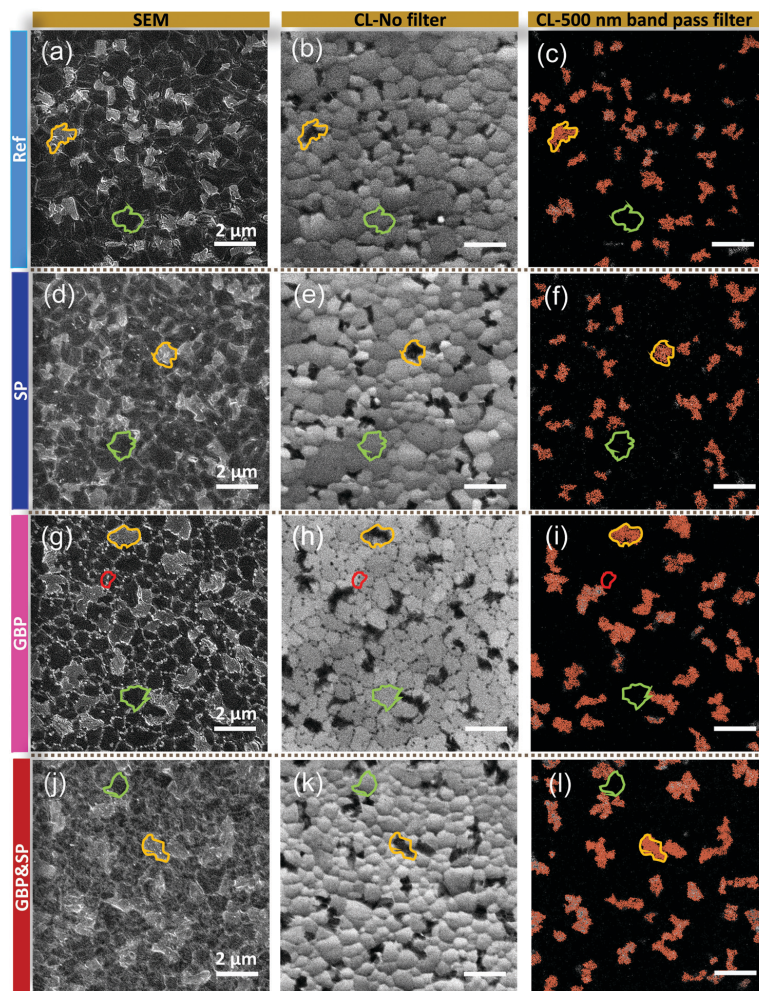


Fig. 4 Scanning electron microscopy (SEM) images, cathodoluminescence (CL) images recorded without any filter and CL images with bandpass ( $500 \pm 40$  nm) filter for perovskite absorbers prepared (a–c) without any modification (Ref), (d–f) with surface passivation (SP), (g–i) grain boundary passivation (GBP) and (j–l) grain boundary & surface passivation (GBP&SP), respectively. The green encircled grains represent the expected 3D perovskite phase with a bandgap of  $\sim 1.57$  eV. The yellow encircled grains are attributed to  $\text{PbI}_2$ -rich crystallites. The small red encircled grains appear close to the grain boundaries for GBP films.

when we apply the  $500 \text{ nm} \pm 40 \text{ nm}$  bandpass filter, only the features related to  $\text{PbI}_2$ -rich grains can be observed, whereas no signal or feature correlated with the small bright grains is traceable (Fig. 4i). This indicates that these are not related to  $\text{PbI}_2$  or  $\text{PbCl}_2$ . Finally, for GBP&SP film no small grains are visible in SEM anymore due to their dispersion after surface treatment (Fig. 4j) and thus can no longer be identified in the CL image either without or with the bandpass filter (Fig. 4k and l). Consistent with the PLQY and TRPL results, the GBP&SP film (Fig. 4k) exhibits the highest CL intensity at a wavelength of  $\sim 774 \text{ nm}$  (Fig. S25, ESI<sup>†</sup>).

This enhancement is attributed to the passivation of various recombination centres in the grain boundaries and/or at the surface of the perovskite layer.<sup>126</sup> Importantly, an additional CL peak at  $\sim 620 \text{ nm}$  appears, which cannot be related to either the 3D perovskite phase or the  $\text{PbI}_2$ -rich phase. We find similar peaks in PL measurements of GBP&SP films as well as for SP films when using a higher PEACl concentration of  $3 \text{ mg ml}^{-1}$  (see Fig. S26, ESI<sup>†</sup>). We correlate this observation to the formation of a thin emissive 2D  $(\text{PEA})_2(\text{Cs}_y\text{FA}_{1-y})_{n-1}\text{Pb}_n(\text{I}_{1-x}\text{Cl}_x)_{3n+1}$  RP phase with  $n = 2$  at the surface of the films, as will be discussed in the following.<sup>75,127</sup>

To analyse the crystal structure of our films, we perform X-ray diffraction (XRD) measurements (Fig. S27a, ESI†). All perovskite films exhibit the expected peaks at  $14.2^\circ$ ,  $20.1^\circ$ ,  $24.6^\circ$  and  $28.4^\circ$  from the (100), (110), (111) and (200) crystal planes of the 3D cubic  $\alpha$ - $\text{Cs}_{0.18}\text{FA}_{0.82}\text{PbI}_3$  phase,<sup>25,112,128</sup> as well as a peak at  $\sim 12.9^\circ$  related to  $\text{PbI}_2$ . The peak positions, intensities and FWHM of the XRD peaks are largely unchanged for SP films as observed in our previous work when using BABr for surface treatment.<sup>59</sup> For GBP films the intensity of the  $\text{PbI}_2$  peak slightly increases (Fig. S27a, ESI†), in agreement with the larger number of  $\text{PbI}_2$ -rich crystallites observed in SEM and CL. Furthermore, the ratio of the (100) to (111) peak slightly decreases for GBP films as compared to Ref and SP films, implying a slightly less preferred (100) orientation of the perovskite grains (Fig. S27b, ESI†).<sup>25,99</sup> Similar to SP films, GBP&SP films exhibit a largely unchanged XRD spectrum as compared to GBP films. We do not observe a signal related to a 2D RP phase for the SP and GBP&SP films, which could be related to either the passivation layer being too thin to be

detected by XRD, the presence of a heterogeneous distribution of  $(\text{PEA})_2(\text{Cs}_y\text{FA}_{1-y})_{n-1}\text{Pb}_n(\text{I}_{1-x}\text{Cl}_x)_{3n+1}$  phases with various  $n$ , or the presence of a non-crystalline PEA-based passivation layer.<sup>14,59,68,69</sup> Yet, upon further increasing the PEACl concentration to  $4.5 \text{ mg ml}^{-1}$  or  $10 \text{ mg ml}^{-1}$ , peaks at  $\sim 5.3^\circ$ ,  $10.5^\circ$ ,  $15.7^\circ$ ,  $20.9^\circ$ ,  $26.1^\circ$  and  $31.8^\circ$  start to appear. These can be attributed to a pure 2D ( $n = 1$ )  $(\text{PEA})_2\text{Pb}(\text{I}_{1-x}\text{Cl}_x)_4$  RP phase with a superlattice spacing of  $\sim 1.7 \text{ nm}$  that forms at the surface of the perovskite films (Fig. S28, ESI†).<sup>77,129–132</sup>

We perform XPS measurements of ITO/2PACz/perovskite stacks to get a better understanding of the elemental composition at the surface of our perovskite films and prove the presence of a PEACl-based passivation layer. For the Ref film, the XPS core-level spectra in Fig. 5a–c and Fig. S29a–c (ESI†) for the different elements in the 3D  $\text{Cs}_{0.18}\text{FA}_{0.82}\text{PbI}_3$  absorber show the expected peaks with binding energies of  $\sim 138.7 \text{ eV}$  ( $\text{Pb } 4f_{7/2}$ ),  $\sim 400.8 \text{ eV}$  ( $\text{N } 1s$ ),  $\sim 288.6 \text{ eV}$  ( $\text{C } 1s$  from FA's  $\text{N}=\text{C}=\text{N}$  bonding),  $\sim 619.6 \text{ eV}$  ( $\text{I } 3d_{5/2}$ ) and  $\sim 725.3 \text{ eV}$  ( $\text{Cs } 3d_{5/2}$ ).<sup>133</sup> The additional  $\text{C } 1s$  peak at  $\sim 284.8 \text{ eV}$  is attributed to adventitious carbon ( $\text{sp}^3$  C–C bonding)

This article is licensed under a Creative Commons Attribution 3.0 Unported Licence.

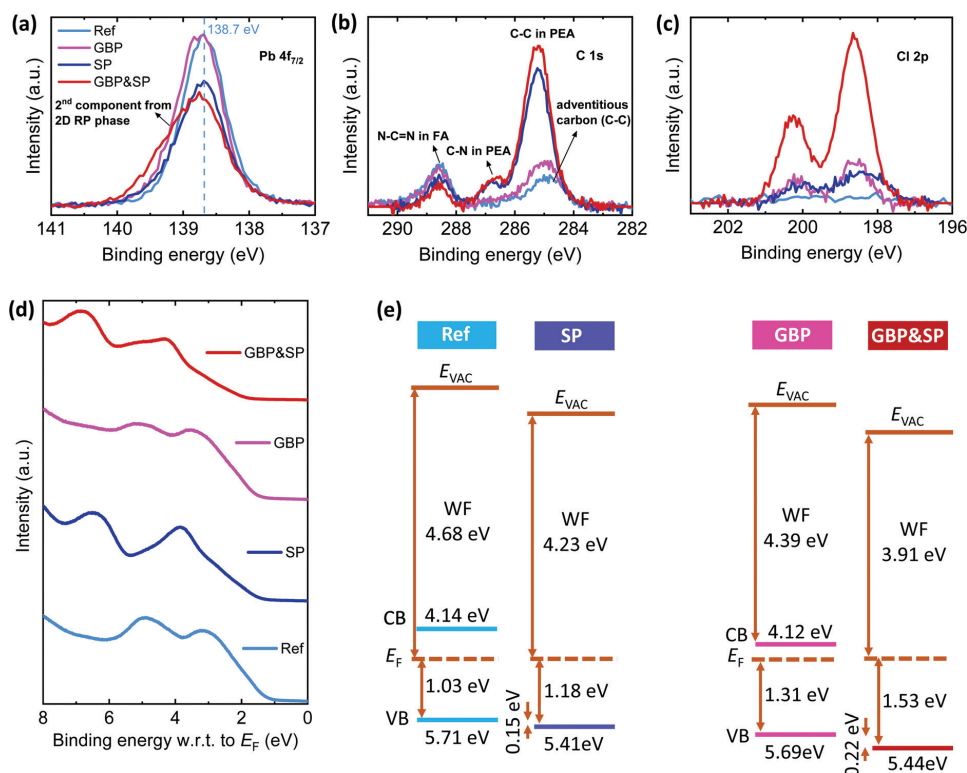


Fig. 5 X-ray photoelectron spectroscopy (XPS) spectra of (a)  $\text{Pb } 4f_{7/2}$ , (b)  $\text{C } 1s$  and (c)  $\text{Cl } 2p$  core levels for perovskite films prepared on ITO/2PACz substrates without (Ref), with surface passivation (SP), grain boundary passivation (GBP), and grain boundary & surface passivation (GBP&SP) processes. (d) Proposed energy-level scheme based on ultraviolet photoelectron spectroscopy (UUPS) measurements and (e) the respective spectra of the region close to the valence band onset.  $E_F$  is the Fermi level,  $E_{\text{vac}}$  is the vacuum level, and CB and VB show the conduction and valence band, respectively. The CB position of the 3D perovskite was calculated from the corresponding value of the optical gap.

at the film surface.<sup>17,95</sup> There is no signal related to a Cl 2p doublet at a binding energy of  $\sim 198.6$  eV and  $\sim 200.2$  eV despite using CsCl in the precursor solution which can be explained by the sublimation of FACl during the annealing process.<sup>16,112,134</sup> We note that we do not observe a peak related to metallic lead (Pb<sub>0</sub>) at  $\sim 137$  eV which emphasizes the high quality of our reference perovskite films.<sup>19,20,74,87</sup>

Upon PEACL:PbCl<sub>2</sub> incorporation and/or PEACL surface treatment (GBP, SP and GBP&SP films) there are three key observations as compared to the Ref film. Firstly, for BP films the Pb 4f<sub>7/2</sub> core level slightly shifts toward higher binding energies and exhibits an increased FWHM, while for SP and GBP&SP films the signal intensity at  $\sim 138.7$  eV decreases and the peak becomes broader and asymmetric toward the high-energy side. This asymmetry is stronger for GBP&SP films. Secondly, a Cl signal at  $\sim 198.6$  eV (Cl 2p<sub>3/2</sub>) and  $\sim 200.2$  eV (Cl 2p<sub>1/2</sub>) appears for all films, which is by far strongest for GBP&SP films. Thirdly, two new peaks at  $\sim 285.2$  eV and  $286.7$  eV appear which are similar in intensity for SP and GBP&SP films and only very weak for GBP films. These peaks can be related to the C 1s emission from PEA (C-C and C-N bonds, respectively) with the expected stoichiometric ratio of 7 : 1.

Comparing SP and GBP&SP films using a higher PEACL concentration of  $3 \text{ mg ml}^{-1}$ , we find even more pronounced changes in the Pb 4f core levels (Fig. S30, ESI<sup>†</sup>). We stress that these are not accompanied by changes in the peak position or shape of the I 3d<sub>5/2</sub>, Cs 3d<sub>5/2</sub> and C 1s core levels, which excludes the possibility of a shift due to electronic doping of the perovskite bulk.<sup>87,95,135,136</sup> We therefore relate the damping of the signal at  $\sim 138.7$  eV for SP and GBP&SP, together with the appearance of a second Pb component at  $\sim 139.1$  eV as well as a Cl 2p and PEA signal, to the formation of a thin PEACL-based passivation layer on the surface of the films that has a different chemical environment. The fact that for GBP the damping of the signal at  $\sim 138.7$  eV is less pronounced and the peak becomes broader fits with our observation from SEM and CL that passivation happens mainly close to the grain boundary regions. To further test this interpretation, we show XPS measurements of SP and GBP&SP films with a much thicker passivation layer ( $10 \text{ mg ml}^{-1}$ ) in Fig. S31 (ESI<sup>†</sup>). A single Pb 4f<sub>7/2</sub> peak at  $\sim 139.4$  eV can be observed with no remaining signal at  $\sim 138.7$  eV. In addition, no signals related to FA and Cs are observed anymore, which is an indication for the formation of a 2D RP phase with  $n = 1$  and the composition (PEA)<sub>2</sub>Pb(I<sub>1-x</sub>Cl<sub>x</sub>)<sub>4</sub>, at the film surface that completely damps the Pb signal from the underlying 3D perovskite phase. This is in line with the appearance of the related XRD peaks discussed above. We note that the calculated atomic ratio of (I + Cl)/Pb is 4.71 (SP) and 5.14 (GBP&SP) and thus even larger than the expected 4, which could be related to excess PEAI or PEACL at the film surface possibly forming an amorphous phase as reported recently (see Table S4, ESI<sup>†</sup>).<sup>14,68</sup> Similar shifts of the Pb 4f binding energies have previously been observed when changing the halide, *i.e.* for MAPbCl<sub>3</sub> and PbCl<sub>2</sub> as compared to MAPbI<sub>3</sub> and PbI<sub>2</sub>,<sup>137,138</sup> possibly due to the higher electronegativity of Cl as compared to I.

The formation of an  $n = 1$  2D RP phase has been proposed in several studies that employed PEAI or OAI for surface treatment.<sup>14,61,65,67,70,77,79,80</sup> However, for the thin passivation layer thicknesses studied in this work, the atomic ratio of Cs/Pb for SP and GBP&SP films first increases above the respective values for the Ref and GBP films ( $1.5 \text{ mg ml}^{-1}$ ), and only starts to slightly decrease for a higher PEACL concentration of  $3 \text{ mg ml}^{-1}$  (Table S4 and Fig. S32, ESI<sup>†</sup>). This indicates that Cs is taking part in the formation of the thin 2D RP passivation layer as otherwise the signal should be strictly decreasing because of the damping overlayer. This strict decrease in intensity with the formation of a 2D passivation layer can be seen for the atomic ratio of FA/Pb. This points towards a 2D RP (PEA)<sub>2</sub>(Cs<sub>y</sub>FA<sub>1-y</sub>)<sub>n-1</sub>Pb<sub>n</sub>(I<sub>1-x</sub>Cl<sub>x</sub>)<sub>3n+1</sub> phase with  $y \rightarrow 1$  at the surface of our GBP, SP and GBP&SP films.<sup>10,64,78,80,119,127,132</sup> Another clear observation is that the intensity of the Cl 2p doublet is considerably higher for GBP&SP as compared to SP films (Fig. 5b), while the I 3d<sub>5/2</sub> peak shows the reversed trend (Fig. S29c, ESI<sup>†</sup>). Accordingly, we note larger atomic ratios of Cl/Pb for GBP&SP vs. SP while the atomic ratio of I/Pb is smaller (Table S4 and Fig. S32, ESI<sup>†</sup>). This suggests that the 2D RP (PEA)<sub>2</sub>(Cs<sub>y</sub>FA<sub>1-y</sub>)<sub>n-1</sub>Pb<sub>n</sub>(I<sub>1-x</sub>Cl<sub>x</sub>)<sub>3n+1</sub> phase in case of GBP&SP films is more chloride-rich as compared to SP films ( $x \rightarrow 1$ ). The hypothesis that an  $n > 1$  2D RP (PEA)<sub>2</sub>(Cs<sub>y</sub>FA<sub>1-y</sub>)<sub>n-1</sub>Pb<sub>n</sub>(I<sub>1-x</sub>Cl<sub>x</sub>)<sub>3n+1</sub> phase exist for all thin passivation layers is further corroborated by our observation of a CL and PL peak at  $\sim 620$  nm for the SP ( $3 \text{ mg ml}^{-1}$ ) and GBP&SP films (see Fig. S25 and S26, ESI<sup>†</sup>) which points toward the existence of  $n$  of presumably 2.<sup>75,127</sup> To proof the existence of  $n > 1$ , we performed additional XRD measurements using a more sensitive setup. We specifically analyzed the low-angle region of the XRD spectrum ( $2\theta < 12^\circ$ ) of GBP&SP films employing various concentrations of PEACL for surface treatment ( $3, 3.5, 4$  and  $4.5 \text{ mg ml}^{-1}$ ) and used the (100) peak of a GBP film as reference point. As shown in Fig. S33 (ESI<sup>†</sup>), for all GBP&SP films we observe a clear peak at  $\sim 5.1^\circ$  and a corresponding one at  $\sim 10.2^\circ$  that correlate to an  $n = 1$  2D RP phase, as well a small peak at  $\sim 3.8^\circ$  that correlates to  $n = 2$ . Upon increasing the PEACL concentration, the intensity of the  $n = 1$  peak monotonically increases, while that for  $n = 2$  is comparable in intensity for the lower concentrations and only slightly in-creses for  $4.5 \text{ mg ml}^{-1}$ . Based on the XPS and XRD results together with the existence of a PL signal at  $\sim 620$  nm as discussed above, we conclude that for thin passivation layers the surface consists of a mixture of  $n = 1$  and  $n = 2$  2D RP phases, while for thicker passivation layers  $n = 1$  becomes dominant toward the film surface. In order to give a rough estimate for the film thickness and  $n$  of the passivation layers, we take the Pb 4f<sub>7/2</sub> peak which shows a clear indication for two phases and fit it with two components (see Fig. S34, ESI<sup>†</sup>): one for the 3D bulk phase (I) and one for the 2D RP surface phase (II). Here, for simplicity, we assume that the Pb 4f<sub>7/2</sub> binding energy related to the 2D RP phase is situated at  $139.1$  eV. This allows to separate the relative contribution of the 2D (II) and 3D (I) material to the XPS signal and to evaluate the signal damping of the 3D bulk phase caused by the 2D RP overlayer. From here, we estimate a thickness of the 2D RP phase for a PEACL concentration of  $1.5/3 \text{ mg ml}^{-1}$  of  $\sim 0.7/2.4$  nm for SP films and  $\sim 1.5/4.3$  nm for



GBP&SP films (see Table S5 and further information in the XPS/UPS section in the ESI†). Finally, for simplicity assuming that the complete PEA signal measured in XPS is bound in a 2D RP phase, we can make a rough estimation of the respective  $n$  (averaged over the measured XPS spot) by analysing the atomic ratio of PEA to the 2D Pb (II) signal for 1.5/3 mg ml<sup>-1</sup> PEACl (see Table S5, ESI†). We find that  $n$  for GBP&SP films ( $\sim 2.6/2.3$ ) is larger than for SP films ( $\sim 1.2/1.7$ ).

To assess the effect of the thin (PEA)<sub>2</sub>(Cs<sub>3</sub>FA<sub>1-y</sub>)<sub>n-1</sub>Pb<sub>n</sub>(I<sub>1-x</sub>Cl<sub>x</sub>)<sub>3n+1</sub> surface layer on the energetics of our films we perform UPS measurements. From the onsets of the secondary electron cut-off and valence band spectra (Fig. S35, ESI† and Fig. 5d) we derive the energy band diagrams shown in Fig. 5e. The Ref films exhibit a WF of 4.68 eV and an ionization potential (IP) of 5.71 eV which represents a slightly n-type perovskite film, in line with previous observations.<sup>24,25,66,95,139</sup> For GBP films, the WF considerably decreases to 4.39 eV while the IP stays roughly constant at 5.69 eV, implying that the perovskite becomes more n-type, which could be attributed to a reduced electron trap density, in line with our SCLC results, or a different surface termination.<sup>24,25,66,106,140</sup> The SP and GBP&SP films exhibit a further reduction in WF to 4.23 eV and 3.91 eV, respectively, together with a similar IP of 5.41 eV and 5.44 eV. These changes we attribute to the formation of the thin 2D RP phase with a larger bandgap and different chemical environments at the film surface as observed by CL and XPS. This is further supported by measurements of SP and GBP&SP films with a PEACl concentration of 3 mg ml<sup>-1</sup>, for which the WF further decreases to 3.89 eV and 3.82 eV, while the IP exhibits similar values of 5.45 eV and 5.47 eV, which implies a valence band onset of 1.57 eV and 1.66 eV, respectively, the latter being larger than the 3D perovskite bandgap (Fig. S36, ESI†). We also note that the shape of the VB density of states clearly is affected by surface treatment (Fig. 5e), showing that the electronic properties of the 2D RP surface layer are different compared to the 3D bulk perovskite.<sup>141</sup> Therefore, in addition to the expected chemical passivation,<sup>53</sup> we speculate that the 2D RP phase at the film surface with an increased distance of the VB to the Fermi level results in hole blocking and thus a reduced probability for holes in the 3D perovskite absorber to recombine with electrons in the C<sub>60</sub> layer.<sup>25,53,72,86,142</sup> In our case, electrons can effectively tunnel through the very thin ( $\sim 0.7$ – $1.5$  nm) surface layer into C<sub>60</sub>,<sup>25,38,142</sup> resulting in still efficient charge extraction that allows very high FF for low PEACl concentrations of 1.5 mg ml<sup>-1</sup>. For higher PEACl concentration of 3 mg ml<sup>-1</sup> the passivation layers become too thick ( $\sim 2.4$ – $4.3$  nm), making tunneling less likely which results in a decreased device performance due to a lower FF (Fig. S4, ESI†). Finally, we note that our results indicate band bending at the narrow 2D/3D interface as has recently been shown experimentally for the n-i-p architecture,<sup>139,143</sup> which also could contribute to the enhanced device performance.<sup>10</sup>

So far, our analyses clearly show that our dual passivation strategy effectively reduces non-radiative recombination mainly at the perovskite/C<sub>60</sub> interface, but also the grain boundaries. Moreover, it is evident that a very thin 2D RP interlayer with a

lower WF forms on the surface. The remaining questions are whether the PEACl:PbCl<sub>2</sub> additive passivates mainly defects in the grain interior and/or at the grain boundaries and how heterogeneous the surface passivation is for the different strategies. To shed light on this, we did frequency modulated Kelvin probe force microscopy (FM-KPFM) in the heterodyne KPFM implementation. KPFM measures the local contact potential difference (CPD) between a metallic tip and the sample surface and thus is directly related to the WF.<sup>144,145</sup> We used KPFM to map the effects of passivation on the CPD distribution of ITO/2PACz/perovskite/C<sub>60</sub> layer stacks, especially looking at grain boundaries, PbI<sub>2</sub>-rich grains and extent of heterogeneity (see Fig. 6). We want to stress that KPFM is prone to crosstalk from topography, often leading to KPFM contrast in strongly curved surface regions, such as grain boundaries. To minimize crosstalk artefacts, we use FM-KPFM<sup>146</sup> and carefully analysed the images, comparing the KPFM signal with the topography at the grain boundaries.

The map for the Ref sample (Fig. 6a) shows perovskite grains with a rather uniform CPD of ( $-430 \pm 40$ ) mV interrupted by grains with a less uniform and  $\sim 110$ – $230$  mV lower CPD. The size and the surface distribution of the darker regions correspond to the PbI<sub>2</sub>-rich grains as observed in SEM and CL (Fig. 4 and Fig. S19, ESI†). Here, the negative CPD contrast could be explained by a higher WF in PbI<sub>2</sub> as compared to the 3D perovskite due to its larger bandgap and p-type characteristics,<sup>137,147–149</sup> in line with previous observations.<sup>150,151</sup> The map of the GBP sample (Fig. 6b) shows a similar trend in CPD contrast between more homogeneous perovskite grains with a CPD of ( $-700 \pm 120$ ) mV and less uniform spots with a CPD of ( $-1300 \pm 280$ ) mV. We note that the absolute value of the CPD depends on the tip's WF, which is sensitive to tip wear and contamination during the scanning. This could explain the overall lower absolute CPD in the GBP films. Assuming that the PbI<sub>2</sub> covered regions for the Ref and GBP sample have a comparable WF, we can use these “dark” regions as internal reference surface. Therefore, we first compare the relative change of the CPD value at the 3D perovskite grains with that at the dark PbI<sub>2</sub>-rich grains for the Ref as compared to the GBP samples, *i.e.*  $\Delta\text{CPD}_{3\text{D-PbI}_2}$  ( $\text{CPD}_{3\text{D-grains}} - \text{CPD}_{\text{PbI}_2\text{-grains}}$ ). For the Ref sample  $\Delta\text{CPD}_{3\text{D-PbI}_2}$  is  $\sim 170$  mV, while it is  $\sim 600$  mV for the GBP sample (note the different scales in Fig. 6a and b). This relative difference of  $\Delta\text{CPD}_{3\text{D-PbI}_2}$  of  $\sim 430$  mV is comparable with the reduction in WF of  $\sim 290$  mV for GBP films as determined by UPS. Therefore, we attribute this observation to the fact that the PEACl:PbCl<sub>2</sub> additive mainly lowers the WF of the 3D perovskite grains, while the PbI<sub>2</sub>-rich grains are not modified by this strategy.

To analyse if the CPD at the grain boundaries with respect to the grain interior is modified for the GBP sample as compared to the Ref sample, *i.e.*,  $\Delta\text{CPD}_{\text{GB}}$  ( $\text{CPD}_{\text{grain boundary}} - \text{CPD}_{\text{grain}}$ ), we show line profiles across representative grain boundaries in Fig. S37a and b (ESI†). To allow for a direct comparison, we shifted the CPD values of the grain interior at different positions to zero. For the Ref sample, many of the grain boundaries show a  $\sim 50$ – $100$  mV lower CPD compared to the grains, similarly as



# CHAPTER 3. TWO BIRDS WITH ONE STONE: DUAL GRAIN-BOUNDARY AND INTERFACE PASSIVATION ENABLES >22 % EFFICIENT INVERTED METHYLAMMONIUM-FREE PEROVSKITE SOLAR CELLS

View Article Online

Paper

Energy & Environmental Science

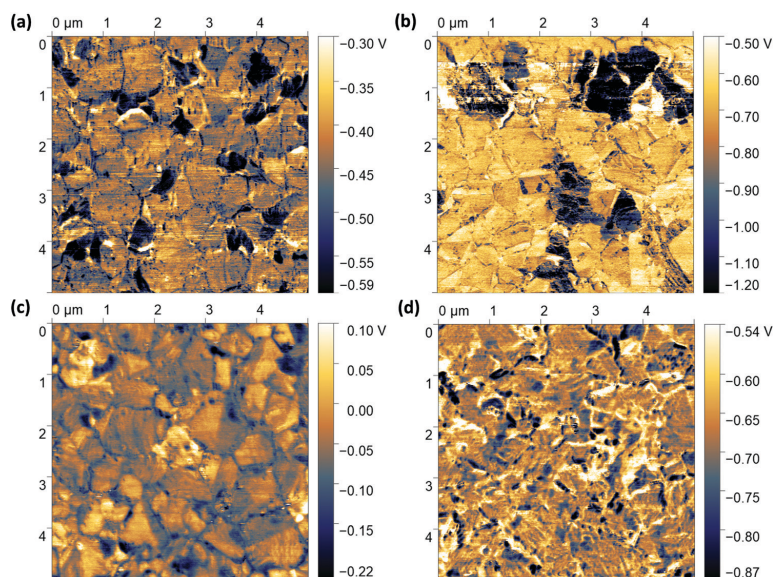


Fig. 6 Kelvin probe force microscopy (KPFM) images for perovskite films with the structure ITO/2PACz/perovskite/C<sub>60</sub> prepared (a) without any modification (Ref), (b) with grain boundary passivation (GBP), (c) surface passivation (SP), and (d) grain boundary & surface passivation (GBP&SP) processes.

This article is licensed under a Creative Commons Attribution 3.0 Unported Licence.



previously reported.<sup>152–155</sup> Such observations have been generally attributed to an enhanced ion and/or defect density, possibly due to a lower energy for defect formation at grain boundary regions.<sup>42,46,154</sup> In contrast, for the GBP sample we observed on average less contrast between grain boundaries and grain interior such that some of them cannot be clearly distinguished in the CPD map and line profiles anymore. We analysed in total a larger number of grain boundaries (~60) (Fig. S38a and b, ESI<sup>†</sup>) for better statistics and found an average reduction from ~93 mV to ~74 mV for the GBP as compared to the Ref sample together with a large number of grain boundaries not showing any CPD contrast (see histogram in Fig. S38c, ESI<sup>†</sup>). A reduction in  $\Delta\text{CPD}_{\text{GB}}$  for the GBP as compared to the Ref sample indicates that the PEACl:PbCl<sub>2</sub> additive could specifically passivate the grain boundaries, resulting in a slightly more pronounced reduction of the WF with respect to the PbI<sub>2</sub>-rich grains as compared to the grain interior. We hypothesize that this is due to the formation of a PEACl-based 2D RP (PEA)<sub>2</sub>(Cs<sub>y</sub>FA<sub>1-y</sub>)<sub>n-1</sub>Pb<sub>n</sub>(I<sub>1-x</sub>Cl<sub>x</sub>)<sub>3n+1</sub> phase specifically close to the grain boundaries, in line with the observations from CL and XPS.

We further analyse the effects of PEACl surface treatment on the CPD (Fig. 6c and d). The SP Sample shows a heterogeneous CPD of  $(-52 \pm 50)$  mV with no clear distinction between high- and low-CPD grains anymore; however, we still observe a slight grain boundary contrast. We attribute this to the very thin 2D RP phase on top of the perovskite film – as identified by XPS – that changes the electrical properties of the film surface, including the regions of the PbI<sub>2</sub>-rich grains. We speculate that PEACl cannot completely penetrate and thus passivate the

grain boundary regions, explaining why we still observe a CPD contrast. The enhanced heterogeneity of the CPD over different grains as compared to the Ref sample could be explained by the fact that the 2D RP (PEA)<sub>2</sub>(Cs<sub>y</sub>FA<sub>1-y</sub>)<sub>n-1</sub>Pb<sub>n</sub>(I<sub>1-x</sub>Cl<sub>x</sub>)<sub>3n+1</sub> phase exhibits various *n*, *i.e.* a mixture of *n* = 1 and *n* = 2 phases with slightly different WF at different regions of the films. For the GBP&SP samples, we observe an even more heterogeneous CPD of  $(-670 \pm 70)$  mV compared to all other samples (Fig. 6d and Fig. S39, ESI<sup>†</sup>). Critically, no grain boundaries and PbI<sub>2</sub>-rich grains can be identified in the CPD map anymore. Taking the CL, XPS and KPFM results together, this indicates that employing both PEACl:PbCl<sub>2</sub> as additive and PEACl for surface treatment leads to a thin heterogeneous 2D RP (PEA)<sub>2</sub>(Cs<sub>y</sub>FA<sub>1-y</sub>)<sub>n-1</sub>Pb<sub>n</sub>(I<sub>1-x</sub>Cl<sub>x</sub>)<sub>3n+1</sub> phase at the grain boundaries and surface of the perovskite film with *n* of ~1–2. Finally, we note that the CPD value can be affected both by the facet orientation as well as the existence of RP phases with various *n*, which makes it difficult to disentangle these effects in detail.<sup>146,153,156–158</sup>

### Stability of passivated PSCs

Defect sites at grain boundaries and surfaces accelerate the degradation of perovskite thin films, since defects facilitate the migration of charged defects and mobile ions.<sup>25,73,159,160</sup> Having demonstrated that our dual passivation strategy reduces defects at the grain boundaries and the surface of the perovskite film, the question arises whether the concept also serves to increase the stability, *i.e.* slows down the degradation of the perovskite films. For this purpose, we compare the activation energy for ion

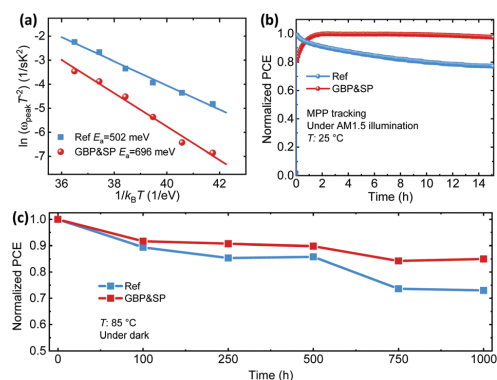


Fig. 7 (a) Arrhenius plots determined from the derivative of admittance spectra to determine the activation energy ( $E_a$ ) for reference (Ref) and grain boundary & surface passivation (GBP&SP) perovskite solar cells. (b) Maximum power point (MPP) tracking of the Ref and GBP&SP perovskite solar cells under continuous solar illumination ( $100 \text{ mW cm}^{-2}$ ) in a nitrogen atmosphere. (c) Thermal stability of devices heated at temperature of  $85 \text{ }^\circ\text{C}$  in dark condition inside of a glovebox. Data points were extracted from  $J-V$  curves at various time intervals.

migration for Ref, SP, GBP and GBP&SP PSCs by thermal admittance spectroscopy (TAS). Fig. S40a–d (ESI<sup>†</sup>) depicts the TAS spectra of the lateral devices measured from 278 to 318 K in the dark. The activation energy ( $E_a$ ) is obtained from the Arrhenius plot using the equation  $\omega_{\text{peak}} = \beta T^2 \exp(-E_a/k_B T)$ , where  $\beta$  is temperature independent prefactor,  $T$  is the absolute temperature,  $k_B$  is the Boltzmann constant, and  $\omega_{\text{peak}}$  is the angular frequency obtained by the maxima of the capacitance logarithmic derivative (Fig. S40e–h, ESI<sup>†</sup>). In line with the previously discussed trends, the GBP&SP PSCs exhibit by far the highest  $E_a$  of 696 meV, surpassing the activation energy for either single passivation strategy (GBP: 580 meV, SP: 551 meV) as well as the Ref PSC (502 meV) (Fig. 7a and Fig. S41, ESI<sup>†</sup>). The trend in  $E_a$  indicates that the simultaneous passivation of grain boundaries and the surface of the perovskite film yields by far the highest energy barrier for ion migration. As a consequence, the accumulation of ionic defects is most effectively suppressed for GBP&SP PSCs. To verify that the reduced ion migration also implies enhanced device stability under illumination,<sup>90,100</sup> the operational stability of GBP&SP and Ref PSCs is examined under constant illumination ( $100 \text{ mW cm}^{-2}$ , AM1.5G, 14 h, room temperature) and MPP tracking conditions. The PCE of the Ref PSC decreases to around 80% of the initial value after only 8 h, whereas the GBP&SP PSC retained almost 98% of the initial PCE after 14 h (Fig. 7b). Furthermore, we investigate the operational stability of PSCs for which the perovskite/ETL interface is passivated using a thin evaporated LiF layer, which is often employed in high-efficiency p–i–n PSCs.<sup>31,35,38,88,89,93</sup> In comparison with our GBP&SP PSCs (Fig. S42, ESI<sup>†</sup>) the p–i–n PSC with LiF passivation layer degrades much faster, reaching 80% of the initial PCE already after 7 h of constant illumination. Similar reports on the fast degradation of LiF containing p–i–n PSC can

be found in literature.<sup>31,93</sup> Next to improved operational stability under constant AM1.5G illumination, the GBP&SP PSCs demonstrate improved thermal stability as compared to Ref PSCs by tracking the photovoltaic performance of the devices after aging under  $85 \text{ }^\circ\text{C}$  heating in the dark over 1000 h (see Fig. 7c). To further evaluate the stability with regard to moisture, we exposed unencapsulated Ref PSCs and GBP&SP PSCs to a relative humidity of  $\sim 50\%$  in ambient atmosphere and at room temperature for 1 day. The photographs and absorption data exhibit no changes for the GBP&SP film, while the Ref film is entirely decomposed to  $\text{PbI}_2$  (Fig. S43a, ESI<sup>†</sup>). The increased contact angle of water droplets from  $55.9^\circ$  for the Ref film to  $78^\circ$  for the GBP&SP film (Fig. S43b, ESI<sup>†</sup>) confirms the better moisture resistance capability in the case of GBP&SP, which is attributed to the presence of hydrophobic  $\text{PEA}^+$  cations at the surface and grain boundaries of the perovskite films that acts as a hydrophobic barrier.<sup>25,71,76</sup> We note that the formation of shallow iodine interstitials upon passivation with iodide-based passivation molecules has recently been proposed to cause accelerated degradation of FAPbI<sub>3</sub> perovskites.<sup>71</sup> Our chloride-based dual passivation approach might potentially mitigate this issue. In summary, the presented fundamental assessment of stability for PSCs employing our dual passivation strategy highlights the importance of passivating defects at both the surface and the grain boundaries of perovskite films for achieving PCSs exhibiting both high efficiency and stability.

## Conclusion

In summary, we demonstrate a dual passivation strategy for p–i–n PSCs that simultaneously passivates defects at the perovskite/ $\text{C}_{60}$  interface as well as in the grain boundaries using the long chain alkylammonium salt phenethylammonium chloride. We achieve a substantial enhancement in charge carrier lifetime and quasi-Fermi level splitting compared to reference films as well as to films with either individual grain boundary or surface passivation. The best PSC with dual passivation achieves a significant absolute enhancement in both  $V_{\text{OC}}$  (76 mV) and FF (4.6%) compared to the best reference device. As a result, a remarkable stabilized PCE of 22.3% is demonstrated, one of the highest reported for p–i–n PSCs. We attribute this improvement in performance to the formation of a heterogeneous 2D RP  $(\text{PEA})_2(\text{Cs}_y\text{FA}_{1-y})_{n-1}\text{Pb}_n(\text{I}_{1-x}\text{Cl}_x)_{3n+1}$  phase with  $n \sim 1-2$  at the surface and grain boundaries of the films, which leads to (1) efficient chemical passivation of grain boundary and surface/interface defects and (2) additional hole blocking at the perovskite/ $\text{C}_{60}$  interface. Finally, we demonstrate that the activation energy for ion migration is strongly increased upon dual passivation, which is reflected by an enhanced device stability under maximum power point (MPP) tracking and prolonged heat treatment. This work highlights the importance of defect management by employing a proper material both for grain boundary as well as surface passivation for achieving high-efficiency and stable inverted p–i–n PSCs. Thereby this work makes a relevant contribution to the advance of perovskite-based flexible and tandem photovoltaics.

# CHAPTER 3. TWO BIRDS WITH ONE STONE: DUAL GRAIN-BOUNDARY AND INTERFACE PASSIVATION ENABLES >22 % EFFICIENT INVERTED METHYLAMMONIUM-FREE PEROVSKITE SOLAR CELLS

View Article Online

Paper

Energy & Environmental Science

## Author contributions

S. G. conceived the initial idea for this study and developed it further with support of P. F., I. M. H. and U. W. P. Furthermore, S. G. designed the experiments, fabricated the perovskite films and performed the  $J-V$ , EQE and long-term stability measurements. P. F. performed the absolute and intensity-dependent PLQY measurements and data analysis. I. M. H. performed the transient photoluminescence measurements and data analysis. S. G. performed the XRD measurements. M. F. performed the XPS/UPS measurements and data analysis and P. F. and J. P. H. supported in data interpretation. M. S. helped for device fabrication. P. R. performed the KPFM measurements, supervised by S. A. L. W., and the data was analysed by P. R., S. G., P. F. and S. A. L. W. The CL measurements were performed by T. D. The TAS measurements were performed by S. G. and M. R. K., and O. A. and M. R. K. analysed the data. T. A. and B. A. N. performed the SEM measurements. F. S. performed the contact angle measurement. T. F. applied and optimized the antireflection coating. R. S. helped for long-term stability measurement. B. A. N. helped with designing the schematics. D. F. performed additional high-resolution XRD measurements. U. L. and U. W. P. supervised the whole project. S. G., P. F. and U. W. P. drafted the manuscript. All authors reviewed and commented on the paper.

## Conflicts of interest

There are no conflicts to declare.

## Acknowledgements

B. A. N. acknowledges the financial support from the European Union's Horizon 2020 research and innovation program under the Marie Skłodowska-Curie grant agreement No [840937]. T. D. acknowledges the financial support from Australian Centre for Advanced Photovoltaics (ACAP). O. A. acknowledges the funding from the European Union's Horizon 2020 research and innovation program under the Photonics Public Private Partnership ([www.photonics21.org](http://www.photonics21.org)) with the project PEROXIS (grant no. 871336). M. S. acknowledges funding from the European Research Council (ERC) under the European Union's Horizon 2020 research and innovation program (Grant agreement No. 947221). Financial support by the Initiating and Networking funding of the Helmholtz Association (HYIG of U. W. P. (VHNG-1148)), the Helmholtz Energy Materials Foundry (HEMF), PEROSEED (ZT0024), the German Federal Ministry for Economic Affairs (BMWi) through the project 27Plus6 (03EE1056B) as well as the project CAPITANO (03EE1038B), and the Karlsruhe School of Optics & Photonics (KSOP) is gratefully acknowledged. Furthermore, this project has received funding from the European Union's Horizon 2020 research and innovation program under grant agreement No 850937 (PERCISTAND). The financial support of this research through the Baden-Württemberg Foundation is acknowledged (project acronym: ANU-KIT-PV).

## References

- 1 NREL Best Research-Cell Efficiency Chart, <https://www.nrel.gov/pv/cell-efficiency.html>, accessed: March 2021.
- 2 O. Almora, D. Baran, G. C. Bazan, C. Berger, C. I. Cabrera, K. R. Catchpole, S. Erten-Ela, F. Guo, J. Hauch, A. W. Y. Ho-Baillie, T. J. Jacobsson, R. A. J. Janssen, T. Kirchartz, N. Kopidakis, Y. Li, M. A. Loi, R. R. Lunt, X. Mathew, M. D. McGehee, J. Min, D. B. Mitzi, M. K. Nazeeruddin, J. Nelson, A. F. Nogueira, U. W. Paetzold, N. Park, B. P. Rand, U. Rau, H. J. Snaith, E. Unger, L. Vaillant-Roca, H. Yip and C. J. Brabec, *Adv. Energy Mater.*, 2021, **11**, 2002774.
- 3 G. Kim, H. Min, K. S. Lee, D. Y. Lee, S. M. Yoon and S. Il Seok, *Science*, 2020, **370**, 108–112.
- 4 M. Jeong, I. W. Choi, E. M. Go, Y. Cho, M. Kim, B. Lee, S. Jeong, Y. Jo, H. W. Choi, J. Lee, J. Bae, S. K. Kwak, D. S. Kim and C. Yang, *Science*, 2020, **1620**, 1615–1620.
- 5 M. Kim, G. Kim, T. K. Lee, I. W. Choi, H. W. Choi, Y. Jo, Y. J. Yoon, J. W. Kim, J. Lee, D. Huh, H. Lee, S. K. Kwak, J. Y. Kim and D. S. Kim, *Joule*, 2019, **3**, 2179–2192.
- 6 E. H. Jung, N. J. Jeon, E. Y. Park, C. S. Moon, T. J. Shin, T. Y. Yang, J. H. Noh and J. Seo, *Nature*, 2019, **567**, 511–515.
- 7 H. Zhu, Y. Ren, L. Pan, O. Ouellette, F. T. Eickemeyer, Y. Wu, X. Li, S. Wang, H. Liu, X. Dong, S. M. Zakeeruddin, Y. Liu, A. Hagfeldt and M. Grätzel, *J. Am. Chem. Soc.*, 2021, **143**, 3231–3237.
- 8 M. A. Mahmud, T. Duong, Y. Yin, J. Peng, Y. Wu, T. Lu, H. T. Pham, H. Shen, D. Walter, H. T. Nguyen, N. Mozaffari, G. D. Tabi, Y. Liu, G. Andersson, K. R. Catchpole, K. J. Weber and T. P. White, *Small*, 2020, **16**, 2005022.
- 9 T.-S. Su, F. T. Eickemeyer, M. A. Hope, F. Jahanbakhshi, M. Mladenović, J. Li, Z. Zhou, A. Mishra, J.-H. Yum, D. Ren, A. Krishna, O. Ouellette, T.-C. Wei, H. Zhou, H.-H. Huang, M. D. Mensi, K. Sivula, S. M. Zakeeruddin, J. V. Milić, A. Hagfeldt, U. Rothlisberger, L. Emsley, H. Zhang and M. Grätzel, *J. Am. Chem. Soc.*, 2020, **142**, 19980–19991.
- 10 J. J. Yoo, S. Wieghold, M. C. Sponseller, M. R. Chua, S. N. Bertram, N. T. P. Hartono, J. S. Tresback, E. C. Hansen, J.-P. Correa-Baena, V. Bulović, T. Buonassisi, S. S. Shin and M. G. Bawendi, *Energy Environ. Sci.*, 2019, **12**, 2192–2199.
- 11 B. Yang, J. Suo, E. Mosconi, D. Ricciarelli, W. Tress, F. De Angelis, H. Kim and A. Hagfeldt, *ACS Energy Lett.*, 2020, **5**, 3159–3167.
- 12 J. Jeong, M. Kim, J. Seo, H. Lu, P. Ahlawat, A. Mishra, Y. Yang, M. A. Hope, F. T. Eickemeyer, M. Kim, Y. J. Yoon, I. W. Choi, B. P. Darwich, S. J. Choi, Y. Jo, J. H. Lee, B. Walker, S. M. Zakeeruddin, L. Emsley, U. Rothlisberger, A. Hagfeldt, D. S. Kim, M. Grätzel and J. Y. Kim, *Nature*, 2021, **592**, 381–385.
- 13 J. J. Yoo, G. Seo, M. R. Chua, T. G. Park, Y. Lu, F. Rotermund, Y. Kim, C. S. Moon, N. J. Jeon, J.-P. Correa-Baena, V. Bulović, S. S. Shin, M. G. Bawendi and J. Seo, *Nature*, 2021, **590**, 587–593.

This article is licensed under a Creative Commons Attribution 3.0 Unported Licence.



- 14 Q. Jiang, Y. Zhao, X. Zhang, X. Yang, Y. Chen, Z. Chu, Q. Ye, X. Li, Z. Yin and J. You, *Nat. Photonics*, 2019, **13**, 460–466.
- 15 P. Wang, R. Li, B. Chen, F. Hou, J. Zhang, Y. Zhao and X. Zhang, *Adv. Mater.*, 2020, **32**, 1905766.
- 16 C. Ma and N.-G. Park, *ACS Energy Lett.*, 2020, **5**, 3268–3275.
- 17 X. Yang, Y. Fu, R. Su, Y. Zheng, Y. Zhang, W. Yang, M. Yu, P. Chen, Y. Wang, J. Wu, D. Luo, Y. Tu, L. Zhao, Q. Gong and R. Zhu, *Adv. Mater.*, 2020, **32**, 2002585.
- 18 E. H. Jung, B. Chen, K. Bertens, M. Vafaie, S. Teale, A. Proppe, Y. Hou, T. Zhu, C. Zheng and E. H. Sargent, *ACS Energy Lett.*, 2020, **5**, 2796–2801.
- 19 Q. Jiang, Z. Ni, G. Xu, Y. Lin, P. N. Rudd, R. Xue, Y. Y. Li, Y. Y. Li, Y. Gao and J. Huang, *Adv. Mater.*, 2020, **32**, 2001581.
- 20 X. Yang, D. Luo, Y. Xiang, L. Zhao, M. Anaya, Y. Shen, J. Wu, W. Yang, Y. H. Chiang, Y. Tu, R. Su, Q. Hu, H. Yu, G. Shao, W. Huang, T. P. Russell, Q. Gong, S. D. Stranks, W. Zhang and R. Zhu, *Adv. Mater.*, 2021, **33**, 2006435.
- 21 J. Zhuang, P. Mao, Y. Luan, N. Chen, X. Cao, G. Niu, F. Jia, F. Wang, S. Cao and J. Wang, *Adv. Funct. Mater.*, 2021, **31**, 2010385.
- 22 H. Lu, Y. Liu, P. Ahlawat, A. Mishra, W. R. Tress, F. T. Eickemeyer, Y. Yang, F. Fu, Z. Wang, C. E. Avalos, B. I. Carlsen, A. Agarwalla, X. Zhang, X. Li, Y. Zhan, S. M. Zakeeruddin, L. Emsley, U. Rothlisberger, L. Zheng, A. Hagfeldt and M. Grätzel, *Science*, 2020, **370**, eabb8985.
- 23 M. Green, E. Dunlop, J. Hohl-Ebinger, M. Yoshita, N. Kopidakis and X. Hao, *Prog. Photovoltaics*, 2021, **29**, 3–15.
- 24 F. Li, X. Deng, F. Qi, Z. Li, D. Liu, D. Shen, M. Qin, S. Wu, F. Lin, S. Jang, J. Zhang, X. Lu, D. Lei, C. Lee, Z. Zhu and A. K.-Y. Jen, *J. Am. Chem. Soc.*, 2020, **142**, 20134–20142.
- 25 X. Zheng, Y. Hou, C. Bao, J. Yin, F. Yuan, Z. Huang, K. Song, J. Liu, J. Troughton, N. Gasparini, C. Zhou, Y. Lin, D.-J. Xue, B. Chen, A. K. Johnston, N. Wei, M. N. Hedhili, M. Wei, A. Y. Alsalloum, P. Maity, B. Turedi, C. Yang, D. Baran, T. D. Anthopoulos, Y. Han, Z.-H. Lu, O. F. Mohammed, F. Gao, E. H. Sargent and O. M. Bakr, *Nat. Energy*, 2020, **5**, 131–140.
- 26 W. Wu, P. N. Rudd, Q. Wang, Z. Yang and J. Huang, *Adv. Mater.*, 2020, **32**, 2000995.
- 27 S. Wu, J. Zhang, Z. Li, D. Liu, M. Qin, S. H. Cheung, X. Lu, D. Lei, S. K. So, Z. Zhu and A. K.-Y. Jen, *Joule*, 2020, **4**, 1248–1262.
- 28 X. Sun, Z. Li, X. Yu, X. Wu, C. Zhong, D. Liu, D. Lei, A. K.-Y. Jen, Z. Li and Z. Zhu, *Angew. Chem., Int. Ed.*, 2021, **60**, 7227–7233.
- 29 X. Hu, C. Liu, Z. Zhang, X. Jiang, J. Garcia, C. Sheehan, L. Shui, S. Priya, G. Zhou, S. Zhang and K. Wang, *Adv. Sci.*, 2020, **7**, 2001285.
- 30 A. Y. Alsalloum, B. Turedi, K. Almasabi, X. Zheng, R. Naphade, S. D. Stranks, O. F. Mohammed and O. M. Bakr, *Energy Environ. Sci.*, 2021, **14**, 2263–2268.
- 31 A. Al-Ashouri, E. Köhnen, B. Li, A. Magomedov, H. Hempel, P. Caprioglio, J. A. Márquez, A. B. Morales Vilches, E. Kasparavičius, J. A. Smith, N. Phung, D. Menzel, M. Grischek, L. Kegelmann, D. Skroblin, C. Gollwitzer, T. Malinauskas, M. Jošt, G. Matič, B. Rech, R. Schlattmann, M. Topič, L. Korte, A. Abate, B. Stannowski, D. Neher, M. Stolterfoht, T. Unold, V. Getautis and S. Albrecht, *Science*, 2020, **370**, 1300–1309.
- 32 A. Al-Ashouri, A. Magomedov, M. Roš, M. Jošt, M. Talaikis, G. Chistiakova, T. Bertram, J. A. Márquez, E. Köhnen, E. Kasparavičius, S. Levenco, L. Gil-Escrig, C. J. Hages, R. Schlattmann, B. Rech, T. Malinauskas, T. Unold, C. A. Kaufmann, L. Korte, G. Niaura, V. Getautis and S. Albrecht, *Energy Environ. Sci.*, 2019, **12**, 3356–3369.
- 33 X. Lin, D. Cui, X. Luo, C. Zhang, Q. Han, Y. Wang and L. Han, *Energy Environ. Sci.*, 2020, **13**, 3823–3847.
- 34 M. Stolterfoht, M. Grischek, P. Caprioglio, C. M. Wolff, E. Gutierrez-Partida, F. Peña-Camargo, D. Rothhardt, S. Zhang, M. Raoufi, J. Wolansky, M. Abdi-Jalebi, S. D. Stranks, S. Albrecht, T. Kirchartz and D. Neher, *Adv. Mater.*, 2020, **32**, 2000080.
- 35 M. Stolterfoht, P. Caprioglio, C. M. Wolff, J. A. Márquez, J. Nordmann, S. Zhang, D. Rothhardt, U. Hörmann, Y. Amir, A. Redinger, L. Kegelmann, F. Zu, S. Albrecht, N. Koch, T. Kirchartz, M. Saliba, T. Unold and D. Neher, *Energy Environ. Sci.*, 2019, **12**, 2778–2788.
- 36 D. Luo, R. Su, W. Zhang, Q. Gong and R. Zhu, *Nat. Rev. Mater.*, 2020, **5**, 44–60.
- 37 C. M. Wolff, P. Caprioglio, M. Stolterfoht and D. Neher, *Adv. Mater.*, 2019, **31**, 1902762.
- 38 M. Stolterfoht, C. M. Wolff, J. A. Márquez, S. Zhang, C. J. Hages, D. Rothhardt, S. Albrecht, P. L. Burn, P. Meredith, T. Unold and D. Neher, *Nat. Energy*, 2018, **3**, 847–854.
- 39 S. Zhang, P. E. Shaw, G. Zhang, H. Jin, M. Tai, H. Lin, P. Meredith, P. L. Burn, D. Neher and M. Stolterfoht, *ACS Appl. Mater. Interfaces*, 2020, **12**, 37647–37656.
- 40 J.-W. Lee, S.-H. Bae, N. De Marco, Y.-T. Hsieh, Z. Dai and Y. Yang, *Mater. Today Energy*, 2018, **7**, 149–160.
- 41 A. Castro-Méndez, J. Hidalgo and J. Correa-Baena, *Adv. Energy Mater.*, 2019, **9**, 1901489.
- 42 J.-S. Park and A. Walsh, *Annu. Rev. Condens. Matter Phys.*, 2021, **12**, 042020annurev-conmatphys-.
- 43 Y. Shao, Y. Fang, T. Li, Q. Wang, Q. Dong, Y. Deng, Y. Yuan, H. Wei, M. Wang, A. Gruverman, J. Shield and J. Huang, *Energy Environ. Sci.*, 2016, **9**, 1752–1759.
- 44 J. S. Yun, J. Seidel, J. Kim, A. M. Soufiani, S. Huang, J. Lau, N. J. Jeon, S. Il Seok, M. A. Green and A. Ho-Baillie, *Adv. Energy Mater.*, 2016, **6**, 1600330.
- 45 L. Liu, S. Huang, Y. Lu, P. Liu, Y. Zhao, C. Shi, S. Zhang, J. Wu, H. Zhong, M. Sui, H. Zhou, H. Jin, Y. Li and Q. Chen, *Adv. Mater.*, 2018, **30**, 1800544.
- 46 N. Phung, A. Al-Ashouri, S. Meloni, A. Mattoni, S. Albrecht, E. L. Unger, A. Merdasa and A. Abate, *Adv. Energy Mater.*, 2020, **10**, 1903735.
- 47 L. McGovern, I. Koschany, G. Grimaldi, L. A. Muscarella and B. Ehrler, *J. Phys. Chem. Lett.*, 2021, 2423–2428.
- 48 S. P. Dunfield, L. Bliss, F. Zhang, J. M. Luther, K. Zhu, M. F. A. M. Hest, M. O. Reese and J. J. Berry, *Adv. Energy Mater.*, 2020, **10**, 1904054.



# CHAPTER 3. TWO BIRDS WITH ONE STONE: DUAL GRAIN-BOUNDARY AND INTERFACE PASSIVATION ENABLES >22 % EFFICIENT INVERTED METHYLAMMONIUM-FREE PEROVSKITE SOLAR CELLS

View Article Online

Paper

Energy & Environmental Science

- 49 L. Fu, H. Li, L. Wang, R. Yin, B. Li and L.-W. Yin, *Energy Environ. Sci.*, 2020, **13**, 4017–4056.
- 50 Q. Sun, P. Fassel, D. Becker-Koch, A. Bausch, B. Rivkin, S. Bai, P. E. Hopkinson, H. J. Snaith and Y. Vaynzof, *Adv. Energy Mater.*, 2017, **7**, 1700977.
- 51 J. P. Bastos, G. Uytterhoeven, W. Qiu, U. W. Paetzold, D. Cheyns, S. Surana, J. Rivas, M. Jaysankar, W. Song, T. Aernouts, J. Poortmans and R. Gehlhaar, *ACS Appl. Mater. Interfaces*, 2019, **11**, 16517–16526.
- 52 S. Akin, N. Arora, S. M. Zakeeruddin, M. Grätzel, R. H. Friend and M. I. Dar, *Adv. Energy Mater.*, 2020, **10**, 1903090.
- 53 E. Aydin, M. Bastiani and S. Wolf, *Adv. Mater.*, 2019, **31**, 1900428.
- 54 F. Gao, Y. Zhao, X. Zhang and J. You, *Adv. Energy Mater.*, 2020, **10**, 1902650.
- 55 H. Zhang, M. K. Nazeeruddin and W. C. H. Choy, *Adv. Mater.*, 2019, **31**, 1805702.
- 56 W. Qi, X. Zhou, J. Li, J. Cheng, Y. Li, M. J. Ko, Y. Zhao and X. Zhang, *Sci. Bull.*, 2020, **65**, 2022–2032.
- 57 Y. Li, H. Wu, W. Qi, X. Zhou, J. Li, J. Cheng, Y. Zhao, Y. Li and X. Zhang, *Nano Energy*, 2020, **77**, 105237.
- 58 S. Akin, B. Dong, L. Pfeifer, Y. Liu, M. Graetzel and A. Hagfeldt, *Adv. Sci.*, 2021, **8**, 2004593.
- 59 S. Gharibzadeh, B. Abdollahi Nejad, M. Jakoby, T. Abzieher, D. Hauschild, S. Moghadamzadeh, J. A. Schwenzler, P. Brenner, R. Schmager, A. A. Haghighirad, L. Weinhardt, U. Lemmer, B. S. Richards, I. A. Howard and U. W. Paetzold, *Adv. Energy Mater.*, 2019, **9**, 1803699.
- 60 S. Gharibzadeh, I. M. Hossain, P. Fassel, B. A. Nejad, T. Abzieher, M. Schultes, E. Ahlsvede, P. Jackson, M. Powalla, S. Schäfer, M. Rienäcker, T. Wietler, R. Peibst, U. Lemmer, B. S. Richards and U. W. Paetzold, *Adv. Funct. Mater.*, 2020, **30**, 1909919.
- 61 Y. Liu, S. Akin, L. Pan, R. Uchida, N. Arora, J. V. Milić, A. Hinderhofer, F. Schreiber, A. R. Uhl, S. M. Zakeeruddin, A. Hagfeldt, M. I. Dar and M. Grätzel, *Sci. Adv.*, 2019, **5**, eaaw2543.
- 62 Z. Li, J. Zhang, S. Wu, X. Deng, F. Li, D. Liu, C. Lee, F. Lin, D. Lei, C.-C. Chueh, Z. Zhu and A. K. Y. Jen, *Nano Energy*, 2020, **78**, 105377.
- 63 M. A. Mahmud, T. Duong, Y. Yin, H. T. Pham, D. Walter, J. Peng, Y. Wu, L. Li, H. Shen, N. Wu, N. Mozaffari, G. Andersson, K. R. Catchpole, K. J. Weber and T. P. White, *Adv. Funct. Mater.*, 2020, **30**, 1907962.
- 64 T. Duong, H. Pham, T. C. Kho, P. Phang, K. C. Fong, D. Yan, Y. Yin, J. Peng, M. A. Mahmud, S. Gharibzadeh, B. A. Nejad, I. M. Hossain, M. R. Khan, N. Mozaffari, Y. Wu, H. Shen, J. Zheng, H. Mai, W. Liang, C. Samundsett, M. Stocks, K. McIntosh, G. G. Andersson, U. Lemmer, B. S. Richards, U. W. Paetzold, A. Ho-Ballie, Y. Liu, D. Macdonald, A. Blakers, J. Wong-Leung, T. White, K. Weber and K. Catchpole, *Adv. Energy Mater.*, 2020, **10**, 1903553.
- 65 T. Zhu, D. Zheng, J. Liu, L. Coolen, T. Pauporté, T. Pauporte and T. Pauporté, *ACS Appl. Mater. Interfaces*, 2020, **12**, 37197–37207.
- 66 D. Luo, W. Yang, Z. Wang, A. Sadhanala, Q. Hu, R. Su, R. Shivanna, G. F. Trindade, J. F. Watts, Z. Xu, T. Liu, K. Chen, F. Ye, P. Wu, L. Zhao, J. Wu, Y. Tu, Y. Zhang, X. Yang, W. Zhang, R. H. Friend, Q. Gong, H. J. Snaith and R. Zhu, *Science*, 2018, **360**, 1442–1446.
- 67 K. Lee, J. Kim, H. Yu, J. W. Lee, C. M. Yoon, S. K. Kim and J. Jang, *J. Mater. Chem. A*, 2018, **6**, 24560–24568.
- 68 F. Zhang, Q. Huang, J. Song, Y. Zhang, C. Ding, F. Liu, D. Liu, X. Li, H. Yasuda, K. Yoshida, J. Qu, S. Hayase, T. Toyoda, T. Minemoto and Q. Shen, *Sol. RRL*, 2020, **4**, 1900243.
- 69 H. Dong, M. Yue, S. Pang, W. Zhu, D. Chen, H. Xi, Z. Lin, J. Chang, J. Zhang, Y. Hao and C. Zhang, *Sol. RRL*, 2019, **3**, 1900291.
- 70 C. Zhang, S. Wu, L. Tao, G. M. Arumugam, C. Liu, Z. Wang, S. Zhu, Y. Yang, J. Lin, X. Liu, R. E. I. Schropp and Y. Mai, *Adv. Energy Mater.*, 2020, **10**, 2002004.
- 71 S. Tan, I. Yavuz, M. H. Weber, T. Huang, C. Chen, R. Wang, H. Wang, J. H. Ko, S. Nuryeva, J. Xue, Y. Zhao, K. Wei, J. Lee and Y. Yang, *Joule*, 2020, **4**, 2426–2442.
- 72 H. Kim, S. Lee, D. Y. Lee, M. J. Paik, H. Na, J. Lee and S. Il Seok, *Adv. Energy Mater.*, 2019, **9**, 1902740.
- 73 X. Zheng, B. Chen, J. Dai, Y. Fang, Y. Bai, Y. Lin, H. Wei, X. C. Zeng and J. Huang, *Nat. Energy*, 2017, **2**, 17102.
- 74 Q. Zhou, Y. Gao, C. Cai, Z. Zhang, J. Xu, Z. Yuan and P. Gao, *Angew. Chem.*, 2021, **133**, 8384–8393.
- 75 H. Wang, C. Zhu, L. Liu, S. Ma, P. Liu, J. Wu, C. Shi, Q. Du, Y. Hao, S. Xiang, H. Chen, P. Chen, Y. Bai, H. Zhou, Y. Li and Q. Chen, *Adv. Mater.*, 2019, **31**, 1904408.
- 76 T. M. Koh, V. Shanmugam, X. Guo, S. S. Lim, O. Filonik, E. M. Herzig, P. Müller-Buschbaum, V. Swamy, S. T. Chien, S. G. Mhaisalkar and N. Mathews, *J. Mater. Chem. A*, 2018, **6**, 2122–2128.
- 77 K. T. Cho, G. Grancini, Y. Lee, E. Oveisi, J. Ryu, O. Almora, M. Tschumi, P. A. Schouwink, G. Seo, S. Heo, J. Park, J. Jang, S. Paek, G. Garcia-Belmonte and M. K. Nazeeruddin, *Energy Environ. Sci.*, 2018, **11**, 952–959.
- 78 Y. Cho, A. M. Soufiani, J. S. Yun, J. Kim, D. S. Lee, J. Seidel, X. Deng, M. A. Green, S. Huang and A. W. Y. Ho-Baillie, *Adv. Energy Mater.*, 2018, **8**, 1703392.
- 79 P. Chen, Y. Bai, S. Wang, M. Lyu, J.-H. Yun and L. Wang, *Adv. Funct. Mater.*, 2018, **28**, 1706923.
- 80 Y. Lin, Y. Bai, Y. Fang, Z. Chen, S. Yang, X. Zheng, S. Tang, Y. Liu, J. Zhao and J. Huang, *J. Phys. Chem. Lett.*, 2018, **9**, 654–658.
- 81 M. Malekshahi Byranvand, F. Behboodi-Sadabad, A. Alrhman Eliwi, V. Trouillet, A. Welle, S. Ternes, I. M. Hossain, M. R. Khan, J. A. Schwenzler, A. Farooq, B. S. Richards, J. Lahann and U. W. Paetzold, *J. Mater. Chem. A*, 2020, **8**, 20122–20132.
- 82 J. Peng, D. Walter, Y. Ren, M. Tebyetekerwa, Y. Wu, T. Duong, Q. Lin, J. Li, T. Lu, M. A. Mahmud, O. L. C. Lem, S. Zhao, W. Liu, Y. Liu, H. Shen, L. Li, F. Kremer, H. T. Nguyen, D. Choi, K. J. Weber, K. R. Catchpole and T. P. White, *Science*, 2021, **371**, 390–395.

This article is licensed under a Creative Commons Attribution 3.0 Unported Licence.



- 83 R. Wang, J. Xue, K.-L. Wang, Z.-K. K. Wang, Y. Luo, D. Fenning, G. Xu, S. Nuryyeva, T. Huang, Y. Zhao, J. L. Yang, J. Zhu, M. Wang, S. Tan, I. Yavuz, K. N. Houk and Y. Yang, *Science*, 2019, **366**, 1509–1513.
- 84 X. Liu, Z. Yu, T. Wang, K. L. Chiu, F. Lin, H. Gong, L. Ding and Y. Cheng, *Adv. Energy Mater.*, 2020, **10**, 2001958.
- 85 S. Yang, J. Dai, Z. Yu, Y. Shao, Y. Zhou, X. Xiao, X. C. Zeng and J. Huang, *J. Am. Chem. Soc.*, 2019, **141**, 5781–5787.
- 86 C. M. Wolff, L. Canil, C. Rehermann, N. Ngoc Linh, F. Zu, M. Ralaierisoa, P. Caprioglio, L. Fiedler, M. Stolterfoht, S. Kogikoski, I. Bald, N. Koch, E. L. Unger, T. Dittrich, A. Abate and D. Neher, *ACS Nano*, 2020, **14**, 1445–1456.
- 87 Z. Liu, F. Cao, M. Wang, M. Wang and L. Li, *Angew. Chem.*, 2020, **132**, 4190–4196.
- 88 J. Xu, C. C. Boyd, Z. J. Yu, A. F. Palmstrom, D. J. Witter, B. W. Larson, R. M. France, J. Werner, S. P. Harvey, E. J. Wolf, W. Weigand, S. Manzoor, M. F. A. M. van Hest, J. J. Berry, J. M. Luther, Z. C. Holman and M. D. McGehee, *Science*, 2020, **367**, 1097–1104.
- 89 F. Peña-Camargo, P. Caprioglio, F. Zu, E. Gutierrez-Partida, C. M. Wolff, K. Brinkmann, S. Albrecht, T. Riedl, N. Koch, D. Neher and M. Stolterfoht, *ACS Energy Lett.*, 2020, **5**, 2728–2736.
- 90 S. Yang, S. Chen, E. Mosconi, Y. Fang, X. Xiao, C. Wang, Y. Zhou, Z. Yu, J. Zhao, Y. Gao, F. De Angelis and J. Huang, *Science*, 2019, **365**, 473–478.
- 91 F. Wang, Y. Zhang, M. Yang, D. Han, L. Yang, L. Fan, Y. Sui, Y. Sun, X. Liu, X. Meng and J. Yang, *Adv. Funct. Mater.*, 2021, **31**, 2008052.
- 92 P. Caprioglio, M. Stolterfoht, C. M. Wolff, T. Unold, B. Rech, S. Albrecht and D. Neher, *Adv. Energy Mater.*, 2019, **9**, 1901631.
- 93 J. Dagar, M. Fenske, A. Al-Ashouri, C. Schultz, B. Li, H. Köbler, R. Munir, G. Parmasivam, J. Li, I. Levine, A. Merdasa, L. Kegelman, H. Näsström, J. A. Marquez, T. Unold, D. M. Töbrens, R. Schlattmann, B. Stegemann, A. Abate, S. Albrecht and E. Unger, *ACS Appl. Mater. Interfaces*, 2021, **13**, 13022–13033.
- 94 B. Park, N. Kedem, M. Kulbak, D. Y. Lee, W. S. Yang, N. J. Jeon, J. Seo, G. Kim, K. J. Kim, T. J. Shin, G. Hodes, D. Cahen and S. Il Seok, *Nat. Commun.*, 2018, **9**, 3301.
- 95 P. Fassel, V. Lami, A. Bausch, Z. Wang, M. T. Klug, H. J. Snaith and Y. Vaynzof, *Energy Environ. Sci.*, 2018, **11**, 3380–3391.
- 96 P. Fassel, Y. Zakharko, L. M. Falk, K. P. Goetz, F. Paulus, A. D. Taylor, J. Zaumseil and Y. Vaynzof, *J. Mater. Chem. C*, 2019, **7**, 5285–5292.
- 97 K. Wang, W. S. Subhani, Y. Wang, X. Zuo, H. Wang, L. Duan and S. (Frank) Liu, *Adv. Mater.*, 2019, **31**, 1902037.
- 98 D. Kim, H. J. Jung, I. J. Park, B. W. Larson, S. P. Dunfield, C. Xiao, J. Kim, J. Tong, P. Boonmongkolras, S. G. Ji, F. Zhang, S. R. Pae, M. Kim, S. B. Kang, V. Dravid, J. J. Berry, J. Y. Kim, K. Zhu, D. H. Kim and B. Shin, *Science*, 2020, **3433**, eaba3433.
- 99 D. S. Lee, J. S. Yun, J. Kim, A. M. Souffiani, S. Chen, Y. Cho, X. Deng, J. Seidel, S. Lim, S. Huang and A. W. Y. Ho-Baillie, *ACS Energy Lett.*, 2018, **3**, 647–654.
- 100 J.-W. Lee, Z. Dai, T.-H. Han, C. Choi, S.-Y. Chang, S.-J. Lee, N. De Marco, H. Zhao, P. Sun, Y. Huang and Y. Yang, *Nat. Commun.*, 2018, **9**, 3021.
- 101 M. Jung, T. J. Shin, J. Seo, G. Kim and S. Il Seok, *Energy Environ. Sci.*, 2018, **11**, 2188–2197.
- 102 Z. Wang, Q. Lin, F. P. Chmiel, N. Sakai, L. M. Herz and H. J. Snaith, *Nat. Energy*, 2017, **2**, 17135.
- 103 D. H. Kim, C. P. Muzzillo, J. Tong, A. F. Palmstrom, B. W. Larson, C. Choi, S. P. Harvey, S. Glynn, J. B. Whitaker, F. Zhang, Z. Li, H. Lu, M. F. A. M. van Hest, J. J. Berry, L. M. Mansfield, Y. Huang, Y. Yan and K. Zhu, *Joule*, 2019, **3**, 1734–1745.
- 104 C. Fei, M. Zhou, J. Ogle, D.-M. Smilgies, L. Whittaker-Brooks and H. Wang, *J. Mater. Chem. A*, 2019, **7**, 23739–23746.
- 105 N. Li, Z. Zhu, C. C. Chueh, H. Liu, B. Peng, A. Petrone, X. Li, L. Wang and A. K.-Y. Jen, *Adv. Energy Mater.*, 2017, **7**, 1–9.
- 106 S. Xiong, Z. Hou, S. Zou, X. Lu, J. Yang, T. Hao, Z. Zhou, J. Xu, Y. Zeng, W. Xiao, W. Dong, D. Li, X. Wang, Z. Hu, L. Sun, Y. Wu, X. Liu, L. Ding, Z. Sun, M. Fahlman and Q. Bao, *Joule*, 2021, **5**, 467–480.
- 107 X. Wang, K. Rakstys, K. Jack, H. Jin, J. Lai, H. Li, C. S. K. Ranasinghe, J. Saghaei, G. Zhang, P. L. Burn, I. R. Gentle and P. E. Shaw, *Nat. Commun.*, 2021, **12**, 52.
- 108 F. Zhang and K. Zhu, *Adv. Energy Mater.*, 2020, **10**, 1902579.
- 109 S. Liu, Y. Guan, Y. Sheng, Y. Hu, Y. Rong, A. Mei and H. Han, *Adv. Energy Mater.*, 2020, **10**, 1902492.
- 110 J. Wang, G. Jin, Q. Zhen, C. He and Y. Duan, *Adv. Mater. Interfaces*, 2021, **8**, 2002078.
- 111 X. Zhou, W. Qi, J. Li, J. Cheng, Y. Li, J. Luo, M. J. Ko, Y. Li, Y. Zhao and X. Zhang, *Sol. RRL*, 2020, **4**, 2000308.
- 112 D. Prochowicz, R. Runjhun, M. M. Tavakoli, P. Yadav, M. Sasaki, A. Q. Alanazi, D. J. Kubicki, Z. Kaszukur, S. M. Zakeeruddin, J. Lewiński and M. Grätzel, *Chem. Mater.*, 2019, **31**, 1620–1627.
- 113 L. Krückemeier, U. Rau, M. Stolterfoht and T. Kirchartz, *Adv. Energy Mater.*, 2020, **10**, 1902573.
- 114 L. Krückemeier, B. Krogmeier, Z. Liu, U. Rau and T. Kirchartz, *Adv. Energy Mater.*, 2021, **11**, 2003489.
- 115 Z. Liu, L. Krückemeier, B. Krogmeier, B. Klingebiel, J. A. Márquez, S. Levchenko, S. Öz, S. Mathur, U. Rau, T. Unold and T. Kirchartz, *ACS Energy Lett.*, 2019, **4**, 110–117.
- 116 B. Krogmeier, F. Staub, D. Grabowski, U. Rau and T. Kirchartz, *Sustainable Energy Fuels*, 2018, **2**, 1027–1034.
- 117 T. Kirchartz, J. A. Márquez, M. Stolterfoht and T. Unold, *Adv. Energy Mater.*, 2020, **10**, 1904134.
- 118 P. Fassel, V. Lami, F. J. Berger, L. M. Falk, J. Zaumseil, B. S. Richards, I. A. Howard, Y. Vaynzof and U. W. Paetzold, *Matter*, 2021, **4**, 1391–1412.
- 119 S. Zhang, S. M. Hosseini, R. Gunder, A. Petsiuk, P. Caprioglio, C. M. Wolff, S. Shoaee, P. Meredith, S. Schorr, T. Unold, P. L. Burn, D. Neher and M. Stolterfoht, *Adv. Mater.*, 2019, **31**, 1901090.
- 120 H. Jin, E. Debroye, M. Keshavarz, I. G. Scheblykin, M. B. J. Roeflaers, J. Hofkens and J. A. Steele, *Mater. Horizons*, 2020, **7**, 397–410.



# CHAPTER 3. TWO BIRDS WITH ONE STONE: DUAL GRAIN-BOUNDARY AND INTERFACE PASSIVATION ENABLES >22 % EFFICIENT INVERTED METHYLAMMONIUM-FREE PEROVSKITE SOLAR CELLS

View Article Online

Paper

Energy & Environmental Science

- 121 W.-Q. Wu, P. N. Rudd, Z. Ni, C. H. Van Brackle, H. Wei, Q. Wang, B. R. Ecker, Y. Gao and J. Huang, *J. Am. Chem. Soc.*, 2020, **142**, 3989–3996.
- 122 P. Caprioglio, C. M. Wolff, O. J. Sandberg, A. Armin, B. Rech, S. Albrecht, D. Neher and M. Stollerfoht, *Adv. Energy Mater.*, 2020, **10**, 2000502.
- 123 N. E. Courtier, *Phys. Rev. Appl.*, 2020, **14**, 024031.
- 124 M. A. Green and A. W. Y. Ho-Baillie, *ACS Energy Lett.*, 2019, **4**, 1639–1644.
- 125 Z. Liu, J. Siekmann, B. Klingebiel, U. Rau and T. Kirchartz, *Adv. Energy Mater.*, 2021, 2003386.
- 126 H. Guthrey and J. Moseley, *Adv. Energy Mater.*, 2020, **10**, 1903840.
- 127 J. Hu, I. W. H. Oswald, S. J. Stuard, M. M. Nahid, N. Zhou, O. F. Williams, Z. Guo, L. Yan, H. Hu, Z. Chen, X. Xiao, Y. Lin, Z. Yang, J. Huang, A. M. Moran, H. Ade, J. R. Neilson and W. You, *Nat. Commun.*, 2019, **10**, 1276.
- 128 B. G. H. M. Groeneveld, S. Adjokatse, O. Nazarenko, H. Fang, G. R. Blake, G. Portale, H. Duim, G. H. ten Brink, M. V. Kovalenko and M. A. Loi, *Energy Technol.*, 2020, **8**, 1901041.
- 129 K. Du, Q. Tu, X. Zhang, Q. Han, J. Liu, S. Zauscher and D. B. Mitzi, *Inorg. Chem.*, 2017, **56**, 9291–9302.
- 130 K. Thirumal, W. K. Chong, W. Xie, R. Ganguly, S. K. Muduli, M. Sherburne, M. Asta, S. Mhaisalkar, T. C. Sum, H. Sen Soo and N. Mathews, *Chem. Mater.*, 2017, **29**, 3947–3953.
- 131 P. Cai, X. Wang, H. J. Seo and X. Yan, *Appl. Phys. Lett.*, 2018, **112**, 153901.
- 132 X. Chen, H. Lu, Z. Li, Y. Zhai, P. F. Ndione, J. J. Berry, K. Zhu, Y. Yang and M. C. Beard, *ACS Energy Lett.*, 2018, **3**, 2273–2279.
- 133 S. Béchu, M. Ralajarisoa, A. Etcheberry and P. Schulz, *Adv. Energy Mater.*, 2020, **10**, 1904007.
- 134 R. D. Chavan, D. Prochowicz, P. Yadav, M. M. Tavakoli, A. Nimbalkar, S. P. Bhoite and C. K. Hong, *Sol. RRL*, 2019, **3**, 1900294.
- 135 T. Hellmann, C. Das, T. Abzieher, J. A. Schwenzer, M. Wussler, R. Dachauer, U. W. Paetzold, W. Jaegermann and T. Mayer, *Adv. Energy Mater.*, 2020, **10**, 2002129.
- 136 N. K. Noel, S. N. Habisreutinger, A. Pellaroque, F. Pulvirenti, B. Wenger, F. Zhang, Y.-H. Lin, O. G. Reid, J. Leisen, Y. Zhang, S. Barlow, S. R. Marder, A. Kahn, H. J. Snaith, C. B. Arnold and B. P. Rand, *Energy Environ. Sci.*, 2019, **12**, 3063–3073.
- 137 M. Caputo, N. Cefarin, A. Radivo, N. Demitri, L. Gigli, J. R. Plaisier, M. Panighel, G. Di Santo, S. Moretti, A. Giglia, M. Polentarutti, F. De Angelis, E. Mosconi, P. Umari, M. Tormen and A. Goldoni, *Sci. Rep.*, 2019, **9**, 15159.
- 138 B. Philippe, B. Park, R. Lindblad, J. Oscarsson, S. Ahmadi, E. M. J. Johansson and H. Rensmo, *Chem. Mater.*, 2015, **27**, 1720–1731.
- 139 A. A. Sultanto, P. Caprioglio, N. Drigo, Y. J. Hofstetter, I. Garcia-Benito, V. I. E. Queloz, D. Neher, M. K. Nazeeruddin, M. Stollerfoht, Y. Vaynzof and G. Grancini, *Chem*, 2021, **7**, 1903–1916.
- 140 S. Draguta, J. A. Christians, Y. V. Morozov, A. Mucunzi, J. S. Manser, P. V. Kamat, J. M. Luther and M. Kuno, *Energy Environ. Sci.*, 2018, **11**, 960–969.
- 141 J. Emar, T. Schnier, N. Pourdavoud, T. Riedl, K. Meerholz and S. Olthof, *Adv. Mater.*, 2016, **28**, 553–559.
- 142 Q. Wang, Q. Dong, T. Li, A. Gruverman and J. Huang, *Adv. Mater.*, 2016, **28**, 6734–6739.
- 143 H. Kanda, N. Shibayama, A. J. Huckaba, Y. Lee, S. Paek, N. Klipfel, C. Roldán-Carmona, V. I. E. Queloz, G. Grancini, Y. Zhang, M. Abuhelaiqa, K. T. Cho, M. Li, M. D. Mensi, S. Kinge and M. K. Nazeeruddin, *Energy Environ. Sci.*, 2020, **13**, 1222–1230.
- 144 A. Axt, I. M. Hermes, V. W. Bergmann, N. Tausendpfund and S. A. L. Weber, *Beilstein J. Nanotechnol.*, 2018, **9**, 1809–1819.
- 145 J. L. Garrett and J. N. Munday, *Nanotechnology*, 2016, **27**, 245705.
- 146 E. M. Lanzoni, T. Gallet, C. Spindler, O. Ramirez, C. K. Boumenou, S. Siebentritt and A. Redinger, *Nano Energy*, 2021, **88**, 106270.
- 147 D. H. Cao, C. C. Stoumpos, C. D. Malliakas, M. J. Katz, O. K. Farha, J. T. Hupp and M. G. Kanatzidis, *APL Mater.*, 2014, **2**, 091101.
- 148 R. A. Street, S. E. Ready, F. Lemmi, K. S. Shah, P. Bennett and Y. Dmitriyev, *J. Appl. Phys.*, 1999, **86**, 2660–2667.
- 149 Y. Sun, Z. Zhou, Z. Huang, J. Wu, L. Zhou, Y. Cheng, J. Liu, C. Zhu, M. Yu, P. Yu, W. Zhu, Y. Liu, J. Zhou, B. Liu, H. Xie, Y. Cao, H. Li, X. Wang, K. Liu, X. Wang, J. Wang, L. Wang and W. Huang, *Adv. Mater.*, 2019, **31**, 1806562.
- 150 Y.-M. Xie, X. Xu, C. Ma, M. Li, Y. Ma, C.-S. Lee and S.-W. Tsang, *ACS Appl. Mater. Interfaces*, 2019, **11**, 25909–25916.
- 151 S. Chen, X. Wen, J. S. Yun, S. Huang, M. Green, N. J. Jeon, W. S. Yang, J. H. Noh, J. Seo, S. Il Seok and A. Ho-Baillie, *ACS Appl. Mater. Interfaces*, 2017, **9**, 6072–6078.
- 152 S. I. Rahman, B. S. Lamsal, A. Gurung, A. H. Chowdhury, K. M. Reza, N. Ghimire, B. Bahrami, W. Luo, R. S. Bobba, J. Pokharel, A. Baniya, A. R. Laskar, K. Emshadi, M. T. Rahman and Q. Qiao, *ACS Appl. Mater. Interfaces*, 2020, **12**, 41312–41322.
- 153 T. Gallet, R. G. Poeira, E. M. Lanzoni, T. Abzieher, U. W. Paetzold and A. Redinger, *ACS Appl. Mater. Interfaces*, 2021, **13**, 2642–2653.
- 154 K. M. Reza, A. Gurung, B. Bahrami, A. H. Chowdhury, N. Ghimire, R. Pathak, S. I. Rahman, M. A. R. Laskar, K. Chen, R. S. Bobba, B. S. Lamsal, L. K. Biswas, Y. Zhou, B. Logue and Q. Qiao, *Sol. RRL*, 2021, **5**, 2000740.
- 155 D. Toth, B. Hailegnaw, F. Richteimer, F. A. Castro, F. Kienberger, M. C. Scharber, S. Wood and G. Gramse, *ACS Appl. Mater. Interfaces*, 2020, **12**, 48057–48066.
- 156 D. Kim, J.-H. Yun, M. Lyu, J. Kim, S. Lim, J. S. Yun, L. Wang and J. Seidel, *J. Phys. Chem. C*, 2019, **123**, 14144–14151.
- 157 T. Gallet, D. Grabowski, T. Kirchartz and A. Redinger, *Nanoscale*, 2019, **11**, 16828–16836.
- 158 J. Yang, S. Xiong, J. Song, H. Wu, Y. Zeng, L. Lu, K. Shen, T. Hao, Z. Ma, F. Liu, C. Duan, M. Fahlman and Q. Bao, *Adv. Energy Mater.*, 2020, **10**, 2000687.

This article is licensed under a Creative Commons Attribution 3.0 Unported Licence.



- 159 C. Chen, Z. Song, C. Xiao, R. A. Awni, C. Yao, N. Shrestha, C. Li, S. S. Bista, Y. Zhang, L. Chen, R. J. Ellingson, C.-S. Jiang, M. Al-Jassim, G. Fang and Y. Yan, *ACS Energy Lett.*, 2020, 5, 2560–2568.
- 160 S. Tan, I. Yavuz, N. De Marco, T. Huang, S. Lee, C. S. Choi, M. Wang, S. Nuryyeva, R. Wang, Y. Zhao, H. Wang, T. Han, B. Dunn, Y. Huang, J. Lee and Y. Yang, *Adv. Mater.*, 2020, 32, 1906995.

This article is licensed under a Creative Commons Attribution 3.0 Unported Licence.



## CHAPTER 3. TWO BIRDS WITH ONE STONE: DUAL GRAIN-BOUNDARY AND INTERFACE PASSIVATION ENABLES >22 % EFFICIENT INVERTED METHYLAMMONIUM-FREE PEROVSKITE SOLAR CELLS

---

Electronic Supplementary Material (ESI) for Energy & Environmental Science.  
This journal is © The Royal Society of Chemistry 2021

### **Two Birds with One Stone: Dual Grain-Boundary and Interface Passivation Enables > 22% Efficient Inverted Methylammonium-Free Perovskite Solar Cells**

Saba Gharibzadeh,<sup>a,b,†</sup> Paul Fassl,<sup>a,b,†</sup> Ihteaz M. Hossain,<sup>a,b</sup> Pascal Rohrbeck,<sup>c</sup> Markus Frericks,<sup>d,e</sup> Moritz Schmidt,<sup>a,b,f</sup> The Duong,<sup>g</sup> Motiur Rahman Khan,<sup>a</sup> Tobias Abzieher,<sup>a</sup> Bahram Abdollahi Nejand,<sup>a,b</sup> Fabian Schackmar,<sup>a,b</sup> Osbel Almora,<sup>h</sup> Thomas Feeney,<sup>a</sup> Roja Singh,<sup>a,b</sup> Dirk Fuchs,<sup>i</sup> Uli Lemmer,<sup>a</sup> Jan P. Hofmann,<sup>d,e</sup> Stefan L.A. Weber,<sup>c</sup> and Ulrich W. Paetzold<sup>a,b,\*</sup>

<sup>a</sup> Light Technology Institute, Karlsruhe Institute of Technology, Engesserstrasse 13, 76131 Karlsruhe, Germany.

<sup>b</sup> Institute of Microstructure Technology, Karlsruhe Institute of Technology, Hermann-von Helmholtz-Platz 1, 76344 Eggenstein-Leopoldshafen, Germany.

<sup>c</sup> Max Planck Institute for polymer research, department physics at interfaces, Ackermannweg 10, 55128 Mainz, Germany

<sup>d</sup> Technische Universität Darmstadt, Otto-Berndt-Straße 3, Darmstadt 64287, Germany.

<sup>e</sup> InnovationLab GmbH, Speyerer Strasse 4, 69115 Heidelberg, Germany.

<sup>f</sup> Center for Nanophotonics, AMOLF, 1098 XG Amsterdam, The Netherlands.

<sup>g</sup> School of Engineering, The Australian National University, Canberra, 2601 Australia.

<sup>h</sup> Institute of Advanced Materials, Universitat Jaume I, 12006 Castelló, Spain.

<sup>i</sup> Insitute for Quantum Materials and Technologies, Karlsruhe Institute of Technology, Herrmann-von-Helmholtz-Platz 1, 76344 Eggenstein-Leopoldshafen, Germany.

<sup>†</sup>These authors contributed equally

Corresponding author: Jun.-Prof. Ulrich Paetzold (Email: ulrich.paetzold@kit.edu)

---

## Device and Material Characterization

**Current density–voltage (*J–V*) measurements.** The *J–V* characteristics of the PSCs were measured with a class AAA xenon-lamp solar simulator (Newport Oriol Sol3A) with a scan rate set at 0.6 V/s using a sourcemeter (Keithley 2400) with an air-mass 1.5 global (AM1.5G) spectra (100 mW/cm<sup>2</sup>). The solar simulator irradiation intensity was calibrated using a certified Si solar cell (Fraunhofer ISE) equipped with a KG5 band pass filter. The stabilized PCE of the PSCs was determined by measuring the photocurrent at the maximum power point (MPP) by using a perturb and observing algorithm under continuous AM 1.5G illumination, while the temperature of the devices was controlled at 25 °C by a Peltier element connected to a microcontroller during the measurements. The measurement was performed in a nitrogen-filled glovebox.

**External Quantum Efficiency Measurements (EQE).** The EQE was measured using a PVE300 photovoltaic QE system (Bentham EQE system). A chopping frequency of ~570 Hz with an integration time of 500 ms to acquire the spectra in a wavelength range from 300 to 850 nm was used. An illumination spot (1.5mm) was utilized to obtain the average over possible variations in the EQE spectra.

**Scanning electron microscopy (SEM).** High-resolution field emission cross-sectional and top-view SEM images of the perovskite thin films based grain boundary-incorporation and surface treatment processes were taken using a Zeiss LEO1530 VP scanning electron microscope with an in-lens detector and an aperture size of 20 µm. The SEM images were captured using a 3-kV acceleration voltage.

**X-ray diffraction (XRD).** The crystal structure of the perovskite layers was carried out utilizing XRD (Bruker D2Phaser system) with Cu-K<sub>α</sub> radiation (λ = 1.5405 Å) in Bragg–Brentano configuration using a LynxEye detector. The XRD was taken from the perovskite layer deposited on the ITO/2Pac substrate to obtain the same perovskite nucleation as well as crystallization as in the solar cells.

**UV-Vis Spectrophotometry (UV).** Transmittance and reflectance spectra of the perovskite thin films were measured using a Bentham PVE300 spectrophotometry setup equipped with a monochromator and a modulated source. A chopper frequency in the range of 400 Hz was applied.

**Cathodoluminescence (CL).** Cathodoluminescence (CL) measurement is performed on an FEI Verios scanning electron microscope (SEM) equipped with a GatanMonoCL4 Elite. The measurements are performed at 3 kV / 25 pA. CL images were captured in panchromatic mode with appropriate dichroic filters (band pass filter with 500 ± 40 nm).

**X-ray and Ultraviolet Photoelectron Spectroscopy (XPS and UPS).** Photoelectron spectroscopy was performed with a PHI 5000 VersaProbe at the Clustertool at InnovationLab GmbH in Heidelberg. The samples were introduced from the glovebox with exposures to air <1 min. The pressure in the ultra-high vacuum system is around 10<sup>-9</sup> mbar. For XPS, monochromatic Al K<sub>α</sub> radiation with an excitation energy of 1486.6 eV was used. UPS was carried out with a He-discharge lamp using the He-I emission with an energy of 21.22 eV. Pass energies of 11.75, 2.95, and 0.59 eV were used for XPS core-level spectra, UPS valence band and UPS secondary electron cut-offs, respectively. For the measurements of the secondary electron cut-off, a bias of -5 V was applied. The take-off angle for all measurements was 90°. The binding energies of the spectra were calibrated with respect to the Fermi level of an Ar<sup>+</sup>-ion etched silver foil. For the XPS core level spectra shown in this work a background subtraction was performed using a Shirley type or linear background.<sup>1–3</sup> Stoichiometric ratios were determined using corrected peak areas using CasaXPS software. For the correction of the peak areas, we used calculated photoionization cross-sections by Scofield,<sup>4</sup> angular distribution correction for a source-analyzer-angle of 45° based on Reilman et al.,<sup>5</sup> an empirical transmission function determined for the used system, and an escape depth correction with a kinetic energy exponent of 0.7. The peak area correction was verified using the I 3d and I 4d emissions from a survey spectrum. The derived corrected area ratio of I3d/I4d is 1.03 and thereby in good agreement with the expected value of 1. The inelastic mean free path (IMFP) for the calculation of the 2D passivation overlayer thickness was estimated using the TPP-2M equation in the NIST database software.<sup>6,7</sup> We estimated a IMFP value of 3.1 nm for the photoelectrons of the Pb 4f<sub>7/2</sub> emission. This IMFP value and a Lambert-Beer type exponential law were used to calculate the 2D passivation overlayer thickness from the intensity decay of the Pb 4f<sub>7/2</sub> component emitted from the underlying 3D bulk phase (see Fig. S28).

**Kelvin probe force microscopy (KPFM).** KPFM was measured on an Oxford Instruments/Asylum Research MFP-3D AFM in an argon glovebox (level of humidity below 0.2 ppm, level of oxygen below 0.1 ppm) for all experiments. The typical resonance frequency of the cantilevers (Bruker Model: SCM-PIT-V2) was ~65 kHz, spring constant of 2 N/m, a tip radius of 25 nm and a tip height of 10 to 15 µm. Tip, tip cone and cantilever are coated with PtIr (work function ~5.5 eV)<sup>8</sup> on both sides. The topography feedback was performed with amplitude

## CHAPTER 3. TWO BIRDS WITH ONE STONE: DUAL GRAIN-BOUNDARY AND INTERFACE PASSIVATION ENABLES >22 % EFFICIENT INVERTED METHYLAMMONIUM-FREE PEROVSKITE SOLAR CELLS

---

modulation (AM) on the first eigenmode and the oscillation amplitude was kept to approximately  $\approx 20\text{-}30$  nm for all measurements. To perform the KPFM feedback, we used a Zurich Instruments HF2 Lock-In amplifier for all heterodyne frequency modulation (FM) experiments. The electric drive amplitude of the  $\omega_E$  signal was 2 V. We grounded the sample via the sample holder with an external wire to ground level of the Zürich Lock-In Amplifier. The compensating  $U_{bc}$  was applied to the tip, minimizing electrostatic tip-sample interactions.<sup>9</sup> In the tip-bias configuration, the measured CPD signal,  $U_{CPD}$ , is connected to the work functions of sample,  $\Phi_{\text{sample}}$ , and tip,  $\Phi_{\text{tip}}$ , by

$$U_{CPD} = \frac{1}{e} (\Phi_{\text{tip}} - \Phi_{\text{sample}})$$

Thus, a lower value of  $U_{CPD}$  corresponds to a higher sample work function.

**Photoluminescence Quantum Yield (PLQY).** PLQY measurements were carried out inside an integrating sphere (LabSphere, 15 cm diameter) in ambient air (relative humidity <30%). A green laser (Coherent or LD-515-10MG from Roithner Lasertechnik) was directed into the sphere *via* a small entrance port. An optical fiber was used to collect the emission from the exit port of the sphere and guide it to the spectrometers (QE65 Pro from Ocean Optics and AvaSpec-ULS2048x64TEC from Avantes). The spectral response was calibrated using a calibration lamp (HL-3plus-INT-Cal from Ocean Optics). Raw measured spectra were recalculated to give power spectra using the integration time. The PLQY was determined using the method described by de Mello *et al.*<sup>10</sup> The samples were placed at an angle of  $15^\circ$  with respect to the laser beam to avoid specular reflectance toward the entrance port. The radiative limit of the  $V_{oc}$  ( $V_{oc-rad}$ ), the implied  $V_{oc}$  ( $V_{oc-imp}$ ) (Fig. 3c) and the pseudo  $JV$ -curves (Fig. S14) were determined from the (intensity-dependent) PLQY measurements as described by Stolterfoht *et al.*<sup>11</sup> and Kirchartz *et al.*<sup>12</sup>

**Time-resolved photoluminescence (TRPL).** Time-resolved photoluminescence (TRPL) measurements were carried out in gated-mode with a pulsed laser of 532 nm. A repetition rate of 1 kHz and a pulse width of 0.8 ns was used for the excitation of the samples. All measurements were performed with a pump fluence of  $\sim 20\text{-}30$  nJ/cm<sup>2</sup>. The photoluminescence was captured using an ACTON spectrometer and a CCD camera PIMAX512 at room temperature. The measurements were carried out in the air.

**Thermal admittance spectroscopy (TAS).** The thermal admittance spectroscopy (TAS) measurements were performed on Paios (Fluxim AG)- platform for all-in-one-characterization of solar cells and OLEDs at short circuit in the dark with the perturbation AC voltage amplitude of 35 mV in a frequency range 0.5 Hz-1M Hz. The temperature was varied between 278 and 318 K using liquid-cooled Peltier cryostat where the sample chamber was filled with nitrogen gas. The theoretical formalism of the TAS can be found in the literature.<sup>13-16</sup>

**Space charge limited current (SCLC) measurements.** Space charge limited current (SCLC) measurements were performed on Paios (Fluxim AG)- platform for all-in-one-characterization of solar cells and OLEDs. The dark  $J$ - $V$  measurements are plotted on a log-log scale. Generally, three distinct regions are observed in the  $J$ - $V$  plot: (1) Ohmic region with slope 1, (2) trap filling region with a slope higher than 2 and (3) trap-free SCLC region with a slope of 2. The mobility value is typically extracted by the quadratic region of the  $J$ - $V$  curve which is governed by the Mott-Gurney equation:

$$J = \frac{9}{8} \epsilon \epsilon_0 \mu \frac{V^2}{d^3}$$

where  $\epsilon_0$  is the permittivity of vacuum,  $\epsilon$  is the dielectric constant of the material,  $\mu$  is the mobility of the charge carrier and  $d$  is the thickness of the active layer. The electron mobility is extracted by fitting the above equation. It should be noted that the dielectric constant is taken as 26 which is calculated from the capacitance-frequency measurement. The trap densities for the devices are calculated from the trap-filled-limit voltage:

$$V_{TFL} = \frac{qn_t d^2}{2\epsilon \epsilon_0}$$

Where  $q$  is the elementary charge,  $n_t$  is the trap density and  $d$  is the thickness of the active layer. The trap-filled-limit-voltage  $V_{TFL}$  is the voltage at the intersection point of the tangent with slope 1 and tangent with slope higher than 2.<sup>17,18</sup>

---

## Experimental Section

### Materials:

2PACz (TCI, CAS: 20999-38-6), Lead iodide (PbI<sub>2</sub>: TCI, CAS: 10101-63-0), Formamidinium iodide (FAI: Dyenamo, CAS: 879643-71-7), Cesium chloride (abcr, CAS: 7647-17-8), 2-phenylethylammonium chloride (PEACl: Sigma-Aldrich; CAS: 156-28-5), *n*-Octylammonium Chloride (OACl: Greatcell solar materials, CAS: 142-95-0), *n*-Butylammonium Chloride (BACl: TCI, CAS: 3858784, Fullerene-C<sub>60</sub> (C<sub>60</sub>: Sigma-Aldrich, CAS: 99685-96-8), Bathocuproine (BCP: Lumtec, CAS: 4733-39-5), (MgF<sub>2</sub>: Sigma-Aldrich, CAS: 7783-40-6). All solvents including *N,N*-dimethylformamide, ≥99.9% (DMF, CAS: 68-12-2), Dimethyl sulfoxide (DMSO) anhydrous, ≥99.9% CAS: 67-68-5), Chlorobenzene (CB) anhydrous, 99.8%, CAS: 108-90-7), 2-Propanol, ≥98%, (IPA, CAS: 67-63-0) were ordered from Sigma-Aldrich. Ethanol absolute 99.8% was ordered from VWR Chemicals.

### Perovskite solar cell Fabrication:

The planar p-i-n perovskite solar cells were fabricated with the architecture of: glass/ITO/2PACz/Cs<sub>0.18</sub>FA<sub>0.82</sub>PbI<sub>3</sub>/C<sub>60</sub>/BCP/Ag.

ITO substrates (sheet resistance 15 Ω/sq, Luminescence Technology, CAS: 50926-11-9) were cut in 0.16 cm × 0.16 cm and cleaned with acetone and isopropanol in an ultrasonic bath for 10 minutes each. The substrates were further treated with oxygen plasma for 3 min before the deposition of the hole transport layer (HTL).

A thin layer of 2PACz HTL was deposited on the ITO substrate by spin-coating at 3000 rpm for 30 s and subsequently annealed at 100 °C for 10 min. The 2PACz precursor solution was prepared by dissolving 2PACz in anhydrous Ethanol with a concentration of 1 mmol/l. The prepared solution was put in an ultrasonic bath for 15 min before it was used. The reference double cation perovskite Cs<sub>0.18</sub>FA<sub>0.82</sub>PbI<sub>3</sub> precursor solution was prepared by mixing PbI<sub>2</sub> (507 mg: 10% excess of PbI<sub>2</sub>), CsCl (30 mg) and FAI (172 mg) in 1 mL solvent mixture of DMF:DMSO 4:1 volume ratio.<sup>17</sup> The reference perovskite film was deposited on the substrate at 1000 rpm (acceleration 2000 rpm s<sup>-1</sup>) for 10 s and 5000 rpm (acceleration rate 2000 rpm s<sup>-1</sup>) for 30 s. 20 s after the start of the second step spin-coating, 150 μL Chlorobenzene was quickly dropped on the spinning substrate. The samples were then annealed at 150 °C for 30 min in an inert atmosphere. For preparing surface passivation (SP) perovskite layer, PEACl dissolved in IPA with different concentrations (1.5 and 3mg) was dynamically spin-coated on top of the reference perovskite film at 5000 rpm (acceleration 2000 rpm s<sup>-1</sup>) for 30 s, followed by annealing at 100 °C for 5 min. For preparing the grain boundary passivation (GBP) perovskite layer, 25 μL of PbCl<sub>2</sub>:PEACl solution with a molar ratio of 1:1 dissolved in 1 mL DMSO was added in the reference perovskite precursor solution and then was heated at 150 °C for 30 min. In the case of preparing the grain boundary perovskite layer based on other chloride-based long-chain organic alkylammonium salts BACl and OACl, the same procedure was applied. Finally, for preparing grain boundary passivation & surface passivation (GBP&SP) perovskite layer, the PEACl interlayer was spin-coated on top of the GBP perovskite film, followed by annealing at 100 °C for 5 min. The electron transport layer, 23 nm C<sub>60</sub> and 3 nm BCP, were thermally evaporated at an evaporation rate of 0.1-0.2 Å/s at a pressure of around 10<sup>-6</sup> mbar. Afterwards, 100 nm Ag was thermally evaporated using a shadow mask with an active area of 0.12 mm<sup>2</sup> to complete the perovskite solar cells with 4 pixels per substrate. It should be noted that in order to reduce the reflection in perovskite solar cell, 125 nm MgF<sub>2</sub> as an antireflection layer was evaporated on top of the Ag.

## CHAPTER 3. TWO BIRDS WITH ONE STONE: DUAL GRAIN-BOUNDARY AND INTERFACE PASSIVATION ENABLES >22 % EFFICIENT INVERTED METHYLAMMONIUM-FREE PEROVSKITE SOLAR CELLS

---

Table S1: Photovoltaic parameters in reverse (BW) and forward (FW) bias of perovskite solar cells based on the reference (Ref), grain boundary passivation (GBP), surface passivation (SP), and combination of grain boundary & surface passivation (GBP&SP) processes.

		$V_{oc}$ (V)	$J_{sc}$ (mA/cm <sup>2</sup> )	FF	PCE (%)
Ref	BW	1.086	23.9	78.6	20.4
	FW	1.08	23.6	75.6	19.3
GBP	BW	1.114	23.5	79.3	20.8
	FW	1.11	23.6	77.9	20.4
SP	BW	1.131	23.7	82.3	22.1
	FW	1.131	23.6	79.9	21.3
GBP&SP	BW	1.162	23.5	83.2	22.7
	FW	1.153	23.6	80.6	22.0

---

Table S2: The calculated electron mobilities and trap densities for the perovskite solar cells based on the reference (Ref), surface passivation (SP), grain boundary passivation (GBP), and combination of grain boundary & surface passivation (GBP&SP) processes.

Device	Electron mobility ( $\text{cm}^2\text{V}^{-1}\text{s}^{-1}$ )	$n_t$ ( $\text{cm}^{-3}$ )
Ref	$4.9 \times 10^{-3}$	$9.2 \times 10^{15}$
GBP	$7.2 \times 10^{-3}$	$6.5 \times 10^{15}$
SP	$6.3 \times 10^{-3}$	$5.4 \times 10^{15}$
GBP&SP	$10.0 \times 10^{-3}$	$3.7 \times 10^{15}$

## CHAPTER 3. TWO BIRDS WITH ONE STONE: DUAL GRAIN-BOUNDARY AND INTERFACE PASSIVATION ENABLES >22 % EFFICIENT INVERTED METHYLAMMONIUM-FREE PEROVSKITE SOLAR CELLS

---

Table S3: The calculated hole mobilities and trap densities for the perovskite solar cells based on the reference (Ref), surface passivation (SP), grain boundary passivation (GBP), and combination of grain boundary & surface passivation (GBP&SP) processes.

Device	Hole mobility ( $\text{cm}^2\text{V}^{-1}\text{s}^{-1}$ )	$n_t$ ( $\text{cm}^{-3}$ )
Ref	$4.0 \times 10^{-4}$	$4.2 \times 10^{15}$
GBP	$6.2 \times 10^{-4}$	$3.4 \times 10^{15}$
SP	$5.3 \times 10^{-4}$	$3.0 \times 10^{15}$
GBP&SP	$7.9 \times 10^{-4}$	$2.9 \times 10^{15}$

Table S4: The atomic ratio of I/Pb, Cl/Pb, Cs/Pb, FA/Pb, and I+Cl/Pb for the reference (Ref) and grain boundary (GBP) perovskite films treated with different concentration of PEACl (1.5, 3 and 10 mg/ml) as a surface passivation layer (referred to as: SP(1.5), SP(3), SP(10), GBP&SP(1.5), GBP&SP(3) and GBP&SP(10), respectively).

Atomic ratio	I / Pb	Cl / Pb	I+Cl / Pb	Cs / Pb	FA / Pb
Ref	3.06	0.00	3.06	0.11	0.55
SP(1.5)	2.95	0.31	3.26	0.14	0.43
SP(3)	2.64	0.90	3.55	0.11	0.27
SP(10)	1.41	3.30	4.71	0.00	0.00
GBP	2.67	0.22	2.89	0.16	0.43
GBP&SP(1.5)	1.87	1.15	3.02	0.29	0.24
GBP&SP(3)	1.49	1.79	3.28	0.24	0.17
GBP&SP(10)	1.07	4.07	5.14	0.00	0.00

## CHAPTER 3. TWO BIRDS WITH ONE STONE: DUAL GRAIN-BOUNDARY AND INTERFACE PASSIVATION ENABLES >22 % EFFICIENT INVERTED METHYLAMMONIUM-FREE PEROVSKITE SOLAR CELLS

---

Table S5: Estimation for the 2D RP passivation layer thickness, the atomic ratio of PEA to the 2D Pb (II) phase and the corresponding calculated n.

	estimated 2D thickness	PEA / Pb II	calculated n
Ref	0.00	0.00	0.00
SP(1.5)	0.75	1.68	1.19
SP(3)	2.38	1.19	1.69
SP(10)	-	1.74	1.15
GBP	0.00	0.41	4.85
GBP&SP(1.5)	1.53	0.77	2.59
GBP&SP(3)	4.30	0.85	2.35
GBP&SP(10)	-	2.10	0.95

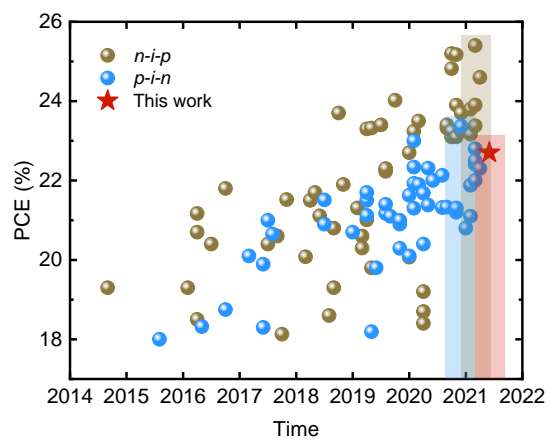


Fig. S1: Reported champion power conversion efficiencies (PCEs) measured in the *J-V*-scan for *n-i-p* vs. *p-i-n* perovskite solar cells compared to the champion PCE of 22.7% reported in this work.

CHAPTER 3. TWO BIRDS WITH ONE STONE: DUAL GRAIN-BOUNDARY AND INTERFACE PASSIVATION ENABLES  $>22\%$  EFFICIENT INVERTED METHYLAMMONIUM-FREE PEROVSKITE SOLAR CELLS

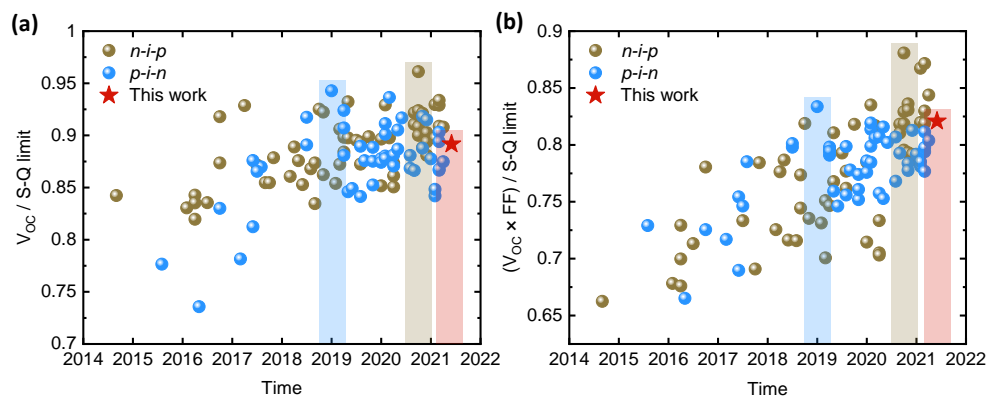


Fig. S2: (a) Reported champion open-circuit voltage ( $V_{oc}$ ) with respect to the Shockley-Queisser (S-Q) limit for the respective bandgap for *n-i-p* vs. *p-i-n* perovskite solar cells (PSCs). The bandgap of all PSCs was determined from the inflection point of the external quantum efficiency spectra extracted from literature as suggested by Kirchartz *et al.*<sup>12</sup> (b) Reported champion  $V_{oc} \times \text{fill factor (FF)}$  product of *n-i-p* vs. *p-i-n* PSCs with respect to the S-Q limit. We note that the highest reported value in 2019 was based on a PSC with PCE  $<21\%$  given the rather low  $J_{sc}$ .<sup>20</sup>

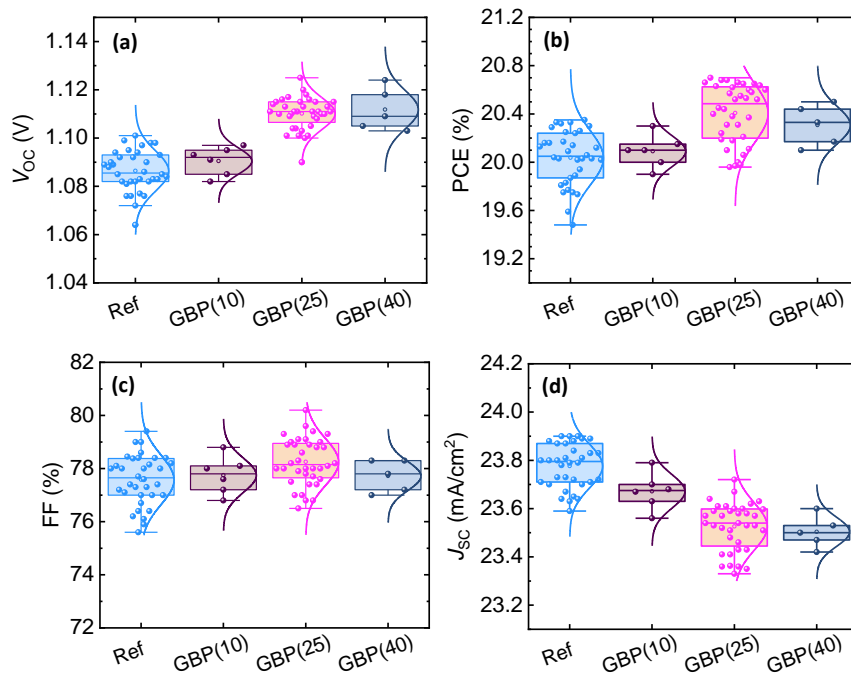


Fig. S3: Comparison of photovoltaic parameters (extracted from the reverse scan of the  $J$ - $V$  curves) of reference (Ref) and grain boundary passivation perovskite solar cells prepared with various amounts of PEACl:PbCl<sub>2</sub> solution added into the Ref perovskite solution (10, 25 and 40  $\mu\text{L}$ , referred to as GBP(10), GBP(25) and GBP(40), respectively). (a) Power conversion efficiency (PCE), (b) open-circuit voltage ( $V_{oc}$ ), (c) short-circuit current density ( $J_{sc}$ ), and (d) fill factor (FF).

CHAPTER 3. TWO BIRDS WITH ONE STONE: DUAL GRAIN-BOUNDARY AND INTERFACE PASSIVATION ENABLES  $>22\%$  EFFICIENT INVERTED METHYLAMMONIUM-FREE PEROVSKITE SOLAR CELLS

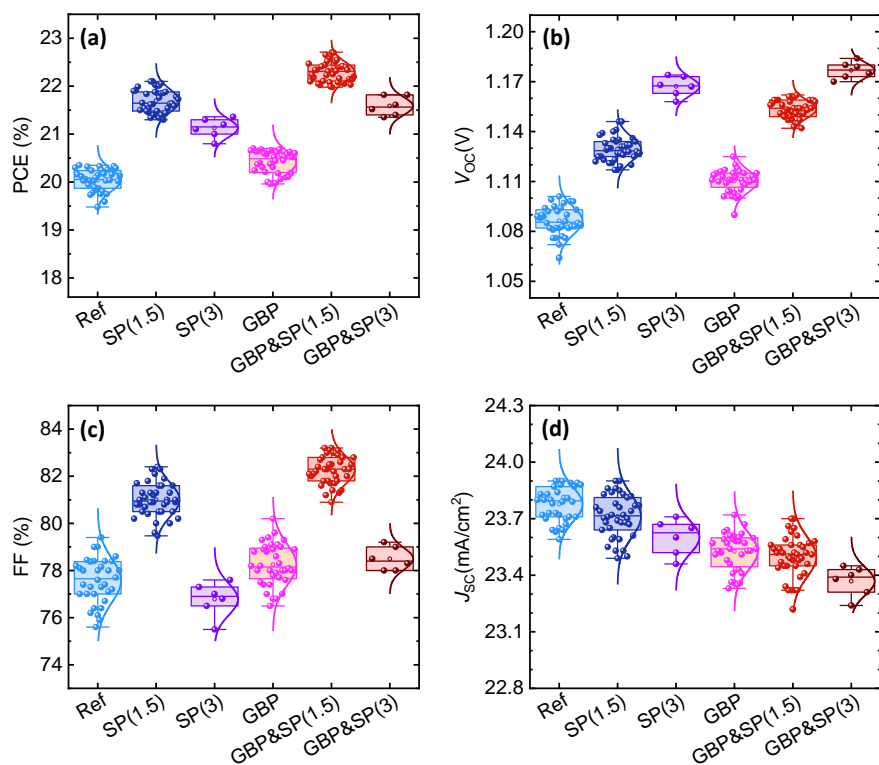


Fig. S4: The effect of the PEACl concentration (1.5 mg/ml and 3 mg/mL) as a surface passivation interlayer on photovoltaic parameters of reference (Ref) and grain boundary passivation (GBP) perovskite solar cells (referred to as: SP(1.5), SP(3), GBP&SP(1.5) and GBP&SP(3) respectively). (a) Power conversion efficiency (PCE), (b) open-circuit voltage ( $V_{oc}$ ), (c) short-circuit current density ( $J_{sc}$ ), and (d) fill factor (FF).

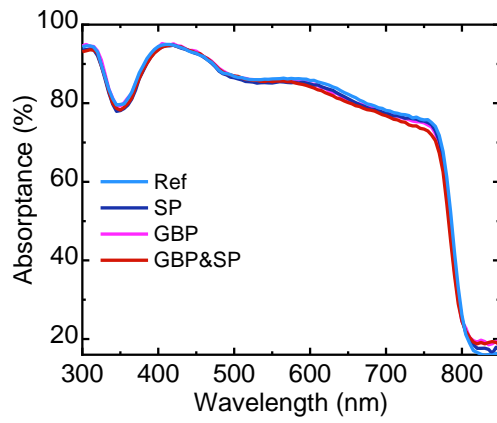


Fig. S5: Absorbance spectra of double-cation Cs<sub>0.18</sub>FA<sub>0.82</sub>PbI<sub>3</sub> perovskite films deposited on the glass substrates prepared without any modification (Ref) as well as with surface passivation (SP), grain boundary passivation (GBP), and grain boundary & surface passivation (GBP&SP).

CHAPTER 3. TWO BIRDS WITH ONE STONE: DUAL GRAIN-BOUNDARY AND INTERFACE PASSIVATION ENABLES >22 % EFFICIENT INVERTED METHYLAMMONIUM-FREE PEROVSKITE SOLAR CELLS

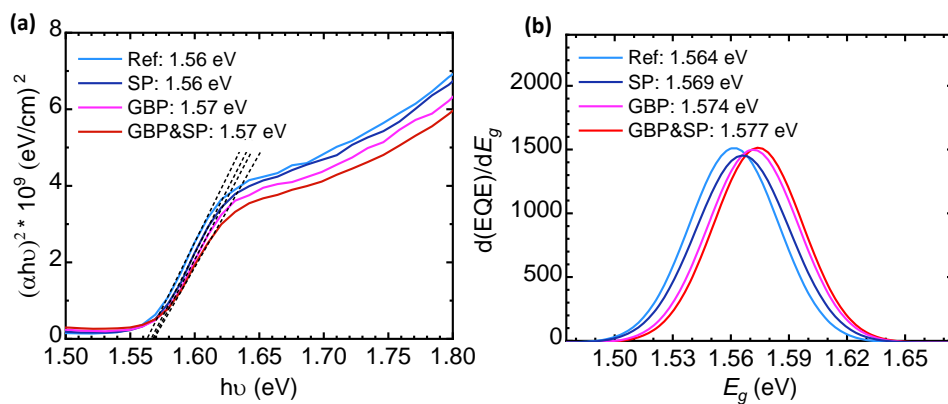


Fig. S6: Optical bandgap extracted from (a) the Tauc plot assuming a direct bandgap and (b) the inflection point of the external quantum efficiency (EQE) spectra of double-cation  $\text{Cs}_{0.18}\text{FA}_{0.82}\text{PbI}_3$  perovskite films prepared without any modification (Ref) and with surface passivation (SP), grain boundary passivation (GBP) and grain boundary & surface passivation (GBP&SP).

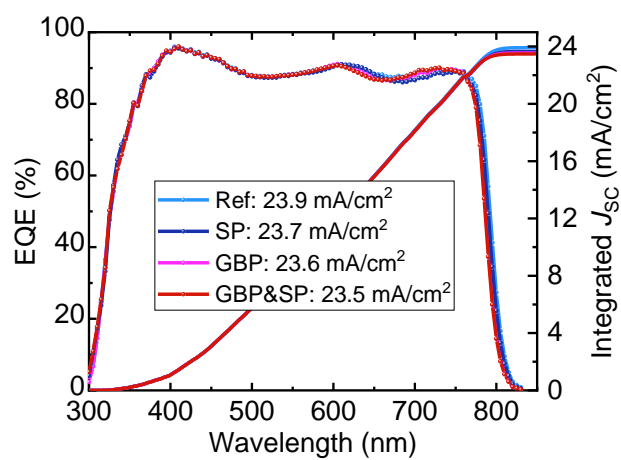


Fig. S7: External quantum efficiency (EQE) and corresponding integrated short-circuit current density ( $J_{sc}$ ) of the best-performing perovskite solar cells prepared without any modification (Ref) and with surface passivation (SP), grain boundary passivation (GBP), and grain boundary & surface passivation (GBP&SP). The inset shows the respective integrated  $J_{sc}$ .

### CHAPTER 3. TWO BIRDS WITH ONE STONE: DUAL GRAIN-BOUNDARY AND INTERFACE PASSIVATION ENABLES >22 % EFFICIENT INVERTED METHYLAMMONIUM-FREE PEROVSKITE SOLAR CELLS

---

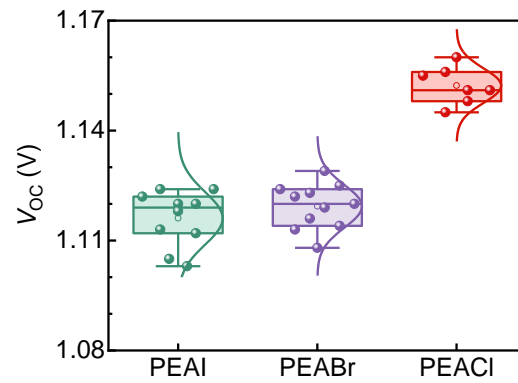


Fig. S8: Comparison of the open-circuit voltage ( $V_{oc}$ ) of dual passivated perovskite solar cells based on the incorporation of PEAI:PbCl<sub>2</sub>, PEABr:PbCl<sub>2</sub> and PEACl:PbCl<sub>2</sub> in the precursor solution, as well as surface treatment with PEAI, PEABr and PEACl solution, respectively (referred to as: Ph-Cl/PEAI, Ph-Br/PEABr and Ph-Cl/PEACl).

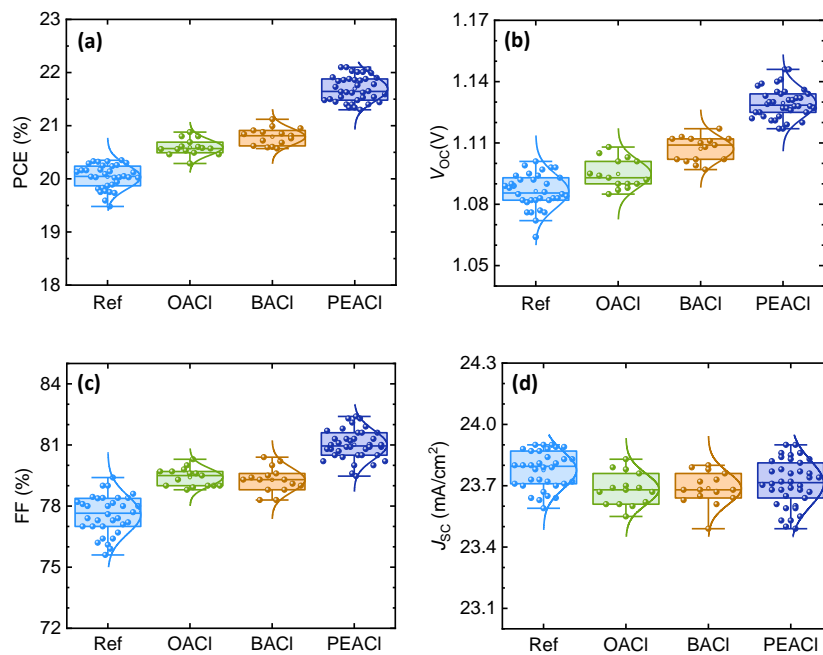


Fig. S9: Photovoltaic parameters of the perovskite solar cells without any modification (Ref) and with surface passivation process, treated with OACI, BACI and PEACI solution on top of the reference perovskite layer respectively. (a) Power conversion efficiency (PCE), (b) open-circuit voltage ( $V_{oc}$ ), (c) fill factor (FF), (d) short-circuit current density ( $J_{sc}$ ).

CHAPTER 3. TWO BIRDS WITH ONE STONE: DUAL GRAIN-BOUNDARY AND INTERFACE PASSIVATION ENABLES  $>22\%$  EFFICIENT INVERTED METHYLAMMONIUM-FREE PEROVSKITE SOLAR CELLS

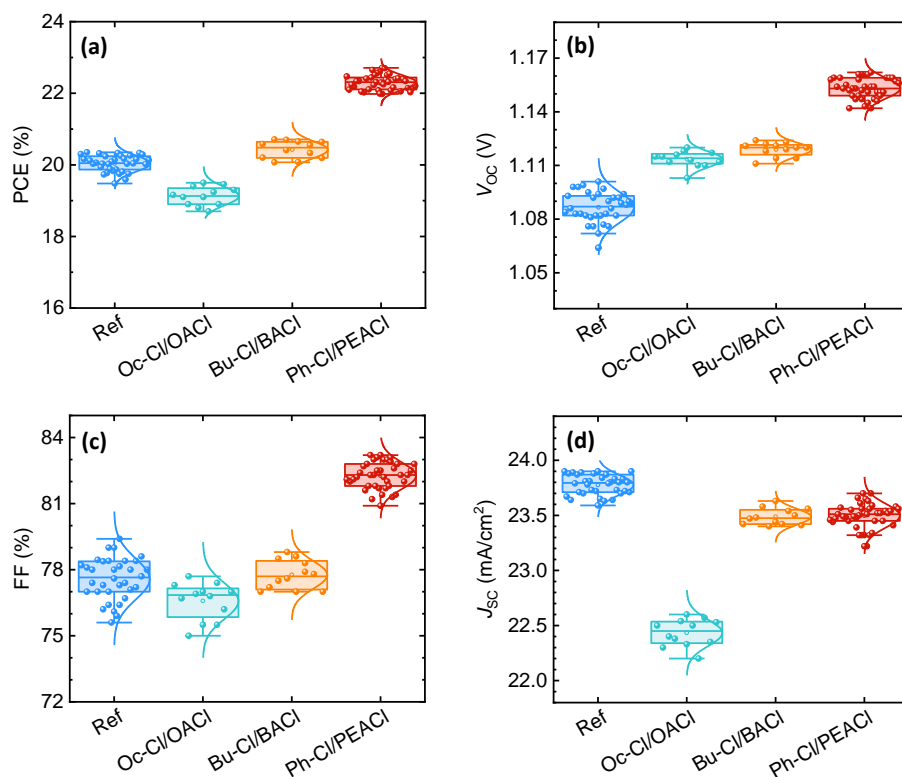


Fig. S10: Photovoltaic parameters of the perovskite solar cells without any modification (Ref) and with combined grain boundary & surface passivation processes based on the incorporation of OAcI:PbCl<sub>2</sub> (Oc-Cl), BACI:PbCl<sub>2</sub> (Bu-Cl) and PEACI:PbCl<sub>2</sub> (Ph-Cl) in the precursor solution, as well as surface treatment with OAcI, BACI and PEACI solution, respectively (referred to as: Oc-Cl/OAcI, Bu-Cl/BACI and Ph-Cl/PEACI). (a) Power conversion efficiency (PCE), (b) open-circuit voltage ( $V_{oc}$ ), (c) fill factor (FF), (d) short-circuit current density ( $J_{sc}$ ).

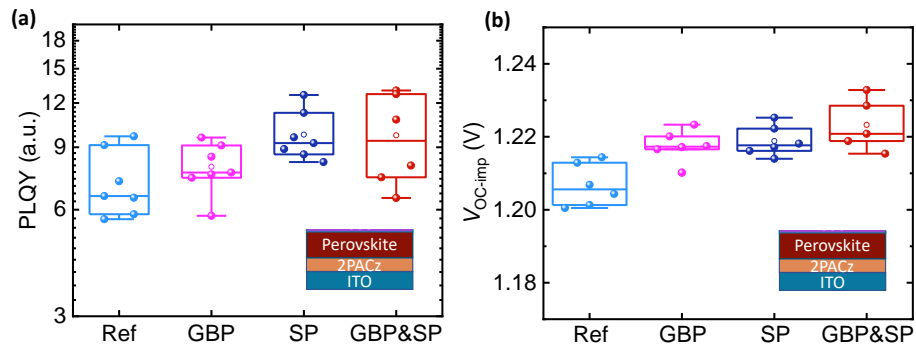


Fig. S11. Photoluminescence quantum yield (PLQY) and the obtained implied  $V_{OC}$  ( $V_{OC-imp}$ ) of perovskite films prepared on ITO/2PACz substrates without any modification (Ref) and with surface passivation (SP), grain boundary passivation (GBP), and grain boundary & surface passivation (GBP&SP) processes.

### CHAPTER 3. TWO BIRDS WITH ONE STONE: DUAL GRAIN-BOUNDARY AND INTERFACE PASSIVATION ENABLES >22 % EFFICIENT INVERTED METHYLAMMONIUM-FREE PEROVSKITE SOLAR CELLS

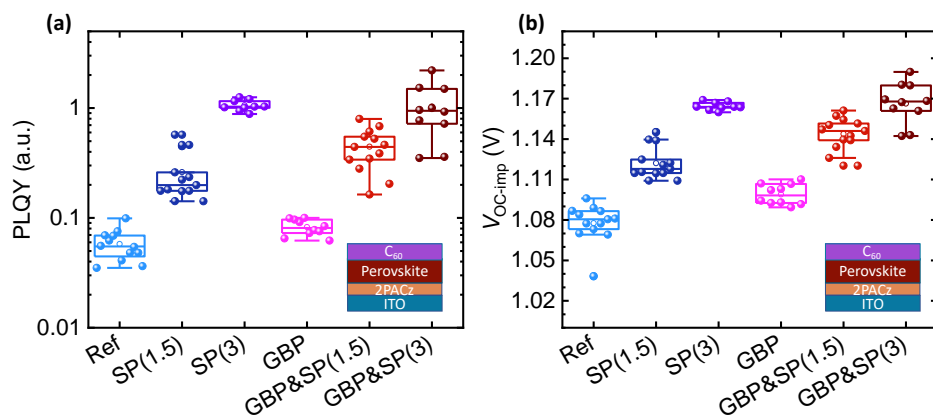


Fig. S12. The effect of PEACl concentration (1.5 mg/ml and 3 mg/ml) as a surface passivation interlayer on (a) photoluminescence quantum yield (PLQY) and (b) the obtained implied  $V_{oc}$  ( $V_{oc-imp}$ ) of the reference (Ref) and grain boundary passivation (GBP) perovskite solar cells (referred to as: SP(1.5), SP(3), GBP&SP(1.5) and GBP&SP(3), respectively).

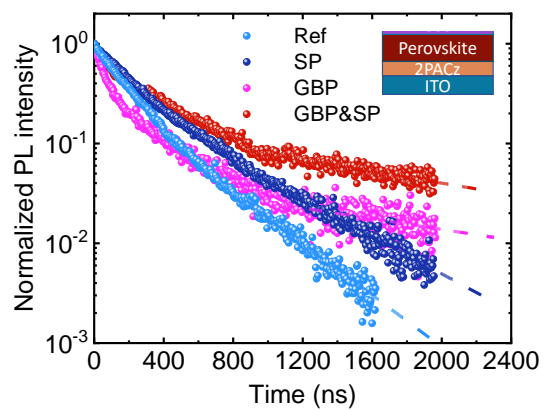


Fig. S13: Time-resolved photoluminescence (TRPL) for perovskite films prepared on ITO/2PACz substrates without any modification (Ref) and with surface passivation (SP), grain boundary passivation (GBP) and grain boundary & surface passivation (GBP&SP).

CHAPTER 3. TWO BIRDS WITH ONE STONE: DUAL GRAIN-BOUNDARY AND INTERFACE PASSIVATION ENABLES >22 % EFFICIENT INVERTED METHYLAMMONIUM-FREE PEROVSKITE SOLAR CELLS

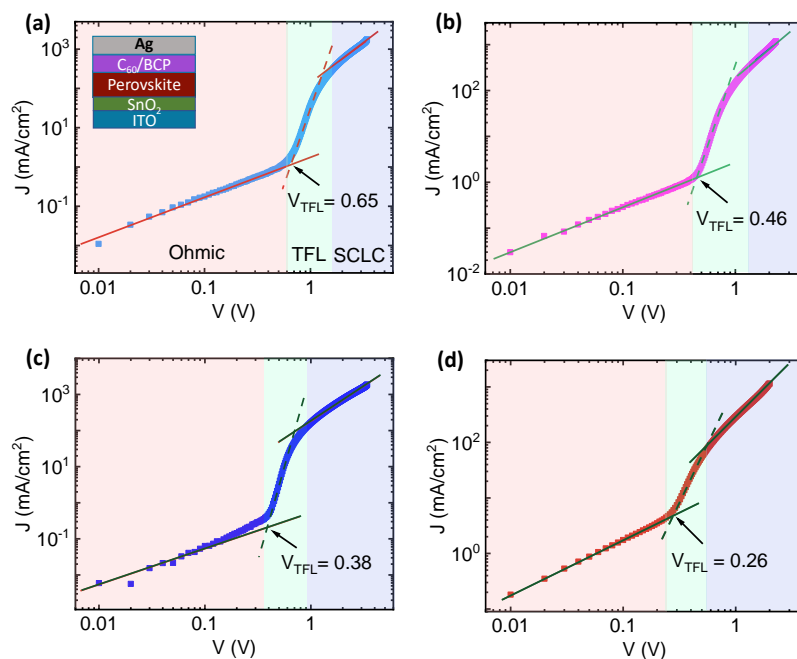


Fig S14: The J-V characteristics (log-log plot) of electron-only devices demonstrating three different regimes, marked with ohmic, trap-filled, and trap-free space charge limited current (SCLC) regime measured in the dark for (a) reference (Ref), (b) grain boundary passivation (GBP), (c) surface passivation (SP), and (d) grain boundary & surface passivation (GBP&SP) films. The electron trap density ( $n_t$ ) could be determined by the trap-filled limited voltage ( $V_{TFL}$ ) from electron-only devices.

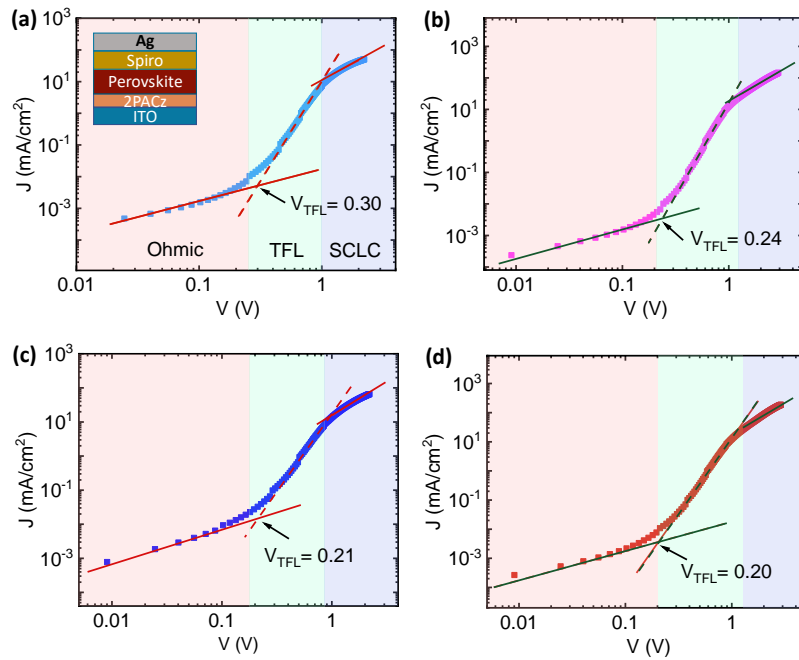


Fig S15. The J-V characteristics (log-log plot) of hole-only devices demonstrating three different regimes, marked with Ohmic, trap-filled, and trap-free space charge limit current regime measured in the dark for (a) reference (Ref), (b) grain boundary passivation (GBP), (c) surface passivation (SP), and (d) grain boundary & surface passivation (GBP&SP) films. The insert shows the device configuration: ITO/2PACz/Perovskite/Spiro-MeOTAD/Ag.

### CHAPTER 3. TWO BIRDS WITH ONE STONE: DUAL GRAIN-BOUNDARY AND INTERFACE PASSIVATION ENABLES >22 % EFFICIENT INVERTED METHYLAMMONIUM-FREE PEROVSKITE SOLAR CELLS

---

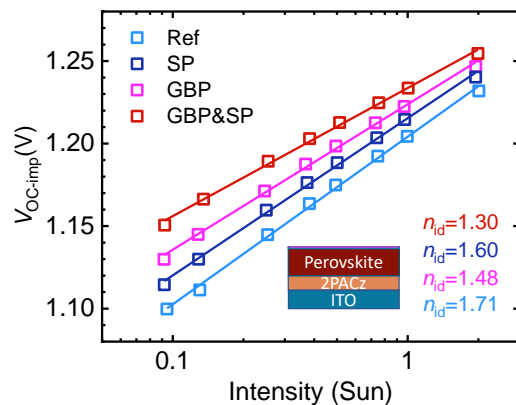


Fig. S16: Ideality factor ( $n_{id}$ ) extracted from a fit to the implied  $V_{oc}$  ( $V_{oc-imp}$ ) (derived from intensity-dependent photoluminescence quantum yield measurements) for perovskite films prepared on ITO/2PACz substrates without any modification (Ref) and with surface passivation (SP), grain boundary passivation (GBP) and grain boundary & surface passivation (GBP&SP).

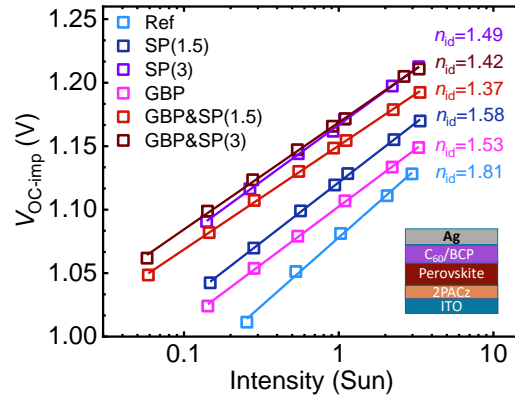


Fig. S17: The effect of PEACl concentration (1.5 mg/ml and 3 mg/ml) as a surface passivation interlayer (referred to as: SP(1.5) and SP(3)) on the ideality factor ( $n_{id}$ ) extracted from a fit to the implied  $V_{oc}$  ( $V_{OC-imp}$ ) of the reference (Ref) and grain boundary passivation (GBP) perovskite solar cells (referred as: SP(1.5), SP(3), GBP&SP(1.5) and GBP&SP(1.5), respectively).

CHAPTER 3. TWO BIRDS WITH ONE STONE: DUAL GRAIN-BOUNDARY AND INTERFACE PASSIVATION ENABLES  $>22\%$  EFFICIENT INVERTED METHYLAMMONIUM-FREE PEROVSKITE SOLAR CELLS

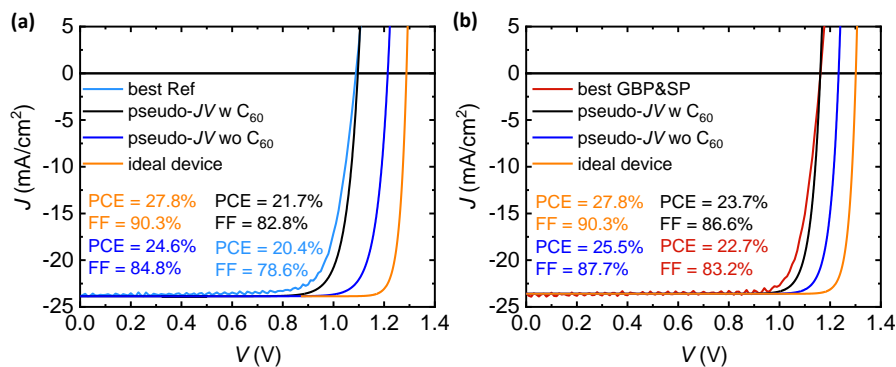


Fig. S18: The  $JV$ -curves of (a) the best GBP&SP PSC and (b) the best Ref PSC are compared to pseudo- $JV$  curves calculated from the intensity-dependent PLQY data for perovskite films prepared on ITO/2Pacz with (w) and without (wo) a C<sub>60</sub> layer on top as well as to an ideal device ( $n_{id} = 1$ ) that has the same  $J_{SC}$  as the best PSC, as described by Stolterfoht et al.<sup>11</sup>

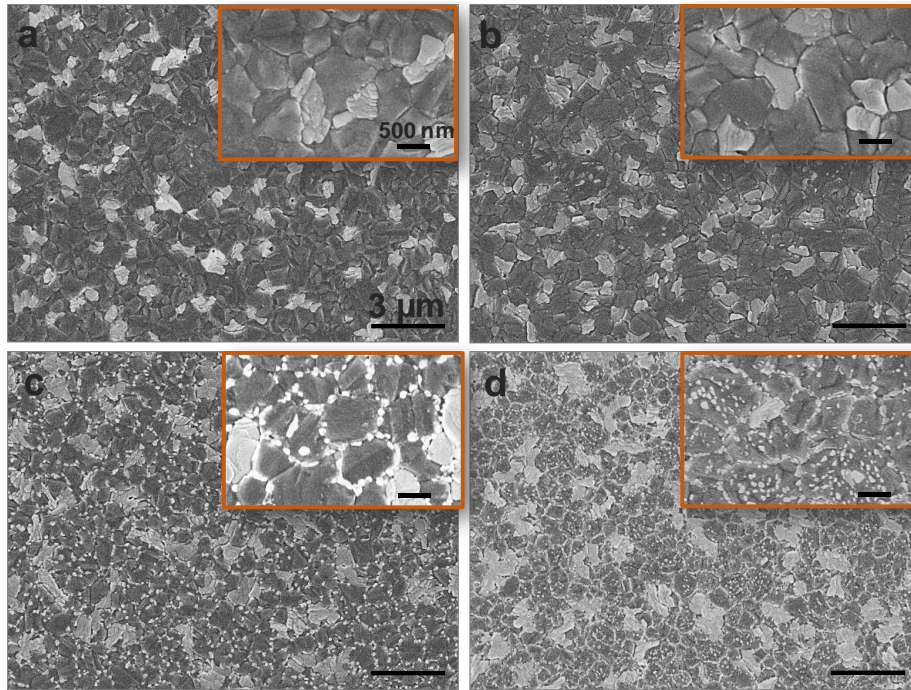


Fig. S19: Top-view scanning electron microscopy (SEM) images of double-cation  $\text{Cs}_{0.18}\text{FA}_{0.82}\text{PbI}_3$  perovskite films prepared (a) without any modification and with (b) surface passivation (c) grain boundary passivation, and (d) grain boundary & surface passivation processes. The insets show higher magnification images.

### CHAPTER 3. TWO BIRDS WITH ONE STONE: DUAL GRAIN-BOUNDARY AND INTERFACE PASSIVATION ENABLES >22 % EFFICIENT INVERTED METHYLAMMONIUM-FREE PEROVSKITE SOLAR CELLS

---

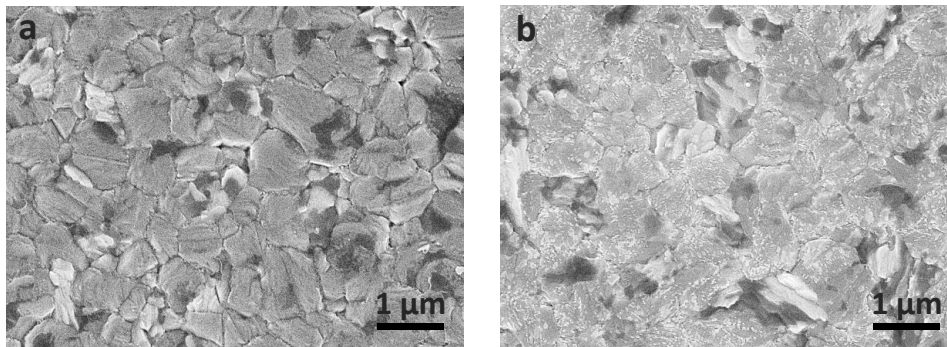


Fig. S20: Top-view scanning electron microscopy (SEM) images of double-cation  $\text{Cs}_{0.18}\text{FA}_{0.82}\text{PbI}_3$  perovskite film treated with a high-concentration of PEACl (3 mg/ml) on top of the (a) reference and (b) grain boundary passivated perovskite layers.

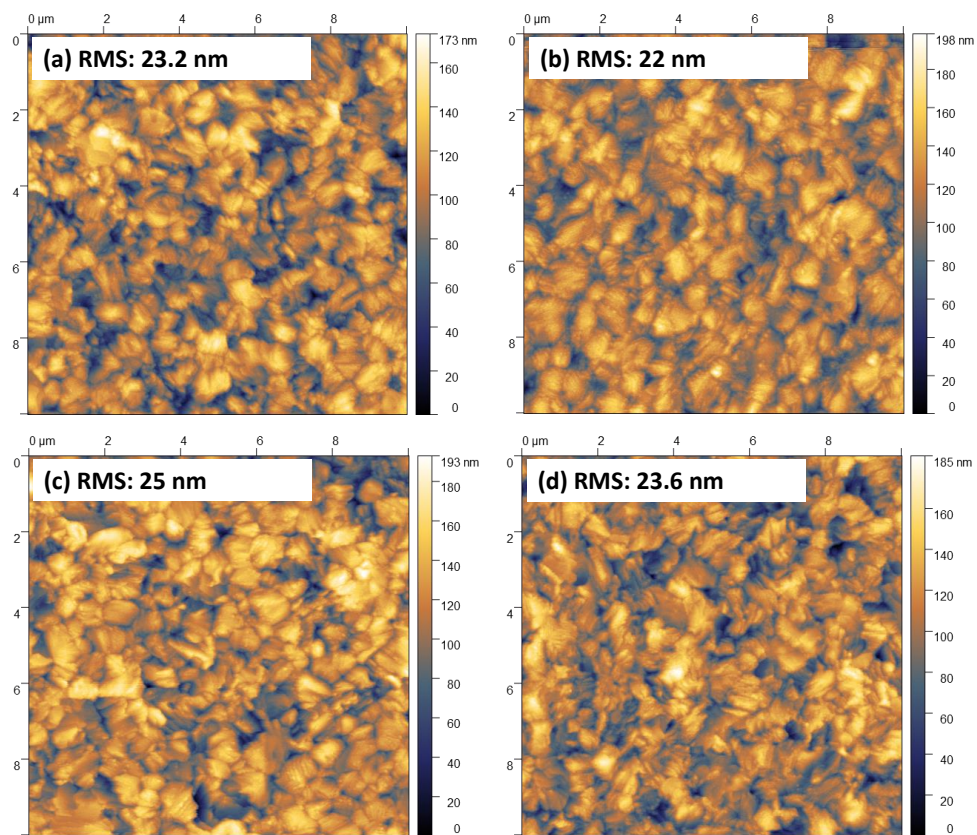


Fig. S21: Atomic force microscopy (AFM) analysis of double-cation  $\text{Cs}_{0.18}\text{FA}_{0.82}\text{PbI}_3$  perovskite films prepared (a) without any modification and with (b) surface passivation (c) grain boundary passivation, and (d) grain boundary & surface passivation processes. The surface roughness of each perovskite film is noted as the root-mean-square (RMS) value.

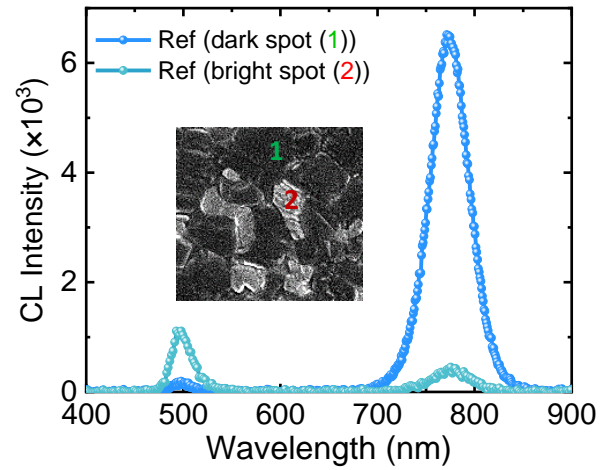


Fig. S22: Cathodoluminescence (CL) spectra of the reference perovskite film at two different spots.

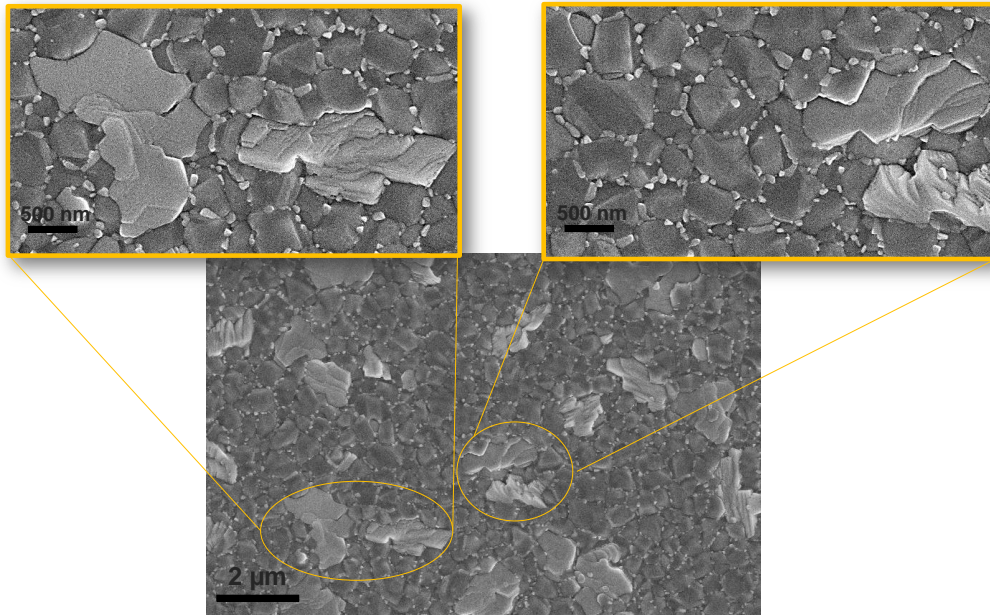


Fig S23: Top-view scanning electron microscopy (SEM) images of grain boundary passivated perovskite films. The insets show higher magnification images of the large bright grains related to  $\text{PbI}_2$ -rich crystallites.

### CHAPTER 3. TWO BIRDS WITH ONE STONE: DUAL GRAIN-BOUNDARY AND INTERFACE PASSIVATION ENABLES >22 % EFFICIENT INVERTED METHYLAMMONIUM-FREE PEROVSKITE SOLAR CELLS

---

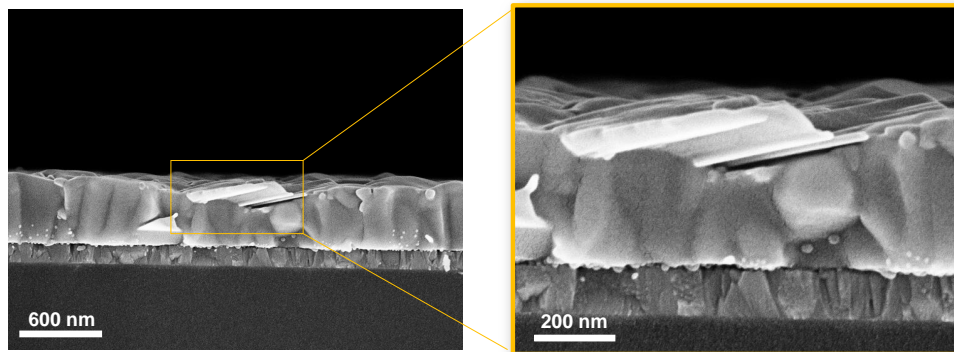


Fig. S24: Left: Cross-sectional scanning electron microscopy (SEM) images of grain boundary passivated perovskite films with the configuration of ITO/2PACz/perovskite. Right: The magnified image of a large bright grain - related to a PbI<sub>2</sub>-rich crystallite as identified by cathodoluminescence and top-view SEM (see Figs. S4 and S22-S23) - indicates that these are situated on top of 3D perovskite grains.

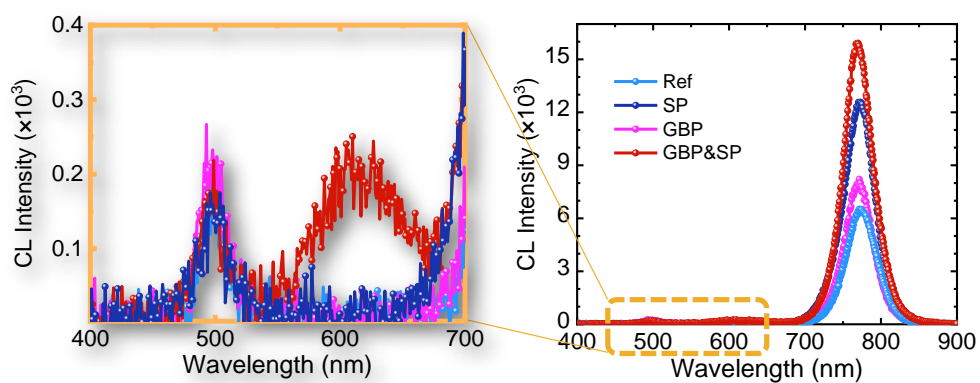


Fig. S25: Cathodoluminescence (CL) spectra of perovskite films prepared without any modification (Ref) and with surface passivation (SP), grain boundary passivation (GBP), and grain boundary & surface passivation (GBP&SP). The left panel is a magnified view of the same CL spectra in the visible range of 400 to 700 nm.

### CHAPTER 3. TWO BIRDS WITH ONE STONE: DUAL GRAIN-BOUNDARY AND INTERFACE PASSIVATION ENABLES >22 % EFFICIENT INVERTED METHYLAMMONIUM-FREE PEROVSKITE SOLAR CELLS

---

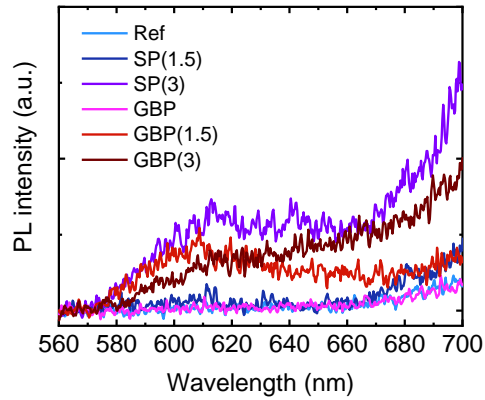


Fig. S26: Steady-state photoluminescence (PL) of the perovskite films prepared on ITO/2PACz substrates for the reference (Ref), surface passivation with different PEACl concentrations (SP(1.5), SP(3)), grain boundary passivation (GBP), and grain boundary passivated films treated with different PEACl concentrations (GBP&SP(1.5), GBP&SP(3)) in the visible range of 560-700 nm.

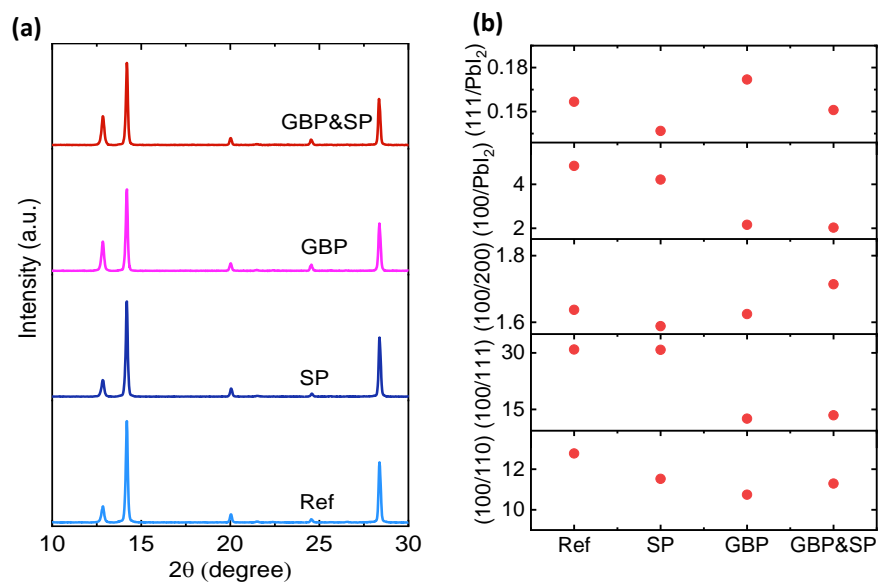


Fig. S27: (a) X-ray diffraction (XRD) pattern of perovskite films prepared without any modification (Ref) and with surface passivation (SP), grain boundary passivation (GBP), and grain boundary & surface passivation (GBP&SP). (b) Calculated intensity ratios of the various crystal planes.

CHAPTER 3. TWO BIRDS WITH ONE STONE: DUAL GRAIN-BOUNDARY AND INTERFACE PASSIVATION ENABLES >22 % EFFICIENT INVERTED METHYLAMMONIUM-FREE PEROVSKITE SOLAR CELLS

---

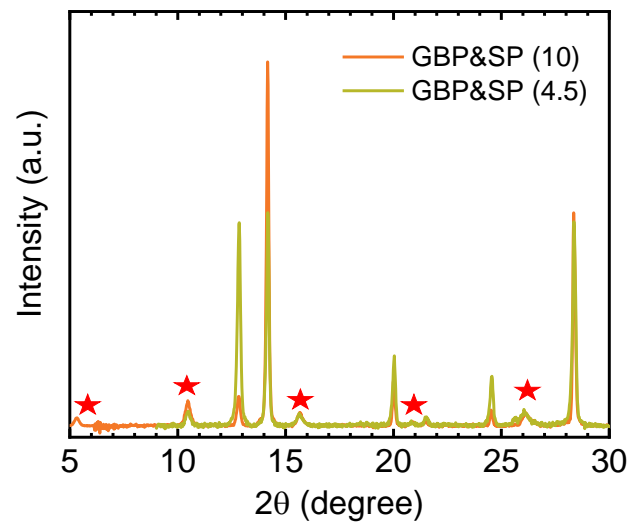


Fig. S28: XRD patterns of grain boundary & surface (GBP&SP) perovskite films treated with a high concentration of PEACl (4.5 mg/ml and 10 mg/ml). The red stars denote the diffraction peaks resulting from a pure ( $n = 1$ ) 2D Ruddlesden-Popper  $(\text{PEA})_2\text{Pb}(\text{I}_{1-y}\text{Cl}_y)_4$  phase with a superlattice spacing of  $\sim 1.7$  nm.

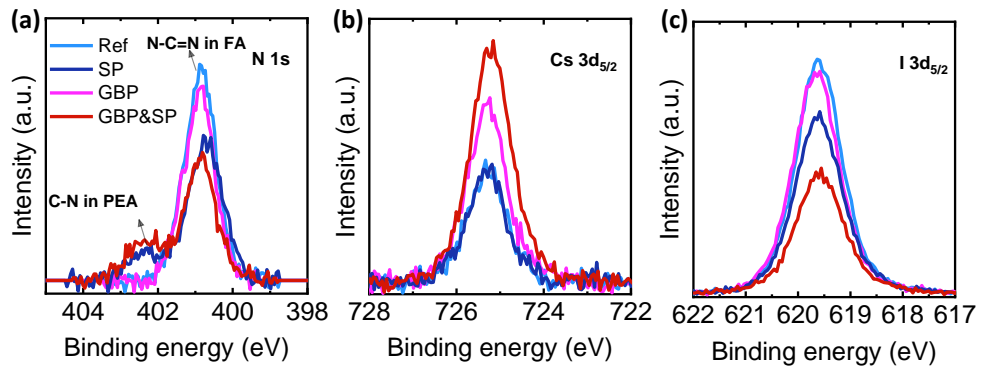


Fig. S29: X-ray photoelectron spectroscopy (XPS) spectra of (a) N 1s, (b) Cs 3d<sub>5/2</sub>, and (c) I 3d<sub>5/2</sub> core-levels for perovskite films prepared on ITO/2PACz substrates without any modification (Ref) and with surface passivation (SP), grain boundary passivation (GBP), and grain boundary & surface passivation (GBP&SP).

# CHAPTER 3. TWO BIRDS WITH ONE STONE: DUAL GRAIN-BOUNDARY AND INTERFACE PASSIVATION ENABLES >22 % EFFICIENT INVERTED METHYLAMMONIUM-FREE PEROVSKITE SOLAR CELLS

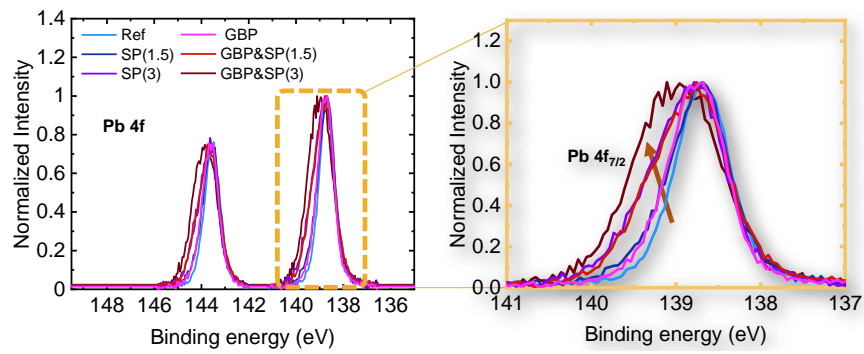


Fig. S30: Normalized X-ray photoelectron spectroscopy (XPS) spectra of the Pb 4f core levels (same data as in Fig. 5 a) including perovskite films with a PEACl concentration of 3 mg/ml (SP (3) and GBP&SP(3)) (left) and a higher magnification of the Pb 4f<sub>7/2</sub> peak.

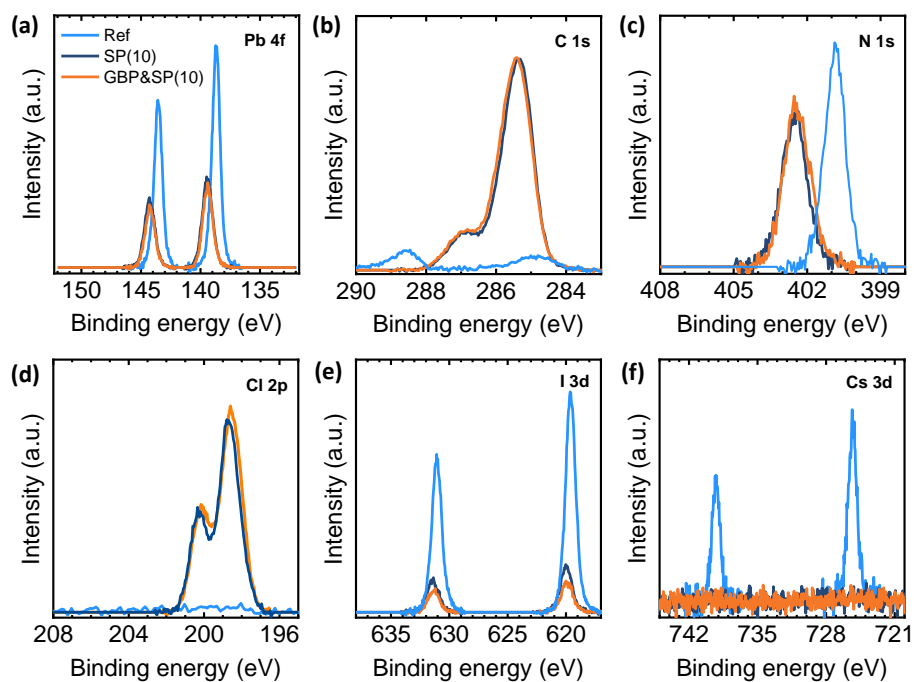


Fig. S31: X-ray photoelectron spectroscopy (XPS) spectra of the denoted core levels for reference (Ref) and grain boundary passivated perovskite films treated with a PEACl concentration of 10 mg/ml (SP (10) and GBP&SP(10)) and comparison to the data for the reference perovskite film.

CHAPTER 3. TWO BIRDS WITH ONE STONE: DUAL GRAIN-BOUNDARY AND INTERFACE PASSIVATION ENABLES >22 % EFFICIENT INVERTED METHYLAMMONIUM-FREE PEROVSKITE SOLAR CELLS

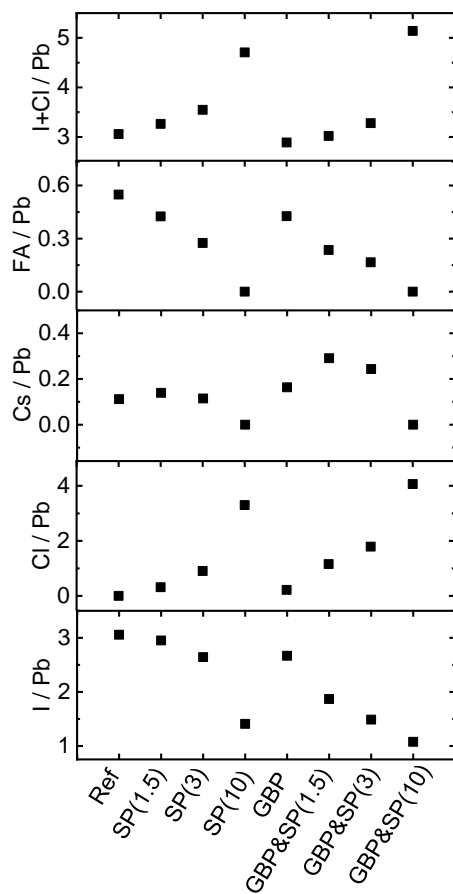


Fig. S32: The atomic ratio of I+Cl/Pb, Cl/Pb, Cs/Pb, FA/Pb, and I/Pb for the reference (Ref) and grain boundary (GBP) perovskite films treated with different concentration of PEACl (1.5, 3 and 10 mg/ml).

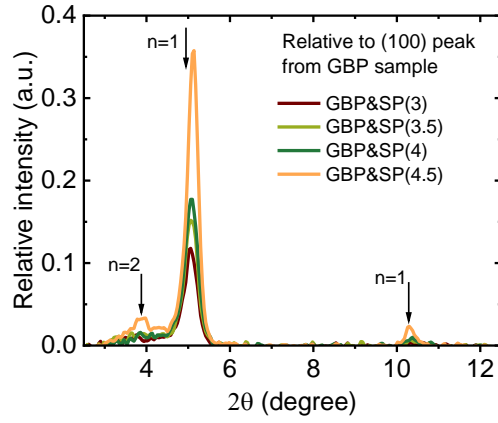


Fig. S33: Additional XRD measurements of grain boundary & surface passivated films (GBP&SP) employing various concentrations of PEACL for surface treatment (3, 3.5, 4 and 4.5 mg/ml). The data is plotted relative to the (100) peak of a GBP reference sample in order to study the trend when going from rather thin to thicker passivation layers. The peaks at  $\sim 5.1^\circ$  and  $\sim 10.2^\circ$  correlate to an  $n = 1$  2D RP phase with superlattice spacing of  $\sim 1.7$  nm and the peak at  $\sim 3.8^\circ$  correlates to  $n = 2$  with a superlattice spacing of  $\sim 2.34$  nm.

# CHAPTER 3. TWO BIRDS WITH ONE STONE: DUAL GRAIN-BOUNDARY AND INTERFACE PASSIVATION ENABLES >22 % EFFICIENT INVERTED METHYLAMMONIUM-FREE PEROVSKITE SOLAR CELLS

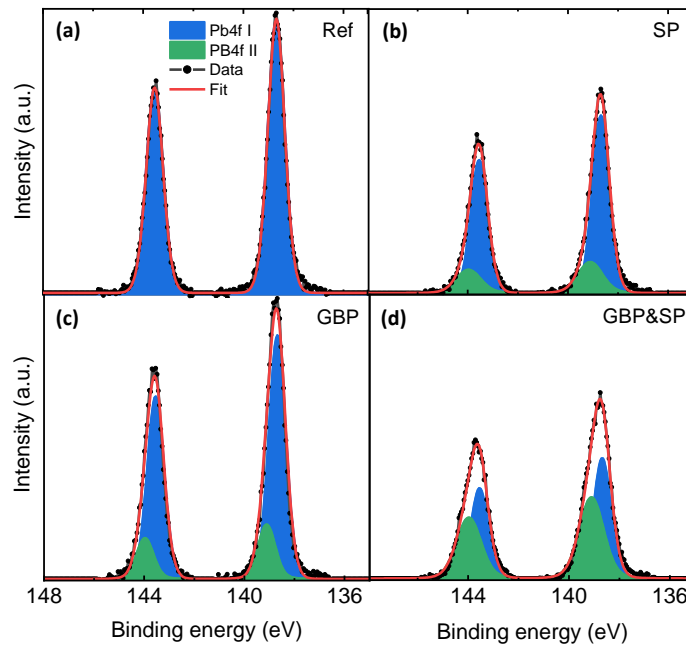


Fig. S34: (a) Fit to Pb4f core levels of the reference perovskite film, which yields peak positions of  $\sim 138.7$  eV and  $\sim 143.5$  eV with a FWHM of 0.8. For (b), (c) and (d), the peak position and FWHM for the 3D perovskite peak are fixed (blue area) and the second component is fixed to 139.1 eV (green area).

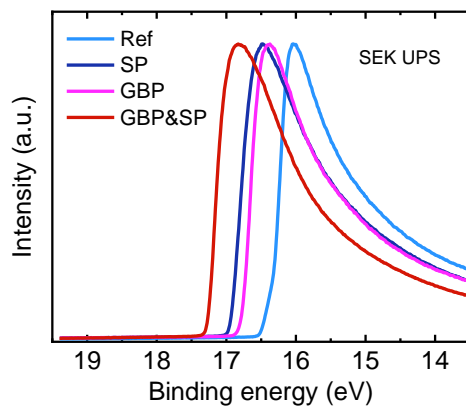


Fig. S35: Secondary electron cut-off spectra from ultraviolet photoelectron spectroscopy (UPS) were used to determine the work function of the perovskite films.

CHAPTER 3. TWO BIRDS WITH ONE STONE: DUAL GRAIN-BOUNDARY AND INTERFACE PASSIVATION ENABLES >22 % EFFICIENT INVERTED METHYLAMMONIUM-FREE PEROVSKITE SOLAR CELLS

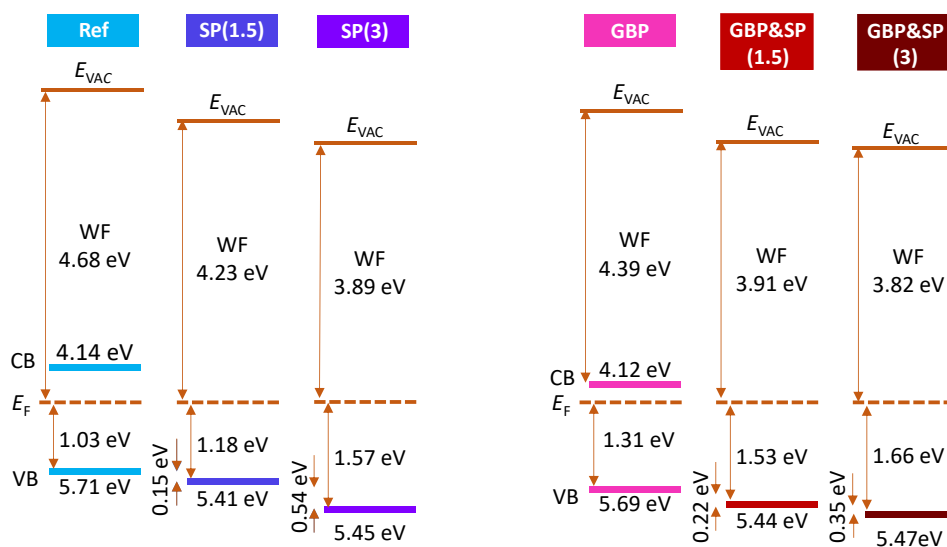


Fig. S36: Proposed energy band diagrams from ultraviolet photoelectron spectroscopy (UPS) measurements. Same data as in Fig. 5d, but including data for films with a higher PEACl concentration (SP(3) and GBP&SP(3)).

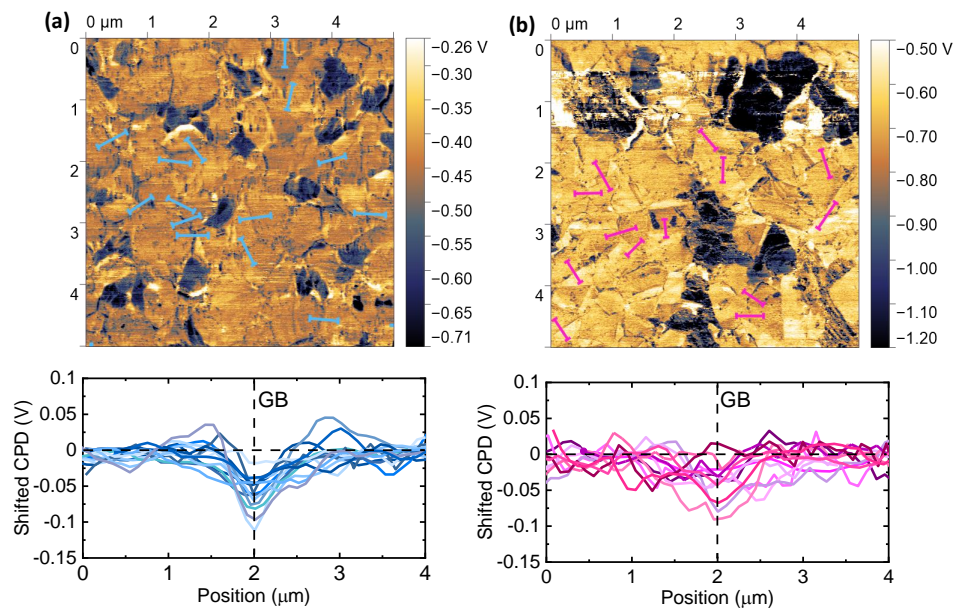


Fig. S37: Visualization of random grain boundary regions demonstrated by blue and pink lines in contact potential difference (CPD) map to determine the CPD offset and CPD profile lines between grain boundary and grain interior for (a) reference (Ref) and (b) grain boundary passivation (GBP) perovskite films.

CHAPTER 3. TWO BIRDS WITH ONE STONE: DUAL GRAIN-BOUNDARY AND INTERFACE PASSIVATION ENABLES >22 % EFFICIENT INVERTED METHYLAMMONIUM-FREE PEROVSKITE SOLAR CELLS

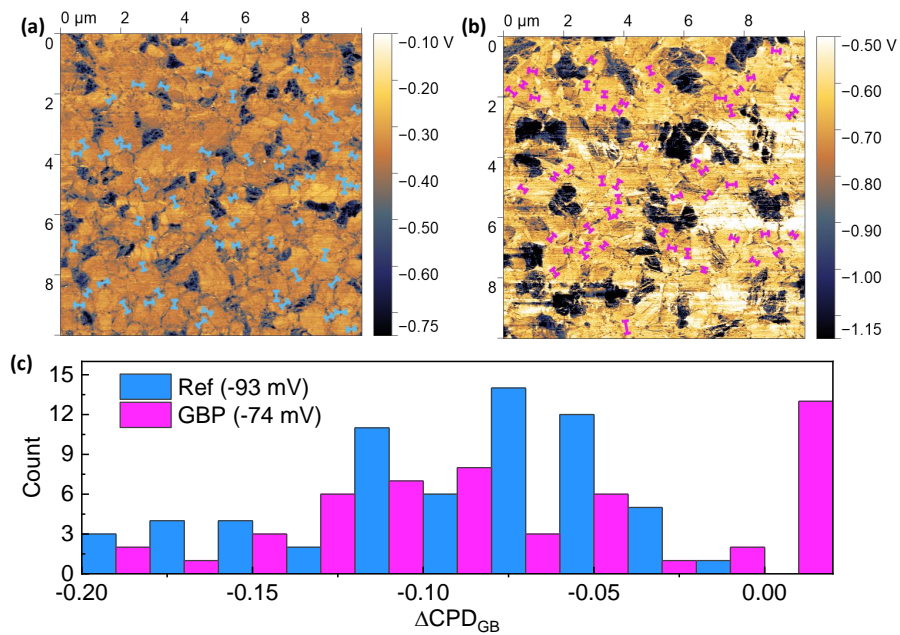


Fig. S38: (a) Visualization of ~60 different grain boundary regions to estimate the average contact potential difference (CPD) offset between grain boundary and grain interior for (a) reference (Ref) and (b) grain boundary passivated (GBP) perovskite films. (c) Respective histogram of the extracted  $\Delta\text{CPD}_{\text{GB}}$  (CPD<sub>grain boundary</sub> - CPD<sub>grain</sub>).

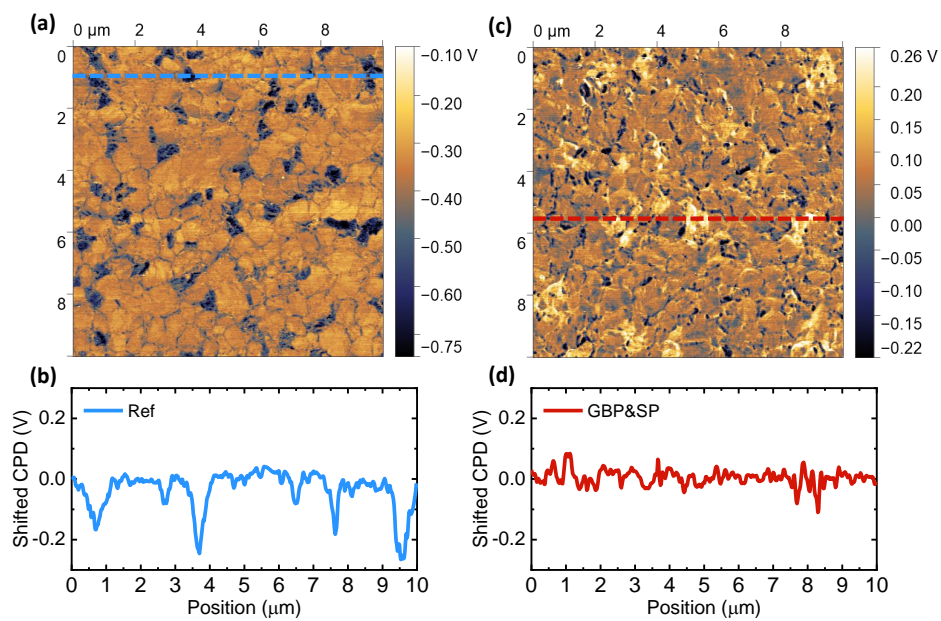


Fig. S39: Contact potential difference (CPD) images and CPD variation recorded in dark for (a), (b) reference (Ref) and (c), (d) grain boundary & surface passivation (GBP&SP) films. The line profiles were analyzed along the blue line and red line indicated in the CPD maps for Ref and GBP&SP films, respectively.

CHAPTER 3. TWO BIRDS WITH ONE STONE: DUAL GRAIN-BOUNDARY AND INTERFACE PASSIVATION ENABLES >22 % EFFICIENT INVERTED METHYLAMMONIUM-FREE PEROVSKITE SOLAR CELLS

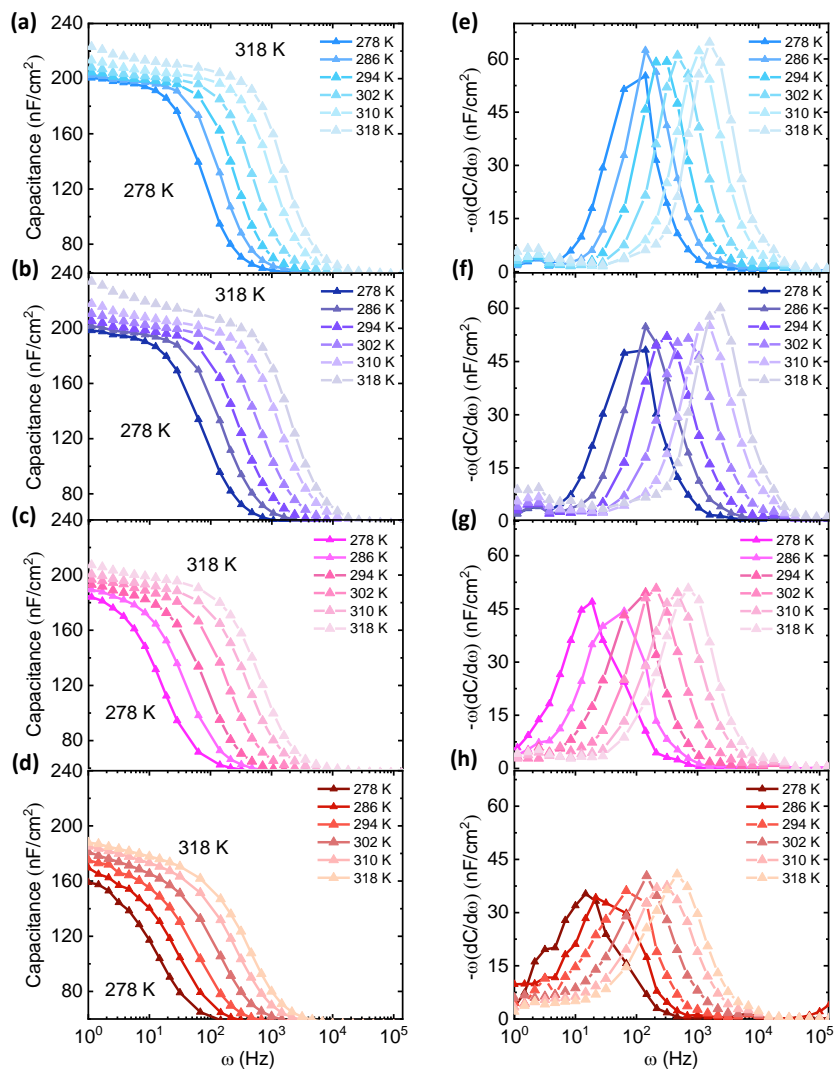


Fig. S40: (a, b, c, d) Capacitance ( $C$ ) versus angular frequency ( $\omega$ ) spectra and (e, f, g, h) corresponding logarithmic derivative of the reference (Ref), surface passivation (SP), grain boundary passivation (GBP), and grain boundary & surface passivation (GBP&SP) perovskite solar cells respectively, measured in a temperature range of 278 to 318 K.

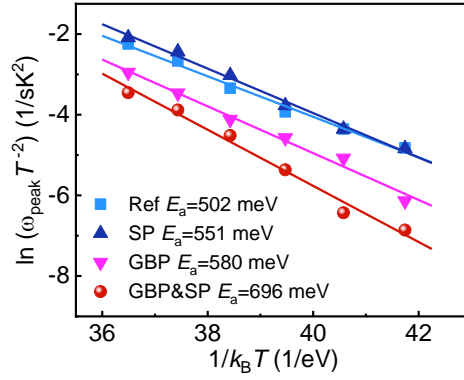


Fig. S41: Arrhenius plots of  $\ln(\omega_{\text{peak}} T^{-2})$  versus  $1/k_B T$  extracted from the derivative of admittance spectra to determine the activation energy ( $E_a$ ) for reference (Ref), surface passivation (SP), grain boundary passivation (GBP), and grain boundary & surface passivation (GBP&SP) perovskite solar cells.

### CHAPTER 3. TWO BIRDS WITH ONE STONE: DUAL GRAIN-BOUNDARY AND INTERFACE PASSIVATION ENABLES >22 % EFFICIENT INVERTED METHYLAMMONIUM-FREE PEROVSKITE SOLAR CELLS

---

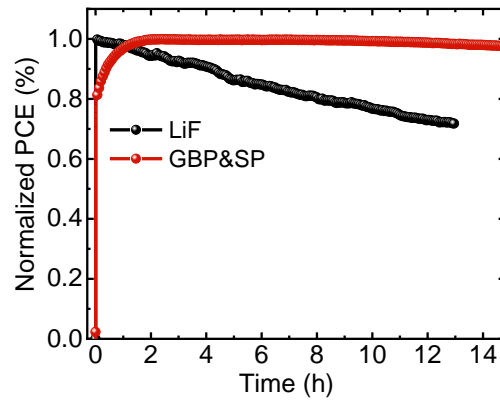


Fig. S42: Comparison of maximum power point (MPP) tracking of the grain boundary & surface passivation (GBP&SP) and LiF-based perovskite solar cell measured during continuous AM 1.5G illumination at room temperature in a nitrogen-filled glovebox.

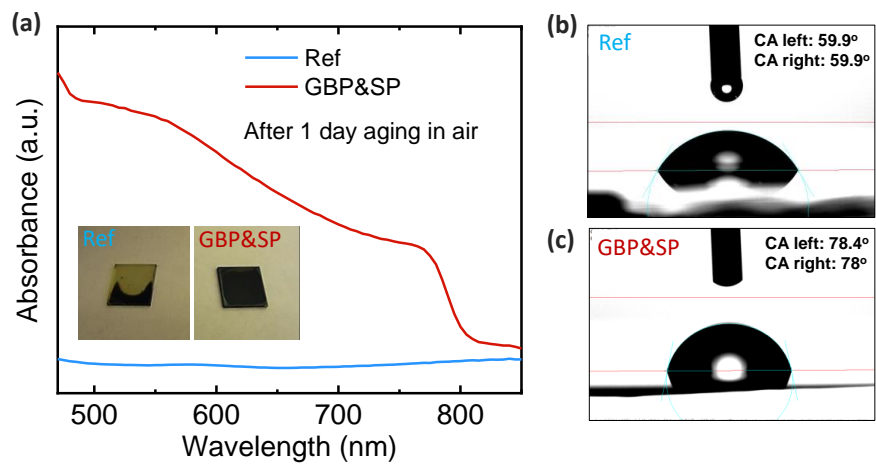


Fig. S43. (a) The ultraviolet-visible absorption spectra of grain boundary & surface (GBP&SP) passivation and reference (Ref) perovskite films after 1 day of their exposure to the 50% humidity. Contact angle measurements with a water droplet on top of the (b) Ref (c) GBP&SP perovskite films.

## CHAPTER 3. TWO BIRDS WITH ONE STONE: DUAL GRAIN-BOUNDARY AND INTERFACE PASSIVATION ENABLES >22 % EFFICIENT INVERTED METHYLAMMONIUM-FREE PEROVSKITE SOLAR CELLS

---

### **References:**

- 1 R. Schäfer and P. C. Schmidt, in *Methods in Physical Chemistry*, Wiley-VCH Verlag GmbH & Co. KGaA, 2012.
- 2 D. A. Shirley, *Phys. Rev. B*, 1972, **5**, 4709–4714.
- 3 A. Proctor and P. M. A. Sherwood, *Anal. Chem.*, 1982, **54**, 13–19.
- 4 J. H. Scofield, *J. Electron Spectros. Relat. Phenomena*, 1976, **8**, 129–137.
- 5 R. F. Reilman, A. Msezane and S. T. Manson, *J. Electron Spectros. Relat. Phenomena*, 1976, **8**, 389–394.
- 6 S. Tanuma, C. J. Powell and D. R. Penn, *Surf. Interface Anal.*, 1994, **21**, 165–176.
- 7 C. J. Powell and A. Jablonski, *Natl. Inst. Stand. Technol.*
- 8 R. Sydam, R. K. Kokal and M. Deepa, *ChemPhysChem*, 2015, **16**, 1042–1051.
- 9 D. Ziegler, N. Naujoks and A. Stemmer, *Rev. Sci. Instrum.*, 2008, **79**, 063704.
- 10 J. C. de Mello, H. F. Wittmann and R. H. Friend, *Adv. Mater.*, 1997, **9**, 230–232.
- 11 M. Stolterfoht, M. Grischek, P. Caprioglio, C. M. Wolff, E. Gutierrez-Partida, F. Peña-Camargo, D. Röthhardt, S. Zhang, M. Raoufi, J. Wolansky, M. Abdi-Jalebi, S. D. Stranks, S. Albrecht, T. Kirchartz and D. Neher, *Adv. Mater.*, 2020, **32**, 2000080.
- 12 L. Krückemeier, U. Rau, M. Stolterfoht and T. Kirchartz, *Adv. Energy Mater.*, 2020, **10**, 1902573.
- 13 O. Almora, M. García-Batlle and G. Garcia-Belmonte, *J. Phys. Chem. Lett.*, 2019, **10**, 3661–3669.
- 14 T. Walter, R. Herberholz, C. Müller and H. W. Schock, *J. Appl. Phys.*, 1996, **80**, 4411–4420.
- 15 J. A. Carr, M. Elshobaki and S. Chaudhary, *Appl. Phys. Lett.*, 2015, **107**, 203302.
- 16 S. Wang, P. Kaienburg, B. Klingebiel, D. Schillings and T. Kirchartz, *J. Phys. Chem. C*, 2018, **122**, 9795–9803.
- 17 M. A. Lampert and R. B. Schilling, 1970, pp. 1–96.
- 18 H. Min, M. Kim, S.-U. Lee, H. Kim, G. Kim, K. Choi, J. H. Lee and S. Il Seok, *Science*, 2019, **366**, 749–753.
- 19 D. Prochowicz, R. Runjhun, M. M. Tavakoli, P. Yadav, M. Saski, A. Q. Alanazi, D. J. Kubicki, Z. Kaszukur, S. M. Zakeeruddin, J. Lewiński and M. Grätzel, *Chem. Mater.*, 2019, **31**, 1620–1627.
- 20 Z. Liu, L. Krückemeier, B. Krogmeier, B. Klingebiel, J. A. Márquez, S. Levchenko, S. Öz, S. Mathur, U. Rau, T. Unold and T. Kirchartz, *ACS Energy Lett.*, 2019, **4**, 110–117.





---

## 4 Nanoscale Surface Photovoltage Spectroscopy

Reproduced via CC BY-NC 4.0 from Ref. 'Yalcinkaya, Y.; Rohrbeck, P. N.; Schütz, E. R.; Fakharuddin, A.; Schmidt-Mende, L.; Weber, S. A. L. Nanoscale Surface Photovoltage Spectroscopy. *Adv. Opt. Mater.* **2024**, 12 (8), 1–12. DOI: 10.1002/adom.202301318.<sup>98</sup> with permission from John Wiley and Sons.

In this paper, we introduce tr-KPFM-based methods to investigate defect and free charge carrier dynamics within halide perovskites materials. Therefore, we show a new investigation methods called nanoscale surface photovoltage spectroscopy (nano-SPV) and nanoscale ideality factor mapping (nano-IFM) to map and investigate charge carrier recombination, ion migration, and defects in halide perovskite samples with different morphologies and passivation and their respective dynamics.

Pascal Niko Rohrbeck and Mehmet Yenel Yalçinkaya are equal shared first authors of this paper. Pascal Niko Rohrbeck measured the solvent-annealed pristine sample (Figure 3) and the solvent-annealed and passivated sample (Figure 4) via the developed nano-SPV method to make defect areas visible in the AFM and investigate the role of passivation in this.



## RESEARCH ARTICLE

## Nanoscale Surface Photovoltage Spectroscopy

Yenal Yalcinkaya, Pascal N. Rohrbeck, Emilia R. Schütz, Azhar Fakharuddin, Lukas Schmidt-Mende, and Stefan A.L. Weber\*

Understanding electron and ion dynamics is an important task for improving modern energy materials, such as photovoltaic perovskites. These materials usually have delicate nano- and microstructures that influence the device parameters. To resolve detailed structure–function relationships on the relevant micro- and nanometer length scales, the current macroscopic and microscopic measurement techniques are often not sufficient. Here, nanoscale surface photovoltage spectroscopy (nano-SPV) and nanoscale ideality factor mapping (nano-IFM) via time-resolved Kelvin probe force microscopy are introduced. These methods can map nanoscale variations in charge carrier recombination, ion migration, and defects. To show the potential of nano-SPV and nano-IFM, these methods are applied to perovskite samples with different morphologies. The results clearly show an improved uniformity of the SPV and SPV decay distribution within the perovskite films upon passivation and increasing the grain size. Nevertheless, nano-SPV and nano-IFM can still detect local variations in the defect density on these optimized samples, guiding the way for further optimization.

## 1. Introduction

Lead halide perovskites are promising materials for optoelectronic applications due to their direct adjustable band gap,<sup>[1–3]</sup> high defect tolerance,<sup>[4]</sup> and long charge carrier lifetimes.<sup>[5–7]</sup> Unlike conventional semiconductors, lead halide perovskites do not possess a high density of deep trap states.<sup>[8]</sup> The trap states due to crystal defects within the halide perovskites appear

within or close to the energy bands. This defect tolerance allows high-quality perovskite films to be fabricated from simple solution processes. Nonetheless, energy losses still occur at areas with high defect density, such as grain boundaries (GB) of the halide perovskites or interfaces within perovskite solar cells (PSCs), increasing non-radiative recombination losses during device operations.<sup>[9]</sup>

Defects related to non-radiative recombination in perovskites mainly occur as 1D point defects such as interstitials, antisites, or vacancies; 2D defects such as GBs, interfaces, and surfaces; and 3D defects such as clusters of iodine or lead or defects at the contacts. Interfacial recombination may originate from energy alignment mismatch between layers, surface defects, and charge carrier back transfer.<sup>[10–14]</sup> Improving the perovskite film quality by means of passivation is a common strategy to improve device efficiency.<sup>[15,16]</sup> Common surface

passivation methods use chemical agents that partially fill the vacancies on the perovskite film surface. Here, the active group (ammonium, for example) fills the A<sup>+</sup> cation vacancies, whereas other parts of the passivation agent can be used, for example, for increasing the hydrophobicity of the perovskite surface. A good example is phenylethylammonium ion (PEA<sup>+</sup>), which contains an ammonium and a hydrophobic phenyl group.<sup>[15]</sup>

The main goal of defect passivation is to increase the efficiency of PSCs. The most common and straightforward way to characterize the perovskite film quality is therefore to measure the efficiency of PSC devices. To understand the mechanisms behind efficiency losses, however, it is helpful to characterize the perovskite layer itself. Commonly used methods aim at monitoring the charge carrier dynamics such as photoluminescence (PL)<sup>[17]</sup>; transient absorption<sup>[18]</sup>; Terahertz, microwave, or electrical impedance spectroscopy<sup>[19,20]</sup>; surface photovoltage (SPV)<sup>[21]</sup>; and surface photocurrent<sup>[22]</sup> measurements. These methods are usually conducted on macroscopic length scales and therefore yield measurements that are averaged over many different grains, GBs, and other interfaces. Local measurements such as PL microscopy<sup>[23]</sup> and fluorescence lifetime microscopy (FLIM)<sup>[24]</sup> can record and map the charge carrier dynamics. However, the lateral resolution of these optical methods is diffraction-limited and cannot fully resolve effects at the GBs. Alternatively, qualitative SPV mapping can be performed via scanning electron microscopy (SEM). Here, the electric fields generated by the local photovoltage modulate the secondary electron emission and

Y. Yalcinkaya, P. N. Rohrbeck, S. A. Weber  
Max Planck Institute for Polymer Research  
Ackermannweg 10, 55128 Mainz, Germany  
E-mail: webers@mpip-mainz.mpg.de

Y. Yalcinkaya, S. A. Weber  
Institute of Physics  
Johannes Gutenberg University Mainz  
Duesbergweg 10-14, 55128 Mainz, Germany  
E. R. Schütz, A. Fakharuddin, L. Schmidt-Mende  
Department of Physics  
University of Konstanz  
Universitätsstr. 10, 78464 Konstanz, Germany

The ORCID identification number(s) for the author(s) of this article can be found under <https://doi.org/10.1002/adom.202301318>

© 2023 The Authors. Advanced Optical Materials published by Wiley-VCH GmbH. This is an open access article under the terms of the Creative Commons Attribution-NonCommercial License, which permits use, distribution and reproduction in any medium, provided the original work is properly cited and is not used for commercial purposes.

DOI: 10.1002/adom.202301318

thereby the image contrast. Irde et al.<sup>[25]</sup> have demonstrated the SEM-based mapping of SPV dynamics on methylammonium lead iodide thin films within seconds to hours.<sup>[25]</sup> Pietralunga et al.<sup>[26]</sup> used SEM-based SPV spectroscopy to study charge transport dynamics, internal electric field configurations, and interface energetics of perovskite films under illumination.<sup>[26]</sup> Generally, the irradiation with high-energy electrons under high vacuum conditions can damage delicate perovskite samples,<sup>[27]</sup> even though electron beam damage can be reduced via the use of low-energy electron beams<sup>[28]</sup> or by reducing the electron dose,<sup>[29]</sup> limiting the spatial resolution and the signal-to-noise ratio.<sup>[25,30]</sup>

Here, atomic force microscopy (AFM) is a more gentle and versatile alternative. Next to the sample topography, AFM can detect many other surface properties and sub-granular structures.<sup>[31–33]</sup> Using conductive AFM (C-AFM), Shao et al.<sup>[34]</sup> measured the current values on the perovskite grains and the GBs in between. These measurements demonstrated that ion migration is faster at GBs compared to grain interiors. Conings et al.<sup>[35]</sup> used C-AFM to track the degradation of methylammonium lead iodide films after annealing. Recently, we showed via C-AFM that an increased grain size as a result of methylamine treatment resulted in a higher conductivity and a lower charge accumulation at the GBs, indicating more efficient charge dissociation and transport within the grains. Another important AFM method is Kelvin probe force microscopy (KPFM). KPFM maps the electrostatic surface potential and has been used to reveal interfacial charges within perovskite devices<sup>[36–38]</sup> and band bending behavior at the GBs.<sup>[15,39]</sup> KPFM is particularly powerful in combination with sample excitation, for example, using voltage or light.<sup>[38,40]</sup> Since the contact potential difference (CPD) is depending on the electrostatic landscape on the surface, sample excitation by means of voltage or light pulses adds a modulation to the measured CPD value. Thus, KPFM can track charge carrier dynamics with high spatial resolution. Collins et al. carried out dynamic KPFM measurements by using general-mode KPFM (G-Mode KPFM)<sup>[41,42]</sup> to do fast KPFM measurements in the time range of tens of microseconds.<sup>[41]</sup> Other methods such as pump-probe KPFM (pp-KPFM)<sup>[43–46]</sup> can even locally resolve processes down to 1 ps.<sup>[43]</sup> Nevertheless, these methods require short excitation pulses at high repetition rates, limiting the application to fast and ultrafast processes (<μms).

In this study, we demonstrate KPFM-based nanoscale surface photovoltage spectroscopy (nano-SPV) and nanoscale ideality factor mapping (nano-IFM) as a tool to map the nanoscale distribution of defects. Using these methods, we investigate triple cation Cs<sub>0.05</sub>FA<sub>0.8</sub>MA<sub>0.15</sub>PbI<sub>3</sub> perovskite films with different morphologies and surface passivation. We use nano-SPV to visualize the charge carrier dynamics at grains and GBs on perovskite half-cells with an architecture of (ITO/TiO<sub>2</sub>-SnO<sub>2</sub>/perovskite) with small, large, and PEA-passivated perovskite grains. Our nano-SPV measurements offer two types of measurement: i) tracking the SPV dynamics during and after a light pulse to track the extraction and recombination time of photo-generated charge carriers (nano-SPV) and ii) tracking the SPV as a function of light illumination to obtain the local ideality factor,  $n_{id}$  (nano-IFM). The results show suppressed ion migration when the number of GBs is lower due to large grains. Furthermore, half-cells showed more uniform and lower defect densities when the perovskite films were PEA-passivated or had larger grains.

## 2. Theory

Here, we introduce some common macroscopic SPV-based measurement methods and how we implement them in nano-SPV operation mode using KPFM.

### 2.1. Surface Photovoltage and Surface Photovoltage Decay

Upon illumination of a photovoltaic sample, the electrostatic potential on the surface will change. This SPV is commonly measured by means of a macroscopic Kelvin Probe. Here, a millimeter-sized metal plate mechanically vibrates above the sample. In the presence of a voltage difference between the plate and the surface, the periodic variations in the plate distance will lead to a capacitive current. By compensating the voltage difference via an external voltage, the capacitive current can be minimized. Already without external voltage, there is an intrinsic voltage difference called the contact potential difference (CPD). The CPD corresponds to the difference in work functions or the position of the Fermi Level,  $E_F$ , of the probe and the sample material:

$$V_{CPD} = \frac{E_F^{np} - E_F^{sample}}{e} \quad (1)$$

where  $e$  is the elemental charge. Any illumination-induced change in the measured CPD value corresponds to the SPV:

$$V_{SPV} = V_{CPD, illum.} - V_{CPD, dark} \quad (2)$$

The SPV signal can have different contributions: i) band flattening at the semiconductor surface and ii) charge separation at buried interfaces. At the surface, defect states lead to Fermi-level pinning and band bending. The increased charge carrier concentration during illumination screens the trapped surface charges, leading to band flattening<sup>[47]</sup> (Figure S1, Supporting Information). The resulting change in the surface potential can be observed as a SPV signal, where the polarity depends on the majority charge carriers as in n- or p-type doping (Figure S1, Supporting Information). Typically, n-type semiconductors yield positive SPV while the SPV values are negative for p-type semiconductors. Therefore, the doping status of the sample can be estimated by the sign of the SPV value.<sup>[48]</sup>

On photovoltaic device stacks, a SPV signal can be caused by band bending at buried interfaces, for example, between the absorber and a charge-selective contact (Figure S2, Supporting Information). Here, photo-generated charge carriers redistribute across the heterojunction depending on the characteristics of the charge-selective layer. If the layer is an electron transport layer (ETL), the electrons will be transported while the holes remain within the semiconductor film and the resulting SPV will be positive due to the imbalance of free charges in the film volume.<sup>[26]</sup> On the contrary, if the charge selective layer is a hole transport layer (HTL), the electrons will remain in the absorber while the holes are transferred, leading to a negative SPV because of an excess of electrons.<sup>[26]</sup>

Since the SPV signal depends on the Fermi level and the Fermi level change under illumination in the sample, it is influenced by band bending,<sup>[49]</sup> and stoichiometry in the sample.<sup>[50]</sup>

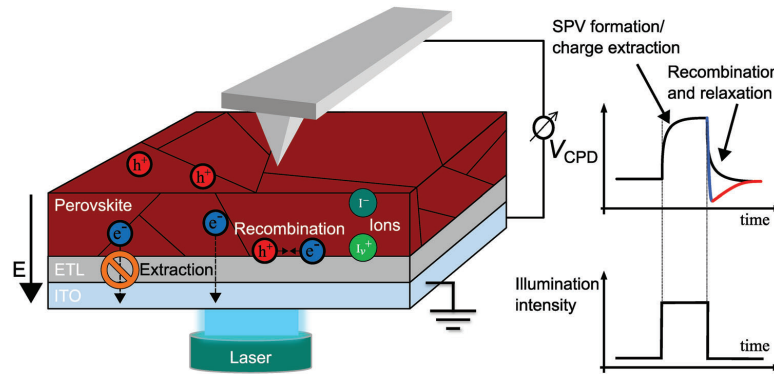


**Figure 1.** Schematic overview of the tr-KPFM setup. The laser intensity is either modulated in a pulse shape or a slow intensity increase with the tip engaged to the surface while the local CPD signal is recorded. The CPD traces contain information about local charge carrier extraction processes, which result in the formation of an electric field  $E$  (arrow on the left). After the light pulse, the CPD trace reveals information about recombination processes and the presence of defect states such as GBs and interfaces, which hinder the extraction of charges (blocking symbol).

To disentangle the different contributions to the SPV signal, we can track the SPV decay after an illumination pulse (SPV spectroscopy). The SPV transients contain information about recombination rates,<sup>[51]</sup> trap density,<sup>[52]</sup> and ion migration<sup>[40]</sup> effects. **Figure 1** shows the illustration of a SPV decay measurement result demonstrating the characteristic voltage decay following an illumination pulse. The decrease pattern gives information about the contributing charge carriers. The fast-decaying component (blue curve in **Figure 1**) is typically the electronic one whereas the slow-decaying one (red curve in **Figure 1**) is usually the ionic component.<sup>[40]</sup> The electronic decay is correlated to the electron–hole recombination mechanisms taking place at the perovskite bulk or the interface between the perovskite and the ETL after the illumination pulse. The more trap-assisted recombination occurs, the faster the SPV decay takes place. The ionic decay is correlated to the re-distribution of the ions from the surface which can be migrating from the crystal lattice or be adsorbed from the environment. Also, the electric field generated by the migration of electrons and the accumulation of holes at the surface influences the movement of ions within the film.

We further interpret the dynamics during the SPV formation at the beginning of a light pulse as the interfacial extraction of charge carriers. Other experimental studies using PL<sup>[53]</sup> or photoconductivity measurements came to a similar conclusion.<sup>[54]</sup> The results by Grill et al. suggest that only the ETL or HTL interface is the charge transport-limiting factor in the device and not the perovskite itself.<sup>[26,54]</sup> This means it is possible to see interfacial properties of the device by tracking the change of the SPV.<sup>[26]</sup>

## 2.2. Ideality Factor

The current–voltage ( $I$ – $V$ ) characteristics of semiconductor diodes such as solar cells can be described by the Shockley diode equation:

$$I = I_L - I_S \left( e^{\frac{V}{n_{id} k_B T / q}} - 1 \right) \quad (3)$$

where  $I$  is the overall current of the solar cell,  $I_L$  is the light-generated current,  $I_S$  is the reverse bias saturation current,  $V$  is the voltage across the solar cell,  $k_B$  is the Boltzmann constant,  $T$  is the temperature, and  $q$  is the elementary charge. Here, the ideality factor,  $n_{id}$ , is a measure of how close a photovoltaic device behaves to an ideal diode ( $n_{id} = 1$ ). Deviations from the ideal diode behavior can be caused by charge carrier recombination mechanisms. Here,  $n_{id}$  can be estimated as the relation between the quasi-Fermi-level splitting,  $\Delta E_F$ , and the recombination rate,  $R$ <sup>[55]</sup>:

$$n_{id,C} = \frac{1}{kT} \frac{d\Delta E_F}{d\ln(R)} \quad (4)$$

where  $n_{id,C}$  is the conceptual ideality factor and  $kT$  is the thermal energy. Typically, a higher  $n_{id}$  suggests that the traps within the semiconductor contribute to the recombination process more.<sup>[56]</sup> Practically, it is hard to obtain values for the recombination rate and local quasi-Fermi level splitting values independently to obtain  $n_{id,C}$ . To work around this obstacle, an approximate value for  $n_{id}$  can be estimated from the current and voltage of the device. Here, the dark current,  $J_d$ , replaces the recombination rate, whereas the external voltage,  $V_e$ , replaces the local quasi-Fermi level splitting to obtain dark ideality factor,  $n_{id,d}$ , in Equation 5:

$$n_{id,d} = \frac{q}{kT} \frac{dV_e}{d\ln(J_d)} \quad (5)$$

This equation uses easily measurable quantities to obtain  $n_{id}$ . Nevertheless, this approach has the disadvantage that shunt or series resistances contribute to the ideality factor, as well as the recombination rates. Therefore, the  $n_{id,d}$  can give misleading results.

At open circuit conditions under illumination, charge generation and recombination rates are equal, as the net charge extraction is zero. Here, the steady-state open-circuit voltage ( $V_{oc}$ ) can be seen as an approximation of the quasi-Fermi level splitting.

By measuring  $V_{oc}$  as a function of light intensity,  $\phi$ , we can vary the recombination/generation rate within the device. Modifying Equation 6 yields

$$n_{id,l} = \frac{q}{kT} \frac{dV_{oc}}{dn(\phi)} \quad (6)$$

which we refer to as the light ideality factor,  $n_{id,l}$ . This value gives information about the recombination mechanisms with a minimum contribution from series or shunt resistances. Thus, a comparison of the  $n_{id,l}$  values between samples allows for determining the degree of trap-assisted recombination.<sup>[57]</sup> Nevertheless, there is an ongoing debate about the interpretation of  $n_{id}$  in PSC devices. Recently, Caprioglio et al.<sup>[58]</sup> reported on optical  $n_{id}$  measurements on half and full perovskite solar cells with different perovskite/transport layer interfaces and compared the  $n_{id}$  values. Their work suggests that the interfacial recombination dominates in  $n_{id}$  over the bulk recombination contribution.

### 2.3. Static and Time-Resolved Kelvin Probe Force Microscopy

The methods discussed so far rely on macroscopic measurements, for example, using a millimeter-sized Kelvin probe or an optical excitation spot.<sup>[59]</sup> KPFM is an AFM-based adaptation of the Kelvin probe measurement principle.<sup>[60–63]</sup> Instead of a capacitive current, KPFM detects the electrostatic force caused by the tip-sample potential to quantify the CPD. KPFM-based CPD maps can give information about facets,<sup>[64]</sup> band bending due to defects,<sup>[65]</sup> and energy level alignment in solar cells.<sup>[38]</sup>

To both map and record the nanoscale CPD and SPV dynamics with KPFM, the conventional scanning mode would be too slow. We recently introduced a point-wise time-resolved KPFM (tr-KPFM) data acquisition method where we record the sample response to a light or voltage pulse subsequently on every pixel of an image (Figure 1).<sup>[38,66]</sup> Here, we collect the CPD dynamics upon light or bias excitation subsequently at individual pixels within a designated area of the sample. Once the whole map is completed, we can either extract snapshots of the CPD distribution at defined positions in time or extract traces of CPD dynamics at defined positions in space (see also Experimental Section for more details). This method has the advantage that it is not limited in terms of the duration of the CPD traces. In particular, on PSC samples, where the full ionic relaxation can take several hundreds of milliseconds,<sup>[38]</sup> it is important to wait long enough to allow the sample to relax back to an equilibrium state. Other dynamic KPFM methods<sup>[41–46,67]</sup> require an excitation at high repetition rates, which might leave the sample effectively in an excited state. Thus, using only standard KPFM equipment (lock-in amplifier and feedback system), tr-KPFM can map the CPD and SPV distribution in the time scale of hundreds of microseconds to seconds. We call this operation mode nano-SPV.

Although flexible in terms of longer timescales, there are physical restrictions in terms of the shortest timescales that can be detected with tr-KPFM and nano-SPV. In the heterodyne KPFM detection mode used in this study,<sup>[68,69]</sup> signals are detected by means of an amplitude change on one of the cantilever's reso-

nances. Therefore, the smallest detectable time scale  $\tau_{min}$  is determined by the damping or  $Q$ -factor on this resonance:

$$\tau_{min,n} = \frac{Q_n}{f_n \cdot \pi} \quad (7)$$

where  $Q_n$  and  $f_n$  are the  $Q$ -factor and frequency of the  $n$ -th resonance of the AFM cantilever, respectively (see Experimental Section and Section S2, Supporting Information, for details). For a typical cantilever used in this study with second eigenmode frequency  $f_2 = 977$  kHz and  $Q_2 = 461$ , the smallest timescale is, therefore,  $\tau_{lim} = 150$   $\mu$ s. This limit could be further pushed by using cantilevers with higher resonance frequency, or by using frequency modulation detection.

## 3. Results and Discussion

To investigate the correlation between sample structure, surface treatment, and defect distribution in perovskite thin films, we prepared triple cation perovskite films with 0.95:1.05  $A^+/B^{2+}$  cation ratio with different structures (see Experimental Section for details). The topography images obtained via AFM are shown in Figure S3 in Section S4, Supporting Information. These include: i) a reference sample with small ( $\langle d \rangle_{Ref} = 200 \pm 60$  nm) grains (Ref), ii) a dimethyl sulfoxide (DMSO) vapor solvent annealed ( $SA_{Pristine}$ ) ( $\langle d \rangle_{SA_{Pristine}} = 590 \pm 160$  nm), iii) solvent-annealed triple cation sample with PEA-I surface passivation ( $SA_{Pass}$ ) ( $\langle d \rangle_{SA_{Pass}} = 670 \pm 210$  nm), and iv) a methylamine gas-treated triple cation sample with large ( $\langle d \rangle_{MA80} > 100$   $\mu$ m) grains (MA80). By comparing the reference perovskite film to the solvent vapor-annealed and/or passivated perovskite films, we aim to identify surface structures with locally higher or lower defect concentrations.

### 3.1. Reference Sample

The topography on the reference sample (Figure 2a) shows a structure of grains with a size of  $\langle d \rangle_{Ref} = 200 \pm 60$  nm. The correlated equilibrium CPD map before the voltage pulse (Figure 2b) mostly shows the contrast between the grains and the GBs due to band bending at the GBs,<sup>[15]</sup> where CPD increase and decrease correspond to downward and upward band bending, respectively. The CPD varies at the GBs within a range of 2 to 30 mV (Figure S4, Supporting Information). Furthermore, most GBs show higher CPD values compared to the grain interiors with minor exceptions (Figure S4e, Supporting Information). Since the band bending direction is determined by the type of defects, we argue that the minority GBs that show smaller CPD compared to the grains indicate different type of defects compared to the rest of the GBs within the film. Apart from that, some grains exhibited around 240 mV lower CPD value than the rest of the image (average value of  $760 \pm 90$  mV). By subtracting the CPD values before illumination from the CPD values during illumination, we obtained a map of the SPV distribution (Figure 2c). The illumination pulse ( $0$  ms  $< t < 201.6$  ms) resulted in an average photopotential of  $280 \pm 90$  mV. Interestingly, grains with initially lower CPD exhibited about 190 mV higher SPV compared to the rest of the sample. The heterogeneous distribution of the SPV

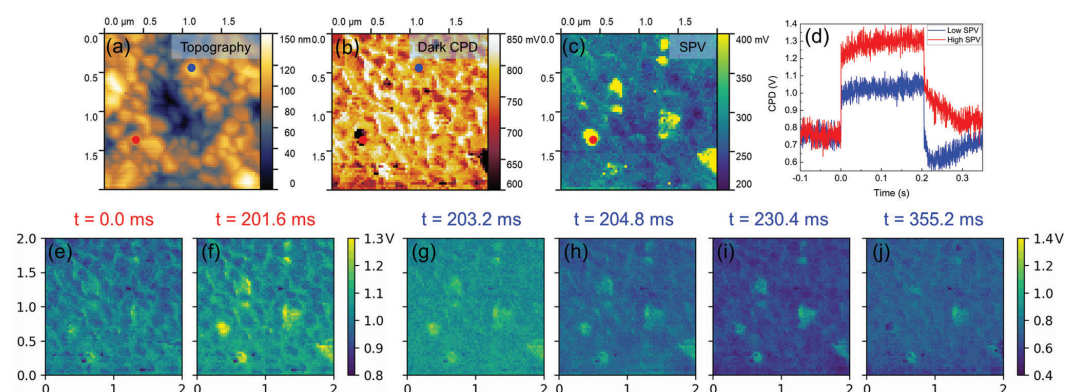


**Figure 2.** a) Topography, b) CPD in dark, c) SPV, and d) SPV plots over time from marked areas of reference perovskite sample. Panels (e)–(j) show the CPD maps at different time frames. The maps have 150x150 pixels.

suggests either non-uniform defect distribution or non-uniform chemical stoichiometry within the reference perovskite film. The former possibility would be causing changes in the local Fermi levels, whereas the latter would change the Fermi level shift during illumination.<sup>[50]</sup>

When comparing the dynamics at high and low SPV areas (Figure 2d; red and blue markers in Figure 2c and Figure S5b, Supporting Information), the SPV decay at the high SPV grain shows a slower decay compared to SPV decay at the low SPV grain (Figure 2d). Furthermore, the SPV decay at the blue marker shows a rapid decrease to negative SPV values before returning to the equilibrium dark CPD value. This undershoot could be caused by ion migration as illustrated in Figure 1.<sup>[40]</sup> During illumination, the electric field caused by the SPV polarizes mobile ions within the perovskite layer. After the illumination, the electronic polarization rapidly decays, leaving behind the ionic field that generates a negative surface voltage. The slower SPV decays within the high SPV grain (red and orange markers) suggest that the defect density is lower at the high SPV areas of the reference sample. Furthermore, the absence of an SPV undershoot during decay also suggests that the ion migration is suppressed at the high SPV areas.

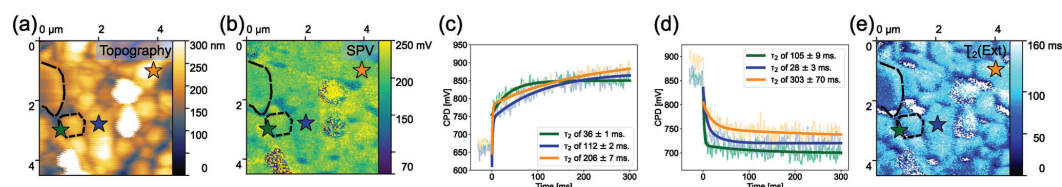
The snapshots of the CPD distribution of the reference perovskite film at different times during the nano-SPV measurement show the time-evolution of the SPV before (Figure 2b), during (Figure 2e,f), and after (Figure 2g–j) the illumination pulse (see also Video S1, Supporting Information). Directly after the laser was switched on, the CPD distribution remained rather uniform at  $1030 \pm 40$  mV; 200 ms later, the contrast between the low and high SPV grains was clearly visible. Directly upon switching off the laser, the CPD values started to decrease due to the charge carrier recombination (Figure S6, Supporting Information). The electronic recombination for most of the image occurred within the first  $\approx 30$  ms after the laser was switched off (Figure 2i) at which the average CPD reached a minimum (Figure S6, Supporting Information). After reaching the minimum, the average CPD of the whole map increased again due to the slow decay of the ionic polarization that occurs in low SPV areas (blue plot in

Figure 2d), and most grains relaxed back to their original dark CPD values (Figure 2j). The high SPV grains, however, showed longer decay times without the ionic undershoot, as also shown in Figure 2d. The absence of ionic polarization and the longer SPV decay time suggest that the defect density is lower at the high SPV areas of the reference sample.

### 3.2. Solvent-Annealed Pristine Sample

To investigate the effect of solvent annealing on the defect density, we prepared triple cation perovskite films with a post-treatment of DMSO solvent annealing. This post-treatment should lead to a better crystallinity of larger grains and decreased GB density.<sup>[70]</sup> It also has been shown that the larger grain size reduces the defect density within the perovskite layer.<sup>[71]</sup> The topography of the SA<sub>pristine</sub> sample (Figure 3a) showed larger perovskite grains ( $\langle d \rangle_{SA_{pristine}} = 590 \pm 160$  nm) compared to the reference ( $\langle d \rangle_{Ref} = 200 \pm 60$  nm) due to the solvent annealing.<sup>[72]</sup> The dark CPD picture of SA<sub>pristine</sub> can be found in Figure S16 in Section S6, Supporting Information. The distortions in the form of comb-like artifacts were caused by sample drift.

The nano-SPV map of the SA<sub>pristine</sub> sample (Figure 3b) shows a pattern that matches some features in the topography map. The ETL of the reference sample and the SA<sub>pristine</sub> are SnO<sub>2</sub> and c-TiO<sub>2</sub>, respectively (see Experimental Section). Nevertheless, compared to the reference, the SPV value decreased slightly, from  $280 \pm 90$  to  $210 \pm 50$  mV on the SA<sub>pristine</sub> sample. This lower SPV signal could be the result of a reduced band bending at the top surface due to the improved film quality<sup>[73,74]</sup> or a reduced charge transfer at the ETL interface, for example, due to energy barriers. Furthermore, at some of the GBs, we observed a stronger SPV contrast compared to the reference sample (SPV profiles in Figure S12b, Supporting Information). These profiles reveal a  $73 \pm 15$  mV lower SPV at the GB compared to the grain interior. This value is in agreement with previous reports.<sup>[15]</sup> The lower SPV at the GBs could be caused by band bending at the GBs.<sup>[48]</sup> Furthermore, we see a SPV contrast of about  $32 \pm 5$  mV between



**Figure 3.** a) The topography; b) SPV map; c) CPD spectroscopy curves with 30 ms pre-zero data of spots marked in (a), (b), and (e) with a calculated slow timescale of electron extraction ( $\tau_2$ (extraction)) in respect to turning on the laser; d) CPD spectroscopy curves with 30 ms pre-zero data of spots marked in (a), (b), and (e) with a calculated slow timescale of electron recombination ( $\tau_2$ (recombination)) in respect to turning off the laser; and e) SPV rise time  $\tau_2$ (ext) map of  $\text{Cs}_{0.05}\text{FA}_{0.8}\text{MA}_{0.15}\text{PbI}_3$  perovskite film with 0.95:1.05 A/B cation ratio ( $\text{SA}_{\text{Pristine}}$ ). An extended version is available in Figures S7–S9, Supporting Information.

some individual grains and even within the same grain (see Figure S13b,c, Supporting Information). These differences could result from a facet dependency of the SPV,<sup>[75]</sup> stoichiometry differences, or the defect distribution within the perovskite film. The elevated structures that are visible in the topography (Figure 3a) and the corresponding noisy SPV features in Figure 3b, together with a locally lower CPD (Figure S16, Supporting Information) could be caused by a locally higher  $\text{PbI}_2$  concentration.<sup>[15]</sup>

We further analyzed the nano-SPV dynamics in different locations on the map with similar SPV values. One spot was chosen to be on a GB (green star) and two were placed within different grains (blue and orange stars in Figure 3a,b,e). Analyzing the SPV decay curves, it is obvious that the ionic undershoot that we observed on the reference sample disappeared on most grains in Figure 3d (some exceptions are shown in Figure S7 in Section S6, Supporting Information). The suppression of ion migration<sup>[40]</sup> is a result of the increased grain size and fewer GBs.<sup>[74,76]</sup> We want to point out that the increase in the grain size already had a massive impact on the ion migration. This means increasing the grain size alone already improves the defect density at the GBs. Although the grains marked with blue and orange stars exhibited a similar SPV value, the timescale until the SPV reached equilibrium varied from  $112 \pm 2$  to  $206 \pm 7$  ms, respectively. On the GBs, these timescales were even shorter  $\sim 36 \pm 1$  ms ( $< \tau_2(\text{ext}) >(\text{GB}) = 64 \pm 21$  ms;  $< \tau_2(\text{ext}) >(\text{grain}) = 300 \pm 30$  ms; see also Video S2, Supporting Information). Changes of SPV in the time range of seconds have been reported before by tr-SEM measurements<sup>[25]</sup> and by earlier tr-KPFM measurements on device cross sections.<sup>[77,78]</sup>

Since ion migration is suppressed in solvent-annealed samples, the SPV decay is dominated by electron–hole recombination. Therefore, the shorter decay at the GBs can be attributed to faster electron–hole recombination, which points out higher defect density at the GBs. We interpret the equilibration time of the SPV as a local capacitive charging or extraction time, where the photogenerated charges fill up the capacitor between the bottom contact and the perovskite surface. Here, a faster equilibration time is indicative of a higher generation rate or a lower capacitance of the perovskite material. Moreover, the recombination or discharging traces and, therefore, the time in Figure 3d also show a wide variation of  $\tau_2(\text{rec})$  values between  $28 \pm 3$  and  $303 \pm 70$  ms. We did not observe a consistent correlation between the extraction and recombination times, indicating that the mechanisms of charge extraction and charge recombination are different. This is up to future research.

The fact that the nano-SPV measurements yield complete SPV traces for every position on the samples allows for generating maps of the equilibration timescales. We were able to fit most of the nano-SPV traces for excitation (ext) and recombination (rec) with a double exponential fit, indicating that two distinctly different timescales,  $\tau_1$  and  $\tau_2$ , are involved in the dynamics. While all the other timescales showed no clear contrast, we found a distinct contrast between the grain interior and the GB in  $\tau_2(\text{ext})$  (see Figure 3e). Furthermore, there is a weak correlation between the SPV magnitude and the SPV extraction time that could be connected to different crystal facets. Generally, we observed higher SPV extraction times for lower SPV grains or grain facets, for example, the area in Figure 3b right to the long dotted line marked grain. This area had a lower SPV, but a higher extraction time in Figure 3e. This contrast trend could originate from stoichiometric differences or variations in defect density between grains in the triple cation perovskite film. The difference of  $\tau_2(\text{ext})$  between the grain interior and the GB is about  $33 \pm 6$  ms (see Figure S14b, Supporting Information). This observation demonstrates that the extraction of charge carriers usually takes place much faster at GBs compared to the grain interior.

Although Regalado-Pérez et al. have suggested poor electronic transport due to local electric fields at GBs caused by an accumulation of negatively charged ionic defects,<sup>[74]</sup> Tainter et al. performed bulk measurements of photocurrent at excitation–junction separations much larger than topographical feature size and find that large fractions of excited carriers travel across multiple GBs.<sup>[79]</sup> These authors assumed that GBs do not prevent charge diffusion and GBs are not major impediments to charge motion in the polycrystalline films.<sup>[79–81]</sup> Moreover, Shao et al. saw that larger grains have GBs perpendicular to the substrate.<sup>[82]</sup> We, therefore, think that the overall increase in the grain size due to the DMSO vapor annealing has not only improved the crystallinity of the film but also made the GBs fast perpendicular pathways to the underlying substrate. Such a conductive pathway would explain the faster dynamics that we observed at the GBs with nano-SPV. Furthermore, Figure 3e shows not only a difference between the grain interior and the GB but also shows a facet dependence of the timescale of the nano-SPV response (e.g., the top left grain marked with a dashed line in Figure 3a,b,e and Figure S7a–d, Supporting Information).

Comparing the map of extraction/generation time constants (Figure 3e) to the map of the fast recombination/decay timescale in Figure S18, Supporting Information, we see a similar pattern. In particular, positions where the SPV stabilized fast were also

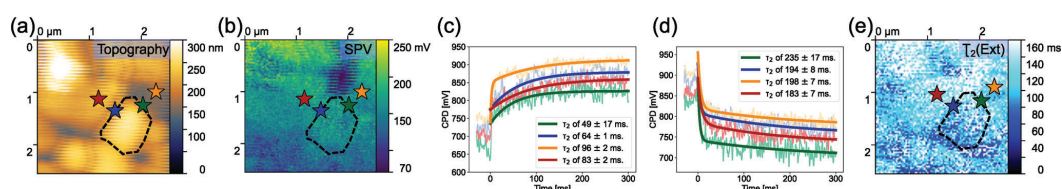


**Figure 4.** a) The topography; b) SPV map; c) CPD spectroscopy curves with 30 ms pre-zero data of spots marked in (a), (b), and (e) with a calculated slow timescale of electron extraction ( $\tau_2$  (extraction)) in respect to turning on the laser; d) CPD spectroscopy curves with 30 ms pre-zero data of spots marked in (a), (b), and (e) with a calculated slow timescale of electron recombination ( $\tau_2$  (recombination)) in respect to turning off the laser; and e) SPV rise time  $\tau_2$  (ext) map of  $\text{Cs}_{0.05}\text{FA}_{0.8}\text{MA}_{0.15}\text{PbI}_3$  perovskite film with 0.95:1.05 A/B cation ratio and surface passivation ( $\text{SA}_{\text{Pass}}$ ). A combined figure of the CPD spectroscopy trajectory shown in (c) and (d) can be found in Figure S24, Supporting Information.

positions with fast SPV decay after the light was switched off. Interestingly, the second timescale obtained from the fits was very long, up to 1.5 s (see Figure S19, Supporting Information). Mapping the longer timescale, we observed a much more homogeneous contrast. Nevertheless, the exact meaning of this second timescale remains unclear and will be subject to future studies.

### 3.3. Solvent-Annealed and Passivated Sample

The topography of the  $\text{SA}_{\text{Pass}}$  sample Figure 4a shows slightly larger perovskite grains ( $\langle d \rangle_{\text{SA}_{\text{Pass}}} = 670 \pm 210$  nm) compared to the  $\text{SA}_{\text{Pristine}}$  sample (Figure 3a). Again, the comb artifacts are caused by sample drift and should not affect the interpretation of the results. The dark CPD picture of  $\text{SA}_{\text{Pass}}$  can be found in Figure S28 in Section S7, Supporting Information.

The nano-SPV image (Figure 4b) shows a more uniform distribution compared to the SPV image of the  $\text{SA}_{\text{Pristine}}$  sample (Figure 3b). Overall, the SPV value decreased from 210 mV with an RMS variation of 50 mV on the reference sample to 160 mV with an RMS deviation of 30 mV on the passivated sample. The decrease of the SPV could be the result of less band bending (shown in Figure S1, Supporting Information) due to the passivation of surface defect states. Furthermore, the grain–GB contrast decreased as a result of the passivation. The dark CPD decreased probably due to the site-specific passivation of the GBs by forming a 2D perovskite.<sup>[15]</sup> The lower defect density due to the passivation specifically at the GBs may lead to decreased band bending (see Figure S1, Supporting Information). This causes the SPV to be lower since there is less energy needed to flatten the bands.

To further support the homogeneous distribution of the passivation agent, we analyzed again four spots on the  $\text{SA}_{\text{Pass}}$  sample with similar SPV values (see spots in Figure 4b) on GBs and within grains. Figure 4c shows that the curves appear much more similar compared to the  $\text{SA}_{\text{Pristine}}$  (Figure 3c,d). The values of  $\tau_2$ (ext) are only separated by about  $\approx 23$  %. The SPV extraction time map of  $\text{SA}_{\text{Pass}}$  given in Figure 4e shows an overall improved SPV extraction time uniformity compared to the  $\text{SA}_{\text{Pristine}}$  sample (see Figure 3e and Video S3, Supporting Information). There is a medium intergranular difference of  $\tau_2$ (ext) of  $\approx 20$  ms between the grains shown in Figure 4e. Similar to the pristine perovskite film, the fast recombination time map (see Figure S30, Supporting Information) shows a uniform distribution (Figure 4a). Some non-uniformity could be caused by the non-homogeneous distribution of PEA-ions on the surface

during preparation. Nevertheless, the distribution is much more homogeneous compared to the pristine one (Figure S18, Supporting Information). Slower SPV recombination times usually indicate slower recombination<sup>[83]</sup> due to the passivation. Therefore, our results show that surface passivation with PEA leads to a more uniform SPV distribution and SPV extraction time behavior on GBs and within grains due to the homogenized defect density within the perovskite film and/or the formation of 2D-perovskite phases shown in a previous study.<sup>[15]</sup>

### 3.4. Methylamine-Treated Sample

The topography image of the MA80 sample (Figure 5a) shows a structure where the grain size exceeds 100  $\mu\text{m}$ . Due to the limited scan size of the AFM, we were not able to investigate areas with several grains and therefore focused on one particular GB (diagonal line from top left to bottom right in Figure 5a). The CPD map before the illumination (Figure 5b) shows grain–GB contrast without any contrast within grains with no topographical features. The average dark CPD was  $960 \pm 50$  mV within the grains with and about 65 mV higher at the GBs. The SPV map (Figure 5c) obtained during the illumination pulse (0 ms  $< t < 201.6$  ms) shows an average SPV of  $200 \pm 40$  mV with an  $\approx 60$  mV lower value at the GB. The fact that the CPD and SPV contrast are almost identical at the GBs supports the notion of band bending at the GBs that we suggested previously. Apart from the GBs, MA80 shows uniform behavior considering both CPD and SPV distribution. Therefore, we suggest that methylamine treatment heals the perovskite grains and homogenizes the stoichiometry, leading to a more uniform CPD and SPV distribution.

To investigate the nano-SPV dynamics at high and low SPV areas (Figure 5c, blue and red markers, respectively), we looked at the SPV traces located at the grain interiors and a GB, respectively (Figure 5d, blue and red markers in c, respectively). The SPV dynamics upon excitation were comparable to those of the previous samples. Surprisingly, we observed a spike (inset of Figure 5d) in CPD about 3 ms after the light was switched off. Such a  $V_{\text{OC}}$  overshooting effect has also been reported by Herterich et al. during solar cell device measurements.<sup>[84]</sup> These authors suggested that due to the presence of mobile ions in the perovskite layer, a space charge layer forms between the perovskite and the contact layer. This space charge layer decreases the conductivity of the majority charge carriers, leading to a gradient of the quasi-Fermi level splitting at the contact interface. When the light is switched

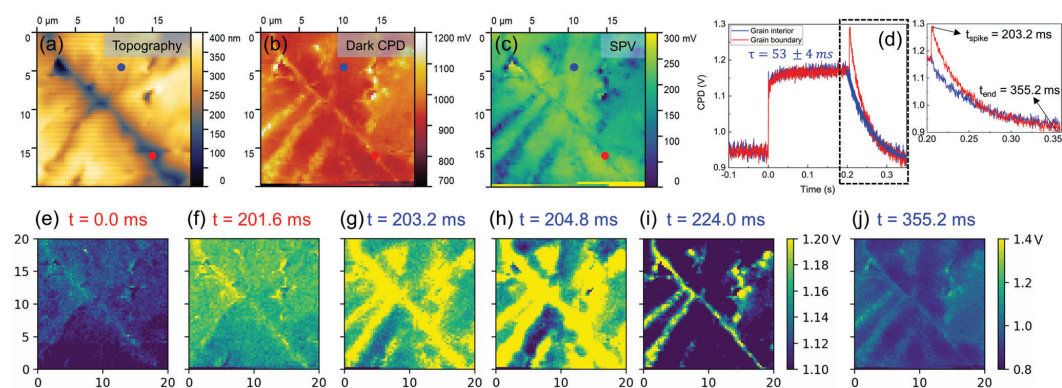


**Figure 5.** a) Topography, b) CPD in dark, c) SPV, and d) SPV plots over time from marked areas of the MA80 sample. Panels (e)–(j) show the CPD maps at different time frames. The maps have 150x150 pixels.

off, this gradient at the interface decreases faster compared to the bulk quasi-Fermi level splitting, resulting in  $V_{OC}$  overshoot.

When we examine a nano-SPV trace within a grain, we see a SPV decay without any overshoot. Furthermore, in both grain and GBs, the decay shows longer SPV decay times compared to the reference sample. The SPV decay given in Figure 5e decays with a characteristic time of  $53 \pm 4$  ms according to the double exponential fit of the signal. This result is also backed by our previous observations on MA gas-treated samples.<sup>[85]</sup> The longer charge recombination times in both tr-PL (Figure S38, Supporting Information) and SPV decay (Figure 5d) indicate reduced defect density of the MA80 film due to the healing effect of methylamine treatment and fewer GBs. The increased crystallinity and grain orientation that we observed from the XRD patterns (Figure S36, Supporting Information) is possibly a contributing factor that leads to increased charge recombination times. The PL spectra given in Figure S37a, Supporting Information, also support the improvements that we see in SPV and XRD results, since the PL full-width half maximum is narrower after the methylamine treatment. The absence of a SPV overshoot further supports our earlier conclusion that decreasing the number of GBs further suppresses ion migration within the perovskite.

The SPV time frames gathered from the MA80 film during the nano-SPV experiment show the CPD distribution before (Figure 5b), during (Figure 5e,f), and after (Figure 5g–j) light illumination (see also Video S4, Supporting Information). When the laser was first switched on, the CPD had an average value of  $1130 \pm 50$  mV, while it evolved to an average of  $1160 \pm 20$  mV within 200 ms (Figure 5e,f). After switching off the laser, the CPD within the grains started to relax back to the original values due to charge carrier recombination. The SPV maps revealed that the SPV overshoot within the first 3 ms after the light pulse had a magnitude of up to 120 mV in the vicinity of the GB. This overshoot leads to a SPV decay contrast between the perovskite grains and the GBs, comparable to the dark CPD distribution. The SPV overshoot contrast between the GB and the grains suggests that the ion accumulation at the interface is higher at GBs. At the end of the nano-SPV recording at  $t = 355.2$  ms, we see that the CPD

image is almost identical to the dark CPD image. This suggests a more uniform SPV decay behavior within the grains of the MA80 film compared to the reference film. Moreover, the absence of CPD contrast within the grains suggests that the methylamine treatment could be working as a passivation treatment by healing the  $A^+$ -cation site defects or causing uniform chemical stoichiometry distribution throughout the film.

### 3.5. Nanoscale Ideality Factor Mapping

As we have shown, CPD and SPV measurements can be used to map sample heterogeneity in terms of Fermi level contrast and SPV decay times, which are mainly related to defects. However, the changes in these parameters could be linked to local stoichiometry changes<sup>[50]</sup> as well as they could be linked to the presence of defects within the perovskite layer or at the interfaces. Furthermore, the time resolution of tr-KPFM during SPV decay is determined by the use of our cantilevers and is in the order of 0.1–1 ms. This limitation makes it difficult to obtain quantitative results from samples with shorter SPV decay times (Figure 2j). Therefore, we introduce a new KPFM-based technique where we locally measure the recombination behavior in the semiconductor film by measuring the  $n_{id,i}$  of our perovskite half-cells named nano-IFM. To use the concept of  $n_{id,i}$  to our advantage, we used our AFM tip as a nanoscale probe for each pixel and measured the SPV as a function of illumination intensity. By doing so, we are able to map the  $n_{id,i}$  in the scan area of the sample (see Section S10, Supporting Information).

The topography image (Figure 6a) shows the granular structure of the same reference perovskite film given in Figure 2. The grain size varied between 100 and 400 nm. The SPV map shows an average SPV of  $110 \pm 20$  mV (Figure 6b). Some grains show higher SPV values up to 200 mV compared to the rest of the sample. Furthermore, SPV values decreased between 10 and 20 mV at the GBs. As we suggested previously, the SPV contrast could be related to the stoichiometry or defect density distribution within the reference perovskite film. The  $n_{id,i}$  distribution within the grains shows the same trend as the SPV distribution, where the

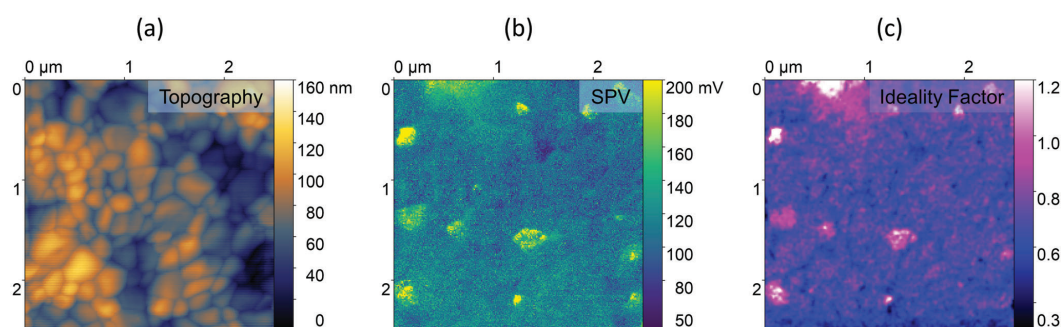


Figure 6. a) Topography, b) SPV, and c)  $n_{id,1}$  maps of reference perovskite film. The map contains 200x200 pixels. The nano-IFM map was 1x1 pixel Gaussian filtered.

average  $n_{id,1}$  value is  $0.69 \pm 0.11$ , with up to 0.3 higher  $n_{id,1}$  values within the grains with higher SPV in Figure 6b, suggesting that these grains exhibit a lower defect density (Figure 6c). Thus, we conclude that the defect density at the grain interiors is not uniform within the perovskite film, in agreement with the earlier interpretation of the SPV decay (Figure 2a–f) and SPV distribution (Figure 2h). Moreover, this result also suggests a direct correlation between the quasi-Fermi level splitting and the  $n_{id,1}$ , which demonstrates the dominance of interfacial recombination in our perovskite half-cells.<sup>[58,59]</sup> The GBs in Figure 6d show lower  $n_{id,1}$  values between 15 and 20 compared to the grain interiors, which points out the higher defect density at the GBs.

On the MA80 sample, we again focused on a region with a GB (Figure 5g). Here, we observed two GBs: the crack-like boundary on the left and the more subtle boundary on the right (Figure 7a). Apart from these boundaries, the topography was smooth with 36 nm RMS roughness (Figure 7a). The SPV map (Figure 7b) shows a uniform distribution within the grains with an average value of  $370 \pm 50$  mV and about 20 mV lower SPV values at the GB. However, SPV values of the grains near the GB were about 50 mV higher compared to the average SPV. The features appearing in these areas in the dark CPD map (Figure S42b, Supporting Information) suggest that this effect could be related to a stoichiometric change. The  $n_{id,1}$  map, like the SPV map, shows uniform

distribution within the MA80 film with an average value of  $0.92 \pm 0.28$  (Figure 7c). Some areas within the grains show an about 0.4 lower  $n_{id,1}$  value compared to the average value. This decrease could be related to the topographical features (Figure 7a). The grain–GB contrast in Figure 7d exhibits a  $n_{id,1}$  drop of around 0.1 at the GB. This shows that the GBs still possess higher defect density, even after the methylamine treatment. Interestingly, the SPV contrast (Figure 7b) and the  $n_{id,1}$  contrast (Figure 7c) do not exactly overlap. This supports our previous notion that SPV increases near the GBs are caused by the chemical stoichiometry changes. Therefore, a comparison of the SPV and the  $n_{id,1}$  maps can give us stoichiometry and defect contrasts within the same film after a single nano-IFM measurement.

Comparing the overall  $n_{id,1}$  values of the measured films, we see that the average  $n_{id,1}$  increased after the methylamine treatment from  $0.69 \pm 0.18$  to  $0.92 \pm 0.28$ . Therefore, our nano-IFM results suggest that the methylamine treatment increases the grain sizes and decreases the defect density inside the grains. The non-conventional  $n_{id,1}$  values below 1 could be related to the fact that the measurements are carried out on perovskite half-cells with ITO/ETL/perovskite structure in which there is a charge carrier imbalance due to the absence of an HTL layer. Previously,  $n_{id,1}$  values below 1 have been reported to be caused by energy misalignment between the absorber layer and the HTL in organic

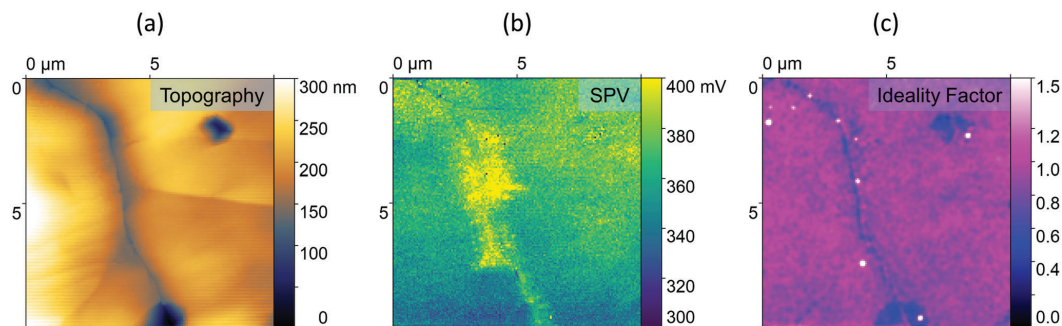


Figure 7. a) Topography, b) SPV, and c)  $n_{id,1}$  maps of MA80 film. The map contains 150x150 pixels. The  $n_{id,1}$  map was 1x1 pixel Gaussian filtered.

solar cells.<sup>[86]</sup> Also, the effect of ion migration and the possible space charge layers at the interfaces on  $n_{id,1}$  is not entirely clear in the classical diode theory.<sup>[87]</sup> The quantities obtained via nano-IFM could be the subject of future research.

#### 4. Conclusion

Using nano-SPV and nano-IFM, we demonstrate the effect of GBs on the lateral defect distribution in triple-cation perovskite films. Using pulsed and ramped laser illumination during tr-KPFM measurements, we showed the occurring changes within the perovskite films with small grains, large grains, and passivated grains. These measurements enabled us to experimentally demonstrate the effect of chemical processing on the nanostructures and charge carrier dynamics within the halide perovskite devices. Fewer GBs within the perovskite film lead to longer SPV lifetimes, which agrees with longer electron–hole lifetimes as observed in tr-PL. Furthermore, the ion migrations within the perovskite films were suppressed in solvent-annealed ( $SA_{\text{Pristine}}$  and  $SA_{\text{Pass}}$ ) and MA80 films due to a lower density of GBs and higher crystallinity. The nano-SPV and SPV decay maps showed more uniformity when defects were passivated via PEA coating. Also, the nano-SPV map showed that the MA80 film shows a more uniform SPV distribution compared to the reference perovskite film. We furthermore showed the different recombination behavior of reference and MA80 perovskite films by nano-IFM. Our  $n_{id,1}$  mapping results show that different GBs can show varying recombination mechanisms but they are still the main locations for trap-assisted recombination within the perovskite films. According to our results, the negative effects of GBs are suppressed by surface passivation. On top of that, the grain interiors are also positively affected by the passivation agent coating as the higher SPV decay values measured in the grains suggest. Nevertheless, even the optimized films still exhibited some lateral variations in the defect density, thus guiding the way for targeted optimization of perovskite solar cells. Our results highlight the potential of nano-SPV and nano-IFM for the investigation of nanoscale structure–function relationships in optoelectronic materials beyond perovskites.

#### 5. Experimental Section

**Preparation of Perovskite Films:** The planar ETL/perovskite half solar cells had the architecture of ITO/c-TiO<sub>2</sub>/Cs<sub>0.05</sub>FA<sub>0.8</sub>MA<sub>0.15</sub>PbI<sub>3</sub>.

The triple-cation perovskites (Cs<sub>0.05</sub>FA<sub>0.8</sub>MA<sub>0.15</sub>PbI<sub>3</sub>) used for the tr-KPFM measurements were prepared on Ossila ITO-coated glass substrates with a conductivity of 20 Ω. After being brushed with Hellmanex III (Hellma), the ITO substrates were washed with hot tap water and milliQ water and then dried with an air gun. Afterward, the ITO substrates were treated with UV–ozone for 30 min freshly before the preparation of the compact TiO<sub>2</sub> (c-TiO<sub>2</sub>) and once more before the perovskite layer. The c-TiO<sub>2</sub> layer was prepared by spin coating 80 μL of a 0.75 mol L<sup>-1</sup> aqueous TiCl<sub>4(aq)</sub> solution on the ITO glass. The substrates were dried for 5 min @ 100 °C and then heated for 30 min on a high-temperature hot plate at a temperature of 500 °C. The perovskite precursor solution of 1.0:1.0, 0.9:1.1, and 0.8:1.2 A<sup>+</sup>:B<sup>2+</sup> cation ratio were prepared each with the concentration of 1.3 mol L<sup>-1</sup> for PbI<sub>2</sub> in DMSO: *N,N*-dimethylformamide (DMF) (both anhydrous, Sigma-Aldrich) in a 1:4 volume ratio (v:v). For spin coating, 100 μL of the perovskite precursor solution was placed on the substrate and spin coated for 10 s @ 1000 rpm followed by 20 s @

6000 rpm. 5 s before the end of the second step, 200 μL of chlorobenzene (CB) was used as an antisolvent. The substrate was then put on a hot plate with a temperature of 100 °C first until the substrate turned black and the film dried completely (≈10 s) and then for 15 min in an atmosphere of DMSO under a petri dish for solvent annealing. For each six samples, one petri dish was used with 90 μL of DMSO. The solvent annealing step was followed by a step of thermal annealing at 100 °C for another 15 min without DMSO for drying.

The passivated films were prepared by letting the samples cool after the thermal annealing step and then using a 10 mM solution of PEA-I solution in dry 2-propanol (IPA). 100 μL of the passivation solution was put on the perovskite substrates and spin-coated for 20 s @ 3000 rpm. The samples were then dried by thermal annealing for 10 min @ 100 °C on the hot plate. In addition, the samples were put in a dry and dark atmosphere for at least 11 days; some were left in there for 36 days.

The samples for grain size effect investigation were prepared on Lumtec ITO-coated glass substrates. The ITO substrates were ultrasonicated for 30 min in detergent solution in deionized water, acetone, and isopropanol. After cleaning, the ITO substrates were treated with oxygen plasma for 7 min. The SnO<sub>2</sub> precursor was prepared by the reflux method,<sup>[88]</sup> which involved preparing a 0.1 M solution of tin(II) chloride dihydrate (SnCl<sub>2</sub> · H<sub>2</sub>O, Alfa Aesar) in a 1:19 butanol (Sigma-Aldrich)/deionized water mixture and heating it at 110 °C for 4 h. Then, the solution was spin-coated at 2000 rpm for 30 s and annealed at 130 °C for 60 min to obtain the SnO<sub>2</sub> layer. The perovskite precursor solution was prepared by dissolving 507.1 mg PbI<sub>2</sub>, 73.4 mg PbBr<sub>2</sub> (Sigma-Aldrich), 22.4 mg methylammonium bromide (Sigma-Aldrich), and 172 mg formamidine iodide (Greatcell Solar) in 1:4 DMSO:DMF. Then, 53 μL of 389.7 mg mL<sup>-1</sup> cesium iodide (Sigma-Aldrich) in DMSO solution was added to the perovskite precursor solution. The perovskite precursor solution was then spin-coated at 1000 rpm for 10 s and then at 6000 rpm for 20 s. 250 μL of CB (anhydrous, Sigma-Aldrich) was dropped onto the sample roughly 5 s before the end of the program. After the coating, the films were annealed at 100 °C for 60 min on a hot plate.

The perovskite films with extremely large grains were obtained via a methylamine treatment.<sup>[85]</sup> The methylamine treatment was carried out with 230 mbar of methylamine partial pressure. The perovskite film was kept under this methylamine atmosphere for 10 s before the pressure was pumped up to 600 mbar, decreasing the methylamine partial pressure to ≈170 mbar during recrystallization.

**Kelvin Probe Force Microscopy Measurements:** KPFM was measured on an Oxford Instruments/Asylum Research MFP-3D Infinity AFM in a nitrogen glovebox (level of humidity below 0.3 %, level of oxygen below 0.1 %) for all experiments. The Pt/Ir-coated conductive cantilevers (Bruker Model: SCM-PIT-V2) had a typical resonance frequency of ≈75 kHz, a spring constant of 2 N m<sup>-1</sup>, a tip radius of 25 nm, and a tip height of 10 to 15 μm. The topography feedback was performed with amplitude modulation (AM) on the first eigenmode, and the oscillation amplitude was kept to ≈20–30 nm for all measurements. A Zurich Instruments HF2 Lock-In amplifier was used for all heterodyne KPFM experiments,<sup>[68,69]</sup> to perform the KPFM feedback. The electric drive amplitude of the ω<sub>c</sub> signal varied between 2 and 5 V depending on the obtained signal from the sample. The sample was grounded via the sample holder with an external wire to the ground level of the Zurich Lock-In Amplifier. The compensating V<sub>DC</sub> was applied to the tip, minimizing the electrostatic tip–sample interactions. For SPV measurements, the sample was illuminated from below by a pulsed laser (Cobolt 06-01 Series) at 488 nm. The laser power was controlled by a custom-written code within the MFP3D's control software by the AFM controller (Asylum Research ARC2), which provided analog voltage to activate the illumination.

**Optical Measurements:** PL and tr-PL measurements were performed on a PicoQuant FluoTime300 fluorescence spectrometer with an excitation wavelength of 405 nm. The repetition rate was set as 40 and 1 MHz for steady-state and time-resolved measurements, respectively. A 455 nm longpass filter was placed between the sample and the detector to block the stray laser light.

UV–vis absorbance spectroscopy was carried out with a CARY 5000 UV-Vis spectrometer by Agilent Technologies.

**X-ray Diffraction Measurements:** The XRD measurements were performed on a Bruker D8 X-ray diffractometer with a Cu anode using the K(alpha) emission line between 5° and 70°. The measurements were made with a step resolution of 0.02° and a 192 s integration time per step.

### Supporting Information

Supporting Information is available from the Wiley Online Library or from the author.

### Acknowledgements

Y.Y. and P.N.R. contributed equally to this work. Y.Y. and S.A.L.W. acknowledge the SPP2196 project (Deutsche Forschungsgemeinschaft) for funding. The authors also thank Stefan Glunz (ISE Freiburg) for the discussions that inspired the implementation of the nano-IFM method.

Open access funding enabled and organized by Projekt DEAL.

### Conflict of Interest

The authors declare no conflict of interest.

### Data Availability Statement

The data that support the findings of this study are available from the corresponding author upon reasonable request.

### Keywords

atomic force microscopy, charge carrier dynamics, Ideality factor, Kelvin probe force microscopy, perovskites, surface photovoltage spectroscopy

Received: June 5, 2023

Revised: July 31, 2023

Published online:

- [1] L. Protesescu, S. Yakunin, M. I. Bodnarchuk, F. Krieg, R. Caputo, C. H. Hendon, R. X. Yang, A. Walsh, M. V. Kovalenko, *Nano Lett.* **2015**, *15*, 3692.
- [2] C. C. Stoumpos, C. D. Malliakas, M. G. Kanatzidis, *Inorg. Chem.* **2013**, *52*, 9019.
- [3] T. J. Jacobsson, J.-P. Correa-Baena, M. Pazoki, M. Saliba, K. Schenk, M. Grätzel, A. Hagfeldt, *Energy Environ. Sci.* **2016**, *9*, 1706.
- [4] K. X. Steirer, P. Schulz, G. Teeter, V. Stevanovic, M. Yang, K. Zhu, J. J. Berry, *ACS Energy Lett.* **2016**, *1*, 360.
- [5] M. B. Johnston, L. M. Herz, *Acc. Chem. Res.* **2016**, *49*, 146.
- [6] S. D. Stranks, G. E. Eperon, G. Grancini, C. Menelaou, M. J. Alcocer, T. Leijtens, L. M. Herz, A. Petrozza, H. J. Snaith, *Science* **2013**, *342*, 341.
- [7] D. Shi, V. Adinolfi, R. Comin, M. Yuan, E. Alarousu, A. Buin, Y. Chen, S. Hoogland, A. Rothenberger, K. Katsiev, Y. Losovyj, X. Zhang, P. A. Dowben, O. F. Mohammed, E. H. Sargent, O. M. Bakr, *Science* **2015**, *347*, 519.
- [8] R. E. Brandt, J. R. Poindexter, P. Gorai, R. C. Kurchin, R. L. Hoyer, L. Nienhaus, M. W. Wilson, J. A. Polizzotti, R. Sereika, R. Zaltauskas, L. C. Lee, J. L. MacManus-Driscoll, M. Bawendi, V. Stevanovic, T. Buonassisi, *Chem. Mater.* **2017**, *29*, 4667.
- [9] Y. Lei, Y. Xu, M. Wang, G. Zhu, Z. Jin, *Small* **2021**, *17*, 2005495.
- [10] C. Aranda, A. Guerrero, J. Bisquert, *ACS Energy Lett.* **2019**, *4*, 741.
- [11] D. Yang, X. Zhang, K. Wang, C. Wu, R. Yang, Y. Hou, Y. Jiang, S. Liu, S. Priya, *Nano Lett.* **2019**, *19*, 3313.
- [12] M. Abdi-Jalebi, M. Ibrahim Dar, S. P. Senanayak, A. Sadhanala, Z. Andaji-Garmaroudi, L. M. Pazos-Outón, J. M. Richter, A. J. Pearson, H. Sirringhaus, M. Grätzel, R. H. Friend, *Sci. Adv.* **2019**, *5*, eaav2012.
- [13] E. Halvani Anaraki, A. Kermanpur, M. T. Mayer, L. Steier, T. Ahmed, S.-H. Turren-Cruz, J. Seo, J. Luo, S. M. Zakeeruddin, W. R. Tress, T. Edvinsson, M. Grätzel, A. Hagfeldt, J.-P. Correa-Baena, *ACS Energy Lett.* **2018**, *3*, 773.
- [14] N. Arora, M. I. Dar, A. Hinderhofer, N. Pellet, F. Schreiber, S. M. Zakeeruddin, M. Grätzel, *Science* **2017**, *358*, 768.
- [15] S. Gharibzadeh, P. Fassel, I. M. Hossain, P. N. Rohrbeck, M. Frericks, M. Schmidt, T. Duong, M. R. Khan, T. Abzieher, B. A. Nejjad, F. Schackmar, O. Almora, T. Feeny, R. Singh, D. Fuchs, U. Lemmer, J. P. Hofmann, S. A. L. Weber, U. W. Paetzold, *Energy Environ. Sci.* **2021**, *14*, 5875.
- [16] C. Ma, N.-G. Park, *ACS Energy Lett.* **2020**, *5*, 3268.
- [17] M. Stolterfoht, V. M. Le Corre, M. Feuerstein, P. Caprioglio, L. J. A. Koster, D. Neher, *ACS Energy Lett.* **2019**, *4*, 2887.
- [18] E. Serpetzoglou, I. Konidakis, G. Kakavelakis, T. Maksudov, E. Kymakis, E. Stratakis, *ACS Appl. Mater. Interfaces* **2017**, *9*, 43910.
- [19] H. Hempel, T. J. Savenjie, M. Stolterfoht, J. Neu, M. Failla, V. C. Paingad, P. Kuzel, E. J. Heilweil, J. A. Spies, M. Schleunig, J. Zhao, D. Friedrich, K. Schwarzburg, L. D. A. Siebbeles, P. Dörflinger, V. Dyakonov, R. Katoh, M. J. Hong, J. G. Labram, M. Monti, E. Butler-Caddle, J. Lloyd-Hughes, M. M. Taheri, J. B. Baxter, T. J. Magnanelli, S. Luo, J. M. Cardon, S. Ardo, T. Unold, *Adv. Energy Mater.* **2022**, *12*, 2102776.
- [20] E. Von Hauff, D. Klotz, *J. Mater. Chem. C* **2022**, *10*, 742.
- [21] Y.-C. Chin, M. Daboczi, C. Henderson, J. Luke, J.-S. Kim, *ACS Energy Lett.* **2022**, *7*, 560.
- [22] N. Li, A. Feng, X. Guo, J. Wu, S. Xie, Q. Lin, X. Jiang, Y. Liu, Z. Chen, X. Tao, *Adv. Energy Mater.* **2022**, *12*, 2103241.
- [23] S. Zouhair, S.-M. Yoo, D. Bogachuk, J. P. Herterich, J. Lim, H. Kanda, B. Son, H. J. Yun, U. Würfel, A. Chahboun, M. K. Nazeeruddin, A. Hinsch, L. Wagner, H. Kim, *Adv. Energy Mater.* **2022**, *12*, 2200837.
- [24] Y. Zhang, Y. Zhu, M. Hu, N. Pai, T. Qin, Y.-B. Cheng, U. Bach, A. N. Simonov, J. Lu, *J. Phys. Chem. Lett.* **2022**, *13*, 2792.
- [25] G. Irde, S. M. Pietralunga, V. Sala, M. Zani, J. M. Ball, A. J. Barker, A. Petrozza, G. Lanzani, A. Tagliaferri, *Micron* **2019**, *121*, 53.
- [26] S. M. Pietralunga, G. Irde, A. J. Barker, J. M. Ball, A. Petrozza, V. Sala, M. Zani, G. Lanzani, A. Tagliaferri, *Adv. Mater. Interfaces* **2020**, *7*, 2000297.
- [27] S. K. Yadavalli, M. Chen, M. Hu, Z. Dai, Y. Zhou, N. P. Padture, *Scr. Mater.* **2020**, *187*, 88.
- [28] D. Zhang, Y. Zhu, L. Liu, X. Ying, C.-E. Hsiung, R. Sougrat, K. Li, Y. Han, *Science* **2018**, *359*, 675.
- [29] R. Egerton, P. Li, M. Malac, *Micron* **2004**, *35*, 399.
- [30] J. Ran, O. Dyck, X. Wang, B. Yang, D. B. Geohegan, K. Xiao, *Adv. Energy Mater.* **2020**, *10*, 1903191.
- [31] I. M. Hermes, S. A. Bretschneider, V. W. Bergmann, D. Li, A. Klases, J. Mars, W. Tremel, F. Laquai, H.-J. Butt, M. Mezger, R. Berger, B. J. Rodriguez, S. A. L. Weber, *J. Phys. Chem. C* **2016**, *120*, 5724.
- [32] I. M. Hermes, A. Best, L. Winkelmann, J. Mars, S. M. Vorpahl, M. Mezger, L. Collins, H.-J. Butt, D. S. Ginger, K. Koynov, S. A. L. Weber, *Energy Environ. Sci.* **2020**, *13*, 4168.
- [33] Y. Yalcinkaya, I. M. Hermes, T. Seewald, K. Amann-Winkel, L. Veith, L. Schmidt-Mende, S. A. Weber, *Adv. Energy Mater.* **2022**, 2202442.
- [34] Y. Shao, Y. Fang, T. Li, Q. Wang, Q. Dong, Y. Deng, Y. Yuan, H. Wei, M. Wang, A. Gruverman, J. Shialda, J. Huang, *Energy Environ. Sci.* **2016**, *9*, 1752.

- [35] B. Conings, J. Drijkoningen, N. Gauquelin, A. Babayigit, J. D'Haen, L. D'Olieslaeger, A. Ethirajan, J. Verbeeck, J. Manca, E. Mosconi, F. De Angelis, H.-G. Boyen, *Adv. Energy Mater.* **2015**, *5*, 1500477.
- [36] V. W. Bergmann, S. A. Weber, F. Javier Ramos, M. K. Nazeeruddin, M. Grätzel, D. Li, A. L. Domanski, I. Lieberwirth, S. Ahmad, R. Berger, *Nat. Commun.* **2014**, *5*, 5001.
- [37] I. M. Hermes, Y. Hou, V. W. Bergmann, C. J. Brabec, S. A. Weber, *J. Phys. Chem. Lett.* **2018**, *9*, 6249.
- [38] S. A. Weber, I. M. Hermes, S.-H. Turren-Cruz, C. Gort, V. W. Bergmann, L. Gilson, A. Hagfeldt, M. Graetzel, W. Tress, R. Berger, *Energy Environ. Sci.* **2018**, *11*, 2404.
- [39] E. M. Lanzoni, T. Gallet, C. Spindler, O. Ramirez, C. K. Boumenou, S. Siebentritt, A. Redinger, *Nano Energy* **2021**, *88*, 106270.
- [40] E. Strelcov, S. Jesse, Y.-L. Huang, Y.-C. Teng, I. I. Kravchenko, Y.-H. Chu, S. V. Kalinin, *ACS Nano* **2013**, *7*, 6806.
- [41] L. Collins, A. Belianinov, S. Somnath, N. Balke, S. V. Kalinin, S. Jesse, *Sci. Rep.* **2016**, *6*, 30557.
- [42] L. Collins, M. Ahmadi, J. Qin, Y. Liu, O. S. Ovchinnikova, B. Hu, S. Jesse, S. V. Kalinin, *Nanotechnology* **2018**, *29*, 44.
- [43] Z. Schumacher, A. Spielhofer, Y. Miyahara, P. Grutter, *Appl. Phys. Lett.* **2017**, *110*, 5.
- [44] B. Grévin, O. Bardagot, R. Demadrille, *Beilstein J. Nanotechnol.* **2020**, *11*, 323.
- [45] V. Aubriet, K. Courouble, O. Bardagot, R. Demadrille, Ł. Borowik, B. Grévin, *Nanotechnology* **2022**, *33*, 225401.
- [46] J. Murawski, T. Graupner, P. Milde, R. Raupach, U. Zerweck-Trogisch, *L. Eng. J. Appl. Phys.* **2015**, *118*, 15.
- [47] E. Johnson, *Phys. Rev.* **1958**, *111*, 153.
- [48] D. Cavalcoli, A. Cavallini, *Phys. Status Solidi c* **2010**, *7*, 1293.
- [49] J. T.-W. Wang, Z. Wang, S. Pathak, W. Zhang, D. W. DeQuilettes, F. Wisnivesky-Rocca-Rivarola, J. Huang, P. K. Nayak, J. B. Patel, H. A. M. Yusuf, Y. Vaynzof, R. Zhu, I. Ramirez, J. Zhang, C. Ducati, C. Grovenor, M. B. Johnston, D. S. Ginger, R. J. Nicholas, H. J. Snaith, *Energy Environ. Sci.* **2016**, *9*, 2892.
- [50] G. Alkhalifah, A. D. Marshall, F. Rudayni, S. Wanigasekara, J. Z. Wu, W.-L. Chan, *J. Phys. Chem. Lett.* **2022**, *13*, 6711.
- [51] S. Wood, D. O'Connor, C. W. Jones, J. D. Claverley, J. C. Blakesley, C. Giusca, F. A. Castro, *Sol. Energy Mater. Sol. Cells* **2017**, *161*, 89.
- [52] L. Kronik, Y. Shapira, *Surf. Sci. Rep.* **1999**, *37*, 1.
- [53] Q. Zhou, B. Wang, R. Meng, J. Zhou, S. Xie, X. Zhang, J. Wang, S. Yue, B. Qin, H. Zhou, Y. Zhang, *Adv. Funct. Mater.* **2020**, *30*, 2000550.
- [54] I. Grill, M. F. Ayyüler, T. Bein, P. Docampo, N. F. Hartmann, M. Handloser, A. Hartschuh, *ACS Appl. Mater. Interfaces* **2017**, *9*, 37655.
- [55] T. Kirchartz, F. Deledalle, P. S. Tuladhar, J. R. Durrant, J. Nelson, *J. Phys. Chem. Lett.* **2013**, *4*, 2371.
- [56] C. Van Berkel, M. Powell, A. Franklin, I. French, *J. Appl. Phys.* **1993**, *73*, 5264.
- [57] D. Prochowicz, R. Runjhun, M. M. Tavakoli, P. Yadav, M. Sasaki, A. Q. Alanazi, D. J. Kubicki, Z. Kaszukur, S. M. Zakeeruddin, J. Lewiński, M. Grätzel, *Chem. Mater.* **2019**, *31*, 1620.
- [58] P. Caprioglio, C. M. Wolff, O. J. Sandberg, A. Armin, B. Rech, S. Albrecht, D. Neher, M. Stollerfoht, *Adv. Energy Mater.* **2020**, *10*, 2000502.
- [59] A. Dasgupta, S. Mahesh, P. Caprioglio, Y.-H. Lin, K.-A. Zaininger, R. D. Oliver, P. Holzhey, S. Zhou, M. M. McCarthy, J. A. Smith, M. Frenzel, M. G. Christoforo, J. M. Ball, B. Wenger, H. J. Snaith, *ACS Energy Lett.* **2022**, *7*, 2311.
- [60] M. Nonnenmacher, M. o'Boyle, H. K. Wickramasinghe, *Appl. Phys. Lett.* **1991**, *58*, 2921.
- [61] L. Kelvin, *Lond. Edinb. Dublin Philos. Mag. J. Sci.* **1898**, *46*, 82.
- [62] J. Weaver, D. W. Abraham, *J. Vac. Sci. Technol. B Microelectron. Nanometer Struct. Process. Meas. Phenom.* **1991**, *9*, 1559.
- [63] Y. Martin, D. W. Abraham, H. K. Wickramasinghe, *Appl. Phys. Lett.* **1988**, *52*, 1103.
- [64] U. J. Bahnmüller, H. Kuper, T. Seewald, Y. Yalcinkaya, J. A. Becker, L. Schmidt-Mende, S. A. Weber, S. Polarz, *Nanomaterials* **2021**, *11*, 3057.
- [65] W. Zhang, S. Pathak, N. Sakai, T. Stergiopoulos, P. K. Nayak, N. K. Noel, A. A. Haghighirad, V. M. Burlakov, D. W. DeQuilettes, A. Sadhanala, W. Li, L. Wang, D. S. Ginger, R. H. Friend, H. J. Snaith, *Nat. Commun.* **2015**, *6*, 10030.
- [66] P. Rohrbeck, *Master thesis*, Johannes Gutenberg University Mainz, **2021**.
- [67] D. Toth, B. Hailegnaw, F. Richeimer, F. A. Castro, F. Kienberger, M. C. Scharber, S. Wood, G. Gramse, *ACS Appl. Mater. Interfaces* **2020**, *12*, 48057.
- [68] J. L. Garrett, J. N. Munday, *Nanotechnology* **2016**, *27*, 24.
- [69] A. Axt, I. M. Hermes, V. W. Bergmann, N. Tausendpfund, S. A. L. Weber, *Beilstein J. Nanotechnol.* **2018**, *9*, 1809.
- [70] Z. Xiao, Q. Dong, C. Bi, Y. Shao, Y. Yuan, J. Huang, *Adv. Mater.* **2014**, *26*, 6503.
- [71] X. Yang, Y. Wei, F. Huang, S. Jin, D. Luo, Y. Fang, Y. Zhao, Q. Guo, Y. Huang, L. Fan, J. Wu, *Sol. Energy* **2019**, *177*, 299.
- [72] J. Bing, S. Huang, A. W. Y. Ho-Baillie, *Energy Technol.* **2020**, *8*, 1901114.
- [73] Y. Guo, S. Yuan, D. Zhu, M. Yu, H.-Y. Wang, J. Lin, Y. Wang, Y. Qin, J.-P. Zhang, X.-C. Ai, *Phys. Chem. Chem. Phys.* **2021**, *23*, 6162.
- [74] E. Regalado-Pérez, E. B. Díaz-Cruz, J. Landa-Bautista, N. R. Mathews, X. Mathew, *ACS Appl. Mater. Interfaces* **2021**, *13*, 11833.
- [75] S. Y. Leblebici, L. Leppert, Y. Li, S. E. Reyes-Lillo, S. Wickenburg, E. Wong, J. Lee, M. Melli, D. Ziegler, D. K. Angell, D. F. Ogletree, P. D. Ashby, F. M. Toma, J. B. Neaton, I. D. Sharp, A. Weber-Bargioni, *Nat. Energy* **2016**, *1*, 16093.
- [76] D. Prochowicz, R. Runjhun, M. M. Tavakoli, P. Yadav, M. Sasaki, A. Q. Alanazi, D. J. Kubicki, Z. Kaszukur, S. M. Zakeeruddin, J. Lewiński, M. Grätzel, *Chem. Mater.* **2019**, *31*, 1620.
- [77] V. W. Bergmann, S. A. L. Weber, F. Javier Ramos, M. K. Nazeeruddin, M. Grätzel, D. Li, A. L. Domanski, I. Lieberwirth, S. Ahmad, R. Berger, *Nat. Commun.* **2014**, *5*, 5001.
- [78] V. W. Bergmann, Y. Guo, H. Tanaka, I. M. Hermes, D. Li, A. Klases, S. A. Bretschneider, E. Nakamura, R. Berger, S. A. Weber, *ACS Appl. Mater. Interfaces* **2016**, *8*, 19402.
- [79] G. D. Tainter, M. T. Hörantner, L. M. Pazos-Outón, R. D. Lamboll, H. Åboliņš, T. Leijtens, S. Mahesh, R. H. Friend, H. J. Snaith, H. J. Joyce, F. Deschler, *Joule* **2019**, *3*, 1301.
- [80] R. Ciesielski, F. Schäfer, N. F. Hartmann, N. Giesbrecht, T. Bein, P. Docampo, A. Hartschuh, *ACS Appl. Mater. Interfaces* **2018**, *10*, 7974.
- [81] D. W. DeQuilettes, S. Jariwala, S. Burke, M. E. Ziffer, J. T.-W. Wang, H. J. Snaith, D. S. Ginger, *ACS Nano* **2017**, *11*, 11488.
- [82] Y. Shao, Y. Fang, T. Li, Q. Wang, Q. Dong, Y. Deng, Y. Yuan, H. Wei, M. Wang, A. Gruverman, J. Shield, J. Huang, *Energy Environ. Sci.* **2016**, *9*, 1752.
- [83] K. Fu, C. T. Nelson, M. C. Scott, A. Minor, N. Mathews, L. H. Wong, *Nanoscale* **2016**, *8*, 4181.
- [84] J. Herterich, M. Unmüßig, L. Wagner, G. Loukeris, J. Faisst, M. List, M. Kohlstädt, U. Würfel, *Energy Technol.* **2022**, *10*, 2100868.
- [85] E. R. Schütz, A. Fakharuddin, Y. Yalcinkaya, E. Ochoa-Martinez, S. Bijani, A. R. b. Mohd Yusoff, M. Vasilopoulou, T. Seewald, U. Steiner, S. A. Weber, L. Schmidt-Mende, *APL Mater.* **2022**, *10*, 081110.
- [86] S. Wheeler, F. Deledalle, N. Tokmoldin, T. Kirchartz, J. Nelson, J. R. Durrant, *Phys. Rev. Appl.* **2015**, *4*, 024020.
- [87] N. Courtier, *Phys. Rev. Appl.* **2020**, *14*, 024031.
- [88] C. Chen, Y. Jiang, J. Guo, X. Wu, W. Zhang, S. Wu, X. Gao, X. Hu, Q. Wang, G. Zhou, Y. Chen, J.-M. Liu, K. Kempa, J. Gao, *Adv. Funct. Mater.* **2019**, *29*, 1900557.

**ADVANCED  
OPTICAL  
MATERIALS**

Supporting Information

for *Adv. Optical Mater.*, DOI 10.1002/adom.202301318

Nanoscale Surface Photovoltage Spectroscopy

*Yenal Yalcinkaya, Pascal N. Rohrbeck, Emilia R. Schütz, Azhar Fakharuddin, Lukas Schmidt-Mende and Stefan A.L. Weber\**

# Supporting Information

## Nanoscale Surface Photovoltage Spectroscopy

### S1 Band bending at interfaces

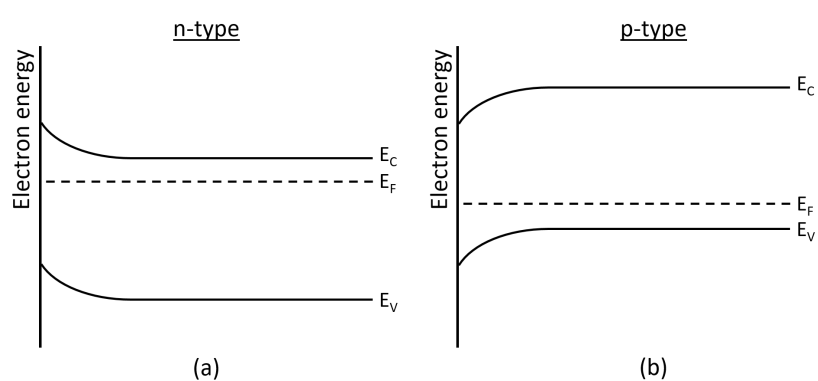


Figure S1: Band bending of (a) n-type and (b) p-type semiconductors.

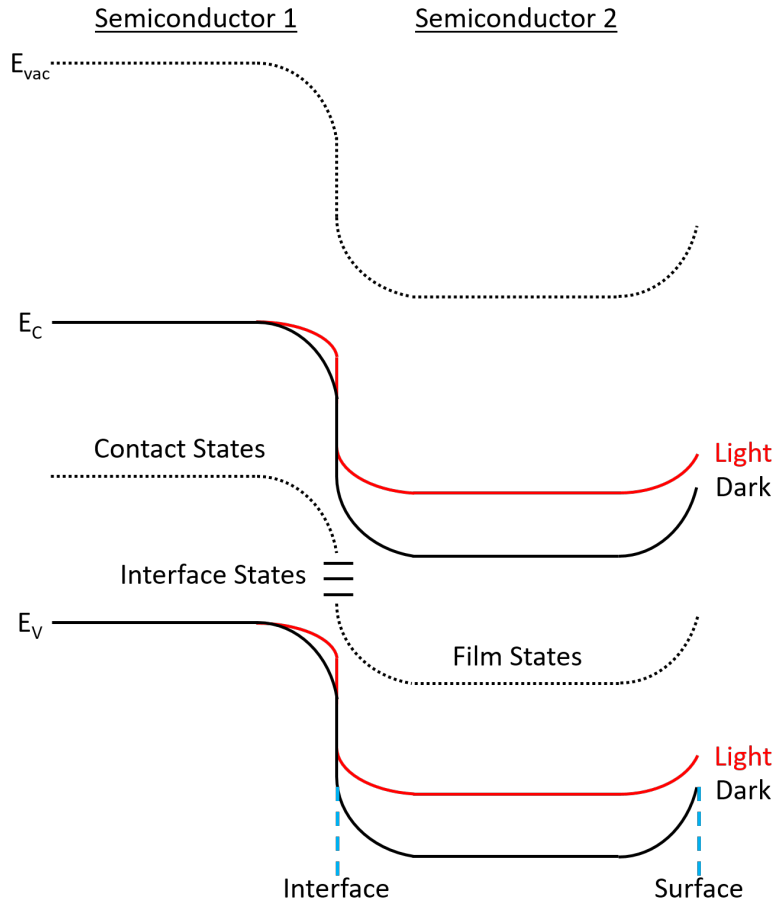


Figure S2: Band alignment illustration for two semiconductor heterojunction.

## S2 Time limitation of the tr-KPFM method

tr-KPFM gives us the ability to map the charge carrier dynamics within the perovskite thin films and locate the defects. This method has a time resolution limit to detect fast changes due to the intrinsic amplitude modulation (AM) detection mode limit which is proportional to  $\frac{Q}{f_0\sigma}$  [1].  $Q$  is the damping factor (also known as  $Q$ -factor) of the oscillation of the cantilever, and  $f_0$  is the mechanical resonance frequency at which the cantilever oscillates.

The  $Q$ -factor of the detection of the electric signal can be calculated by Equation (S8) [2, 3].

$$Q = \frac{f \cdot \sqrt{2}}{FWHM} \quad (S8)$$

$FWHM$  is the full width at half maximum of the resonance peak for the amplitude curve and  $f$  is the resonance frequency.

---

### S3 Fit of tr-KPFM data

The CPD spectra was fitted with an exponential fit of the form seen in Equation (S9).

$$\text{CPD}(t) = \text{CPD}_{\text{eq.}} + A_1 \cdot \exp\left(\frac{x_0 - x}{\tau_1}\right) + A_2 \cdot \exp\left(\frac{x_0 - x}{\tau_2}\right) \quad (\text{S9})$$

$\text{CPD}_{\text{eq.}}$  is the equilibrium CPD value during light state or respectively dark state CPD.  $A_1$  and  $A_2$  are the values how much the CPD is changing with the respective time scales  $\tau_1$  or  $\tau_2$ .

S4 Topography comparison

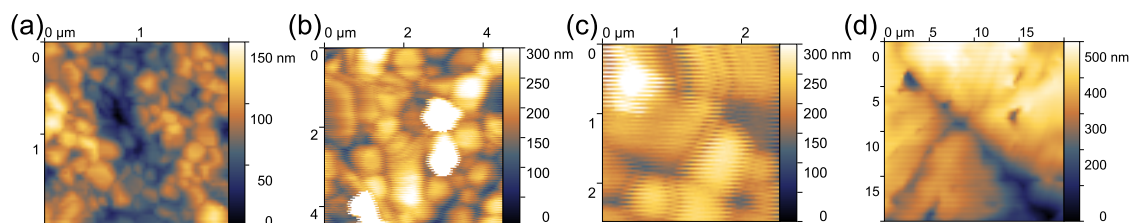


Figure S3: The topography of (a) Reference, (b)  $SA_{\text{Pristine}}$ , (c)  $SA_{\text{Pass}}$ , (d) MA80 sample.

## S5 Further Analysis of the Reference sample

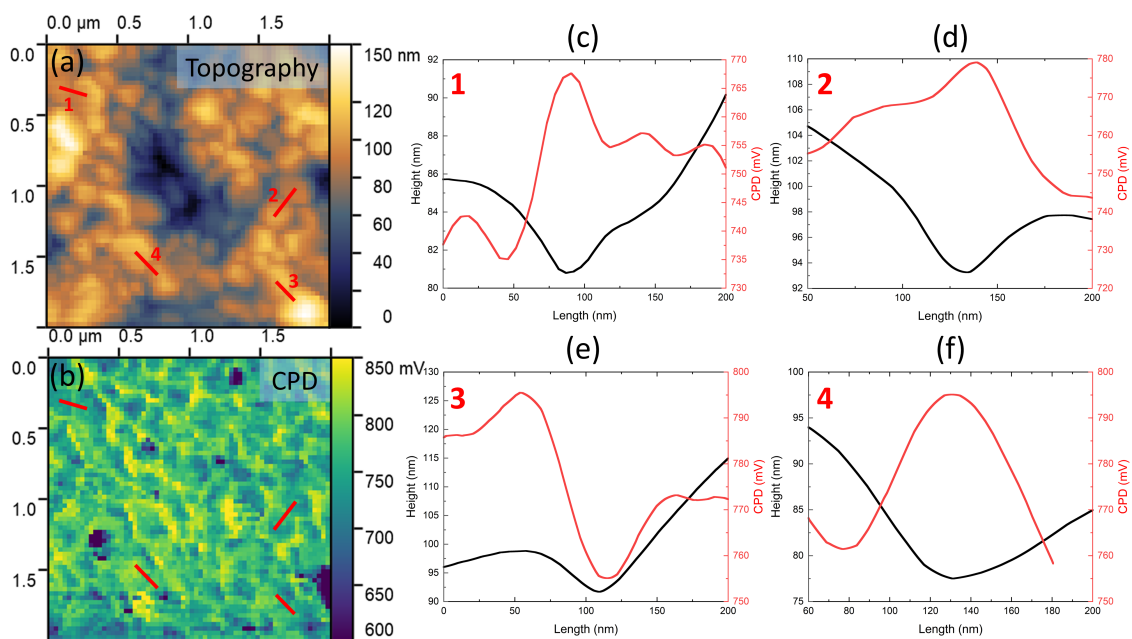


Figure S4: (a) Topography and (b) CPD of reference perovskite sample in dark conditions. (c-f) The profiles showing the changes of topography and CPD at GBs. The drawn profiles enable us to locate the CPD changes accurately.

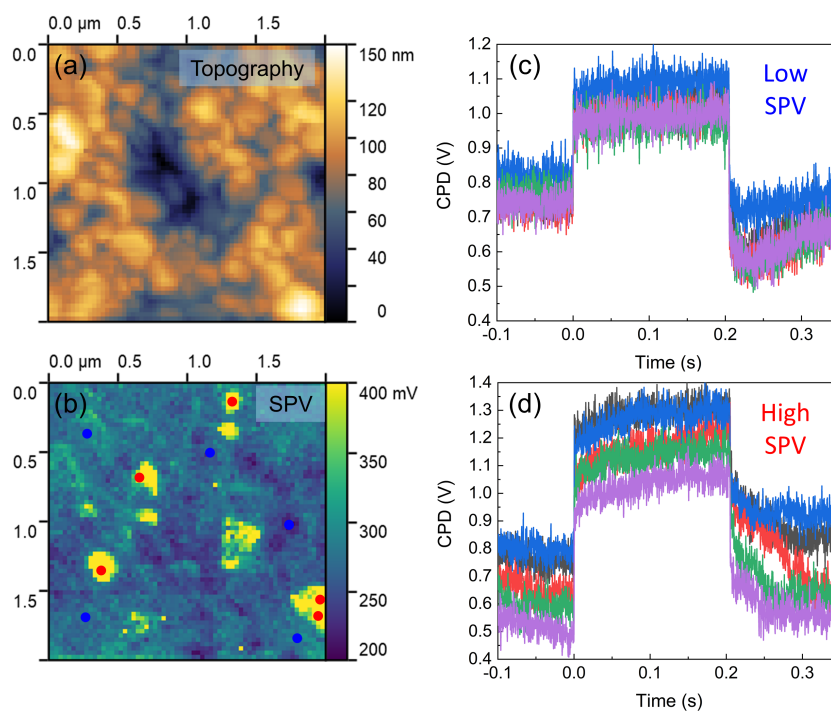


Figure S5: (a) Topography, (b) SPV, and further CPD profiles from (c) low SPV and (d) high SPV areas in the reference sample.

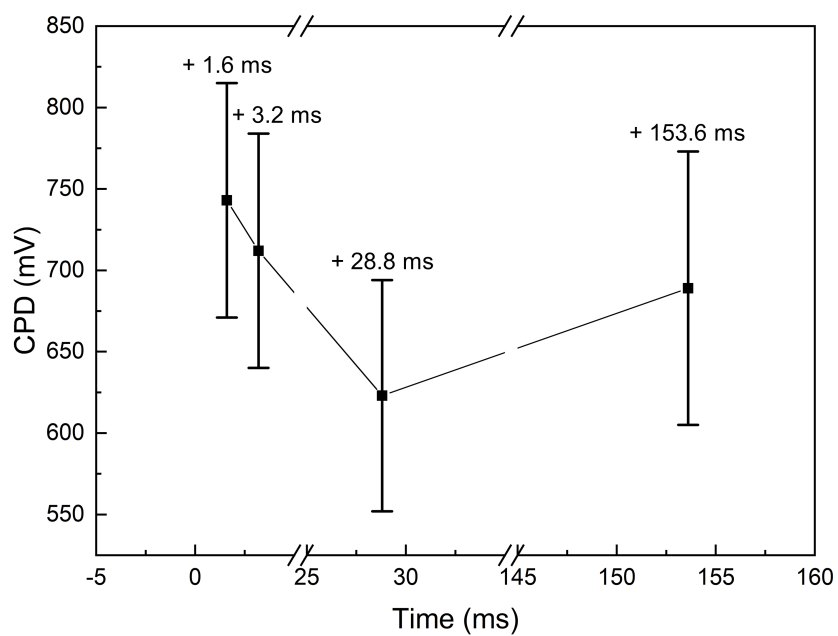


Figure S6: Time dependant CPD evolution of the reference perovskite film after laser was switched off. The average CPD values corresponds to the timeframes from Figure 2(g-j).

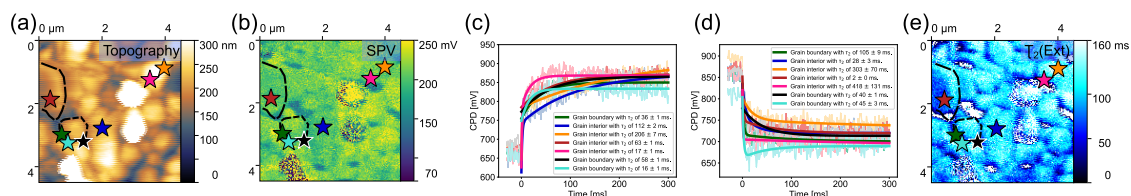
S6 Further Analysis of the pristine solvent annealed sample SA<sub>Pristine</sub>


Figure S7: (a) The topography, (b) SPV map, (c) CPD spectroscopy curves of spots marked in (a), (b) and (e) with calculated slow time scale of electron extraction ( $\tau_2(\text{ext})$ ) in respect to turning on the laser, (d) CPD spectroscopy curves with 30 ms pre-zero data of spots marked in (a), (b) and (e) with calculated slow time scale of electron recombination ( $\tau_2(\text{rec})$ ) in respect to turning off the laser and (e) SPV rise time  $\tau_2(\text{ext})$  map of Cs<sub>0.05</sub>FA<sub>0.8</sub>MA<sub>0.15</sub>PbI<sub>3</sub> perovskite film with 0.95:1.05 A/B cation ratio (SA<sub>Pristine</sub>).

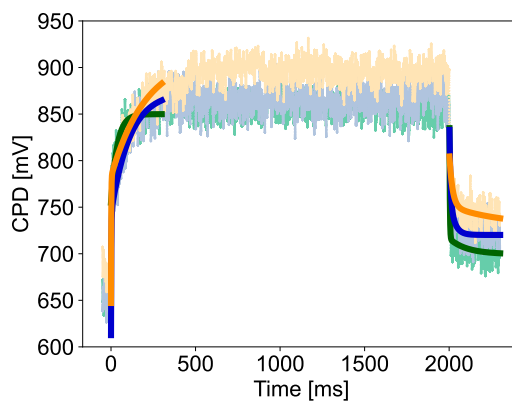


Figure S8: Whole CPD spectroscopy trajectory curves of spots marked in (a), (b) and (e) in Figure 3 with fitted slow time scale of electron extraction ( $\tau_2(\text{ext})$ ) and electron recombination ( $\tau_2(\text{rec})$ ) in respect to turning on the laser of Cs<sub>0.05</sub>FA<sub>0.8</sub>MA<sub>0.15</sub>PbI<sub>3</sub> perovskite film with 0.95:1.05 A/B cation ratio (SA<sub>Pristine</sub>).

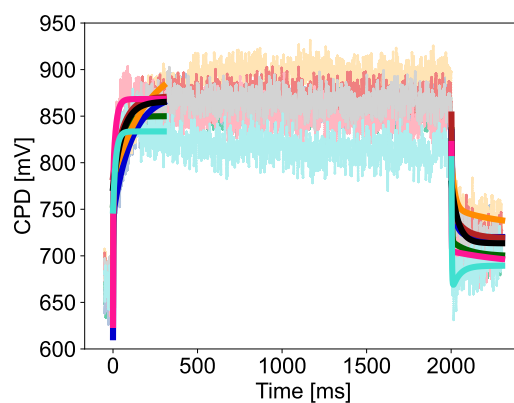


Figure S9: Whole CPD spectroscopy trajectory curves of spots marked in (a), (b) and (e) in Figure S7 with fitted slow time scale of electron extraction ( $\tau_2(\text{ext})$ ) and electron recombination ( $\tau_2(\text{rec})$ ) in respect to turning on the laser of  $\text{Cs}_{0.05}\text{FA}_{0.8}\text{MA}_{0.15}\text{PbI}_3$  perovskite film with 0.95:1.05 A/B cation ratio ( $\text{SA}_{\text{Pristine}}$ ).

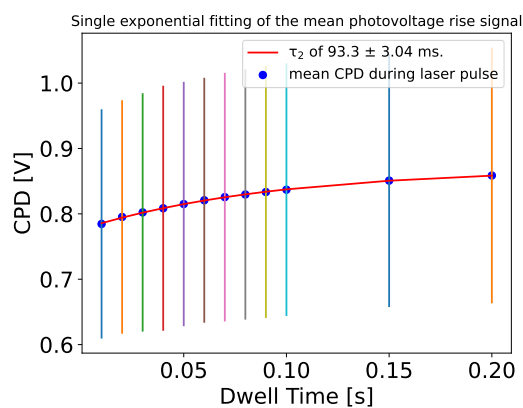


Figure S10: Time dependant CPD evolution of the overall  $\text{SA}_{\text{Pristine}}$  film after laser was switched on. The average CPD values were calculated in 10 ms steps away from each other compared to the switch on of the laser.

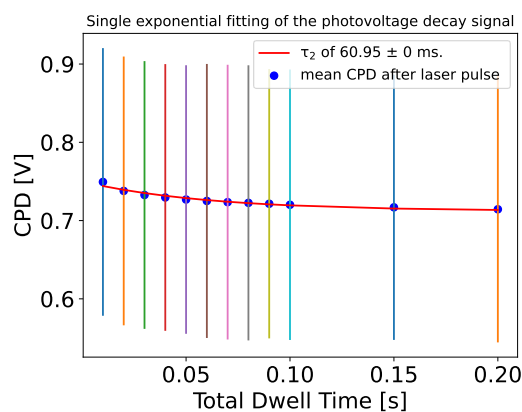


Figure S11: Time dependant CPD evolution of the overall SA<sub>Pristine</sub> film after laser was switched off. The average CPD values were calculated in 10 ms steps away from each other compared to the switch off of the laser.

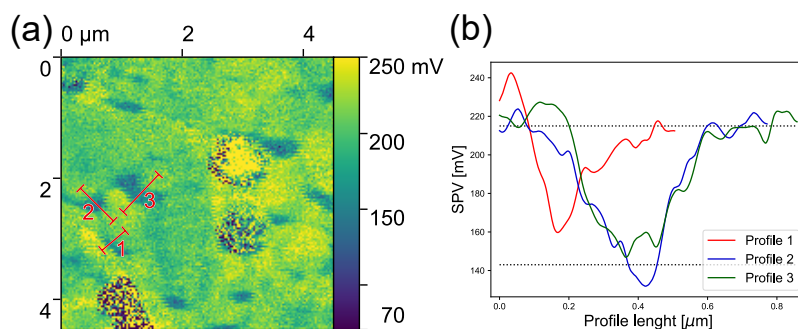


Figure S12: Profile analysis of the SPV picture shown in Figure 3(b). The profile lines averaged over 6 lines marked from 1 - 3 in (a) are shown in (b) with the dotted lines showing the average of SPV value of the grain interior and GB, respectively.

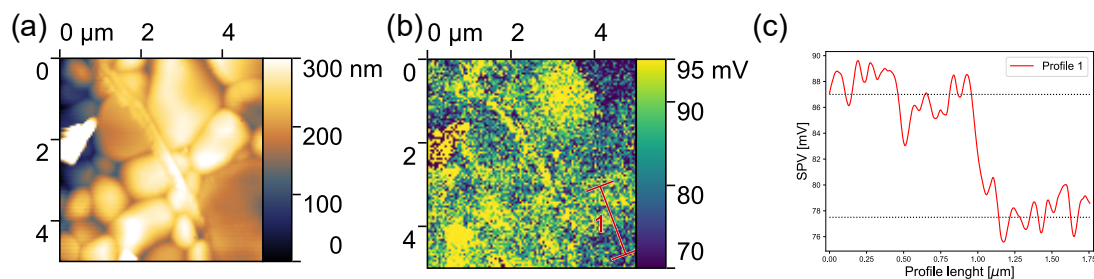


Figure S13: (a) Topography, (b) SPV map and (c) profile analysis of the SPV change within a grain marked in (b) of Cs<sub>0.05</sub>FA<sub>0.8</sub>MA<sub>0.15</sub>PbI<sub>3</sub> perovskite film with 1:1 A/B cation ratio. The profile lines averaged over 14 lines marked in (b) are shown in (c) with the dotted lines showing the average of SPV value along the grain interior of 87 ± 2 mV and 78 ± 2 mV which leads to intragranular difference of 9 ± 2 mV.

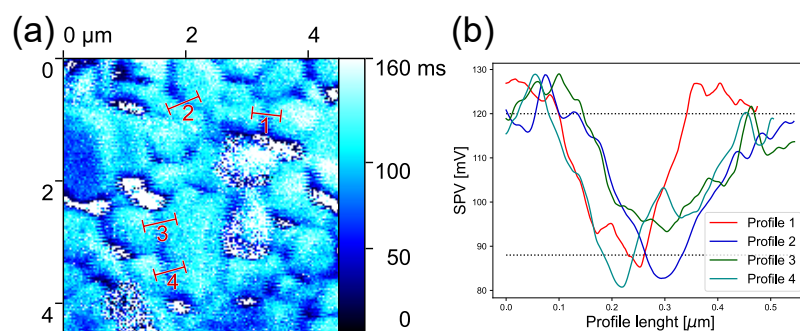


Figure S14: Profile analysis of the  $\tau_2(\text{ext})$  map shown in Figure 3(e). The profile lines averaged over 7 lines marked from 1 - 4 in (a) are shown in (b) with the dotted lines showing the average of  $\tau_2(\text{ext})$  value of  $122 \pm 6$  ms and  $88 \pm 6$  ms the grain interior and grain boundary, respectively. This leads to difference between grain interior and grain boundary of  $32 \pm 6$  ms.

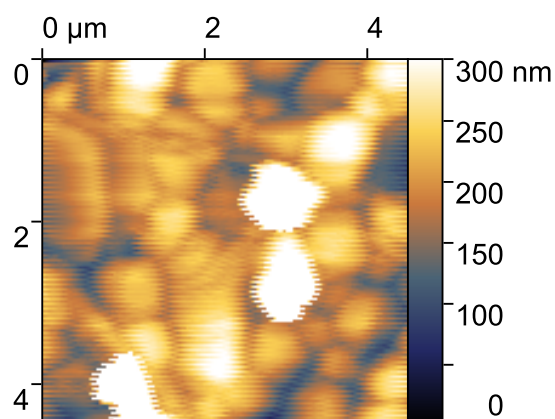


Figure S15: Topography map of  $\text{Cs}_{0.05}\text{FA}_{0.8}\text{MA}_{0.15}\text{PbI}_3$  perovskite film with 0.95:1.05 A/B cation ratio.

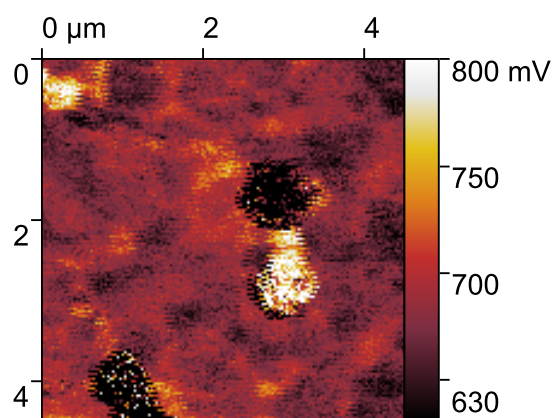


Figure S16: Dark CPD map of  $\text{Cs}_{0.05}\text{FA}_{0.8}\text{MA}_{0.15}\text{PbI}_3$  perovskite film with 0.95:1.05 A/B cation ratio.

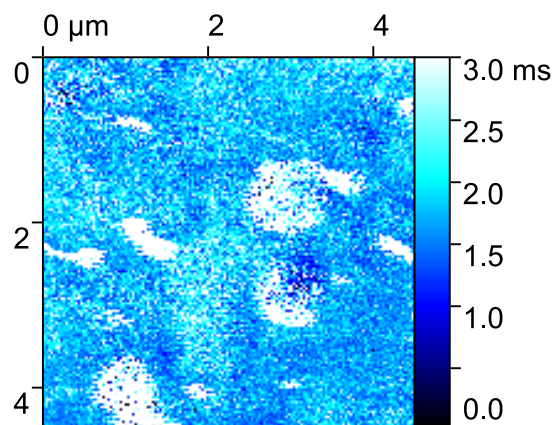


Figure S17: SPV rise time ( $\tau_1(\text{ext})$ ) map of  $\text{Cs}_{0.05}\text{FA}_{0.8}\text{MA}_{0.15}\text{PbI}_3$  perovskite film with 0.95:1.05 A/B cation ratio.

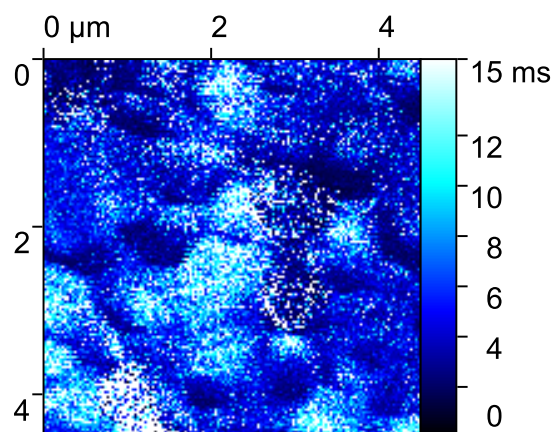


Figure S18: SPV decay time ( $\tau_1(\text{rec})$ ) map of  $\text{Cs}_{0.05}\text{FA}_{0.8}\text{MA}_{0.15}\text{PbI}_3$  perovskite film with 0.95:1.05 A/B cation ratio.

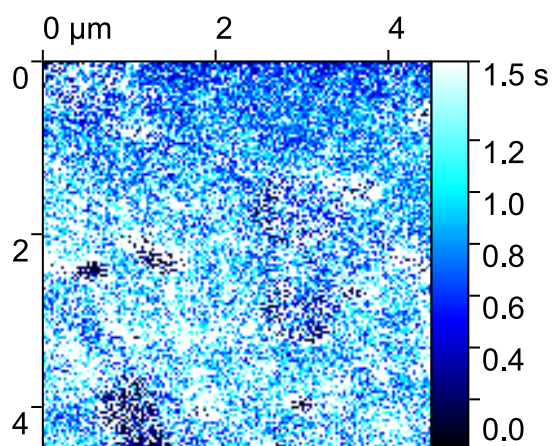


Figure S19: SPV decay time ( $\tau_2(\text{rec})$ ) map of  $\text{Cs}_{0.05}\text{FA}_{0.8}\text{MA}_{0.15}\text{PbI}_3$  perovskite film with 0.95:1.05 A/B cation ratio.

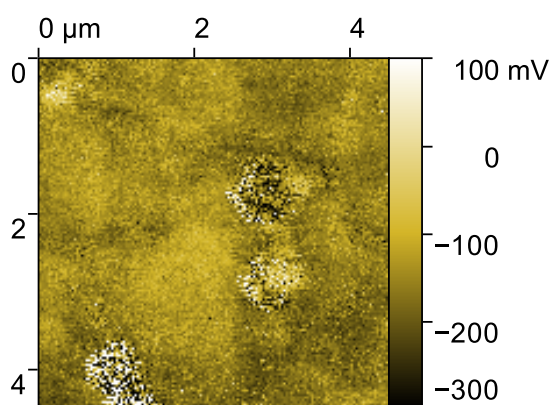


Figure S20: SPV rise amplitude ( $A_1(\text{ext})$ ) map of  $\text{Cs}_{0.05}\text{FA}_{0.8}\text{MA}_{0.15}\text{PbI}_3$  perovskite film with 0.95:1.05 A/B cation ratio.

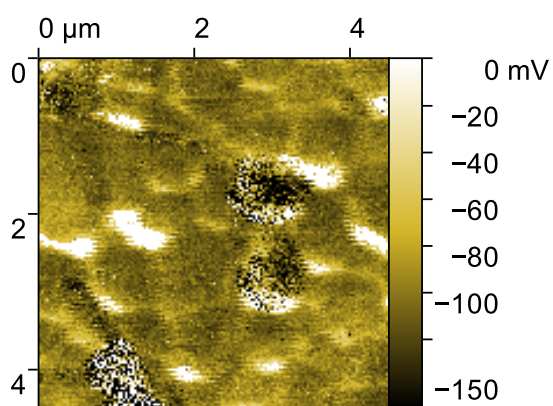


Figure S21: SPV rise amplitude ( $A_2(\text{ext})$ ) map of  $\text{Cs}_{0.05}\text{FA}_{0.8}\text{MA}_{0.15}\text{PbI}_3$  perovskite film with 0.95:1.05 A/B cation ratio.

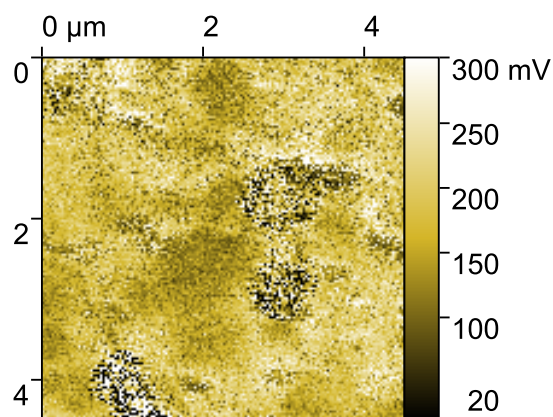


Figure S22: SPV decay amplitude ( $A_1(\text{rec})$ ) map of  $\text{Cs}_{0.05}\text{FA}_{0.8}\text{MA}_{0.15}\text{PbI}_3$  perovskite film with 0.95:1.05 A/B cation ratio.

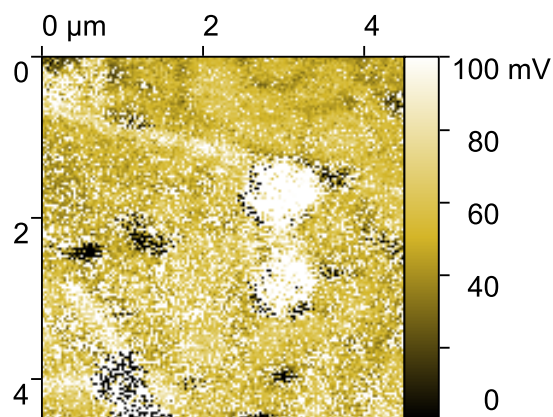


Figure S23: SPV decay amplitude ( $A_2(\text{rec})$ ) map of  $\text{Cs}_{0.05}\text{FA}_{0.8}\text{MA}_{0.15}\text{PbI}_3$  perovskite film with 0.95:1.05 A/B cation ratio.

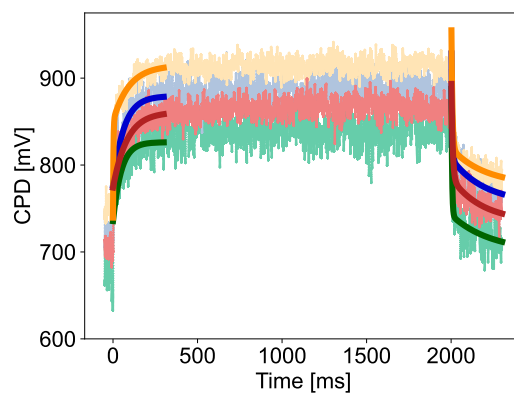
S7 Further Analysis of the passivated solvent annealed sample SA<sub>Pass</sub>

Figure S24: Whole CPD spectroscopy trajectory curves of spots marked in (a), (b) and (e) in Figure 4 with fitted slow time scale of electron extraction ( $\tau_2(\text{ext})$ ) and electron recombination ( $\tau_2(\text{rec})$ ) in respect to turning on the laser of  $\text{Cs}_{0.05}\text{FA}_{0.8}\text{MA}_{0.15}\text{PbI}_3$  perovskite film with surface passivation and 0.95:1.05 A/B cation ratio (SA<sub>Pass</sub>).

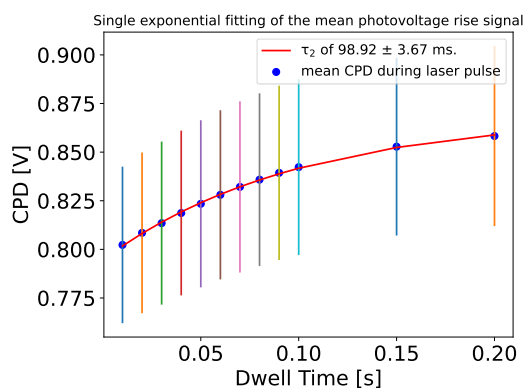


Figure S25: Time dependant CPD evolution of the overall SA<sub>Pass</sub> film after laser was switched on. The average CPD values were calculated in 10ms steps away from each other compared to the switch on of the laser.

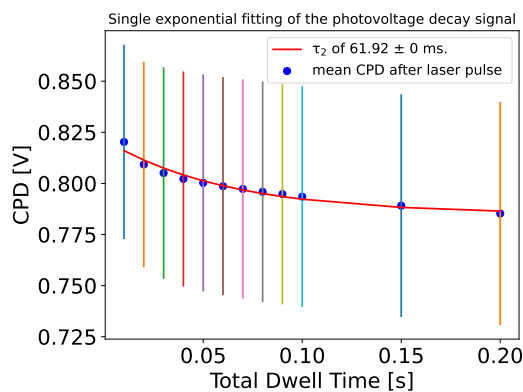


Figure S26: Time dependant CPD evolution of the overall  $\text{SA}_{\text{Pass}}$  film after laser was switched off. The average CPD values were calculated in 10 ms steps away from each other compared to the switch off of the laser.

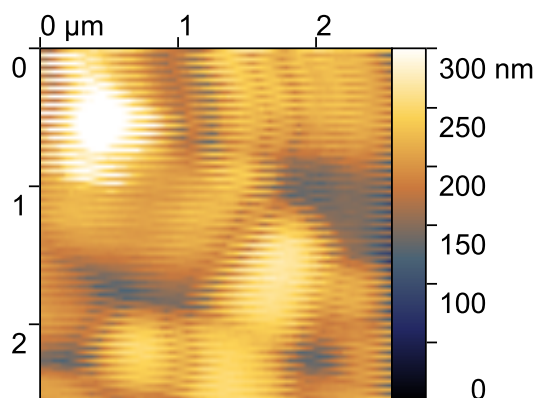


Figure S27: Topography map of PEA-passivated  $\text{Cs}_{0.05}\text{FA}_{0.8}\text{MA}_{0.15}\text{PbI}_3$  perovskite film with 0.95:1.05 A/B cation ratio.

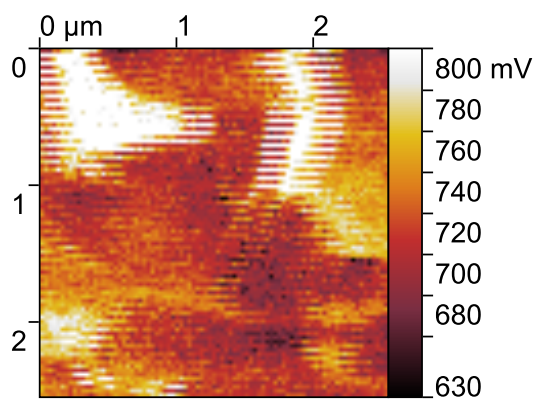


Figure S28: Dark CPD map of PEA-passivated  $\text{Cs}_{0.05}\text{FA}_{0.8}\text{MA}_{0.15}\text{PbI}_3$  perovskite film with 0.95:1.05 A/B cation ratio.

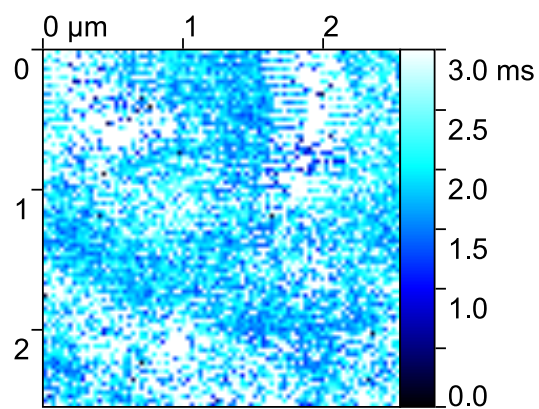


Figure S29: SPV rise time ( $\tau_1(\text{ext})$ ) map of PEA-passivated  $\text{Cs}_{0.05}\text{FA}_{0.8}\text{MA}_{0.15}\text{PbI}_3$  perovskite film with 0.95:1.05 A/B cation ratio.

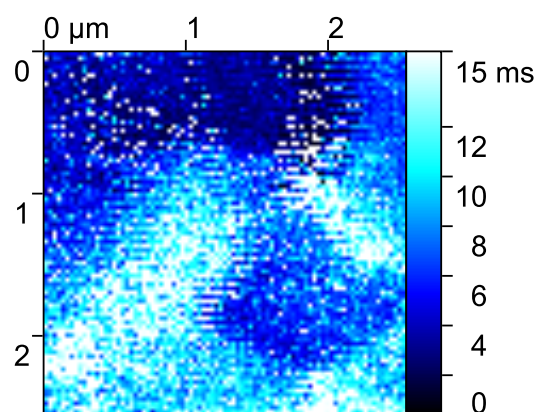


Figure S30: SPV decay time ( $\tau_1(\text{rec})$ ) map of PEA-passivated  $\text{Cs}_{0.05}\text{FA}_{0.8}\text{MA}_{0.15}\text{PbI}_3$  perovskite film with 0.95:1.05 A/B cation ratio.

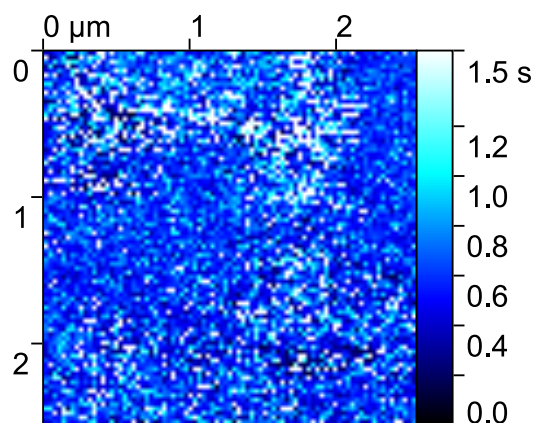


Figure S31: SPV decay time ( $\tau_2(\text{rec})$ ) map of PEA-passivated  $\text{Cs}_{0.05}\text{FA}_{0.8}\text{MA}_{0.15}\text{PbI}_3$  perovskite film with 0.95:1.05 A/B cation ratio.

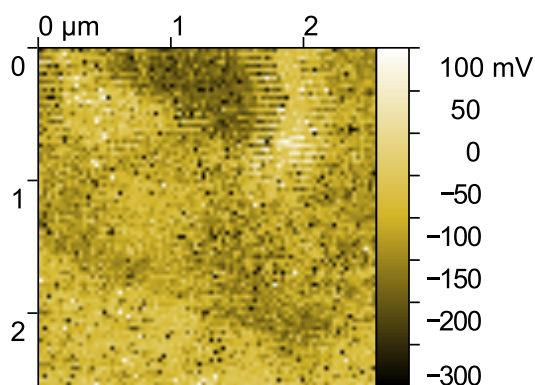


Figure S32: SPV rise amplitude ( $A_1(\text{ext})$ ) map of PEA-passivated  $\text{Cs}_{0.05}\text{FA}_{0.8}\text{MA}_{0.15}\text{PbI}_3$  perovskite film with 0.95:1.05 A/B cation ratio.

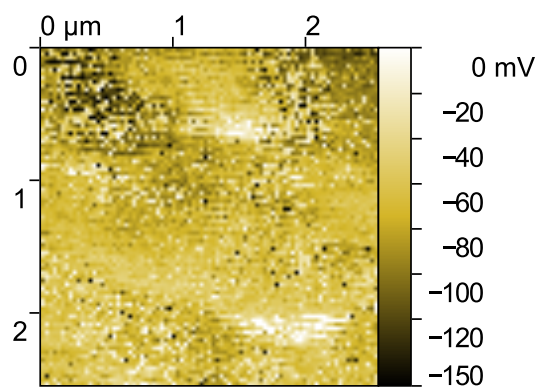


Figure S33: SPV rise amplitude ( $A_2(\text{ext})$ ) map of PEA-passivated  $\text{Cs}_{0.05}\text{FA}_{0.8}\text{MA}_{0.15}\text{PbI}_3$  perovskite film with 0.95:1.05 A/B cation ratio.

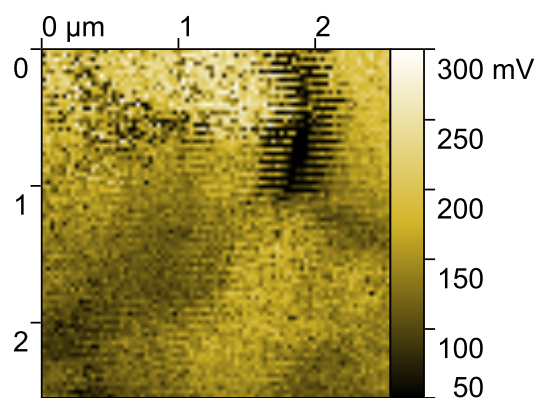


Figure S34: SPV decay amplitude ( $A_1(\text{rec})$ ) map of PEA-passivated  $\text{Cs}_{0.05}\text{FA}_{0.8}\text{MA}_{0.15}\text{PbI}_3$  perovskite film with 0.95:1.05 A/B cation ratio.

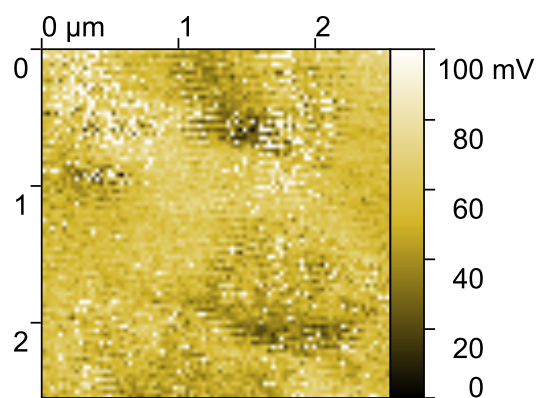


Figure S35: SPV decay amplitude ( $A_2(\text{rec})$ ) map of PEA-passivated  $\text{Cs}_{0.05}\text{FA}_{0.8}\text{MA}_{0.15}\text{PbI}_3$  perovskite film with 0.95:1.05 A/B cation ratio.

## S8 Further Analysis of the MA80 sample

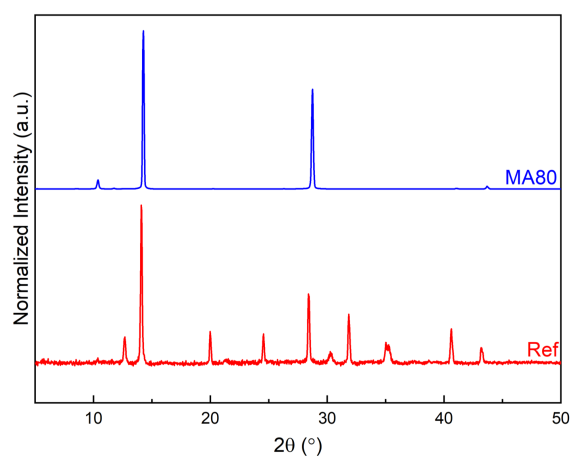


Figure S36: XRD patterns of reference and MA80 perovskite films.

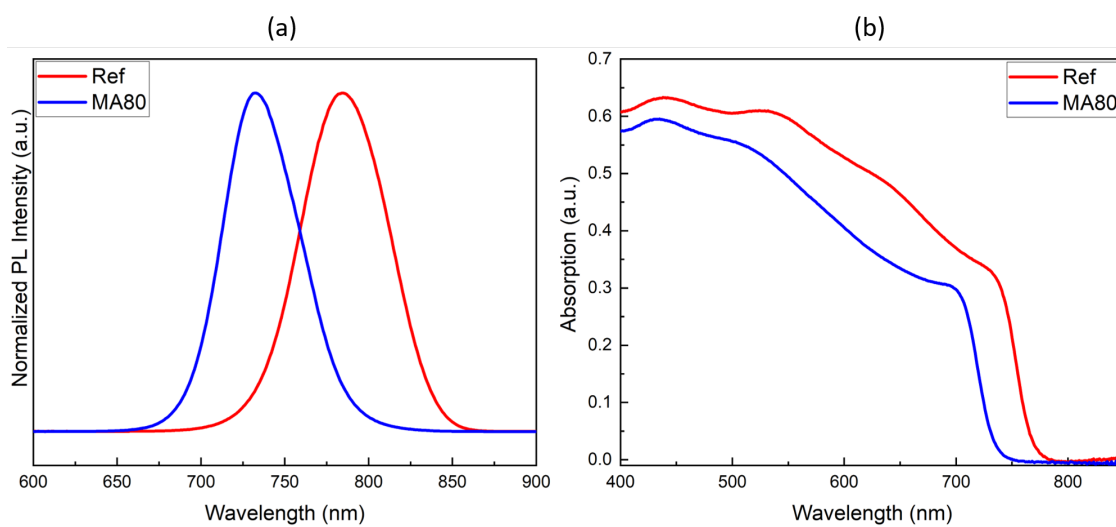


Figure S37: Photoluminescence and absorption spectra of reference and MA80 perovskite films.

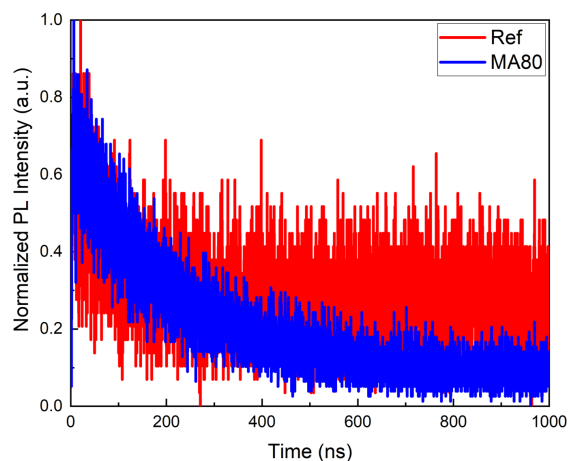


Figure S38: Time-resolved photoluminescence spectra of reference and MA80 perovskite films.

## S9 Long-time measurements

Long-time measurements of the trajectory is shown in **Figure S39**.

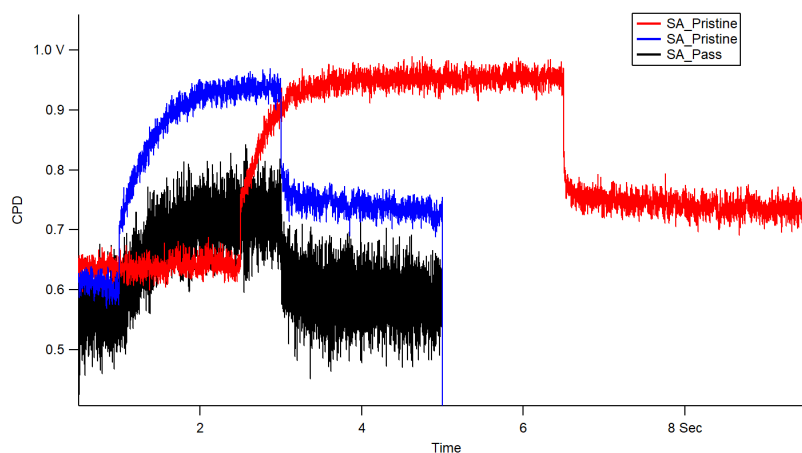


Figure S39: Whole CPD spectroscopy trajectory curves before the respective force maps of  $SA_{\text{Pristine}}$  (red and blue curve) and  $SA_{\text{Pass}}$  (black curve) of  $Cs_{0.05}FA_{0.8}MA_{0.15}PbI_3$  perovskite films with 0.95:1.05 A/B cation ratio.

In Figure S39 the long-time CPD change due to the illumination according to Figure 1 shows that the  $CPD_{\text{dark}}$  is not the same compared to the CPD value directly after the light pulse. Interestingly, this is independent of the dwell time (see red and blue curve in Figure S39). Moreover, the red and blue curve was measured right after each other. So, after applying the erase pulse to the red curve the  $CPD_{\text{dark}}$  value of the blue curve is very comparable to the  $CPD_{\text{dark}}$  value of the red curve. This difference of the CPD value is not visible in the  $SA_{\text{Pass}}$  sample (see black curve in Figure S39).

## S10 Nanoscale Ideality Factor Mapping

The intensity of the laser is controlled by the analog voltage that is provided by the controller of our AFM and the analog voltage dependence of the laser intensity is measured to be linear. This relation gives us the ramp up parameters of the laser intensity. By using this we can plot the SPV against the logarithmic light intensity and obtain the  $n_{id,l}$  which reveals the information about the recombination behavior of the sample. Since the recombination mechanisms are closely related to the trap density within the perovskite films, mapping  $n_{id,l}$  this way enables us to map the defects on a nanoscale.

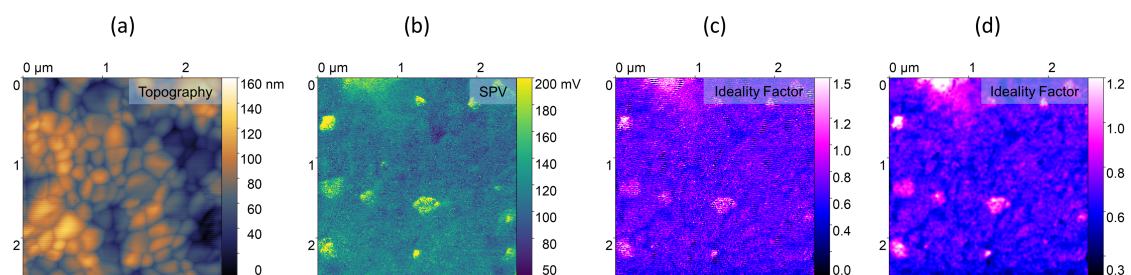


Figure S40: (a) Topography, (b) SPV, (c)  $n_{id,l}$ , and (d) 1x1 pixel Gaussian filtered  $n_{id,l}$  maps of reference perovskite film. The map contains 200x200 pixels.

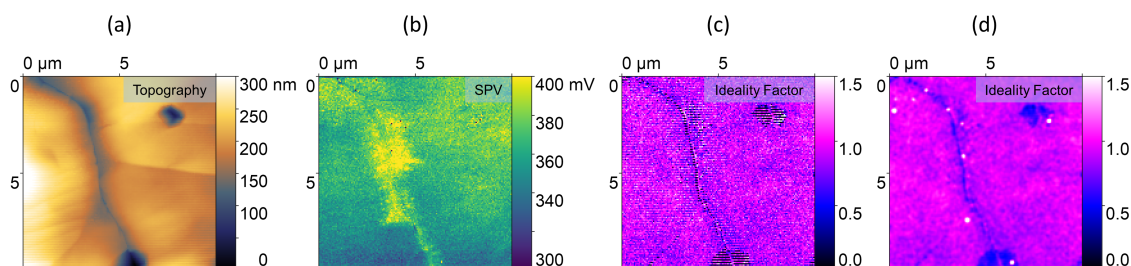


Figure S41: (a) Topography, (b) SPV, (c)  $n_{id,l}$ , and (d) 1x1 pixel Gaussian filtered  $n_{id,l}$  maps of MA80 film. The map contains 150x150 pixels.

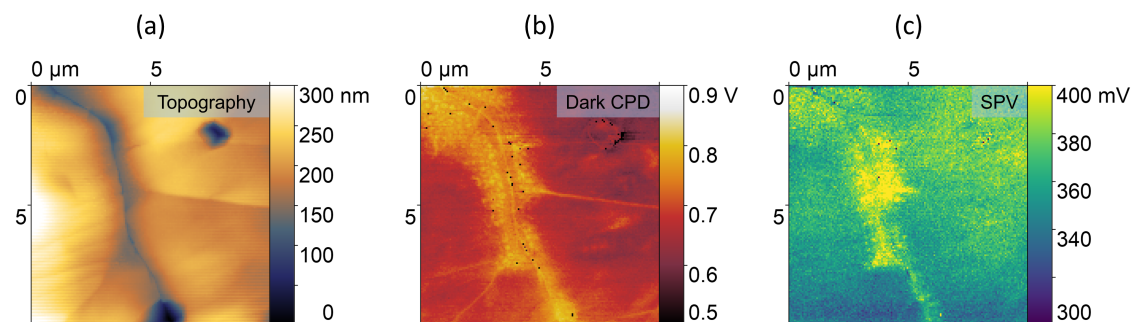


Figure S42: (a) Topography, (b) dark CPD, and (c) SPV maps of MA80 film.

### Bibliography

- [1] B. Voigtländer, *Scanning Probe Microscopy*, NanoScience and Technology. Springer Berlin Heidelberg, Berlin, Heidelberg, **2015**.
- [2] A. Varol, I. Gunev, B. Orun, C. Basdogan, *Nanotechnology* **2008**, *19*, 7 075503.
- [3] A. Perez-Cruz, A. Dominguez-Gonzalez, I. Stiharu, R. A. Osornio-Rios, *Ultramicroscopy* **2012**, *115* 61.





---

# 5 Nanoscale capacitance spectroscopy based on multi-frequency electrostatic force microscopy

Reproduced via CC BY-NC 4.0 from Ref. 'Rohrbeck, P. N.; Cavar, L. D.; Weber, F.; Reichel, P. G.; Niebling, M.; Weber, S. A. L. *Beilstein J. Nanotechnol.* **2025**, *16*, 637–651. DOI: 10.3762/bjnano.16.49.<sup>99</sup> with permission from the Beilstein-Institut.

In this paper, we introduce a new multi-frequency-EFM method named multi-frequency heterodyne Electrostatic Force Microscopy (MFH-EFM) to show an easy method that combines the superior lateral resolution and stray capacitance suppression of heterodyne EFM with the possibility of measuring at arbitrary frequencies by means of a multi-frequency excitation.

Pascal Niko Rohrbeck is first author of this paper. Pascal Niko Rohrbeck measured and analyzed all the data, developed the concept and wrote the manuscript. The project as well as the manuscript was overseen and corrected by Stefan A. L. Weber.



## Nanoscale capacitance spectroscopy based on multifrequency electrostatic force microscopy

Pascal N. Rohrbeck<sup>1,2</sup>, Lukas D. Cavar<sup>1,3</sup>, Franjo Weber<sup>1,2</sup>, Peter G. Reichel<sup>1</sup>,  
Mara Niebling<sup>1,3</sup> and Stefan A. L. Weber<sup>\*1,3,4</sup>

### Full Research Paper

Open Access

#### Address:

<sup>1</sup>Max Planck Institute for Polymer Research, Ackermannweg 10, 55128 Mainz, Germany, <sup>2</sup>Department of Chemistry, University of Mainz, Duesbergweg 10-14, 55128 Mainz, Germany, <sup>3</sup>Department of Physics, University of Mainz, Staudingerweg 7, 55128 Mainz, Germany and <sup>4</sup>Institute for Photovoltaics, University of Stuttgart, Pfaffenwaldring 47, 70569 Stuttgart, Germany

#### Email:

Stefan A. L. Weber<sup>\*</sup> - Stefan.Weber@ipv.uni-stuttgart.de

\* Corresponding author

#### Keywords:

atomic force microscopy; capacitance gradients; dielectric constant; dielectric spectroscopy; heterodyne frequency mixing; Kelvin probe force microscopy; multifrequency AFM; quantitative force spectroscopy; scanning capacitance force microscopy

*Beilstein J. Nanotechnol.* **2025**, *16*, 637–651.  
<https://doi.org/10.3762/bjnano.16.49>

Received: 20 December 2024

Accepted: 25 April 2025

Published: 08 May 2025

This article is part of the thematic issue "At the cutting edge of atomic force microscopy".

Associate Editor: T. Glatzel



© 2025 Rohrbeck et al.; licensee Beilstein-Institut.  
License and terms: see end of document.

### Abstract

We present multifrequency heterodyne electrostatic force microscopy (MFH-EFM) as a novel electrostatic force microscopy method for nanoscale capacitance characterization at arbitrary frequencies above the second cantilever resonance. Besides a high spatial resolution, the key advantage of the multifrequency approach of MFH-EFM is that it measures the second-order capacitance gradient at almost arbitrary frequencies, enabling the measurement of the local dielectric function over a wide range of frequencies. We demonstrate the reliable operation of MFH-EFM using standard atomic force microscopy equipment plus an external lock-in amplifier up to a frequency of 5 MHz, which can in principle be extended to gigahertz frequencies and beyond. Our results show a significant reduction of signal background from long-range electrostatic interactions, resulting in highly localized measurements. Combined with refined tip-sample capacitance models, MFH-EFM will enhance the precision of quantitative studies on dielectric effects in nanoscale systems across materials science, biology, and nanotechnology, complementing established methods in the field.

### Introduction

Technological progress in fields including electronics, energy storage, photonics, and biomedical devices would not have been possible without the development of new materials. Progress in

these areas requires a detailed understanding of material properties, particularly at the nanoscale, where phenomena such as quantum confinement, interface effects, and defect dynamics

play a critical role. Innovations in characterization techniques have enabled researchers to explore these properties with unprecedented precision, paving the way for the design of materials with tailored functionalities [1-6].

Dielectric properties are fundamental for understanding the behavior and performance of various material systems, as they directly influence charge storage, polarization, and energy dissipation mechanisms. For instance, in microelectronic devices, high- $\kappa$  dielectric materials such as  $\text{HfO}_2$  and  $\text{ZrO}_2$  are critical for minimizing leakage currents and enhancing gate capacitance in transistors [7-9]. In energy storage systems, the dielectric constants of polymer-ceramic composites determine the efficiency and reliability of capacitors [10]. Similarly, in next-generation photovoltaic devices, the dielectric properties of absorber layers, such as lead-halide perovskites, affect carrier recombination and electric field distribution, thereby influencing power conversion efficiency [11].

At the nanoscale, the importance of dielectric properties becomes even more pronounced. Many advanced materials exhibit nanoscale structural heterogeneity, where quantum confinement, phase composition, and interfacial effects cause significant deviations in dielectric behavior compared to bulk materials [12,13]. These nanoscale variations influence key properties such as charge transport, polarization dynamics, and defect distributions, directly impacting the performance of microelectronic and energy systems [14,15]. Understanding these effects requires correlating nanoscale dielectric properties with structural and morphological features.

Scanning probe techniques have revolutionized nanoscale material characterization. Since the invention of scanning tunneling microscopy (STM) [16] and atomic force microscopy (AFM) [17], various electric force-based methods, called electrostatic force microscopy (EFM) methods, have emerged to study materials such as perovskite solar cells [18-20] and Li-ion batteries [21-23]. AFM enables simultaneous acquisition of topographic and electronic data by applying AC or DC voltages across the tip-sample gap, allowing for the detection of capacitive forces [24,25] or contact potential difference (CPD) [18]. Its exceptional spatial resolution, ranging from sub-micrometer [24,26] to atomic scales [27,28], makes AFM a powerful tool for nanoscale analysis.

Scanning probe-based capacitance mapping methods can be divided into two categories: Methods measuring the tip-sample capacitance directly are referred to as scanning capacitance microscopy (SCM) [29-54], whereas methods measuring the capacitive tip-sample force are referred to as scanning capacitance force microscopy (SCFM) [24,25,55-73]. Compared to

optical ellipsometry or reflectance spectroscopy, SCM and SCFM can map surface properties such as film thickness [35,39] and dielectric constants [35,74], with superior spatial resolution. However, in particular, SCM techniques face limitations due to nonlocal stray capacitances [40] from cantilever, tip cone, and the electrical connection, which hamper precise measurements and decrease resolution [55,61].

The advantage of SCFM methods is that capacitive forces depend on the first- or higher-order capacitance gradients with respect to the tip-sample distance, automatically canceling out the background capacitance caused by electrical connections and – to some degree – by the cantilever and the tip cone [24,25,55-73]. For example, Cherniavskaya et al. and Crider et al. laid the groundwork for EFM-based nanoscale dielectric measurements such as SCFM [68,69]. Generally, EFM methods using higher-order capacitance gradients exhibit superior lateral resolution [75].

An interesting extension of SCM and SCFM is the possibility to vary the electrostatic excitation frequency, enabling broadband dielectric nanospectroscopy experiments. While it is relatively straightforward to measure the frequency-dependent capacitance in SCM [29,54,76,77], force-based SCFM measurements are usually coupled to the cantilever resonances, limiting the available frequency space. Single-pass second-harmonic EFM in the attractive regime has been used to detect the cantilever response at the second harmonic of the electrostatic force ( $2\omega$ ) [68-70,72] generated when  $\Delta\omega_e$  spans the range from 8 kHz to 2 MHz [70]. SCFM in the megahertz regime has been implemented [70,71] as well as a heterodyne-based EFM mode [59,72,73,78]. By using a low-frequency modulation of a high-frequency electrostatic drive, the response can be picked up either via a frequency shift or by an electrostatic response at one of the cantilever's resonance frequencies. Thus, the dielectric response can be studied at almost arbitrary frequencies. Using this method, Gramse et al. have demonstrated broadband spectroscopy of dielectric layers in air [72] and water [59].

Building on this idea, we propose a novel, multifrequency AFM-based method for nanoscale capacitance characterization at arbitrary frequencies above the second cantilever resonance. Our approach measures the second capacitance gradient, enhancing localization by minimizing stray capacitance contributions [65]. This method enables high-frequency capacitance gradient spectroscopy without requiring specialized equipment beyond a lock-in amplifier (LIA).

The following sections introduce the theoretical framework of multifrequency EFM, demonstrate its resolution enhancement experimentally, and validate its spectroscopic capabilities by

measuring nanoscale dielectric properties of microfabricated SiO<sub>2</sub> samples. Finally, we compare its performance with established techniques through capacitance imaging of a model microcapacitor system and a perfluoroalkyl-alkane F(CF<sub>2</sub>)<sub>14</sub>(CH<sub>2</sub>)<sub>20</sub>H (F14H20) sample.

## Theory

### Multifrequency electrostatic force microscopy

The electrostatic force  $F_{ES}$  between tip and sample can be understood in terms of the gradient of the energy,  $W_C$ , stored in the tip–sample capacitor  $C$  with respect to the tip–sample separation  $z$ , as given by

$$F_{ES} = \frac{\partial W_C}{\partial z} = \frac{1}{2} \cdot \frac{\partial C}{\partial z} \cdot V_{\text{tip-sample}}^2, \quad (1)$$

where  $V_{\text{tip-sample}}$  specifies the electrical voltage across the tip–sample gap. In conventional EFM with single-frequency excitation,  $V_{\text{tip-sample}}$  is given by Equation 2 [18]:

$$V_{ES} = V_{DC} - V_{CPD} + V_{AC} \cdot \sin(\omega_e \cdot t), \quad (2)$$

with  $V_{DC}$  the DC voltage offset applied to the tip,  $V_{AC}$  the AC voltage amplitude with the frequency  $\omega_{AC}$  at a certain time  $t$  and  $V_{CPD}$  the CPD, which corresponds to the difference in tip and sample work function [18]. Inserting Equation 2 into Equation 1, we obtain the following expression:

$$F_{ES} = \frac{1}{2} \frac{\partial C}{\partial z} \left( (V_{DC} - V_{CPD})^2 + \frac{V_{AC}^2}{2} \right) \quad (3)$$

$$+ \frac{\partial C}{\partial z} (V_{DC} - V_{CPD}) V_{AC} \sin(\omega_e t) \quad (4)$$

$$+ \frac{\partial C}{\partial z} \frac{V_{AC}^2}{4} \cos(2\omega_e t). \quad (5)$$

Alongside a static component in Equation 3, the electrostatic force has periodic time-dependent components at frequencies  $\omega_e$  and  $2\omega_e$ , which correspond to Equation 4 and Equation 5, respectively. In the case of an oscillating AFM tip, the tip–sample distance  $z$  and, thereby, the tip–sample capacitance and its gradients are changing periodically. This periodic fluctuation of the capacitance gradient  $C'(t) = \frac{\partial C}{\partial z}(t)$  adds an additional dynamic component to Equations Equation 3–Equation 5. Using a Fourier expansion for the capacitance gradient  $C'(t) = \frac{\partial C}{\partial z}(t)$  yields [18]:

$$C'(t) = C'(z_0) + C''(z_0) \cdot A_m \cdot \cos(\omega_m t) + \dots \quad (6)$$

By inserting Equation 6 into Equations Equation 3–Equation 5, we find that frequency mixing between  $C'(t)$  and the electrostatic excitation leads to sidebands at frequencies  $\omega_{SB,1} = (\omega_m \pm \omega_{AC})$  and  $\omega_{SB,2} = (\omega_m \pm 2\omega_{AC})$  besides the mechanical oscillation at  $\omega_m$ [18]. The amplitude of the first harmonic frequency components is used in conventional amplitude modulation (AM) and sideband or heterodyne Kelvin probe force microscopy (KPFM) [18,26,79]. The second harmonic signals are proportional to the local capacitance gradients, providing information about the local tip–sample capacitance. To ensure a sufficient signal-to-noise ratio, the resulting frequencies should coincide with one of the cantilever’s resonance frequencies, limiting the choice of excitation frequencies.

We can avoid this limitation by using a multifrequency excitation approach. With a double-frequency excitation, we can write the tip–sample voltage as

$$V_{\text{tip-sample}} = V_{AC,1} \cdot \sin(\omega_{e,1} t) + V_{AC,2} \cdot \sin(\omega_{e,2} t). \quad (7)$$

In the case of two drives with identical amplitude  $V_{AC,1} = V_{AC,2} = \frac{V_{AC}}{2}$ , Equation 7 can be rearranged as

$$V_{\text{tip-sample}} = V_{AC} \cdot \sin\left(\frac{\omega_{e,1} - \omega_{e,2}}{2} t\right) \cdot \sin\left(\frac{\omega_{e,1} + \omega_{e,2}}{2} t\right). \quad (8)$$

Thus, the waveform can be viewed as a high-frequency oscillation at  $(\omega_{e,1} + \omega_{e,2})/2 = \omega_{\text{mod}}/2$  with a low-frequency amplitude modulation at frequency  $(\omega_{e,1} - \omega_{e,2})/2 = \Delta\omega_e/2$ . This effect is also known as “beating” and is utilized in the AFM context for example in intermodulation AFM [80-83].

By inserting Equation 6 and Equation 8 in Equations Equation 3–Equation 5, we obtain the full expression for the electrostatic force. Here, we will focus on the DC force component in Equation 3 and set  $V_{DC} - V_{CPD} = \Delta$ :

$$F_{DC} = \frac{1}{2} (C' + C'' A_m \sin(\omega_m t) + \dots) \cdot \left[ \Delta^2 + \frac{V_{AC}^2}{2} \sin^2\left(\frac{\Delta\omega_e}{2} t\right) \right] \quad (9)$$

$$= \frac{1}{2} C' \left[ \Delta^2 + \frac{V_{AC}^2}{4} \right] + \frac{1}{8} C'' V_{AC}^2 \cos(\Delta\omega_e t) \quad (10)$$

$$+\frac{1}{2}C''A_m\left[\Delta^2+\frac{V_{AC}^2}{4}\right]\sin(\omega_m t)+\frac{1}{16}C''A_mV_{AC}^2\sin[(\omega_m\pm\Delta\omega_e)t]. \quad (11)$$

In addition to a static force term identical to Equation 3, Equation 10 contains a term proportional to  $C''$  at frequency  $2\omega_{\text{mod}} = \Delta\omega_e$ . This force has been used for AM-based dielectric spectroscopy [63,69,74,84–88]. The second term, Equation 11, contains a force component at the mechanical drive frequency  $\omega_m$  and at a sideband frequency  $\omega_m \pm 2\omega_{\text{mod}}$ . The latter one is independent of the local CPD, making it interesting for dielectric measurements. As the magnitude of this force component depends on  $C''$ , we can expect a superior lateral resolution through a reduction of long-range force contributions from tip cone and cantilever. As in the case of conventional EFM, signal-to-noise is greatly improved by choosing  $\Delta\omega_e$  such that one of the induced sidebands falls on one of the cantilever's mechanical resonances. We call this method multifrequency heterodyne electrostatic force microscopy (MFH-EFM).

To calculate the second capacitance gradient, we need to calculate the electrostatic force from the detected amplitude signal,  $A_{\text{det}}$ , taking into account the cantilever's frequency-dependent spring constant or transfer function,  $k(\omega)$ :

$$\frac{\partial^2 C}{\partial z^2} = C'' = \frac{16A_{\text{det}} \cdot k(\omega)}{A_m \cdot V_{AC}^2}. \quad (12)$$

Interestingly, the forces in Equation 11 only depend on the frequency difference,  $\Delta\omega_e$ , of the electrical drive frequencies.

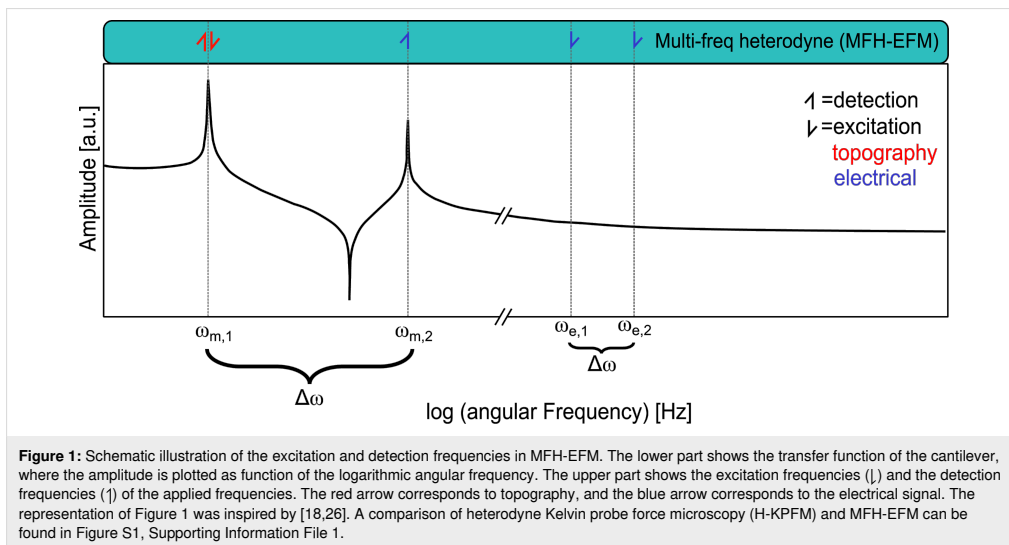
Thus, the experiments can be performed at almost arbitrarily high AC frequencies. The lower limit for the frequency range is given by the second resonance of the cantilever. Towards higher frequencies, the impedance of the electrical connection will introduce a damping of the excitation signal that has to be considered in Equation 12. By using appropriate means of coupling the electrical excitation into the tip-sample gap, experiments at microwave or even at optical frequencies are possible. In our setup, the two excitation frequencies can be varied in frequency from  $\approx 600$  kHz up to at least 50 MHz, limited by the bandwidth of the LIA. To reach a nanoscale-sensitive measurement of the dielectric constant in media besides air, a detection at higher excitation frequencies in the megahertz regime is strictly necessary [59].

The indirect detection of local capacitance variations by means of an electrostatic force has the advantage that it does not require additional devices for the measurement except for the LIA similar to that in the work of Gramse and colleagues [56]. Nevertheless, quantifying the total tip-sample capacitance will require varying the distance, for example, by force-distance spectroscopy.

## Methods

### Multifrequency heterodyne electrostatic force microscopy to measure the second capacitive gradient $C''$

We perform MFH-EFM using a conductive AFM cantilever in tapping mode with a mechanical drive near the fundamental



cantilever eigenmode  $\omega_{m,1}$  with a mechanical amplitude  $A_m$ . Additionally, we apply two high-frequency electrical excitations of identical magnitude ( $V_{AC,1} = V_{AC,2}$ ) at the frequencies  $\omega_{e,1}$  and  $\omega_{e,2}$  (see Equation 7). A schematic of the excitation frequencies is shown in Figure 1.

We select the excitation frequencies at the  $n$ -th and the  $(n + 1)$ -th multiple of the frequency gap  $\Delta\omega = (\omega_{m,2} - \omega_{m,1})$  (see Figure 1). Note that the use of integer multiples is a technical limitation coming from our LIA. In principle, any combination of frequencies with  $\Delta\omega = (\omega_{m,2} - \omega_{m,1})$  would work. We then use lock-in detection to measure the induced mechanical excitation exactly at the second mechanical resonance of the cantilever ( $\omega_{m,2}$ ).

#### Single-frequency electrostatic force microscopy to measure the first capacitive gradient $C'$

To obtain a quantitative comparison of the signal contributions to the signals based on the first and the second capacitance gradient, we performed single-frequency excitation EFM (SF-EFM) measurements as comparison to the multifrequency approach described above. In the fixed-frequency configuration, we use lock-in amplification to detect the second harmonic force component at  $2\omega_e$  induced by a single-frequency ( $\omega_E$ ) stimulus (see Equation 5).

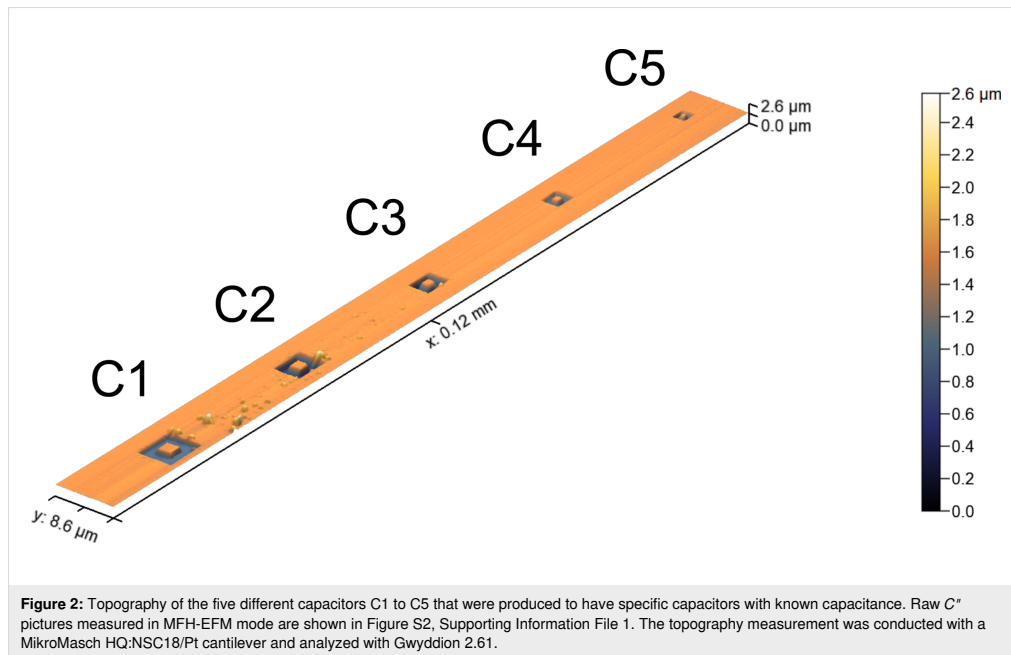
To enhance the signal, we select  $\omega_E$  such that  $2\omega_E$  coincides with the second resonance of the cantilever ( $2\omega_E = \omega_{m,2}$ ). We connect the numerical value of the capacitance gradient to the detected amplitude using the cantilever's frequency-dependent transfer function or spring constant  $k(\omega)$  by

$$\frac{\partial C}{\partial z} = C' = \frac{4A_{\text{det}} \cdot k(\omega)}{V_{AC}^2}. \quad (13)$$

For the variable-frequency detection of  $C'$ , we apply two AC voltages of the same magnitude ( $V_{AC,1} = V_{AC,2}$ ) at frequencies  $n$  and  $(n + 1)$  times the second resonance frequency  $\omega_{m,2}$ . According to Equation 10, this will excite an oscillation at  $\omega_{m,2}$  with an amplitude proportional to  $C'$ .

#### Silicon microcapacitors

To generate structures with a defined dielectric response, we prepared a series of microcapacitors. We used these structures to compare the  $C'$  and  $C''$  distance dependencies from several force–distance curves with model calculations using tip–sample models from the literature, as well as for dielectric nanospectroscopy experiments. The microcapacitors were produced by focused ion beam (FIB) milling on a silicon wafer with a 300 nm layer of  $\text{SiO}_2$  and a 14 nm sputtered layer of Pt on it (Figure 2).

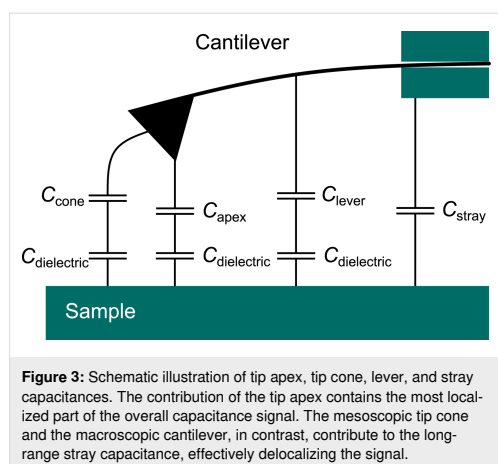


## Results and Discussion

To investigate whether the  $C''$ -sensitive detection leads to an improved spatial resolution of MFH-EFM as compared to conventional methods, we calculate the distance dependence of the first- and second-order capacitance gradients in an ideal cantilever. We compare our calculations to experimentally obtained force–distance curves. We then show the first practical examples of high-frequency capacitive spectra obtained by this method on etched SiO<sub>2</sub> microcapacitors, along with high-resolution high-frequency capacitance images obtained over self-assembled molecular F14H20.

### Tip–sample capacitance

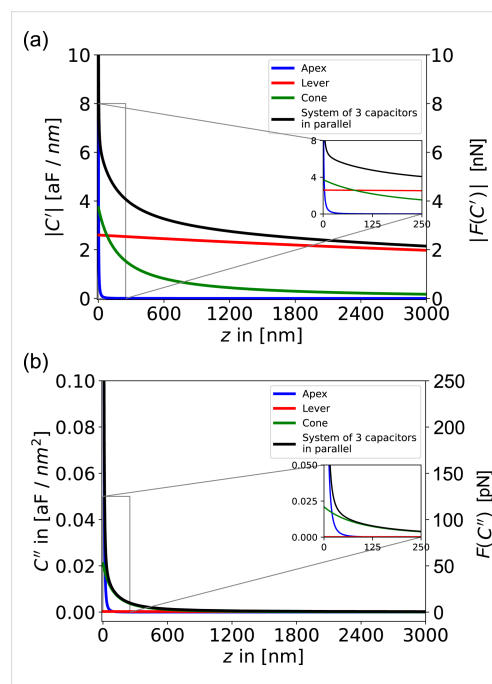
The total capacitance between sample and cantilever consists of contributions from tip apex, tip cone, lever, and some additional stray capacitance caused by the signal cables in the AFM head (Figure 3). In the case of a dielectric sample, the tip-, apex- and lever-surface capacitors are connected in series with capacitors formed by the sample dielectric layer. The exact configuration for these capacitors depends strongly on the local electric field distribution around tip apex, tip cone, and cantilever. Whereas the apex capacitance contains the desired local information, the stray capacitance from cone, lever, and cables produces a background signal that effectively reduces the lateral resolution of the local capacitance measurement. Practically, these signal contributions can be discerned by their respective distance dependence.



To further investigate this distance dependence, we compare experimental force–distance spectra to analytical and numeric models from the literature. In particular, we combine the models for the apex contribution of Hudlet et al. [89] with the cone and lever contributions from Colchero and colleagues

[90,91]. The full equations for the force together with the resulting capacitance used here are given in the Appendix section (see Equations Equation 16–Equation 21 and Figure 10 below).

In Figure 4, we compare the respective contributions to the first and second capacitance gradients together with the corresponding electrostatic forces during a typical AFM experiment as functions of tip–sample distance  $z$ . For the force calculations, we used Equation 12 together with the parameters of a regular EFM cantilever (NuNano SPARK 70 Pt) and an electrical drive of  $V = 2$  V and a mechanical amplitude of  $A_m = 10$  nm. Comparing the graphs, we can immediately see that the total  $C'$  signal retains a significant long-range contribution even at a tip–sample separation of 3000 nm (Figure 4a). In contrast, the  $C''$  signal drops more rapidly over a short distance  $z$  (Figure 4b), indicating a reduced influence of long-range contributions to the force signals.



A measure of how much the signal is disturbed by non-local long-range contributions is the apex contribution to the total signal at a given distance  $z$ . At a typical tip–sample separation of 10 nm, the apex signal makes up more than 82% of the complete  $C''$  signal, while the apex contribution to the first capacitance gradient only makes up less than 10% of the total  $C'$  signal. In closer proximity of 1 nm distance to the sample, the apex contribution to the  $C''$  signal increases to 99.8%, whereas the  $C'$  signal still contains a significant amount of non-local signal contributions with 62% apex vs 38% cone and lever signal. Another way to quantify the “locality” of a force signal is to investigate the tip–sample separation at which the tip apex contribution surpasses the lever-plus-cone contributions within Figure 4. This is true in Figure 4a for distances smaller than  $\approx 3$  nm, while in Figure 4b, this is the case even for distances smaller than  $\approx 20$  nm. Comparing the absolute values of the forces, however, we see that MFH-EFM yields much weaker forces: At a tip–sample distance of 10 nm, the AM-based operation leads to a force of  $F_{ES}(C') = 6.7$  nN, as compared to  $F_{ES}(C'') = 280$  pN for MFH-EFM. Hence, the resulting electrostatic force and, thereby, the expected force is by more than a factor of 24 lower for MFH-EFM. Thus, the improved lateral resolution comes at the price of a reduced signal-to-noise ratio.

To reproduce these findings experimentally, we performed force–distance spectroscopy on the etched microcapacitors shown in Figure 2. The resulting curves of the  $C'$  and  $C''$  signals qualitatively reproduced the simulation results (Figure 5). Whereas the  $C''$  signal only emerged from the noise at distances

of less than 500 nm, the  $C'$  signal shows a monotonic decrease over the full 3  $\mu\text{m}$  of vertical travel. Compared to the simulations, the experimental  $C'$  signal shows a slower decrease, indicating a stronger influence from the tip cone. The direct comparison of the model and the data of the second and first capacitance gradients can be found in Figure S16 and Figure S17, Supporting Information File 1, respectively. These results clearly show that the MFH-EFM method produced an electrostatic force signal that is highly local with suppressed stray contributions from cone and lever.

### Dielectric nanospectroscopy

The advantage of the multifrequency excitation approach of MFH-EFM is that we can choose arbitrary frequencies above the detection frequency for the electrostatic excitation. As the tip–sample capacitance is influenced by the dielectric properties of the material in the tip–sample gap (see Figure 3), the frequency-dependent electrostatic force represents the local dielectric function. To demonstrate the feasibility of dielectric nanospectroscopy, we performed MFH-EFM frequency spectroscopy at three different locations on the microcapacitor sample. The first spectrum was recorded on one of the microcapacitors ( $C3$ , see Figure 2). Then, we measured in one of the FIB-etched trenches around the capacitors. Here, we assume that the bare silicon surface is covered by a thin native oxide layer (Si). Last, we measured on a particle of unknown origin (Dirt, visible in Figure 2). The frequency sweeps were performed by keeping the tip position and amplitude fixed, varying the two heterodyne excitation frequencies while keeping their separation

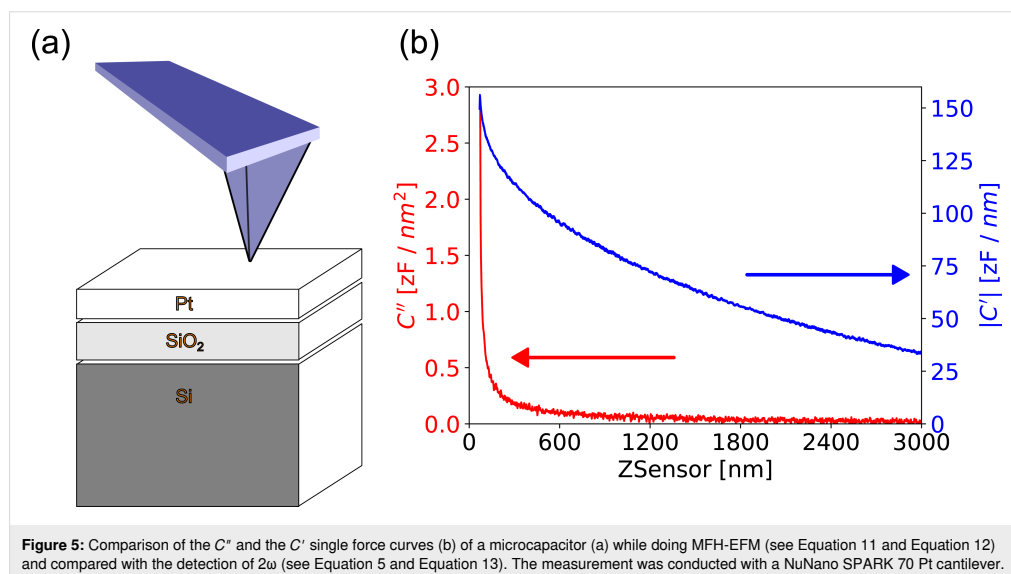


**Figure 5:** Comparison of the  $C''$  and the  $C'$  single force curves (b) of a microcapacitor (a) while doing MFH-EFM (see Equation 11 and Equation 12) and compared with the detection of  $2\omega$  (see Equation 5 and Equation 13). The measurement was conducted with a NuNano SPARK 70 Pt cantilever.

fixed, and recording the resulting excitation amplitude at the second mechanical resonance. All spectra were normalized against a reference spectrum recorded on the bare substrate far away from the capacitors to compensate any frequency response arising from the stray capacitance in the signal paths and cantilever. The electrostatic signal of the capacitor C3 showed a drop at around 2 MHz in Figure 6. When considering the capacitance of C3 of  $183 \pm 1$  aF and the drop-off frequency  $\omega_d$  of the capacitance at 1.7 MHz, we can calculate the resistance  $R$  via the RC time ( $RC = 1/\omega_d$ ) as  $R \approx 3200$  M $\Omega$ . This value is much smaller compared to the calculated value of the resistance of SiO<sub>2</sub>, which is  $25 \cdot 10^{21}$   $\Omega$ , taking into account the electrical resistivity of silicon dioxide of  $\rho_{\text{SiO}_2} = 25 \cdot 10^{16}$   $\Omega\text{m}$  [92] and a thickness of the SiO<sub>2</sub> layer of 300 nm on an area of 9  $\mu\text{m}^2$ . The observed discrepancy may be attributed to the increased conductivity of the microcapacitors, which is a result of the incorporation of Ga<sup>+</sup> ions into the SiO<sub>2</sub> layer.

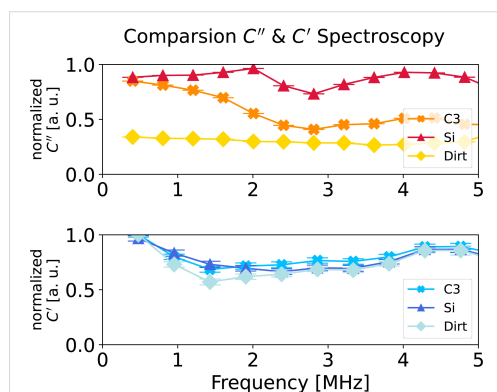


**Figure 6:** Comparison of the normalized  $C''$  (red colors on top) and normalized  $C'$  (blue colors at the bottom) frequency sweep on one of the capacitors (C3, see Figure 2, cross symbols), on milled silicon (Si, triangle symbols), and on a particle of unknown origin (Dirt, square symbols). This experiment was conducted with a MikroMasch HQ:NSC18/Pt cantilever. The non-normalized data, as well as normalized data over a wider frequency range, can be viewed in Figures S3–S6 and S9–S12, Supporting Information File 1.

The  $C''$  signal of the bare Si was stable over the whole range of excitation frequencies and only dropped at a much higher frequency around 24 MHz (see Figure S5, Supporting Information File 1). The dielectric response of the undefined particle was significantly lower compared to the response of the capacitor structures. In the frequency response, we found little to no signal response, even at low excitation frequency. A rise of the signal at around 6 MHz could be observed in all the  $C''$  signals at that frequency (see Figure S3, Supporting Information File 1), which we attribute to a capacitive singularity in the electrical connection to the sample. We observed a similar be-

havior in the frequency range between 5 and 10 MHz and around 17 MHz. We want to point out that we used standard AFM equipment with no special means to control the impedance of the electrical connections. To obtain more trustworthy data in the frequency range above 5 MHz, specialized sample and cantilever holders with coaxial electric connections will be required.

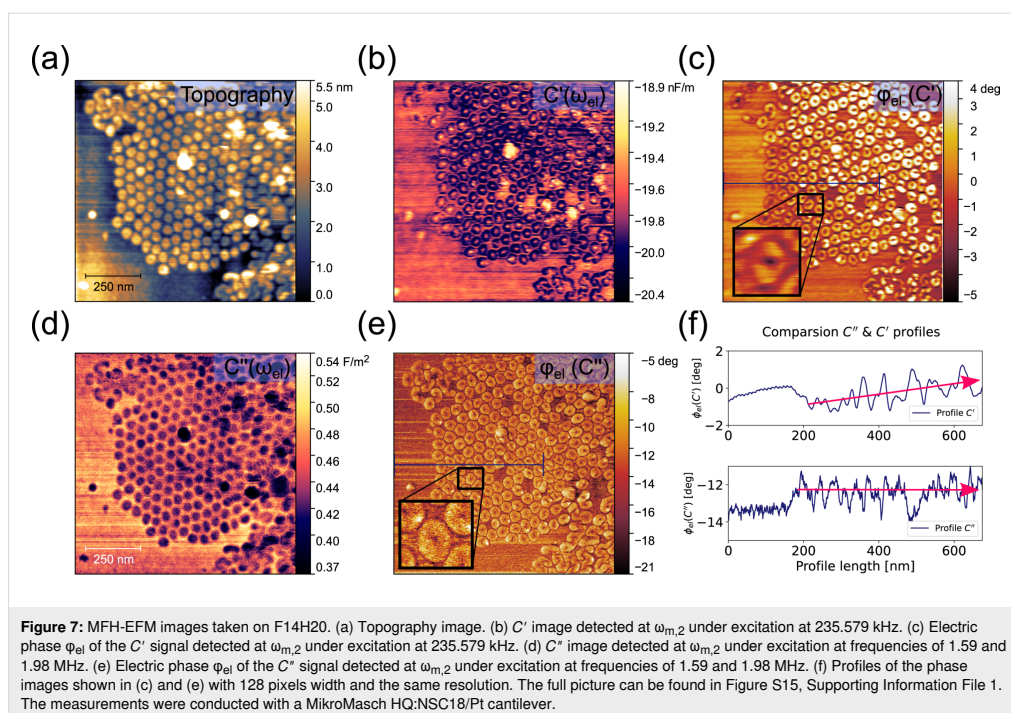
To compare these results with the conventional AM-based EFM approach, we repeated the spectroscopy experiments for the  $C'$  signal based on the second term in Equation 10 (Figure 6, non-normalized data in Figures S9–S11, Supporting Information File 1). In comparison to the MFH-EFM data, the  $C'$  frequency sweep looked very similar on the different structures. We think that this reduction in contrast is caused by the stronger influence of the long-range interactions from tip cone and cantilever in the  $C'$  signal. Thus, the overall impact of the local surface dielectric properties under the tip apex is reduced as compared to the impact of the dielectric properties probed by tip cone and cantilever (see Figure 3).

### Imaging $C'$ versus $C''$

To demonstrate the capabilities of MFH-EFM as an imaging method, we performed experiments on self-assembled nanostructures consisting of the amphiphilic molecule F14H20 (Figure 7). F14H20 exhibits a strong dipole moment of 3.1 D oriented along the chains consisting of fluorinated and hydrogenated parts [93], leading to a strong nanoscale contrast in the dielectric signal.

On the silicon substrate, F14H20 formed groups of spherical particles with a diameter of  $40 \pm 5$  nm (Figure 7a) [94,95]. Simultaneously with the topography, we recorded the  $C''$  amplitude and phase at electrical excitation frequencies of 1.59 and 1.98 MHz. In the dielectric spectroscopy images, we see a sharp contrast between the F14H20 particles and the silicon substrate, both in  $C'$  (Figure 7b,c) and  $C''$  (Figure 7d,e). Within all images, the particles exhibit a lower amplitude signal than the surroundings [95]. The latter is formed by a thin fluoroalkane layer with molecules lying along the sample surface [95]. The contrast within the particles correlates with variations of dielectric permittivity, and the latter is related to averaged dipole values [95]. Similar work [96] indicated that the response increases with an increase of sample permittivity [95,96]. We measured a CPD difference between Si and F14H20 of  $-0.72 \pm 0.08$  V (see Figure S15, Supporting Information File 1), which is close to the literature value of  $-0.8$  V [97].

Interestingly, the image of the  $C'$  signal (Figure 7c,e) showed a more blurry structure (compare the insets in Figure 7b,c). Another effect that can be observed in the  $C'$  phase images is



that the individual contrast on the particles changes when going towards the center of the particle agglomerate (upper graph in Figure 7f). While there is only a very shallow contrast for the first two to five particles, both the contrast and the baseline signals increased towards the center of the agglomerate. In the  $C'$  images, however, the dielectric contrast remained the same across the particle agglomerate, demonstrating once more that MFH-EFM provides more local information and is less affected by long-range electrostatic effects.

## Conclusion

We have presented a novel method for high-resolution nanoscale capacitance characterization based on multifrequency electrostatic force microscopy, complementing established methods in the field. The key advantage of the multifrequency approach of MFH-EFM is that it allows for measurements of higher-order tip-sample capacitance gradients at almost arbitrary frequencies above the second cantilever resonance, enabling the measurement of the local dielectric function over a wide range of frequencies. In comparison to many existing SCM operation modes, MFH-EFM leads to a significant reduction of signal background, which results in higher locality of the measurements with less cross talk. This is due to the fact that the second capacitance gradient is less affected by long-range

interactions, such as those from tip cone and lever. We demonstrate the reliable operation using standard AFM equipment together with an external LIA up to a frequency of 5 MHz. At higher frequencies (up to 50 MHz in our case), the signals were dominated by impedance effects from the signal connections. Thus, to move towards reliable measurements at higher frequencies, specialized high-frequency equipment with coaxial signal connections will be required.

Our analytical simulations of the distance-dependent tip-sample capacitance showed that current models are not able to fully simulate the experimental data. Thus, to enable quantitative measurements of the tip-sample capacitance, further measures such as improved tip-sample models or full numerical simulations will be required. Here, the suppression of long-range electrostatic interactions in MFH-EFM could simplify the simulations. Thus, MFH-EFM could further improve quantitative studies on dielectric effects in nanoscale systems across materials science, biology, and nanotechnology.

## Experimental Polymer blend samples

We used F14H20 samples that we bought from SPM Labs LLC, Tempe, AZ, USA.

### Microcapacitors

Si wafers “CZ” were bought from “Si-Mat” with a diameter of 150 mm, (100) surface orientation, a thickness of  $675 \pm 20 \mu\text{m}$ , a resistivity of  $1.5\text{--}4.0 \Omega\text{cm}$ , and with p-type doping with B atoms. These wafers were thermally oxidized with 300 nm  $\text{SiO}_2$ . A compact coating unit 010/LV with the sputter head SP010 was used to sputter 14 nm of Pt on top of the wafer. The microcapacitors were then milled out of the surface using a FEI Nova600 Nanolab FIB apparatus with a dual  $\text{Ga}^+$  ion beam.

### Multifrequency heterodyne electrostatic force microscopy

MFH-EFM was measured on an Oxford Instruments/Asylum Research MFP-3D Infinity AFM in a nitrogen glovebox (level of humidity below 0.3%, level of oxygen below 0.1%). The typical resonance frequency of the Pt/Ir-coated conductive cantilevers (NuNano SPARK-150Pt and MikroMasch HQ:NSC18/Pt) was  $\approx 75 \text{ kHz}$ ; the levers had a spring constant of  $2\text{--}3 \text{ N}\cdot\text{m}^{-1}$ , a tip radius of 18 nm, and a tip height of  $10\text{--}18 \mu\text{m}$ . The topography feedback measurements were performed with amplitude modulation on the first eigenmode  $\omega_{m,1}$ , and the oscillation amplitude was kept to  $70\text{--}90 \text{ nm}$  for all measurements. The force spectroscopy measurements were done with a  $z$  rate of 0.2 Hz and a force distance of  $8 \mu\text{m}$  for all samples.

We used a Zurich Instruments HF2 LIA for all experiments. The electric drive amplitude of the  $V_{AC,1} = V_{AC,2}$  signal varied

between 3 and 5 V, depending on the obtained signal from the sample. We grounded the sample via the sample holder with an external wire to ground level of the LIA. The  $V_{AC}$  was applied to the tip directly, while the AFM head connections were switched off. The setup of the AFM is shown in Figure 8. The electrical connection from the LIA to the cantilever with the two excitation voltages was realized by using a direct cable connection.

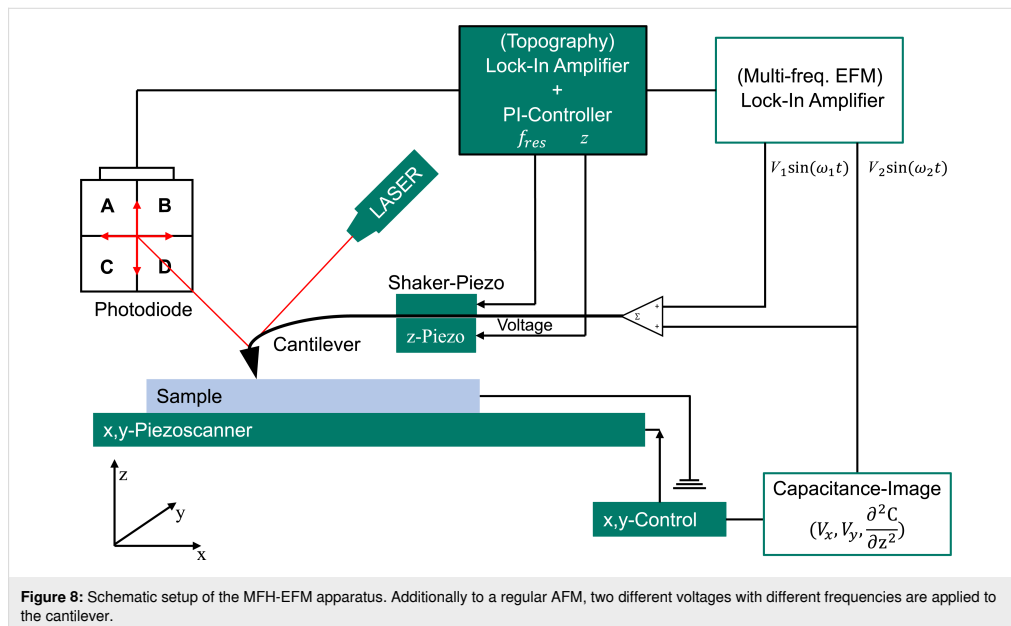
### Focused ion beam milling

FIB milling of the cantilever was conducted using a LEO Gemini instrument from Zeiss. It was used with an acceleration voltage of 3 kV.

### Appendix

#### Equations to calculate the $C''$ and $C'$ signal from the voltages

Equation 14 shows a detailed expression of Equation 12. The detected amplitude from the LIA,  $A_{\text{det}}$ , contains the voltage from the LIA ( $V_{\text{MFH-EFM}}$ ) and  $\Xi_{\text{amp,d2C}}$ , the amplification factor of this voltage from the LIA in MFH-EFM mode. The frequency-dependent spring constant  $k(\omega)$  in Equation 12 contains the inverse optical lever sensitivity (InvOLS) of the second harmonic ( $\text{InvOLS}_2$ ), the spring constant of the second resonance ( $k_2$ ), and the Q-factor shown in Equation 14. It is important to note that the InvOLS and the spring constant on the



second resonance are not the same as measured on the first resonance by the method of Sader and colleagues [98]. It is rather necessary to calculate the properties of the cantilever for the respective eigenmodes [99].

$$\frac{\partial^2 C}{\partial z^2}(\omega) = C''(\omega) = \frac{16 \cdot V_{\text{MFH-SCM}}(\omega) \cdot \text{InvOLS}_2(\omega) \cdot k_2(\omega)}{A_m \cdot V_{\text{AC}}^2 \cdot \Xi_{\text{amp,d2C}} \cdot Q} \quad (14)$$

Equation 15 shows a detailed expression of Equation 13. Again, the expression  $A_{\text{det}}$  contains the detected voltage from the LIA ( $V_{\text{SF-EFM}}$ ) and an amplification factor  $\Xi_{\text{amp,dC}}$  of the signal captured with the LIA in SF-EFM mode. The frequency-dependent spring constant  $k(\omega)$  is the same as above and consists of  $\text{InvOLS}_2$ ,  $k_2$ , and the Q-factor.

$$\frac{\partial C}{\partial z}(\omega) = C'(\omega) = \frac{4 \cdot V_{\text{SF-EFM}}(\omega) \cdot \text{InvOLS}_2(\omega) \cdot k_2(\omega)}{V_{\text{AC}}^2 \cdot \Xi_{\text{amp,dC}} \cdot Q} \quad (15)$$

### Full double excitation force equations

This section gives a full overview of the electric amplitude contributions at various frequencies while activating the MFH-EFM mode. For simplicity, we will use the following substitutions:  $\omega_{\text{m}t}^1 = O$ ,  $\omega_{\text{t}} = E$ ,  $\omega_{\text{mod}t} = M$ ,  $V_{\text{CPD}} - V_{\text{DC}} = \Delta$ ,  $V_{\text{AC}} = V$ , and  $A_m^1 = A$ . Table 1 shows the overview of the force components at various frequencies for the resulting static  $\omega$  and 2 $\omega$  force components acting on the cantilever.

**Table 1:** Overview of the components of the multifrequency electrostatic force microscopy.

Frequency	Amplitude
DC	$1/2 C' [\Delta^2 + U^2/4]$
2M	$1/8 C' U^2$
O	$1/2 C'' A [\Delta^2 + U^2/4]$
$O \pm 2M$	$1/16 C'' A U^2$
$E \pm M$	$1/2 C' U \Delta$
$O \pm (E \pm M)$	$1/4 C'' A U \Delta$
2E	$1/8 C' U^2$
$2(M \pm E)$	$1/16 C' U^2$
$O \pm 2E$	$1/16 C'' A U^2$
$O \pm 2(E \pm M)$	$1/32 C'' A U^2$

### Tip-sample capacitance model

We used the model of Hudlet et al. [89] for the tip apex and, in addition, used the sum of cone and lever distribution of Colchero and colleagues [90,91]. The cantilever can be modeled as a tilted plate capacitor with a truncated cone at the end of the cantilever and with a sharp round tip apex at the end of the tip cone. This is shown schematically in Figure 9.

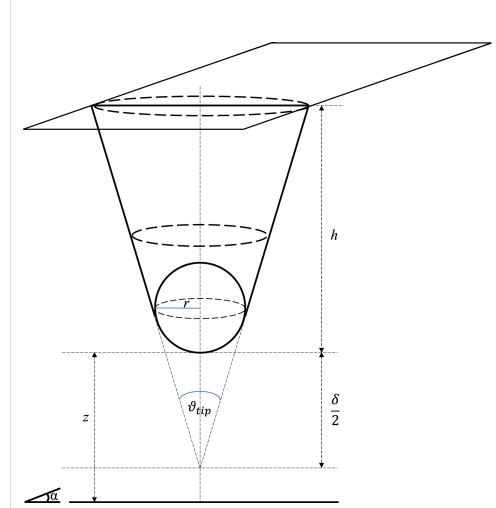


**Figure 9:** Sketch of the capacitance model of the truncated cone with spherical apex. Here  $h$  is the height of the tip,  $r$  is the radius of the sphere,  $\theta_{\text{tip}}$  is the opening angle of the tip,  $\delta$  is the truncated part of the cone, and  $z$  is the distance between sample and tip apex with respect to the surface normal of the sample.  $\alpha$  is the angle between the surface and the lever of the cantilever.

In this case, the electrostatic force for the lever is given by Equation 16[90,91]:

$$F_{\text{lever}}(z) = \frac{2 \tan^2\left(\frac{\alpha}{2}\right)}{\alpha^2} \epsilon_0 V_{\text{tip-sample}}^2 \frac{lw}{h^2} \cdot \frac{1}{\left(1 + \frac{z}{h}\right) \cdot \left(1 + \frac{z + 2l \tan\left(\frac{\alpha}{2}\right)}{h}\right)} \quad (16)$$

Integration taking into account Equation 1 yields:

$$C_{\text{lever}}(z) = \frac{2 \tan^2\left(\frac{\alpha}{2}\right)}{\alpha^2} \epsilon_0 V_{\text{tip-sample}}^2 \frac{lw}{h^2} \cdot \frac{h^2 \cot\left(\frac{\alpha}{2}\right) \left\{ \ln(h+z) - \ln\left[\cos\left(\frac{\alpha}{2}\right)(h+z) + 2l \sin\left(\frac{\alpha}{2}\right)\right] \right\}}{2l} \quad (17)$$

where  $\epsilon_0$  is the dielectric constant of the vacuum. The dimensions of the lever are given by its width  $w$ , its length  $l$ , and the height of the tip cone  $h$ . The lever is tilted by the angle  $\alpha = \theta_{\text{lever}}$ .

The tip cone can be approximated by a truncated cone (Figure 9). The electrostatic force as a function of the distance between tip cone and sample is given by Equation 18[90,91]:

$$F_{\text{cone}}(z) = \frac{4\pi}{(\pi - \vartheta_{\text{tip}})^2} \varepsilon_0 V_{\text{tip-sample}}^2 \cdot \left[ \ln \left( \frac{z - \frac{\delta}{2} + h}{z + \frac{\delta}{2}} \right) - \sin \left( \frac{\vartheta_{\text{tip}}}{2} \right) \frac{h - \delta}{z - \frac{\delta}{2} + h} \cdot \frac{z - \frac{\delta}{2}}{z + \frac{\delta}{2}} \right] \quad (18)$$

with the open angle of the tip cone ( $\vartheta_{\text{tip}}$ ) and the height of the truncated part of the cone ( $\delta = r/\tan^2(\vartheta_{\text{tip}}/2)$ ) [90,91]. Integration of this equation to obtain the capacitance yields

$$C_{\text{cone}}(z) = 2 \frac{4\pi\varepsilon_0}{(\vartheta_{\text{tip}} - \pi)^2} \cdot \left\{ \sin \left( \frac{\vartheta_{\text{tip}}}{2} \right) \left[ h \ln(2f_1) - \delta \ln f_2 \right] + f_1 \ln \left( \frac{f_2}{2f_1} \right) + (\delta - h) \ln f_2 \right\}, \quad (19)$$

where  $f_1 = z - \frac{\delta}{2} + h$  and  $f_2 = 2z + \delta$ .

The tip apex is approximated as a sphere over an infinite surface (Figure 9). The corresponding electrostatic force between a tip apex and the surface is given by Equation 20[89]:

$$F_{\text{apex}}(z) = \pi\varepsilon_0 r^2 V_{\text{tip-sample}}^2 \left( \frac{1 - \sin \left( \frac{\vartheta_{\text{tip}}}{2} \right)}{z \left\{ z + r \left[ 1 - \sin \left( \frac{\vartheta_{\text{tip}}}{2} \right) \right] \right\}} \right) \quad (20)$$

Hence, the capacitance is given by

$$C_{\text{apex}}(z) = 2\pi\varepsilon_0 r \ln \left( \frac{z + r \left[ 1 - \sin \left( \frac{\vartheta_{\text{tip}}}{2} \right) \right]}{z} \right) \quad (21)$$

When the capacitance of the cantilever is plotted as function of the distance between the tip and the sample,  $z$ , Figure 10 is obtained. The parameters were taken from the website of the producer of the NuNano SPARK 70 Pt cantilever:  $w = 30 \mu\text{m}$ ,  $l = 225 \mu\text{m}$ ,  $\alpha = 11^\circ$ ,  $h = 12 \mu\text{m}$ ,  $\vartheta_{\text{cone}} = 25^\circ$ ,  $r = 18 \text{ nm}$ , and  $V_{\text{AC}} = 2 \text{ V}$ .

In order to get the first,  $C'$ , and second capacitance gradient,  $C''$ , of the relevant parts of the cantilever, we used the onward and

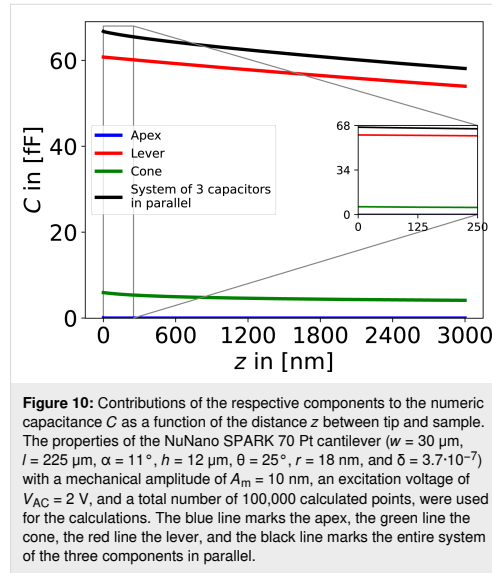


**Figure 10:** Contributions of the respective components to the numeric capacitance  $C$  as a function of the distance  $z$  between tip and sample. The properties of the NuNano SPARK 70 Pt cantilever ( $w = 30 \mu\text{m}$ ,  $l = 225 \mu\text{m}$ ,  $\alpha = 11^\circ$ ,  $h = 12 \mu\text{m}$ ,  $\theta = 25^\circ$ ,  $r = 18 \text{ nm}$ , and  $\delta = 3.7 \cdot 10^{-7}$ ) with a mechanical amplitude of  $A_m = 10 \text{ nm}$ , an excitation voltage of  $V_{\text{AC}} = 2 \text{ V}$ , and a total number of 100,000 calculated points, were used for the calculations. The blue line marks the apex, the green line the cone, the red line the lever, and the black line marks the entire system of the three components in parallel.

backward differentiation given in Equation 22 and the central differential quotient of the second order given in Equation 23, respectively. The step size was chosen to be  $1 \cdot 10^{-10} \text{ m}$  with a total number of 1,000,000 steps. Models of the first and the second capacitance gradient can be found in Figure 4a and Figure 4b, respectively.

$$f'(x) = \frac{f(x+h) - f(x-h)}{2h} \quad (22)$$

$$f''(x) = \frac{f(x+h) - 2f(x) + f(x-h)}{h^2} \quad (23)$$

## Supporting Information

Supporting information features a comparison of the working principles of H-KPFM and MFH-EFM, all the raw and normalized data of the MFH-EFM frequency spectroscopy measurements, the full comparison of the MFH-EFM, SF-EFM, and H-KPFM images on the F14H20 structures, and finally a comparison of the model data and the measured data on the microcapacitors.

### Supporting Information File 1

Additional experimental data.

[<https://www.beilstein-journals.org/bjnano/content/supplementary/2190-4286-16-49-S1.pdf>]

## Acknowledgements

This work is based on the preliminary results previously reported in the Bachelor Thesis in Physics named “Tip–sample capacitance in electrostatic force microscopy” by Peter Gregor Reichel (2021, Johannes Gutenberg-Universität Mainz). We acknowledge Dr. Pravash Bista giving helpful ideas in the process of the research. Also, we acknowledge Maren Müller, our technician, for the help to prepare the capacitors.

## Author Contributions

Pascal N. Rohrbeck: conceptualization; data curation; formal analysis; investigation; methodology; project administration; resources; software; validation; visualization; writing – original draft; writing – review & editing. Lukas D. Cavar: resources; software; writing – review & editing. Franjo Weber: software. Peter G. Reichel: investigation. Mara Niebling: resources; software. Stefan A. L. Weber: conceptualization; funding acquisition; resources; supervision; validation; writing – original draft; writing – review & editing.

## ORCID® iDs

Pascal N. Rohrbeck - <https://orcid.org/0000-0002-1514-6008>

## Data Availability Statement

Data generated and analyzed during this study is available from the corresponding author upon reasonable request.

## Preprint

A non-peer-reviewed version of this article has been previously published as a preprint: <https://doi.org/10.3762/bxiv.2024.72.v1>

## References

- Elayarani, P.; Sumathi, T.; Sivakumar, G.; Pragadeswaran, S.; Suthakaran, S.; Sathiyamurthy, S.; Seshadhri, J.; Ayyar, M.; Arularasu, M. V. *Z. Phys. Chem.* **2024**, *238*, 1019–1042. doi:10.1515/zpch-2023-0531
- Majid, F.; Bashir, M.; Bibi, I.; Ayub, M.; Khan, B. S.; Somaily, H. H.; Al-Mijalli, S. H.; Nazir, A.; Iqbal, S.; Iqbal, M. Z. *Phys. Chem.* **2023**, *237*, 1345–1360. doi:10.1515/zpch-2022-0097
- Iqbal, Z.; Imran, M.; Latif, S.; Nazir, A.; Ibrahim, S. M.; Ahmad, I.; Iqbal, M.; Iqbal, S. Z. *Phys. Chem.* **2023**, *237*, 1139–1152. doi:10.1515/zpch-2022-0113
- Ali, F.; Safdar, A.; Younas, U.; Sillanpaa, M.; Pervaiz, M.; Nazir, A.; Naem, M.; Iqbal, M.; Al-Kahtani, A. A.; Tighezza, A. M. *Z. Phys. Chem.* **2023**, *237*, 599–616. doi:10.1515/zpch-2022-0098
- Nazir, A.; Alam, S.; Alwadai, N.; Abbas, M.; Bibi, I.; Ali, A.; Ahmad, N.; Al Huwayz, M.; Iqbal, M. Z. *Phys. Chem.* **2023**, *237*, 1733–1751. doi:10.1515/zpch-2023-0331
- Arif, H.; Yasir, M.; Ali, F.; Nazir, A.; Ali, A.; Al Huwayz, M.; Alwadai, N.; Iqbal, M. Z. *Phys. Chem.* **2023**, *237*, 689–705. doi:10.1515/zpch-2023-0224
- Sahoo, K. K.; Pradhan, D.; Ghosh, S. P.; Gartia, A.; Kar, J. P. *Phys. Scr.* **2024**, *99*, 025934. doi:10.1088/1402-4896/ad196b
- Zhu, C.; Liu, A.; Liu, G.; Jiang, G.; Meng, Y.; Fortunato, E.; Martins, R.; Shan, F. *J. Mater. Chem. C* **2016**, *4*, 10715–10721. doi:10.1039/c6tc02607a
- Paily, R.; DasGupta, A.; DasGupta, N.; Bhattacharya, P.; Misra, P.; Ganguli, T.; Kukreja, L. M.; Balamurugan, A. K.; Rajagopalan, S.; Tyagi, A. K. *Appl. Surf. Sci.* **2002**, *187*, 297–304. doi:10.1016/s0169-4332(01)01040-6
- Robertson, J. *Rep. Prog. Phys.* **2006**, *69*, 327–396. doi:10.1088/0034-4885/69/2/r02
- Werner, F.; Babbe, F.; Elanzeery, H.; Siebentritt, S. *Prog. Photovoltaics* **2019**, *27*, 1045–1058. doi:10.1002/pip.3196
- Barsoukov, E.; Macdonald, J. R., Eds. *Impedance Spectroscopy*; John Wiley & Sons: Hoboken, NJ, USA, 2005. doi:10.1002/0471716243
- Shi, N.; Ramprasad, R. *J. Comput.-Aided Mater. Des.* **2007**, *14*, 133–139. doi:10.1007/s10820-006-9034-9
- Pang, H.-S.; Xu, H.; Tang, C.; Meng, L.-K.; Ding, Y.; Xiao, J.; Liu, R.-L.; Pang, Z.-Q.; Huang, W. *Org. Electron.* **2019**, *65*, 275–299. doi:10.1016/j.orgel.2018.09.025
- Yalcinkaya, Y.; Rohrbeck, P. N.; Schütz, E. R.; Fakharuddin, A.; Schmidt-Mende, L.; Weber, S. A. L. *Adv. Opt. Mater.* **2024**, *12*, 2301318. doi:10.1002/adom.202301318
- Binnig, G.; Rohrer, H.; Gerber, C.; Weibel, E. *Phys. Rev. Lett.* **1982**, *49*, 57–61. doi:10.1103/physrevlett.49.57
- Binnig, G.; Quate, C. F.; Gerber, C. *Phys. Rev. Lett.* **1986**, *56*, 930–933. doi:10.1103/physrevlett.56.930
- Axt, A.; Hermes, I. M.; Bergmann, V. W.; Tausendpfund, N.; Weber, S. A. L. *Beilstein J. Nanotechnol.* **2018**, *9*, 1809–1819. doi:10.3762/bjnano.9.172
- Hermes, I. M.; Best, A.; Winkelmann, L.; Mars, J.; Vorpahl, S. M.; Mezger, M.; Collins, L.; Butt, H.-J.; Ginger, D. S.; Koynov, K.; Weber, S. A. L. *Energy Environ. Sci.* **2020**, *13*, 4168–4177. doi:10.1039/d0ee01016b
- Rohrbeck, P. N. Untersuchung von lokalen Aufladungsdynamiken an Perowskit-Korngrenzen mit zeitaufgelösten KPFM Methoden. Master thesis, Johannes Gutenberg University Mainz, 2021.
- Bergmann, V. W.; Weber, S. A. L.; Javier Ramos, F.; Nazeeruddin, M. K.; Grätzel, M.; Li, D.; Domanski, A. L.; Lieberwirth, I.; Ahmad, S.; Berger, R. *Nat. Commun.* **2014**, *5*, 5001. doi:10.1038/ncomms6001
- Weber, S. A. L.; Hermes, I. M.; Turren-Cruz, S.-H.; Gort, C.; Bergmann, V. W.; Gilson, L.; Hagfeldt, A.; Graetzel, M.; Tress, W.; Berger, R. *Energy Environ. Sci.* **2018**, *11*, 2404–2413. doi:10.1039/c8ee01447g
- Zhu, C.; Fuchs, T.; Weber, S. A. L.; Richter, F. H.; Glasser, G.; Weber, F.; Butt, H.-J.; Janek, J.; Berger, R. *Nat. Commun.* **2023**, *14*, 1300. doi:10.1038/s41467-023-36792-7
- Martin, Y.; Abraham, D. W.; Wickramasinghe, H. K. *Appl. Phys. Lett.* **1988**, *52*, 1103–1105. doi:10.1063/1.99224
- Abraham, D. W.; Williams, C.; Slinkman, J.; Wickramasinghe, H. K. *J. Vac. Sci. Technol., B: Microelectron. Nanometer Struct.–Process., Mater. Relat.* **1991**, *9*, 703–706. doi:10.1116/1.585536
- Garrett, J. L.; Munday, J. N. *Nanotechnology* **2016**, *27*, 245705. doi:10.1088/0957-4484/27/24/245705
- Eaton, P.; West, P. *Atomic Force Microscopy*; Oxford University Press: Oxford, UK, 2010. doi:10.1093/acprof:oso/9780199570454.001.0001
- Biberger, R.; Benstetter, G.; Goebel, H.; Hofer, A. *Microelectron. Reliab.* **2010**, *50*, 1511–1513. doi:10.1016/j.microrel.2010.07.052
- Jaensch, S.; Schmidt, H.; Grundmann, M. *Phys. B (Amsterdam, Neth.)* **2006**, *376-377*, 913–915. doi:10.1016/j.physb.2005.12.227

30. Tran, T.; Oliver, D. R.; Thomson, D. J.; Bridges, G. E. Sub-zeptofarad sensitivity scanning capacitance microscopy. In *IEEE CCECE2002. Canadian Conference on Electrical and Computer Engineering. Conference Proceedings (Cat. No.02CH37373)*, 2002; pp 455–459. doi:10.1109/ccece.2002.1015268
31. Raineri, V.; Giannazzo, F. *Solid State Phenom.* **2001**, *78–79*, 425. doi:10.4028/www.scientific.net/ssp.78-79.425
32. Barrett, R. C.; Quate, C. F. *J. Appl. Phys.* **1991**, *70*, 2725–2733. doi:10.1063/1.349388
33. Goto, K.; Hane, K. *Rev. Sci. Instrum.* **1997**, *68*, 120–123. doi:10.1063/1.1147749
34. Fumagalli, L.; Ferrari, G.; Sampietro, M.; Casuso, I.; Martínez, E.; Samitier, J.; Gomila, G. *Nanotechnology* **2006**, *17*, 4581–4587. doi:10.1088/0957-4484/17/18/009
35. Gomila, G.; Toset, J.; Fumagalli, L. *J. Appl. Phys.* **2008**, *104*, 024315. doi:10.1063/1.2957069
36. Fumagalli, L.; Ferrari, G.; Sampietro, M.; Gomila, G. *Nano Lett.* **2009**, *9*, 1604–1608. doi:10.1021/nl803851u
37. Matey, J. R.; Blanc, J. *J. Appl. Phys.* **1985**, *57*, 1437–1444. doi:10.1063/1.334506
38. Arakawa, H.; Nishitani, R. *J. Vac. Sci. Technol., B: Microelectron. Nanometer Struct.–Process., Mater. Sci. Phenom.* **2001**, *19*, 1150–1153. doi:10.1116/1.1379796
39. Lee, D. T.; Pelz, J. P.; Bhushan, B. *Nanotechnology* **2006**, *17*, 1484–1491. doi:10.1088/0957-4484/17/5/054
40. Lee, D. T.; Pelz, J. P.; Bhushan, B. *Rev. Sci. Instrum.* **2002**, *73*, 3525–3533. doi:10.1063/1.1505655
41. Isenbart, J.; Born, A.; Wiesendanger, R. *Appl. Phys. A: Mater. Sci. Process.* **2001**, *72* (Suppl. 2), S243–S251. doi:10.1007/s003390100793
42. Kopanski, J. J.; Mayo, S. *Appl. Phys. Lett.* **1998**, *72*, 2469–2471. doi:10.1063/1.121397
43. Casuso, I.; Fumagalli, L.; Gomila, G.; Padrós, E. *Appl. Phys. Lett.* **2007**, *91*, 063111. doi:10.1063/1.2767979
44. Biburger, R.; Benstetter, G.; Schweinboeck, T.; Breitschopf, P.; Goebel, H. *Microelectron. Reliab.* **2008**, *48*, 1339–1342. doi:10.1016/j.microrel.2008.06.013
45. Smoliner, J.; Basnar, B.; Golka, S.; Gornik, E.; Löffler, B.; Schatzmayr, M.; Enichlmair, H. *Appl. Phys. Lett.* **2001**, *79*, 3182–3184. doi:10.1063/1.1415044
46. Brezna, W.; Schramboeck, M.; Lugstein, A.; Harasek, S.; Enichlmair, H.; Bertagnolli, E.; Gornik, E.; Smoliner, J. *Appl. Phys. Lett.* **2003**, *83*, 4253–4255. doi:10.1063/1.1628402
47. Giannazzo, F.; Raineri, V.; Mirabella, S.; Impellizzeri, G.; Priolo, F.; Fedele, M.; Mucciato, R. *J. Vac. Sci. Technol., B: Microelectron. Nanometer Struct.–Process., Mater. Sci. Phenom.* **2006**, *24*, 370–374. doi:10.1116/1.2151907
48. Brezna, W.; Fischer, M.; Wanzenboeck, H. D.; Bertagnolli, E.; Smoliner, J. *Appl. Phys. Lett.* **2006**, *88*, 122116. doi:10.1063/1.2189030
49. Futscher, M. H.; Lee, J. M.; McGovern, L.; Muscarella, L. A.; Wang, T.; Haider, M. I.; Fakhruddin, A.; Schmidt-Mende, L.; Ehrler, B. *Mater. Horiz.* **2019**, *6*, 1497–1503. doi:10.1039/c9mh00445a
50. Kopanski, J. J.; Marchiando, J. F.; Lowney, J. R. *Mater. Sci. Eng., B* **1997**, *44*, 46–51. doi:10.1016/s0921-5107(96)01797-7
51. Kopanski, J. J.; Marchiando, J. F.; Lowney, J. R. *J. Vac. Sci. Technol., B: Microelectron. Nanometer Struct.–Process., Mater. Sci. Phenom.* **1996**, *14*, 242–247. doi:10.1116/1.588455
52. Goto, K.; Hane, K. *J. Appl. Phys.* **1998**, *84*, 4043–4048. doi:10.1063/1.368617
53. de Voogd, J. M.; van Spronsen, M. A.; Kalf, F. E.; Bryant, B.; Ostojčić, O.; den Haan, A. M. J.; Groot, I. M. N.; Oosterkamp, T. H.; Otte, A. F.; Rost, M. J. *Ultramicroscopy* **2017**, *181*, 61–69. doi:10.1016/j.ultramic.2017.05.009
54. Hiranaga, Y.; Cho, Y. *Rev. Sci. Instrum.* **2019**, *90*, 083705. doi:10.1063/1.5097906
55. Kobayashi, K.; Yamada, H.; Matsushige, K. *Appl. Phys. Lett.* **2002**, *81*, 2629–2631. doi:10.1063/1.1510582
56. Gramse, G.; Casuso, I.; Toset, J.; Fumagalli, L.; Gomila, G. *Nanotechnology* **2009**, *20*, 395702. doi:10.1088/0957-4484/20/39/395702
57. Fumagalli, L.; Gramse, G.; Esteban-Ferrer, D.; Edwards, M. A.; Gomila, G. *Appl. Phys. Lett.* **2010**, *96*, 183107. doi:10.1063/1.3427362
58. Fumagalli, L.; Esteban-Ferrer, D.; Cuervo, A.; Carrascosa, J. L.; Gomila, G. *Nat. Mater.* **2012**, *11*, 808–816. doi:10.1038/nmat3369
59. Gramse, G.; Edwards, M. A.; Fumagalli, L.; Gomila, G. *Appl. Phys. Lett.* **2012**, *101*, 213108. doi:10.1063/1.4768164
60. Gramse, G.; Dols-Perez, A.; Edwards, M. A.; Fumagalli, L.; Gomila, G. *Biophys. J.* **2013**, *104*, 1257–1262. doi:10.1016/j.bpj.2013.02.011
61. Kimura, K.; Kobayashi, K.; Yamada, H.; Matsushige, K. *Appl. Surf. Sci.* **2003**, *210*, 93–98. doi:10.1016/s0169-4332(02)01486-1
62. Henning, A. K.; Hochwitz, T. *Mater. Sci. Eng., B* **1996**, *42*, 88–98. doi:10.1016/s0921-5107(96)01688-1
63. Checa, M.; Neumayer, S. M.; Susner, M. A.; McGuire, M. A.; Maksymovych, P.; Collins, L. *Appl. Phys. Lett.* **2021**, *119*, 252905. doi:10.1063/5.0078034
64. Li, Z.-Y.; Gu, B.-Y.; Yang, G.-Z. *Phys. Rev. B* **1998**, *57*, 9225–9233. doi:10.1103/physrevb.57.9225
65. Gil, A.; Colchero, J.; Gómez-Herrero, J.; Baró, A. M. *Nanotechnology* **2003**, *14*, 332–340. doi:10.1088/0957-4484/14/2/345
66. Fukuzawa, R.; Takahashi, T. *Rev. Sci. Instrum.* **2020**, *91*, 023702. doi:10.1063/1.5127219
67. Izumi, R.; Miyazaki, M.; Li, Y. J.; Sugawara, Y. *Beilstein J. Nanotechnol.* **2023**, *14*, 175–189. doi:10.3762/bjnano.14.18
68. Cherniavskaya, O.; Chen, L.; Weng, V.; Yuditisky, L.; Brus, L. E. *J. Phys. Chem. B* **2003**, *107*, 1525–1531. doi:10.1021/jp0265438
69. Crider, P. S.; Majewski, M. R.; Zhang, J.; Oukris, H.; Israeloff, N. E. *Appl. Phys. Lett.* **2007**, *91*, 013102. doi:10.1063/1.2753539
70. Cadena, M. J.; Sung, S. H.; Boudouris, B. W.; Reifenberger, R.; Raman, A. *ACS Nano* **2016**, *10*, 4062–4071. doi:10.1021/acsnano.5b06893
71. Riedel, C.; Arinero, R.; Tordjeman, P.; Lévêque, G.; Schwartz, G. A.; Alegria, A.; Colmenero, J. *Phys. Rev. E* **2010**, *81*, 010801. doi:10.1103/physreve.81.010801
72. Gramse, G.; Schönhals, A.; Kienberger, F. *Nanoscale* **2019**, *11*, 4303–4309. doi:10.1039/c8nr05880f
73. Gramse, G.; Kölker, A.; Škernež, T.; Stock, T. J. Z.; Aeppli, G.; Kienberger, F.; Fuhrer, A.; Curson, N. J. *Nat. Electron.* **2020**, *3*, 531–538. doi:10.1038/s41928-020-0450-8
74. Fumagalli, L.; Ferrari, G.; Sampietro, M.; Gomila, G. *Appl. Phys. Lett.* **2007**, *91*, 243110. doi:10.1063/1.2821119
75. Söngen, H.; Rahe, P.; Neff, J. L.; Bechstein, R.; Ritala, J.; Foster, A. S.; Kühnle, A. J. *Appl. Phys.* **2016**, *119*, 025304. doi:10.1063/1.4939619
76. Tran, T.; Oliver, D. R.; Thomson, D. J.; Bridges, G. E. *Rev. Sci. Instrum.* **2001**, *72*, 2618–2623. doi:10.1063/1.1369637
77. Moertelmaier, M.; Huber, H. P.; Rankl, C.; Kienberger, F. *Ultramicroscopy* **2014**, *136*, 67–72. doi:10.1016/j.ultramic.2013.07.011
78. Millan-Solsona, R.; Checa, M.; Fumagalli, L.; Gomila, G. *Nanoscale* **2020**, *12*, 20658–20668. doi:10.1039/d0nr05723a

79. Sugawara, Y.; Kou, L.; Ma, Z.; Kamijo, T.; Naitoh, Y.; Jun Li, Y. *Appl. Phys. Lett.* **2012**, *100*, 223104. doi:10.1063/1.4723697
80. Platz, D.; Tholén, E. A.; Pesen, D.; Haviland, D. B. *Appl. Phys. Lett.* **2008**, *92*, 153106. doi:10.1063/1.2909569
81. Borgani, R.; Forchheimer, D.; Bergqvist, J.; Thorén, P.-A.; Inganäs, O.; Haviland, D. B. *Appl. Phys. Lett.* **2014**, *105*, 143113. doi:10.1063/1.4897966
82. Garrett, J. L.; Leite, M. S.; Munday, J. N. *ACS Appl. Mater. Interfaces* **2018**, *10*, 28850–28859. doi:10.1021/acsami.8b08097
83. Dobryden, I.; Borgani, R.; Rigoni, F.; Ghangosar, P.; Concina, I.; Almqvist, N.; Vomiero, A. *Nanoscale Adv.* **2021**, *3*, 4388–4394. doi:10.1039/d1na00319d
84. Labardi, M.; Prevosto, D.; Nguyen, K. H.; Capaccioli, S.; Lucchesi, M.; Rolla, P. *J. Vac. Sci. Technol., B: Microelectron. Nanometer Struct.–Process., Mater., Phenom.* **2010**, *28*, C4D11–C4D17. doi:10.1116/1.3368597
85. Schwartz, G. A.; Riedel, C.; Arinero, R.; Tordjeman, P.; Alegría, A.; Colmenero, J. *Ultramicroscopy* **2011**, *111*, 1366–1369. doi:10.1016/j.ultramicro.2011.05.001
86. Miccio, L. A.; Kummali, M. M.; Schwartz, G. A.; Alegría, Á.; Colmenero, J. *Ultramicroscopy* **2014**, *146*, 55–61. doi:10.1016/j.ultramicro.2014.06.006
87. Miccio, L. A.; Kummali, M. M.; Schwartz, G. A.; Alegría, Á.; Colmenero, J. *J. Appl. Phys.* **2014**, *115*, 184305. doi:10.1063/1.4875836
88. Miccio, L. A.; Schwartz, G. A. *AIP Conf. Proc.* **2014**, *1599*, 150–153. doi:10.1063/1.4876800
89. Hudlet, S.; Saint Jean, M.; Guthmann, C.; Berger, J. *Eur. Phys. J. B* **1998**, *2*, 5–10. doi:10.1007/s100510050219
90. Colchero, J.; Gil, A.; Baró, A. M. *Phys. Rev. B* **2001**, *64*, 245403. doi:10.1103/physrevb.64.245403
91. Law, B. M.; Rieutord, F. *Phys. Rev. B* **2002**, *66*, 035402. doi:10.1103/physrevb.66.035402
92. Halpern, A.; Eribach, E. *Schaum's outline of theory and problems of beginning physics II: waves, electromagnetism, optics, and modern physics*; McGraw-Hill: New York, NY, USA, 1998.
93. Lyubchenko, Y. L., Ed. *Nanoscale Imaging*; Springer: New York, NY, USA, 2018. doi:10.1007/978-1-4939-8591-3
94. Mourran, A.; Tartsch, B.; Gallyamov, M.; Magonov, S.; Lambrea, D.; Ostrovskii, B. I.; Dolbnya, I. P.; de Jeu, W. H.; Moeller, M. *Langmuir* **2005**, *21*, 2308–2316. doi:10.1021/la048069y
95. Magonov, S.; Alexander, J. *Beilstein J. Nanotechnol.* **2011**, *2*, 15–27. doi:10.3762/bjnano.2.2
96. Sugimura, H.; Ishida, Y.; Hayashi, K.; Takai, O.; Nakagiri, N. *Appl. Phys. Lett.* **2002**, *80*, 1459–1461. doi:10.1063/1.1455145
97. Abed, A. E.; Fauré, M.-C.; Pouzet, E.; Abillon, O. *Phys. Rev. E* **2002**, *65*, 051603. doi:10.1103/physreve.65.051603
98. Sader, J. E.; Chon, J. W. M.; Mulvaney, P. *Rev. Sci. Instrum.* **1999**, *70*, 3967–3969. doi:10.1063/1.1150021
99. Labuda, A.; Kocun, M.; Lysy, M.; Walsh, T.; Meinhold, J.; Proksch, T.; Meinhold, W.; Anderson, C.; Proksch, R. *Rev. Sci. Instrum.* **2016**, *87*, 073705. doi:10.1063/1.4955122

## License and Terms

This is an open access article licensed under the terms of the Beilstein-Institut Open Access License Agreement (<https://www.beilstein-journals.org/bjnano/terms>), which is identical to the Creative Commons Attribution 4.0 International License (<https://creativecommons.org/licenses/by/4.0>). The reuse of material under this license requires that the author(s), source and license are credited. Third-party material in this article could be subject to other licenses (typically indicated in the credit line), and in this case, users are required to obtain permission from the license holder to reuse the material.

The definitive version of this article is the electronic one which can be found at:

<https://doi.org/10.3762/bjnano.16.49>



BEILSTEIN JOURNAL OF NANOTECHNOLOGY

## Supporting Information

for

### **Nanoscale capacitance spectroscopy based on multifrequency electrostatic force microscopy**

Pascal N. Rohrbeck, Lukas D. Cavar, Franjo Weber, Peter G. Reichel, Mara Niebling  
and Stefan A. L. Weber

*Beilstein J. Nanotechnol.* **2025**, *16*, 637–651. doi:10.3762/bjnano.16.49

## Additional experimental data

License and Terms: This is a supporting information file under the terms of the Creative Commons Attribution License (<https://creativecommons.org/licenses/by/4.0>). Please note that the reuse, redistribution and reproduction in particular requires that the author(s) and source are credited and that individual graphics may be subject to special legal provisions.

The license is subject to the *Beilstein Journal of Nanotechnology* terms and conditions: (<https://www.beilstein-journals.org/bjnano/terms>)

This Supporting Information features a comparison of the working principles of heterodyne Kelvin probe force microscopy (H-KPFM) and multi-frequency heterodyne electrostatic force microscopy (MFH-EFM), all the raw and normalized data of the MFH-EFM frequency spectroscopy, the full comparison of the MFH-EFM, SF-EFM, and H-KPFM images on the perfluoroalkyl-alkane  $F(CF_2)_{14}(CH_2)_{20}H$  (F14H20) structures, and finally a comparison of the model data and the measured data on the microcapacitors.

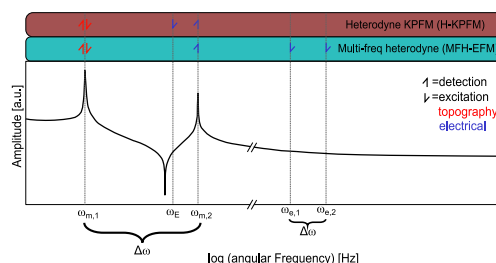


**Figure S1:** Schematic comparison of the excitation and detection frequencies in H-KPFM and MFH-EFM. The lower part shows the transfer function of the cantilever, where the amplitude is plotted vs the logarithmic angular frequency. The upper part shows the excitation frequencies (2) and the detection frequencies (1) of the applied frequencies. The red arrow corresponds to topography- and the blue arrow to the electrical signal. Representation of Figure S1 was inspired by [1,2].

**Table S1:** Known capacitance methods from the literature compared to our new MFH-EFM method.

Reference in the Paper, DOI	Force detection method	Detecting second capacity gradient	High Freq. Sweep possible	Remarks
Jaensch2006 [3], 10.1016/j.physb.2005.12.227	NO	NO	NO	dC/dV
Tran2002 [4], 10.1109/CCECE.2002.1015268	NO	NO	NO	
Continued on next page				

Table S1 – continued from previous page

<b>Reference in the Paper, DOI</b>	<b>Force detection method</b>	<b>Detecting second capacity gradient</b>	<b>High Freq. Sweep possible</b>	<b>Remarks</b>
Raineri2001 [5], <small>10.4028/www.scientific.net/SSP.78-79.425</small>	NO	NO	NO	dC/dV
Barrett1991 [6], <small>10.1063/1.349388</small>	NO	NO	NO	
Yamamoto1996 [7], <small>10.1143/JJAP.35.3793</small>	NO	NO	NO	dC/dV
Goto1997a [8], <small>10.1063/1.1147749</small>	NO	NO	NO	dC/dV
Goto1997 [9], <small>10.1117/12.271216</small>	NO	NO	NO	C
Fumagalli2006 [10], <small>10.1088/0957-4484/17/18/009</small>	NO	NO	NO	
Fumagalli2007 [11], <small>10.1063/1.2821119</small>	NO	NO	NO	
Gomila2008 [12], <small>10.1063/1.2957069</small>	NO	NO	NO	
Fumagalli2009 [13], <small>10.1021/nl803851u</small>	NO	NO	NO	
Matey1985 [14], <small>10.1063/1.334506</small>	NO	NO	NO	C
Arakawa2001 [15], <small>10.1116/1.1379796</small>	NO	NO	NO	V

Continued on next page

CHAPTER 5. NANOSCALE CAPACITANCE SPECTROSCOPY BASED ON  
MULTI-FREQUENCY ELECTROSTATIC FORCE MICROSCOPY

---

Table S1 – continued from previous page

<b>Reference in the Paper, DOI</b>	<b>Force detection method</b>	<b>Detecting second capacity gradient</b>	<b>High Freq. Sweep possible</b>	<b>Remarks</b>
Lee2006 [16], 10.1088/0957-4484/17/5/054	NO	NO	NO	dC/dV
Lee2002 [17], 10.1063/1.1505655	NO	NO	NO	dC/dV
Isenbart2001 [18], 10.1007/s003390100793	NO	NO	NO	dC/dV
Kopanski1998 [19], 10.1063/1.121397	NO	NO	NO	C
Casuso2007 [20], 10.1063/1.2767979	NO	NO	NO	C
Biberger2008 [21], 10.1016/j.microrel.2008.06.013	NO	NO	NO	dC/dV
Smoliner2001 [22], 10.1063/1.1415044	NO	NO	NO	dC/dV
Brezna2003 [23] 10.1063/1.1628402	NO	NO	NO	dC/dV
Giannazzo2006 [24], 10.1116/1.2151907	NO	NO	NO	C
Brezna2006 [25], 10.1063/1.2189030	NO	NO	NO	dC/dV
Futscher2019 [26], 10.1039/C9MH00445A	NO	NO	NO	C

Continued on next page

Table S1 – continued from previous page

<b>Reference in the Paper, DOI</b>	<b>Force detection method</b>	<b>Detecting second capacity gradient</b>	<b>High Freq. Sweep possible</b>	<b>Remarks</b>
Kopanski1997 [27], 10.1016/S0921-5107(96)01797-7	NO	NO	NO	dC/dV
Kopanski1996a [28], 10.1116/1.588455	NO	NO	NO	
Goto1998 [29], 10.1063/1.368617	NO	NO	NO	C
DeVoogd2017 [30], 10.1016/j.ultramic.2017.05.009	NO	NO	NO	C
Hiranaga2019 [31], 10.1063/1.5097906	NO	NO	NO	
Kobayashi2002 [32], 10.1063/1.1510582	YES	NO	NO	dC/dV
Martin1988 [33], 10.1063/1.99224	YES	NO	NO	
Abraham1991 [34], 10.1116/1.585536	YES	NO	NO	
Gramse2009 [35], 10.1088/0957-4484/20/39/395702	YES	NO	NO	
Fumagalli2010 [36], 10.1063/1.3427362	YES	NO	NO	
Fumagalli2012 [37], 10.1038/nmat3369	YES	NO	NO	

Continued on next page

CHAPTER 5. NANOSCALE CAPACITANCE SPECTROSCOPY BASED ON  
MULTI-FREQUENCY ELECTROSTATIC FORCE MICROSCOPY

---

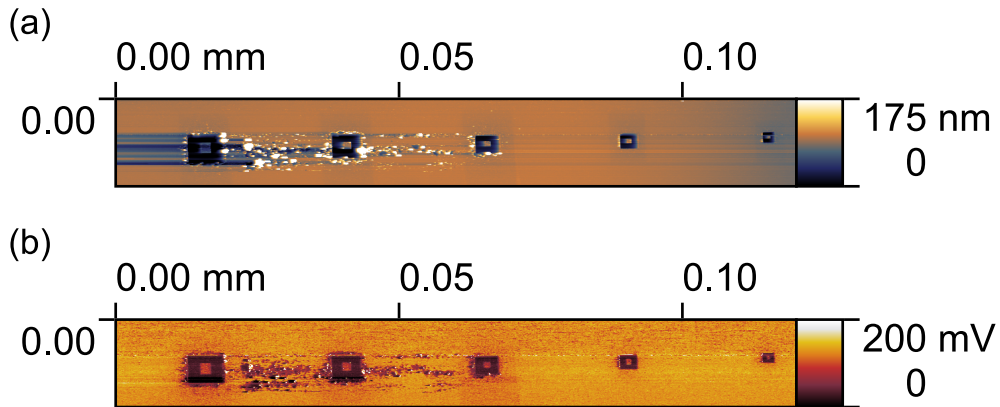
Table S1 – continued from previous page

Reference in the Paper, DOI	Force detection method	Detecting second capacity gradient	High Freq. Sweep possible	Remarks
Gramse2012 [38], 10.1063/1.4768164	YES	NO	YES	
Gramse2013 [39], 10.1016/j.bj.2013.02.011	YES	NO	NO	
Kimura2003 [40], 10.1016/S0169-4332(02)01486-1	YES	NO	NO	dC/dV
Henning1996 [41], 10.1016/S0921-5107(96)01688-1	YES	NO	NO	
Checa2021 [42], 10.1063/5.0078034	YES	NO	NO	
Li1998 [43], 10.1103/PhysRevB.57.9225	YES	NO	NO	
Gil2003 [44], 10.1088/0957-4484/14/2/345	YES	NO	NO	
Fukuzawa2020 [45], 10.1063/1.5127219	YES	NO	NO	dC/dV
Izumi2023 [46], 10.3762/bjnano.14.18	YES	NO	NO	
Cherniavskaya2003 [47], 10.1021/jp0265438	YES	NO	NO	
Crider2007a [48], 10.1063/1.2753539	YES	YES	NO	low freq. sweeps

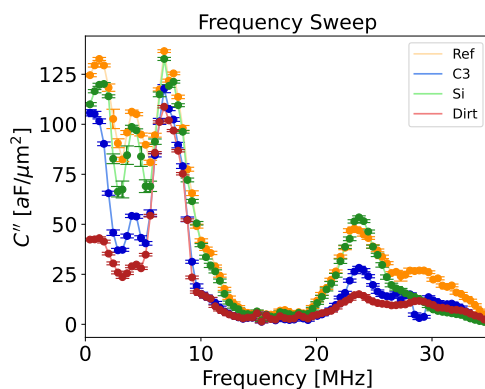
Continued on next page

Table S1 – continued from previous page

Reference in the Paper, DOI	Force detection method	Detecting second capacity gradient	High Freq. Sweep possible	Remarks
Cadena2016 [49], 10.1021/jp0265438	YES	NO	YES	lift mode, freq. tracking *: phase modulation : limited to 1 MHz
Riedel2010 [50], 10.1103/PhysRevE.81.010801	YES	YES	NO	
Gramse2019 [51], 10.1039/C8NR05880F	YES	YES	YES*	
Gramse2020 [52], 10.1038/s41928-020-0450-8	YES	YES	YES	
Our Method: MFH-EFM	YES	YES	YES	dC/dV possible



**Figure S2:** Raw data taken from the microcapacitors shown in Figure 2 in MFH-EFM mode. (a) The topography and (b) the  $A_{det}$  from the measurement. The image is not converted into  $C''$  values but the relation is the same.



**Figure S3:** Non-normalized data of the comparison of the  $C''$  frequency sweep shown in Figure 6 on the four spots while in MFH-EFM (see Equation 12). This was conducted with the  $\mu\text{masch}$ 's HQ:NSC18/Pt cantilever.

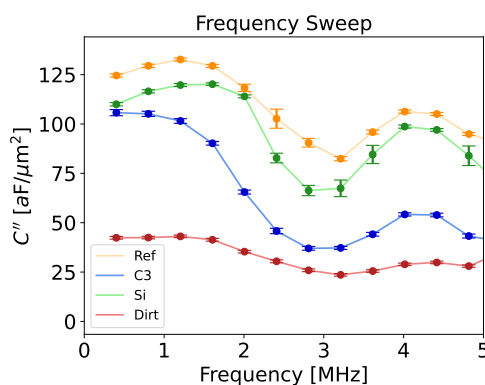


**Figure S4:** Zoom of the non-normalized data from the comparison of the  $C''$  frequency sweep shown in Figure 6 on the four spots while in MFH-EFM (see Equation 12). This was conducted with the  $\mu\text{masch}$ 's HQ:NSC18/Pt cantilever.

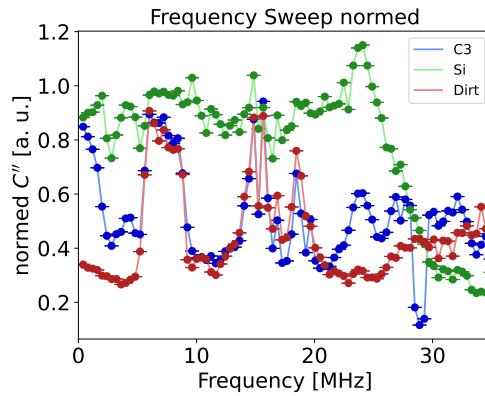


**Figure S5:** Normalized data of the  $C''$  frequency sweep shown in Figure 6 on the three spots while in MFH-EFM (see Equation 12). This was conducted with the  $\mu$ masch's HQ:NSC18/Pt cantilever.

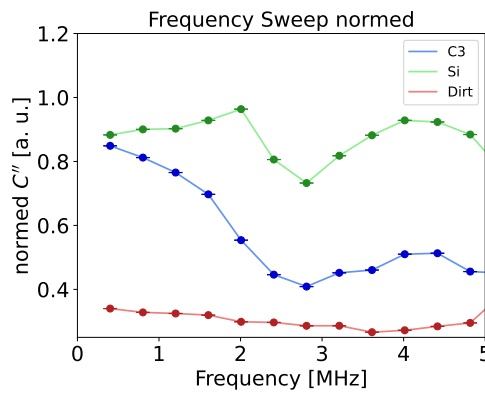


**Figure S6:** Zoomed and normalized data of the  $C''$  frequency sweep shown in Figure 6 on the three spots while in MFH-EFM (see Equation 12). This was conducted with the  $\mu$ masch's HQ:NSC18/Pt cantilever.

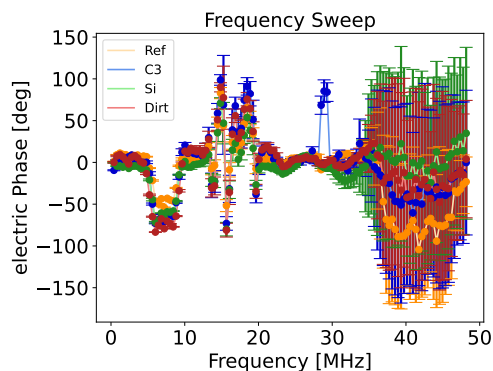


**Figure S7:** Non-normalized data of the phase signal  $\varphi$  spectra of the comparison from the  $C''$  frequency sweep shown in Figure 6 on the four spots while in MFH-EFM (see Equation 12). This was conducted with the  $\mu$ masch's HQ:NSC18/Pt cantilever.

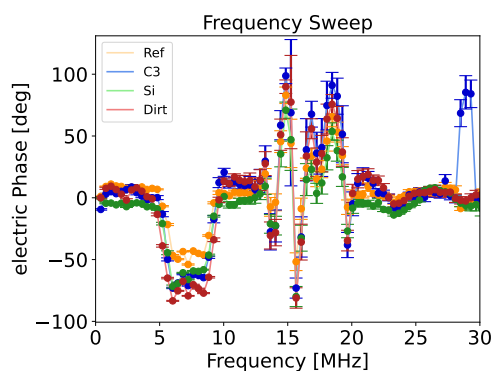


**Figure S8:** Zoom of the non-normalized data of the phase signal  $\varphi$  spectra of the comparison from the  $C''$  frequency sweep shown in Figure 6 on the four spots while in MFH-EFM (see Equation 12). This was conducted with the  $\mu$ masch's HQ:NSC18/Pt cantilever.

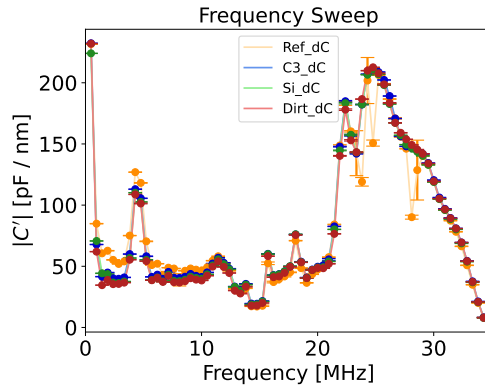


**Figure S9:** Non-normalized data of the comparison of the  $C'$  frequency sweep shown in Figure 6 on the four spots while in SF-EFM mode (see Equation 13). This was conducted with the  $\mu$ masch's HQ:NSC18/Pt cantilever.

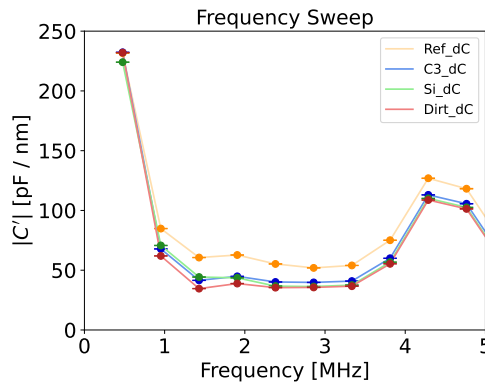


**Figure S10:** Zoom of the non-normalized data of the comparison of the  $C'$  frequency sweep shown in Figure 6 on the four spots while in SF-EFM mode (see Equation 13). This was conducted with the  $\mu$ masch's HQ:NSC18/Pt cantilever.

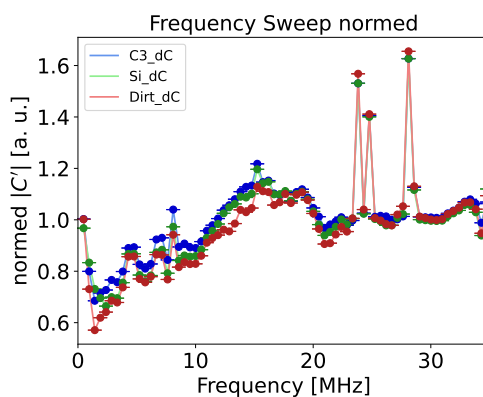


**Figure S11:** Normalized data of the  $C'$  frequency sweep shown in Figure 6 on the three spots while in SF-EFM mode (see Equation 13). This was conducted with the  $\mu$ masch's HQ:NSC18/Pt cantilever.

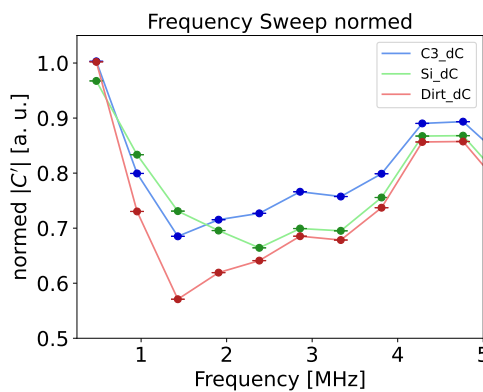


**Figure S12:** Zoomed and normalized data of the  $C'$  frequency sweep shown in Figure 6 on the three spots while in SF-EFM mode (see Equation 13). This was conducted with the  $\mu$ masch's HQ:NSC18/Pt cantilever.

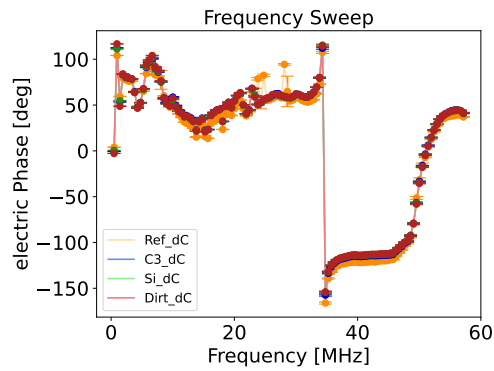


**Figure S13:** Non-normalized data of the phase signal  $\varphi$  spectra of the comparison of the  $C'$  frequency sweep shown in Figure 6 on the four spots while in SF-EFM mode (see Equation 13). This was conducted with the  $\mu$ masch's HQ:NSC18/Pt cantilever.

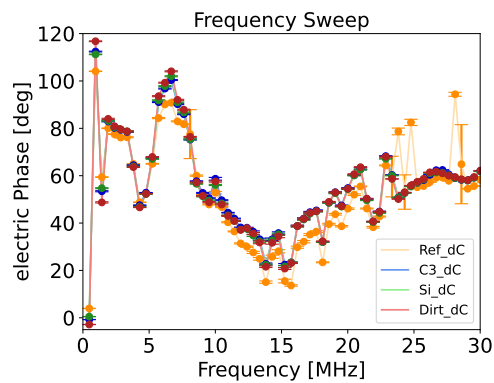


**Figure S14:** Zoom of the non-normalized data of the phase signal  $\varphi$  spectra of the comparison of the  $C'$  frequency sweep shown in Figure 6 on the four spots while in SF-EFM mode (see Equation 13). This was conducted with the  $\mu$ masch's HQ:NSC18/Pt cantilever.

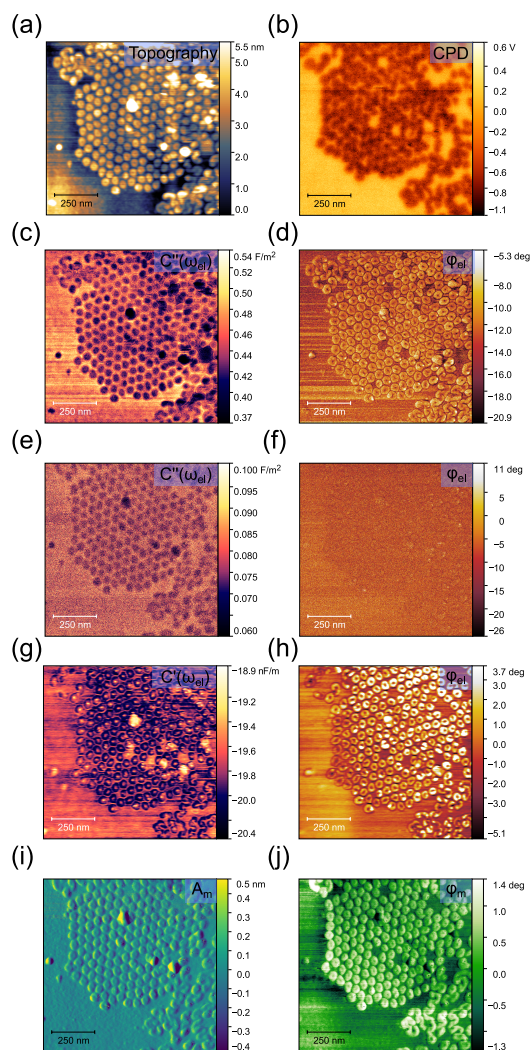


**Figure S15:** Full version of the MFH-EFM pictures given in Figure 7. MFH-EFM pictures made on F14H20 with (a) the topography, (b) the contact potential difference (CPD) picture, (c) the  $C''$  picture detected at  $\omega_{m,2}$ , while excitation took place at frequencies 1.59 and 1.98 MHz, (d) electric phase  $\varphi_{el}$  of the  $C''$  signal detected at  $\omega_{m,2}$ , while excitation took place at frequencies 1.59 and 1.98 MHz, (e) the  $C''$  picture detected at  $\omega_{m,2}$ , while excitation took place at frequencies 15.88 and 16.28 MHz, (f) electric phase  $\varphi_{el}$  of the  $C''$  signal detected at  $\omega_{m,2}$ , while excitation took place at frequencies 15.88 and 16.28 MHz, (g) the  $C'$  picture detected at  $\omega_{m,2}$ , while excitation took place at 235.579 kHz, (h) electric phase  $\varphi_{el}$  of the  $C'$  signal detected at  $\omega_{m,2}$ , while excitation took place at frequency 235.579 kHz, (i) the picture of the mechanical amplitude at the resonance frequency of 74.580 kHz, and (j) the picture of the mechanical phase at the resonance frequency of 74.580 kHz. This was conducted with the  $\mu$ masch's HQ:NSC18/Pt Cantilever.

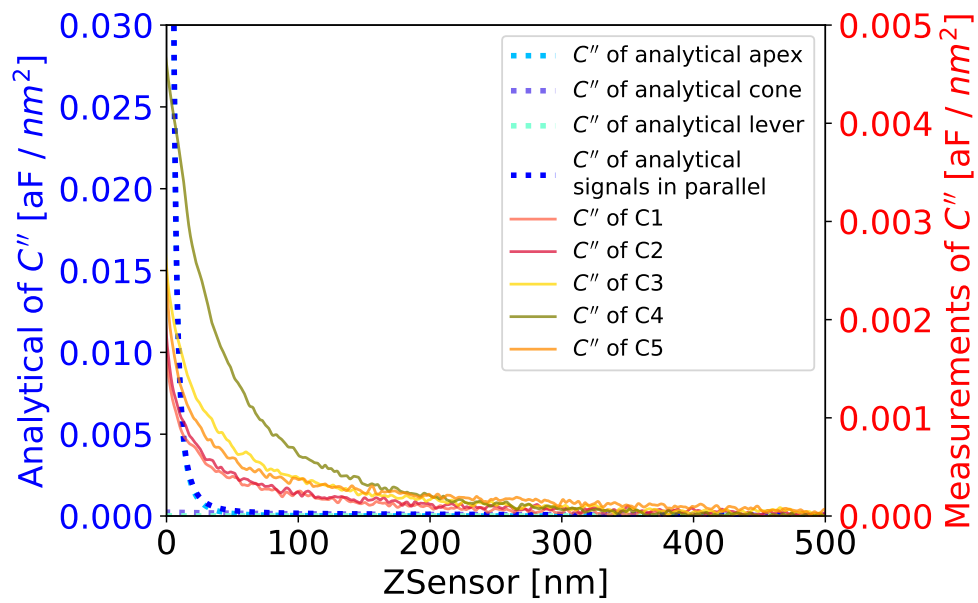


**Figure S16:** A comparison of the measured  $C''$  values on various capacitors, as shown in Figure 2, is presented. The measurements, performed using the NuNano SPARK 70 Pt cantilever (solid lines), are contrasted with the theoretical contributions of the respective components to the first numerical derivative  $C'$  of the capacitance (dotted lines) as a function of the tip-to-sample distance,  $z$ . For the theoretical calculations, the properties of the NuNano SPARK 70 Pt cantilever ( $w = 30 \mu\text{m}$ ,  $l = 225 \mu\text{m}$ ,  $\alpha = 11 \text{ deg}$ ,  $h = 12 \mu\text{m}$ ,  $\theta = 25 \text{ deg}$ ,  $r = 18 \text{ nm}$ ,  $\delta = 3.7 \cdot 10^{-7}$ ) with an mechanical amplitude of  $A_m = 10 \text{ nm}$ , an excitation voltage of  $V_{AC} = 2 \text{ V}$ , and a total amount of calculated points of 100,000, was used for these.

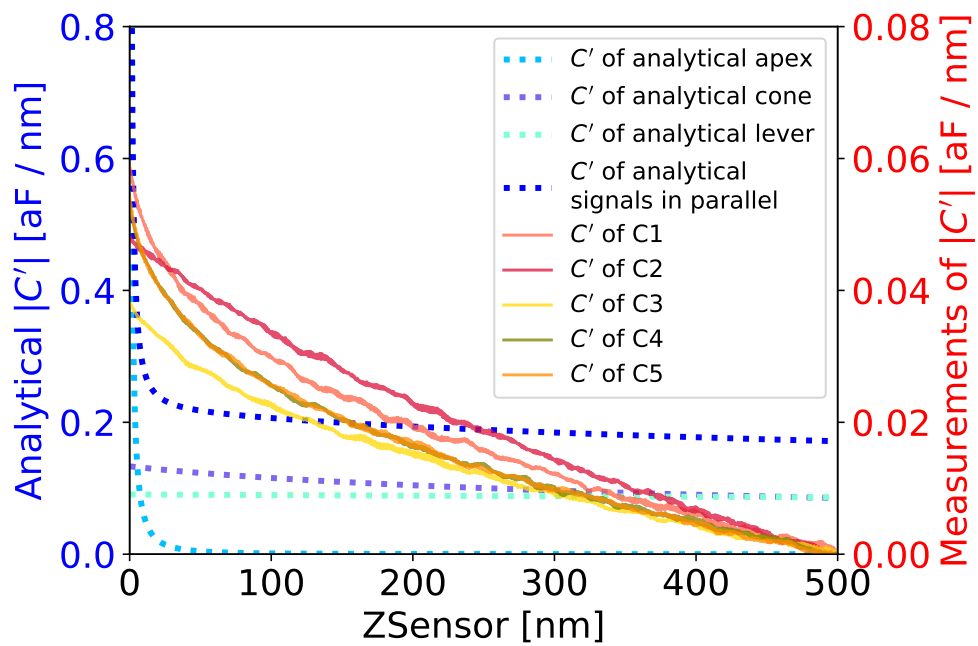


**Figure S17:** A comparison of the measured  $C'$  values on various capacitors, as shown in Figure 2, is presented. The measurements, performed using the NuNano SPARK 70 Pt cantilever (solid lines), are contrasted with the theoretical contributions of the respective components to the first numerical derivative  $C'$  of the capacitance (dotted lines) as a function of the tip-to-sample distance,  $z$ . For the theoretical calculations, the properties of the NuNano SPARK 70 Pt cantilever ( $w = 30 \mu\text{m}$ ,  $l = 225 \mu\text{m}$ ,  $\alpha = 11 \text{ deg}$ ,  $h = 12 \mu\text{m}$ ,  $\theta = 25 \text{ deg}$ ,  $r = 18 \text{ nm}$ ,  $\delta = 3.7 \cdot 10^{-7}$ ) with an mechanical amplitude of  $A_m = 10 \text{ nm}$ , an excitation voltage of  $V_{AC} = 2 \text{ V}$ , and a total amount of calculated points of 100,000, was used for these.

---

## References

1. Garrett, J. L.; Munday, J. N. *Nanotechnology* **2016**, *27* (24), 14. doi:10.1088/0957-4484/27/24/245705.
2. Axt, A.; Hermes, I. M.; Bergmann, V. W.; Tausendpfund, N.; Weber, S. A. L. *Beilstein J. Nanotechnol.* **2018**, *9* (1), 1809–1819. doi:10.3762/bjnano.9.172.
3. Jaensch, S.; Schmidt, H.; Grundmann, M. *Phys. B Condens. Matter* **2006**, *376-377* (1), 913–915. doi:10.1016/j.physb.2005.12.227.
4. Tran, T.; Oliver, D.; Thomson, D.; Bridges, G. Sub-zeptofarad sensitivity scanning capacitance microscopy. In *IEEE CCECE2002. Can. Conf. Electr. Comput. Eng. Conf. Proc. (Cat. No.02CH37373)*; IEEE, 2002; pp 455–459. doi:10.1109/CCECE.2002.1015268.
5. Raineri, V.; Giannazzo, F. *Solid State Phenom.* **2001**, *78-79*, 425–0. doi:10.4028/www.scientific.net/SSP.78-79.425.
6. Barrett, R. C.; Quate, C. F. *J. Appl. Phys.* **1991**, *70* (5), 2725–2733. doi:10.1063/1.349388.
7. Yamamoto, T.; Suzuki, Y.; Hiroyuki Sugimura, H. S.; Nobuyuki Nakagiri, N. N. *Jpn. J. Appl. Phys.* **1996**, *35* (6S), 3793. doi:10.1143/JJAP.35.3793.
8. Goto, K.; Hane, K. *Rev. Sci. Instrum.* **1997**, *68* (1), 120–123. doi:10.1063/1.1147749.
9. Goto, K.; Hane, K. <title>Tapping mode scanning capacitance microscopy: feasibility of quantitative capacitance measurement</title>. In *Micromach. Imaging*; Michalske, T. A., Wendman, M. A., Eds.; 1997; pp 84–91. doi:10.1117/12.271216.
10. Fumagalli, L.; Ferrari, G.; Sampietro, M.; Casuso, I.; Martínez, E.; Samitier, J.; Gomila, G. *Nanotechnology* **2006**, *17* (18), 4581–4587. doi:10.1088/0957-4484/17/18/009.
11. Fumagalli, L.; Ferrari, G.; Sampietro, M.; Gomila, G. *Appl. Phys. Lett.* **2007**, *91* (24), 243110. doi:10.1063/1.2821119.

12. Gomila, G.; Toset, J.; Fumagalli, L. *J. Appl. Phys.* **2008**, *104* (2), 024315. doi:10.1063/1.2957069.
13. Fumagalli, L.; Ferrari, G.; Sampietro, M.; Gomila, G. *Nano Lett.* **2009**, *9* (4), 1604–1608. doi:10.1021/nl803851u.
14. Matey, J. R.; Blanc, J. *J. Appl. Phys.* **1985**, *57* (5), 1437–1444. doi:10.1063/1.334506.
15. Arakawa, H.; Nishitani, R. *J. Vac. Sci. Technol. B Microelectron. Nanom. Struct. Process. Meas. Phenom.* **2001**, *19* (4), 1150–1153. doi:10.1116/1.1379796.
16. Lee, D. T.; Pelz, J. P.; Bhushan, B. *Nanotechnology* **2006**, *17* (5), 1484–1491. doi:10.1088/0957-4484/17/5/054.
17. Lee, D. T.; Pelz, J. P.; Bhushan, B. *Rev. Sci. Instrum.* **2002**, *73* (10), 3525–3533. doi:10.1063/1.1505655.
18. Isenbart, J.; Born, A.; Wiesendanger, R. *Appl. Phys. A Mater. Sci. Process.* **2001**, *72* (S2), S243–S251. doi:10.1007/s003390100793.
19. Kopanski, J. J.; Mayo, S. *Appl. Phys. Lett.* **1998**, *72* (19), 2469–2471. doi:10.1063/1.121397.
20. Casuso, I.; Fumagalli, L.; Gomila, G.; Padrós, E. *Appl. Phys. Lett.* **2007**, *91* (6), 063111. doi:10.1063/1.2767979.
21. Biberger, R.; Benstetter, G.; Schweinboeck, T.; Breitschopf, P.; Goebel, H. *Microelectron. Reliab.* **2008**, *48* (8-9), 1339–1342. doi:10.1016/j.microrel.2008.06.013.
22. Smoliner, J.; Basnar, B.; Golka, S.; Gornik, E.; Löffler, B.; Schatzmayr, M.; Enichlmair, H. *Appl. Phys. Lett.* **2001**, *79* (19), 3182–3184. doi:10.1063/1.1415044.
23. Brezna, W.; Schramboeck, M.; Lugstein, A.; Harasek, S.; Enichlmair, H.; Bertagnolli, E.; Gornik, E.; Smoliner, J. *Appl. Phys. Lett.* **2003**, *83* (20), 4253–4255. doi:10.1063/1.1628402.

- 
24. Giannazzo, F.; Raineri, V.; Mirabella, S.; Impellizzeri, G.; Priolo, F.; Fedele, M.; Mucciato, R. *J. Vac. Sci. Technol. B Microelectron. Nanom. Struct. Process. Meas. Phenom.* **2006**, *24* (1), 370–374. doi:10.1116/1.2151907.
  25. Brezna, W.; Fischer, M.; Wanzenboeck, H. D.; Bertagnolli, E.; Smoliner, J. *Appl. Phys. Lett.* **2006**, *88* (12), 122116. doi:10.1063/1.2189030.
  26. Futscher, M. H.; Lee, J. M.; McGovern, L.; Muscarella, L. A.; Wang, T.; Haider, M. I.; Fakharuddin, A.; Schmidt-Mende, L.; Ehrler, B. *Mater. Horizons* **2019**, *6* (7), 1497–1503. doi:10.1039/C9MH00445A.
  27. Kopanski, J. J.; Marchiando, J. F.; Lowney, J. R. *Mater. Sci. Eng. B* **1997**, *44* (1-3), 46–51. doi:10.1016/S0921-5107(96)01797-7.
  28. Kopanski, J. J.; Marchiando, J. F.; Lowney, J. R. *J. Vac. Sci. Technol. B Microelectron. Nanom. Struct. Process. Meas. Phenom.* **1996**, *14* (1), 242–247. doi:10.1116/1.588455.
  29. Goto, K.; Hane, K. *J. Appl. Phys.* **1998**, *84* (8), 4043–4048. doi:10.1063/1.368617.
  30. de Voogd, J.; van Spronsen, M.; Kalff, F.; Bryant, B.; Ostojić, O.; den Haan, A.; Groot, I.; Oosterkamp, T.; Otte, A.; Rost, M. *Ultramicroscopy* **2017**, *181*, 61–69. doi:10.1016/j.ultramic.2017.05.009.
  31. Hiranaga, Y.; Cho, Y. *Rev. Sci. Instrum.* **2019**, *90* (8), 1–12. doi:10.1063/1.5097906.
  32. Kobayashi, K.; Yamada, H.; Matsushige, K. *Appl. Phys. Lett.* **2002**, *81* (14), 2629–2631. doi:10.1063/1.1510582.
  33. Martin, Y.; Abraham, D. W.; Wickramasinghe, H. K. *Appl. Phys. Lett.* **1988**, *52* (13), 1103–1105. doi:10.1063/1.99224.
  34. Abraham, D. W.; Williams, C.; Slinkman, J.; Wickramasinghe, H. K. *J. Vac. Sci. Technol. B Microelectron. Nanom. Struct. Process. Meas. Phenom.* **1991**, *9* (2), 703–706. doi:10.1116/1.585536.

35. Gramse, G.; Casuso, I.; Toset, J.; Fumagalli, L.; Gomila, G. *Nanotechnology* **2009**, *20* (39), 395702. doi:10.1088/0957-4484/20/39/395702.
36. Fumagalli, L.; Gramse, G.; Esteban-Ferrer, D.; Edwards, M. A.; Gomila, G. *Appl. Phys. Lett.* **2010**, *96* (18), 183107. doi:10.1063/1.3427362.
37. Fumagalli, L.; Esteban-Ferrer, D.; Cuervo, A.; Carrascosa, J. L.; Gomila, G. *Nat. Mater.* **2012**, *11* (9), 808–816. doi:10.1038/nmat3369.
38. Gramse, G.; Edwards, M. A.; Fumagalli, L.; Gomila, G. *Appl. Phys. Lett.* **2012**, *101* (21), 213108. doi:10.1063/1.4768164.
39. Gramse, G.; Dols-Perez, A.; Edwards, M.; Fumagalli, L.; Gomila, G. *Biophys. J.* **2013**, *104* (6), 1257–1262. doi:10.1016/j.bpj.2013.02.011.
40. Kimura, K.; Kobayashi, K.; Yamada, H.; Matsushige, K. *Appl. Surf. Sci.* **2003**, *210* (1-2), 93–98. doi:10.1016/S0169-4332(02)01486-1.
41. Henning, A.; Hochwitz, T. *Mater. Sci. Eng. B* **1996**, *42* (1-3), 88–98. doi:10.1016/S0921-5107(96)01688-1.
42. Checa, M.; Neumayer, S. M.; Susner, M. A.; McGuire, M. A.; Maksymovych, P.; Collins, L. *Appl. Phys. Lett.* **2021**, *119* (25), 252905. doi:10.1063/5.0078034.
43. Li, Z.-y.; Gu, B.-y.; Yang, G.-z. *Phys. Rev. B* **1998**, *57* (15), 9225–9233. doi:10.1103/PhysRevB.57.9225.
44. Gil, A.; Colchero, J.; Gomez Herrero, J.; Bar, A. M. *Nanotechnology* **2003**, *14* (2), 332–340. doi:10.1088/0957-4484/14/2/345.
45. Fukuzawa, R.; Takahashi, T. *Rev. Sci. Instrum.* **2020**, *91* (2), 023702. doi:10.1063/1.5127219.
46. Izumi, R.; Miyazaki, M.; Li, Y. J.; Sugawara, Y. *Beilstein J. Nanotechnol.* **2023**, *14*, 175–189. doi:10.3762/bjnano.14.18.

- 
47. Cherniavskaya, O.; Chen, L.; Weng, V.; Yuditsky, L.; Brus, L. E. *J. Phys. Chem. B* **2003**, *107* (7), 1525–1531. doi:10.1021/jp0265438.
48. Crider, P. S.; Majewski, M. R.; Zhang, J.; Oukris, H.; Israeloff, N. E. *Appl. Phys. Lett.* **2007**, *91* (1), 2–5. doi:10.1063/1.2753539.
49. Cadena, M. J.; Sung, S. H.; Boudouris, B. W.; Reifenberger, R.; Raman, A. *ACS Nano* **2016**, *10*, 4062–4071. doi:10.1021/acsnano.5b06893. PMID: 26972782
50. Riedel, C.; Arinero, R.; Tordjeman, P.; L ev eque, G.; Schwartz, G. A.; Alegria, A.; Colmenero, J. *Phys. Rev. E* **2010**, *81* (1), 010801. doi:10.1103/PhysRevE.81.010801.
51. Gramse, G.; Sch onhals, A.; Kienberger, F. *Nanoscale* **2019**, *11* (10), 4303–4309. doi:10.1039/C8NR05880F.
52. Gramse, G.; K olker, A.; Škere n, T.; Stock, T. J. Z.; Aeppli, G.; Kienberger, F.; Fuhrer, A.; Curson, N. J. *Nat. Electron.* **2020**, *3* (9), 531–538. doi:10.1038/s41928-020-0450-8.



---

## 6 Summary and Outlook

In this PhD Thesis, the primary objective was to develop novel Atomic Force Microscopy (AFM) techniques and to utilize existing AFM techniques to gain a comprehensive understanding of the impact of passivation and the structural characteristics of perovskites, including grain boundaries (GBs) and interfaces, on the dynamics of free carriers and the migration of ions. This approach enabled the demonstration of efficient methods for studying interfaces and identifying device bottlenecks with new Electrostatic Force Microscopy (EFM)-based approaches.

The study in Chapter 3 addresses the critical challenge of non-radiative recombination losses in inverted (p-i-n) perovskite solar cells (PSCs), which arise from defects at GBs and interfacial recombination at the perovskite/ $C_{60}$  interface. While defect passivation strategies for GBs or interfaces had been explored individually, prior approaches failed to simultaneously mitigate both recombination pathways, leaving a gap in understanding how coordinated defect management across these distinct regions could synergistically enhance device performance and stability.

The hypothesis of this study was that phenethylammonium chloride ( $\text{Ph}-\text{C}_2\text{H}_4-\text{NH}_3^+ + \text{Cl}^-$ ) (PEACl) used as both a GB additive and surface treatment (dual passivation) would homogenize the perovskite surface and GBs by forming a heterogeneous 2D RUDDLESDEN-POPPER phase. The Kelvin Probe Force Microscopy (KPFM) data yielded substantial evidence that dual passivation homogenizes the perovskite surface and GBs by demonstrating a more uniform work function distribution across dual-passivated films in comparison to the control sample. This process enables concurrent enhancements in open circuit voltage ( $V_{\text{OC}}$ ), fill factor (FF), and operational stability. Furthermore, the heterogeneous 2D RUDDLESDEN-POPPER phase  $(\text{PEA})_2(\text{Cs}_{1-x}\text{FA}_x)_{n-1}\text{Pb}_n(\text{I}_{1-y}\text{Cl}_y)_{3n+1}$  with  $n \sim 1 - 2$  was demonstrated to prolong the lifetime of charge carriers and mitigate the process of non-radiative recombination, as indicated by the time-resolved photoluminescence (tr-PL) and photoluminescence quantum yield (PLQY) measurements. Furthermore, thermal admittance spectroscopy (TAS) revealed that passivation increased the activation energy for ion migration, thereby enhancing the device's stability under operational stresses such as light, heat, and humidity.

Notwithstanding these advancements, several unresolved inquiries persist. First, the precise mechanisms by which the PEACl-based RUDDLESDEN-POPPER phase interacts with different defect types at the GBs and interfaces require further elucidation. In consideration of the GBs and the formation of the phase, a definitive localization of the passivation molecules remains elusive. However, the advent of methodologies such as Time-of-Flight Secondary Ion Mass Spectrometry (ToF-SIMS) may in the future facilitate the confirmation of the unequal distribution of passivation molecules and the optimization of their density, thereby further enhancing the efficacy of passivation. Furthermore, while the strategy enhances stability, the scalability of this dual passivation method for industrial applications remains uncertain, particularly with regard to cost-effectiveness and reproducibility. A comprehensive investigation into the long-term effects of potential ion migration on device performance under continuous operation is imperative to ascertain commercial viability.

The study in Chapter 4 examined the correlation between nanoscale defect distributions (e.g., at grain boundaries or grain interiors) and localized charge carrier dynamics (e.g., recombination, ion migration) on the nanoscale. This investigation utilized time-resolved Kelvin Probe Force Microscopy (tr-KPFM) to perform nanoscale surface photovoltage spectroscopy (nano-SPV) and nanoscale ideality factor mapping (nano-IFM) spectroscopy. Lead halide perovskites have been shown to exhibit exceptional optoelectronic properties; however, they are subject to non-radiative recombination losses at GBs and interfaces, which serve to limit device efficiency. While macroscopic techniques, such as PL and surface photovoltage (SPV) measurements, provide averaged insights, they lack the spatial resolution to resolve nanoscale variations in defect density and charge carrier dynamics. Optical methods, such as PL microscopy, are inherently constrained by diffraction-limited resolution, typically ranging from  $\sim 200 - 300$  nm. Conversely, Scanning Electron Microscopy (SEM)-based surface photovoltage (SPV) spectroscopy entails the potential risk of sample damage due to the application of high-energy electron beams. Conventional KPFM lacks temporal resolution, which precludes its use in tracking dynamic processes such as ion migration and recombination at GBs.

The hypothesis was developed that nanoscale variations in defect density directly govern charge carrier recombination rates and ion migration kinetics, with GBs acting as hotspots for these losses. To test this hypothesis, a methodology based on tr-KPFM was developed that entailed the implementation of nano-SPV and nano-IFM. The utilization of these techniques enabled the spatial resolution of SPV dynamics during and immediately after light pulses. Additionally, a correlation was established between local ideality factors ( $n_{id}$ ) and defect density.

However, some open questions remain unsolved in this study. Initially, it should be noted

---

that while the study demonstrated reduced defect densities with larger grains and passivation, the exact formation and stability, similar to the work mentioned in Chapter 3, remains unclear. Furthermore, the role of chemical stoichiometry variations in influencing SPV dynamics remains unclear and warrants further investigation. The observed variations in SPV decay times across different grain facets suggest a facet-dependence of charge carrier dynamics that requires further elucidation. Finally, the interpretation of nanoscale ideality factor ( $n_{id}$ ) values below 1 in half-cell configurations prompts inquiries into their association with interfacial recombination and ion migration effects. These inquiries could be addressed in future studies to refine the understanding of recombination mechanisms in perovskite materials.

The study presented in Chapter 5 addresses a critical limitation in the field of nanoscale dielectric characterization. Conventional EFM methods are constrained by cantilever resonance frequencies and long-range electrostatic interactions, which impede high-frequency measurements and spatial resolution. Although Scanning Capacitance Microscopy (SCM) and single-frequency EFM have been demonstrated to offer insights into dielectric properties, both techniques are limited by non-local stray capacitances and frequency restrictions that are tied to mechanical resonances. A novel methodology has been developed, multi-frequency heterodyne Electrostatic Force Microscopy (MFH-EFM), that overcomes the aforementioned limitations. This methodology utilizes the probing of the second-order capacitance gradient ( $C''$ ), which inherently suppresses long-range force interactions. The result of this suppression is a reduction in signal background and the ability to perform frequency-dependent dielectric spectroscopy measurements. The method demonstrated a high degree of efficacy in measuring nanoscale dielectric properties across a broad frequency range, extending up to 50 MHz, by employing standard AFM equipment in conjunction with an external lock-in amplifier (LIA). The experimental findings on microfabricated  $\text{SiO}_2$  capacitors confirmed the enhanced locality of  $C''$ -based measurements. According to theoretical calculations, the signal from the tip alone contributes 82% of the total signal at a distance of 10 nm. Furthermore, high-frequency capacitance imaging of molecular structures yielded sharper contrasts in comparison with conventional methods, underscoring the potential of MFH-EFM for quantitative dielectric studies in materials science, biology, and nanotechnology.

Despite the notable advancements in the field, the existing models for tip-sample capacitance do not fully align with the experimental data, underscoring the necessity for enhanced theoretical frameworks or numerical simulations to facilitate precise extraction of capacitance values  $C$  and  $\epsilon_r$ . Furthermore, while MFH-EFM permits operation at elevated frequencies (up to 50 MHz), signal quality at these ranges is diminished by impedance effects in the electrical con-

nections. Subsequent endeavors should prioritize the optimization of the system configuration, encompassing the incorporation of specialized high-frequency hardware equipped with coaxial connections, with the objective of attaining reliable measurements at elevated frequencies. Furthermore, the extension of the method to extract dielectric properties with greater ease and accuracy will require advancements in calibration techniques and algorithms for analyzing complex nanoscale systems. These developments will lay the foundation for the utilization of these techniques in a more extensive manner for the characterization of dielectric heterogeneities at the nanoscale.

In summary, this PhD Thesis pioneered advanced AFM techniques to probe interfacial dynamics in solar cells and energy materials, yielding critical insights and methodologies. Noteworthy achievements include the development of MFH-EFM for nanoscale dielectric spectroscopy, enabling dielectric mapping and frequency-dependent analysis with high precision. A remarkable discovery was that 82 % of MFH-EFM force signal arises from the tip apex even at 10 nm distances, thereby emphasizing the locality of the measurement. The application of enhanced KPFM and tr-KPFM revealed the homogenization of electron-hole separation times at GBs by passivation, leading to a direct improvement in device efficiency. These methodologies establish the foundation for applications involving 2D materials, including dielectric breakdown measurements, investigations of interfaces in tandem solar cells, and (organic) light-emitting diode (LED) optimization. The MFH-EFM principle facilitates the profiling of dopants in semiconductors through the implementation of  $\partial C/\partial V$  measurements, thereby ensuring an unparalleled degree of resolution. The study underscored the imperative for artificial intelligence (AI)-driven automation to manage large datasets from advanced AFM modes, including conductive Atomic Force Microscopy (c-AFM), KPFM, general acquisition mode Kelvin Probe Force Microscopy (G-mode KPFM), tr-KPFM, and MFH-EFM. This approach is expected to expedite material discovery for photovoltaics and organic electronics. The future of this field lies in multi-frequency approaches, such as the detection of higher-order capacitance gradients (e.g.,  $C'''$ ), and the standardization of AFM data into machine-learning-compatible formats to bridge the materials science and computational communities. The thesis establishes the foundation for real-time, nanoscale diagnostics by integrating MFH-EFM with AI platforms, thereby promising "unknown-speed" analysis from sample preparation to imaging and interpretation. The integration of nanoscale metrology and intelligent automation has the potential to transform the design of next-generation energy devices, thereby fostering interdisciplinary innovation across various fields.<sup>1</sup>

---

<sup>1</sup>This chapter has been initially prepared with the help of artificial intelligence (AI) chatbot Perplexity AI, which provided a first version of the summary and outlook chapter. The text created by an AI algorithm has been further edited by the human author.

---

## 7 Bibliography

- (1) Al-Ashouri, A. et al. Monolithic perovskite/silicon tandem solar cell with >29% efficiency by enhanced hole extraction. *Science (80-. )*. **2020**, *370*, 1300–1309, DOI: 10.1126/science.abd4016.
- (2) Al-Ashouri, A. et al. Conformal monolayer contacts with lossless interfaces for perovskite single junction and monolithic tandem solar cells. *Energy Environ. Sci.* **2019**, *12*, 3356–3369, DOI: 10.1039/C9EE02268F.
- (3) Lin, X.; Cui, D.; Luo, X.; Zhang, C.; Han, Q.; Wang, Y.; Han, L. Efficiency progress of inverted perovskite solar cells. *Energy Environ. Sci.* **2020**, *13*, 3823–3847, DOI: 10.1039/D0EE02017F.
- (4) Stolterfoht, M.; Grischek, M.; Caprioglio, P.; Wolff, C. M.; Gutierrez-Partida, E.; Peña-Camargo, F.; Rothhardt, D.; Zhang, S.; Raoufi, M.; Wolansky, J.; Abdi-Jalebi, M.; Stranks, S. D.; Albrecht, S.; Kirchartz, T.; Neher, D. How To Quantify the Efficiency Potential of Neat Perovskite Films: Perovskite Semiconductors with an Implied Efficiency Exceeding 28%. *Adv. Mater.* **2020**, *32*, DOI: 10.1002/adma.202000080.
- (5) Stolterfoht, M. et al. The impact of energy alignment and interfacial recombination on the internal and external open-circuit voltage of perovskite solar cells. *Energy Environ. Sci.* **2019**, *12*, 2778–2788, DOI: 10.1039/C9EE02020A.
- (6) Luo, D.; Su, R.; Zhang, W.; Gong, Q.; Zhu, R. Minimizing non-radiative recombination losses in perovskite solar cells. *Nat. Rev. Mater.* **2019**, *5*, 44–60, DOI: 10.1038/s41578-019-0151-y.
- (7) Wolff, C. M.; Caprioglio, P.; Stolterfoht, M.; Neher, D. Nonradiative Recombination in Perovskite Solar Cells: The Role of Interfaces. *Adv. Mater.* **2019**, *31*, DOI: 10.1002/adma.201902762.
- (8) Stolterfoht, M.; Wolff, C. M.; Márquez, J. A.; Zhang, S.; Hages, C. J.; Rothhardt, D.; Albrecht, S.; Burn, P. L.; Meredith, P.; Unold, T.; Neher, D. Visualization and suppression of interfacial recombination for high-efficiency large-area pin perovskite solar cells. *Nat. Energy* **2018**, *3*, 847–854, DOI: 10.1038/s41560-018-0219-8.

- (9) Zhang, S.; Shaw, P. E.; Zhang, G.; Jin, H.; Tai, M.; Lin, H.; Meredith, P.; Burn, P. L.; Neher, D.; Stolterfoht, M. Defect/Interface Recombination Limited Quasi-Fermi Level Splitting and Open-Circuit Voltage in Mono- and Triple-Cation Perovskite Solar Cells. *ACS Appl. Mater. Interfaces* **2020**, *12*, 37647–37656, DOI: 10.1021/acsami.0c02960.
- (10) Li, Z.; Zhang, J.; Wu, S.; Deng, X.; Li, F.; Liu, D.; Lee, C.-C.; Lin, F.; Lei, D.; Chueh, C.-C.; Zhu, Z.; Jen, A. K.-Y. Minimized surface deficiency on wide-bandgap perovskite for efficient indoor photovoltaics. *Nano Energy* **2020**, *78*, 105377, DOI: 10.1016/j.nanoen.2020.105377.
- (11) Zhu, T.; Zheng, D.; Liu, J.; Coolen, L.; Pauporté, T. PEAI-Based Interfacial Layer for High-Efficiency and Stable Solar Cells Based on a MAI-Mediated Grown FA 0.94 MA 0.06 PbI<sub>3</sub> Perovskite. *ACS Appl. Mater. Interfaces* **2020**, *12*, 37197–37207, DOI: 10.1021/acsami.0c09970.
- (12) Dong, H.; Yue, M.; Pang, S.; Zhu, W.; Chen, D.; Xi, H.; Lin, Z.; Chang, J.; Zhang, J.; Hao, Y.; Zhang, C. A Modulated Double-Passivation Strategy Toward Highly Efficient Perovskite Solar Cells with Efficiency Over 21%. *Sol. RRL* **2019**, *3*, DOI: 10.1002/solr.201900291.
- (13) Cho, K. T.; Grancini, G.; Lee, Y.; Oveisi, E.; Ryu, J.; Almora, O.; Tschumi, M.; Schouwink, P. A.; Seo, G.; Heo, S.; Park, J.; Jang, J.; Paek, S.; Garcia-Belmonte, G.; Nazeeruddin, M. K. Selective growth of layered perovskites for stable and efficient photovoltaics. *Energy Environ. Sci.* **2018**, *11*, 952–959, DOI: 10.1039/C7EE03513F.
- (14) Lee, D. S.; Yun, J. S.; Kim, J.; Soufiani, A. M.; Chen, S.; Cho, Y.; Deng, X.; Seidel, J.; Lim, S.; Huang, S.; Ho-Baillie, A. W. Passivation of Grain Boundaries by Phenethylammonium in Formamidinium-Methylammonium Lead Halide Perovskite Solar Cells. *ACS Energy Lett.* **2018**, *3*, 647–654, DOI: 10.1021/acsenenergylett.8b00121.
- (15) Kim, D. H. et al. Bimolecular Additives Improve Wide-Band-Gap Perovskites for Efficient Tandem Solar Cells with CIGS. *Joule* **2019**, *3*, 1734–1745, DOI: 10.1016/j.joule.2019.04.012.
- (16) Fakharuddin, A.; Schmidt-Mende, L.; Garcia-Belmonte, G.; Jose, R.; Mora-Sero, I. Interfaces in Perovskite Solar Cells. *Adv. Energy Mater.* **2017**, *7*, DOI: 10.1002/aenm.201700623.
- (17) Schulz, P. Interface Design for Metal Halide Perovskite Solar Cells. *ACS Energy Lett.* **2018**, *3*, 1287–1293, DOI: 10.1021/acsenenergylett.8b00404.

- 
- (18) Zhou, G.; Luo, J.; Liu, C.; Chu, L.; Crittenden, J. Efficient heavy metal removal from industrial melting effluent using fixed-bed process based on porous hydrogel adsorbents. *Water Res.* **2018**, *131*, 246–254, DOI: 10.1016/j.watres.2017.12.067.
- (19) Roose, B.; Wang, Q.; Abate, A. The Role of Charge Selective Contacts in Perovskite Solar Cell Stability. *Adv. Energy Mater.* **2019**, *9*, 1–20, DOI: 10.1002/aenm.201803140.
- (20) Bergmann, V. W.; Guo, Y.; Tanaka, H.; Hermes, I. M.; Li, D.; Klasen, A.; Bretschneider, S. A.; Nakamura, E.; Berger, R.; Weber, S. A. Local Time-Dependent Charging in a Perovskite Solar Cell. *ACS Appl. Mater. Interfaces* **2016**, *8*, 19402–19409, DOI: 10.1021/acsami.6b04104.
- (21) Wang, H.; Guerrero, A.; Bou, A.; Al-Mayouf, A. M.; Bisquert, J. Kinetic and material properties of interfaces governing slow response and long timescale phenomena in perovskite solar cells. *Energy Environ. Sci.* **2019**, *12*, 2054–2079, DOI: 10.1039/C9EE00802K.
- (22) Steirer, K. X.; Schulz, P.; Teeter, G.; Stevanovic, V.; Yang, M.; Zhu, K.; Berry, J. J. Defect tolerance in methylammonium lead triiodide perovskite. *ACS Energy Letters* **2016**, *1*, 360–366.
- (23) Lei, Y.; Xu, Y.; Wang, M.; Zhu, G.; Jin, Z. Origin, influence, and countermeasures of defects in perovskite solar cells. *Small* **2021**, *17*, 2005495.
- (24) Zouhair, S.; Yoo, S.-M.; Bogachuk, D.; Herterich, J. P.; Lim, J.; Kanda, H.; Son, B.; Yun, H. J.; Würfel, U.; Chahboun, A.; Nazeeruddin, M. K.; Hinsch, A.; Wagner, L.; Kim, H. Employing 2D-Perovskite as an Electron Blocking Layer in Highly Efficient (18.5%) Perovskite Solar Cells with Printable Low Temperature Carbon Electrode. *Adv. Energy Mater.* **2022**, *12*, DOI: 10.1002/aenm.202200837.
- (25) Zhang, Y.; Zhu, Y.; Hu, M.; Pai, N.; Qin, T.; Cheng, Y.-B.; Bach, U.; Simonov, A. N.; Lu, J. Self-Enhancement of Efficiency and Self-Attenuation of Hysteretic Behavior of Perovskite Solar Cells with Aging. *J. Phys. Chem. Lett.* **2022**, *13*, 2792–2799, DOI: 10.1021/acs.jpcllett.2c00278.
- (26) Cox, P. A., *The Electronic Structure and Chemistry of Solids*; Oxford University Press: New York, 1987, p 270.
- (27) Bisquert, J., *The Physics of Solar Cells*; CRC Press: Boca Raton, FL : CRC Press, Taylor & Francis Group, [2018], 2017, DOI: 10.1201/b22380.
- (28) Shen, C., *Atomic Force Microscopy for Energy Research*; CRC Press: Boca Raton, 2022, DOI: 10.1201/9781003174042.

- (29) Yang, Y.; Antoniou, N.; Chintala, R. In *At. Force Microsc. Energy Res.* CRC Press: Boca Raton, 2022, pp 185–212, DOI: 10.1201/9781003174042-5.
- (30) Garcia, R.; Herruzo, E. T. The emergence of multifrequency force microscopy. *Nat. Nanotechnol.* **2012**, *7*, 217–226, DOI: 10.1038/nnano.2012.38.
- (31) Kobayashi, K.; Yamada, H.; Matsushige, K. Dopant profiling on semiconducting sample by scanning capacitance force microscopy. *Appl. Phys. Lett.* **2002**, *81*, 2629–2631, DOI: 10.1063/1.1510582.
- (32) Martin, Y.; Abraham, D. W.; Wickramasinghe, H. K. High-resolution capacitance measurement and potentiometry by force microscopy. *Appl. Phys. Lett.* **1988**, *52*, 1103–1105, DOI: 10.1063/1.99224.
- (33) Abraham, D. W.; Williams, C.; Slinkman, J.; Wickramasinghe, H. K. Lateral dopant profiling in semiconductors by force microscopy using capacitive detection. *J. Vac. Sci. Technol. B Microelectron. Nanom. Struct. Process. Meas. Phenom.* **1991**, *9*, 703–706, DOI: 10.1116/1.585536.
- (34) Gramse, G.; Casuso, I.; Toset, J.; Fumagalli, L.; Gomila, G. Quantitative dielectric constant measurement of thin films by DC electrostatic force microscopy. *Nanotechnology* **2009**, *20*, 395702, DOI: 10.1088/0957-4484/20/39/395702.
- (35) Fumagalli, L.; Gramse, G.; Esteban-Ferrer, D.; Edwards, M. A.; Gomila, G. Quantifying the dielectric constant of thick insulators using electrostatic force microscopy. *Appl. Phys. Lett.* **2010**, *96*, 183107, DOI: 10.1063/1.3427362.
- (36) Fumagalli, L.; Esteban-Ferrer, D.; Cuervo, A.; Carrascosa, J. L.; Gomila, G. Label-free identification of single dielectric nanoparticles and viruses with ultraweak polarization forces. *Nat. Mater.* **2012**, *11*, 808–816, DOI: 10.1038/nmat3369.
- (37) Gramse, G.; Edwards, M. A.; Fumagalli, L.; Gomila, G. Dynamic electrostatic force microscopy in liquid media. *Appl. Phys. Lett.* **2012**, *101*, 213108, DOI: 10.1063/1.4768164.
- (38) Gramse, G.; Dols-Perez, A.; Edwards, M.; Fumagalli, L.; Gomila, G. Nanoscale Measurement of the Dielectric Constant of Supported Lipid Bilayers in Aqueous Solutions with Electrostatic Force Microscopy. *Biophys. J.* **2013**, *104*, 1257–1262, DOI: 10.1016/j.bpj.2013.02.011.
- (39) Kimura, K.; Kobayashi, K.; Yamada, H.; Matsushige, K. Two-dimensional dopant profiling by scanning capacitance force microscopy. *Appl. Surf. Sci.* **2003**, *210*, 93–98, DOI: 10.1016/S0169-4332(02)01486-1.

- 
- (40) Henning, A.; Hochwitz, T. Scanning probe microscopy for 2-D semiconductor dopant profiling and device failure analysis. *Mater. Sci. Eng. B* **1996**, *42*, 88–98, DOI: 10.1016/S0921-5107(96)01688-1.
- (41) Checa, M.; Neumayer, S. M.; Susner, M. A.; McGuire, M. A.; Maksymovych, P.; Collins, L. Simultaneous mapping of nanoscale dielectric, electrochemical, and ferroelectric surface properties of van der Waals layered ferroelectric via advanced SPM. *Appl. Phys. Lett.* **2021**, *119*, 252905, DOI: 10.1063/5.0078034.
- (42) Li, Z.-y.; Gu, B.-y.; Yang, G.-z. Scanning-electrostatic-force microscopy: Self-consistent method for mesoscopic surface structures. *Phys. Rev. B* **1998**, *57*, 9225–9233, DOI: 10.1103/PhysRevB.57.9225.
- (43) Gil, A.; Colchero, J.; Gomez-Herrero, J.; Bar, A. M. Electrostatic force gradient signal: resolution enhancement in electrostatic force microscopy and improved Kelvin probe microscopy. *Nanotechnology* **2003**, *14*, 332–340, DOI: 10.1088/0957-4484/14/2/345.
- (44) Fukuzawa, R.; Takahashi, T. Development of dual bias modulation electrostatic force microscopy for variable frequency measurements of capacitance. *Rev. Sci. Instrum.* **2020**, *91*, 023702, DOI: 10.1063/1.5127219.
- (45) Izumi, R.; Miyazaki, M.; Li, Y. J.; Sugawara, Y. High–low Kelvin probe force spectroscopy for measuring the interface state density. *Beilstein J. Nanotechnol.* **2023**, *14*, 175–189, DOI: 10.3762/bjnano.14.18.
- (46) Cherniavskaya, O.; Chen, L.; Weng, V.; Yuditsky, L.; Brus, L. E. Quantitative Noncontact Electrostatic Force Imaging of Nanocrystal Polarizability. *J. Phys. Chem. B* **2003**, *107*, 1525–1531, DOI: 10.1021/jp0265438.
- (47) Crider, P. S.; Majewski, M. R.; Zhang, J.; Oukris, H.; Israeloff, N. E. Local dielectric spectroscopy of polymer films. *Appl. Phys. Lett.* **2007**, *91*, 2–5, DOI: 10.1063/1.2753539.
- (48) Cadena, M. J.; Sung, S. H.; Boudouris, B. W.; Reifenberger, R.; Raman, A. Nanoscale Mapping of Dielectric Properties of Nanomaterials from KiloHertz to Megahertz Using Ultrasmall Cantilevers. *ACS Nano* **2016**, *10*, 4062–4071, DOI: 10.1021/acsnano.5b06893.
- (49) Riedel, C.; Arinero, R.; Tordjeman, P.; L ev eque, G.; Schwartz, G. A.; Alegria, A.; Colmenero, J. Nanodielectric mapping of a model polystyrene-poly(vinyl acetate) blend by electrostatic force microscopy. *Phys. Rev. E* **2010**, *81*, 010801, DOI: 10.1103/PhysRevE.81.010801.

- (50) Gramse, G.; Schönhals, A.; Kienberger, F. Nanoscale dipole dynamics of protein membranes studied by broadband dielectric microscopy. *Nanoscale* **2019**, *11*, 4303–4309, DOI: 10.1039/C8NR05880F.
- (51) Gramse, G.; Kölker, A.; Škereň, T.; Stock, T. J. Z.; Aeppli, G.; Kienberger, F.; Fuhrer, A.; Curson, N. J. Nanoscale imaging of mobile carriers and trapped charges in delta doped silicon p–n junctions. *Nat. Electron.* **2020**, *3*, 531–538, DOI: 10.1038/s41928-020-0450-8.
- (52) Jaensch, S.; Schmidt, H.; Grundmann, M. Quantitative scanning capacitance microscopy. *Phys. B Condens. Matter* **2006**, *376-377*, 913–915, DOI: 10.1016/j.physb.2005.12.227.
- (53) Tran, T.; Oliver, D.; Thomson, D.; Bridges, G. In *IEEE CCECE2002. Can. Conf. Electr. Comput. Eng. Conf. Proc. (Cat. No.02CH37373)*, IEEE: 2002; Vol. 1, pp 455–459, DOI: 10.1109/CCECE.2002.1015268.
- (54) Raineri, V.; Giannazzo, F. Scanning Capacitance Microscopy on Semiconductor Materials. *Solid State Phenom.* **2001**, *78-79*, 425–, DOI: 10.4028/www.scientific.net/SSP.78-79.425.
- (55) Barrett, R. C.; Quate, C. F. Charge storage in a nitride-oxide-silicon medium by scanning capacitance microscopy. *J. Appl. Phys.* **1991**, *70*, 2725–2733, DOI: 10.1063/1.349388.
- (56) Goto, K.; Hane, K. Tapping mode capacitance microscopy. *Rev. Sci. Instrum.* **1997**, *68*, 120–123, DOI: 10.1063/1.1147749.
- (57) Fumagalli, L.; Ferrari, G.; Sampietro, M.; Casuso, I.; Martínez, E.; Samitier, J.; Gomila, G. Nanoscale capacitance imaging with attofarad resolution using ac current sensing atomic force microscopy. *Nanotechnology* **2006**, *17*, 4581–4587, DOI: 10.1088/0957-4484/17/18/009.
- (58) Gomila, G.; Toset, J.; Fumagalli, L. Nanoscale capacitance microscopy of thin dielectric films. *J. Appl. Phys.* **2008**, *104*, 024315, DOI: 10.1063/1.2957069.
- (59) Fumagalli, L.; Ferrari, G.; Sampietro, M.; Gomila, G. Quantitative Nanoscale Dielectric Microscopy of Single-Layer Supported Biomembranes. *Nano Lett.* **2009**, *9*, 1604–1608, DOI: 10.1021/nl803851u.
- (60) Matey, J. R.; Blanc, J. Scanning capacitance microscopy. *J. Appl. Phys.* **1985**, *57*, 1437–1444, DOI: 10.1063/1.334506.

- 
- (61) Arakawa, H.; Nishitani, R. Spatially resolved measurements of the capacitance by scanning tunneling microscope combined with a capacitance bridge. *J. Vac. Sci. Technol. B Microelectron. Nanom. Struct. Process. Meas. Phenom.* **2001**, *19*, 1150–1153, DOI: 10.1116/1.1379796.
- (62) Lee, D. T.; Pelz, J. P.; Bhushan, B. Scanning capacitance microscopy for thin film measurements. *Nanotechnology* **2006**, *17*, 1484–1491, DOI: 10.1088/0957-4484/17/5/054.
- (63) Lee, D. T.; Pelz, J. P.; Bhushan, B. Instrumentation for direct, low frequency scanning capacitance microscopy, and analysis of position dependent stray capacitance. *Rev. Sci. Instrum.* **2002**, *73*, 3525–3533, DOI: 10.1063/1.1505655.
- (64) Isenbart, J.; Born, A.; Wiesendanger, R. The physical principles of scanning capacitance spectroscopy. *Appl. Phys. A Mater. Sci. Process.* **2001**, *72*, S243–S251, DOI: 10.1007/s003390100793.
- (65) Kopanski, J. J.; Mayo, S. Intermittent-contact scanning capacitance microscope for lithographic overlay measurement. *Appl. Phys. Lett.* **1998**, *72*, 2469–2471, DOI: 10.1063/1.121397.
- (66) Casuso, I.; Fumagalli, L.; Gomila, G.; Padrós, E. Nondestructive thickness measurement of biological layers at the nanoscale by simultaneous topography and capacitance imaging. *Appl. Phys. Lett.* **2007**, *91*, 063111, DOI: 10.1063/1.2767979.
- (67) Biberger, R.; Benstetter, G.; Schweinboeck, T.; Breitschopf, P.; Goebel, H. Intermittent-contact scanning capacitance microscopy versus contact mode SCM applied to 2D dopant profiling. *Microelectron. Reliab.* **2008**, *48*, 1339–1342, DOI: 10.1016/j.microrel.2008.06.013.
- (68) Smoliner, J.; Basnar, B.; Golka, S.; Gornik, E.; Löffler, B.; Schatzmayr, M.; Enichlmair, H. Mechanism of bias-dependent contrast in scanning-capacitance-microscopy images. *Appl. Phys. Lett.* **2001**, *79*, 3182–3184, DOI: 10.1063/1.1415044.
- (69) Brezna, W.; Schramboeck, M.; Lugstein, A.; Harasek, S.; Enichlmair, H.; Bertagnolli, E.; Gornik, E.; Smoliner, J. Quantitative scanning capacitance spectroscopy. *Appl. Phys. Lett.* **2003**, *83*, 4253–4255, DOI: 10.1063/1.1628402.
- (70) Giannazzo, F.; Raineri, V.; Mirabella, S.; Impellizzeri, G.; Priolo, F.; Fedele, M.; Mucciato, R. Scanning capacitance microscopy: Quantitative carrier profiling down to nanostructures. *J. Vac. Sci. Technol. B Microelectron. Nanom. Struct. Process. Meas. Phenom.* **2006**, *24*, 370–374, DOI: 10.1116/1.2151907.

- (71) Brezna, W.; Fischer, M.; Wanzenboeck, H. D.; Bertagnolli, E.; Smoliner, J. Electron-beam deposited SiO<sub>2</sub> investigated by scanning capacitance microscopy. *Appl. Phys. Lett.* **2006**, *88*, 122116, DOI: 10.1063/1.2189030.
- (72) Futscher, M. H.; Lee, J. M.; McGovern, L.; Muscarella, L. A.; Wang, T.; Haider, M. I.; Fakharuddin, A.; Schmidt-Mende, L.; Ehrler, B. Quantification of ion migration in CH<sub>3</sub>NH<sub>3</sub>PbI<sub>3</sub> perovskite solar cells by transient capacitance measurements. *Mater. Horizons* **2019**, *6*, 1497–1503, DOI: 10.1039/C9MH00445A.
- (73) Kopanski, J. J.; Marchiando, J. F.; Lowney, J. R. Scanning capacitance microscopy applied to two-dimensional dopant profiling of semiconductors. *Mater. Sci. Eng. B* **1997**, *44*, 46–51, DOI: 10.1016/S0921-5107(96)01797-7.
- (74) Kopanski, J. J.; Marchiando, J. F.; Lowney, J. R. Scanning capacitance microscopy measurements and modeling: Progress towards dopant profiling of silicon. *J. Vac. Sci. Technol. B Microelectron. Nanom. Struct. Process. Meas. Phenom.* **1996**, *14*, 242–247, DOI: 10.1116/1.588455.
- (75) Goto, K.; Hane, K. Tip-sample capacitance in capacitance microscopy of dielectric films. *J. Appl. Phys.* **1998**, *84*, 4043–4048, DOI: 10.1063/1.368617.
- (76) De Voogd, J.; van Spronsen, M.; Kalff, F.; Bryant, B.; Ostojić, O.; den Haan, A.; Groot, I.; Oosterkamp, T.; Otte, A.; Rost, M. Fast and reliable pre-approach for scanning probe microscopes based on tip-sample capacitance. *Ultramicroscopy* **2017**, *181*, 61–69, DOI: 10.1016/j.ultramicro.2017.05.009.
- (77) Hiranaga, Y.; Cho, Y. Carrier distribution imaging using  $\partial C/\partial z$ -mode scanning nonlinear dielectric microscopy. *Rev. Sci. Instrum.* **2019**, *90*, 1–12, DOI: 10.1063/1.5097906.
- (78) Kitamura, S.; Iwatsuki, M. High-resolution imaging of contact potential difference with ultrahigh vacuum noncontact atomic force microscope. *Applied Physics Letters* **1998**, *72*, 3154–3156.
- (79) Miccio, L. A.; Kummali, M. M.; Schwartz, G. A.; Alegría, Á.; Colmenero, J. AFM based dielectric spectroscopy: Extended frequency range through excitation of cantilever higher eigenmodes. *Ultramicroscopy* **2014**, *146*, 55–61, DOI: 10.1016/j.ultramicro.2014.06.006.
- (80) Yamada, H. Present status and future prospects of electric force microscopy. *Nonlinear Theory and Its Applications, IEICE* **2017**, *8*, 80–84.

- 
- (81) Sahoo, K. K.; Pradhan, D.; Ghosh, S. P.; Gartia, A.; Kar, J. P. Modulation of electrical properties of sputtered Ta<sub>2</sub>O<sub>5</sub> films by variation of RF power and substrate temperature. *Phys. Scr.* **2024**, *99*, 025934, DOI: 10.1088/1402-4896/ad196b.
- (82) Zhu, C.; Liu, A.; Liu, G.; Jiang, G.; Meng, Y.; Fortunato, E.; Martins, R.; Shan, F. Low-temperature, nontoxic water-induced high-k zirconium oxide dielectrics for low-voltage, high-performance oxide thin-film transistors. *J. Mater. Chem. C* **2016**, *4*, 10715–10721, DOI: 10.1039/C6TC02607A.
- (83) Paily, R.; DasGupta, A.; DasGupta, N.; Bhattacharya, P.; Misra, P.; Ganguli, T.; Kukreja, L. M.; Balamurugan, A.; Rajagopalan, S.; Tyagi, A. Pulsed laser deposition of TiO<sub>2</sub> for MOS gate dielectric. *Appl. Surf. Sci.* **2002**, *187*, 297–304, DOI: 10.1016/S0169-4332(01)01040-6.
- (84) Robertson, J. High dielectric constant gate oxides for metal oxide Si transistors. *Reports Prog. Phys.* **2006**, *69*, 327–396, DOI: 10.1088/0034-4885/69/2/R02.
- (85) Werner, F.; Babbe, F.; Elanzeery, H.; Siebentritt, S. Can we see defects in capacitance measurements of thin-film solar cells? *Prog. Photovoltaics Res. Appl.* **2019**, *27*, 1045–1058, DOI: 10.1002/pip.3196.
- (86) Rodríguez, T. R.; García, R. Compositional mapping of surfaces in atomic force microscopy by excitation of the second normal mode of the microcantilever. *Appl. Phys. Lett.* **2004**, *84*, 449–451, DOI: 10.1063/1.1642273.
- (87) Lozano, J. R.; Garcia, R. Theory of Multifrequency Atomic Force Microscopy. *Phys. Rev. Lett.* **2008**, *100*, 076102, DOI: 10.1103/PhysRevLett.100.076102.
- (88) Platz, D.; Tholén, E. A.; Pesen, D.; Haviland, D. B. Intermodulation atomic force microscopy. *Appl. Phys. Lett.* **2008**, *92*, 153106, DOI: 10.1063/1.2909569.
- (89) Hutter, C.; Platz, D.; Tholén, E. A.; Hansson, T. H.; Haviland, D. B. Reconstructing Nonlinearities with Intermodulation Spectroscopy. *Phys. Rev. Lett.* **2010**, *104*, 050801, DOI: 10.1103/PhysRevLett.104.050801.
- (90) Kilpatrick, J. I.; Kargin, E.; Rodriguez, B. J. Comparing the performance of single and multifrequency Kelvin probe force microscopy techniques in air and water. *Beilstein J. Nanotechnol.* **2022**, *13*, 922–943, DOI: 10.3762/bjnano.13.82.
- (91) Santos, S.; Lai, C.-Y.; Olukan, T.; Chiesa, M. Multifrequency AFM: from origins to convergence. *Nanoscale* **2017**, *9*, 5038–5043, DOI: 10.1039/C7NR00993C.

- (92) Preiner, J.; Tang, J.; Pastushenko, V.; Hinterdorfer, P. Higher Harmonic Atomic Force Microscopy: Imaging of Biological Membranes in Liquid. *Phys. Rev. Lett.* **2007**, *99*, 046102, DOI: 10.1103/PhysRevLett.99.046102.
- (93) Cartagena-Rivera, A. X.; Wang, W.-H.; Geahlen, R. L.; Raman, A. Fast, multi-frequency and quantitative nanomechanical mapping of live cells using the atomic force microscope. *Sci. Rep.* **2015**, *5*, 11692, DOI: 10.1038/srep11692.
- (94) Harcombe, D. M.; Ruppert, M. G.; Fleming, A. J. A review of demodulation techniques for multifrequency atomic force microscopy. *Beilstein J. Nanotechnol.* **2020**, *11*, 76–91, DOI: 10.3762/bjnano.11.8.
- (95) Dobryden, I.; Borgani, R.; Rigoni, F.; Ghamgosar, P.; Concina, I.; Almqvist, N.; Vomiero, A. Nanoscale characterization of an all-oxide core–shell nanorod heterojunction using intermodulation atomic force microscopy (AFM) methods. *Nanoscale Adv.* **2021**, *3*, 4388–4394, DOI: 10.1039/D1NA00319D.
- (96) Miyazaki, M.; Sugawara, Y.; Li, Y. J. Dual-bias modulation heterodyne Kelvin probe force microscopy in FM mode. *Appl. Phys. Lett.* **2022**, *121*, 241602, DOI: 10.1063/5.0129433.
- (97) Gharibzadeh, S. et al. Two birds with one stone: dual grain-boundary and interface passivation enables >22% efficient inverted methylammonium-free perovskite solar cells. *Energy Environ. Sci.* **2021**, *14*, 5875–5893, DOI: 10.1039/D1EE01508G.
- (98) Yalcinkaya, Y.; Rohrbeck, P. N.; Schütz, E. R.; Fakharuddin, A.; Schmidt-Mende, L.; Weber, S. A. Nanoscale Surface Photovoltage Spectroscopy. *Adv. Opt. Mater.* **2024**, *12*, 1–12, DOI: 10.1002/adom.202301318.
- (99) Rohrbeck, P. N.; Cavar, L. D.; Weber, F.; Reichel, P. G.; Niebling, M.; Weber, S. A. L. Nanoscale capacitance spectroscopy based on multifrequency electrostatic force microscopy. *Beilstein J. Nanotechnol.* **2025**, *16*, 637–651, DOI: 10.3762/bjnano.16.49.
- (100) Liang, J.; Ender, C. P.; Rohrbeck, P.; Graf, R.; Lieberwirth, I.; Räder, H.-J.; Wagner, M.; Weber, S. A.; Müllen, K.; Weil, T. High pressure induced formation of carbon nanorods from tetracosane. *Diam. Relat. Mater.* **2024**, *143*, 110913, DOI: 10.1016/j.diamond.2024.110913.
- (101) Hassan, A.; Wang, Z.; Ahn, Y. H.; Azam, M.; Khan, A. A.; Farooq, U.; Zubair, M.; Cao, Y. Recent defect passivation drifts and role of additive engineering in perovskite photovoltaics. *Nano Energy* **2022**, *101*, 107579, DOI: 10.1016/j.nanoen.2022.107579.

- 
- (102) Tennyson, E. M.; Howard, J. M.; Leite, M. S. Mesoscale Functional Imaging of Materials for Photovoltaics. *ACS Energy Lett.* **2017**, *2*, 1825–1834, DOI: 10.1021/acsenerylett.7b00382.
- (103) Howard, J. M.; Lahoti, R.; Leite, M. S. Imaging Metal Halide Perovskites Material and Properties at the Nanoscale. *Adv. Energy Mater.* **2020**, *10*, 1903161, DOI: 10.1002/aenm.201903161.
- (104) Hidalgo, J.; Castro-Méndez, A. F.; Correa-Baena, J. P. Imaging and Mapping Characterization Tools for Perovskite Solar Cells. *Adv. Energy Mater.* **2019**, *9*, 1–30, DOI: 10.1002/aenm.201900444.
- (105) Rohrbeck, P. N. Untersuchung von lokalen Aufladungsdynamiken an Perowskit-Korngrenzen mit zeitaufgelösten KPFM Methoden, Master thesis, Johannes Gutenberg University Mainz, 2021, pp 1–116.
- (106) De Amorim, W. S.; Valduga, I. B.; Ribeiro, J. M. P.; Williamson, V. G.; Krauser, G. E.; Magtoto, M. K.; de Andrade Guerra, J. B. S. O. The nexus between water, energy, and food in the context of the global risks: An analysis of the interactions between food, water, and energy security. *Environ. Impact Assess. Rev.* **2018**, *72*, 1–11, DOI: 10.1016/j.eiar.2018.05.002.
- (107) M, D.; Prem, A.; Mohan, B. Accident alert using GPS technology & automated traffic light control for ambulance. *IJARCCCE* **2015**, 284–286, DOI: 10.17148/IJARCCCE.2015.4164.
- (108) Rabaia, M. K. H.; Abdelkareem, M. A.; Sayed, E. T.; Elsaid, K.; Chae, K.-J.; Wilberforce, T.; Olabi, A. Environmental impacts of solar energy systems: A review. *Sci. Total Environ.* **2020**, *754*, 141989, DOI: 10.1016/j.scitotenv.2020.141989.
- (109) Wiatros-Motyka, M.; Fulghum, Nicolas Jones, D. *Global Electricity Review*; tech. rep.; 2024, p 191.
- (110) Kannan, N.; Vakeesan, D. Solar energy for future world: - A review. *Renew. Sustain. Energy Rev.* **2016**, *62*, 1092–1105, DOI: 10.1016/j.rser.2016.05.022.
- (111) Furlan, C.; Mortarino, C. Forecasting the impact of renewable energies in competition with non-renewable sources. *Renew. Sustain. Energy Rev.* **2018**, *81*, 1879–1886, DOI: 10.1016/j.rser.2017.05.284.
- (112) Elsaid, K.; Sayed, E. T.; Abdelkareem, M. A.; Baroutaji, A.; Olabi, A. Environmental impact of desalination processes: Mitigation and control strategies. *Sci. Total Environ.* **2020**, *740*, 140125, DOI: 10.1016/j.scitotenv.2020.140125.

- (113) Elsaid, K.; Sayed, E. T.; Abdelkareem, M. A.; Mahmoud, M. S.; Ramadan, M.; Olabi, A. Environmental impact of emerging desalination technologies: A preliminary evaluation. *J. Environ. Chem. Eng.* **2020**, *8*, 104099, DOI: 10.1016/j.jece.2020.104099.
- (114) Elsaid, K.; Kamil, M.; Sayed, E. T.; Abdelkareem, M. A.; Wilberforce, T.; Olabi, A. Environmental impact of desalination technologies: A review. *Sci. Total Environ.* **2020**, *748*, 141528, DOI: 10.1016/j.scitotenv.2020.141528.
- (115) Friedlingstein, P. et al. Global Carbon Budget 2023. *Earth Syst. Sci. Data* **2023**, *15*, 5301–5369, DOI: 10.5194/essd-15-5301-2023.
- (116) Lan, X.; Tans, P.; Thoning, K. *Trends in globally-averaged CO<sub>2</sub> determined from NOAA Global Monitoring Laboratory measurements*; tech. rep.; Global Monitoring Laboratory, 2025, DOI: <https://doi.org/10.15138/9NOH-ZH07>.
- (117) Morice, C. P.; Kennedy, J. J.; Rayner, N. A.; Winn, J. P.; Hogan, E.; Killick, R. E.; Dunn, R. J. H.; Osborn, T. J.; Jones, P. D.; Simpson, I. R. An Updated Assessment of Near-Surface Temperature Change From 1850: The HadCRUT5 Data Set. *J. Geophys. Res. Atmos.* **2021**, *126*, DOI: 10.1029/2019JD032361.
- (118) Dracup, J. A.; Lee, K. S.; Paulson, E. G. On the definition of droughts. *Water Resour. Res.* **1980**, *16*, 297–302, DOI: 10.1029/WR016i002p00297.
- (119) Kallis, G. Droughts. *Annu. Rev. Environ. Resour.* **2008**, *33*, 85–118, DOI: 10.1146/annurev.enviro.33.081307.123117.
- (120) Bukhary, S.; Ahmad, S.; Batista, J. Analyzing land and water requirements for solar deployment in the Southwestern United States. *Renew. Sustain. Energy Rev.* **2018**, *82*, 3288–3305, DOI: 10.1016/j.rser.2017.10.016.
- (121) Trenberth, K. E.; Fasullo, J. T.; Balmaseda, M. A. Earth’s Energy Imbalance. *J. Clim.* **2014**, *27*, 3129–3144, DOI: 10.1175/JCLI-D-13-00294.1.
- (122) MacDougall, A. H.; Friedlingstein, P. The Origin and Limits of the Near Proportionality between Climate Warming and Cumulative CO<sub>2</sub> Emissions. *J. Clim.* **2015**, *28*, 4217–4230, DOI: 10.1175/JCLI-D-14-00036.1.
- (123) Supran, G.; Rahmstorf, S.; Oreskes, N. Assessing ExxonMobil’s global warming projections. *Science (80-. )*. **2023**, *379*, DOI: 10.1126/science.abk0063.
- (124) In *Hybrid Perovskite Solar Cells*; John Wiley & Sons, Ltd: 2021, pp i–xix, DOI: <https://doi.org/10.1002/9783527825851.fmatter>.

- (125) Malinauskaite, J.; Jouhara, H.; Egilegor, B.; Al-Mansour, F.; Ahmad, L.; Pusnik, M. Energy efficiency in the industrial sector in the EU, Slovenia, and Spain. *Energy* **2020**, *208*, 118398, DOI: 10.1016/j.energy.2020.118398.
- (126) Jouhara, H.; Olabi, A. G. Editorial: Industrial waste heat recovery. *Energy* **2018**, *160*, 1–2, DOI: 10.1016/j.energy.2018.07.013.
- (127) Abdelkareem, M. A.; Elsaid, K.; Wilberforce, T.; Kamil, M.; Sayed, E. T.; Olabi, A. Environmental aspects of fuel cells: A review. *Sci. Total Environ.* **2020**, *752*, 141803, DOI: 10.1016/j.scitotenv.2020.141803.
- (128) De l'Epine, M.; Kaizuka, I. *Trends in Photovoltaic Applications 2024*; tech. rep.; 2024, DOI: 10.69766/JNEW6916.
- (129) Dupont, E.; Koppelaar, R.; Jeanmart, H. Global available solar energy under physical and energy return on investment constraints. *Appl. Energy* **2020**, *257*, 113968, DOI: 10.1016/j.apenergy.2019.113968.
- (130) Of World Energy (2024); Population based on various sources (2023) – with major processing by Our World in Data, E. ( E. I. -. S. R. Energy, Website, accessed on 19.02.2025, 2024.
- (131) Binnig, G.; Rohrer, H.; Gerber, C.; Weibel, E. Surface Studies by Scanning Tunneling Microscopy. *Phys. Rev. Lett.* **1982**, *49*, 57–61, DOI: 10.1103/PhysRevLett.49.57.
- (132) Sadewasser, S.; Glatzel, T., *Kelvin Probe Force Microscopy*, 65th ed.; Sadewasser, S., Glatzel, T., Eds.; Springer Series in Surface Sciences, Vol. 65; Springer International Publishing: Cham, 2018, p 530, DOI: 10.1007/978-3-319-75687-5.
- (133) Binnig, G.; Quate, C. F.; Gerber, C. Atomic Force Microscope. *Phys. Rev. Lett.* **1986**, *56*, 930–933, DOI: 10.1103/PhysRevLett.56.930.
- (134) Garrett, J. L.; Munday, J. N. Fast, high-resolution surface potential measurements in air with heterodyne Kelvin probe force microscopy. *Nanotechnology* **2016**, *27*, 14, DOI: 10.1088/0957-4484/27/24/245705.
- (135) Axt, A.; Hermes, I. M.; Bergmann, V. W.; Tausendpfund, N.; Weber, S. A. L. Know your full potential: Quantitative Kelvin probe force microscopy on nanoscale electrical devices. *Beilstein J. Nanotechnol.* **2018**, *9*, 1809–1819, DOI: 10.3762/bjnano.9.172.
- (136) Kojima, A.; Teshima, K.; Shirai, Y.; Miyasaka, T. Organometal Halide Perovskites as Visible-Light Sensitizers for Photovoltaic Cells. *J. Am. Chem. Soc.* **2009**, *131*, 6050–6051, DOI: 10.1021/ja809598r.

- (137) National Renewable Energy Lab (NREL) Best Research-Cell Efficiency Chart, Washington, DC, <https://www.nrel.gov/pv/cell-efficiency.html> ; Accessed on 19.02.2025, 2025, DOI: <https://www.nrel.gov/pv/cell-efficiency.html>.
- (138) Agrawal, G. P.; Dutta, N. K., *Semiconductor lasers*; Springer Science & Business Media: 2013.
- (139) Tremel, W.; Seshadri, R.; Finckh, E. Metall oder Nichtmetall? Das ist hier die Frage!: Festkörperphysik für Chemiker. *Chemie unserer Zeit* **2001**, *35*, 42–58, DOI: 10.1002/1521-3781(200101)35:1<42::AID-CIUZ42>3.0.CO;2-H.
- (140) Mahan, G. D. Excitons in Degenerate Semiconductors. *Phys. Rev.* **1967**, *153*, 882–889, DOI: 10.1103/PhysRev.153.882.
- (141) Gay, J. G. Screening of Excitons in Semiconductors. *Phys. Rev. B* **1971**, *4*, 2567–2575, DOI: 10.1103/PhysRevB.4.2567.
- (142) Gao, T.; Lu, Q.; Li, C.; Gao, K.; Xie, S. Thermally Induced Exciton Diffusion and Dissociation in Organic Semiconductors. *J. Phys. Chem. C* **2019**, *123*, 28527–28532, DOI: 10.1021/acs.jpcc.9b06789.
- (143) Lin, J. D. A.; Mikhnenko, O. V.; van der Poll, T. S.; Bazan, G. C.; Nguyen, T.-Q. Temperature Dependence of Exciton Diffusion in a Small-Molecule Organic Semiconductor Processed With and Without Additive. *Adv. Mater.* **2015**, *27*, 2528–2532, DOI: 10.1002/adma.201404590.
- (144) Mikhnenko, O. V.; Blom, P. W. M.; Nguyen, T.-Q. Exciton diffusion in organic semiconductors. *Energy Environ. Sci.* **2015**, *8*, 1867–1888, DOI: 10.1039/C5EE00925A.
- (145) Gerhard, M.; Arndt, A. P.; Bilal, M.; Lemmer, U.; Koch, M.; Howard, I. A. Field-induced exciton dissociation in PTB7-based organic solar cells. *Phys. Rev. B* **2017**, *95*, 195301, DOI: 10.1103/PhysRevB.95.195301.
- (146) Zhang, L.; Zhang, X.; Yu, Y.; Xu, X.; Tang, J.; He, X.; Wu, J.; Lan, Z. Efficient planar perovskite solar cells based on high-quality perovskite films with smooth surface and large crystal grains fabricated in ambient air conditions. *Sol. Energy* **2017**, *155*, 942–950, DOI: 10.1016/j.solener.2017.07.039.
- (147) Kurpiers, J.; Ferron, T.; Roland, S.; Jakoby, M.; Thiede, T.; Jaiser, F.; Albrecht, S.; Janietz, S.; Collins, B. A.; Howard, I. A.; Neher, D. Probing the pathways of free charge generation in organic bulk heterojunction solar cells. *Nat. Commun.* **2018**, *9*, 2038, DOI: 10.1038/s41467-018-04386-3.
- (148) Nelson, J. A., *The physics of solar cells*; World Scientific Publishing Company: 2003.

- (149) Jin, H.; Debroye, E.; Keshavarz, M.; Scheblykin, I. G.; Roeffaers, M. B.; Hofkens, J.; Steele, J. A. It's a trap! On the nature of localised states and charge trapping in lead halide perovskites. *Materials Horizons* **2020**, *7*, 397–410.
- (150) Stranks, S. D.; Burlakov, V. M.; Leijtens, T.; Ball, J. M.; Goriely, A.; Snaith, H. J. Recombination kinetics in organic-inorganic perovskites: excitons, free charge, and subgap states. *Physical Review Applied* **2014**, *2*, 034007.
- (151) Yalcinkaya, M. Y. Investigation of Sub-Granular Dynamics in Halide Perovskites via Atomic Force Microscopy, Ph.D. Thesis, Johannes Gutenberg University Mainz, 2023, p 158.
- (152) Demtröder, W., *Experimentalphysik 3: Atome, Moleküle und Festkörper*; Springer-Verlag: 2010.
- (153) Gerlach, W.; Schlangenotto, H.; Maeder, H. On the radiative recombination rate in silicon. *physica status solidi (a)* **1972**, *13*, 277–283.
- (154) Trupke, T.; Green, M. A.; Würfel, P.; Altermatt, P.; Wang, A.; Zhao, J.; Corkish, R. Temperature dependence of the radiative recombination coefficient of intrinsic crystalline silicon. *Journal of Applied Physics* **2003**, *94*, 4930–4937.
- (155) Michaelis, W.; Pilkuhn, M. Radiative recombination in silicon p-n junctions. *physica status solidi (b)* **1969**, *36*, 311–319.
- (156) Varshni, Y. P. Temperature dependence of the energy gap in semiconductors. *physica* **1967**, *34*, 149–154.
- (157) Klasen, A.; Baumli, P.; Sheng, Q.; Johannes, E.; Bretschneider, S. A.; Hermes, I. M.; Bergmann, V. W.; Gort, C.; Axt, A.; Weber, S. A. L.; Kim, H.; Butt, H.-J.; Tremel, W.; Berger, R. Removal of Surface Oxygen Vacancies Increases Conductance Through TiO<sub>2</sub> Thin Films for Perovskite Solar Cells. *J. Phys. Chem. C* **2019**, *123*, 13458–13466, DOI: 10.1021/acs.jpcc.9b02371.
- (158) Butt, H.-J.; Graf, K.; Kappl, M., *Physics and Chemistry of Interfaces*; Wiley: 2003, DOI: 10.1002/3527602313.
- (159) Abou-Ras, D.; Kirchartz, T.; Rau, U., *Advanced Characterization Techniques for Thin Film Solar Cells*; Abou-Ras, D., Kirchartz, T., Rau, U., Eds.; Wiley-VCH Verlag GmbH & Co. KGaA: Weinheim, Germany, 2016; Vol. 1-2, pp 1–681, DOI: 10.1002/9783527699025.
- (160) Araújo, G. L.; Martí, A. Absolute limiting efficiencies for photovoltaic energy conversion. *Solar energy materials and solar cells* **1994**, *33*, 213–240.

- (161) Thorp, H. H. Shockley was a racist and eugenicist. *Science (80-. )*. **2022**, *378*, 683–683, DOI: 10.1126/science.adf8117.
- (162) Ehrler, B.; Hutter, E. M.; Berry, J. J. The Complicated Morality of Named Inventions. *ACS Energy Lett.* **2021**, *6*, 565–567, DOI: 10.1021/acsenerylett.0c02657.
- (163) Shockley, W.; Queisser, H. J. Detailed balance limit of efficiency of p-n junction solar cells. *J. Appl. Phys.* **1961**, *32*, 510–519, DOI: 10.1063/1.1736034.
- (164) Xu, Y.; Gong, T.; Munday, J. N. The generalized Shockley-Queisser limit for nanostructured solar cells. *Sci. Rep.* **2015**, *5*, 1–9, DOI: 10.1038/srep13536.
- (165) Rühle, S. Tabulated values of the Shockley–Queisser limit for single junction solar cells. *Sol. Energy* **2016**, *130*, 139–147, DOI: 10.1016/j.solener.2016.02.015.
- (166) Bisquert, J.; Cahen, D.; Hodes, G.; Rühle, S.; Zaban, A. Physical chemical principles of photovoltaic conversion with nanoparticulate, mesoporous dye-sensitized solar cells. *The Journal of Physical Chemistry B* **2004**, *108*, 8106–8118.
- (167) Peng, J.; Lu, L.; Yang, H. Review on life cycle assessment of energy payback and greenhouse gas emission of solar photovoltaic systems. *Renew. Sustain. Energy Rev.* **2013**, *19*, 255–274, DOI: 10.1016/j.rser.2012.11.035.
- (168) Ganose, A. M.; Savory, C. N.; Scanlon, D. O. Beyond methylammonium lead iodide: prospects for the emergent field of ns<sub>2</sub> containing solar absorbers. *Chem. Commun.* **2017**, *53*, 20–44, DOI: 10.1039/c6cc06475b.
- (169) Wadia, C.; Alivisatos, A. P.; Kammen, D. M. Materials Availability Expands the Opportunity for Large-Scale Photovoltaics Deployment. *Environ. Sci. Technol.* **2009**, *43*, 2072–2077, DOI: 10.1021/es8019534.
- (170) Dhere, N. G. Toward GW/year of CIGS production within the next decade. *Sol. Energy Mater. Sol. Cells* **2007**, *91*, 1376–1382, DOI: 10.1016/j.solmat.2007.04.003.
- (171) Baikie, T.; Fang, Y.; Kadro, J. M.; Schreyer, M.; Wei, F.; Mhaisalkar, S. G.; Graetzel, M.; White, T. J. Synthesis and crystal chemistry of the hybrid perovskite (CH<sub>3</sub>NH<sub>3</sub>)PbI<sub>3</sub> for solid-state sensitised solar cell applications. *J. Mater. Chem. A* **2013**, *1*, 5628, DOI: 10.1039/c3ta10518k.
- (172) D’Innocenzo, V.; Grancini, G.; Alcocer, M. J. P.; Kandada, A. R. S.; Stranks, S. D.; Lee, M. M.; Lanzani, G.; Snaith, H. J.; Petrozza, A. Excitons versus free charges in organolead tri-halide perovskites. *Nat. Commun.* **2014**, *5*, 3586, DOI: 10.1038/ncomms4586.

- (173) Walsh, A.; Scanlon, D. O.; Chen, S.; Gong, X. G.; Wei, S.-H. Self-Regulation Mechanism for Charged Point Defects in Hybrid Halide Perovskites. *Angew. Chemie* **2015**, *127*, 1811–1814, DOI: 10.1002/ange.201409740.
- (174) Deng, Y.; Peng, E.; Shao, Y.; Xiao, Z.; Dong, Q.; Huang, J. Scalable fabrication of efficient organolead trihalide perovskite solar cells with doctor-bladed active layers. *Energy Environ. Sci.* **2015**, *8*, 1544–1550, DOI: 10.1039/C4EE03907F.
- (175) Xing, G.; Mathews, N.; Sun, S.; Lim, S. S.; Lam, Y. M.; Grätzel, M.; Mhaisalkar, S.; Sum, T. C. Long-Range Balanced Electron- and Hole-Transport Lengths in Organic-Inorganic CH<sub>3</sub>NH<sub>3</sub>PbI<sub>3</sub>. *Science (80-. )*. **2013**, *342*, 344–347, DOI: 10.1126/science.1243167.
- (176) Shao, Y.; Xiao, Z.; Bi, C.; Yuan, Y.; Huang, J. Origin and elimination of photocurrent hysteresis by fullerene passivation in CH<sub>3</sub>NH<sub>3</sub>PbI<sub>3</sub> planar heterojunction solar cells. *Nat. Commun.* **2014**, *5*, 5784, DOI: 10.1038/ncomms6784.
- (177) Wehrenfennig, C.; Liu, M.; Snaith, H. J.; Johnston, M. B.; Herz, L. M. Homogeneous Emission Line Broadening in the Organo Lead Halide Perovskite CH<sub>3</sub>NH<sub>3</sub>PbI<sub>3-x</sub>Cl<sub>x</sub>. *J. Phys. Chem. Lett.* **2014**, *5*, 1300–1306, DOI: 10.1021/jz500434p.
- (178) Zhao, Y.; Zhu, K. Charge Transport and Recombination in Perovskite (CH<sub>3</sub>NH<sub>3</sub>)PbI<sub>3</sub> Sensitized TiO<sub>2</sub> Solar Cells. *J. Phys. Chem. Lett.* **2013**, *4*, 2880–2884, DOI: 10.1021/jz401527q.
- (179) Navrotsky, A.; Weidner, D. J. Perovskite: a structure of great interest to geophysics and materials science. *Washington DC American Geophysical Union Geophysical Monograph Series* **1989**, *45*.
- (180) Brivio, F.; Butler, K. T.; Walsh, A.; van Schilfgaarde, M. Relativistic quasiparticle self-consistent electronic structure of hybrid halide perovskite photovoltaic absorbers. *Phys. Rev. B* **2014**, *89*, 155204, DOI: 10.1103/PhysRevB.89.155204.
- (181) Eames, C.; Frost, J. M.; Barnes, P. R.; O'Regan, B. C.; Walsh, A.; Islam, M. S. Ionic transport in hybrid lead iodide perovskite solar cells. *Nat. Commun.* **2015**, *6*, 2–9, DOI: 10.1038/ncomms8497.
- (182) Leguy, A. M.; Frost, J. M.; McMahon, A. P.; Sakai, V. G.; Kochelmann, W.; Law, C.; Li, X.; Foglia, F.; Walsh, A.; O'Regan, B. C.; Nelson, J.; Cabral, J. T.; Barnes, P. R. The dynamics of methylammonium ions in hybrid organic-inorganic perovskite solar cells. *Nat. Commun.* **2015**, *6*, DOI: 10.1038/ncomms8124.

- (183) Pitaro, M.; Tekelenburg, E. K.; Shao, S.; Loi, M. A. Tin halide perovskites: from fundamental properties to solar cells. *Advanced Materials* **2022**, *34*, 2105844.
- (184) Ong, K. P.; Goh, T. W.; Xu, Q.; Huan, A. Structural evolution in methylammonium lead iodide CH<sub>3</sub>NH<sub>3</sub>PbI<sub>3</sub>. *The Journal of Physical Chemistry A* **2015**, *119*, 11033–11038.
- (185) Cohen, R. E.; Krakauer, H. Electronic structure studies of the differences in ferroelectric behavior of BaTiO<sub>3</sub> and PbTiO<sub>3</sub>. *Ferroelectrics* **1992**, *136*, 65–83.
- (186) De Wolf, S.; Holovsky, J.; Moon, S.-J.; Loper, P.; Niesen, B.; Ledinsky, M.; Haug, F.-J.; Yum, J.-H.; Ballif, C. Organometallic halide perovskites: sharp optical absorption edge and its relation to photovoltaic performance. *The journal of physical chemistry letters* **2014**, *5*, 1035–1039.
- (187) Umari, P.; Mosconi, E.; De Angelis, F. Infrared dielectric screening determines the low exciton binding energy of metal-halide perovskites. *The journal of physical chemistry letters* **2018**, *9*, 620–627.
- (188) Stranks, S. D.; Eperon, G. E.; Grancini, G.; Menelaou, C.; Alcocer, M. J.; Leijtens, T.; Herz, L. M.; Petrozza, A.; Snaith, H. J. Electron-hole diffusion lengths exceeding 1 micrometer in an organometal trihalide perovskite absorber. *Science* **2013**, *342*, 341–344.
- (189) Unger, E.; Kegelmann, L.; Suchan, K.; Sörell, D.; Korte, L.; Albrecht, S. Roadmap and roadblocks for the band gap tunability of metal halide perovskites. *Journal of Materials Chemistry A* **2017**, *5*, 11401–11409.
- (190) Kim, G.-W.; Petrozza, A. Defect Tolerance and Intolerance in Metal-Halide Perovskites. *Advanced Energy Materials* **2020**, *10*, 2001959.
- (191) Barrows, A. T.; Pearson, A. J.; Kwak, C. K.; Dunbar, A. D. F.; Buckley, A. R.; Lidzey, D. G. Efficient planar heterojunction mixed-halide perovskite solar cells deposited via spray-deposition. *Energy Environ. Sci.* **2014**, *7*, 2944–2950, DOI: 10.1039/C4EE01546K.
- (192) Bhachu, D. S.; Scanlon, D. O.; Saban, E. J.; Bronstein, H.; Parkin, I. P.; Carmalt, C. J.; Palgrave, R. G. Scalable route to CH<sub>3</sub>NH<sub>3</sub>PbI<sub>3</sub> perovskite thin films by aerosol assisted chemical vapour deposition. *J. Mater. Chem. A* **2015**, *3*, 9071–9073, DOI: 10.1039/C4TA05522E.
- (193) Hodes, G.; Cahen, D. Perovskite cells roll forward. *Nat. Photonics* **2014**, *8*, 87–88, DOI: 10.1038/nphoton.2014.5.

- (194) Christians, J. A.; Manser, J. S.; Kamat, P. V. Best Practices in Perovskite Solar Cell Efficiency Measurements. Avoiding the Error of Making Bad Cells Look Good. *J. Phys. Chem. Lett.* **2015**, *6*, 852–857, DOI: 10.1021/acs.jpcllett.5b00289.
- (195) Nagabhushana, G. P.; Shivaramaiah, R.; Navrotsky, A. Direct calorimetric verification of thermodynamic instability of lead halide hybrid perovskites. *Proc. Natl. Acad. Sci.* **2016**, *113*, 7717–7721, DOI: 10.1073/pnas.1607850113.
- (196) Park, B.-w.; Seok, S. I. Intrinsic instability of inorganic–organic hybrid halide perovskite materials. *Advanced Materials* **2019**, *31*, 1805337.
- (197) Guarnera, S.; Abate, A.; Zhang, W.; Foster, J. M.; Richardson, G.; Petrozza, A.; Snaith, H. J. Improving the Long-Term Stability of Perovskite Solar Cells with a Porous Al<sub>2</sub>O<sub>3</sub> Buffer Layer. *J. Phys. Chem. Lett.* **2015**, *6*, 432–437, DOI: 10.1021/jz502703p.
- (198) Niu, G.; Guo, X.; Wang, L. Review of recent progress in chemical stability of perovskite solar cells. *J. Mater. Chem. A* **2015**, *3*, 8970–8980, DOI: 10.1039/C4TA04994B.
- (199) Yang, J.; Kelly, T. L. Decomposition and Cell Failure Mechanisms in Lead Halide Perovskite Solar Cells. *Inorg. Chem.* **2017**, *56*, 92–101, DOI: 10.1021/acs.inorgchem.6b01307.
- (200) Haddad, J.; Krogmeier, B.; Klingebiel, B.; Krückemeier, L.; Melhem, S.; Liu, Z.; Hüpkens, J.; Mathur, S.; Kirchartz, T. Analyzing Interface Recombination in Lead-Halide Perovskite Solar Cells with Organic and Inorganic Hole-Transport Layers. *Advanced materials interfaces* **2020**, *7*, 2000366.
- (201) Adhyaksa, G. W.; Brittman, S.; Āboliņš, H.; Lof, A.; Li, X.; Keelor, J. D.; Luo, Y.; Duevski, T.; Heeren, R. M.; Ellis, S. R., et al. Understanding detrimental and beneficial grain boundary effects in halide perovskites. *Advanced Materials* **2018**, *30*, 1804792.
- (202) Weber, S. A.; Hermes, I. M.; Turren-Cruz, S.-H.; Gort, C.; Bergmann, V. W.; Gilson, L.; Hagfeldt, A.; Graetzel, M.; Tress, W.; Berger, R. How the formation of interfacial charge causes hysteresis in perovskite solar cells. *Energy & environmental science* **2018**, *11*, 2404–2413.
- (203) Goldschmidt, V. M. Die gesetze der krystallochemie. *Naturwissenschaften* **1926**, *14*, 477–485.
- (204) Kieslich, G.; Sun, S.; Cheetham, A. K. Solid-state principles applied to organic–inorganic perovskites: new tricks for an old dog. *Chemical Science* **2014**, *5*, 4712–4715.
- (205) Klasen, A. Synthesis and Analysis of Thin Films for Perovskite Solar Cells, PhD thesis, Johannes Gutenberg University Mainz, 2020.

- (206) Chouhan, L.; Ghimire, S.; Subrahmanyam, C.; Miyasaka, T.; Biju, V. Synthesis, optoelectronic properties and applications of halide perovskites. *Chemical Society Reviews* **2020**, *49*, 2869–2885.
- (207) Koutselas, I. B.; Ducasse, L.; Papavassiliou, G. C. Electronic properties of three- and low-dimensional semiconducting materials with Pb halide and Sn halide units. *Journal of Physics: Condensed Matter* **1996**, *8*, 1217.
- (208) Fabini, D. H.; Seshadri, R.; Kanatzidis, M. G. The underappreciated lone pair in halide perovskites underpins their unusual properties. *MRS Bulletin* **2020**, *45*, 467–477.
- (209) Goyal, A.; McKechnie, S.; Pashov, D.; Tumas, W.; Van Schilfgaarde, M.; Stevanovic, V. Origin of pronounced nonlinear band gap behavior in lead–tin hybrid perovskite alloys. *Chemistry of Materials* **2018**, *30*, 3920–3928.
- (210) Liang, J.; Chen, C.; Hu, X.; Chen, Z.; Zheng, X.; Li, J.; Wang, H.; Ye, F.; Xiao, M.; Lu, Z., et al. Suppressing the phase segregation with potassium for highly efficient and photostable inverted wide-band gap halide perovskite solar cells. *ACS Applied Materials & Interfaces* **2020**, *12*, 48458–48466.
- (211) Goesten, M. G.; Hoffmann, R. Mirrors of bonding in metal halide perovskites. *Journal of the American Chemical Society* **2018**, *140*, 12996–13010.
- (212) Protesescu, L.; Yakunin, S.; Bodnarchuk, M. I.; Krieg, F.; Caputo, R.; Hendon, C. H.; Yang, R. X.; Walsh, A.; Kovalenko, M. V. Nanocrystals of cesium lead halide perovskites (CsPbX<sub>3</sub>, X= Cl, Br, and I): novel optoelectronic materials showing bright emission with wide color gamut. *Nano letters* **2015**, *15*, 3692–3696.
- (213) Stoumpos, C. C.; Malliakas, C. D.; Kanatzidis, M. G. Semiconducting tin and lead iodide perovskites with organic cations: phase transitions, high mobilities, and near-infrared photoluminescent properties. *Inorganic chemistry* **2013**, *52*, 9019–9038.
- (214) Kitazawa, N.; Watanabe, Y.; Nakamura, Y. Optical properties of CH<sub>3</sub>NH<sub>3</sub>PbX<sub>3</sub> (X= halogen) and their mixed-halide crystals. *Journal of materials science* **2002**, *37*, 3585–3587.
- (215) Paik, M. J.; Yoo, J. W.; Park, J.; Noh, E.; Kim, H.; Ji, S.-G.; Kim, Y. Y.; Seok, S. I. SnO<sub>2</sub>–TiO<sub>2</sub> hybrid electron transport layer for efficient and flexible perovskite solar cells. *ACS Energy Letters* **2022**, *7*, 1864–1870.
- (216) Rombach, F. M.; Haque, S. A.; Macdonald, T. J. Lessons learned from spiro-OMeTAD and PTAA in perovskite solar cells. *Energy & Environmental Science* **2021**, *14*, 5161–5190.

- (217) Liang, L.; Cai, Y.; Li, X.; Nazeeruddin, M. K.; Gao, P. All that glitters is not gold: Recent progress of alternative counter electrodes for perovskite solar cells. *Nano Energy* **2018**, *52*, 211–238.
- (218) Abdi-Jalebi, M.; Dar, M. I.; Sadhanala, A.; Senanayak, S. P.; Giordano, F.; Zakeeruddin, S. M.; Grätzel, M.; Friend, R. H. Impact of a mesoporous titania–perovskite interface on the performance of hybrid organic–inorganic perovskite solar cells. *The journal of physical chemistry letters* **2016**, *7*, 3264–3269.
- (219) Ma, C.; Park, N.-G. Paradoxical approach with a hydrophilic passivation layer for moisture-stable, 23% efficient perovskite solar cells. *ACS Energy Letters* **2020**, *5*, 3268–3275.
- (220) Sajid, S.; Elseman, A. M.; Huang, H.; Ji, J.; Dou, S.; Jiang, H.; Liu, X.; Wei, D.; Cui, P.; Li, M. Breakthroughs in NiOx-HTMs towards stable, low-cost and efficient perovskite solar cells. *Nano Energy* **2018**, *51*, 408–424.
- (221) Xu, J.; Dai, J.; Dong, H.; Li, P.; Chen, J.; Zhu, X.; Wang, Z.; Jiao, B.; Hou, X.; Li, J., et al. Surface-tension release in PTAA-based inverted perovskite solar cells. *Organic Electronics* **2022**, *100*, 106378.
- (222) Lee, H.-J.; Na, S.-I. Investigation of PCBM/ZnO and C60/BCP-based electron transport layer for high-performance pin perovskite solar cells. *Journal of Alloys and Compounds* **2022**, *921*, 166007.
- (223) Klasen, A.; Baumli, P.; Sheng, Q.; Johannes, E.; Bretschneider, S. A.; Hermes, I. M.; Bergmann, V. W.; Gort, C.; Axt, A.; Weber, S. A., et al. Removal of surface oxygen vacancies increases conductance through TiO<sub>2</sub> thin films for perovskite solar cells. *The Journal of Physical Chemistry C* **2019**, *123*, 13458–13466.
- (224) Min, H.; Lee, D. Y.; Kim, J.; Kim, G.; Lee, K. S.; Kim, J.; Paik, M. J.; Kim, Y. K.; Kim, K. S.; Kim, M. G., et al. Perovskite solar cells with atomically coherent interlayers on SnO<sub>2</sub> electrodes. *Nature* **2021**, *598*, 444–450.
- (225) Byranvand, M. M.; Saliba, M. Defect passivation of perovskite films for highly efficient and stable solar cells. *Solar RRL* **2021**, *5*, 2100295.
- (226) Uratani, H.; Yamashita, K. Charge carrier trapping at surface defects of perovskite solar cell absorbers: a first-principles study. *The journal of physical chemistry letters* **2017**, *8*, 742–746.

- (227) De Quilettes, D. W.; Vorpahl, S. M.; Stranks, S. D.; Nagaoka, H.; Eperon, G. E.; Ziffer, M. E.; Snaith, H. J.; Ginger, D. S. Impact of microstructure on local carrier lifetime in perovskite solar cells. *Science* **2015**, *348*, 683–686.
- (228) Park, J.-S.; Calbo, J.; Jung, Y.-K.; Whalley, L. D.; Walsh, A. Accumulation of deep traps at grain boundaries in halide perovskites. *ACS Energy Letters* **2019**, *4*, 1321–1327.
- (229) Tress, W.; Marinova, N.; Moehl, T.; Zakeeruddin, S. M.; Nazeeruddin, M. K.; Grätzel, M. Understanding the rate-dependent J–V hysteresis, slow time component, and aging in CH<sub>3</sub>NH<sub>3</sub>PbI<sub>3</sub> perovskite solar cells: the role of a compensated electric field. *Energy & Environmental Science* **2015**, *8*, 995–1004.
- (230) Slotcavage, D.; Karunadasa, H.; McGehee, M. *ACS Energy Lett.* **1**, 1199 (2016).
- (231) Kato, Y.; Ono, L. K.; Lee, M. V.; Wang, S.; Raga, S. R.; Qi, Y. Silver iodide formation in methyl ammonium lead iodide perovskite solar cells with silver top electrodes. *Advanced Materials Interfaces* **2015**, *2*, 1500195.
- (232) Zhang, H.; Nazeeruddin, M. K.; Choy, W. C. Perovskite Photovoltaics: The Significant Role of Ligands in Film Formation, Passivation, and Stability. *Adv. Mater.* **2019**, *31*, 1–29, DOI: 10.1002/adma.201805702.
- (233) Lee, D. S.; Yun, J. S.; Kim, J.; Soufiani, A. M.; Chen, S.; Cho, Y.; Deng, X.; Seidel, J.; Lim, S.; Huang, S.; Ho-Baillie, A. W. Passivation of Grain Boundaries by Phenethylammonium in Formamidinium-Methylammonium Lead Halide Perovskite Solar Cells. *ACS Energy Lett.* **2018**, *3*, 647–654, DOI: 10.1021/acsenergylett.8b00121.
- (234) Yuan, Y.; Huang, J. Ion migration in organometal trihalide perovskite and its impact on photovoltaic efficiency and stability. *Accounts of chemical research* **2016**, *49*, 286–293.
- (235) Zhu, W.; Wang, S.; Zhang, X.; Wang, A.; Wu, C.; Hao, F. Ion migration in organic–inorganic hybrid perovskite solar cells: current understanding and perspectives. *Small* **2022**, *18*, 2105783.
- (236) Fu, L.; Li, H.; Wang, L.; Yin, R.; Li, B.; Yin, L. Defect passivation strategies in perovskites for an enhanced photovoltaic performance. *Energy Environ. Sci.* **2020**, *13*, 4017–4056, DOI: 10.1039/D0EE01767A.
- (237) Akin, S.; Arora, N.; Zakeeruddin, S. M.; Grätzel, M.; Friend, R. H.; Dar, M. I. New Strategies for Defect Passivation in High-Efficiency Perovskite Solar Cells. *Adv. Energy Mater.* **2020**, *10*, DOI: 10.1002/aenm.201903090.

- (238) Aydin, E.; De Bastiani, M.; De Wolf, S. Defect and Contact Passivation for Perovskite Solar Cells. *Adv. Mater.* **2019**, *31*, DOI: 10.1002/adma.201900428.
- (239) Gao, F.; Zhao, Y.; Zhang, X.; You, J. Recent Progresses on Defect Passivation toward Efficient Perovskite Solar Cells. *Adv. Energy Mater.* **2020**, *10*, DOI: 10.1002/aenm.201902650.
- (240) Zhang, H.; Nazeeruddin, M. K.; Choy, W. C. H. Perovskite Photovoltaics: The Significant Role of Ligands in Film Formation, Passivation, and Stability. *Adv. Mater.* **2019**, *31*, DOI: 10.1002/adma.201805702.
- (241) Qi, W.; Zhou, X.; Li, J.; Cheng, J.; Li, Y.; Ko, M. J.; Zhao, Y.; Zhang, X. Inorganic material passivation of defects toward efficient perovskite solar cells. *Sci. Bull.* **2020**, *65*, 2022–2032, DOI: 10.1016/j.scib.2020.07.017.
- (242) Li, Y.; Wu, H.; Qi, W.; Zhou, X.; Li, J.; Cheng, J.; Zhao, Y.; Li, Y.; Zhang, X. Passivation of defects in perovskite solar cell: From a chemistry point of view. *Nano Energy* **2020**, *77*, 105237, DOI: 10.1016/j.nanoen.2020.105237.
- (243) Akin, S.; Dong, B.; Pfeifer, L.; Liu, Y.; Graetzel, M.; Hagfeldt, A. Organic Ammonium Halide Modulators as Effective Strategy for Enhanced Perovskite Photovoltaic Performance. *Adv. Sci.* **2021**, *8*, DOI: 10.1002/advs.202004593.
- (244) Zheng, X.; Chen, B.; Dai, J.; Fang, Y.; Bai, Y.; Lin, Y.; Wei, H.; Zeng, X. C.; Huang, J. Defect passivation in hybrid perovskite solar cells using quaternary ammonium halide anions and cations. *Nat. Energy* **2017**, *2*, 17102, DOI: 10.1038/nenergy.2017.102.
- (245) Chen, P.; Bai, Y.; Wang, S.; Lyu, M.; Yun, J.-H.; Wang, L. In Situ Growth of 2D Perovskite Capping Layer for Stable and Efficient Perovskite Solar Cells. *Adv. Funct. Mater.* **2018**, *28*, DOI: 10.1002/adfm.201706923.
- (246) Cho, Y.; Soufiani, A. M.; Yun, J. S.; Kim, J.; Lee, D. S.; Seidel, J.; Deng, X.; Green, M. A.; Huang, S.; Ho-Baillie, A. W. Y. Mixed 3D–2D Passivation Treatment for Mixed-Cation Lead Mixed-Halide Perovskite Solar Cells for Higher Efficiency and Better Stability. *Adv. Energy Mater.* **2018**, *8*, DOI: 10.1002/aenm.201703392.
- (247) Koh, T. M.; Shanmugam, V.; Guo, X.; Lim, S. S.; Filonik, O.; Herzig, E. M.; Müller-Buschbaum, P.; Swamy, V.; Chien, S. T.; Mhaisalkar, S. G.; Mathews, N. Enhancing moisture tolerance in efficient hybrid 3D/2D perovskite photovoltaics. *J. Mater. Chem. A* **2018**, *6*, 2122–2128, DOI: 10.1039/C7TA09657G.

- (248) Lee, K.; Kim, J.; Yu, H.; Lee, J. W.; Yoon, C.-M.; Kim, S. K.; Jang, J. A highly stable and efficient carbon electrode-based perovskite solar cell achieved via interfacial growth of 2D PEA 2 PbI 4 perovskite. *J. Mater. Chem. A* **2018**, *6*, 24560–24568, DOI: 10.1039/C8TA09433K.
- (249) Lin, Y.; Bai, Y.; Fang, Y.; Chen, Z.; Yang, S.; Zheng, X.; Tang, S.; Liu, Y.; Zhao, J.; Huang, J. Enhanced Thermal Stability in Perovskite Solar Cells by Assembling 2D/3D Stacking Structures. *J. Phys. Chem. Lett.* **2018**, *9*, 654–658, DOI: 10.1021/acs.jpcclett.7b02679.
- (250) Luo, D. et al. Enhanced photovoltage for inverted planar heterojunction perovskite solar cells. *Science (80-. )*. **2018**, *360*, 1442–1446, DOI: 10.1126/science.aap9282.
- (251) Gharibzadeh, S.; Abdollahi Nejad, B.; Jakoby, M.; Abzieher, T.; Hauschild, D.; Moghadamzadeh, S.; Schwenzler, J. A.; Brenner, P.; Schmager, R.; Haghighirad, A. A.; Weinhardt, L.; Lemmer, U.; Richards, B. S.; Howard, I. A.; Paetzold, U. W. Record Open-Circuit Voltage Wide-Bandgap Perovskite Solar Cells Utilizing 2D/3D Perovskite Heterostructure. *Adv. Energy Mater.* **2019**, *9*, DOI: 10.1002/aenm.201803699.
- (252) Jiang, Q.; Zhao, Y.; Zhang, X.; Yang, X.; Chen, Y.; Chu, Z.; Ye, Q.; Li, X.; Yin, Z.; You, J. Surface passivation of perovskite film for efficient solar cells. *Nat. Photonics* **2019**, *13*, 460–466, DOI: 10.1038/s41566-019-0398-2.
- (253) Jung, E. H.; Jeon, N. J.; Park, E. Y.; Moon, C. S.; Shin, T. J.; Yang, T.-Y.; Noh, J. H.; Seo, J. Efficient, stable and scalable perovskite solar cells using poly(3-hexylthiophene). *Nature* **2019**, *567*, 511–515, DOI: 10.1038/s41586-019-1036-3.
- (254) Kim, H.; Lee, S.-U.; Lee, D. Y.; Paik, M. J.; Na, H.; Lee, J.; Seok, S. I. Optimal Interfacial Engineering with Different Length of Alkylammonium Halide for Efficient and Stable Perovskite Solar Cells. *Adv. Energy Mater.* **2019**, *9*, DOI: 10.1002/aenm.201902740.
- (255) Liu, Y.; Akin, S.; Pan, L.; Uchida, R.; Arora, N.; Milić, J. V.; Hinderhofer, A.; Schreiber, F.; Uhl, A. R.; Zakeeruddin, S. M.; Hagfeldt, A.; Dar, M. I.; Grätzel, M. Ultrahydrophobic 3D/2D fluoroarene bilayer-based water-resistant perovskite solar cells with efficiencies exceeding 22%. *Sci. Adv.* **2019**, *5*, DOI: 10.1126/sciadv.aaw2543.
- (256) Wang, H. et al. Interfacial Residual Stress Relaxation in Perovskite Solar Cells with Improved Stability. *Adv. Mater.* **2019**, *31*, DOI: 10.1002/adma.201904408.

- (257) Yoo, J. J.; Wieghold, S.; Sponseller, M. C.; Chua, M. R.; Bertram, S. N.; Hartono, N. T. P.; Tresback, J. S.; Hansen, E. C.; Correa-Baena, J.-P.; Bulović, V.; Buonassisi, T.; Shin, S. S.; Bawendi, M. G. An interface stabilized perovskite solar cell with high stabilized efficiency and low voltage loss. *Energy Environ. Sci.* **2019**, *12*, 2192–2199, DOI: 10.1039/C9EE00751B.
- (258) Duong, T. et al. High Efficiency Perovskite-Silicon Tandem Solar Cells: Effect of Surface Coating versus Bulk Incorporation of 2D Perovskite. *Adv. Energy Mater.* **2020**, *10*, DOI: 10.1002/aenm.201903553.
- (259) Gharibzadeh, S. et al. 2D/3D Heterostructure for Semitransparent Perovskite Solar Cells with Engineered Bandgap Enables Efficiencies Exceeding 25% in Four-Terminal Tandems with Silicon and CIGS. *Adv. Funct. Mater.* **2020**, *30*, DOI: 10.1002/adfm.201909919.
- (260) Jeong, M.; Choi, I. W.; Go, E. M.; Cho, Y.; Kim, M.; Lee, B.; Jeong, S.; Jo, Y.; Choi, H. W.; Lee, J.; Bae, J.-H.; Kwak, S. K.; Kim, D. S.; Yang, C. Stable perovskite solar cells with efficiency exceeding 24.8% and 0.3-V voltage loss. *Science (80-. )*. **2020**, *369*, 1615–1620, DOI: 10.1126/science.abb7167.
- (261) Kim, G.; Min, H.; Lee, K. S.; Lee, D. Y.; Yoon, S. M.; Seok, S. I. Impact of strain relaxation on performance of  $\alpha$ -formamidinium lead iodide perovskite solar cells. *Science (80-. )*. **2020**, *370*, 108–112, DOI: 10.1126/science.abc4417.
- (262) Lu, H. et al. Vapor-assisted deposition of highly efficient, stable black-phase FAPbI<sub>3</sub> perovskite solar cells. *Science (80-. )*. **2020**, *370*, DOI: 10.1126/science.abb8985.
- (263) Mahmud, M. A.; Duong, T.; Yin, Y.; Pham, H. T.; Walter, D.; Peng, J.; Wu, Y.; Li, L.; Shen, H.; Wu, N.; Mozaffari, N.; Andersson, G.; Catchpole, K. R.; Weber, K. J.; White, T. P. Double-Sided Surface Passivation of 3D Perovskite Film for High-Efficiency Mixed-Dimensional Perovskite Solar Cells. *Adv. Funct. Mater.* **2020**, *30*, DOI: 10.1002/adfm.201907962.
- (264) Tan, S.; Yavuz, I.; Weber, M. H.; Huang, T.; Chen, C.-H.; Wang, R.; Wang, H.-C.; Ko, J. H.; Nuryyeva, S.; Xue, J.; Zhao, Y.; Wei, K.-H.; Lee, J.-W.; Yang, Y. Shallow Iodine Defects Accelerate the Degradation of  $\alpha$ -Phase Formamidinium Perovskite. *Joule* **2020**, *4*, 2426–2442, DOI: 10.1016/j.joule.2020.08.016.
- (265) Yang, B.; Suo, J.; Mosconi, E.; Ricciarelli, D.; Tress, W.; De Angelis, F.; Kim, H.-S.; Hagfeldt, A. Outstanding Passivation Effect by a Mixed-Salt Interlayer with Internal Interactions in Perovskite Solar Cells. *ACS Energy Lett.* **2020**, *5*, 3159–3167, DOI: 10.1021/acsenerylett.0c01664.

- (266) Zhang, C.; Wu, S.; Tao, L.; Arumugam, G. M.; Liu, C.; Wang, Z.; Zhu, S.; Yang, Y.; Lin, J.; Liu, X.; Schropp, R. E. I.; Mai, Y. Fabrication Strategy for Efficient 2D/3D Perovskite Solar Cells Enabled by Diffusion Passivation and Strain Compensation. *Adv. Energy Mater.* **2020**, *10*, DOI: 10.1002/aenm.202002004.
- (267) Zhang, F.; Huang, Q.; Song, J.; Zhang, Y.; Ding, C.; Liu, F.; Liu, D.; Li, X.; Yasuda, H.; Yoshida, K.; Qu, J.; Hayase, S.; Toyoda, T.; Minemoto, T.; Shen, Q. Growth of Amorphous Passivation Layer Using Phenethylammonium Iodide for High-Performance Inverted Perovskite Solar Cells. *Sol. RRL* **2020**, *4*, DOI: 10.1002/solr.201900243.
- (268) Yang, X. et al. Buried Interfaces in Halide Perovskite Photovoltaics. *Adv. Mater.* **2021**, *33*, DOI: 10.1002/adma.202006435.
- (269) Yoo, J. J.; Seo, G.; Chua, M. R.; Park, T. G.; Lu, Y.; Rotermund, F.; Kim, Y.-K.; Moon, C. S.; Jeon, N. J.; Correa-Baena, J.-P.; Bulović, V.; Shin, S. S.; Bawendi, M. G.; Seo, J. Efficient perovskite solar cells via improved carrier management. *Nature* **2021**, *590*, 587–593, DOI: 10.1038/s41586-021-03285-w.
- (270) Zhou, Q.; Gao, Y.; Cai, C.; Zhang, Z.; Xu, J.; Yuan, Z.; Gao, P. Dually-Passivated Perovskite Solar Cells with Reduced Voltage Loss and Increased Super Oxide Resistance. *Angew. Chemie* **2021**, *133*, 8384–8393, DOI: 10.1002/ange.202017148.
- (271) Ma, C.; Park, N.-G. Paradoxical Approach with a Hydrophilic Passivation Layer for Moisture-Stable, 23% Efficient Perovskite Solar Cells. *ACS Energy Lett.* **2020**, *5*, 3268–3275, DOI: 10.1021/acsenergylett.0c01848.
- (272) Jiang, Q.; Ni, Z.; Xu, G.; Lin, Y.; Rudd, P. N.; Xue, R.; Li, Y.; Li, Y.; Gao, Y.; Huang, J. Interfacial Molecular Doping of Metal Halide Perovskites for Highly Efficient Solar Cells. *Adv. Mater.* **2020**, *32*, DOI: 10.1002/adma.202001581.
- (273) Li, F. et al. Regulating Surface Termination for Efficient Inverted Perovskite Solar Cells with Greater Than 23% Efficiency. *J. Am. Chem. Soc.* **2020**, *142*, 20134–20142, DOI: 10.1021/jacs.0c09845.
- (274) Liu, L.; Huang, S.; Lu, Y.; Liu, P.; Zhao, Y.; Shi, C.; Zhang, S.; Wu, J.; Zhong, H.; Sui, M.; Zhou, H.; Jin, H.; Li, Y.; Chen, Q. Grain-Boundary “Patches” by In Situ Conversion to Enhance Perovskite Solar Cells Stability. *Adv. Mater.* **2018**, *30*, DOI: 10.1002/adma.201800544.

- (275) Malekshahi Byranvand, M.; Behboodi-Sadabad, F.; Alrhman Eliwi, A.; Trouillet, V.; Welle, A.; Ternes, S.; Hossain, I. M.; Khan, M. R.; Schwenzer, J. A.; Farooq, A.; Richards, B. S.; Lahann, J.; Paetzold, U. W. Chemical vapor deposited polymer layer for efficient passivation of planar perovskite solar cells. *J. Mater. Chem. A* **2020**, *8*, 20122–20132, DOI: 10.1039/D0TA06646J.
- (276) Peng, J. et al. Nanoscale localized contacts for high fill factors in polymer-passivated perovskite solar cells. *Science (80-. )*. **2021**, *371*, 390–395, DOI: 10.1126/science.abb8687.
- (277) Wang, R. et al. Constructive molecular configurations for surface-defect passivation of perovskite photovoltaics. *Science (80-. )*. **2019**, *366*, 1509–1513, DOI: 10.1126/science.aay9698.
- (278) Liu, X.; Yu, Z.; Wang, T.; Chiu, K. L.; Lin, F.; Gong, H.; Ding, L.; Cheng, Y. Full Defects Passivation Enables 21% Efficiency Perovskite Solar Cells Operating in Air. *Adv. Energy Mater.* **2020**, *10*, DOI: 10.1002/aenm.202001958.
- (279) Yang, S.; Dai, J.; Yu, Z.; Shao, Y.; Zhou, Y.; Xiao, X.; Zeng, X. C.; Huang, J. Tailoring Passivation Molecular Structures for Extremely Small Open-Circuit Voltage Loss in Perovskite Solar Cells. *J. Am. Chem. Soc.* **2019**, *141*, 5781–5787, DOI: 10.1021/jacs.8b13091.
- (280) Wolff, C. M. et al. Perfluorinated Self-Assembled Monolayers Enhance the Stability and Efficiency of Inverted Perovskite Solar Cells. *ACS Nano* **2020**, *14*, 1445–1456, DOI: 10.1021/acsnano.9b03268.
- (281) Liu, Z.; Cao, F.; Wang, M.; Wang, M.; Li, L. Observing Defect Passivation of the Grain Boundary with 2-Aminoterephthalic Acid for Efficient and Stable Perovskite Solar Cells. *Angew. Chemie* **2020**, *132*, 4190–4196, DOI: 10.1002/ange.201915422.
- (282) Xu, J. et al. Triple-halide wide-band gap perovskites with suppressed phase segregation for efficient tandems. *Science (80-. )*. **2020**, *367*, 1097–1104, DOI: 10.1126/science.aaz5074.
- (283) Peña-Camargo, F.; Caprioglio, P.; Zu, F.; Gutierrez-Partida, E.; Wolff, C. M.; Brinkmann, K.; Albrecht, S.; Riedl, T.; Koch, N.; Neher, D.; Stolterfoht, M. Halide Segregation versus Interfacial Recombination in Bromide-Rich Wide-Gap Perovskite Solar Cells. *ACS Energy Lett.* **2020**, *5*, 2728–2736, DOI: 10.1021/acsenergylett.0c01104.
- (284) Aydin, E.; De Bastiani, M.; De Wolf, S. Defect and Contact Passivation for Perovskite Solar Cells. *Adv. Mater.* **2019**, *31*, DOI: 10.1002/adma.201900428.

- (285) Yang, S.; Chen, S.; Mosconi, E.; Fang, Y.; Xiao, X.; Wang, C.; Zhou, Y.; Yu, Z.; Zhao, J.; Gao, Y.; De Angelis, F.; Huang, J. Stabilizing halide perovskite surfaces for solar cell operation with wide-bandgap lead oxysalts. *Science (80-. )*. **2019**, *365*, 473–478, DOI: 10.1126/science.aax3294.
- (286) Wang, F.; Zhang, Y.; Yang, M.; Han, D.; Yang, L.; Fan, L.; Sui, Y.; Sun, Y.; Liu, X.; Meng, X.; Yang, J. Interface Dipole Induced Field-Effect Passivation for Achieving 21.7% Efficiency and Stable Perovskite Solar Cells. *Adv. Funct. Mater.* **2021**, *31*, 1–10, DOI: 10.1002/adfm.202008052.
- (287) Zheng, X. et al. Managing grains and interfaces via ligand anchoring enables 22.3%-efficiency inverted perovskite solar cells. *Nat. Energy* **2020**, *5*, 131–140, DOI: 10.1038/s41560-019-0538-4.
- (288) Caprioglio, P.; Stolterfoht, M.; Wolff, C. M.; Unold, T.; Rech, B.; Albrecht, S.; Neher, D. On the Relation between the Open-Circuit Voltage and Quasi-Fermi Level Splitting in Efficient Perovskite Solar Cells. *Adv. Energy Mater.* **2019**, *9*, DOI: 10.1002/aenm.201901631.
- (289) Tennyson, E. M.; Garrett, J. L.; Frantz, J. A.; Myers, J. D.; Bekele, R. Y.; Sanghera, J. S.; Munday, J. N.; Leite, M. S. Nanoimaging of Open-Circuit Voltage in Photovoltaic Devices. *Adv. Energy Mater.* **2015**, *5*, DOI: 10.1002/aenm.201501142.
- (290) Weber, S. A. L.; Hermes, I. M.; Turren-Cruz, S.-H.; Gort, C.; Bergmann, V. W.; Gilson, L.; Hagfeldt, A.; Graetzel, M.; Tress, W.; Berger, R. How the formation of interfacial charge causes hysteresis in perovskite solar cells. *Energy Environ. Sci.* **2018**, *11*, 2404–2413, DOI: 10.1039/C8EE01447G.
- (291) Bian, K.; Gerber, C.; Heinrich, A. J.; Müller, D. J.; Scheuring, S.; Jiang, Y. Scanning probe microscopy. *Nat. Rev. Methods Prim.* **2021**, *1*, 36, DOI: 10.1038/s43586-021-00033-2.
- (292) Gries, T. W. Masterarbeit: Perovskite Thin Films under the Microscope: The Impact of Grain Passivation on Morphology and Stability, Master thesis, ETH Zürich, 2020.
- (293) Zurich Instruments Kelvin Probe Force Microscopy (KPFM) (<https://www.zhinst.com/others/en/applications/scanning-probe-microscopy/kelvin-probe-force-microscopy-kpfm>; Abgerufen am 28.02.2021), 2021, DOI: <https://www.zhinst.com/others/en/applications/scanning-probe-microscopy/kelvin-probe-force-microscopy-kpfm>.

- 
- (294) Voigtländer, B., *Scanning Probe Microscopy*; NanoScience and Technology; Springer Berlin Heidelberg: Berlin, Heidelberg, 2015, p 382, DOI: 10.1007/978-3-662-45240-0.
- (295) Eaton, P.; West, P., *Atomic Force Microscopy*; 4; Oxford University Press: 2010; Vol. 39, pp 379–379, DOI: 10.1093/acprof:oso/9780199570454.001.0001.
- (296) Meyer, G.; Amer, N. M. Novel optical approach to atomic force microscopy. *Appl. Phys. Lett.* **1988**, *53*, 1045–1047, DOI: 10.1063/1.100061.
- (297) Butt, H.-J.; Cappella, B.; Kappl, M. Force measurements with the atomic force microscope: Technique, interpretation and applications. *Surf. Sci. Rep.* **2005**, *59*, 1–152, DOI: 10.1016/j.surfrep.2005.08.003.
- (298) Liu, S.; Wang, Y. Application of AFM in microbiology: a review. *Scanning* **2010**, *32*, 61–73, DOI: 10.1002/sca.20173.
- (299) Hansma, P. K.; Cleveland, J. P.; Radmacher, M.; Walters, D. A.; Hillner, P. E.; Bezanilla, M.; Fritz, M.; Vie, D.; Hansma, H. G.; Prater, C. B.; Massie, J.; Fukunaga, L.; Gurley, J.; Elings, V. Tapping mode atomic force microscopy in liquids. *Appl. Phys. Lett.* **1994**, *64*, 1738–1740, DOI: 10.1063/1.111795.
- (300) Colchero, J.; Gil, A.; Baró, A. M. Resolution enhancement and improved data interpretation in electrostatic force microscopy. *Phys. Rev. B* **2001**, *64*, 245403, DOI: 10.1103/PhysRevB.64.245403.
- (301) Zerweck, U.; Loppacher, C.; Otto, T.; Grafström, S.; Eng, L. M. Accuracy and resolution limits of Kelvin probe force microscopy. *Phys. Rev. B* **2005**, *71*, 125424, DOI: 10.1103/PhysRevB.71.125424.
- (302) Loppacher, C.; Zerweck, U.; Teich, S.; Beyreuther, E.; Otto, T.; Grafström, S.; Eng, L. M. FM demodulated Kelvin probe force microscopy for surface photovoltage tracking. *Nanotechnology* **2005**, *16*, S1–S6, DOI: 10.1088/0957-4484/16/3/001.
- (303) Moores, B.; Hane, F.; Eng, L.; Leonenko, Z. Kelvin probe force microscopy in application to biomolecular films: Frequency modulation, amplitude modulation, and lift mode. *Ultramicroscopy* **2010**, *110*, 708–711, DOI: 10.1016/j.ultramicro.2010.02.036.
- (304) Ziegler, D.; Stemmer, A. Force gradient sensitive detection in lift-mode Kelvin probe force microscopy. *Nanotechnology* **2011**, *22*, 075501.
- (305) Li, G.; Mao, B.; Lan, F.; Liu, L. Practical aspects of single-pass scan Kelvin probe force microscopy. *Rev. Sci. Instrum.* **2012**, *83*, DOI: 10.1063/1.4761922.

- (306) Schwenk, J.; Kim, S.; Berwanger, J.; Ghahari, F.; Walkup, D.; Slot, M. R.; Le, S. T.; Cullen, W. G.; Blankenship, S. R.; Vranjkovic, S.; Hug, H. J.; Kuk, Y.; Giessibl, F. J.; Stroscio, J. A. Achieving  $\mu$  eV tunneling resolution in an in-operando scanning tunneling microscopy, atomic force microscopy, and magnetotransport system for quantum materials research. *Rev. Sci. Instrum.* **2020**, *91*, 071101, DOI: 10.1063/5.0005320.
- (307) Herruzo, E. T.; Perrino, A. P.; Garcia, R. Fast nanomechanical spectroscopy of soft matter. *Nat. Commun.* **2014**, *5*, 3126, DOI: 10.1038/ncomms4126.
- (308) Berger, R.; Domanski, A. L.; Weber, S. A. Electrical characterization of organic solar cell materials based on scanning force microscopy. *Eur. Polym. J.* **2013**, *49*, 1907–1915, DOI: 10.1016/j.eurpolymj.2013.03.005.
- (309) Berger, R.; Butt, H. J.; Retschke, M. B.; Weber, S. A. Electrical modes in scanning probe microscopy. *Macromol. Rapid Commun.* **2009**, *30*, 1167–1178, DOI: 10.1002/marc.200900220.
- (310) Giannazzo, F.; Schilirò, E.; Greco, G.; Roccaforte, F. Conductive atomic force microscopy of semiconducting transition metal dichalcogenides and heterostructures. *Nanomaterials* **2020**, *10*, 1–21, DOI: 10.3390/nano10040803.
- (311) Si, H.; Zhang, S.; Ma, S.; Xiong, Z.; Kausar, A.; Liao, Q.; Zhang, Z.; Sattar, A.; Kang, Z.; Zhang, Y. Emerging Conductive Atomic Force Microscopy for Metal Halide Perovskite Materials and Solar Cells. *Adv. Energy Mater.* **2020**, *10*, DOI: 10.1002/aenm.201903922.
- (312) Almora, O.; Zarazua, I.; Mas-Marza, E.; Mora-Sero, I.; Bisquert, J.; Garcia-Belmonte, G. Capacitive Dark Currents, Hysteresis, and Electrode Polarization in Lead Halide Perovskite Solar Cells. *J. Phys. Chem. Lett.* **2015**, *6*, 1645–1652, DOI: 10.1021/acs.jpcllett.5b00480.
- (313) Garcia-Belmonte, G.; Bisquert, J. Distinction between Capacitive and Noncapacitive Hysteretic Currents in Operation and Degradation of Perovskite Solar Cells. *ACS Energy Lett.* **2016**, *1*, 683–688, DOI: 10.1021/acsenergylett.6b00293.
- (314) Cui, A.; Deng, M.; Ye, Y.; Wang, X.; Hu, Z. In *At. Force Microsc. Energy Res.* CRC Press: Boca Raton, 2022, pp 1–43, DOI: 10.1201/9781003174042-1.
- (315) Ko, J.; Song, J.; Yoon, H.; Kim, T.; Lee, C.; Berger, R.; Char, K. Controlled Mutual Diffusion between Fullerene and Conjugated Polymer Nanopillars in Ordered Heterojunction Solar Cells. *Adv. Mater. Interfaces* **2016**, *3*, DOI: 10.1002/admi.201600264.

- 
- (316) Ko, J.; Kim, Y.; Kang, J. S.; Berger, R.; Yoon, H.; Char, K. Enhanced Vertical Charge Transport of Homo- and Blended Semiconducting Polymers by Nanoconfinement. *Adv. Mater.* **2020**, *32*, DOI: 10.1002/adma.201908087.
- (317) Sadewasser, S.; Barth, C. Electrostatic force microscopy and Kelvin probe force microscopy. *Characterization of Materials* **2002**, 1–12.
- (318) Lanza, M., *Conductive atomic force microscopy: applications in nanomaterials*; John Wiley & Sons: 2017.
- (319) Checa, M.; Neumayer, S. M.; Tsai, W.-Y.; Collins, L. In *At. Force Microsc. Energy Res.* CRC Press: Boca Raton, 2022, pp 45–104, DOI: 10.1201/9781003174042-2.
- (320) Barnea-Nehoshtan, L.; Kirmayer, S.; Edri, E.; Hodes, G.; Cahen, D. Surface Photovoltage Spectroscopy Study of Organo-Lead Perovskite Solar Cells. *J. Phys. Chem. Lett.* **2014**, *5*, 2408–2413, DOI: 10.1021/jz501163r.
- (321) Nonnenmacher, M.; O’Boyle, M. P.; Wickramasinghe, H. K. Kelvin probe force microscopy. *Appl. Phys. Lett.* **1991**, *58*, 2921–2923, DOI: 10.1063/1.105227.
- (322) Zisman, W. A. A NEW METHOD OF MEASURING CONTACT POTENTIAL DIFFERENCES IN METALS. *Rev. Sci. Instrum.* **1932**, *3*, 367–370, DOI: 10.1063/1.1748947.
- (323) Kelvin, L. V. Contact electricity of metals. *London, Edinburgh, Dublin Philos. Mag. J. Sci.* **1898**, *46*, 82–120, DOI: 10.1080/14786449808621172.
- (324) Collins, L.; Kilpatrick, J. I.; Weber, S. A. L.; Tselev, A.; Vlassioux, I. V.; Ivanov, I. N.; Jesse, S.; Kalinin, S. V.; Rodriguez, B. J. Open loop Kelvin probe force microscopy with single and multi-frequency excitation. *Nanotechnology* **2013**, *24*, 475702, DOI: 10.1088/0957-4484/24/47/475702.
- (325) Sadewasser, S.; Leendertz, C.; Streicher, F.; Lux-Steiner, M. C. The influence of surface topography on Kelvin probe force microscopy. *Nanotechnology* **2009**, *20*, 505503, DOI: 10.1088/0957-4484/20/50/505503.
- (326) Mélin, T.; Barbet, S.; Diesinger, H.; Théron, D.; Deresmes, D. Note: Quantitative (artifact-free) surface potential measurements using Kelvin force microscopy. *Rev. Sci. Instrum.* **2011**, *82*, DOI: 10.1063/1.3516046.
- (327) Sugawara, Y.; Kou, L.; Ma, Z.; Kamijo, T.; Naitoh, Y.; Jun Li, Y. High potential sensitivity in heterodyne amplitude-modulation Kelvin probe force microscopy. *Appl. Phys. Lett.* **2012**, *100*, 2–5, DOI: 10.1063/1.4723697.

- (328) Glatzel, T.; Sadewasser, S.; Lux-Steiner, M. C. Amplitude or frequency modulation-detection in Kelvin probe force microscopy. *Appl. Surf. Sci.* **2003**, *210*, 84–89, DOI: 10.1016/S0169-4332(02)01484-8.
- (329) Barbet, S.; Popoff, M.; Diesinger, H.; Deresmes, D.; Theron, D.; Melin, T. Cross-talk artefacts in Kelvin probe force microscopy imaging: a comprehensive study. *Journal of Applied Physics* **2014**, *115*.
- (330) Jönsson, M.; Thierry, D.; LeBozec, N. The influence of microstructure on the corrosion behaviour of AZ91D studied by scanning Kelvin probe force microscopy and scanning Kelvin probe. *Corrosion Science* **2006**, *48*, 1193–1208.
- (331) Abdellatif, M.; Salerno, M.; Polovitsyn, A.; Marras, S.; De Angelis, F. Sensing the facet orientation in silver nano-plates using scanning Kelvin probe microscopy in air. *Applied Surface Science* **2017**, *403*, 371–377.
- (332) Rosenwaks, Y.; Shikler, R.; Glatzel, T.; Sadewasser, S. Kelvin probe force microscopy of semiconductor surface defects. *Physical Review B* **2004**, *70*, 085320.
- (333) Lanzoni, E. M.; Gallet, T.; Spindler, C.; Ramirez, O.; Boumenou, C. K.; Siebentritt, S.; Redinger, A. The impact of Kelvin probe force microscopy operation modes and environment on grain boundary band bending in perovskite and Cu (In, Ga) Se<sub>2</sub> solar cells. *Nano Energy* **2021**, *88*, 106270.
- (334) Kronik, L. Surface photovoltage phenomena: theory, experiment, and applications. *Surf. Sci. Rep.* **1999**, *37*, 1–206, DOI: 10.1016/S0167-5729(99)00002-3.
- (335) Gal, D.; Beier, J.; Moons, E.; Hodes, G.; Cahen, D.; Kronik, L.; Burstein, L.; Mishori, B.; Leibovitch, M.; Shapira, Y.; Hariskos, D.; Klenk, R.; Schock, H.-W. In *AIP Conf. Proc.* AIP: 1996; Vol. 353, pp 453–464, DOI: 10.1063/1.49432.
- (336) Gross, D.; Mora-Seró, I.; Dittrich, T.; Belaidi, A.; Mauser, C.; Houtepen, A. J.; Como, E. D.; Rogach, A. L.; Feldmann, J. Charge Separation in Type II Tunneling Multilayered Structures of CdTe and CdSe Nanocrystals Directly Proven by Surface Photovoltage Spectroscopy. *J. Am. Chem. Soc.* **2010**, *132*, 5981–5983, DOI: 10.1021/ja101629c.
- (337) Wang, J. T.-W.; Wang, Z.; Pathak, S.; Zhang, W.; deQuilettes, D. W.; Wisnivesky-Rocca-Rivarola, F.; Huang, J.; Nayak, P. K.; Patel, J. B.; Yusof, H. A. M., et al. Efficient perovskite solar cells by metal ion doping. *Energy & Environmental Science* **2016**, *9*, 2892–2901.

- (338) Alkhalifah, G.; Marshall, A. D.; Rudayni, F.; Wanigasekara, S.; Wu, J. Z.; Chan, W.-L. Defect-Polaron and Enormous Light-Induced Fermi-Level Shift at Halide Perovskite Surface. *The Journal of Physical Chemistry Letters* **2022**, *13*, 6711–6720.
- (339) Johnson, E. Large-signal surface photovoltage studies with germanium. *Physical Review* **1958**, *111*, 153.
- (340) Cavalcoli, D.; Cavallini, A. Surface photovoltage spectroscopy - method and applications. *Phys. status solidi c* **2010**, *7*, 1293–1300, DOI: 10.1002/pssc.200983124.
- (341) Petrović, M.; Chellappan, V.; Ye, T.; Ramakrishna, S. Charge carrier decay and diffusion in organic-inorganic CH<sub>3</sub>NH<sub>3</sub>PbI<sub>3-x</sub>Cl<sub>x</sub> perovskite based solar cell. *Phys. status solidi - Rapid Res. Lett.* **2015**, *9*, 682–686, DOI: 10.1002/pssr.201510389.
- (342) Carnie, M. J.; Troughton, J.; Regan, B. O.; Barnes, P.; Bryant, D.; Watson, T.; Worsley, D. In *2015 IEEE 42nd Photovolt. Spec. Conf.* IEEE: 2015, pp 1–3, DOI: 10.1109/PVSC.2015.7355675.
- (343) Wood, S.; O'Connor, D.; Jones, C. W.; Claverley, J. D.; Blakesley, J. C.; Giusca, C.; Castro, F. A. Transient photocurrent and photovoltage mapping for characterisation of defects in organic photovoltaics. *Solar Energy Materials and Solar Cells* **2017**, *161*, 89–95.
- (344) Strelcov, E.; Jesse, S.; Huang, Y.-L.; Teng, Y.-C.; Kravchenko, I. I.; Chu, Y.-H.; Kalinin, S. V. Space-and time-resolved mapping of ionic dynamic and electroresistive phenomena in lateral devices. *ACS nano* **2013**, *7*, 6806–6815.
- (345) Yalcinkaya, Y.; Hermes, I. M.; Seewald, T.; Amann-Winkel, K.; Veith, L.; Schmidt-Mende, L.; Weber, S. A. Chemical Strain Engineering of MAPbI<sub>3</sub> Perovskite Films. *Adv. Energy Mater.* **2022**, *12*, 2202442, DOI: 10.1002/aenm.202202442.
- (346) Zhou, Q.; Wang, B.; Meng, R.; Zhou, J.; Xie, S.; Zhang, X.; Wang, J.; Yue, S.; Qin, B.; Zhou, H.; Zhang, Y. Understanding Temperature-Dependent Charge Extraction and Trapping in Perovskite Solar Cells. *Adv. Funct. Mater.* **2020**, *30*, 2000550, DOI: 10.1002/adfm.202000550.
- (347) Grill, I.; Aygüler, M. F.; Bein, T.; Docampo, P.; Hartmann, N. F.; Handloser, M.; Hartschuh, A. Charge Transport Limitations in Perovskite Solar Cells: The Effect of Charge Extraction Layers. *ACS Appl. Mater. Interfaces* **2017**, *9*, 37655–37661, DOI: 10.1021/acsami.7b09567.

- (348) Pietralunga, S. M.; Irde, G.; Barker, A. J.; Ball, J. M.; Petrozza, A.; Sala, V.; Zani, M.; Lanzani, G.; Tagliaferri, A. Dynamical Imaging of Surface Photopotentials in Hybrid Lead Iodide Perovskite Films under High Optical Irradiance and the Role of Selective Contacts. *Adv. Mater. Interfaces* **2020**, *7*, 2000297, DOI: 10.1002/admi.202000297.
- (349) Kelley, K. P.; Ziatdinov, M.; Collins, L.; Susner, M. A.; Vasudevan, R. K.; Balke, N.; Kalinin, S. V.; Jesse, S. Fast Scanning Probe Microscopy via Machine Learning: Non-Rectangular Scans with Compressed Sensing and Gaussian Process Optimization. *Small* **2020**, *16*, 2002878, DOI: 10.1002/sm11.202002878.
- (350) Checa, M.; Fuhr, A. S.; Sun, C.; Vasudevan, R.; Ziatdinov, M.; Ivanov, I.; Yun, S. J.; Xiao, K.; Sehirliglu, A.; Kim, Y.; Sharma, P.; Kelley, K. P.; Domingo, N.; Jesse, S.; Collins, L. High-speed mapping of surface charge dynamics using sparse scanning Kelvin probe force microscopy. *Nat. Commun.* **2023**, *14*, 7196, DOI: 10.1038/s41467-023-42583-x.
- (351) Murawski, J.; Graupner, T.; Milde, P.; Raupach, R.; Zerweck-Trogisch, U.; Eng, L. M. Pump-probe Kelvin-probe force microscopy: Principle of operation and resolution limits. *J. Appl. Phys.* **2015**, *118*, 8, DOI: 10.1063/1.4933289.
- (352) Grévin, B.; Bardagot, O.; Demadrille, R. Implementation of data-cube pump-probe KPFM on organic solar cells. *Beilstein J. Nanotechnol.* **2020**, *11*, 323–337, DOI: 10.3762/bjnano.11.24.
- (353) Aubriet, V.; Courouble, K.; Bardagot, O.; Demadrille, R.; Borowik, Ł.; Grévin, B. Hidden surface photovoltages revealed by pump probe KPFM. *Nanotechnology* **2022**, *33*, 225401, DOI: 10.1088/1361-6528/ac5542.
- (354) Collins, L.; Ahmadi, M.; Wu, T.; Hu, B.; Kalinin, S. V.; Jesse, S. Breaking the Time Barrier in Kelvin Probe Force Microscopy: Fast Free Force Reconstruction Using the G-Mode Platform. *ACS Nano* **2017**, *11*, 8717–8729, DOI: 10.1021/acsnano.7b02114.
- (355) Fumagalli, L.; Ferrari, G.; Sampietro, M.; Gomila, G. Dielectric-constant measurement of thin insulating films at low frequency by nanoscale capacitance microscopy. *Appl. Phys. Lett.* **2007**, *91*, 243110, DOI: 10.1063/1.2821119.
- (356) Palmer, R.; RC, P.; EJ, D., et al. In *CAPACITIVE-PICKUP CIRCUITY FOR VIDEODISCS*, 1982.
- (357) McCoy, D. The RCA " SelectaVision " VideoDisc System. *RCA Corporation* **1978**, *39*, 7.

- 
- (358) Tran, T.; Oliver, D. R.; Thomson, D. J.; Bridges, G. E. “Zeptofarad” (10-21 F) resolution capacitance sensor for scanning capacitance microscopy. *Rev. Sci. Instrum.* **2001**, *72*, 2618–2623, DOI: 10.1063/1.1369637.
- (359) Borgani, R.; Forchheimer, D.; Bergqvist, J.; Thorén, P.-A.; Inganäs, O.; Haviland, D. B. Intermodulation electrostatic force microscopy for imaging surface photo-voltage. *Appl. Phys. Lett.* **2014**, *105*, 143113, DOI: 10.1063/1.4897966.
- (360) Garrett, J. L.; Leite, M. S.; Munday, J. N. Multiscale Functional Imaging of Interfaces through Atomic Force Microscopy Using Harmonic Mixing. *ACS Appl. Mater. Interfaces* **2018**, *10*, 28850–28859, DOI: 10.1021/acsami.8b08097.
- (361) Labardi, M.; Prevosto, D.; Nguyen, K. H.; Capaccioli, S.; Lucchesi, M.; Rolla, P. Local dielectric spectroscopy of nanocomposite materials interfaces. *J. Vac. Sci. Technol. B, Nanotechnol. Microelectron. Mater. Process. Meas. Phenom.* **2010**, *28*, C4D11–C4D17, DOI: 10.1116/1.3368597.
- (362) Schwartz, G.; Riedel, C.; Arinero, R.; Tordjeman, P.; Alegría, A.; Colmenero, J. Broad-band nanodielectric spectroscopy by means of amplitude modulation electrostatic force microscopy (AM-EFM). *Ultramicroscopy* **2011**, *111*, 1366–1369, DOI: 10.1016/j.ultramicro.2011.05.001.
- (363) Miccio, L. A.; Kummali, M. M.; Schwartz, G. A.; Alegría, Á.; Colmenero, J. Dielectric spectroscopy at the nanoscale by atomic force microscopy: A simple model linking materials properties and experimental response. *J. Appl. Phys.* **2014**, *115*, 184305, DOI: 10.1063/1.4875836.
- (364) Miccio, L. A.; Schwartz, G. A. In *AIP Conf. Proc.* AIP Publishing LLC: 2014; Vol. 1599, pp 150–153, DOI: 10.1063/1.4876800.
- (365) Millan-Solsona, R.; Checa, M.; Fumagalli, L.; Gomila, G. Mapping the capacitance of self-assembled monolayers at metal/electrolyte interfaces at the nanoscale by in-liquid scanning dielectric microscopy. *Nanoscale* **2020**, *12*, 20658–20668, DOI: 10.1039/D0NR05723A.
- (366) Hudlet, S.; Saint Jean, M.; Guthmann, C.; Berger, J. Evaluation of the capacitive force between an atomic force microscopy tip and a metallic surface. *Eur. Phys. J. B* **1998**, *2*, 5–10, DOI: 10.1007/s100510050219.

- (367) Sanchez, R. S.; Gonzalez-Pedro, V.; Lee, J.-W.; Park, N.-G.; Kang, Y. S.; Mora-Sero, I.; Bisquert, J. Slow Dynamic Processes in Lead Halide Perovskite Solar Cells. Characteristic Times and Hysteresis. *J. Phys. Chem. Lett.* **2014**, *5*, 2357–2363, DOI: 10.1021/jz5011187.
- (368) Juarez-Perez, E. J.; Sanchez, R. S.; Badia, L.; Garcia-Belmonte, G.; Kang, Y. S.; Mora-Sero, I.; Bisquert, J. Photoinduced Giant Dielectric Constant in Lead Halide Perovskite Solar Cells. *J. Phys. Chem. Lett.* **2014**, *5*, 2390–2394, DOI: 10.1021/jz5011169.
- (369) Reichel, P. Tip-sample capacitance in electrostatic force microscopy, Bachelor thesis, University of Mainz, 2021.
- (370) Sader, J. E.; Chon, J. W. M.; Mulvaney, P. Calibration of rectangular atomic force microscope cantilevers. *Rev. Sci. Instrum.* **1999**, *70*, 3967–3969, DOI: 10.1063/1.1150021.
- (371) Labuda, A.; Kocun, M.; Lysy, M.; Walsh, T.; Meinhold, J.; Proksch, T.; Meinhold, W.; Anderson, C.; Proksch, R. Calibration of higher eigenmodes of cantilevers. *Rev. Sci. Instrum.* **2016**, *87*, 073705, DOI: 10.1063/1.4955122.

---

# 8 List of Figures

1.1	Electricity production from fossil fuels, nuclear and renewables on the entire world measured in TWh from 1985 to 2023. <sup>109</sup> . . . . .	1
1.2	(a) CO <sub>2</sub> emissions by fuel or industry type on the entire world measured in billion t from 1750 to 2023 <sup>115</sup> and (b) the global atmospheric CO <sub>2</sub> concentration from January 15, 1979 to October 15, 2024 measured in parts per million (ppm). <sup>116</sup> . . . . .	2
1.3	Summary of all global warming projections (nominal scenarios) reported by ExxonMobil scientists in internal documents and peer-reviewed publications (gray lines), superimposed on historically observed temperature change (red). <sup>123</sup> . . . . .	2
2.1	Orbital Energies of (a) an atom, (b) a small molecule, (c) a large molecule, (d) a solid, and (e) the density of states corresponding to (d). . . . .	7
2.2	Density of states (DOS) in (a) non-metallic solid with the band gap $E_g$ , and (b) metal. The respective FERMI level is marked with $EF$ . Shading represents occupied levels. . . . .	8
2.3	Simple point defects. (a) Lattice vacancy. (b) Interstitial atom. (c) SCHOTTKY defect, consisting of cation and anion vacancy. (d) FRENKEL defect, with vacancy balanced by interstitial. . . . .	13
2.4	Electronic consequences of defects in semiconductors are illustrated with the respected valence band (VB) and the conduction band (CB). FERMI-DIRAC distribution in a (a) pure crystalline solid; (b) p-type; and (c) n-type semiconductor with extra holes or electrons in valence or conduction band. (d) and (e): Defect levels providing free electrons or holes by thermal excitation. (f) and (g): Defect levels acting as traps for electrons or holes. (h): Levels giving optical absorption at energies below the band gap. (i) the corresponding band gap $E_g$ of the semiconductor. Shading represents occupied levels. . . . .	14
2.5	Illustration of recombination mechanisms in semiconductors. (a) Radiative, (b) non-radiative, and (c) AUGER. <sup>151</sup> . . . . .	17

2.6	Energy band alignment illustration for two semiconductor heterojunction. (a) Band bending shown at the interface between two semiconductors and (b) the band bending at the surface of a n-type semiconductor. <sup>98</sup> . . . . .	22
2.7	Schematic illustration of energy diagram of a semiconductor layer with CB for electrons $E_c$ and VB for holes $E_v$ and two contacts: an electron selective contact (ETL) with work function $\Phi_{\text{ETL}}$ and hole selective contact (HTL) with work function $\Phi_{\text{HTL}}$ . The contacts are considered as metals in which the carrier energy level is at the respective FERMI level. Contacting, forward bias voltage or light illumination modifies the FERMI level of the ETL with respect to $E_c$ , while holes remain at equilibrium at the left contact (HTL). (a) Energies of the separate materials. (b,c) Different situations of bias voltage $V$ indicating the FERMI levels of electrons ( $E_{F_e}$ ) and holes ( $E_{F_h}$ ). In (d), the semiconductor is illuminated and minority carrier generation raises the FERMI level of electrons consequently producing a photovoltage (SPV). <sup>27</sup> . . . . .	24
2.8	Crystal structure of metal halide perovskites of the molecular formula $\text{ABX}_3$ in the cubic phase ( $T > 330\text{ K}$ ). A MA molecule occupies the A site in the crystal surrounded by 12 direct iodine neighbor atoms and corner-linked octahedra. The octahedra are built up by the iodine atoms (purple) sitting on the A-position. The lead atoms (black) form the centers of the octahedra on the B-position. <sup>105,180–182</sup> . . . . .	27
2.9	Band diagram of a typical perovskite solar cell. Light passes through the ITO layer and the ETL and is absorbed by the perovskite layer (red), where an electron is promoted from the VB into the CB as indicated by the arrow in between the valence and CB. Excited electrons can migrate into the CB of the electron transport layer. Since the hole transport layer has no corresponding energy level, that layer act as an electron blocking layer. The photon-generated electrons migrate from the ETL into the bottom electrode, the ITO. The remaining hole in the VB of the perovskite layer is filled with electrons from the VB of the hole transport layer. This process corresponds to migration of holes from the perovskite layer into the hole transport layer (violet). Since the ETL has no corresponding energy level, that layer acts as a hole blocking layer. The holes migrate from the HTL into the gold electrode. <sup>205</sup> . . . . .	29
2.10	Typical architecture for a PSC. . . . .	30
2.11	Fundamental setup of an contact mode AFM during operation. <sup>132,292–295</sup> . . . . .	34
2.12	Fundamental setup of an dynamic / AC mode AFM during operation. <sup>132,292–295</sup> . . . . .	36

---

2.13	Fundamental setup of an c-AFM during operation. <sup>132,292-295</sup> . . . . .	37
2.14	The following illustration provides a visual representation of the band gap diagrams, illustrating the principle behind the KELVIN method, which is utilized in KPFM. The potential energy diagram for the probe and the sample, with work functions $\Phi_{\text{tip}}$ and $\Phi_{\text{sample}}$ , initially not connected and thus sharing a common vacuum level $E_{\text{vac}}$ , is depicted in (a). (b) If the two materials are connected by a conducting wire, the FERMI levels $E_{F,1}$ and $E_{F,2}$ of the two materials align. A buildup of surface charge leads to a macroscopic potential gradient, which compensates the difference between the work functions ( $\Delta\Phi$ ) of the two materials. (c) The surface charges and the corresponding electric field $E$ vanish if a voltage $V_{\text{DC}} = V_{\text{CPD}} = (\Phi_{\text{sample}} - \Phi_{\text{tip}})/e = \Delta\Phi/e$ is applied between the materials. <sup>27,28,151,294,319</sup> . . . . .	38
2.15	Fundamental setup of an EFM during operation. <sup>132,292-295</sup> . . . . .	39
2.16	Fundamental setup of an KPFM during operation. <sup>105,132,294</sup> . . . . .	41
2.17	The upward and downward band bending effecting the VB, the CB, the vacuum level $E_{\text{vac}}$ , and the CPD signal at a defect position like a GB. <sup>98,151</sup> . . . . .	46
2.18	Fundamental setup of an tr-KPFM during operation. <sup>98</sup> . . . . .	48
2.19	Schematic illustration of tip apex, tip cone, lever, and stray capacitances. The contribution of the tip apex contains the most localized part of the overall capacitance signal. The mesoscopic tip cone and the macroscopic cantilever, in contrast, contribute to the long- range stray capacitance, effectively delocalizing the signal. <sup>99</sup> . . . . .	51
2.20	The fundamental setup of a MFH-EFM during operation is demonstrated in the presence of a schematic intermodulation signal consisting of two sinusoidal frequencies, specifically 2 Hz and 2.5 Hz. <sup>99</sup> . . . . .	53
2.21	Comparison of the $C''$ and the $C'$ single force curves of a microcapacitor while doing MFH-EFM (see Equations (2.32b) and (2.33)) and compared with the detection of $2\omega$ (see Equation (2.23)). <sup>99</sup> . . . . .	55
2.22	Schematic illustration of the excitation and detection frequencies in MFH-EFM. The lower part shows the transfer function of the cantilever, where the amplitude is plotted vs the logarithmic angular frequency. The upper part shows the excitation frequencies ( $\downarrow$ ) and the detection frequencies ( $\uparrow$ ) of the applied frequencies. The red arrow corresponds to topography- and the blue arrow to the electrical signal. <sup>99,134,135,369</sup> A comparison of H-KPFM and MFH-EFM can be found in the work of ROHRBECK ET AL. <sup>99</sup> . . . . .	56



---

## 9 Nutzung KI-Tools

In Table 9.1 the usage of "AI Tools" that I used during the preparation of this PhD thesis is documented.

**Table 9.1:** Anhang Nutzung KI-Tools:

KI-Tool	Genutzt für	Warum	Wann
DeepL Write	Neuformulierung meiner Textentwürfe	bessere Lesbarkeit und Verständnis	über die gesamte Arbeit hinweg
DeepL Translate	Erstellung der Kurzzusammenfassung	Hilfe für die erste Version	Kurzzusammenfassung
Perplexity Pro Reasoning with o3-model	Erstellung der ersten Version der Zusammenfassung und beim Umfang der Arbeit	schnelle Erstellung einer ersten Textentwurfs	Scope, Zusammenfassung



---

## 10 Curriculum Vitae

I hereby confirm that the following document is the most recent iteration of the Curriculum Vitae of PASCAL NIKO ROHRBECK, dated Wednesday, May 14, 2025.



## Pascal Niko Rohrbeck

PhD student in chemistry,  
Max Planck Institute for Polymer Research, Mainz

10.10.1995



[Redacted email address]



[Redacted phone number]



rohrbeckp@mpip-mainz.mpg.de



German

## Social Network

LinkedIn  
 ORCID  
 Google Scholar  
 X (Twitter)

## Languages

German ●●●●●  
*Mother Tongue, C2*

English ●●●●●  
*Proficient User, C1*

Swedish ●●●●●  
*Basic User, A2*

French ●●●●●  
*Basic User, A1*

## Hard Skills

Atomic Force Microscope (AFM)  
 Kelvin Probe Force Microscope (KPFM)  
 Data Analysis  
 Physical Vapor Deposition (PVD)  
 Nanoscale Device Fabrication  
 Plasma etching  
 Capacitance Measurements  
 Python &  $\LaTeX$

## Work Experience

- June 2021–Now **PhD Student** Max Planck Institute for Polymer Research, Mainz  
 ○ Investigating perovskite solar cells with electric modes of scanning probe microscopy system  
 ○ Preparation of perovskite solar half-cells  
 ○ Writing and using Python code to analyze data  
 ○ Working in an international working group  
 ○ Helping organize events and activities for other PhD students
- September 2023 – November 2023 **Research stay in the USA as a guest student** Oak Ridge, TN, USA  
 Spending two months abroad learning and usage of ultra fast scanning probe force microscopy methods to investigate dynamics at perovskite solar cell materials. The research was conducted at the Center for Nanophase Materials Sciences (CNMS) on the campus of the Oak Ridge National Laboratory (ORNL) in Tennessee, USA.
- June – August and January – April 2021 **Tutor of the physical chemistry IV exercise** Johannes Gutenberg University, Mainz  
 Lecture held by Prof. Dr. Stefan Weber, Prof. Dr. Michael Kappl, respectively
- November 2019 – June 2021 **Assisting scientist** Max Planck Institute for Polymer Research, Mainz  
 I studied new techniques to measure capacitance differences with Kelvin Probe Force Microscopy (KPFM)- and Scanning Capacitance Microscopy (SCM) Technique.
- August – October 2019 **Research internship** Max Planck Institute for Polymer Research, Mainz  
 In this internship I studied ferroelastic domains in Methylammonium lead iodide perovskite surfaces with Piezo Force Microscopy (PFM).

## Education

- March 2019–June 2021 **Master of Science Chemistry** Johannes Gutenberg University, Mainz  
 ∅ Grade: 1.3
- Master thesis, ∅ 1.0** Max Planck Institute for Polymer Research, Mainz  
 Investigation of local charging dynamics of perovskite grain boundaries with time-resolved Kelvin Probe Force Microscopy (KPFM) methods, Supervisor: Prof. Dr. Stefan Weber, 2. Supervisor: Prof. Dr. Wolfgang Tremel
- October 2014–March 2019 **Bachelor of Science Chemistry** Johannes Gutenberg University, Mainz  
 ∅ Grade: 2.2
- Bachelor thesis, ∅ 1.5** Johannes Gutenberg University, Mainz  
 Linkage of Water-soluble chlorophyll protein (WSCP)-Modifications at spherical gold nanoparticles, Supervisor: Prof. Dr. Thomas Basché, 2. Supervisor: Prof. Dr. Wolfgang Tremel
- 2014 **High school diploma** Gutenbergschule, Wiesbaden  
 ∅ Grade: 1.9
- 2006–2014 **High School** Gutenbergschule, Wiesbaden  
 Major: chemistry and mathematics

## Certificates

- March 2024 **Certified Project manager business chemistry GDCh** Münster, Germany  
 Corporate strategies, competitive analysis and innovation management in the chemical industry, Course-ID: 414/24

# Pascal Niko Rohrbeck

PhD student in chemistry,  
Max Planck Institute for Polymer Research, Mainz

## Soft Skills

- Project management
- Team work
- Leadership
- Networking
- Communication
- Organization and lead of Projects
- Adaptability to new techniques
- Presentation
- Scientific writing

## References

Jun. Prof. Dr. Stefan A.L. Weber  
Max Planck Institute for Polymer Research,  
Mainz  
Institute for Photovoltaic, Stuttgart



Stefan.Weber@mpip-mainz.mpg.de  
Stefan.Weber@ipv.uni-stuttgart.de  
+49 711 685 69209

Prof. Dr. Hans-Jürgen Butt  
Max Planck Institute for Polymer Research



butt@mpip-mainz.mpg.de  
+49 6131 379 111

Dr. Liam Collins  
Center For Nanophase Materials Sciences  
Oak Ridge National Laboratory, TN, USA



collinslf@ornl.gov  
+1 865-347-8435

Dr. Martí Nualart Checa  
Center For Nanophase Materials Sciences  
Oak Ridge National Laboratory, TN, USA



checam@ornl.gov  
+1 865-348 8373

## Publications

- 2025 **Rohrbeck, P. N.; Cavar, L. D.; Weber, F.; Reichel, P. G.; Niebling, M.; Weber, S. A. L. Nanoscale capacitance spectroscopy based on multifrequency electrostatic force microscopy.** *Beilstein J. Nanotechnol.*, **2025**, *16*, 637–651. DOI: 10.3762/bjnano.16.49.
- 2025 **Pious, J. K.; Rohrbeck, P. N.; Widmer, R.; Oechsle, A. H.; Shivarudraiah, S. B.; Kothandaraman, R. K.; Siegrist, S.; Shih, C.; Jung, T. A.; Weber, S. A. L.; Tiwari, A. N.; Fu, F. Efficient Blade-Coated Wide-Bandgap Perovskite Solar Cells via Interface Engineering.** *ACS Appl. Mater. Interfaces*, **2025**, *17* (16), 24040–24047. DOI: 10.1021/acsami.5c03709.
- 2024 **Liang, J.; Ender, C. P.; Rohrbeck, P. N.; Graf, R.; Lieberwirth, I.; Räder, H.-J.; Wagner, M.; Weber, S. A. L.; Müllen, K.; Weil, T. High Pressure Induced Formation of Carbon Nanorods from Tetracosane.** *Diam. Relat. Mater.*, **2024**, *143*, 110913. DOI: 10.1016/j.diamond.2024.110913.
- 2023 **Yalcinkaya, Y.\*; Rohrbeck, P. N.\*; Schütz, E. R.; Fakhruddin, A.; Schmidt-Mende, L.; Weber, S. A. L., Nanoscale Surface Photovoltage Spectroscopy.** *Adv. Opt. Mater.*, **2023**, 2301318. DOI: 10.1002/adom.202301318.
- 2021 **Gharibzadeh, S.; Fassl, P.; Hossain, I. M.; Rohrbeck, P. N.; Frericks, M.; Schmidt, M.; Duong, T.; Khan, M. R.; Abzieher, T.; Nejang, B. A.; Schackmar, F.; Almora, O.; Feeney, T.; Singh, R.; Fuchs, D.; Lemmer, U.; Hofmann, J. P.; Weber, S. A. L.; Paetzold, U. W., Two birds with one stone: dual grain-boundary and interface passivation enables > 22% efficient inverted methylammonium-free perovskite solar cells.** *Energy Environ. Sci.*, **2021**, *14* (11), 5875–5893. DOI: 10.1039/D1EE01508G.

## Scholarships and Awards

- Mai 2023 Partial scholarship of the German Chemical Society (GDCh e.V.) for the time as a guest student in the USA in fall 2023, Partial scholarship No. 468
- March 2024 **Joint Poster Award of the 26th annual Spring Symposium of the JCF** Ulm, Germany  
Young Chemists Network (JungChemikerForum, JCF) of the German Chemical Society (GDCh e.V.) and the Società Chimica Italiana Gruppo Giovani certify that Pascal Rohrbeck has been selected for the Poster Award.

## Hobbies and Interests

- Association **Student member in the German Chemical Society (GDCh)**  
Member since February 2019
- Association **Active member in the Young Chemists Network (JCF) in the regional forum Mainz / Wiesbaden of the GDCh**  
Member since February 2019
- Honorary office **Speaker of the Young Chemists Network (JCF) in the regional forum Mainz / Wiesbaden of the GDCh**  
Speaker February 2022 - February 2024
- Association **Student member in the Association of Employed Academics and Executives in the Chemical Industry (VAA e.V.)**  
Member since February 2019
- Association **Member of the sport club TG Eltville**  
Active member from June 2019 - December 2024
- Hobbies Volleyball, Musicals and Operas, Board games

(Pascal Rohrbeck)  
Mainz, May 14, 2025

## Scientific Symposiums and Conferences

- 2021 **Time-resolution in dynamic Kelvin Probe Force Microscopy**  
*Max Planck Institute for Polymer Research Group Retreat*  
 Berlin, Germany
- 2022 **Effects of passivation on perovskite solar cells**  
*Poster Session at the spring symposium (FJS) of the Young Chemists Network (JCF)*  
 Hanover, Germany
- 2022 **Nanoscale capacitance and dielectric permittivity measurements**  
*Poster session on the German Physicist Society (DPG) Conference of the Session of condense matter*  
 Regensburg, Germany
- 2022 **Investigation of Grains and Grain Boundaries on Free Charges in Lead Halide Perovskite Films**  
*Poster session in the Max Planck Institute for Polymer Research*  
 Mainz, Germany
- 2022 **Advanced Kelvin Probe Force Microscopy Methods to Study Mixed Halide Perovskites**  
*Poster session at the conference of the Materials Research Society (MRS)*  
 Boston, USA
- 2022 **Time-resolved Kelvin Probe Force Microscopy to Investigate Grains of Mixed Halide Perovskite Solar Cell Materials**  
*Poster session at the conference of the Materials Research Society (MRS)*  
 Boston, USA
- 2023 **Investigation of defects inside of mixed halide perovskite solar cells**  
*Pitch talk at the spring symposium (FJS) of the Young Chemists Network (JCF)*  
 Gießen, Germany
- 2023 **Investigation of defects in mixed halide perovskite solar cells**  
*Presentation on the German Physicist Society (DPG) Conference of the Session of condense matter*  
 Dresden, Germany
- 2023 **Local Charge Carrier Dynamics in Lead Halide Perovskites by Nano Surface Photovoltage Spectroscopy**  
*Max Planck Institute for Polymer Research Group Retreat*  
 Hirschegg, Austria
- 2023 **Nanoscale Surface Photovoltage Spectroscopy**  
*Poster Session at the OPERANDO SPM Conference*  
 Berlin, Germany
- 2024 **Nanoscale Surface Photovoltage Spectroscopy (Nano-SPV) to study defect densities on halide perovskite solar cells**  
*Poster Session at the spring symposium (FJS) of the Young Chemists Network (JCF)*  
 Ulm, Germany
- 2024 **Advanced Atomic Force Microscopy Methods on Energy Materials**  
*Invited Lecture Talk at the Summer School themed "Bulk and Surface Microscopy Techniques for Soft Matter"*  
 FORTH, Heraklion, Greece